JUSTUS-LIEBIG-
UNIVERSITÄT
GIESSEN

Silver-bismuth double perovskite semiconductors: variations on a theme

Dissertation

Zur Erlangung des akademischen Doktorgrades

„Doctor rerum naturalium“

- Dr. rer. nat. –

eingereicht am Fachbereich 08

Biologie und Chemie

Der Justus-Liebig-Universität Gießen

von

Fabian Schmitz

Februar 2024

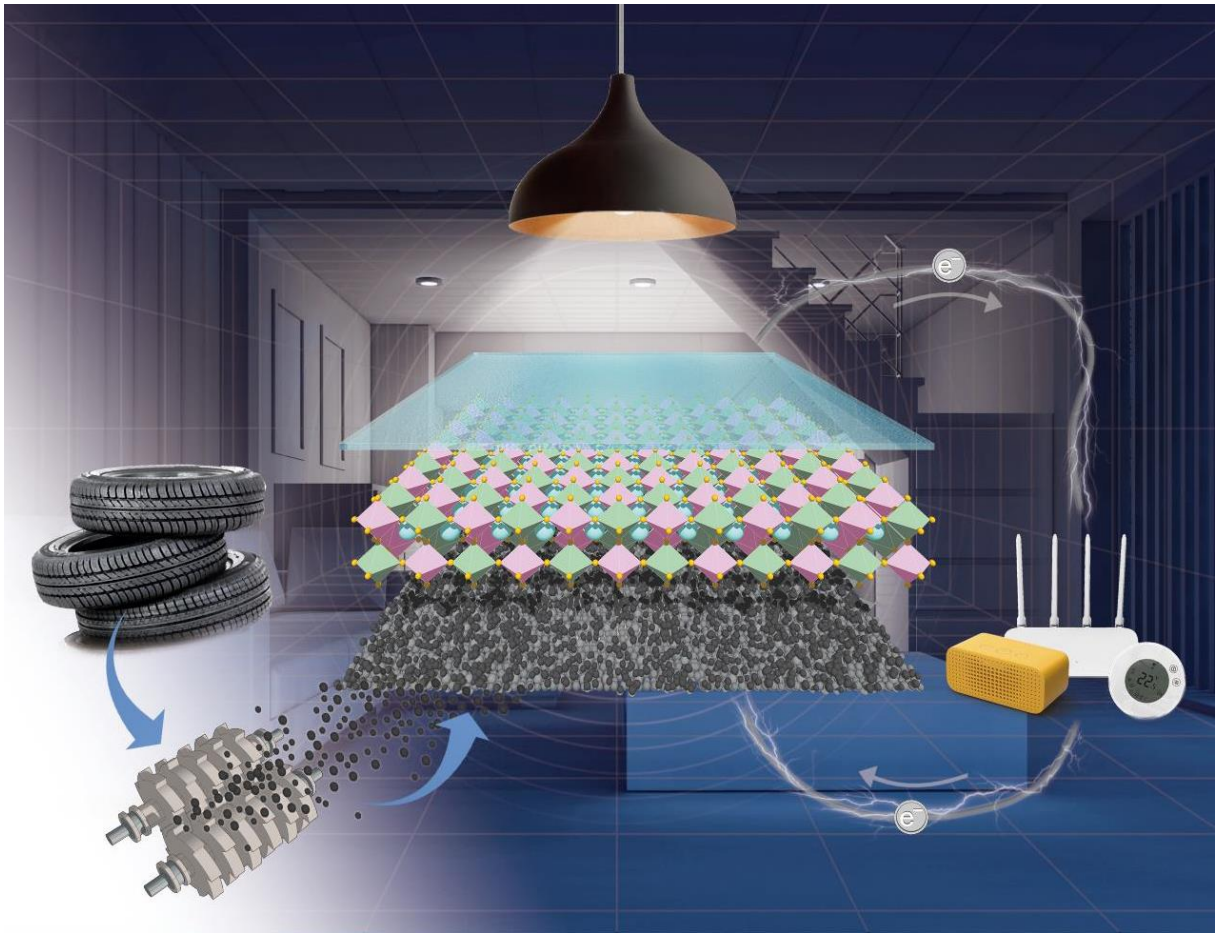

Front cover: High Open-Circuit Voltage $Cs_2AgBiBr_6$ Carbon-Based Perovskite Solar Cells via Green Processing of Ultrasonic Spray-Coated Carbon Electrodes from Waste Tire Sources ***(Publication 5)*** *(ChemSusChem 22/2022)*

Selbstständigkeitserklärung

Ich erkläre: Ich habe die vorgelegte Dissertation selbstständig und ohne unerlaubte fremde Hilfe und nur mit den Hilfen angefertigt, die ich in der Dissertation angegeben habe. Alle Textstellen, die wörtlich oder sinngemäß aus veröffentlichten Schriften entnommen sind, und alle Angaben, die auf mündlichen Auskünften beruhen, sind als solche kenntlich gemacht. Ich stimme einer evtl. Überprüfung meiner Dissertation durch eine Antiplagiat-Software zu. Bei den von mir durchgeführten und in der Dissertation erwähnten Untersuchungen habe ich die Grundsätze guter wissenschaftlicher Praxis, wie sie in der „Satzung der Justus-Liebig-Universität Gießen zur Sicherung guter wissenschaftlicher Praxis“ niedergelegt sind, eingehalten.

_____ _____

Die vorliegende Arbeit und die zugrunde liegenden Experimente wurden in der Zeit von September 2019 – Februar 2024 am Physikalisch-Chemischen Institut der Justus-Liebig-Universität Gießen in der Arbeitsgruppe von Prof. Dr. Teresa Gatti angefertigt.

Erstgutachterin: Prof. Dr. T. Gatti

Zweitgutachter: Prof. Dr. D. Schlettwein

Abstract

Lead-halide perovskites (LHPs) have experienced tremendous development within 15 years from their first report as light harvesters in solar cells until today, in which their power conversion efficiency has been gradually improved from 3.8% to 26.1%. These high efficiencies in combination with their easy and low-cost processability as thin films make them a potential alternative to conventional silicon-based solar cells. However, compared to the latter they possess a low environmental stability and pose an environmental and human health hazard due to their lead content. While the stability has been gradually improved by extensive chemical engineering and encapsulating techniques, the toxicity aspect can only be tackled by substituting lead. $Cs_2AgBiBr_6$ is such a material – which this dissertation revolves around - in which lead is substituted by equal amounts of silver and bismuth, thus named double perovskite, which is characterized by high environmental stability and low toxicity.

This dissertation can be divided into two main topics: The tuning of absorption and emissive processes in Ag-Bi double perovskites *via* structural engineering and the investigation and improvement of hole transport material (HTM)-free $Cs_2AgBiBr_6$ solar cells.

The first topic covers two different approaches to influence the emission of Ag-Bi double perovskites. On the one hand, $Cs_2AgBiBr_6$ was doped with the lanthanides Eu^{3+} and Yb^{3+}, resulting in two new emission features: A weak emission from dopant-introduced trap states (Eu^{3+}) and strong emission due to an efficient energy transfer towards the dopant (Yb^{3+}), respectively. On the other hand, $Cs_2AgBiBr_6$ has been dimensionally reduced to create monolayered 2D perovskites which enlarges the material's bandgap and introduces new characteristic emission.

Regarding the second topic, HTM-free $Cs_2AgBiBr_6$ solar cells have been prepared using ultrasonic spray-coating to deposit electrodes that consist of carbon black, won from upcycled industry waste. Thus, this approach represents an end-of-waste strategy to fabricate "green" solar cells. To further improve these devices, the surface of the $Cs_2AgBiBr_6$ thin films has been modified to create 2D/3D mixed phases. The 2D/3D modification improves the perovskite's band alignment towards the back electrode and theoretical calculations further suggest that it reduces the defect concentration close to the perovskite/electrode interface. Accordingly, the application of the 2D/3D modification represents a valuable alternative to HTMs for $Cs_2AgBiBr_6$ solar cells that utilize carbon-based electrodes.

Zusammenfassung

Seit ihrer ersten Erwähnung vor 15 Jahren bis heute haben Bleiperowskite, die als Photoabsorber in Solarzellen eingesetzt werden, eine enorme Entwicklung durchgemacht, die in einer Wirkungsgradsteigerung von 3.8% auf 26.1% resultiert hat. Da sie zusätzlich relativ einfach und günstig herstellbar sind, stellen Perowskitsolarzellen eine potentielle Alternative zu konventionellen Siliziumsolarzellen dar. Im Vergleich zu diesen besitzen Perowskitsolarzellen allerdings eine geringe Stabilität und stellen aufgrund ihres Bleigehalts ein Gesundheits- sowie Umweltrisiko dar. Während die Stabilität dank umfangreicher Forschung über die chemische Zusammensetzung der Perowskite und Verkapselungstechniken erhöht werden konnte, kann die Toxizität dieser Materialien letztendlich nur durch die Substitution von Blei gelöst werden. $Cs_2AgBiBr_6$ ist ein solches Material, das die zentrale Thematik der vorliegenden Dissertation darstellt und in dem Blei durch gleiche Anteile Wismut und Silber substituiert ist - daher die Bezeichnung Doppelperowskit - und welches sich durch eine hohe Stabilität und geringe Toxizität auszeichnet.

Die vorliegende Dissertation kann in zwei Schwerpunkte aufgeteilt werden: Die Anpassung der Absorption und Emission von Ag-Bi Doppelperowskiten mittels struktureller Beeinflussung des Materials, sowie die Untersuchung lochleiterfreier $Cs_2AgBiBr_6$-basierter Solarzellen.

Der erste Schwerpunkt behandelt zwei unterschiedliche Vorgehensweisen, um die Emission von Ag-Bi Doppelperowskiten zu beeinflussen. Zum einen wurde $Cs_2AgBiBr_6$ mit den Lanthaniden Eu^{3+} bzw. Yb^{3+} dotiert, was zwei neue charakteristische Emission zur Folge hat: Eine schwache Emission, die aufgrund von Fehlstellen entsteht, welche durch Eu^{3+} erzeugt werden und eine starke Emission dank eines effizienten Energietransfers von $Cs_2AgBiBr_6$ zu Yb^{3+}. Zum anderen wurden 2D Monolagenperowskite hergestellt, deren Bandlücke im Vergleich zu der von $Cs_2AgBiBr_6$ vergrößert wurde und die neue charakteristische Emissionen aufwiesen.

Im Zuge des zweiten Schwerpunkts dieser Arbeit wurden lochleiterfrei $Cs_2AgBiBr_6$ Solarzellen hergestellt, indem Ruß, der aus upcycelten Industrieabfall gewonnen wurde, mittels Ultraschallsprühbeschichtung als Kohlenstoffelektroden abgeschieden wurden. Dieser Ansatz stellt eine Möglichkeit das Anfallen von Müll obsolet zu machen, um „grüne“ Solarzellen herzustellen. Um die Effizienz der Solarzellen zu erhöhen, wurde die Oberfläche von $Cs_2AgBiBr_6$ zum Erhalt einer gemischten 2D/3D Phase modifiziert. Die 2D/3D Modifikation verbessert die Bandanpassung des Perowskiten gegenüber der Rückelektrode und theoretische Berechnungen lassen vermuten, dass sie die Defektkonzentration nahe der Perowskit-/Elektrodengrenzfläche verringern. Entsprechend stellt die 2D/3D Modifikation eine wertvolle Alternative gegenüber Lochleitermaterialien in $Cs_2AgBiBr_6$ mit Kohlenstoffrückelektroden dar.

Abbreviation list

Abbreviation	Description	Abbreviation	Description
AE2T	5,5′-diylbis(aminoethyl)-[2,2′-bithiophene]	NIR	near-infrared
AFM	atomic force microscopy	PA	propylammonium
BA	n-butylammonium	PCE	power conversion efficiency
CBE	carbon black back electrode	PEA	phenethylammonium
CBM	conduction band minimum	PIM	perovskite-inspired material
CTL	charge-selective transport layer	PL	photoluminescence
DFT	density functional theory	PLE	photoluminescence excitation
DJ	Dion-Jacobsen	PLQY	photoluminescence quantum yield
DLS	diffuse light scattering	PMMA	polymethyl methacrylate
DP	double perovskite	PSC	perovskite Solar Cell
DSSC	dye-sensitized solar cell	P-XRD	powder x-ray diffraction
EDX	energy-dispersive x-ray spectroscopy	RP	Ruddlesden-Popper
ETM	electron transport material	rpm	revolutions per minute
FA	formamidinium	SAED	selective area electron diffraction
FF	fill factor	SC-XRD	single crystal x-ray diffraction
FTO	fluorine doped tinoxide	SEM	scanning electron microscopy
GIXRD	grazing incidence x-ray diffraction	spiro-OMeTAD	2,2′,7,7′-tetrakis[*N,N*-di(4-methoxyphenyl)amino]-9,9′-spirobifluorene
HTM	hole transport material	STE	self-trapped exciton
iBA	iso-butylammonium	TCO	transparent conductive oxide
ICP-OES	inductively coupled plasma – optical emission spectroscopy	TEM	transmission electron microscopy
IoT	Internet of Things	TGA	thermogravimetric analysis
IPV	indoor photovoltaics	TR-PL	time-resolved photoluminescence
ITO	indium tinoxide	USSC	ultrasonic spray-coating
J_{SC}	short-circuit current density	UV-vis	UV-visible
KPFM	Kelvin probe force microscopy	VBM	valence band maximum
LED	light-emitting diode	V_{OC}	open-circuit voltage
LHP	lead-halide perovskite	WLED	white light-emitting diode
LUMO	lowest unoccupied molecule orbital	XPS	x-ray photoelectron spectroscopy
MA	methylammonium	XRD	x-ray diffraction

Contents

1 Introduction

Since the beginning of the 20th century until today, the majority of global energy demand has been met by fossil fuels, i.e. coal, oil, and natural gas.[1,2] However, the slowing but still ongoing rise of the world population is accompanied by an increasing demand for energy supply.[2,3] This development creates several consequences: Firstly, fossil fuels are limited resources and reserves will exhaust, eventually.[2] Secondly, countries search for alternatives to replace fossil fuels to counteract the anthropogenic global climate change as well as to strengthen their energetic independence.[2] Photovoltaics, devices that harvest light and convert it into electricity, represent one potential alternative to fossil fuels. The sun provides an average energy of $4.4 \cdot 10^{13}$ kW that reaches the Earth's surface per year.[4]

Consequently, solar cells have been utilized as power plants to harvest solar radiation for many decades. Most fabricated solar cells are silicon-based due to the semiconductor's optimum bandgap that enables maximum energy conversion from the solar spectrum.

In 2009, a new type of material for solar cells was reported by the group of Miyasaka: A hybrid organic-inorganic lead halide perovskite (LHP), specifically, methylammonium lead iodide and methylammonium lead bromide.[5] Within 15 years, the scientific interest in this material class grew drastically and perovskite solar cells (PSCs) reached record lab-scale power conversion efficiencies (PCEs) of 26.1%,[6] equaling record PCEs of monocrystalline solar cells.[7]

Advantages of LHPs, in contrast to silicon as solar cell material, are their solution-processability at relatively low temperatures, their high absorption coefficients[8,9] which allow the fabrication of thin films with thicknesses of around 1 µm, and their bandgap tunability.[10,11] Additional optoelectronic properties such as their high charge carrier diffusion lengths, high charge carrier lifetimes,[12,13] and high defect tolerance[14,15] enabled LHP-based solar cells to reach such high PCEs. However, the main hindrances of PSCs being widely utilized in solar power plants are the high health and environmental hazards that lead poses, and the low device durability due to their fast degradation in the presence of water, heat, as well as UV light – all of which solar cells must be exposed to while operating. The stability issues have been tackled by chemical engineering and encapsulation techniques.[16–18]

To resolve the health hazard of lead, research on perovskite-based solar cells has expanded towards materials in which lead is substituted by less or non-toxic materials, i.e. tin (Sn), germanium (Ge), or copper (Cu). From those elements, Sn-based perovskite solar cells achieve the best PCEs with record values of around 14%.[19–21] Still, due to its low redox potential, Sn^{2+} tends to oxidize to Sn^{4+} in ambient atmosphere, thus leading to degradation of the perovskite thin film.

Then, in 2016, the all-inorganic, lead-free elpasolite, often also named *double perovskite* (DP), $Cs_2AgBiBr_6$ was reported for the first time.[22] The material is characterized by a long charge carrier lifetime,[22–24] and high stability in humid atmosphere.[25–27] However, its large indirect bandgap,[25,28,29] low electron diffusion lengths,[30,31] a strong electron-phonon coupling,[32–34] and a resulting polaron-hopping transport mechanism[24,35,36] suppress the PCE improvement of $Cs_2AgBiBr_6$-based solar cells.

Accordingly, a deeper understanding of this material's optoelectronic characteristics is necessary to overcome those efficiency-hampering properties. For example, record PCEs of $Cs_2AgBiBr_6$-based solar cells have stagnated between 2% and 3.5% for years before the PCE could be increased to a record value of 6.37% through interstitial doping with hydrogen atoms in 2022.[37] This effective improvement is an example of the unexploited potential within $Cs_2AgBiBr_6$. Furthermore, even if PCEs cannot be further boosted in the future, insights into the highly reported $Cs_2AgBiBr_6$ can pave the way for other lead-free materials that possess optoelectronic features like LHPs although they do not share the perovskite structure - so-called perovskite-inspired materials (PIMs).[38,39]

It is important to note that the indirect bandgap of $Cs_2AgBiBr_6$ is reported to be 2-2.2 eV[25,28,29] which is far too wide to achieve optimum PCEs when utilized as a sunlight harvester, according to the Shockley-Queisser limit (1.1 – 1.4 eV).[40] Since indoor light sources, mostly white light-emitting diodes (WLEDs) and fluorescent lamps, possess a completely different spectrum than sunlight, the bandgap to achieve maximum PCEs almost equals that of $Cs_2AgBiBr_6$ or can be slightly lower, depending on the light warmth.[41–44] Thus, $Cs_2AgBiBr_6$ and other PIMs, are well-suited as light-harvesting materials for indoor photovoltaics (IPV).[45,46]

For example, as the number of interconnected smart devices (sensors, processors, small displays, etc.) that form the Internet of Things (IoT) is increasing annually, IPV have the prospect of reducing the required maintenance on a mass of remote devices, i.e. checking battery levels and exchanging dead batteries. Especially for IoT devices that are handled in everyday direct contact by humans, i.e., rearrangeable smart price labels, it is vital that such devices are powered by non-hazardous IPV.

Still, $Cs_2AgBiBr_6$ may also play a crucial role in solar cells: $Cs_2AgBiBr_6$ could be applied on top of a Si-based solar cell as a second light harvester to create a two-junction tandem device.[47] However, the second light-harvesting material's optimum bandgap in tandem devices is 1.65 – 1.75 eV.[47] Such a bandgap reduction can be achieved, for example, through the aforementioned hydrogenation of $Cs_2AgBiBr_6$.[37]

The objective of this dissertation is divided into two main topics: The first one is the study whether lanthanide doping and dimensional reduction from 3D to 2D affect the structural and optoelectronic properties of $Cs_2AgBiBr_6$. Additionally, the 2D perovskite was further synthesized as a mixed halide perovskite to tune its bandgap. The second one is the fabrication and characterization of low-cost, non-toxic

$Cs_2AgBiBr_6$ solar cells in which carbon black back electrodes substitute the commonly used expensive hole transport material (HTM) and metal back electrodes. Furthermore, the surface of $Cs_2AgBiBr_6$ in those solar cells was modified with mixed 3D/2D layers and the origin of the resulting improved solar cell performances was investigated.

In **publication 1**, the doping of $Cs_2AgBiBr_6$ with the lanthanides Eu^{3+} and Yb^{3+} is discussed. Only small quantities of those lanthanides could be introduced into the elpasolite structure so that the dopants formed sub-band defect gap states but did not affect the bandgap size. However, new emissive features arose through the lanthanide doping. The emission originated from an efficient energy transfer from $Cs_2AgBiBr_6$ towards the dopant in the case of Yb^{3+} doping but from the creation of a trap state in the $Cs_2AgBiBr_6$ structure that has been formed by the dopant in the case of Eu^{3+} doping.

Another path to tune the absorption and emission of perovskites, the dimensional reduction from a 3D material towards 2D material,[48–50] is reported in **publication 2**. Cs^+ was fully substituted by one of four different large organic cations to create two-dimensional (2D) monolayered double perovskites. The choice of the organic cation strongly influenced the resulting 2D perovskite's morphological, electronic, and optical properties. Even when comparing the isomers n-butylammonium (BA) and isobutylammonium (iBA), completely different morphologies and emission processes were observed.

The structural and optical tuning was continued in **publication 3** via the fabrication of bromide/iodide mixed halide 2D double perovskites. Since the (partial) substitution of bromide with iodide reduces the bandgap of LHPs[51] and the bandgaps had been widely unaffected by the organic cation exchange in **publication 2**, the effects of halide substitution on n-butylammonium based 2D perovskite thin films were investigated. A consistent bandgap decrease with an increasing iodide/bromide ratio was observed. Yet, with progressing perovskite thin film aging, resulting in progressive iodide-loss, the bandgap increased again due to progressive iodide loss.

Publication 4 included the contribution of a chapter about HTM-free perovskite solar cells with a strong focus on carbon-based back electrodes that substitute both the HTM and the metal back electrode. This chapter provides information about the differences between the high-temperature and low-temperature fabrication of carbon back electrodes, various deposition methods, as well as strategies on how to improve the injection into various carbon electrode materials and increase their conductivity.

Publication 5 reports on $Cs_2AgBiBr_6$-based HTM-free solar cells with back electrodes consisting of additive-free carbon black that was deposited via ultrasonic spray-coating. The carbon black was won from upcycled waste tires and, therefore, the report presents an end-of-waste strategy to fabricate low-cost, non-toxic solar cells that can perspectively be applied to power IoT devices. While pure $Cs_2AgBiBr_6$ was utilized as light-harvesting material in **publication 5**, a 2D/3D mixed perovskite layer was introduced at

the $Cs_2AgBiBr_6$/carbon back electrode interface in **publication 7**. This layer improved the electrode's selectivity, the $Cs_2AgBiBr_6$/electrode band alignment, and the device durability at the same time.

Finally, the prospect of applying $Cs_2AgBiBr_6$, as well as the PIMs BiOI and $Cs_3Sb_2I_{9-x}Cl_x$ in IPVs to power IoT devices is thoroughly reviewed in **publication 6**. It discusses the electronic and structural differences between LHPs and PIMs and offers an overview of up-to-date research on the 3 PIMs as well as their respective potential to be utilized as IPVs.

2 Background

Investigations on the double perovskite $Cs_2AgBiBr_6$ and its related materials are the topic of this dissertation and while **publication 6** summarizes recent research advances with a focus on its potential as a light-harvesting material in IPVs to power IoT devices, this chapter provides a more general overview of this material. To elucidate the special structure of $Cs_2AgBiBr_6$ as well as the bottlenecks that are investigated in current research on $Cs_2AgBiBr_6$-based photovoltaics, a short introduction to LHPs and (HTM-free) PSCs is necessary. Many established concepts for those material systems can be adapted to $Cs_2AgBiBr_6$, which is why they will be described first, followed by a description of $Cs_2AgBiBr_6$.

Finally, due to their frequent and most prominent use within this work, the thin film deposition methods spin-coating and ultrasonic spray-coating are described.

2.1 Perovskites for photovoltaics

The perovskite structure is derived from the material $CaTiO_3$ which carries the same name: *perovskite*. Its sum formula is typically abbreviated as ABX_3. In oxidic perovskite structures, A is a divalent cation, B is a tetravalent cation, and X is the divalent oxygen anion. However, the perovskite structure is not limited to oxides. For example, for LHPs, all ionic charges in ABX_3 are halved in comparison to oxidic perovskites which maintains a neutral overall charge.

In LHPs, the monovalent A site is typically occupied by the small organic ions methylammonium (MA), or formamidinium (FA) but also Cs^+ or Rb^+ are commonly used. The B site is occupied by divalent lead and the X site is occupied by iodide, bromide, or chloride. One of the most advantageous properties of LHPs is the tunability of their optoelectronic and structural properties depending on their composition. While the choice of the X site halide mainly determines the LHP's bandgap size – it increases with decreasing halide radius -,[52–54] the choice of the A site cation can influence its structural stability,[55] i.e., by suppressing the LHP's ion migration.[56]

The convenient A and X site interchangeability leads to a broad spectrum of utilizable LHPs: Some possess only one ion type per A or X site, like $MAPbI_3$ which was the first reported LHP light harvester (together with $MAPbBr_3$) in a solar cell in 2009[57] and is still used to fabricate solar cells with PCEs exceeding 25%.[58] Other LHPs consist of multiple ions on the A and X sites, for example, the quadruple cation perovskite $Rb_{0.05}Cs_{0.05}FA_{0.72}MA_{0.18}Pb(I_{0.83}Br_{0.17})$.[59]

The first reported LHP-based solar cells reached a maximum PCE of 3.8% by utilizing $MAPbI_3$ and $MAPbBr_3$ nanocrystals, respectively, that were deposited on porous TiO_2 in a dye-sensitized solar cell (DSSC), thus using a liquid electrolyte that degraded the perovskites rapidly.[57]

Later, in 2012, the first reported solid-state perovskite solar cell, which was based on $MAPbI_2Cl$ as light-harvesting material, reached a PCE of 10.9%.[60] The solar cell architecture, like the deposition of the LHP onto mesoporous TiO_2 that works as ETM, was closely related to the architecture of DSSCs and is still commonly used. However, the removal of the liquid electrolyte enabled the creation of new architectures, i.e. the use of planar ETMs, or the deposition of LHPs on top of planar or porous HTMs in so-called inverted solar cell architectures.[61–63]

In **Figure 1**, the commonly utilized PSC architectures are depicted: The perovskite layer is sandwiched between an ETM and an HTM. One of the charge-selective transport layers (CTLs) is in contact with a transparent conductive oxide (TCO)-covered glass substrate, the other one is covered with a back electrode consisting of silver or gold in the case of high-efficiency PSCs.[61,64] When the ETL is in contact with the TCO, the architecture is named n-i-p or "regular".

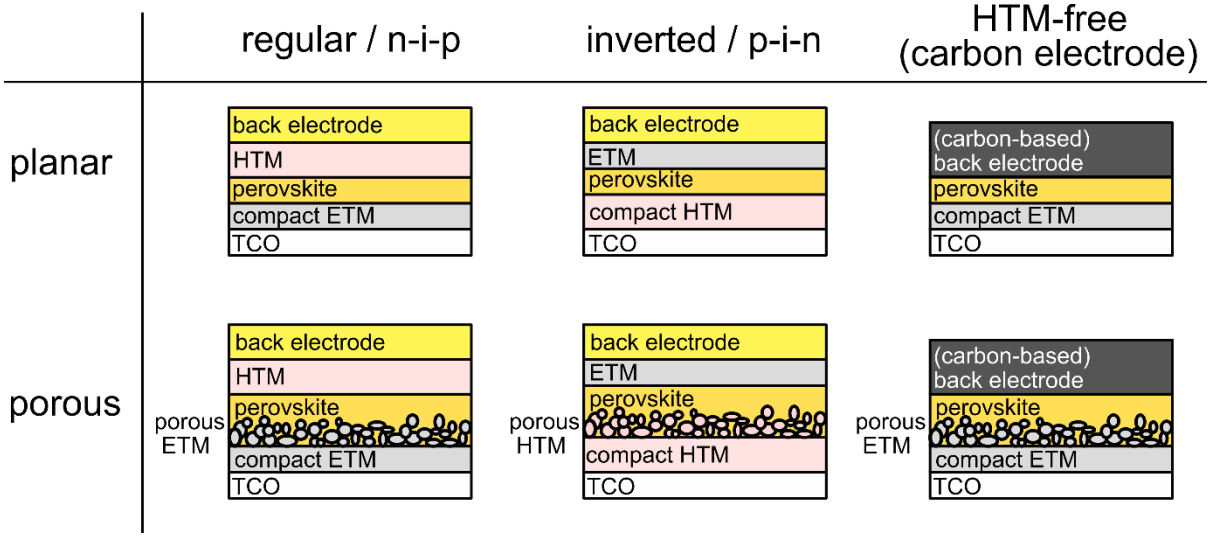

Figure 1. *Sketches of perovskite solar cell architectures, sorted by planar and porous, as well as regular, inverted, and HTM-free architectures.*

When the HTL is in contact with the TCO, it is named p-i-n or "inverted".[61,64] The respective opposite CTL is in contact with the back electrode. Inverted PSC architectures show the advantage to apply new materials that cannot be used in regular devices. For example, high-efficiency devices do not rely on the HTM spiro-OMeTAD 2,2′,7,7′-tetrakis[*N*,*N*-di(4-methoxyphenyl)amino]-9,9′-spirobifluorene (spiro-OMeTAD) which is used for the best-performing reported n-i-p PSCs[6,65,66] but at the same time limits their device lifetime due its hygroscopic character.[67,68] Also, inverted architectures are typically used in tandem devices.[69,70] Within this dissertation, solely regular PSC architectures have been utilized (**publications 5**

and **7**) in which both the HTM and the metal electrode were substituted with carbon black back electrodes (CBEs).

The simplified mechanism of how PSCs transform light into electricity is depicted in **Figure 2**. First, it is important to point out that for a photon to be able to reach the perovskite, it must transmit several layers (the bottom layers below the perovskite in **Figure 1**) without being absorbed or reflected.

Therefore, transparent conductive oxides, for example, fluorine doped tin oxide (FTO) or indium tin oxide (ITO), are deposited on transparent substrates and work either as anode (regular architecture) or as cathode (inverted architecture). The transparent substrate consists typically of glass but also flexible materials such as polymers can be used.[71–73] As a side note, since light passes through the backside of PSCs, the *substrate* should correctly be named *superstrate*.[74,75] However, this nomenclature is barely used in literature.

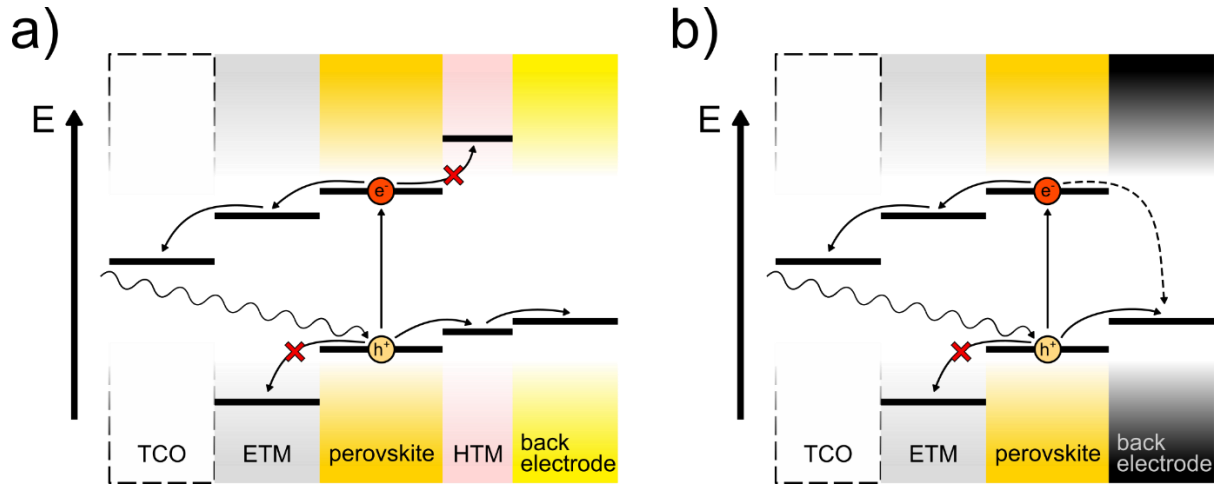

Figure 2. *Excited charge carriers in a sketched band diagram of **a)** a regular and **b)** an HTM-free PSC. The removal of the HTM creates a recombination pathway due to the extermination of an energy barrier for electrons created by the HTM's valence band/LUMO. For the sake of simplicity, factors like the formation of a Schottky barrier at the perovskite/electrode interface or the formation of a built-in electric field are not considered in the sketch.*

For the ETM or HTM that covers the TCO, large bandgap materials that do not absorb the light are utilized, e.g., TiO_2, SnO (both ETMs in regular devices), or NiO_x (HTM in inverted devices). When photons with an energy equal to or larger than the perovskite's bandgap energy reach the perovskite layer, they excite electrons from the perovskite's valence band to its conduction band, as depicted in **Figure 2**. On the one hand, CTLs provide energy barriers that hinder electrons and holes from being injected into the HTL and ETL, respectively, to suppress recombination (red crosses in **Figure 2a**). On the other hand, the lowered energy difference between the perovskite's and HTM's valence band, and the perovskite's and ETM's conduction band enhance the respective charge transfer kinetics.

It is important to note that this description of how PSCs transform photon energy into electric energy as well as the scheme depicted in **Figure 2** are simplified. For example, the band alignment between respective CTLs and the perovskite creates depletion regions which result in a built-in field within the device[76–80] that can be spatially tracked *via* Kelvin probe force microscopy (KPFM) of PSC cross-sections.[80–82] This electric field exerts force on the ions in the perovskite structure which can result in the migration of mobile ions, promoting the material's degradation and/or shielding of the electric field.[80,83]

2.2 Hole-transport material (HTM)-free perovskite solar cells

Large fractions of PSC fabrication costs stem from the material prices of the TCO, the HTL, and the silver or gold electrodes.[84,85] Moreover, gold electrodes are deposited via evaporation under vacuum which is not only cost-intensive but also complicates continuous assembly line fabrication. Here, it is important to note that silver electrodes are also deposable from silver pastes.[86,87]

Carbon-based electrodes (CBEs) can be utilized to substitute both the HTM and the metal electrode (depicted in **Figures 1** and **2b**), reducing the fabrication costs of PSCs drastically[88] and enabling scalable deposition methods.[88,89] Additionally, the hygroscopic character of spiro-OMeTAD[67,68] and the metal migration from the electrode towards the perovskite layer[90,91] enhance perovskite degradation and, therefore, reduce the PSC stability. However, the removal of the HTM from a PSC is accompanied by the removal of the energy barrier for electrons as well as the favorable band alignment for holes between perovskite and back electrode that the HTL could deliver (see **Figure 2b**).

Still, the PCE of such devices does not necessarily harshly diminish due to a Schottky junction that can form at the perovskite/back electrode interface, supporting the hole extraction and electron blocking.[92,93] For example, in the HTM-free PSCs reported in **publication 5** a strong built-in field could be determined for $Cs_2AgBiBr_6$-based PSCs that resulted in exceptionally high open-circuit voltages.

An in-depth review of various types of HTM-free PSC designs, the difference between high- and low-temperature deposition of carbon electrodes, and investigations on the interface processes between the back electrode and the perovskite layer can be found in chapter 4 of **publication 4.**

$Cs_2AgBiBr_6$-based HTM-free PSCs that utilize carbon electrodes have been reported multiple times.[94–99] However, only a few of those reports focused on investigating the $Cs_2AgBiBr_6$/electrode interface, i.e., by improving the perovskite/electrode band alignment through incorporating alkali ions into the double perovskite,[96] or by applying a polymethyl methacrylate (PMMA) interlayer to suppress interfacial shunt losses.[97]

2.3 $Cs_2AgBiBr_6$ and its use in optoelectronics

In $Cs_2AgBiBr_6$, the divalent Pb^{2+} on the B site is substituted by equal amounts[100] of monovalent Ag^+ and trivalent Bi^{3+}. Consequently, the general sum formula changes from ABX_3 to $AB_IB_{III}X_3$ by which elpasolites are described. Due to the doubling of B site cation types compared to the perovskite structure, the elpasolite structure is also referred to as *double perovskite* (DP).

The presence of two B sites results in a highly ordered structure in which $[AgBr_6]^{5-}$ and $[BiBr_6]^{3-}$ octahedra are arranged in an alternating fashion, depicted in **Figure 3**, thus forming a chess board pattern that is energetically favored compared to a disordered structure.[101] In **publication 6**, reported effects of disordered $[AgBr_6]^{5-}$ and $[BiBr_6]^{3-}$ octahedra on $Cs_2AgBiBr_6$ such as a decrease of the bandgap and the change from an indirect to a direct or pseudo-direct bandgap are summarized.[101,102]

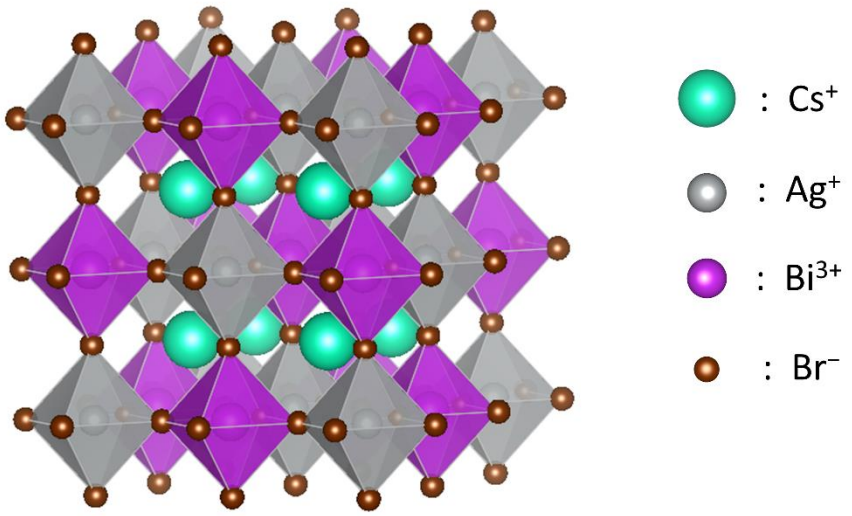

Figure 3. *Double perovskite structure of $Cs_2AgBiBr_6$. The ratios of the ionic radii are not to scale.*

Like LHPs, $Cs_2AgBiBr_6$ can be processed via spin-coating,[28,31,37,97,103–108] spray-coating,[109] thermal evaporation,[110–113] or even pulsed laser deposition[114] due to its relatively high defect-tolerance, meaning that intrinsic defect states are created close to the material's valence or conduction band (shallow trap states) and not deep within the bandgap (deep trap states).[15,115] However, the presence of two B sites in $Cs_2AgBiBr_6$ enables the formation of the antisite defects Bi_{Ag} and Ag_{Bi} that form deep trap states.[115]

In addition to its large indirect bandgap of 2-2.2 eV,[25,28,29] the most prominent feature of $Cs_2AgBiBr_6$ is a local absorption maximum at around 440 nm. Its origin is debated in literature to either be of excitonic nature,[32] to stem from an Ag-to-Bi charge transfer,[49] or to arise from a localized Bi 6s-to-6p transition.[116]

Furthermore, $Cs_2AgBiBr_6$ is characterized by a relatively high hole diffusion length that is contrasted by its low electron diffusion length in respect to its film thickness.[30,31] Additionally, this material possesses charge carrier lifetimes exceeding 1 µs which are highly favorable for photovoltaic applications.[22–24]

In comparison to LHPs and also tin-based perovskites – reaching the highest PCEs of all lead-free perovskite materials - $Cs_2AgBiBr_6$ is highly stable under humid conditions and at elevated temperatures.[25–27] Therefore, $Cs_2AgBiBr_6$-based solar cells already possess high longevity without requiring additional encapsulation that is often applied on LHPs to suppress their degradation under ambient atmosphere.[16,117–119] Still, its optoelectronic properties hamper $Cs_2AgBiBr_6$ solar cells to achieve high PCEs. Although the calculated maximum PCE of solar cells using pure $Cs_2AgBiBr_6$ as sole light harvesters reaches values of up to 11.32% or even 14.23%,[120–122] reported experimental PCEs of such devices do not surpass the 3% threshold[27,97,103,107,109] with a reported maximum of 2.81%.[123]

Thus, the adjustment of the material's optoelectronic properties plays a major role in analyzing and, eventually, overcoming its efficiency-hampering bottlenecks. For example, the aforementioned utilization of disordered $[AgBr_6]^{5-}$ and $[BiBr_6]^{3-}$ octahedra[101,102] is not the only way to exploit a change of the crystal structure to tune the bandgap of $Cs_2AgBiBr_6$. The application of pressure on the system results in a narrowing of the material's bandgap which partially retains when the pressure is released.[124]

Like for LHPs,[125,126] (partial) halide substitution as well as doping can also affect the material's crystallization and optoelectronic properties. Within the first publication to mention $Cs_2AgBiBr_6$ by McClure *et al*., $Cs_2AgBiCl_6$ was also reported, possessing an indirect bandgap of 2.77 eV.[25] In contrast, the substitution of Br with I decreases the material's bandgap[127,128] which would improve its PCE according to the Shockley-Queisser limit.[40]

However, the preparation of Cs_2AgBiI_6 as well as mixed Br/I or Cl/I materials has not been achieved from precursors, yet, due to the thermodynamically favored formation of $Cs_3Bi_2I_9$ and the occurrence of phase separation, respectively.[129–132] Stable Cs_2AgBiI_6 was, however, prepared as nanocrystals which were stabilized by the surface free energy.[132] Additionally, anion exchange on $Cs_2AgBiBr_6$ thin films could be performed using methylammonium iodide, achieving a ratio of up to $Cs_2AgBiBr_2I_4$ and decreasing the bandgap by up to 0.3 eV.[131] Further, when Cs^+ is fully substituted with Cu^+, Cu_2AgBiI_6 thin films that achieved a PCE of 2.4% in solar cells could be fabricated from precursors.[133]

Within this dissertation, **publication 3** describes the fabrication of thin films of the 2D double perovskite $(BA)_4AgBiBr_{8-x}I_x$ (x=1,2,3,4) from precursors to tune its optical properties. Apart from anionic substitutions, the partial substitution of Bi with Sb has been reported to lower the material's bandgap[134] and to increase its charge carrier lifetime in nanocrystals.[135]

Furthermore, the inclusion of small amounts of Zn,[136] and the alkali metals Rb,[96,137] and Li[96] have been reported to improve the film quality and therefore reduce recombination which lead to improved PCEs in solar cells. The hydrogenation of $Cs_2AgBiBr_6$ decreased the material's bandgap to 1.64 eV and strongly improved the PCE to 6.37%.[37] For this modified double perovskite a calculated maximum achievable PCE of 21.28% has been postulated for optimized solar cells.[138]

Doping of $Cs_2AgBiBr_6$ can also be utilized to form additional subbandgap states to enable near-infrared (NIR) absorption to be utilized in NIR photodetectors, for example by introducing small amounts of Fe^{2+} or Cu^{2+} into the crystal structure.[139,140] Other dopants like Na,[141] or Yb[142,143] can also create emissive states to improve the material's photoluminescence quantum yield (PLQY). In **publication 1**, the doping of $Cs_2AgBiBr_6$ with the lanthanides Eu, and Yb is reported and the mechanistic difference in their emissive behavior is investigated.

2.4 Two-dimensional perovskites

A commonly used index to predict the crystal structure stability of a perovskite material is the Goldschmidt tolerance factor *t* which is defined as shown in equation (1).[144]

$$t = \frac{r_A + r_X}{\sqrt{2}(r_B + r_X)} \quad (1)$$

where r_A, r_B, and r_X are the radii of the respective ions in the ABX_3 perovskite sum formula. When $0.8 < t < 1$, a material tends to form a stable cubic perovskite structure. When *t* is larger than 1 or smaller than 0.8, the material will likely form a non-perovskite structure, for example, a hexagonal structure ($t > 1$) or an orthorhombic structure ($t < 0.8$) in the case of $FA_xCs_{1-x}PbI_3$.[145] However, when r_A is drastically increased, usually through the introduction of large organic cations such as, e.g., the often utilized butylammonium (used in **publications 2**, **3**, and **7**),[48,49,146] phenethylammonium (used in **publication 2**),[147,148] or guanidine,[148,149] 2D perovskite structures are formed.

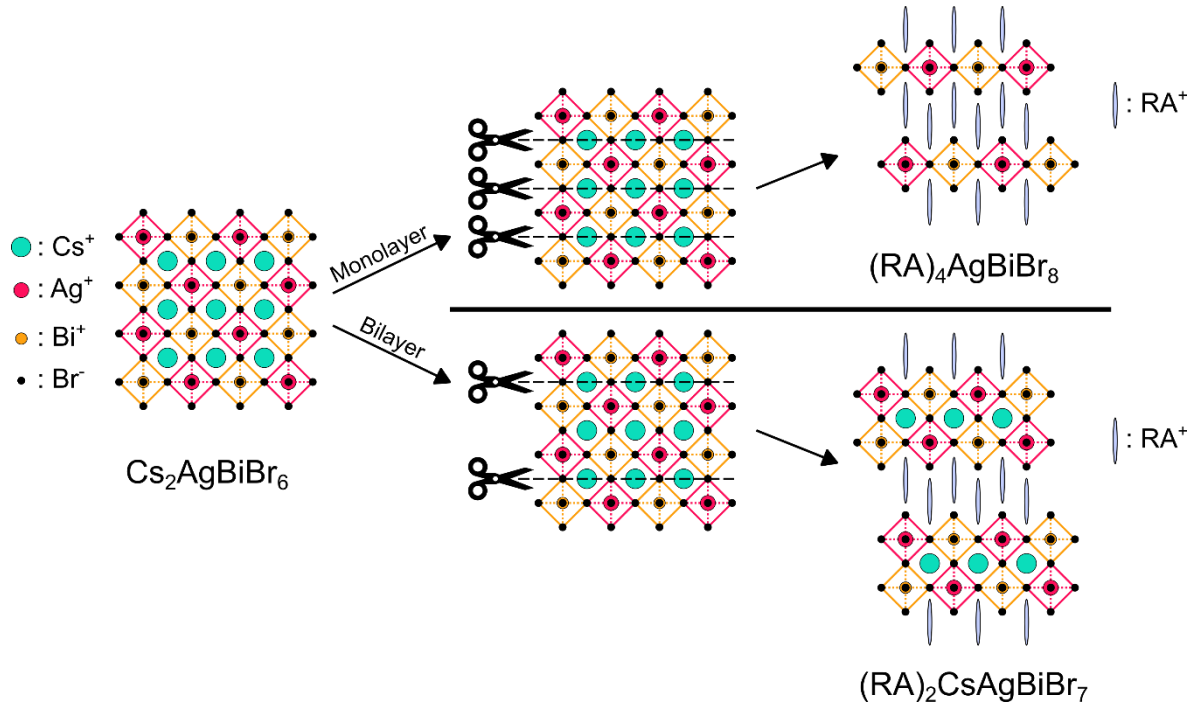

Figure 4. *Dimensional reduction of the 3D double perovskite $Cs_2AgBiBr_6$ into a monolayered (top) and a bilayered (bottom) Ruddlesden Popper 2D double perovskite, respectively. Cs^+ is fully/partially substituted with large organic cations (RA^+) to create the monolayered/bilayered 2D perovskite. The ratios of the ionic radii are not in scale.*

2D perovskite structures consist of alternating layers of interconnected $[BX_6]^{4-}$ octahedra ($[B_IX_6]^{5-}$ and $[B_{III}X_6]^{3-}$ for double perovskites) and layers of organic A-site spacer cations. Depending on whether the

organic spacer cations are mono- or bifunctionalized cations, the 2D perovskite will possess a Ruddlesden-Popper (RP) or a Dion-Jacobsen (DJ) phase, respectively.[150–152]

In the RP phase, bilayers of organic spacer cations separate the perovskite octahedra-dominated layers while the organic cations form monolayers in the DJ phase. 2D double perovskites which were synthesized and analyzed within this dissertation (**publications 2**, **3**, and **6**) solely possessed RP phases. Therefore, the further explanations of 2D perovskites will only describe RP phases which are depicted in **Figure 4**.

When the A-site cation of a 3D perovskite is fully substituted with organic spacer cations, the $[BX_6]^{4-}$ octahedra will form inorganic monolayers, as shown in **Figure 4**.[48,148,153] The monolayered double perovskites in **publications 2** and **3** were synthesized using this approach. On the other hand, when the A-site cation of a 3D perovskite is not fully but only partially substituted, the perovskite octahedra can form multilayers instead of monolayers which are still separated by bilayers of organic spacer cations.[48,49,146,147,154]

The thickness of such multilayers is typically described by the number *n* of octahedra in between two organic bilayers. For this nomenclature, *n*=1 2D perovskites consist of monolayers (**Figure 4**, top right), *n*=2 consist of bilayers (**Figure 4**, bottom right), etc., and *n*=∞ describes a 3D perovskite (**Figure 4**, left). Phases with *n*>1 are referred to as “quasi-2D” perovskites.

In **publication 7**, such *n*=2 quasi-2D layers were identified *via* grazing incidence x-ray diffraction (GIXRD) to be created by partially substituting Cs^+ with butylammonium in $Cs_2AgBiBr_6$ thin films using a post-annealing step.

Furthermore, it is important to mention that, for *n*>1, *n* describes an averaged layer thickness since also layers with smaller and larger *n* can form. Especially, for high *n* values (*n*>3) the layer thickness distribution strongly broadens.[155] Due to the reduction by one dimension and the resulting confinement into two dimensions, the optoelectronic properties of 2D perovskites differ strongly from their 3D analogues: Dielectric confinement increases the exciton binding energies and bandgaps in 2D perovskites compared to 3D perovskites.[156–158] For example, the bandgap of a perovskite can be tuned by changing *n*.[48]

The organic bilayer acts as an insulating layer which strongly reduces the charge carrier mobility perpendicular to the perovskite layer compared to the horizontal direction.[159–161] As a result, the crystallization and orientation of 2D perovskites plays a crucial factor when they are applied in devices such as solar cells: An orthogonal orientation of the 2D perovskite towards the substrate will deliver an optimum conductivity, while a parallel orientation will result in low conductivity.

Thus, large efforts have been put into achieving crystallization orthogonal to the substrate,[162,163] or tuning the organic spacer cation design to improve the conductivity perpendicular to the 2D planes, e.g. by reducing the interlayer distance.[164,165] Most importantly, the introduction of organic spacer cations improves the stability of perovskites against humidity due to the organic spacer cations' hydrophobic character.[166,167]

The character of the spacer cation not only influences the interlayer charge transport but also the crystallization of 2D perovskites,[168] affecting its optical properties, as described in detail for $X_4AgBiBr_8$ 2D perovskites in **publication 2** in which X is butylammonium, isobutylammonium, phenethylammonium, or hexylammonium, respectively.

A noteworthy aspect of silver-bismuth double perovskites is that when the dimension of $Cs_2AgBiBr_6$ is reduced to 2D monolayers, the material's bandgap type changes from indirect to direct.[49,169–171] This is of special interest for the application in solar cells since the excitation of an electron by a photon is distinctly higher for a direct bandgap semiconductor than for an indirect semiconductor.[172]

Pantaler *et al*. reported that, in contrast to LHPs, the dimensional reduction of $Cs_2AgBiBr_6$ towards a 2D material does not strongly influence the exciton binding energy of excited charge carriers due to the soft character of the double perovskite lattice which also explains the large Stokes shift in this materials.[169] The application of a 2D monolayered double perovskite structure also enabled the stabilization of an Ag-Bi-based iodide double perovskite that has not been reported for a 3D double perovskite, yet.[173]

2.5 2D/3D mixed perovskites for photovoltaics

The widened bandgaps, enhanced exciton binding energies, as well as the anisotropic conductivity and charge carrier mobilities seem to make pure low-*n* phases unfavorable materials for photovoltaic applications.[174] Lead-based quasi-2D perovskite solar cells have been reported to exceed PCEs of 20% when their crystallization is carefully controlled.[174,175]

Also, the environmental and thermal stability of such devices is enhanced in comparison to pure 3D perovskite photovoltaics.[174] Another approach to utilize 2D perovskite layers in perovskite photovoltaics is to grow them on top of 3D perovskites, thus fabricating 2D/3D mixed perovskite thin films.[176]

Such thin films combine the properties of both 2D and 3D perovskites to compensate for the drawbacks of the respective opposite material: 3D perovskites, usually constituting the thin film's majority, contribute their isotropic conductivity and charge carrier mobilities,[177] as well as lower exciton binding energies and bandgaps. The 2D perovskites that usually form a comparably thin capping layer on top of the 3D perovskite improve the thin film's overall environmental stability due to their hydrophobicity and at the same time enhance the band level alignment towards the charge carrier selective layer (typically HTL) due to their enhanced valence band maximum (VBM) as depicted in **publication 7**.[79,176,178,179]

To fabricate a 2D perovskite capping layer on top of a 3D perovskite thin film, the latter is first deposited onto a substrate. Subsequently, the thin film's surface is treated with a solution of organic spacer ions to transform the 3D perovskite's surface into 2D and quasi-2D perovskite by substituting the 3D perovskite's A site cation.[79,180] Since the formation of 2D perovskite cannot be controlled stoichiometrically, the choice of the utilized spacer cation and its concentration affect the average dimensionality *n* of the resulting 2D perovskite.[181]

This 2-step preparation method was utilized in **publication 7** to modify the surface of $Cs_2AgBiBr_6$ using butylammonium bromide. Before **publication 7**, the capping of $Cs_2AgBiBr_6$ with a 2D layer has already been reported by Sirtl *et al.*, using phenethylammonium to improve the perovskite's band alignment towards the HTM.[79] However, the application of a 2D capping layer in **publication 7** has explored its role of suppressing recombination at a perovskite/carbon electrode interface in an HTM-free architecture.

2.6 Thin film preparation

PSCs utilize perovskite thin films with thicknesses of hundreds of nanometers up to a few micrometers. In contrast, monocrystalline silicon solar cells typically possess thicknesses of 100-500 µm.[182] The low thickness of perovskite thin films results in low material quantities that are required to prepare PSCs. Furthermore, it allows the fabrication of flexible solar cells.[183,184] Thin film deposition can be conducted either from liquid precursors, for example, by spin-coating,[185–189] dip-coating,[186,190] drop-casting,[188,191] doctor-blading,[192,193] slot-die deposition,[188,194–196] and spray-coating,[197–199] or from gas phase deposition methods like pulsed laser deposition,[200,201] molecular beam epitaxy,[202,203] or atomic layer deposition.[204,205] While many of those deposition methods find application in the fabrication of perovskite thin films for solar cells,[185,188,206,191,193,194,196,198,199,201,205] spin-coating was utilized to fabricate all perovskite thin films within this dissertation.

2.6.1 Spin-coating

Spin-coating enables the preparation of uniform thin films and offers high reproducibility.[207] Drawbacks of this deposition method are its poor scalability, as well as a large amount of precursor excess that is wasted during the deposition process.

To apply this method, a substrate on which the thin film will be prepared is mounted on top of a rotatable plate. The precursor solution is deposited on the substrate and the substrate is turned at a speed of typically several thousand revolutions per minute (rpm). The entire spin-coating process, depicted in **Figure 5**, can be divided into 4 phases: Deposition, spin-up, spin-off, and evaporation.[186,208] The first phase (**Figure 5a**), as its name implies, is the deposition of the precursor solution. It is either deposited before the substrate starts rotating (static spin-coating) or while the substrate is already rotating (dynamic spin-coating).

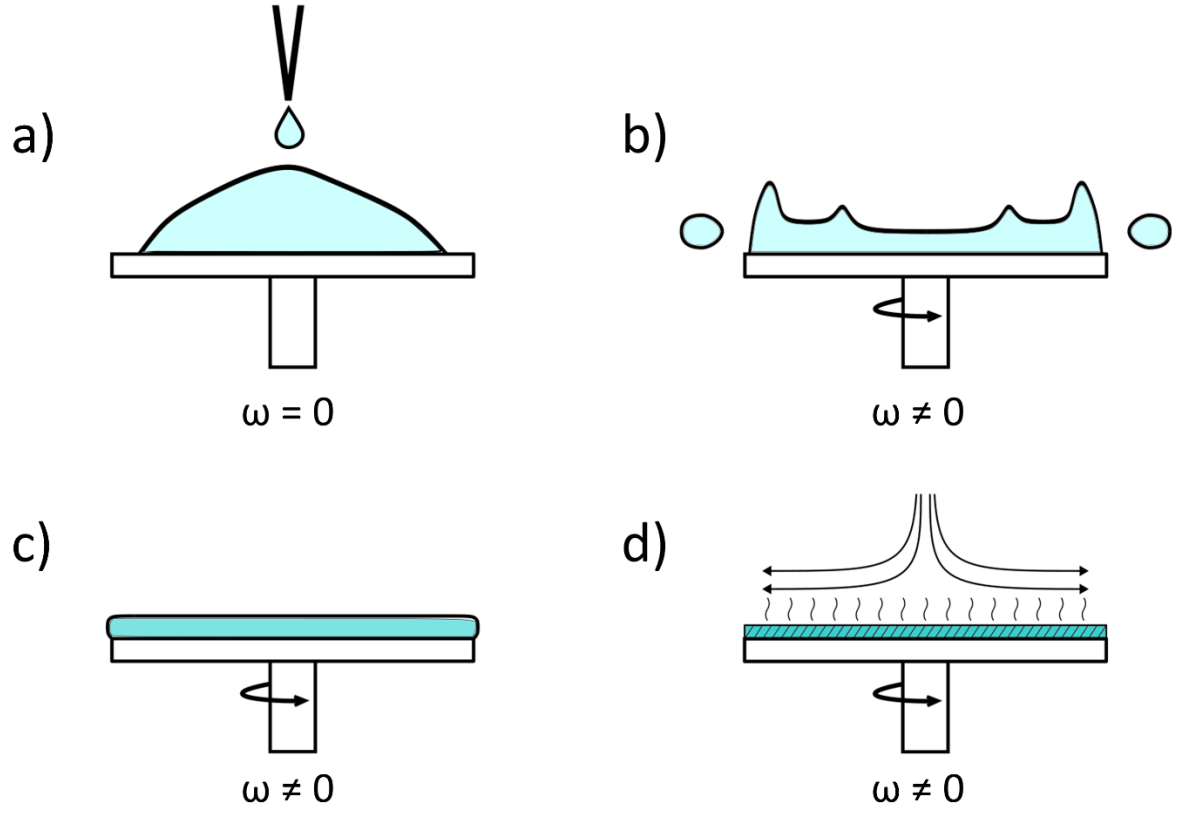

Figure 5. *Schematic depiction of the spin-coating process, divided into its phases: a) Deposition of the precursor solution, b) spin-up phase, c) spin-off phase, and d) evaporation phase.*

In the spin-up phase (**Figure 5b**), which is the first few seconds of spinning the solution-covered substrate, the solution is pushed towards the substrate's edges by the centrifugal force and spread across the substrate. Due to the high initial thickness of the solution that is covering the substrate, spiral vertices can form, originating from the inertia of the top part of the solution in contrast to the substrate's

accelerating spinning velocity (in the case of static spin-coating).[208] Wells of solution form temporarily at the perimeter, from which droplets are ejected off the substrate during the spin-up phase.[186]

As the solution thickness decreases, eventually, the entire fluid will spin at the same velocity as the substrate which results in a uniform fluid thickness when the outward directed centrifugal force and the towards the center of spinning directed viscous force balance (**Figure 5c**).[189] The fluid thickness progressively decreases according to equation (2), where h_0 is the initial thickness of the uniform film, ρ is the fluid density, ω the angular velocity, μ the viscosity, and t the time.[189]

$$h(t) = \frac{h_0}{\sqrt{1 + \frac{4\rho\omega^2 h_0^2}{3\mu} t}} \tag{2}$$

While the solution thickness decreases during the spin-off phase, the flow of liquid slows due to the enhanced resistance of a thinner film.

Finally, the fluid's viscosity starts increasing due to solvent evaporation and the thin film starts to form, beginning the fourth phase (**Figure 5d**).[186,209] The rotating substrate enforces gas convection, drawing gas in orthogonally towards the center of rotation and pushing it radially towards the substrate edges.[186] Thus, the evaporation can be controlled by adjusting the atmosphere, i.e., saturating it with the solvent.[103]

Also, for perovskite thin film fabrication, anti-solvent dripping can be applied to improve the thin film quality. In this method, the initial solvent on the substrate is removed by another solvent that is dropped onto the rotating substrate during the spin-off or evaporation phase, affecting the perovskite crystallization.[210–212]

For perovskite thin films, a consecutive annealing step is often applied, directly after finishing the spin-coating. $Cs_2AgBiBr_6$ is usually annealed at temperatures between 250 °C and 300 °C to improve its crystallization, suppress the formation of side phases, and achieve large grain sizes.[27,28,107]

The homogeneous and pin-hole-free $Cs_2AgBiBr_6$ thin films prepared in the publications of this work were annealed at 285 °C (**publications 1**, **5**, and **7**). Mixed organic-inorganic perovskite thin films are typically annealed at lower temperatures to prevent the degradation of the organic cations. Therefore, the 2D double perovskites fabricated in **publications 2** and **3** were annealed at 100 °C.

2.6.2 Ultrasonic spray-coating (USSC)

Pneumatic spray-coating is a widely known and applied technique not only for thin film deposition but also for the deposition of thick layers in a scale of 100 µm, e.g., industrial painting of cars and other products.[213] For this method, ink is carried through a spray head's nozzle by a pressurized gas flow (i.e. air), atomizing the ink into droplets. The resulting spray consists of a broad distribution of both droplet sizes (10 to 100 µm, see **Figure 6b**) and velocities.[213,214]

When sufficiently thick films are prepared (scale of 100 µm), this broad distribution does not critically impact the film homogeneity. However, thin films of below 1 µm will suffer from strong inhomogeneities due to the large and broadly distributed drop sizes and the high kinetic energies of drops that impact on the substrate surface.[213,214]

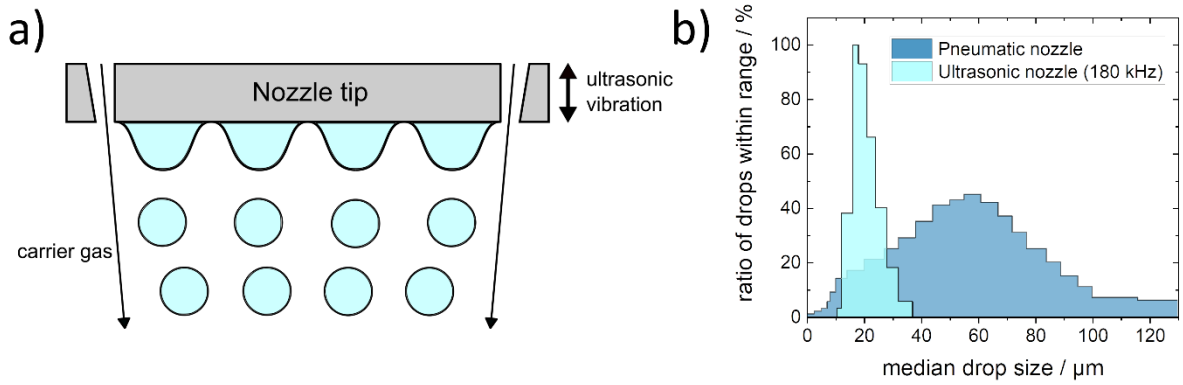

Figure 6. *a) Schematic depiction of the ultrasonic spray-coating process at the nozzle tip. b) Drop size distribution of pneumatic spray-coating vs. ultrasonic spray-coating. Data were taken from reference*[214]

For the deposition of homogeneous thin films, ultrasonic spray-coating (USSC), is far better suited. This method has been applied in **publication 5** to deposit the CBE from carbon black particles that were dispersed in isopropanol. In contrast to pneumatic spray-coating, the ink is atomized at the nozzle not by gas pressure but by ultrasonication: At the nozzle, high-frequency sound creates standing waves of the inks, forming a fine mist as soon as the liquid exits the nozzle, depicted in **Figure 6a**.[214]

Therefore, ultrasonic atomization results in a narrow distribution of drop sizes and supports the homogeneous dispersion of particles in the ink (see **Figure 6b**).[213,215,216] Furthermore, the drop size d_{drop} can be reduced to a few micrometers and controlled by adjusting the frequency f which is applied to the nozzle, according to the proportionality shown in equation (3).[213,215,216]

$$d_{\mathrm{drop}} \sim f^{-\frac{2}{3}} \tag{3}$$

The dispersed ink is directed towards a substrate using a carrier gas (**Figure 6a**). In contrast to pneumatic spray-coating, this carrier gas serves the purpose of shaping the spray into a cone, thus adjusting the spray's density of drops, and not accelerating the drops. Drops with a narrow size distribution and low kinetic energy approach the substrate surface.

Typically, the substrate is heated to evaporate the solvent and create a thin film of (nano)particles that have been dispersed in the ink[217] (i.e. in **publication 5**) or to perform an additional pyrolysis step.[218] Regarding perovskite-based photovoltaics, USSC is not only applied to deposit electrodes but, for example, also to deposit perovskite thin films themselves.[183,219,220]

3 Experimental Section

3.1 Synthesis of $Cs_2AgBiBr_6$ powder

10 mL of HBr (Fisher Scientific, 48%) were added to stoichiometric amounts of CsBr (426 mg, Alfa Aesar, 99.9%), AgBr (188 mg, Alfa Aesar, 99.5%), and $BiBr_3$ (449 mg, Alfa Aesar, 99%) and then stirred for around 2 hours until no undissolved AgBr (yellow particles) remained. An orange powder precipitated after a short time. Then, the solution was transferred to autoclaves. Remaining precipitated powder was also rinsed into the autoclave using a low amount of demineralized water.

The autoclave was heated at 110 °C for 2 hours. Letting the autoclave cool over night did not affect the product quality. After the autoclave cooled down to room temperature, the $Cs_2AgBiBr_6$ powder had precipitated. The excess solution was carefully disposed of.

The precipitated powder was washed in ethanol and centrifuged at 6000 rpm for 10 minutes. Then, the ethanol was carefully disposed of. This washing procedure was repeated another two times. Finally, the powder was dried at 80 °C under ambient atmosphere for 24 hours. The powder could be stored in the dark under ambient atmosphere for several months without observing degradation *via* P-XRD.

3.2 Preparation of $Cs_2AgBiBr_6$ thin films

The pre-synthesized $Cs_2AgBiBr_6$ powder was transferred into an argon-filled glovebox, dimethyl sulfoxide (Thermo Scientific, 99.7+%) was added to prepare a 0.5 M precursor solution, and the solution was stirred for around 1-2 hours until the $Cs_2AgBiBr_6$ was fully dissolved. The precursor solution was a yellow, clear solution. When the dimethyl sulfoxide was too old, the $Cs_2AgBiBr_6$ did not entirely dissolve, and an opaque solution was obtained from which no homogeneous thin films of pure $Cs_2AgBiBr_6$ could be prepared.

The entire thin film preparation process was conducted in an argon-filled glovebox. A substrate was mounted on a spin-coater and covered with the precursor solution. For example, 50 µL were sufficient to cover a 2x2 cm² substrate. The substrate was then rotated at 4000 rpm (3 seconds of acceleration) for 40 seconds. Immediately after finishing the spin-coating process, the substrate was transferred to a 285 °C pre-heated hot plate.

The substrates were annealed for 5 minutes. A prolonged annealing time of several minutes did neither affect the purity, the homogeneity, nor the grain size of the obtained $Cs_2AgBiBr_6$ thin films. The thin films could be stored in the dark under ambient atmosphere for several months without observing degradation *via* GIXRD or UV-Vis absorption spectroscopy.

The pre-treatment of the substrates depended on their type (FTO-covered glass, covered with porous TiO_2, etc) and is described in the experimental sections of the respective publications.

4 Publications

In the following, my publications as first author, a shared first authorship (**publication 5**), and a co-authorship with a considerable contribution (**publication 4**) are listed and described. Each publication is put into the context of literature in the time when it was published, shortly summarized, and each publication's impact on subsequent literature is described. Furthermore, the tasks I took on for each paper are defined, for the sake of assessing my individual achievements within this dissertation and isolating it from work that was performed by co-authors. To avoid phrase repetitions for each publication, information on general tasks that I carried out for every single publication is described in the following paragraph, *General Contributions*. Specific and individual tasks that I carried out at the end of the respective publication descriptions.

General Contributions

All publications have in common that I contributed essential parts of the overall data interpretation in fruitful discussions with my respective co-authors, in particular with my supervisor Teresa Gatti. Furthermore, when not stated differently in the respective publication descriptions, I prepared the manuscripts in close collaboration with and under the supervision of Teresa Gatti. The manuscript drafts were reviewed by, commented by, and discussed with the respective co-authors to be corrected and improved.

4.1 List of considerable publications

Publication 1

"Lanthanide-Induced Photoluminescence in Lead-Free $Cs_2AgBiBr_6$ Bulk Perovskite: Insights from Optical and Theoretical Investigations"

J. Phys. Chem. Lett. 2020, 11, 20, 8893–8900, https://doi.org/10.1021/acs.jpclett.0c02317

Publication 2

"Large Cation Engineering in Two-Dimensional Silver-Bismuth Bromide Double Perovskites"

Chem. Mater. 2021, 33, 12, 4688–4700, https://doi.org/10.1021/acs.chemmater.1c01182

Publication 3

"Tuning the optical properties of 2D monolayer silver-bismuth bromide double perovskite by halide substitution"

Nanotechnology 2022, 33, 215706, https://doi.org/10.1088/1361-6528/ac54df

Publication 4

Considerable co-authorship

"The Non-Innocent Role of Hole-Transporting Materials in Perovskite Solar Cells"

Sol. RRL 2021, 5, 10, 2100514, https://doi.org/10.1002/solr.202100514

Publication 5

Shared first authorship with Nicoló Lago

"High Open-Circuit Voltage $Cs_2AgBiBr_6$ Carbon-Based Perovskite Solar Cells via Green Processing of Ultrasonic Spray-Coated Carbon Electrodes from Waste Tire Sources"

ChemSusChem 2022, 15, 22, e202201590, https://doi.org/10.1002/cssc.202201590

Publication 6

"Heavy pnictogens-based perovskite-inspired materials: sustainable light-harvesters for indoor photovoltaics"

APL Energy 2023, 1, 021502, https://doi.org/10.1063/5.0161023

Publication 7

"Improved hole extraction and band alignment via interface modification in HTM-free Ag/Bi double perovskite solar cells"

Solar RRL 2024, 2300965, https://doi.org/10.1002/solr.202300965

4.1.1 Further publications as co-author

"Controlled Size Reduction of Liquid Exfoliated Graphene Micro-Sheets via Tip Sonication", *Crystals* 2020, 10, 11, 1049, https://doi.org/10.3390/cryst10111049

"Plasmon-Assisted Operando Self-Healing of Cu_2O Photocathodes", *Advanced Sustainable Systems* 2022, 7, 3, 2200397, https://doi.org/10.1002/adsu.202200397

"Transformation of Polarization Mechanisms by Dimensional Reduction in Lead-Free Silver Bismuth Bromide Double-Perovskite Thin Films", *ACS Applied Electronic Materials,* 2024, https://doi.org/10.1021/acsaelm.3c01451

4.2 Publication 1

Lanthanide-Induced Photoluminescence in Lead-Free $Cs_2AgBiBr_6$ Bulk Perovskite: Insights from Optical and Theoretical Investigations

Authors: **Fabian Schmitz**, Kunping Guo, Jonas Horn, Roberto Sorrentino, Gioele Conforto, Francesco Lamberti, Rosaria Brescia, Filippo Drago, Mirko Prato, Zhubing He, Umberto Giovanella, Franco Cacialli, Derck Schlettwein, Daniele Meggiolaro, Teresa Gatti

Before this work was published, $Cs_2AgBiBr_6$ was already reported to possess weak photoluminescence (PL): Zelewski *et al.* reported the PL emission to stem from a color center being effectively excited at an energy of 2.5 eV, while carriers that were excited by energies different from 2.5 eV relax to the respective valence band maximum (VBM) and conduction band minimum (CBM) and recombine non-radiatively.[221] Additionally, the strong broadening of the PL signal as well as the large Stokes shift of around 500 meV between PL and absorption originate from the material's already reported strong electron-phonon coupling.[32,221] Similar results of a strongly Stokes shifted and broad PL emission were reported by Schade *et al.* who suspected grain boundaries to be the origin of charge trapping and non-radiative recombination.[222] The doping of related materials $Cs_2Na_{1-x}Ag_xBiCl_6$,[223] and $Cs_2NaBi_{1-x}In_xCl_6$[224] with Mn^{2+} had already been reported to expand the PL emission by enabling Mn^{2+} emission[223,224] as well as the energy transfer from Mn^{2+} states towards self-trapped excitons (STEs) and the perovskite host.[223] Also, lanthanide doping had already been shown to improve the emission of LHPs.[225,226]

Accordingly, **publication 1** aims to introduce new radiative recombination centers to $Cs_2AgBiBr_6$ by doping the material with the lanthanides Yb^{3+} and Eu^{3+}. $Cs_2AgBiBr_6$ powders doped with the respective lanthanides are synthesized *via* a hydrothermal procedure. The powder is further used as the precursor for the spin-coating fabrication of thin films. Structural and compositional properties of the powders and thin films are analyzed via powder XRD (P-XRD), GIXRD, SEM, SEM-EDX, TEM, Raman spectroscopy and inductively coupled plasma – optical emission spectroscopy (ICP-OES). Optical analysis comprises UV-visible (UV-vis) absorption spectroscopy, steady-state PL, time-resolved PL (TR-PL), and PL excitation (PLE) spectroscopy. Although an initial molar ratio of up to 20% of Bi^{3+} is substituted with either Yb^{3+} or Eu^{3+} when mixing the stoichiometric amount of precursors for the hydrothermal synthesis, a maximum of 0.04% with respect to Bi^{3+} can be detected in the perovskite powder. No major structural changes stem from the small amount of incorporated lanthanides. However, not only the characteristic $Cs_2AgBiBr_6$ emission, centered at 2 eV,[221,222] is observed for each sample but also the appearance of additional PL signals for the Eu^{3+}-doped (centered at 1.30 eV) and the Yb^{3+}-doped (1.25 eV) perovskite. Notably, while the Yb^{3+} emission is characterized by a high intensity and can be assigned to the ion's

$^2F_{5/2} \rightarrow {}^2F_{7/2}$ transition at 1.25 eV, achieving a PL quantum yield (PLQY) of 28%, no characteristic transition can be assigned to the weak emission at 1.3 eV for Eu^{3+}. In combination with simulations from density functional theory (DFT), the differing emissive behaviors of the Eu^{3+}-doped and the Yb^{3+}-doped $Cs_2AgBiBr_6$ are revealed: The Yb^{3+} emission originates from an effective energy transfer from $Cs_2AgBiBr_6$ towards the dopant while the Eu^{3+} emission results from a trap-mediated process.

The work not only presents the fabrication of the first Yb-doped and Eu-doped Bi-based double perovskite thin films but also elaborates on the emission mechanism of Yb^{3+} in $Cs_2AgBiBr_6$ that has not been reported before. Thus, this work supports the utilization of stable, lead-free lanthanide-doped double perovskite thin films in near-infrared (NIR) emitting devices, i.e., NIR light-emitting diodes (LEDs) which have been reported after this work was published.[227–229] Furthermore, other groups reported improved PL quantum yields for Yb-doped $Cs_2AgBiBr_6$ thin films after the publication of this work by depositing the material *via* physical-vapor deposition.[142,143]

In addition to the *General Contributions*, all samples that were analyzed within this work were prepared by my student Gioele Conforto under my supervision and by me. I performed UV-Vis absorption spectroscopy, Raman spectroscopy, SEM, powder-XRD, thin film GIXRD, and SEM-EDX measurements, including the respective data processing.

THE JOURNAL OF PHYSICAL CHEMISTRY Letters

pubs.acs.org/JPCL Letter

Lanthanide-Induced Photoluminescence in Lead-Free $Cs_2AgBiBr_6$ Bulk Perovskite: Insights from Optical and Theoretical Investigations

Fabian Schmitz, Kunping Guo,⊕ Jonas Horn,⊕ Roberto Sorrentino, Gioele Conforto, Francesco Lamberti, Rosaria Brescia, Filippo Drago, Mirko Prato, Zhubing He, Umberto Giovanella, Franco Cacialli, Derck Schlettwein,* Daniele Meggiolaro,* and Teresa Gatti*

Cite This: J. Phys. Chem. Lett. 2020, 11, 8893−8900 Read Online

ACCESS | Metrics & More | Article Recommendations | Supporting Information

ABSTRACT: Emphasis was recently placed on the $Cs_2AgBiBr_6$ double perovskite as a possible candidate to substitute toxic lead in metal halide perovskites. However, its poor light-emissive features currently make it unsuitable for solid-state lighting. Lanthanide doping is an established strategy to implement luminescence in poorly emissive materials, with the additional advantage of fine-tuning the emission wavelength. We discuss here the impact of Eu and Yb doping on the optical properties of $Cs_2AgBiBr_6$ thin films, obtained from the solution processing of hydrothermally synthesized bulk crystalline powders, by combining experiments and density functional theory calculations. Eu(III) incorporation does not lead to the characteristic $^5D_0 \rightarrow {}^7F_2$ emission feature at 2 eV, while only a weak trap-assisted sub-band gap radiative emission is reported. Oppositely, we demonstrate that incorporated Yb(III) leads to an intense and exclusive photoluminescence emission in the near-infrared as a result of the efficient sensitization of the lanthanide $^2F_{5/2} \rightarrow {}^2F_{7/2}$ transition.

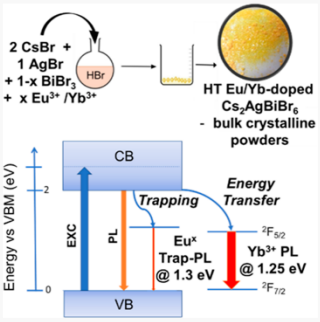

The development of lead-free halide perovskites for optoelectronic applications [solar cells, light-emitting diodes (LEDs), lasers, and photodetectors] is central to current materials research,[1−4] with the aim of finding valuable alternatives to lead-based perovskites currently leading the field. Lead halide perovskites (LHP) feature a problematic toxicity caused by lead and a limited environmental stability.[5] Double perovskite structures, containing pairs of cations in the +I and +III oxidation states in substitution of Pb^{2+}, are particularly appealing due to the impressive resistance to ambient stress (humidity, light, and heat). Among others, bismuth(III)-based compounds such as $Cs_2AgBiBr_6$ have been the subject of extensive investigations because of the excellent stability and low toxicity.[6−8] The optoelectronic properties of $Cs_2AgBiBr_6$ are, however, strongly limited by the indirect nature of the band gap, originated by the alternating Ag/Bi-based hexabromide octahedra in the lattice. The existence of a highly localized Bi-based optical transition with a pronounced excitonic character and strong electron−phonon coupling further limit the efficiency of the exciton separation and promote charge recombination in the material, as described in detail by some of us in previous work.[9] These drawbacks, in conjunction with the difficulties in obtaining good-quality thin films,[7,10,11] are the cause of the poor power conversion efficiency (generally below the 3% threshold) achieved up to now by $Cs_2AgBiBr_6$ as the photosensitizer in multilayered photovoltaic architectures.[12,13] The use of $Cs_2AgBiBr_6$ in an LED is also hampered by its poor photoluminescence (PL) properties caused by the nonradiative deactivation of injected electron−hole pairs.[14]

Lanthanide doping is a well-established strategy to improve the luminescence features of wide band gap inorganic semiconductors[15] and other hybrid solid-state materials,[16] with the possibility of tuning the emission wavelength. As the f-f transitions in lanthanides have normally very low absorption coefficients, crystalline host matrices play the role of sensitizers for boosting an efficient emission from these dopants. Lanthanide doping has been extensively applied also in low band gap halide perovskites to tune luminescence while maintaining excellent light-absorption and charge-transport properties. The success of this structural modification is ensured by the octahedral coordination that characterizes the metal ions in the perovskite lattice.[17,18] In particular, Eu(III) ions and Yb(III) have been employed to tune the PL of LHP nanocrystals in the visible and near-infrared (NIR) ranges, respectively, resulting in materials characterized by very narrow emission peaks typical of the lanthanide-based f-f electronic transitions and high values of the PL quantum yield (PLQY). Quantum cutting processes are associated with Yb doping in

Received: July 28, 2020
Accepted: September 30, 2020
Published: September 30, 2020

https://dx.doi.org/10.1021/acs.jpclett.0c02317
J. Phys. Chem. Lett. 2020, 11, 8893−8900

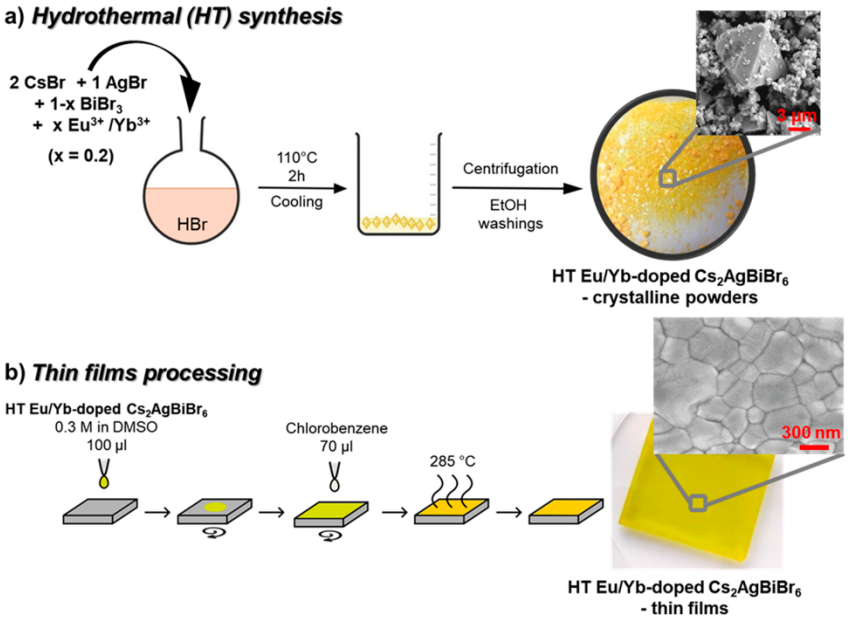

Figure 1. Synthesis, characterization, and thin-film processing of bulk Eu- and Yb-doped HT $Cs_2AgBiBr_6$. (a) Sketch of the HT synthesis process, with a picture and SEM image of a prototypical crystalline product. (b) Sketch of the antisolvent method used for the preparation of thin films, with a picture and top-view SEM image of a prototypical film.

lead halide perovskite nanocrystals,[19] a phenomenon for which a PLQY exceeding the ideal value of 100% is measured, thus prospecting application in devices such as NIR-LEDs, with great interest for biomedical applications. Yb doping has been recently implemented also in lead-free $Cs_2AgBiBr_6$ nanocrystals by Chen and co-workers, with dopant concentrations of up to 5%.[20] This process has led to the expected tuning of the PL behavior, with introduction of a narrow and intense PL at ~1.25 eV. These studies indicate that the activation of a Yb^{3+} ion emission is possible also in an indirect band gap halide perovskite. The successful sensitization of Yb(III) with the associated NIR emission has been also observed in porous silicon,[21] another indirect band gap semiconductor,[22] highlighting that the indirect nature of the band gap does not affect the emission properties of rare-earth dopants.

Despite their versatility and the generally high PLQY,[23] halide perovskite nanocrystals still find limited use in solid-state applications due to the difficulties in obtaining homogeneous layers employing standard solution-processing methods, coupled to the presence of surface defects, which quench PL and trap electrical charges diffusing across the film.[24−26]

In this work we explore the possibility of doping bulk $Cs_2AgBiBr_6$ with lanthanides so as to obtain easy-to-process and homogeneous thin films for light-emitting devices. The impact of Eu and Yb doping on the absorption and emission properties of $Cs_2AgBiBr_6$ polycrystalline thin films is evaluated through a combined experimental-computational approach. Our analysis shows that both Eu(III) and Yb(III) are incorporated in bulk $Cs_2AgBiBr_6$ and can be photoexcited through the electron transfer from the conduction band (CB) of the host perovskite to midgap unoccupied f orbitals. These defects, however, undergo different emissive decay channels. Eu(III) incorporation does not lead to the characteristic $^5D_0 \rightarrow {}^7F_2$ emission feature at ~2 eV but mainly decays through a trap-like recombination mechanism, while Yb(III) shows an intense emission in the NIR, as a result of the efficient sensitization of the lanthanide $^2F_{5/2} \rightarrow {}^2F_{7/2}$ transition.

$Cs_2AgBiBr_6$ is not normally processed into photoactive thin films by applying the typical protocols used for lead-based perovskites but requires a previous step of hydrothermal (HT) synthesis to produce its crystalline powder. Once isolated, the product is redissolved in a suitable solvent for halide perovskite processing [typically dimethyl sulfoxide (DMSO)] and then undergoes the same process employed for the lead-based analogues. Indeed, the simple direct mixing of the metal salt precursors (namely, CsBr, AgBr, and $BiBr_3$) in DMSO and subsequent processing does not generally provide phase-pure thin films of the $Cs_2AgBiBr_6$ double perovskite, as residual peaks of the components or other side phases (such as the bismuth perovskite $Cs_3Bi_2Br_9$) are often detected in the X-ray diffraction (XRD) profiles.[27]

The HT process used for the production of Eu(III)- and Yb(III)-doped $Cs_2AgBiBr_6$ is sketched in Figure 1a (details in the Experimental Section in the Supporting Information) and leads to two orange crystalline solids identical to the undoped $Cs_2AgBiBr_6$, containing crystals with sizes ranging from 500 nm to 6 μm (see also Figure S1 for a transmission electron microscopy image), with the typical octahedral shape of this compound.[12] Employing this synthetic method, we attempted substitution of the Bi^{3+} ions in the double perovskite lattice by either Eu^{3+} or Yb^{3+} up to 20% (the Goldschmidt tolerance factor is not expected to change significantly even at concentrations of these particular dopants up to 50%). In all cases, we could not achieve more than the 0.04% atomic substitution of Bi^{3+} with the lanthanides (as determined through elemental analysis; details in the Supporting

https://dx.doi.org/10.1021/acs.jpclett.0c02317
J. Phys. Chem. Lett. 2020, 11, 8893−8900

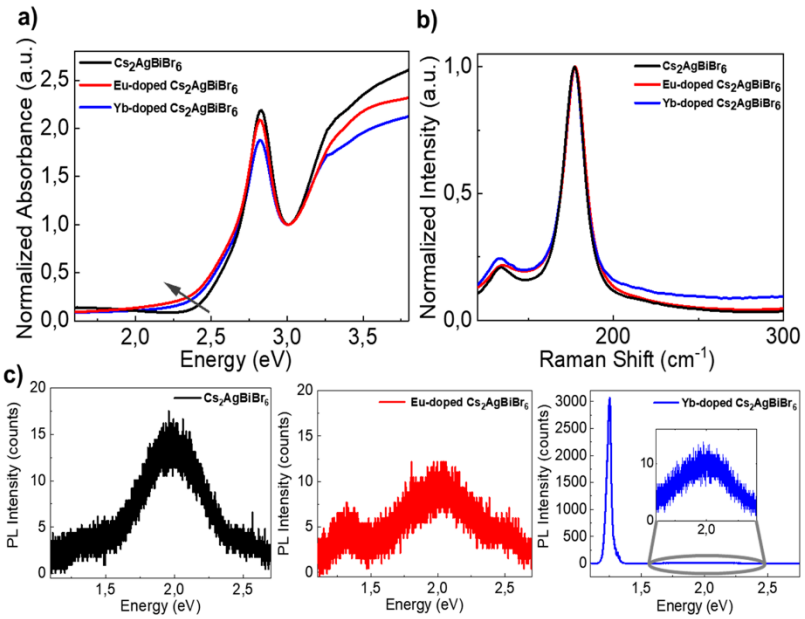

Figure 2. Optical properties of Eu- and Yb-doped $Cs_2AgBiBr_6$ thin films. (a) Normalized (at 3 eV) thin films absorption and (b) Raman spectra of Eu- and Yb-doped $Cs_2AgBiBr_6$ and of pristine $Cs_2AgBiBr_6$ (532 nm laser excitation). (c) Thin-film steady-state PL (excitation at 2.88 eV).

Information), pointing at a very low doping level in the final product.

The powder XRD of the Eu- and Yb-doped $Cs_2AgBiBr_6$ bulk crystalline powder is reported in Figure S2 of the Supporting Information indicating preparation of the undoped and doped materials in a constant crystal structure, without the presence of any additional compound, but of at least two phases characterized by a higher and lower symmetry. Detailed peak analysis of the (004) reflection at ~31° (the most intense one) was performed, showing that the signal is constituted of more than one single component (the same accounts for all the other peaks in the XRD powder pattern), due to the presence of at least two phases characterized by different symmetries. The results of this analysis are purely qualitative and are discussed in the Supporting Information.

Bulk doping through the HT method is apparently characterized by a dramatically lower doping efficiency compared to the nanocrystalline form of the material. Differences are likely associated with the dissimilar dimensionality of the host materials; that is, nanocrystals easily accommodate dopants by forming surface defects and the employed synthetic techniques. The lower doping in the present case can also be due to the high solubility of the lanthanide precursors we employed in HBr (the medium in which the HT reaction takes place).

For the preparation of thin films, the HT product is dissolved in DMSO, and this precursor solution is spin-coated, treated with an antisolvent,[28] and finally annealed to improve the crystallization, as depicted in Figure 1b. The preparation was adapted according to that of refs 9 and 29 and was further optimized with respect to a minimized surface roughness, as measured by confocal microscopy. Variation was performed for rotational speed during spin-coating, concentration of the precursor solution, atmosphere during film preparation, and choice of the antisolvent. The best results were obtained by following the procedure described in the experimental methods in the Supporting Information. Dissolved precursor materials in DMSO were investigated as an alternative precursor solution for thin-film preparation but yielded films of lower quality with smaller crystallites and residues of unreacted precursor materials, leading to additional XRD signals (Figure S3).

The optimized procedure based on dissolved HT product provides thin films with a thickness of 82 ± 5 nm measured by a profilometer and confirmed by scanning electron microscopy (SEM) cross sections (Figure S4), of high quality in terms of grain size (~280 nm) and absence of pinholes, as analyzed by a top-view SEM (inset of Figure 1b). Phase-pure $Cs_2AgBiBr_6$[27,30] is obtained in the films, pointing either at an effective recrystallization of the material upon reprecipitation and annealing that remove the low-symmetry component or at a superposition of the signals within broadened peaks (Figure S3). Furthermore, in SEM-energy-dispersive X-ray (EDX) spectra of the Eu-doped thin film, a very weak signal of Eu was even detected (Figure S5).

To track the possible variations of charge distribution within the band structure of the double perovskite following lanthanide doping, the work function (WF) of the thin films was extracted employing Kelvin probe force microscopy (KPFM) (Figure S6). While the WF value of undoped $Cs_2AgBiBr_6$ is found at 5.07 eV, in agreement with previous reports on $Cs_2AgBiBr_6$ highly crystalline thin films,[10] a 50 meV shift toward smaller values (higher Fermi level) is found for the Eu-doped sample (a small variation is found also for the Yb-doped one, i.e., a small broadening of the overall Gaussian distribution at the lower energy limit). These findings indicate a slight variation of the Fermi level due to the introduction of defects[31] in the double perovskite structure following lanthanide doping.

https://dx.doi.org/10.1021/acs.jpclett.0c02317
J. Phys. Chem. Lett. 2020, 11, 8893−8900

The presence of defects appears more clearly when examining the UV−visible absorption features of the thin films of the lanthanide-doped compared to undoped $Cs_2AgBiBr_6$ reported in Figure 2a. The three absorption spectra do not differ significantly, except for the indicated (dark gray arrow) increase of the absorbance at low energy (from 2.7 eV to almost 2.0 eV) in the two doped samples, indicating an increased density of sub-band gap defect states compared to the undoped semiconductor. As it can be further observed from these spectra, a strong exciton peak centered at 2.83 eV is detected for all the samples, which has been also attributed to a direct s-p electronic transition centered on bismuth[10,32] (the real origin is still under heated debate[33,34]) and can be seen as a highly localized excitation that does not contribute significantly to the photogeneration of charges in the thin film.[9] The intense (and dominant) Raman mode centered at 177 cm^{-1} is strongly related to this excitonic feature and is maintained after doping (Figure 2b, in full agreement with previous literature data[9,35]).

While the impact of the Eu/Yb-doping in $Cs_2AgBiBr_6$ is not significant in the optical properties of the thin films in terms of light absorption (no features ascribable to the direct excitation of lanthanide-based transitions are detected in the spectra in Figure 2a), significant differences emerge when the emissive behaviors are analyzed. The steady-state PL behavior of the undoped, Eu-doped, and Yb-doped thin films of $Cs_2AgBiBr_6$ (Figure 2) has been measured, with a view to detecting the specific emission features from lanthanide dopants in the crystal lattice.[17] The PL of pristine $Cs_2AgBiBr_6$ consists of the broad/weak emission with a large Stokes shift observed earlier (also indicated as a sign of the strong electron−phonon coupling in this material[14]) centered at ∼2 eV (black curve in Figure 2a), which in earlier works was assigned either to an emission from self-trapped excitons[9] or to a color center.[14] After doping the bulk double perovskite with Eu^{3+} ions, no emissive peaks typical of this lanthanide(III) ion (with the most intense $^5D_0 \rightarrow {}^7F_2$ at 2 eV) are observed in response to the photoexcitation of the perovskite matrix.[17,18] On the contrary, an apparently weaker emission of the pristine double perovskite compared to the undoped sample (fair comparison has been done between absorption values and measurements to make the PL intensities among all the thin films comparable) at 2 eV is found, accompanied by a second, even weaker peak at 1.3 eV, which cannot be traced back to any typical Eu PL feature. The PL lifetime of the double perovskite is also considerably reduced (details in the Supporting Information Figure S7). The weak PL signal at 1.3 eV could likely originate from deep defects within the band gap of $Cs_2AgBiBr_6$ as a consequence of Eu-doping and, therefore, could be seen as a sign of a trap-mediated recombination pathway.[36]

Doping with Yb(III) is expected to generate a sharp PL peak in the NIR at ∼1.25 eV (1000 nm), as a result of the $^2F_{5/2} \rightarrow {}^2F_{7/2}$ transition typical of this ion, as it has been seen before in analogous nanocrystal systems.[20] Such a peak is actually present, and it is characterized by an extremely high intensity compared to the native PL of the double perovskite at 2 eV, as it can be observed from Figure 2c (blue curve). The intensity ratio between these two PL contributions in the spectrum is on the order of 300:1. Notably, for the Yb-doped $Cs_2AgBiBr_6$ nanocrystals described by Chen and co-workers,[20] the native PL of the double perovskite was always significant even at the highest 5% doping concentration reported there, and the maximum ratio achieved for the Yb-based peak relative to the double perovskite signal did not surpass the 2.5:1 ratio for the best case (at 2.9% Yb). Our data seem to indicate therefore that the Yb-dopant sensitization process (an energy-transfer process from the photoexcited perovskite sensitizer to the lanthanide-based emissive centers) is much more efficient in the present thin films based on HT-synthesized bulk material than in nanocrystals. Remarkably, a PLQY of 28% (±3%) is determined for the Yb-doped $Cs_2AgBiBr_6$ thin films, with a net improvement from what was found by Hoye et al.[37] for undoped $Cs_2AgBiBr_6$ thin films (0.02%). This is, to the best of our knowledge, the first report on the PLQY extent in Yb-doped $Cs_2AgBiBr_6$ species, since for the case of nanocrystals previously discussed[20] this information was not provided.

We performed a more detailed optical analysis of the NIR emission profile of the Yb-doped $Cs_2AgBiBr_6$ thin film by probing how the NIR-PL intensity varies as a function of the excitation wavelength. As it can be deduced from the excitation-PL three-dimensional (3D) map reported in Figure 3a and from the relative photoluminescence excitation (PLE) spectrum in Figure 3b (comparison with absorption is included for the sake of clarity), the maximum emission from the Yb(III) ions is achieved at an excitation energy of 2.58 eV, and a second maximum of slightly minor intensity is also found at 3.02 eV. Between these two maxima is located a valley, with a minimum at ∼2.8 eV, which is exactly the absorption energy

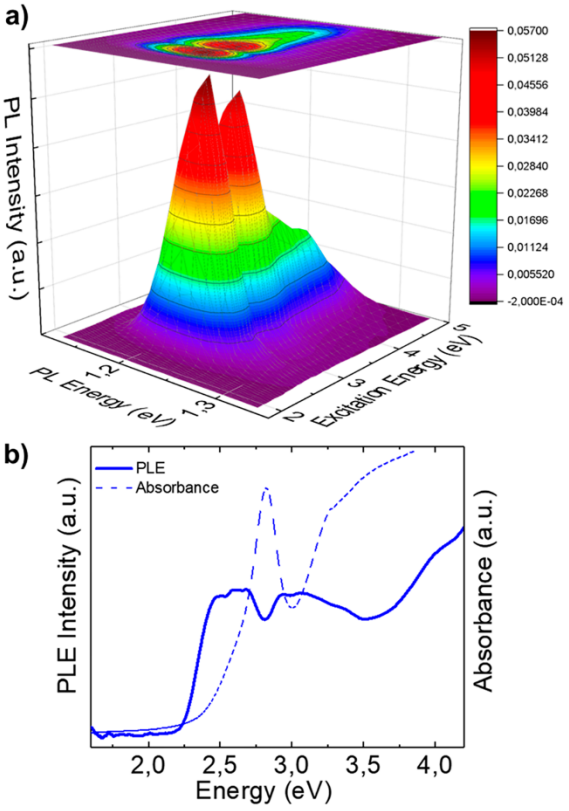

Figure 3. (a) Excitation-NIR PL 3D map of a Yb-doped $Cs_2AgBiBr_6$ thin film and (b) corresponding PLE spectrum and comparison with absorption (dashed line).

https://dx.doi.org/10.1021/acs.jpclett.0c02317
J. Phys. Chem. Lett. 2020, 11, 8893−8900

corresponding to the exciton peak seen in the absorption profile. This behavior was reported previously by Zelewski et al.[14] for the pure $Cs_2AgBiBr_6$ double perovskite single crystal and was interpreted as a further indication of the neutral character of the exciton-centered transition, which does not contribute to generate charges or to populate emissive trap states. It is therefore reasonable to believe that the present case provides further strength to this assumption, as also energy-transfer processes between the exciton of the host semiconductor and the lanthanide dopants seem to be inefficient. A maximum of light emission is, instead, obtained when exciting in the low-energy absorption edge (starting at 2.25 eV). As the relative absorption cross section at these energies is very low (dashed line), it indicates that (i) the population of the Yb states out of them occurs very efficiently and (ii) the optical transition to these states must be strongly forbidden, and they could be associated with those sub-band gap states characteristic of the absorption profile. It is worth mentioning that such a feature has been also found by Zelewski et al. for the undoped double perovskite.[14] The second plateau of the PLE spectrum (and of the excitation/NIR-PL 3D map), which resides in the 2.9−3.1 eV range, was indicated by some of us[9] as the absorption edge of a direct electronic transition in $Cs_2AgBiBr_6$ occurring at 3.2 eV and extrapolated from the relative Tauc plot by applying the formula for direct band gaps.

The effects of Yb and Eu doping on the electronic properties of $Cs_2AgBiBr_6$ have been investigated by density functional theory (DFT), by using the hybrid PBE0 functional (see Computational Details in the Supporting Information).[38,39] Substitutional doping of Eu and Yb at the Bi site has been modeled by simulating dopant densities of ∼3%. In pristine $Cs_2AgBiBr_6$ Bi^{3+} ions are octahedrally coordinated by six Br^- at a distance of 2.85 Å. Upon Eu^{3+} incorporation to form the Eu_{Bi}^0 defect an asymmetric contraction of the lanthanide−bromide bond lengths in the octahedron unit is reported to values between 2.80 and 2.82 Å (Figure 4b). The decreased bond length is ascribed to the smaller Eu^{3+} ionic radius of 109 pm compared to 117 pm for Bi^{3+}, as stated previously. A more pronounced contraction of the bond to Br^- to values of 2.72−2.75 Å was determined for the Yb^{3+} incorporation, that is, the Yb_{Bi}^0 defect, showing an ionic radius even smaller than that of Eu^{3+}, that is, 101 pm (Figure 4e).

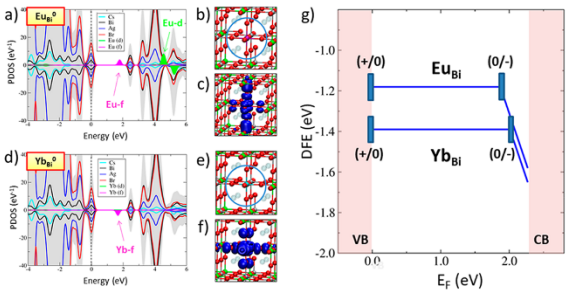

Figure 4. (a) PDOS of Eu substituting Bi in the neutral state of charge, i.e., Eu_{Bi}^0, the top of the VB was set to zero energy. (b) Optimized structure of Eu_{Bi}^0 (Bi = green; Ag = gray; Br = red; Eu = purple; Yb = cyan); (c) plot of the Eu_{Bi}^0 lowest unoccupied molecular orbital (LUMO) single-particle orbital associated with the unoccupied f-state in the band gap of diagram 1a. (d) PDOS of the Yb_{Bi}^0 system. (e) Optimized structure and (f) plot of the Yb_{Bi}^0 LUMO single-particle orbital. (g) Defect formation energies and ionization levels of Eu_{Bi} and Yb_{Bi} defects in the $Cs_2BiAgBr_6$ band gap, highlighting that electrons can be trapped through the deep (0/−) transitions, sensitizing the dopants.

The projected density of states (PDOS) of the Eu- and Yb-doped $Cs_2AgBiBr_6$ perovskite are reported in Figure 4a,d. Eu_{Bi}^0 and Yb_{Bi}^0 show f^6 and f^{13} electronic configurations and introduce unoccupied f-states into the band gap of $Cs_2AgBiBr_6$, placed at 1.70 and 1.59 eV above the valence band (VBM), respectively, with a negligible impact on the band gap of the host perovskite (2.27 eV at the PBE0 level of theory). These single-particle states are spatially localized on the dopants, as confirmed by the plot of the associated wave functions, reported in Figure 4c,f. The emergence of unoccupied f-states within the band gap indicates that dopant sensitization may occur through the vertical transitions of photoexcited electrons from the conduction band (CB) of the host perovskite to the midgap f-orbitals of the dopants.

The defect formation energies (DFE) and thermodynamic ionization levels (TIL) of Eu_{Bi} and Yb_{Bi} defects in different states of charge are reported in Figure 4g. The DFEs were estimated by considering a metal exchange between the $EuCl_3$, $YbCl_3$, and $BiCl_3$ molecules in the gas phase and the pristine perovskite. The DFE diagram in Figure 4g shows that Eu_{Bi} and Yb_{Bi} defects are mainly stable in the neutral form (+III oxidation state) in the $Cs_2AgBiBr_6$ band gap. Favorable substitutional energies of −1.18 and −1.39 eV for Eu_{Bi}^0 and Yb_{Bi}^0 were calculated, respectively, highlighting that the Yb doping is slightly more favored than Eu doping. Eu_{Bi} and Yb_{Bi} show deep (0/−) transitions in the n-doped region of the diagrams placed at 1.87 and 2.01 eV above the VBM, respectively. This indicates that the +II oxidation state of the dopants is thermodynamically stable only in heavily n-doped perovskites. Upon electron trapping on the Eu_{Bi}^0 and Yb_{Bi}^0 centers to form Eu_{Bi}^- and Yb_{Bi}^-, an increase of the Eu−Br and Yb−Br bond lengths to values of 2.92 and 2.80−2.84 Å is observed, respectively. In both cases a remarkable upshift in energy of the occupied f-levels within the host perovskite band gap is reported (Figure S8). On the other hand, (+/0) transitions, associated with the introduction of one hole in the supercells, are only shallow. Holes are delocalized in the VB of doped perovskite and cannot be trapped at the Eu and Yb sites, which are stable only in the +III oxidation state in the Fermi level range delimited by the VBM and the (0/−) transition.

Defect analysis suggests that Eu and Yb dopants, once incorporated in a substitutional position to Bi, can be activated upon photoexcitation through the electron trapping on the empty f-orbitals placed in the band gap. Relaxation of the excited dopant may occur through a recombination of the trapped electron with hole in the VB or through a more complex mechanism involving the electron release and the conversion to form the neutral excited state of the dopant. To predict the possible trap-assisted emission from the defects, that is, the recombination of a trapped electron with hole in the VB, the configuration diagrams of the ground and excited states of Eu_{Bi} and Yb_{Bi} were calculated, and they are reported in Figure S9 of the Supporting Information. Radiative emissions at 1.44 and 1.77 eV are calculated for Eu and Yb, respectively. On the one hand, the calculated emission at 1.44 eV for Eu-doped double perovskite is in close agreement with the weak PL peak at ∼1.3 eV observed in optical experiments; thus, the origin of this PL feature may be ascribed to a trap-mediated process involving the trapping of the electron with the subsequent recombination with hole in the VB. On the other

https://dx.doi.org/10.1021/acs.jpclett.0c02317
J. Phys. Chem. Lett. 2020, 11, 8893−8900

hand, no subgap emissive transition at ~1.7 eV was observed in the Yb-doped perovskite, suggesting that the activated Yb_{Bi}^{-} mainly rearranges to form the $F_{5/2}$ neutral excited state by releasing the trapped electron to the CB and decaying with the characteristic emission at 1.25 eV observed in the PL (Figure 2c, blue line). Such a mechanism is partially justified by the higher optical (0/−) transition of Yb_{Bi} compared to Eu_{Bi}, exceeding the $Cs_2BiAgBr_6$ band gap (see Figure S9). The recombination of trapped electrons with background holes, however, remains a competitive deactivation channel possibly reducing the PL efficiency of the f-f transition.

On the basis of the experimental and theoretical evidence, a Jablonski diagram is proposed as the one reported in Figure 5,

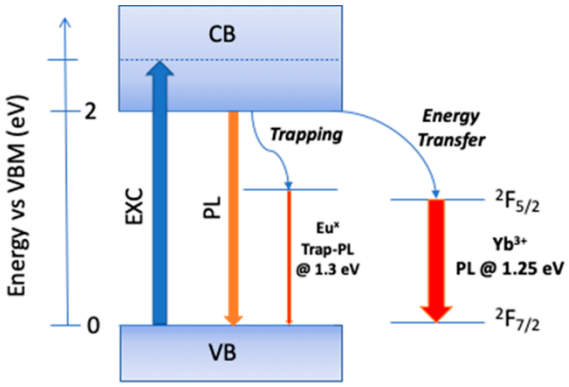

Figure 5. Jablonski diagram depicting the excited state deactivation processes happening in undoped, Eu-, and Yb-doped $Cs_2AgBiBr_6$ thin films. Here CBM is taken at an energy corresponding to the PL maximum of the $Cs_2AgBiBr_6$ thin film, while the excitation (thick blue line) is indicated to take place at a general energy (dashed line in the CB) higher than the energy of the CBM, given the pronounced Stokes shift existing between absorption and emission profiles in the undoped double perovskite. The thickness of the three PL lines (orange to red) is proportional to the relative intensity of the indicated transitions.

depicting the process of lanthanide dopant activation after light excitation of the double perovskite. In this diagram it is shown, together with the native and relatively weak PL of the undoped double perovskite, also the very weak PL originated by the trapping of photoexcited electrons in the Eu-generated deep defects in the band gap and, oppositely, the more efficient energy transfer to the NIR-emissive $^2F_{5/2} \rightarrow {}^2F_{7/2}$ transition of the Yb^{3+} ions.

In conclusion, we have shown that Yb(III) doping in thin films of the lead-free $Cs_2AgBiBr_6$ double perovskite that are processed from the bulk HT powder material can lead to the detection of a narrow and unique PL signal located in the NIR. This points out an efficient energy transfer from the photoexcited double perovskite host to the rare-earth guest that was not observed before in similar nanocrystal systems. We have also provided theoretical insights on the lanthanide-sensitization process, which will be extremely useful for designing future doping strategies in lead-free double perovskites. We believe that the bulk Yb-doped $Cs_2AgBiBr_6$ thin films described in this work hold great promise for the future realization of NIR-emissive solid-state devices after further optimization of the doping level and overall layer quality,[7] as they are easy to process and feature a unique and well-defined emission profile.

■ ASSOCIATED CONTENT

Supporting Information

The Supporting Information is available free of charge at https://pubs.acs.org/doi/10.1021/acs.jpclett.0c02317.

Experimental and computational details; results from analytical and structural characterization (elemental analysis, XRD, TEM, SEM); KPFM data; time-resolved photoluminescence data; additional details from DFT calculations (PDF)

■ AUTHOR INFORMATION

Corresponding Authors

Teresa Gatti − *Center for Materials Research (LaMa) and Institute of Physical Chemistry, Justus Liebig University, 35392 Giessen, Germany;* orcid.org/0000-0001-5343-8055; Email: teresa.gatti@phys.chemie.uni-giessen.de

Daniele Meggiolaro − *Computational Laboratory for Hybrid/Organic Photovoltaics, Istituto CNR di Scienze e Tecnologie Chimiche "Giulio Natta", 06123 Perugia, Italy;* orcid.org/0000-0001-9717-133X; Email: daniele.meggiolaro@cnr.it

Derck Schlettwein − *Center for Materials Research (LaMa) and Institute of Applied Physics, Justus Liebig University, 35392 Giessen, Germany;* orcid.org/0000-0002-3446-196X; Email: derck.schlettwein@app.phys.uni-giessen.de

Authors

Fabian Schmitz − *Center for Materials Research (LaMa) and Institute of Physical Chemistry, Justus Liebig University, 35392 Giessen, Germany*

Kunping Guo − *Department of Physics and Astronomy and London Center for Nanotechnology, University College London, WC1E 6BT London, United Kingdom*

Jonas Horn − *Center for Materials Research (LaMa) and Institute of Applied Physics, Justus Liebig University, 35392 Giessen, Germany*

Roberto Sorrentino − *Istituto CNR di Scienze e Tecnologie Chimiche "Giulio Natta", 20133 Milano, Italy*

Gioele Conforto − *Institute of Physical Chemistry and Institute of Applied Physics, Justus Liebig University, 35392 Giessen, Germany*

Francesco Lamberti − *Department of Chemical Sciences, University of Padova, 35131 Padova, Italy*

Rosaria Brescia − *Electron Microscopy Facility, Istituto Italiano di Tecnologia, 16163 Genova, Italy;* orcid.org/0000-0003-0607-0627

Filippo Drago − *Materials Characterization Facility, Istituto Italiano di Tecnologiass, 16163 Genova, Italy*

Mirko Prato − *Materials Characterization Facility, Istituto Italiano di Tecnologiass, 16163 Genova, Italy;* orcid.org/0000-0002-2188-8059

Zhubing He − *Department of Materials Science and Engineering, Shenzhen Key Laboratory of Full Spectral Solar Electricity Generation, Southern University of Science and Technology, 518055 Shenzhen, Guangdong, China;* orcid.org/0000-0002-2775-0894

Umberto Giovanella − *Istituto CNR di Scienze e Tecnologie Chimiche "Giulio Natta", 20133 Milano, Italy;* orcid.org/0000-0003-2865-050X

https://dx.doi.org/10.1021/acs.jpclett.0c02317
J. Phys. Chem. Lett. 2020, 11, 8893−8900

Franco Cacialli − *Department of Physics and Astronomy and London Center for Nanotechnology, University College London, WC1E 6BT London, United Kingdom;* orcid.org/0000-0001-6821-6578

Complete contact information is available at: https://pubs.acs.org/10.1021/acs.jpclett.0c02317

Author Contributions

⊕(K.-P.G. and J.H.) These two authors contributed equally.

Notes

The authors declare no competing financial interest.

■ ACKNOWLEDGMENTS

F.S., J.H., D.S., and T.G. acknowledge the DFG for financial support via the Research Training Group 2204 "Substitute Materials for Sustainable Energy Technologies". K.G. acknowledges funding from the Royal Society through a Newton International Fellowship. F.L. thanks the Centre Giorgio Levi Cases for Energy Economics and Technology of the University of Padova for the project "AMON-RA". F.C. acknowledges the Royal Society for the award of a Wolfson Foundation Research Merit Award. We thank Prof. L. Franco for insightful discussion.

■ REFERENCES

(1) Wang, R.; Wang, J.; Tan, S.; Duan, Y.; Wang, Z.-K.; Yang, Y. Opportunities and Challenges of Lead-Free Perovskite Optoelectronic Devices. *Trends Chem.* **2019**, *1* (4), 368−379.

(2) Wang, X.; Zhang, T.; Lou, Y.; Zhao, Y. All-Inorganic Lead-Free Perovskites for Optoelectronic Applications. *Mater. Chem. Front.* **2019**, *3* (3), 365−375.

(3) Yu, B.-B.; Liao, M.; Zhu, Y.; Zhang, X.; Du, Z.; Jin, Z.; Liu, D.; Wang, Y.; Gatti, T.; Ageev, O.; et al. Oriented Crystallization of Mixed-Cation Tin Halides for Highly Efficient and Stable Lead-Free Perovskite Solar Cells. *Adv. Funct. Mater.* **2020**, *30* (24), 2002230.

(4) Ke, W.; Kanatzidis, M. G. Prospects for Low-Toxicity Lead-Free Perovskite Solar Cells. *Nat. Commun.* **2019**, *10* (1), 965.

(5) Li, J.; Cao, H.-L.; Jiao, W.-B.; Wang, Q.; Wei, M.; Cantone, I.; Lü, J.; Abate, A. Biological Impact of Lead from Halide Perovskites Reveals the Risk of Introducing a Safe Threshold. *Nat. Commun.* **2020**, *11* (1), 310.

(6) Zhang, L.; Wang, K.; Zou, B. Bismuth Halide Perovskite-Like Materials: Current Opportunities and Challenges. *ChemSusChem* **2019**, *12* (8), 1612−1630.

(7) Jin, Z.; Zhang, Z.; Xiu, J.; Song, H.; Gatti, T.; He, Z. A Critical Review on Bismuth and Antimony Halides Based Perovskites and Derivatives for Photovoltaic Applications: Recent Advances and Challenges. *J. Mater. Chem. A* **2020**, *8* (32), 16166−16188.

(8) Liu, D.; Yu, B.-B.; Liao, M.; Jin, Z.; Zhou, L.; Zhang, X.; Wang, F.; He, H.; Gatti, T.; He, Z. Self-Powered and Broadband Lead-Free Inorganic Perovskite Photodetector with High Stability. *ACS Appl. Mater. Interfaces* **2020**, *12* (27), 30530−30537.

(9) Kentsch, R.; Scholz, M.; Horn, J.; Schlettwein, D.; Oum, K.; Lenzer, T. Exciton Dynamics and Electron−Phonon Coupling Affect the Photovoltaic Performance of the $Cs_2AgBiBr_6$ Double Perovskite. *J. Phys. Chem. C* **2018**, *122* (45), 25940−25947.

(10) Xiu, J.; Shao, Y.; Chen, L.; Feng, Y.; Dai, J.; Zhang, X.; Lin, Y.; Zhu, Y.; Wu, Z.; Zheng, Y.; et al. Defining the Composition and Electronic Structure of Large-Scale and Single-Crystalline like Cs2AgBiBr6 Films Fabricated by Capillary-Assisted Dip-Coating Method. *Mater. Today Energy* **2019**, *12*, 186−197.

(11) Wu, C.; Zhang, Q.; Liu, Y.; Luo, W.; Guo, X.; Huang, Z.; Ting, H.; Sun, W.; Zhong, X.; Wei, S.; et al. The Dawn of Lead-Free Perovskite Solar Cell: Highly Stable Double Perovskite Cs2AgBiBr6 Film. *Adv. Sci.* **2018**, *5* (3), 1700759.

(12) Gao, W.; Ran, C.; Xi, J.; Jiao, B.; Zhang, W.; Wu, M.; Hou, X.; Wu, Z. High-Quality $Cs_2AgBiBr_6$ Double Perovskite Film for Lead-Free Inverted Planar Heterojunction Solar Cells with 2.2% Efficiency. *ChemPhysChem* **2018**, *19* (14), 1696−1700.

(13) Igbari, F.; Wang, R.; Wang, Z.-K.; Ma, X.-J.; Wang, Q.; Wang, K.-L.; Zhang, Y.; Liao, L.-S.; Yang, Y. Composition Stoichiometry of $Cs_2AgBiBr_6$ Films for Highly Efficient Lead-Free Perovskite Solar Cells. *Nano Lett.* **2019**, *19* (3), 2066−2073.

(14) Zelewski, S. J.; Urban, J. M.; Surrente, A.; Maude, D. K.; Kuc, A.; Schade, L.; Johnson, R. D.; Dollmann, M.; Nayak, P. K.; Snaith, H. J.; et al. Revealing the Nature of Photoluminescence Emission in the Metal-Halide Double Perovskite $Cs_2AgBiBr_6$. *J. Mater. Chem. C* **2019**, *7* (27), 8350−8356.

(15) Kumar, V.; Ntwaeaborwa, O. M.; Soga, T.; Dutta, V.; Swart, H. C. Rare Earth Doped Zinc Oxide Nanophosphor Powder: A Future Material for Solid State Lighting and Solar Cells. *ACS Photonics* **2017**, *4* (11), 2613−2637.

(16) Heine, J.; Müller-Buschbaum, K. Engineering Metal-Based Luminescence in Coordination Polymers and Metal−Organic Frameworks. *Chem. Soc. Rev.* **2013**, *42* (24), 9232−9242.

(17) Mir, W. J.; Sheikh, T.; Arfin, H.; Xia, Z.; Nag, A. Lanthanide Doping in Metal Halide Perovskite Nanocrystals: Spectral Shifting, Quantum Cutting and Optoelectronic Applications. *NPG Asia Mater.* **2020**, *12* (1), 9.

(18) Righetto, M.; Meggiolaro, D.; Rizzo, A.; Sorrentino, R.; He, Z.; Meneghesso, G.; Sum, T. C.; Gatti, T.; Lamberti, F. Coupling Halide Perovskites with Different Materials: From Doping to Nanocomposites, beyond Photovoltaics. *Prog. Mater. Sci.* **2020**, *110*, 100639.

(19) Milstein, T. J.; Kroupa, D. M.; Gamelin, D. R. Picosecond Quantum Cutting Generates Photoluminescence Quantum Yields Over 100% in Ytterbium-Doped CsPbCl3 Nanocrystals. *Nano Lett.* **2018**, *18* (6), 3792−3799.

(20) Chen, N.; Cai, T.; Li, W.; Hills-Kimball, K.; Yang, H.; Que, M.; Nagaoka, Y.; Liu, Z.; Yang, D.; Dong, A.; et al. Yb- and Mn-Doped Lead-Free Double Perovskite Cs_2AgBiX_6 (X = Cl−, Br−) Nanocrystals. *ACS Appl. Mater. Interfaces* **2019**, *11* (18), 16855−16863.

(21) Kimura, T.; Yokoi, A.; Nishida, Y.; Saito, R.; Yugo, S.; Ikoma, T. Photoluminescence of Ytterbium-doped Porous Silicon. *Appl. Phys. Lett.* **1995**, *67* (18), 2687−2689.

(22) Iyer, S. S.; Xie, Y.-H. Light Emission from Silicon. *Science* **1993**, *260* (5104), 40−46.

(23) Adjokatse, S.; Fang, H.-H.; Loi, M. A. Broadly Tunable Metal Halide Perovskites for Solid-State Light-Emission Applications. *Mater. Today* **2017**, *20* (8), 413−424.

(24) Yan, F.; Demir, H. V. LEDs Using Halide Perovskite Nanocrystal Emitters. *Nanoscale* **2019**, *11* (24), 11402−11412.

(25) Yan, F.; Tan, S. T.; Li, X.; Demir, H. V. Light Generation in Lead Halide Perovskite Nanocrystals: LEDs, Color Converters, Lasers, and Other Applications. *Small* **2019**, *15* (47), 1902079.

(26) Lamberti, F.; Litti, L.; De Bastiani, M.; Sorrentino, R.; Gandini, M.; Meneghetti, M.; Petrozza, A. High-Quality, Ligands-Free, Mixed-Halide Perovskite Nanocrystals Inks for Optoelectronic Applications. *Adv. Energy Mater.* **2017**, *7* (8), 1601703.

(27) Greul, E.; Petrus, M. L.; Binek, A.; Docampo, P.; Bein, T. Highly Stable, Phase Pure Cs2AgBiBr6 Double Perovskite Thin Films for Optoelectronic Applications. *J. Mater. Chem. A* **2017**, *5* (37), 19972−19981.

(28) Jeon, N. J.; Noh, J. H.; Kim, Y. C.; Yang, W. S.; Ryu, S.; Seok, S. Il. Solvent Engineering for High-Performance Inorganic−Organic Hybrid Perovskite Solar Cells. *Nat. Mater.* **2014**, *13* (9), 897−903.

(29) Pantaler, M.; Cho, K. T.; Queloz, V. I. E.; García Benito, I.; Fettkenhauer, C.; Anusca, I.; Nazeeruddin, M. K.; Lupascu, D. C.; Grancini, G. Hysteresis-Free Lead-Free Double-Perovskite Solar Cells by Interface Engineering. *ACS Energy Lett.* **2018**, *3* (8), 1781−1786.

(30) McClure, E. T.; Ball, M. R.; Windl, W.; Woodward, P. M. Cs_2AgBiX_6 (X = Br, Cl): New Visible Light Absorbing, Lead-Free Halide Perovskite Semiconductors. *Chem. Mater.* **2016**, *28* (5), 1348−1354.

https://dx.doi.org/10.1021/acs.jpclett.0c02317
J. Phys. Chem. Lett. 2020, 11, 8893−8900

(31) Ono, L. K.; Liu, S.; Qi, Y. Reducing Detrimental Defects for High-Performance Metal Halide Perovskite Solar Cells. *Angew. Chem., Int. Ed.* **2020**, *59* (17), 6676−6698.
(32) Bekenstein, Y.; Dahl, J. C.; Huang, J.; Osowiecki, W. T.; Swabeck, J. K.; Chan, E. M.; Yang, P.; Alivisatos, A. P. The Making and Breaking of Lead-Free Double Perovskite Nanocrystals of Cesium Silver−Bismuth Halide Compositions. *Nano Lett.* **2018**, *18* (6), 3502−3508.
(33) Dey, A.; Richter, A. F.; Debnath, T.; Huang, H.; Polavarapu, L.; Feldmann, J. Transfer of Direct to Indirect Bound Excitons by Electron Intervalley Scattering in $Cs_2AgBiBr_6$ Double Perovskite Nanocrystals. *ACS Nano* **2020**, *14* (5), 5855−5861.
(34) Longo, G.; Mahesh, S.; Buizza, L. R. V; Wright, A. D.; Ramadan, A. J.; Abdi-Jalebi, M.; Nayak, P. K.; Herz, L. M.; Snaith, H. J. Understanding the Performance Limiting Factors of $Cs_2AgBiBr_6$ Double-Perovskite Solar Cells. *ACS Energy Lett.* **2020**, *5*, 2200.
(35) Slavney, A. H.; Hu, T.; Lindenberg, A. M.; Karunadasa, H. I. A Bismuth-Halide Double Perovskite with Long Carrier Recombination Lifetime for Photovoltaic Applications. *J. Am. Chem. Soc.* **2016**, *138* (7), 2138−2141.
(36) Motti, S. G.; Gandini, M.; Barker, A. J.; Ball, J. M.; Srimath Kandada, A. R.; Petrozza, A. Photoinduced Emissive Trap States in Lead Halide Perovskite Semiconductors. *ACS Energy Lett.* **2016**, *1*, 726−730.
(37) Hoye, R. L. Z.; Eyre, L.; Wei, F.; Brivio, F.; Sadhanala, A.; Sun, S.; Li, W.; Zhang, K. H. L.; MacManus-Driscoll, J. L.; Bristowe, P. D.; et al. Fundamental Carrier Lifetime Exceeding 1 μs in $Cs_2AgBiBr_6$ Double Perovskite. *Adv. Mater. Interfaces* **2018**, *5* (15), 1800464.
(38) Adamo, C.; Barone, V. Toward Reliable Density Functional Methods without Adjustable Parameters: The PBE0Model. *J. Chem. Phys.* **1999**, *110* (13), 6158−6170.
(39) Perdew, J. P.; Ernzerhof, M.; Burke, K. Rationale for Mixing Exact Exchange with Density Functional Approximations. *J. Chem. Phys.* **1996**, *105*, 9982−9985.

https://dx.doi.org/10.1021/acs.jpclett.0c02317
J. Phys. Chem. Lett. 2020, 11, 8893−8900

Supporting Information for:

Lanthanide Induced Photoluminescence in Lead-Free $Cs_2AgBiBr_6$ Bulk Perovskite: Insights from Optical and Theoretical Investigations

Fabian Schmitz,[1,2] Kunping Guo,[3] Jonas Horn,[1,4] Roberto Sorrentino,[5] Gioele Conforto,[2,4] Francesco Lamberti,[6] Rosaria Brescia,[7] Filippo Drago,[8] Mirko Prato,[8] Zhubing He,[9] Umberto Giovanella,[5] Franco Cacialli,[3] Derck Schlettwein,[1,4]* Daniele Meggiolaro,[10]* Teresa Gatti[1,2]*

[1] Center for Materials Research (LaMa), Justus Liebig University, Heinrich Buff Ring 16, 35392 Giessen, Germany

[2] Institute of Physical Chemistry, Justus Liebig University, Heinrich Buff Ring 17, 35392 Giessen, Germany

[3] Department of Physics and Astronomy and London Center for Nanotechnology, University College London, London, WC1E 6BT, United Kingdom

[4] Institute of Applied Physics, Justus Liebig University, Heinrich-Buff-Ring 16, 35392 Giessen, Germany

[5] Istituto CNR di Scienze e Tecnologie Chimiche "Giulio Natta" (CNR-SCITEC), Via Corti 12, 20133 Milano, Italy

[6] Department of Chemical Sciences, University of Padova, via Marzolo 1, 35131 Padova, Italy

[7] Electron Microscopy Facility, Istituto Italiano di Tecnologia (IIT), via Morego 30, 16163 Genova, Italy

[8] Materials Characterization Facility, Istituto Italiano di Tecnologia, via Morego 30, 16163 Genova, Italy

[9] Department of Materials Science and Engineering, Shenzhen Key Laboratory of Full Spectral Solar Electricity Generation (FSSEG), Southern University of Science and Technology, No. 1088, Xueyuan Rd., Shenzhen 518055, Guangdong, China

[10] Computational Laboratory for Hybrid/Organic Photovoltaics (CLHYO), Istituto CNR di Scienze e Tecnologie Chimiche "Giulio Natta" (CNR-SCITEC), Via Elce di Sotto 8, 06123 Perugia, Italy

Table of Contents

Experimental and computational methods

Materials and methods. All the double perovskite precursors, namely $BiBr_3$ (99%), CsBr (99.9%), AgBr (99.5%) were purchased from Alfa Aesar. $BiBr_3$ was stored in a glovebox due to moisture sensitivity and AgBr in dark due to light sensitivity. The doping precursors $EuCl_3 \cdot 6H_2O$ and $YbCl_3 \cdot 6H_2O$ (also stored in a glovebox) were purchased from Sigma Aldrich, as were all solvents. Powder XRD analysis was performed at ambient temperature with a PANalytical B.V. X'Pert PRO diffractometer employing Cu Kα1 radiation. The instrument operated at 40 kV and 40 mA using a 1° divergence slit for the incident beam. Elemental analysis was carried out via Inductively Couple Plasma Optical Emission (ICP-OES), with an iCAP 7600 DUO (Thermo Fisher Scientific). The RF power of the plasma, the nebulizer gas flow, the coolant gas flow and the auxiliary gas flow were set at 1150 W, 0.5 L min-1, 12 L min-1, 0.5 L min-1, respectively. Samples were weighted and digested (overnight) in a flask with 10% of aqua regia, filled up at volume (10 mL) with Milli-Q and filtered using a 0.45 μm PTFE filter before the analysis. Ar gas was used as Internal Standard and the R2 value of the calibration curve (0.01 - 0.1 – 1 - 10 ppm) for the Bi (λ1 = 223.060 nm; λ2 = 307.770 nm), Eu (λ1 = 381.967; λ2 = 412.970) and Yb (λ 1 = 328.937; λ2 = 369.419) elements was 0.999. ICP-OES was used to determine the amount of dopant in relation to bismuth. Values were evaluated using the Qtegra software (Thermofisher). Micro-Raman analysis was carried out using a Senterra Raman microscope equipped with a λ=532 nm laser. All the measurements were conducted by positioning a small amount of powder on a glass slide, which was placed upon the support inside the instrument. SEM and SEM-EDX was performed on a Zeiss Merlin instrument at a working potential of 20 kV. Powder samples were first coated with a Pt thin layer by sputtering in order to avoid charging effects. TEM images were acquired on a FEI Tecnai G2 F20 TWIN TMP (Schottky emitter), operated at 200 kV, with a Bruker X-Flash 6|T 30 EDS silicon-drift detector (SDD). Powder samples were suspended in ethanol, sonicated and drop casted onto holey carbon-coated Cu grids. Thin film thickness was obtained employing a Alpha-Step 100 profilometer by Tencor Instruments. GIXRD was performed in a range of 3° to 70° (0.05° step size, 0.014 °/s scan speed) with a PANalytical B.V. X'Pert Pro diffractometer using $CuK_{\alpha 1}$ radiation. The diffraction patterns were measured along the 2θ axis with a grazing incidence of ω = 0.5°. KPFM was measured on a VacuScope 1000 AIST-NT microscope, referencing on HOPG (TipNano, ZYA-grade, WF = 4.6 eV[36]) employing OPUS AC GG 160 tips (scan rate = 0.5 Hz, area = 1 μm^2) and measuring in FM-KPFM 2-pass mode (first pass – morphology, second pass CPD, lift < 30 nm). UV-vis absorption measurements of thin films were carried out on an Agilent 8453 UV-Vis spectrometer. PL measurements were performed on a modified NanoLog-TCSPC (Horiba) with a monochromated Xenon lamp excitation source. The excitation-emission map and PLE spectrum of the Yb-doped $Cs_2AgBiBr_6$ thin film were recorded on a Horiba FluoroMax-4 spectrophotometer. All the PL spectra are corrected for the instrument response and measured in backscattering mode in air at room temperature. The PLQY

determination was conducted using an integrating sphere setup and an Andor-Shamrock 163 spectrometer coupled with an Andor-Newton charge-coupled device (CCD) unit. The reported PLQY value is the average values obtained from a set of measurements performed by focusing the 450 nm laser beam (average power <1 mW) on different areas of the films.[1]

Hydrothermal synthesis of $Cs_2AgBiBr_6$ and Eu/Yb-doped $Cs_2AgBiBr_6$ and XRD/ICP-OES characterization. A suspension of $BiBr_3$ (0.449 g, 1 mmol), CsBr (0.426 g, 2 mmol) and AgBr (0.188 g, 1 mmol) in 10 mL of HBr (45-48%) was stirred at room temperature until complete dissolutions of the suspended powders (from 30 minutes to 2 hours). For the preparation of the lanthanide-doped double perovskites, given molar amounts of doping precursors (see text) were added to replace the same molar amounts of $BiBr_3$. The solution was then placed in an autoclave, transferred to an oven and treated at 110 °C for 2 hours. After cooling, the crystalline orange powders precipitated from the reaction mixture and were recovered by centrifugation and washed thoroughly with ethanol after removal of the supernatant. The powders were dried for at least 4 h at 60 °C in the oven and then grinded in a mortar to undergo powder XRD analysis. The results of the ICP-OES analysis are summarized in this table:

		Atomic W	**mg**	**Vf (ml)**		**λ**	**ICP ppm**	**AVERAGE ppm**	**mol**
1	**Bi**	208,98	12,1	10	λ1	223,060	245,14	246,63	1,18E-03
					λ2	307,770	248,11		
	Yb	173,04			λ1	328,937	0,08	0,07	4,19E-07
					λ2	369,419	0,07		
2	**Bi**	208,98	17,4	10	λ1	223,060	261,09	262,42	1,26E-03
					λ2	307,770	263,74		
	Eu	151,96			λ1	381,967	0,07	0,07	4,61E-07
					λ2	412,970	0,07		

Thin films preparation. 0.3 M solutions of the double perovskite powder samples (undoped or doped) were prepared dissolving 0.159 g of the powder obtained from the HT synthesis into 500 µL of DMSO. FTO and quartz glass were used as substrates, depending on the need (the conductive one for SEM and KPFM). Squares of 2.5 cm x 2.5 cm were cut and cleaned using three consecutive sonication steps of 15 min in a RBS solution (purchased from Carl Roth), acetone and isopropanol. Then the substrates were dried with a nitrogen flux and irradiated with an ozone-producing halogen lamp for 10 min. Thin films deposition was performed in a nitrogen-filled glovebox through spin-coating. 100 µL of the solutions were dropped in the middle of the substrates and a rotation at 3000 rpm for 40 s was applied. 15 s before the

rotation end, 70 μL of chlorobenzene were added in the middle of the sample. The films were then dried and finally annealed at 285 °C for 5 min.

Computational details. DFT calculations have been carried out in a 2x2x2 supercell of the conventional cubic lattice of $Cs_2BiAgBr_6$ (320 atoms) by fixing cell parameters to the experimental values.[2] All calculations have been performed by using the CP2K package[3] and the PBE0 hybrid functional[4], by keeping the fraction of Fock exchange α at its original value (0.25). Goedecker-Teter-Hutter pseudopotentials (GTH)[5] along with double-ζ polarized basis sets for the wave functions[6] were used for Cs, Bi, Ag and Br, while for Eu and Yb GTH pseudopotentials and double-ζ basis set developed by Lu et al.[7] have been used. A cutoff of 500 Ry for the expansion of the electron density was adopted in all calculations, by using the cFIT auxiliary basis set for Cs, Bi, Ag and Br elements to speed up hybrid functional calculations.[8] The equilibrium positions of ions within the pristine and doped supercells were found by relaxing ions at the PBE0 level of theory. DFEs and TILs ($\varepsilon(q/q')$)of dopants have been calculated by using the following equations:[9]

$$DFE\ [X^q] = E[X^q] - E[perf] - \sum_i n_i\mu_i + q(\varepsilon_{VB} + \varepsilon_F) + E^q_{\mathrm{corr}}$$

$$\varepsilon(q/q') = \frac{E[X^q] - E[X^{q'}]}{q' - q} + \frac{E^q_{corr} - E^{q'}_{corr}}{q' - q} - \varepsilon_{\mathrm{VB}}$$

where $E[X^q]$ is the energy of the supercell with dopant X in the charge state q and ε_{VB} is the valence band energy of the pristine. Makov-Payne corrections[10] have been used in the E^q_{corr} term by adopting the static dielectric constant of $Cs_2BiAgBr_6$ (ε = 12.7). Chemical potentials in the DFE has been set in order to simulate metal exchange between the $EuCl_3$, $YbCl_3$ and $BiCl_3$ molecules in the gas phase and the un-doped perovskite.

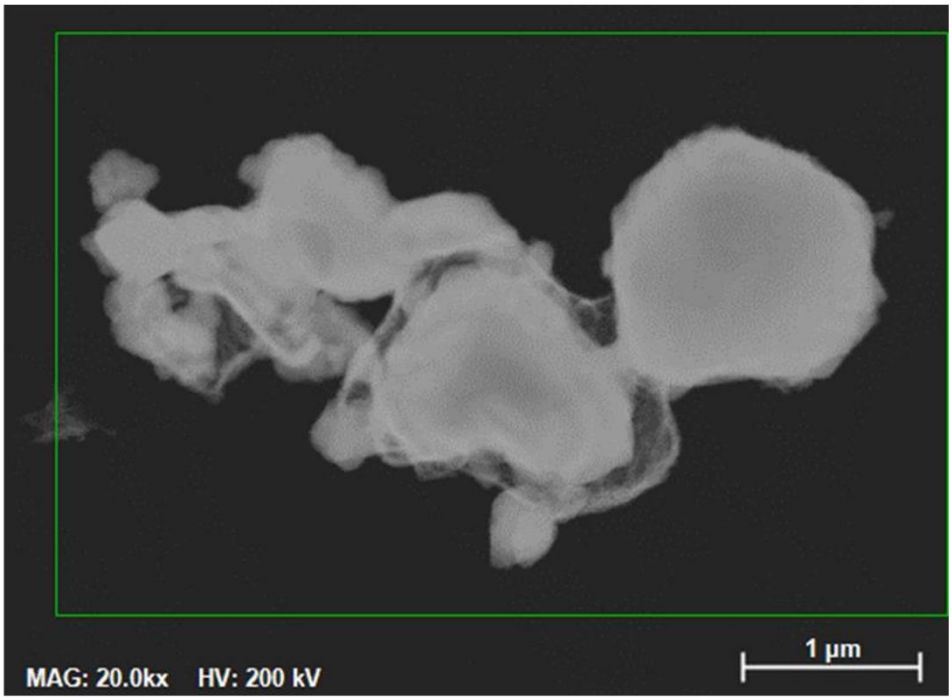

Figure S1. Transmission electron microscopy image of a sample of undoped $Cs_2AgBiBr_6$

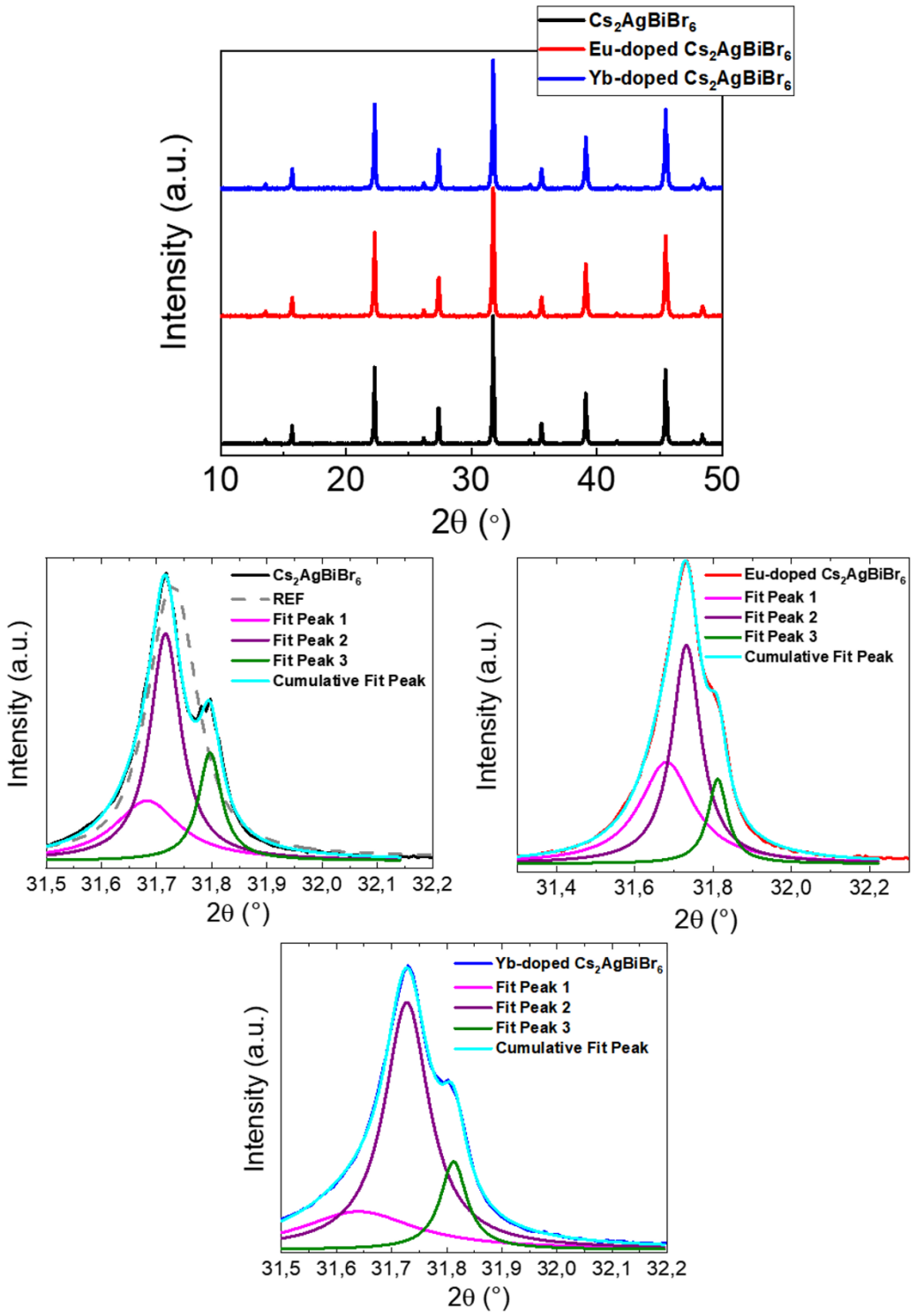

Figure S2. Powder XRD spectra of HT $Cs_2AgBiBr_6$ and of HT Eu- and Yb-doped samples (top), with details and peak analyses of the most intense reflections (bottom).

Table S1 summarizes the outcomes of peak deconvolution (Figure S2). Two are the main components identified, one centered at about 31.71° and one at about 31.79°. Being two different components with very close reflexes, we can state that two similar phases are present, likely characterized by slightly different symmetries, due to structural variations in the crystal lattice. This is justified by the fact that all reflections in the XRD diffractogram feature an identical multi-component shape but no additional, isolated peaks are found, excluding the presence of completely different compounds (such as the pure bismuth perovskite discussed above). We assign the peak centered at 31.71° to a high symmetry phase, which also seems to coincide with the phase found by Woodward and coworkers through single crystal analysis,[11] and the feature centered at 31.79° to a low symmetry phase. These peaks show a slight shift (in the order of 0.05%) towards higher 2θ-values in the lanthanide-doped samples, highlighting a small $Cs_2AgBiBr_6$ lattice contraction upon incorporation of the dopants (as it is expected from the introduction of ions with smaller ionic radii compared to Bi^{3+}). The distribution of crystallite sizes obtained by applying the Scherrer equation to the fitted peaks is found to provide values > 100 nm for all the samples.

Table S1. Summary of the peak analysis conducted on the (004) reflections of HT undoped, Eu- and Yb-doped $Cs_2AgBiBr_6$ bulk crystalline powder samples.

	High symmetry phase	**Low symmetry phase**	
	Peak position (° ±0.01)	Peak position (° ± 0.01)	Peak position variation (%)
$Cs_2AgBiBr_6$	31.71	31.79	-
Eu-doped $Cs_2AgBiBr_6$	31.73	31.81	0.05%
Yb-doped $Cs_2AgBiBr_6$	31.73	31.81	0.05%

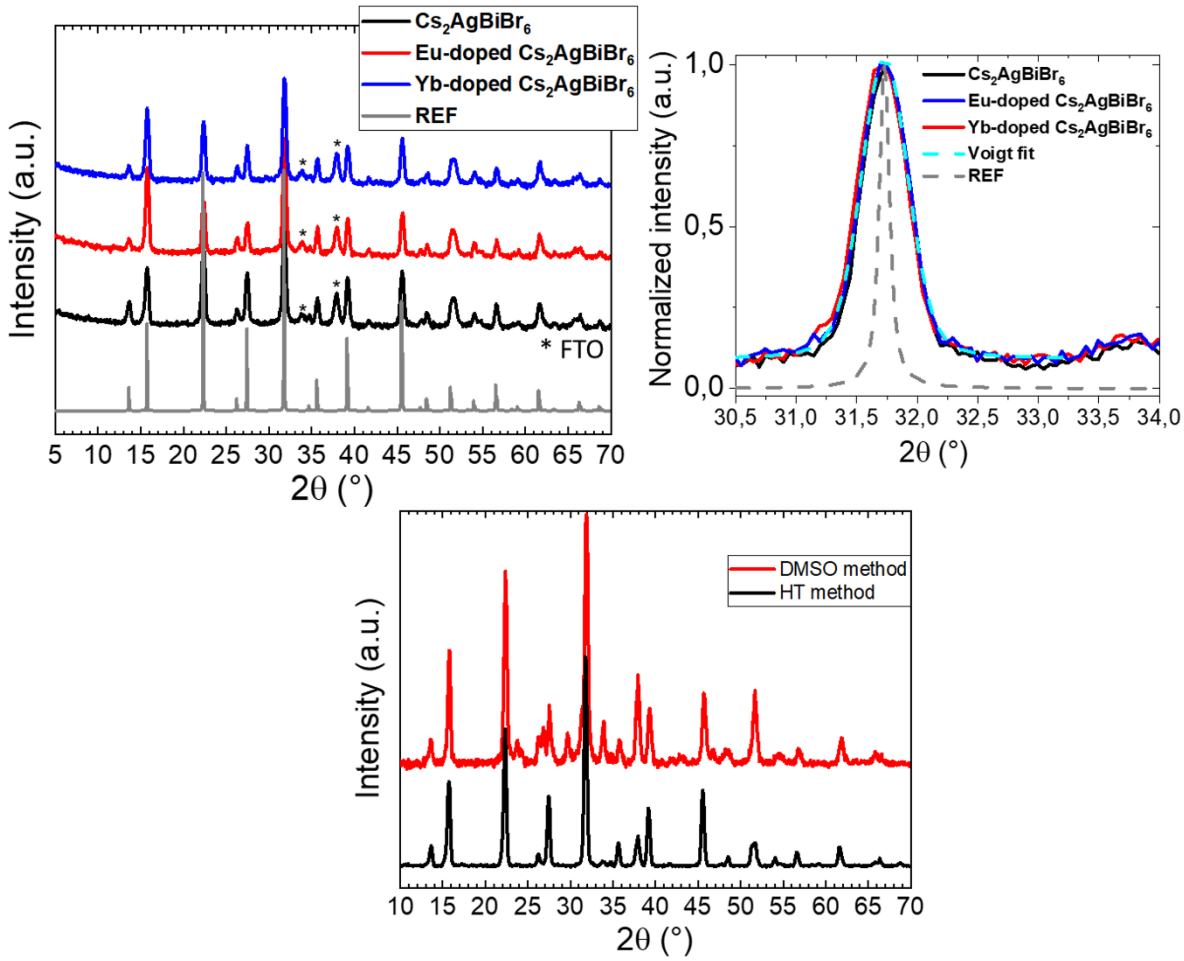

Figure S3. GIXRD spectra of thin films of HT $Cs_2AgBiBr_6$ and of HT Eu- and Yb-doped samples (top left), with details and peak analysis of the most intense reflections (top right). The reference was taken from literature data.[11] Comparison between GIXRD spectra of thin films prepared with the HT method and with the direct dissolution of CsBr, AgBr and $BiBr_3$ precursors in DMSO (bottom). Crystallite sizes of 20-22 nm were found in the undoped and doped thin films, as estimated by Scherrer peak analysis.

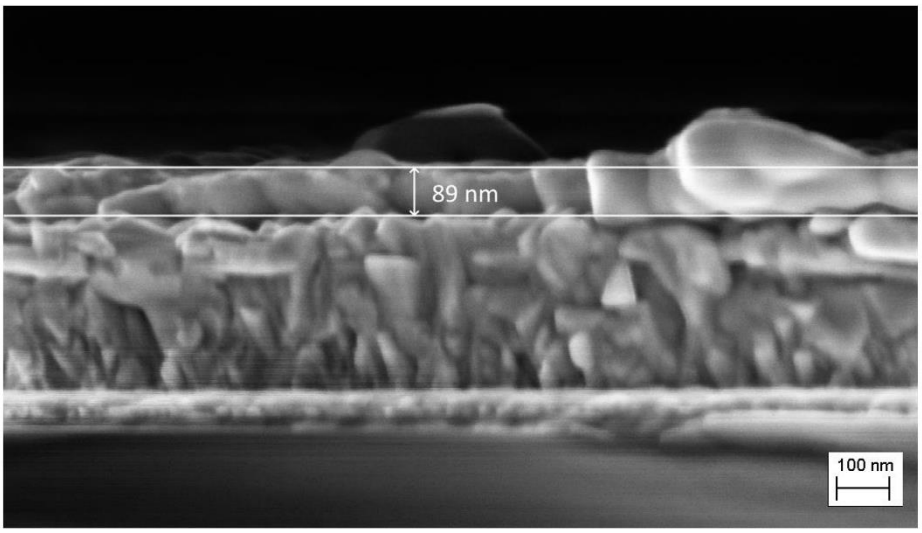

Figure S4. Cross section of an un-doped $Cs_2AgBiBr_6$ thin film on FTO. The average thickness of the double perovskite layer is estimated to be 89 nm.

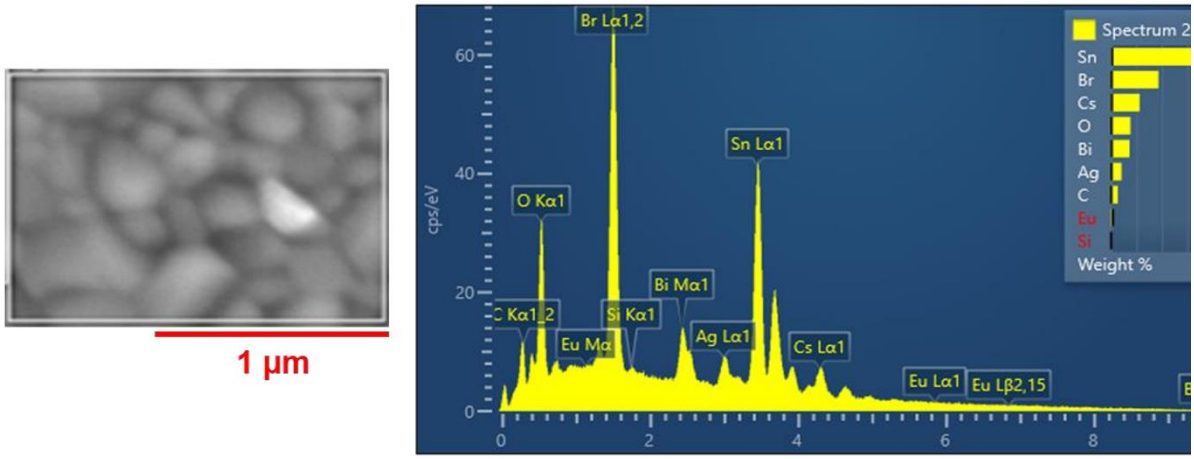

Figure S5. SEM-EDX analysis of Eu-doped $Cs_2AgBiBr_6$ thin film.

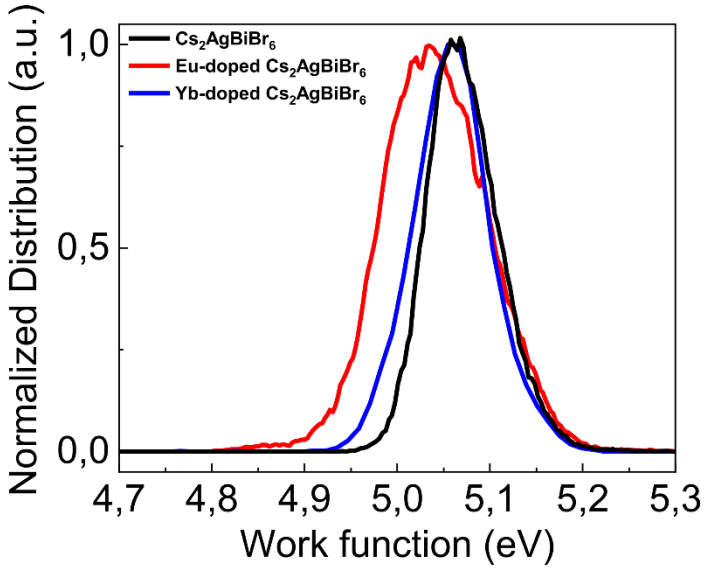

Figure S6. Kelvin probe microscopy analysis of Eu/Yb-doped $Cs_2AgBiBr_6$ and of undoped $Cs_2AgBiBr_6$ thin films.

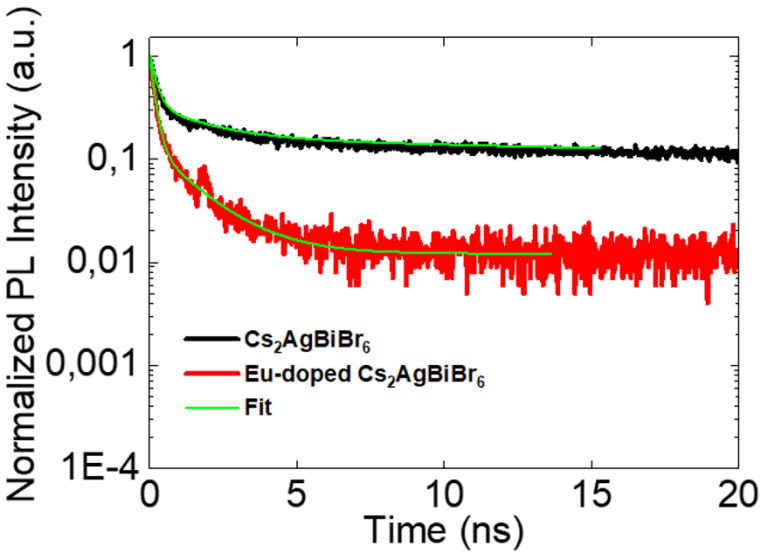

Figure S7. Time resolved photoluminescence decay probed at 2 eV for Eu-doped and undoped $Cs_2AgBiBr_6$ thin films. Photoluminescence lifetimes extracted through the fit result to be equal to 0.944 µs (in line with previous reports[12]) for the undoped double perovskite and 0.9 ns for the Eu-doped double perovskite, with significant shortening due to trapping promoted by the lanthanide-induced deep defects within the band gap.

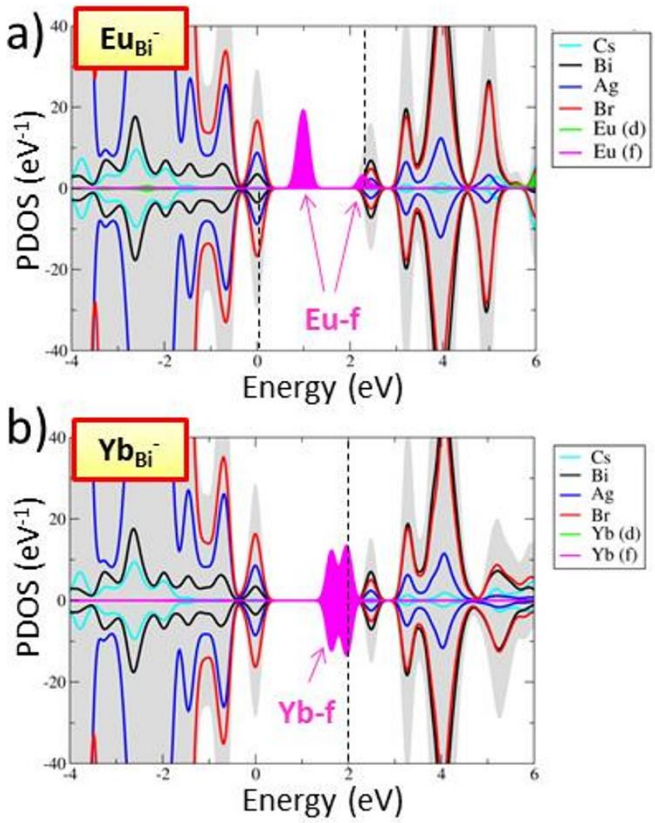

Figure S8. a) PDOS of the Eu_{Bi}^{-} defect, *i.e.* a trapped electron on the Eu_{Bi}^{0} defect; b) PDOS of the Yb_{Bi}^{-} defect.

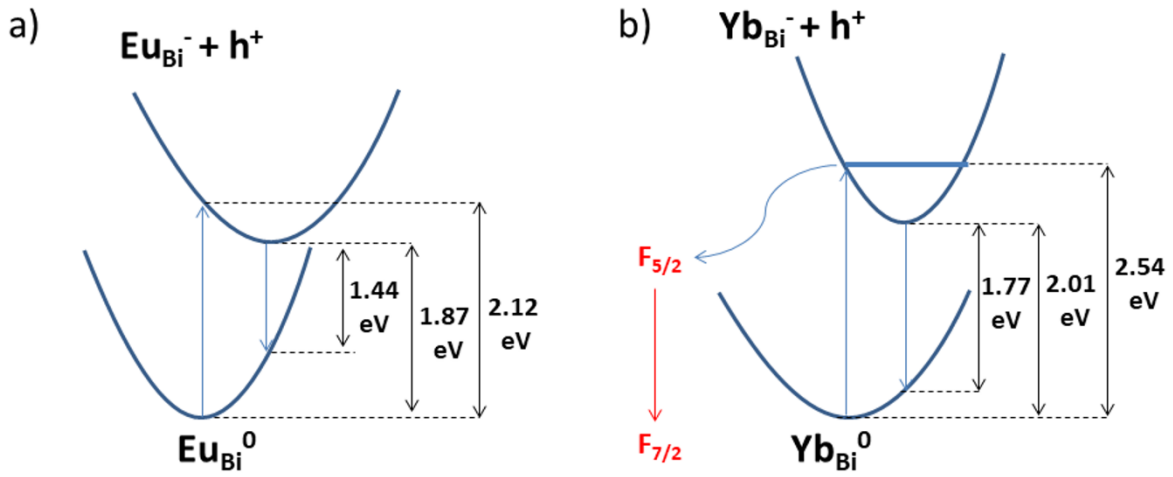

Figure S9. Calculated configuration diagrams (PBE0 level of theory) of the ground and excited states of a) Eu_{Bi} and b) Yb_{Bi} dopants centers in $Cs_2BiAgBr_6$. The excited states refers to the trapping of the electron with hole in VB. The calculated $Cs_2BiAgBr_6$ band gap is 2.27 eV.

References

1) a) de Mello, J.C.; Wittmann, H. F.; Friend, R.H. *Adv. Mater*. **1997**, *9*, 230; b) C. Wurth, C.; Grabolle, M.; Pauli, J.; Spieles, M.; Resch-Genger, U. *Nat. Protoc*. **2013**, *8*, 1535.
2) Slavney, A. H.; Leppert, L.; Bartesaghi, D.; Gold-Parker, A.; Toney, M. F.; Savenije, T. J.; Neaton, J. B.; Karunadasa, H. I. Defect-Induced Band-Edge Reconstruction of a Bismuth-Halide Double Perovskite for Visible-Light Absorption. *J. Am. Chem. Soc.* **2017**, *139*, 5015-5018.
3) VandeVondele, J.; Krack, M.; Mohamed, F.; Parrinello, M.; Chassaing, T.; Hutter, J. Quickstep: Fast and Accurate Density Functional Calculations Using a Mixed Gaussian and Plane Waves Approach. *Comput. Phys. Commun.* **2005**, *167*, 103-128.
4) a) Adamo, C.; Barone, V. Toward Reliable Density Functional Methods without Adjustable Parameters: The Pbe0 Model. *J. Chem. Phys.* **1999**, *110*, 6158-6170. b) Perdew, J. P.; Ernzerhof, M.; Burke, K. Rationale for Mixing Exact Exchange with Density Functional Approximations. *J. Chem. Phys.* **1996**, 105, 9982-9985.
5) Goedecker, S.; Teter, M.; Hutter, J. Separable Dual-Space Gaussian Pseudopotentials. *Phys. Rev. B* **1996**, *54*, 1703-1710.
6) Van de Vondele, J.; Hutter, J. Gaussian Basis Sets for Accurate Calculations on Molecular Systems in Gas and Condensed Phases. *J. Chem. Phys.* **2007**, *127*, 114105.
7) Lu, J.-B.; Cantu, D. C.; Nguyen, M.-T.; Li, J.; Glezakou, V.-A.; Rousseau, R. Norm-Conserving Pseudopotentials and Basis Sets to Explore Lanthanide Chemistry in Complex Environments. *J. Chem. Theory Comp.* **2019**, *15*, 5987-5997.
8) Guidon, M.; Hutter, J.; VandeVondele, J. Auxiliary Density Matrix Methods for Hartree−Fock Exchange Calculations. *J. Chem. Theory Comput.* **2010**, 6, 2348-2364.

9) Van de Walle, C. G.; Neugebauer, J. First-Principles Calculations for Defects and Impurities: Applications to Iii-Nitrides. *J. Appl. Phys.* **2004**, 95, 3851-3879.
10) Makov, G.; Payne, M. C. Periodic Boundary Conditions in Ab Initio Calculations. *Phys. Rev. B* **1995**, 51, 4014-4022.
11) McClure, E. T.; Ball, M. R.; Windl, W.; Woodward, P. M. Cs_2AgBiX_6 (X = Br, Cl): New Visible Light Absorbing, Lead-Free Halide Perovskite Semiconductors. *Chem. Mater.* **2016**, *28*, 1348–1354.
12) Hoye, R. L. Z., Eyre, L., Wei, F., Brivio, F., Sadhanala, A., Sun, S., Li, W., Zhang, K. H. L., MacManus-Driscoll, J. L., Bristowe, P. D., Friend, R. H., Cheetham, A. K., Deschler, F., *Adv. Mater. Interfaces* **2018**, *5*, 1800464.

4.3 Publication 2

Large Cation Engineering in Two-Dimensional Silver-Bismuth Bromide Double Perovskites

Authors: **Fabian Schmitz**, Jonas Horn, Nicolo Dengo, Alexander E. Sedykh, Jonathan Becker, Elena Maiworm, Péter Bélteky, Ákos Kovecz, Silvia Gross, Francesco Lamberti, Klaus Müller-Buschbaum, Derck Schlettwein, Daniele Meggiolaro, Marcello Righetto, Teresa Gatti

2D LHPs as solar absorbers have already been reported in the early stage of perovskite solar cell research,[48,230] first mentioned in 2014 by Smith *et al*.[166]

Connor *et al.* were the first to fabricate mono- (n = 1), and bilayered (n = 2) Ag- and Bi-based 2D double perovskites $(BA)_4AgBiBr_8$ (BA = n-butylammonium), and $(BA)_2CsAgBiBr_7$, respectively.[49] They report a calculated indirect bandgap for $\infty \geq n \geq 2$ materials which becomes direct for the $(BA)_4AgBiBr_8$ monolayer (n = 1). Furthermore, the bandgap increases with decreasing n. $(BA)_2CsAgBiBr_7$ bilayer phase single crystals have also been characterized by a large mobility-lifetime product, making them suitable for application in x-ray detectors.[231] Also, single crystals of the monolayers $(X)_4AgBiBr_8$ and bilayers $(X)_2CsAgBiBr_7$ (with X being propylammonium, octylammonium, and 1,4-butyldiammonium) have been structurally analyzed by Mao *et al.* but their optical properties have not been further investigated.[232]

Publication 2 is a comparative study about the influence of the large organic cations RA on the structural and optical properties of the monolayered 2D $(RA)_4AgBiBr_8$ double perovskite (RA = n-butylammonium [BA], isobutylammonium [iBA], phenylethylammonium [PEA], or hexylammonium [HA]). *Via* P-XRD, the dependence between the inorganic layer distance and the organic cation is determined. Single crystal XRD (SC-XRD) of $(PEA)_4AgBiBr_8$ reveals a herringbone arrangement of the phenyl rings while selective area electron diffraction (SAED) of all systems allows the extraction of the inorganic layers' average lattice constants. Thin films of all four 2D double perovskites have been prepared *via* spin-coating. SEM and AFM images reveal that $(BA)_4AgBiBr_8$ and $(PEA)_4AgBiBr_8$ thin films possess a relatively homogeneous surface with large grains, and $(HA)_4AgBiBr_8$ is characterized by a wax-like character. Meanwhile, $(iBA)_4AgBiBr_8$ thin films consist of square-like grains, interconnected by thin rods, thus creating a porous structure. Also, Kelvin probe force microscopy reveals that the organic cation's dipole moment affects the material's work function, i.e. creating a discrepancy of 500 meV between $(BA)_4AgBiBr_8$ (≈ 4.4 eV) and $(PEA)_4AgBiBr_8$ (≈ 4.9 eV). The choice of cation furthermore impacts the thin film PL. Intense emission bands centered at largely differing energies of 2.6 eV and 1.8 eV exist when the respective isomers BA and iBA are utilized as cations. By combining DFT calculations and experimental results, the origins of the differing emissive processes for $(BA)_4AgBiBr_8$ and $(iBA)_4AgBiBr_8$ are elucidated. For $(iBA)_4AgBiBr_8$, the low energy emission can be ascribed to radiative recombination from a self-trapped electron state, while in

the case of $(BA)_4AgBiBr_8$ the high-energy emission stems from band-to-band exciton recombination or the recombination from a self-trapped hole state.

This work elaborates on the impact of the structure of organic cations on the crystallization and optical properties of 2D Ruddlesden-Popper double perovskites. A mere exchange of a linear BA cation to its branched isomer iBA results in major differences regarding the surface morphology as well as the emission mechanism of thin films although their crystal structures are similar as confirmed by XRD. Thus, the reported structure-property relations create a foundation for a material-by-design approach regarding the 2D double perovskite family. For example, a recombination mechanism based on the one presented for $(BA)_4AgBiBr_8$ in **publication 2** was later reported by Hooijer *et al.* for $(FPEA)_4AgBiBr_8$ (FPEA = 4-fluorophenethylammonium) who revealed ultrafast charge carrier localization for 2D double perovskites.[170]

In addition to the *General Contributions*, all samples that were analyzed within this work were prepared by me. I performed powder-XRD, SEM, UV-Vis absorption spectroscopy, Raman spectroscopy, thermogravimetric analysis (TGA), thin film GIXRD, atomic force microscopy (AFM), and diffuse light scattering (DLS), including the respective data processing.

CHEMISTRY OF MATERIALS

pubs.acs.org/cm Article

Large Cation Engineering in Two-Dimensional Silver–Bismuth Bromide Double Perovskites

Fabian Schmitz, Jonas Horn, Nicola Dengo, Alexander E. Sedykh, Jonathan Becker, Elena Maiworm, Péter Bélteky, Ákos Kukovecz, Silvia Gross, Francesco Lamberti, Klaus Müller-Buschbaum, Derck Schlettwein, Daniele Meggiolaro,* Marcello Righetto,* and Teresa Gatti*

Cite This: *Chem. Mater.* 2021, 33, 4688–4700 Read Online

ACCESS | Metrics & More | Article Recommendations | Supporting Information

ABSTRACT: Double perovskites are promising candidates for less toxic and highly stable metal halide perovskites, but their optoelectronic performances still lag behind those of the lead halide counterpart, due to the indirect nature of the bandgap and the strong electron–phonon coupling. Reducing the dimensionality of $Cs_2AgBiBr_6$ down to a 2D layered form is strategic in order to tune the band gap from indirect to direct and provides new insights into the structure–property relationships of double perovskites. Herein, we report on a series of monolayer 2D hybrid double perovskites of formula $(RA)_4AgBiBr_8$, where RA represents different primary ammonium large cations with alkyl- and aryl-based functionalities. An in-depth experimental characterization of structure, film morphology, and optical properties of these perovskites is carried out. Interestingly, the variation of the ammonium cation and the interplanar distance between adjacent inorganic monolayers has peculiar effects on the film-forming ability and light emission properties of the perovskites. Experiments have been combined with DFT calculations in order to understand the possible origin of the different emissive features. Our study provides a toolbox for future rational developments of 2D double perovskites, with the aim of narrowing the gap with lead halide perovskite optoelectronic properties.

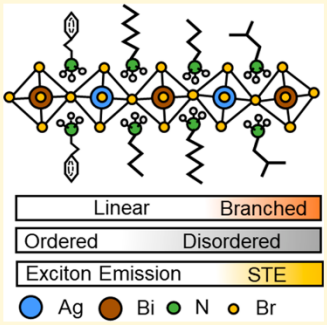

1. INTRODUCTION

Lead halide perovskites have revolutionized the semiconductor field due to their excellent optoelectronic properties, such as the direct band gap, the high absorption coefficient, and the long lifetime of photogenerated charge carriers.[1−3] These properties have been mainly exploited in solar cell devices, where efficiencies beyond 25% have been reached in relatively few years.[4] Despite these outstanding efficiencies, toxicity issues related to the presence of lead[5] and the limited resistance against external agents, e.g., moisture,[6,7] have led to search alternative metals possibly replacing lead.

Within this context, "elpasolites" or double halide perovskites (DHPs) hold great promise due to their excellent stability against environmental degradation.[8] In these materials, such as $Cs_2AgBiBr_6$, lead cations are replaced by iso-electronic metal cation pairs (i.e., mono- and tri- valent metal cations) arranged in alternating $[AgBr_6]$ and $[BiBr_6]$ octahedra. The valence band arises from Ag d^{10} and Bi s^2 orbitals, resulting in a relatively deep valence band, heavy hole masses, and an indirect bandgap of ~2 eV.[9−11] Despite the excellent stability, the indirect nature of the band gap, as well as its relatively wide value, strongly limits their applications in outdoor photovoltaics. On the other hand, interesting and useful applications[12] have been identified for these species in other fields, such as photocatalysis,[13] transparent,[14] indoor[15] and, in general, building-integrated photovoltaics,[16] and radiation detection.[17] The reduction toward two-dimensional (2D) monolayers, however, is an effective strategy to tune the band gap from indirect to direct,[18−20] thus opening new perspectives in the applications of DHPs in efficient optoelectronic devices.[21,22]

The synthesis of (001)-oriented 2D layered perovskites is achieved by introducing bulkier organic cations (e.g., featuring primary ammonium groups) and organic moieties, whose size cannot fit the octahedral cavities in the "elpasolite" structure. The resulting structure is layered, and these large organic cations form bilayers that define the space between adjacent metal-halide octahedra-based inorganic planes.[23] In particular, DHPs (001) monolayers have the formula $A'_4B^IB^{III}X_8$ and a handful of silver–bismuth versions have been recently reported, based on organic cations such as *n*-butyl[21] and *n*-propyl[24] ammonium or more complex ones such as phenylethylammonium[25,26] or dicationic 5,5′-diylbis-(ammoniumethyl)-[2,2′-bithiophene], in line with the many

Received: April 5, 2021
Revised: May 17, 2021
Published: May 28, 2021

https://doi.org/10.1021/acs.chemmater.1c01182
Chem. Mater. 2021, 33, 4688–4700

structural variations carried out on the lead-based counterparts[27] and demonstrating the high versatility of the system.

The above-mentioned studies revealed that subtle structural details (e.g., distortion at the Ag site[28]) play a crucial role in determining the properties of the 2D DHPs. For instance, Connor et al.[21] reported significant changes in the electronic structure of distorted and non-distorted $BA_4AgBiBr_8$. Although this could, in principle, provide control over the properties of these materials to a greater extent, much effort is needed in exploring the space of possible large cations and determining the resulting properties of the corresponding 2D DHPs.

In this study, we performed a systematic investigation of the effects of different aliphatic and aromatic ammonium cations on the structural and optoelectronic properties of the 2D $RA_4AgBiBr_8$ layered perovskites. The study has been focused on a selected list of RA organic cations that constitute the spacer between adjacent 2D inorganic layers, i.e., the aliphatic *n*-butylammonium (BA), isobutylammonium (iBA), and hexylammomium (HA) bromides, featuring two different lengths for the linear alkyl chain and a branched one, and the aromatic phenylethylammonium (PEA) bromide. An in-depth characterization of the structure and morphology of perovskite polycrystalline films is carried out, revealing new insights into the solid-state organization of these hybrid compounds. Then, the impact of different cations on the optical properties of the perovskites has been investigated by optical spectroscopy and density functional theory (DFT) calculations. Interestingly, our analysis shows that change in the monolayer spacing induced by the different cations leads to different film morphologies that may tune selectively sub-bandgap PL emission associated with self-trapping of charge carriers in the 2D moiety.

2. RESULTS AND DISCUSSION

2.1. Synthesis and Structural Properties. The four $A'_4AgBiBr_8$ compounds [henceforth referred to as $(RA)_4AgBiBr_8$] investigated in this work were produced employing the hydrothermal synthesis method reported in the Experimental Section. RA organic cations form in-situ during the synthetic process from the corresponding amines and hydrobromic acid. The structure of the final compounds is sketched for two layers of alternating [$AgBr_6$] and [$BiBr_6$] octahedra in Figure 1a. We obtained four different compounds for the different larger cations as four crystalline powders of yellow color, mainly comprising platelet-like crystals of lateral sizes up to 100 μm (see Figure S1 in the Supporting Information (SI) for an example), that we directly used for powder X-ray diffraction (P-XRD). In Figure 1b, we show the diffractograms for the synthesized samples. A marked difference between the parent 3D structure of $Cs_2AgBiBr_6$ (green diffractogram) and the layered $(RA)_4AgBiBr_8$ compounds can be observed from the presence of intense (001) reflections at 2θ values below 10°. We ascribe these reflections to the periodic spacing between adjacent 2D inorganic sheets created by the large organic cation bilayers. From the position of these reflections, the (001) lattice distance (d_{001}) can be calculated by applying Bragg's law (Table 1).

P-XRD data reveal how large cations affect the geometry of the resulting structure in the first instance. The large cation structure allows the fine-tuning of the spacing distance between the adjacent inorganic sheets. While moving from a linear to a branched alkyl moiety (BA to iBA) does not significantly affect such spacing, longer alkyl chains (HA) and bulkier groups (PEA) effectively increase the spacing. In comparison with others, the $(PEA)_4AgBiBr_8$ sample shows an anomalous P-XRD pattern dominated by the regular reflections belonging to the ⟨00l⟩ family up to (008). This could be related to a very regular 2D stacking order in the structure (i.e., large numbers of PEA double layers are stacked in an ordered way in the crystals), as was observed previously for a lead-based 2D perovskite.[29]

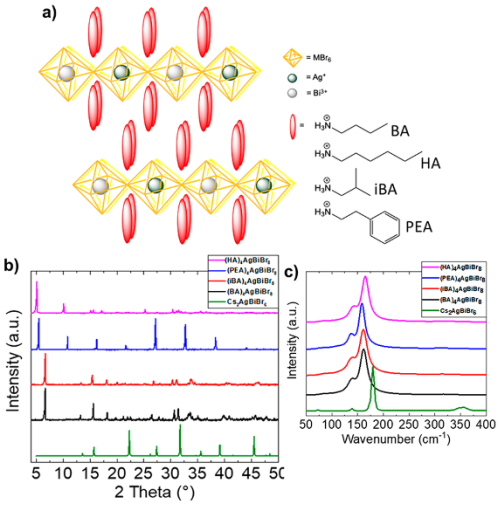

Figure 1. (a) Sketch of the structure of 2D hybrid silver−bismuth double perovskites of general formula $(RA)_4AgBiBr_8$. (b) P-XRD patterns of the four hydrothermally synthesized $(RA)_4AgBiBr_8$ crystalline compounds and of the reference 3D double perovskite $Cs_2AgBiBr_6$. (c) Low wavenumber region of the Raman spectra of the four $(RA)_4AgBiBr_8$ compounds and the reference 3D double perovskite $Cs_2AgBiBr_6$.

Table 1. 2θ Values of the First (001) Reflections in P-XRD of Figure 1b and Calculated (001) Lattice Constants

compound	2θ (deg)	d_{001} (Å)
$(BA)_4AgBiBr_8$	6.7	13.2
$(iBA)_4AgBiBr_8$	6.7	13.2
$(PEA)_4AgBiBr_8$	5.5	16.2
$(HA)_4AgBiBr_8$	5.1	17.4

The dimensional reduction in the four hybrid double perovskites further emerges when tracking the behavior of the most intense phonon mode in the Raman spectra of these compounds in comparison to that of the 3D reference $Cs_2AgBiBr_6$. Figure 1c shows the low wavenumber region of these spectra, dominated by the longitudinal optical A_{1g} mode (symmetric in-phase stretching of the Bi−Br and Ag−Br bonds in the Ag/$BiBr_6$ layers).[30] This phonon mode is located at 177 cm^{-1} for the 3D double perovskite (green line), while shifts to lower wavenumbers in all the three 2D hybrid compounds (at 161, 161, 158, and 165 cm^{-1} for, respectively, RA = BA, iBA, PEA, and HA), still maintaining the highest intensity among all other features within the spectrum (see Figure S2 in the SI for the high wavenumber region, featuring the organic cations vibrational modes). Therefore, the loss of the third dimension in the overall metal-halide octahedra connectivity, which is determined by the generation of the layered species, diminishes the phonon mode energy. Due to the nature of the A_{1g} mode, the phonon softening phenomena observed

https://doi.org/10.1021/acs.chemmater.1c01182
Chem. Mater. 2021, 33, 4688−4700

might be related to weaker Bi−Br and Ag−Br bonds, as a consequence of the loss of the octahedra connectivity in the third dimension for the layered structures (see further discussion in Figure S3 of the SI). Interestingly, the shift appears to be not strictly correlated to the interplanar distance measured via P-XRD; therefore, it cannot be attributed to the mere variation of spacing between layers. There is also no strict correlation to the dipole moment of the organic cations (Table 2, vide infra), which could have an influence on the electronic distribution in the Br^- ions close to the polar head of the organic cations. Recently, Li et al. have demonstrated how distortions of the inorganic framework induced by the organic A-cation soften the lattice of layered lead halide perovskite and result in lower phonon energies.[31] Therefore, we can only speculate that this shift is influenced by the intermolecular packing of organic tail groups and, hence, mechanical flexibility of the different organic interlayers. Nevertheless, we believe that further studies are needed to fully understand the role of organic large cations on the vibrational properties of the inorganic lattice in layered perovskites.

Attempts to grow single crystals suitable for X-ray diffraction (SC-XRD) of the iBA, PEA, and HA 2D monolayer double perovskite derivatives (for the BA derivative, single-crystal details can be found in ref 21) were successful in only one case, i.e., $(PEA)_4AgBiBr_8$. We attribute the unsuccessful obtainment of SC structures for iBA and HA-based 2d DHPs to the extreme disorder present in these structures. Reasonable diffraction intensities could not be obtained with sufficient resolution for structure solution or refinement, which is most likely because the organic cations exhibit consistent disorder (we were successful in crystallizing a structure with BA, but this structure was already reported[21]). The experimental details used for inducing such a crystallization process are reported in the Experimental Section. A crystal structure for the $(PEA)_4AgBiBr_8$ compound was already deposited in the Cambridge database but with a different level of refinement and only to predict the P-XRD pattern for the identification of side phases formed in parallel to a bilayer analogous:[32] on the contrary here we present a detailed description of the structure, which will be helpful for gaining further insights into structure−property relationships existing both in this compound and similar ones (a new structure has been deposited in the database, see details in the Experimental Section). SC-XRD analysis of the structure of $(PEA)_4AgBiBr_8$ reveals a typical monolayer DHP structure with a regular alternation of Ag^+ and Bi^{3+} sites within the inorganic sheets, which are separated by a distance of 16.15 Å (Figure 2a), thus strongly supporting the information obtained from P-XRD. The space group is $P\bar{1}$ (see Table S1 in the SI for the summary of crystallographic data and structure refinement) and the unit cell is defined by four in-plane corner-sharing metal bromide octahedra (two Bi based and two Ag based) and eight PEA cations (Figures 2a and S3 in the SI). The latter was found to be disordered over three positions. Such structural variability also exists for the position of the equatorial bromide atoms (with a conformation that occurs prevalently −91.3% and a less common one −8.7%).

In Figure S4 of SI the heavily distorted geometry of the inorganic monolayers can be clearly observed, with angles between the bismuth- and silver-based octahedra in a square unit of 68° and 112°. Interestingly, the tetragonal distortion at the $[AgBr_6]$ sites observed by Connor et al.[21] in that of $(BA)_4AgBiBr_8$ is not clearly observed in our data on $(PEA)_4AgBiBr_8$. However, the uncertainty associated with

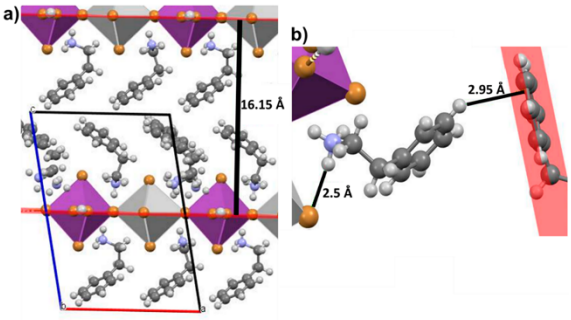

Figure 2. Details of the single-crystal structure of $(PEA)_4AgBiBr_8$. (a) View along the *b*-axis with indicated the interplanar distance between two adjacent inorganic monolayers of metal-bromide octahedra (taken between the planes containing the equatorial bromides). (b) View of the herringbone motif established within the phenylethylammonium-based organic bilayer that highlights the stabilizing CH-π interactions (in red the plane that contains the benzene ring). The hydrogen bond between an ammonium group and a bromide ion is also evidenced (shortest contact of three possible ones).

the silver-bromide distance could contribute to detecting similar equatorial and axial metal-bromide distances (Figure S5). We further examined the SC-XRD data in the search for stabilizing interactions existing at the level of the organic bilayer. Here, the periodic arrangement of the phenyl rings is reminiscent of the classic herringbone motif present, for example, in crystals of the acenes series.[33,34] Within this arrangement, CH−π interactions between edge-to-face arranged aromatic rings play a significant role in driving the formation of such an overall disposition of molecules within the crystal. Figure 2b illustrates a detail of this structural feature, with an estimated CH-π distance of 2.95 Å, therefore in the order of distances typical for this type of van der Waals intermolecular interactions.[35] This stabilizing effect of the π electron density and its interactions, not present in the other compounds investigated in this work, might at least partially explain the slightly higher thermal stability of $(PEA)_4AgBiBr_8$ compared to $(BA)_4AgBiBr_8$, $(iBA)_4AgBiBr_8$, and $(HA)_4AgBiBr_8$ that is seen in the thermograms reported in Figure S6 of the SI.

The structural properties of the four hydrothermally synthesized 2D DHP crystalline compounds were further examined through high-resolution transmission electron microscopy (HR-TEM). All samples presented two different types of populations: one characterized by relatively thin crystalline flakes and one constituted of darker (and thus thicker) regions (see Figures S7−S10 in the SI). Selective area diffraction (SAED) carried out on both the flake-like and darker regions show analogous patterns within each different sample and allows extracting the average in-plane lattice constant for all four 2D DHPs examined (see Figure S11 in the SI).[36] We extracted nearly identical values around 8 Å for all four species (see information on rings 1 inserted as tables in Figure S11 for each SAED pattern). Considering that these are not images taken in cross-section on the crystalline species and thus do not highlight the layered structure, we can safely assign this to repetitive features within the planes of the 2D inorganic sheets, such as the diagonal distance between identical metal centers. This can be verified further for the $(BA)_4AgBiBr_8$ and $(PEA)_4AgBiBr_8$ compounds for which single-crystal structural

https://doi.org/10.1021/acs.chemmater.1c01182
Chem. Mater. 2021, 33, 4688−4700

data are available. From micrographs taken at higher magnifications, we can also distinguish periodic motifs (also shown in Figures S7−S10), characterized by distances that vary from 2.7 to 3.8 Å. We assign these features to in-plane metal-halide distances within the inorganic sheets. To further investigate the structure of these powders, we carried out energy dispersive X-ray analysis (EDX) characterization on a selected sample, i.e., $(BA)_4AgBiBr_8$. Notably, measurement for the two types of populations described above (Figure S12) qualitatively indicate that depletion of silver cations characterizes the first population (orange frame). In contrast, the second (red frame) contains both bismuth and silver. These observations indicate that our powder samples have some degree of heterogeneity and a more complex identity than what could be inferred by merely focusing on P-XRD patterns. For instance, the presence of a Bi-only side phase cannot be inferred from that analysis (we exclude the presence of residual unreacted $BiBr_3$, as there is no trace of its reflexes in the P-XRD). On the other hand, it is known for the case of the 3D double perovskite $Cs_2AgBiBr_6$ that often a bismuth-rich impurity can form either during hydrothermal synthesis or during thin film deposition (the species with formula $Cs_3Bi_2Br_9$, which cannot be present here as no Cesium ions were introduced during the hydrothermal synthesis of the 2D monolayer DHPs);[9] therefore, it seems reasonable to guess that the here identified sample regions lacking silver could be a 2D-version of this bismuth-based compound or some analogous ones that are up to now unreported in literature, to the best of our knowledge.

2.2. Thin-Films Morphology. The four hydrothermally synthesized 2D DHP derivatives were cast into thin-films onto glass substrates. The detailed procedure of the process is provided in the Experimental Section. Briefly, $(RA)_4AgBiBr_8$ crystalline powders were dissolved in DMF and subsequently spun on a glass/FTO substrate and annealed. Thin-film XRD (Figure S13 in the SI) reveals the formation of highly preferentially oriented crystalline phases.[37] Differently from the P-XRD spectra, the intensity of the first reflection at low 2θ values, in all cases significantly more intense than all other reflections, suggests that the crystalline phases are growing parallel to the substrate. A similar behavior has already been reported for 2D lead halide perovskites.[38] On the other hand, the position of this reflection is unvaried with respect to the one in P-XRD (Figure 1b). Therefore, thin-film XRD confirms that the interplanar distance among 2D inorganic sheets is maintained and governed by the length and stereochemistry of different organic cations. The four resulting yellow thin films appeared to have different textures already at the naked eye (photos are visible in Figure S14): BA- and PEA-based films are smooth and homogeneous, the iBA-based film is translucent, and the HA-based film has a wax-like character with a nonhomogeneous distribution on the substrate. Scanning electron microscope (SEM) analysis of thin films prepared on FTO in top-view imaging mode (Figure 3) reveals the microstructure of the four different films.

Here, the film obtained from $(BA)_4AgBiBr_8$ shows a relatively flat surface, where some valleys emerge most likely as an effect of the evaporating solvent. $(PEA)_4AgBiBr_8$ thin films show a similar yet more grain-like morphology with some pinholes.[39] The $(HA)_4AgBiBr_8$ films appear uniform, with many small pinholes. It is worth noting that this is also the thinnest among all four films examined (see Figure S15 for cross-section SEM images). The appearance of the

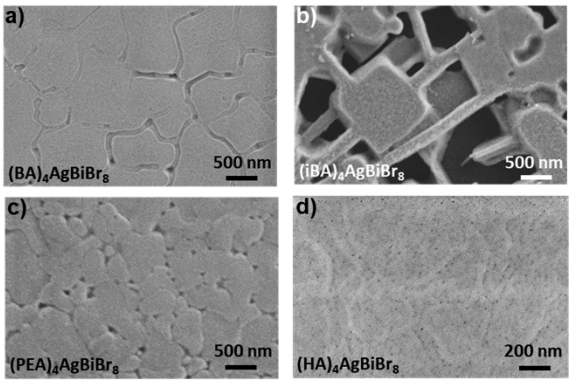

Figure 3. Top-view SEM images of spin-coated thin films of (a) $(BA)_4AgBiBr_8$, (b) $(iBA)_4AgBiBr_8$, (c) $(PEA)_4AgBiBr_8$, and (d) $(HA)_4AgBiBr_8$ on top of FTO substrates.

$(iBA)_4AgBiBr_8$ film is undoubtedly the most peculiar one: micron-sized square-like features have grown during film casting, which are connected one to the other by thinner and longer filaments while leaving around consistent amounts of empty space. This highly microstructured morphology, most likely characterized by a relatively high surface area, could be the reason for the opaque visual appearance of the thin film (Figure S14) as a result of light scattering.

Surface morphologies of the thin films were analyzed in detail through atomic force microscopy (AFM) in tapping mode, with peculiar images obtained for the $(BA)_4AgBiBr_8$ and $(PEA)_4AgBiBr_8$ based samples. The topography scans on the two thin films are reported in Figure S16, accompanied by line-profiles taken in the area of the surface indicated by black lines and numbers. From the $(BA)_4AgBiBr_8$ topography scan, we recognize the presence of many nanometric areas within the main grains, located at a lower height compared to the top smooth surface. When measuring the depth of these areas through depth profiling (right-hand side graphs), we observe that the step corresponds with a good approximation to a single interplanar distance among the 2D inorganic sheets in the layered perovskite (see Table 1). The same can also be inferred for the $(PEA)_4AgBiBr_8$ film (where not only monolayer steps are present but also bilayer ones, as can be seen in relative profile no. 1), even if for this species the surface topography is not flat but rather discontinuous, likely as a result of the more random orientation of the (001) crystallites in the film[40] (which still on average displace mainly parallel to the substrate, as suggested by thin-film XRD). The high tendency to form the inorganic sheets separated by the organic cations is shown by the formation of the terraces in all cases. Dynamic light scattering (DLS) analysis of the solutions used to produce the films (Figure S17) show the presence of scattering particles with diameters of several hundred nm (in most cases, only one distribution of diameters is found, whereas in the case of $(BA)_4AgBiBr_8$ two distributions result). Hence, we hypothesize that, when these crystals are dispersed in a highly coordinating solvent, they disassemble into single or few-layers inorganic sheets. Once cast into thin films, these solutions produce a more ordered stacking, which is reminiscent of a layer-by-layer assembly driven by the evaporation of the solvent.[38] Notably, the growth of thin films can therefore be described as a self-assembly process of pre-existing colloidal species[41] rather than a complete

https://doi.org/10.1021/acs.chemmater.1c01182
Chem. Mater. 2021, 33, 4688−4700

dissolution and regrowth process. This interpretation is confirmed by the fact that similar films could not be prepared from mixed solutions of metal- and ammonium bromides. Figure S18 reports the AFM studies carried out on the iBA and HA-based DHP films. Here, we observe an analogous step-like topography, albeit with much higher steps (around 10 nm) for iBA. These steps correspond to multilayer structures protruding from the surface. In addition, the influence of the cation on the thin film morphology is further confirmed by comparing the surface roughness obtained from AFM measurements (Figures S16 and S18). While the $(HA)_4AgBiBr_8$ film is very flat (RMS 2.1 nm), thin films of $(PEA)_4AgBiBr_8$ and $(BA)_4AgBiBr_8$ are slightly rougher (RMS 4.2 nm) and the $(iBA)_4AgBiBr_8$ film shows a considerably increased surface roughness (RMS 34.1 nm).

Similar to the structural diversity found in the thin film morphology of the four compounds we observed a variability of their work function (WF), as measured by Kelvin probe force microscopy (KPFM), shown in Figure 4 and Table 2.

Table 2. Work Function (WF) and FWHM Obtained by Gauss Fits of the Distribution (Figure 4a) for the Four $(RA)_4AgBiBr_8$ and Calculated Dipole Moments μ of the Organic Cations RA^+

compound	WF (eV)	FWHM (eV)	μ (D)
$(BA)_4AgBiBr_8$	4.43	0.11	1.583
$(HA)_4AgBiBr_8$	4.75	0.05	1.330
$(iBA)_4AgBiBr_8$	4.81	0.06	1.173
$(PEA)_4AgBiBr_8$	4.91	0.07	0.947

The different WF can be directly correlated to the dipole moment calculated for the organic cations RA^+ (Figure S19). The observed work function decreases with the calculated dipole moment of RA^+, well compatible with an orientation of the positive end of the dipole (NH_3^+-group) toward the inorganic sheet and the negative (organic) end toward vacuum, leading to the observed lowered WF. Such direct correlation of the observed WF with μ of the RA^+ reveals an organic termination of the surface. This is also indicated by very similar[42] band structures calculated for $(PEA)_4AgBiBr_8$ and $(BA)_4AgBiBr_8$ despite significant differences in the surface WF of these materials (Table 2). Interestingly, for the layered lead-based perovskite $(PEA)_2PbI_4$ an almost identical WF of 4.87 eV was reported[42] as we find for $(PEA)_4AgBiBr_8$, confirming that the organic moiety dominates the work function of the surface rather than the underlying inorganic sheets.[43] By looking at the FWHM of the WF signals, we find a considerably broader distribution for $(BA)_4AgBiBr_8$ which hints at a lower degree of order of the organic layer when compared to the three other organics, where a stronger intermolecular interaction can be expected that would lead to a higher degree of order and, hence, smaller FWHM of the WF.

2.3. Optical Properties and Computational Modeling.

The optical properties of thin films have been investigated by absorption and PL spectroscopy (see the results in Figure 5a). The UV−visible absorption spectra of the thin film series show well-defined transitions at around 3 eV. Gaussian fitting analysis (Figure 5a and Table 3) reveals that the observed absorption bandwidths have an fwhm larger (up to 380 meV) than for $Cs_2AgBiBr_6$ (about 200 meV, as taken from previous work of some of us[10]). Furthermore, $(iBA)_4AgBiBr_8$ thin films present an additional peak at 2.83 eV.[44,45] These observations suggest the presence of multiple transitions, whose energy is finely controlled by the rotation of the octahedra and the length of the organic spacers.

The assignment of the parent 3D $Cs_2AgBiBr_6$ transition is crucial to understand and interpret the optical response of the 2D $(RA)_4AgBiBr_8$ series. It is well established that bulk $Cs_2AgBiBr_6$ has an indirect bandgap of 1.8−2.2 eV. As discussed by Palummo et al. by computational excited-state methods, the first absorption peak in bulk $Cs_2AgBiBr_6$ is the result of a bound exciton, while the PL spectrum derives from a phonon-assisted radiative recombination process of indirect bound excitons.[46] On the other hand, no consensus has been reached on the nature of the prominent resonant optical feature generally observed at around 2.8 eV.[10,30,47,48] Clarifying its assignment is even more critical for lower dimensional structures, where the 1D/2D confinement of $Cs_2AgBiBr_6$ converts the bandgap from indirect to direct character. Alivisatos et al. postulated a role played by bismuth ion intra-atomic s → p orbital transitions, whose spin-forbidden

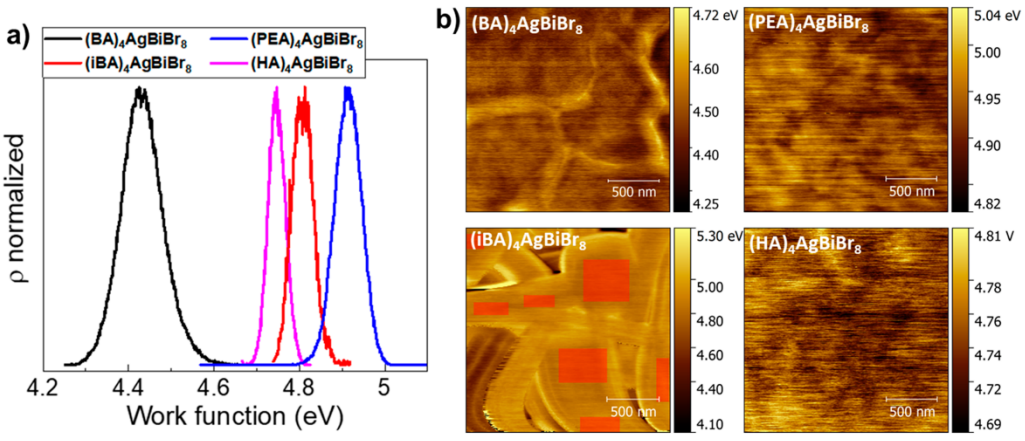

Figure 4. (a) Distribution of work function of the investigated $(RA)_4AgBiBr_8$ thin films. Every histogram contains at least two KPFM measurements, one of which is shown in panel b for each compound. For $(iBA)_4AgBiBr_8$. Only the marked regions were evaluated to avoid an influence of the strongly stepped morphology, whereas the whole area was evaluated for the other three compounds.

https://doi.org/10.1021/acs.chemmater.1c01182
Chem. Mater. 2021, 33, 4688−4700

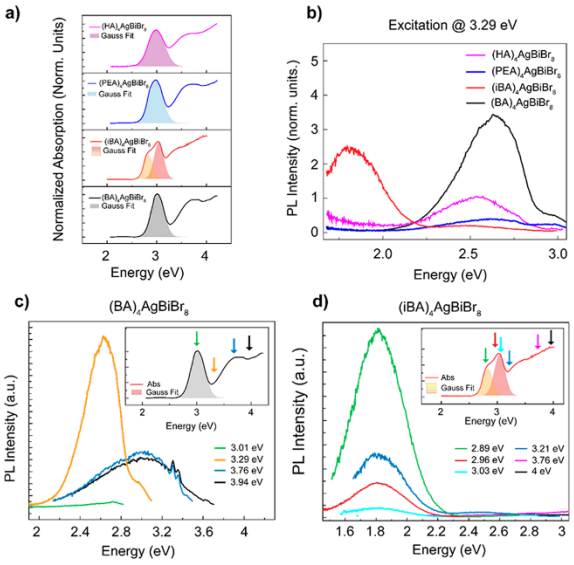

Figure 5. (a) UV−visible absorption spectra of $(RA)_4AgBiBr_8$ thin films (solid lines) and deconvoluted peaks (shaded areas) by Gaussian fitting of the band-edge transitions. (b) Normalized steady-state photoluminescence spectra of $(RA)_4AgBiBr_8$ thin films under 3.29 eV excitation measured at 77 K. Excitation energy-dependent PL spectra for (c) $(iBA)_4AgBiBr_8$ and (d) $(BA)_4AgBiBr_8$ thin films at 77 K. In the insets, the excitation wavelengths are indicated above the absorption profiles by colored arrows.

character is at least partially allowed by the strong spin−orbit coupling of bismuth.[44] On the other hand, Karunadasa et al., based on DFT calculations, suggested additional charge-transfer contributions from Ag-d to Bi-s/Bi-p orbitals.[21] In this context, the comparison between large cations in the $(RA)_4AgBiBr_8$ series provides further insight into the nature of this transition.

To characterize optical fingerprints of the perovskite series more in detail, the diffuse reflectance has been measured and analyzed by Kubelka−Munk theory. The resulting Kubelka−Munk function F(R) spectra, equivalent to absorption spectra, are shown in Figure S20. Notably, the prominent absorption peak lies at ∼3 eV and presents a similar shifting trend with different cations (see Table 3). However, the absorption edge is largely split with an additional peak at ∼2.6 eV, with only minor differences among the cations. Karunadasa et al. observed a similar effect for $(BA)_4AgBiBr_8$ powders, but the authors reported only the band edge.[21]

As shown in Figure 5b, the $(RA)_4AgBiBr_8$ thin films show significant emission peaks under 3.29 eV excitation. Specifically, the comparison (where PL data are normalized for the absorption at 3.29 eV) reveals how $(BA)_4AgBiBr_8$ and $(iBA)_4AgBiBr_8$ show the most intense emission. By comparing the integrated area (see Table S1), the intensity of $(PEA)_4AgBiBr_8$ and $(HA)_4AgBiBr_8$ is reduced with respect to BA-based perovskite by a factor of ∼7 and ∼3, respectively. All of the samples share a broad emission peak at around 2.6 eV with FWHM ranging from 300 to 600 meV (see the normalized comparison in Figure S21). As reported in Table 3, the position of these peaks shifts with different cations from 2.62 eV for $(BA)_4AgBiBr_8$ to 2.47 eV for $(iBA)_4AgBiBr_8$. These results are in excellent agreement with the report by Karunadasa et al., where the emission was assigned to trap-mediated recombination.[21] Differently from other samples, $(iBA)_4AgBiBr_8$ also exhibits a broad (∼400 meV) and highly intense emission band at 1.8 eV. The ratio between this emission and emission under 2.89 eV excitation is about 10, thereby indicating this as an efficient emission channel.

To further explore the excited states of these samples, we measured excitation energy-dependent PL spectra for $(BA)_4AgBiBr_8$ and $(iBA)_4AgBiBr_8$ (Figure 5c,d, respectively). The excitation energy dependence of the PL has already been used to reveal the underlying complex excited-state dynamics of several perovskite and emerging semiconductor systems,[49−51] yet there are no previous reports for 2D Ag−Bi DHPs. For $(BA)_4AgBiBr_8$ thin films, although the emission at 2.6 eV is clearly observed for above band gap excitations (3.29 eV), resonance excitations (3.01 eV) result in a significantly quenched emission. Such behavior indicates the presence of an additional nonradiative recombination mechanism (e.g., trap mediated nonradiative recombination) strongly coupled with the central transition. Furthermore, the use of higher excitation energies produces a broad emission peaked at 3.1 eV. This emission violates the Kasha rule (i.e., the emission takes place from the lowest excited state) and can therefore be tentatively ascribed to the presence of high-lying states which are electronically decoupled from the lower-lying ones, e.g., high-lying trap states or self-trapped exciton (STE) states.[52,53] On the contrary, the emission of $(iBA)_4AgBiBr_8$ thin films under different excitation energies is always dominated by the emission at 1.8 eV. Notably, the intensity of the emission is strongly dependent on the excitation wavelength. Specifically, the emission quenching is observed in correspondence with the main absorption transition (3.01 eV), analogously to what observed for $(BA)_4AgBiBr_8$. Furthermore, the STE emission is fully quenched when excitation energies above 3.7 eV are used. Powder emission PL spectra (Figure S21) confirm the presence of a higher energy emission peak for $(iBA)_4AgBiBr_8$, analogously to what was observed for $(BA)_4AgBiBr_8$.

To delve deeper into the origin of optical excitations in the perovskite series and confirm our assignments, we have

Table 3. Gaussian Fitting Results for Main Absorption and Photoluminescence (under 3.29 eV Excitation) of the $(RA)_4AgBiBr_8$ Thin Film Series

	absorption		photoluminescence	
thin film	position (eV)	FWHM (eV)	position (eV)	FWHM (eV)
$(BA)_4AgBiBr_8$	3.019 ± 0.001	0.30	2.620 ± 0.002	0.37
$(iBA)_4AgBiBr_8$	2.827 ± 0.002	0.21	1,820 ± 0.001	0.38
	3.041 ± 0.001	0.22	2.470 ± 0.002	0.5
$(PEA)_4AgBiBr_8$	2.981 ± 0.001	0.34	2.604 ± 0.002	0.53
$(HA)_4AgBiBr_8$	2.996 ± 0.001	0.39	2.520 ± 0.002	0.44

https://doi.org/10.1021/acs.chemmater.1c01182
Chem. Mater. 2021, 33, 4688−4700

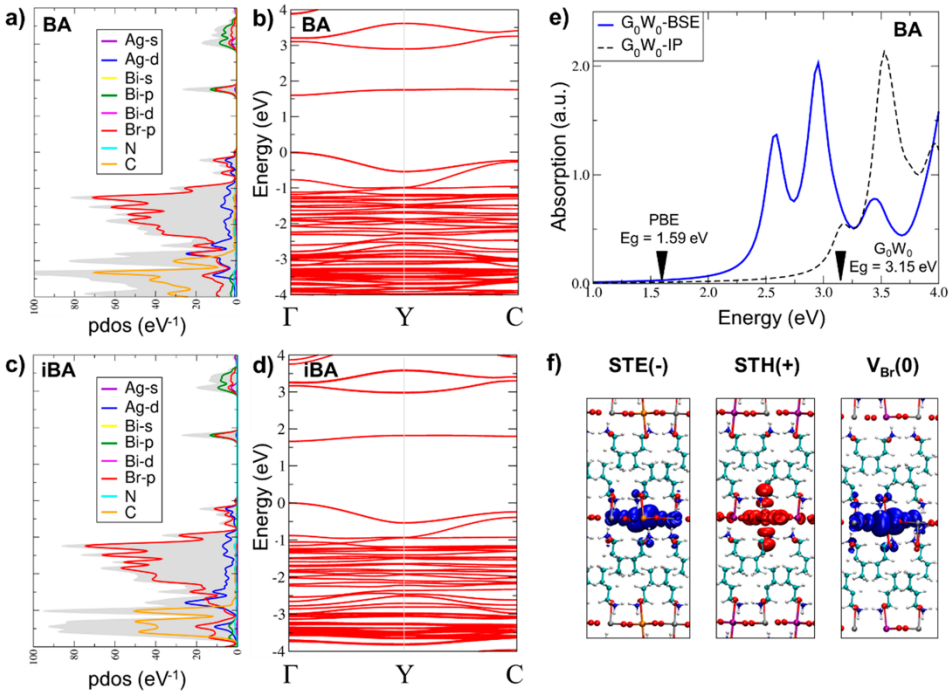

Figure 6. (a) Electronic band structure and PDOS of (a–b) $(BA)_4AgBiBr_8$ and (c–d) $(iBA)_4AgBiBr_8$ layered perovskites, calculated at the PBE-SOC level of theory; (e) optical absorption spectrum of $(BA)_4AgBiBr_8$ calculated at the G_0W_0-independent particle level (G0W0-IP) and by including exciton effects through the solution of the BS equation (G_0W_0-BSE); (f) orbital plots of trapped charge carriers in $(BA)_2AgBiBr_8$: self-trapped electron (STE), self-trapped hole (STH), and trapped-electron at the V_{Br} site.

selected the two isomeric layered perovskites, $(BA)_4AgBiBr_8$ and $(iBA)_4AgBiBr_8$, as model systems. Therefore, we have investigated their electronic and optical properties by ab initio density functional theory (DFT) and many-body perturbation theory (MBPT). The electronic band structures and projected density of states of the (BA, iBA)$_4AgBiBr_8$ perovskites have been calculated at the DFT level by using the Perdew–Burke–Ernzherof (PBE) functional[54] and by including spin–orbit coupling (SOC, see Figure 6a–d).

In both cases cell and ion positions have been relaxed at the PBE level by including DFT-D3 dispersions (see the computational details).[55] Upon structural optimization, a slight contraction of the $(iBA)_4AgBiBr_8$ cell along the *z*-axis is reported with respect to the parent $(BA)_4AgBiBr_8$ perovskite, due to the branched geometry of the iBA cation. The two systems show a similar electronic structure with direct band gaps at the Γ points of 1.59 and 1.66 eV for BA and iBA, respectively. A nearly 2-fold degeneracy of electronic bands at the VBM and CBM is reported. The analysis of PDOS highlights that the VB is mainly composed by Br p and Ag d orbitals, while the CB mainly derives from Bi p and Br p hybridized orbitals with small components of Ag s orbitals, in agreement with previous studies.[21] In both cases, organic cations do not contribute to the electronic states in the proximity of the band edges.

As expected, the calculated band gaps at the PBE-SOC levels strongly underestimate the absorption edges observed in optical experiments. To provide a more accurate estimate of the electronic band gap of these systems, G_0W_0 calculations[56] have been performed on the $BA_4AgBiBr_8$ perovskite by including SOC (see the computational details in the Experimental Section).

Within the G_0W_0 approximation, a significant renormalization of the electronic band gap to 3.15 eV is obtained for $BA_4AgBiBr_8$. The optical absorption spectrum of the perovskite has been simulated at the G_0W_0-independent particle level (G_0W_0-IP) and by including exciton effects by solving the Bethe–Salpeter (BS) equation (G_0W_0-BSE)[57] on top of G_0W_0 corrected eigenvalues (Figure 6e). The solution of the BS equation leads to two main optical absorptions peaks in the low energy range of the spectrum, centered at 2.58 and 2.96 eV. These excitations are mainly associated with transitions between the nearly degenerate levels of the VBM and the CBM, in the proximity of the Γ (0, 0, 0) and C (0.5, 0.5, 0.5) k-points in the Brillouin zone (BZ), respectively. The calculated absorption spectrum is in good agreement with the absorption profile extracted by the Kubelka–Munk analysis (see Figure S20). By considering the energy red-shift of the first exciton peak with respect to the calculated electronic gap, an exciton binding energy of 0.57 eV is estimated. Such a value is naturally higher than in the $Cs_2AgBiBr_6$ bulk perovskite, where an exciton binding energy of 0.34 eV has been reported.[46] The presently observed increase in exciton binding energy and blue-shift by 200 meV in the absorption spectrum with respect to the bulk $Cs_2AgBiBr_6$ are due to a combined effect of dielectric confinement and octahedral distortion.[45] As widely reported for layered lead halide perovskites,[58] the confinement of the carriers arises not only from the restricted motion in a 2D plane (i.e., quantum confinement) but also from the reduced dielectric screening caused by the presence of organic cation layers with lower permittivity compared to

https://doi.org/10.1021/acs.chemmater.1c01182
Chem. Mater. 2021, 33, 4688–4700

3D bulk (i.e., dielectric confinement).[19,20] Furthermore, as demonstrated by Radaelli et al. for $Cs_2AgBiBr_6$, the distortion in Br−Ag−Br angles strongly determines the energy of the direct gap transition.[48] Within this framework, the slight peak shift observed within the 2D perovskite series (i.e., from 2.98 up to 3.04 eV, see Figure 5a and Table 3) can be ascribed to distortions caused by the different steric hindrance of the large cations. These results, in combination with the very similar electronic structure found at the DFT level among the two perovskites, suggest that optical absorption peaks observed at ∼2.7 and ∼3.0 eV may be associated with exciton transitions, and a defect-related origin is likely to be excluded.

PL emissions in the low energy range, i.e., below the first estimated exciton peaks, such as emission at ∼1.8 eV in iBA, are in principle related to emission from defects or self-trapped charge carriers. To investigate this possibility, charge carrier trapping in the perfect lattice and at bromide vacancies defect sites have been studied by performing DFT calculations in 2 × 2 × 1 supercells of BA and iBA systems. PL sub-bandgap emission is studied by simulating the self-trapping of electron (STE) and holes (STH) in the perfect lattice and trapping of the electron at the bromide vacancy V_{Br} site (Figure 6f). To accurately simulate the electronic structures of the perovskites, the hybrid PBE0 functional[59] has been used by increasing the exact exchange fraction α to 0.29. The use of α = 0.29 in combination with a rigid application of SOC provides a band gap of 3.15 eV for BA system, matching the G_0W_0 band gap. SOC is not directly included in PBE0 calculations due to the prohibitive computational cost in supercell calculations. In Table 4 the estimated electronic band gaps at the PBE0-SOC level of theory for the two systems are reported. As already observed at the PBE-SOC level, the modeled phases show similar band gaps.

Table 4. Estimated Electronic Band Gaps of the $(BA)_4AgBiBr_8$ and $(iBA)_4AgBiBr_8$ Perovskites at the PBE0-SOC Level[a] and Calculated TIL and PL Emissions of Self-Trapped Electron (STE), Hole (STH), and Trapped Electron on the V_{Br} Defect, at the PBE0 Level[b]

compound	$(BA)_4AgBiBr_8$		$(iBA)_4AgBiBr_8$	
E_g	3.15		3.24	
defect transition	TIL	PL	TIL	PL
STE (0/−)	3.03	2.03	3.03	2.02
STH (+/0)	0.13	2.59	0.09	2.61
V_{Br} (+/0)	2.27	1.29	2.22	1.25

[a]SOC corrections have been rigidly applied to the PBE0 band gap. [b]All values are in eV.

In Table 4 the calculated thermodynamic ionization levels (TIL) and predicted PL emissions of trapped electrons and holes in the two phases are reported. Notably, calculated transitions show very similar values in the two perovskites, indicating that they share a comparable defect photophysics.

Self-trapping of the electron, simulated by adding a negative charge in the supercell and relaxing ion positions, leads to the electron localization on one Bi ion and to an elongation of the in-plane Bi−Br bonds from ∼2.9 to 3.3 Å (Figure 6f). Electron trapping gives rise to a deep (0/−) thermodynamic transition in the band gap, placed at 3.0 eV above the VB of the perovskites. Radiative decay of the STE with a PL emission at ∼2.0 eV is calculated. Simulation of a self-trapped hole (STH) in the pristine system also shows localization of the hole on a single Ag d orbital hybridized with Br p orbitals in the cell (Figure 6f). Hole trapping leads to a (+/0) transition placed at 0.1 eV above VB and is accompanied by a slight shortening of the Ag−Br bond distances in the localization site from 2.7 to 2.5 Å. A PL emission from STH is calculated at ∼2.6 eV. Electron trapping at the V_{Br}^+ site leads to a deeper (+/0) transition in the band gap with a predicted PL emission in the low energy range at ∼1.2−1.3 eV.

Based on our predictions, the two isomeric perovskites (i.e., iBA and BA-based) show a very similar defect photophysics and no remarkable differences in PL emissions ascribable to the two isomeric cations can be inferred. By considering the cation-induced distortion and the absorption band splitting also observed in the $(iBA)_4AgBiBr_8$ thin-film absorption, the emission peak at ∼1.8 eV is safely ascribed to emission from a self-trapped electron states driven by phonon coupling. Namely, as a consequence of the excitation-phonon coupling, excitations are trapped in the lattice distortion that they generate.[60] Similar emissions from self-trapped carriers have been reported for 2D lead halide perovskites and other corrugated metal−halide complexes.[61,62] On the other hand, the emission at 2.6 eV can be assigned to the band-to-band exciton recombination or to STH emission, where only the hole undergoes localization. In Figure 7, we summarize the photophysics of BA and iBA-based model systems, and the assignment discussed above. We expect this picture to provide a guide for future work delving deeper into the photophysics of two-dimensional $(RA)_4AgBiBr_8$ perovskites.

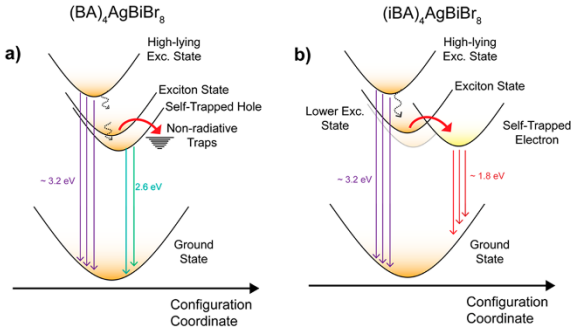

Figure 7. (a and b) Schematic representation of the energetic levels in the configuration coordinate picture, summarizing the structure of the excited states for $(BA)_4AgBiBr_8$ and $(iBA)_4AgBiBr_8$, respectively. Colored arrows represent emission signals and dotted lines represent relaxation processes. The parabolas represent the potential energy surfaces of the different states, their position on the *x*-axis indicates the degree of distortion.

It is worth noting that while ab initio methods give a unique insight into the photophysics of these systems, some of our observation differ from predictions. For instance, as already reported, no STE emission is observed for $(BA)_4AgBiBr_8$. Furthermore, similarly to what observed by Connor et al.,[21] the absorption spectra of thin films do not show strong absorption features at 2.7 eV, which are instead observed for powders. However, we note that extrinsic effects have already demonstrated to be crucial in determining the properties of lower- dimensional lead-halide perovskites.[63] Notably, also the use of corrugated perovskites (obtained via subtle changes in the large cation) has already been proven in white light-emitting 2D lead-based perovskites.[64] While its extent remains

https://doi.org/10.1021/acs.chemmater.1c01182
Chem. Mater. 2021, 33, 4688−4700

an open question, we speculate that morphology could contribute to steering the photophysics of these materials (e.g., by modulating the oscillator strength of some transitions and the carrier-phonon coupling). Such a hypothesis is further confirmed by the significant distribution of WF measured by KPFM on the microstructured surface of $(iBA)_4AgBiBr_8$. We nevertheless expect that future work will be needed to fully elucidate the impact of morphology on the optical properties of 2D-DHPs.

3. CONCLUSIONS

In this work we provide a comprehensive characterization of the structural properties of hydrothermally synthesized 2D monolayer DHP series, with the general formula $(RA)_4AgBiBr_8$. Here, by using four bulky organic cations (RA) with different alkyl chain length, branching, and dipole moments, we finely tuned the interlayer distances in these silver/bismuth bromide 2D DHP. Interestingly, the nature of the large organic cation also chameleonically determines the thin-film morphologies obtained after a recrystallization process of the crystalline powders. The resulting different thin-film microstructures span from the case of very flat and homogeneous surfaces, as found for the $(BA)_4AgBiBr_8$ based thin films, to rougher or extremely soft cases (for $(PEA)_4AgBiBr_8$ and $(BA)_4AgBiBr_8$, respectively) up to the formation of complex porous architectures, as found for the $(iBA)_4AgBiBr_8$ thin films. Notably, the simple isomerization to a branched alkyl ammonium cation (i.e., from butylammonium to isobutylammonium) results in an extreme variation of the film morphology.

A similar multifaceted nature associated with the mere identity of a small molecular component within a hybrid semiconductor primarily drives structure−property relationships, which here have been characterized mainly in terms of basic optical features. Fine-tuning of structure and morphology of the thin films is proven useful to control the optical properties of 2D DHP. By changing from a linear (BA^+) to a branched (iBA^+) cation, the excitonic recombination is outpaced by a broad and relatively intense STE emission. This interplay between structure, morphology and optical properties provides exciting perspectives not only for delving deeper into the optical properties of layered metal halide perovskites but also for a material-by-design approach. Our systematic study of large cation effects on structure, morphology, electronic and optical properties lies the foundation for the future development of the 2D DHP material platform. We expect that future effort will be directed in further expanding the nature (i.e., steric hindrance, chemistry, and electronic properties) of large cations, thus following the development of their lead-based counterparts. Although a complete optoelectronic characterization of these materials will require further studies, the map of the excited states in Figure 7 will provide a valuable guide for future investigations.

This work represents a significant step ahead in the field of non-toxic DHP and casts new hopes for the complete substitution of lead in next-generation low-cost optoelectronic devices.

4. EXPERIMENTAL SECTION

4.1. Materials and Methods. All of the double perovskite precursors, namely $BiBr_3$(99%), CsBr (99.9%), and AgBr (99.5%), were purchased from Alfa Aesar. $BiBr_3$ was stored in a glovebox due to moisture sensitivity and AgBr in dark due to light sensitivity. The crystalline reference 3D double perovskite compound was synthesized through hydrothermal synthesis following a previously reported procedures from some of us.[10] The organic amines were purchased from Sigma-Aldrich, as were all solvents. P-XRD analysis was performed at ambient temperature with a PANalytical B.V. X'Pert PRO diffractometer employing Cu Kα1 radiation. The instrument operated at 40 kV and 40 mA using a 1° divergence slit for the incident beam. SC-XRD was measured at low temperatures (100 K) using φ- and ω-scans on a Bruker D8 Venture system equipped with dual IμS microfocus sources, a PHOTON100 detector, and an OXFORD CRYOSYSTEMS 700 low-temperature system. Mo Kα radiation with wavelength 0.71073 Å and a collimating Quazar multilayer mirror were used. Semiempirical absorption correction from equivalents was applied using SADABS-2016/2[65] and the structures were solved by the dual space algorithm implemented in SHELXT2014/5.[66] Refinement was performed against F^2 on all data by full-matrix least-squares using SHELXL2018/3.[67] All non-hydrogen atoms were refined anisotropically and hydrogen atoms were positioned at geometrically calculated positions and refined using a riding model. The isotropic displacement parameters of all hydrogen atoms were fixed to 1.2× or 1.5× (NH_3 hydrogens) the U_{eq} value of the atoms they are linked to. Disorder was modeled with the help of similarity restraints on bond distances, restraints to a common plane, similarity restraints on anisotropic displacement parameters,[68] and advanced rigid bond restraints.[69] Micro-Raman analysis was carried out using a Senterra Raman microscope equipped with a λ = 532 nm laser. All of the measurements were conducted by positioning a small amount of powder on a glass slide, which was placed upon the support inside the instrument. Ethanolic suspensions of the hydrothermally synthesized 2D double perovskites were drop-casted and dried on 200 mesh copper supported lacey carbon grids, and their morphological characteristics were investigated through a FEI Tecnai G2 20 X Twin TEM using 200 kV accelerating voltage (FEI Corporate Headquarters, Hillsboro, OR, U.S.A.) followed by the crystal structure analysis of the samples through selected area electron diffraction (SAED). Furthermore, and their chemical composition was assessed by energy dispersive X-ray spectroscopy (EDS) using a Bruker XFlash 6T-30 detector mounted onto the TEM (Bruker Corporation, Billerica, MA, U.S.A.). SEM was performed on a Zeiss Merlin instrument at a working potential of 20 kV. GIXRD was performed in a range of 3° to 70° (0.05° step size, 0.014°/s scan speed) with a PANalytical B.V. X'Pert Pro diffractometer using Cu Kα1 radiation. The diffraction patterns were measured along the 2θ axis with a grazing incidence of ω = 0.5°. AFM characterization was carried out with a SmartSPM 1000 from AIST-NT in intermittent contact mode using SEIHR probes (NanoWorld). FM-KPFM was measured using a Vacuscope 2000 from AIST-NT at a pressure below 10−6 mbar using OPUS 160AC-GG cold coated silicon probes operated in two-pass mode. The first pass was used to obtain a surface profile while the contact potential difference was obtained following that profile during the second pass by the sideband method using an AC voltage of 2 V at around 1 kHz. Referencing to the known work function of freshly cleaved HOPG ZYA (4.6 eV,[70] MikroMash) was carried out before and after every measurement to avoid the influence of contamination of the probe. UV−vis absorption measurements of thin films were carried out on an Agilent 8453 UV−vis spectrometer. Diffuse reflectance spectra were acquired on a Cary 5E UV−vis−NIR spectrometer equipped with a diffuse reflectance accessory. DLS measurements were conducted with a Malvern Zetasizer Nano-ZS device (Malvern, U.K.) at 20 °C. The DLS system was operated by the Zetasizer software from Malvern Panlytical (Malvern, U.K.). PL measurements were performed on a HORIBA Jobin Yvon Spex Fluorolog 3 spectrophotometer equipped with a 450 W Xe short-arc lamp, double grated excitation and emission monochromators, and a photomultiplier tube in quartz glass cuvette at 77 K using a special liquid nitrogen-filled Dewar assembly using the FluoroEssence software package. Excitation and emission spectra were corrected for the spectral response of the monochromators and the detector using spectral corrections provided by the manufacturer. The dipole

https://doi.org/10.1021/acs.chemmater.1c01182
Chem. Mater. 2021, 33, 4688−4700

moment of isolated RA^+ cations was calculated by DFT using the B3LYP hybrid functional with the basis set 6-31G* following geometry-optimization of the structures.

4.2. Hydrothermal Synthesis of $(RA)_4AgBiBr_8$ Double Perovskites. A total of 408 mg of $BiBr_3$ (0.9 mmol) and 170 mg of AgBr (0.9 mmol) were transferred to a two-necked 25 mL round-bottom flask. Then, 2.6 mL of HBr (49%) was added with a 5 mL syringe to dissolve inorganic precursors. Last, 3.6 mmol of the primary amine was added with a Labsolute 1000 mL pipet to the stirring mixture, which caused smoke development. The solution was stirred and heated to 100 °C under reflux cooling until all reactants were dissolved. Dissolution occurred between 100 and 120 °C, depending on the amine. While heating, the color of the solution turned from light orange to dark orange. After 30 min, the solutions were cooled to room temperature. Crystalline materials started to participate as soon as the heating was removed. Products were filtered and washed with diethyl ether several times. Subsequent to washing, the products were dried on filtration paper for a few minutes and then transferred to a weighing boat to continue drying overnight. The drying process proceeded under ambient conditions. Single crystals of $(PEA)_4AgBiBr_8$ were obtained by stratifying diethyl ether on top of a supersaturated solution of the polycrystalline powder in DMF and allowing the two solvents to slowly mix overnight. Crystallographic data for $(PEA)_4AgBiBr_8$ was deposited as CCDC 2031528 at the Cambridge Crystallographic Data Centre.

4.3. Preparation of Thin Films. Glass and FTO substrates (1.5 × 1.5 cm^2) were cleaned by successive ultrasonication in deionized water, acetone, and isopropyl alcohol for 15 min each, followed by 15 min of UV-ozone cleaning right before the thin film preparation. The precursor solutions were prepared by dissolving 22 μmol of the respective presynthesized 2D double perovskite powder in 90 μL of DMF and stirred for 2 h at room temperature. The thin film casting was conducted in a nitrogen-filled glovebox and was based on the protocol of Connor et al.[21] To prepare the thin films, the substrates were mounted on a spin-coater, evenly covered with 30 μL of precursor solution and spun at 4000 rpm for 40 s with an acceleration of 200 rpm/s. After spin-coating, the samples were annealed on a hot plate at 100 °C for 4 min.

4.4. DFT Calculations. The electronic structure of (BA, iBA)$_4$AgBiBr$_8$ perovskites has been calculated in periodic boundary conditions by using plane waves basis set and pseudopotentials, as implemented in the Quantum Espresso simulation package.[71] The Perdew–Burke–Ernzerhof (PBE) functional[54] and norm-conserving pseudopotentials were used by including spin–orbit coupling (SOC). An energy cutoff on the wave functions of 60 Ryd and 4 × 4 × 1 k-point grid in the BZ were used. In all cases cell parameters of the phases have been relaxed by using the PBE functional (no SOC included) and including DFT-D3 dispersion corrections.[55] By this approach the following equilibrium cell parameters have been obtained: for BA a = 8.19 Å, b = 8.05 Å, c = 26.78 Å, α = 90.0°, β = 90.1°, γ = 90.0°; for iBA a = 8.20 Å, b = 8.28 Å, c = 25.93 Å, α = 90.0°, β = 88.9°, γ = 90.0°. G_0W_0 and BSE calculations for the BA system have been performed by using the Yambo code[72] on top of PBE-SOC calculations. Due to the prohibitive dimension of the system (460 electrons) a minimal but sufficiently converged computational setup has been adopted (see Table S3 of the SI). G_0W_0 calculations have been carried out in the plasmon-pole approximation[73] by using a cutoff of 30 Ry (3 Ry) for the exchange (correlation) part of the self-energy and by including a total of 2560 bands in the calculation of the dielectric matrix and correlation energy. BSE calculations have been performed on top of QP corrected eigenvalues by using a cutoff of 30 Ry (3 Ry) on the exchange (screening) parts and by including 20 occupied and 20 unoccupied bands. For the screening part the same computational setup employed in G_0W_0 calculations was used. The BSE convergence on the k-point grid has been investigated by performing a BSE scissor operator calculation by enlarging the k-grid up to 6 × 6 × 1 (see Figure S24).

Self-trapping and defect calculations have been carried out in the 2 × 2 × 1 supercells of BA and iBA by using the CP2K software package.[74] Cell parameters of the supercells have been optimized by using the PBE functional and including DFT-D3 dispersions. Equilibrium structures of self-trapped states and defects have been calculated by fixing cell parameters to the optimized values and relaxing ion positions by using the hybrid PBE0 functional[75] with a fraction of exact exchange α = 0.29, in order to reproduce the G_0W_0 band gap of the BA system, and by including van der Waals interactions through the DFT-D3 scheme.[55] Calculations have been carried out with Goedecker-Teter-Hutter pseudopotentials,[76] double-ζ polarized basis sets,[77] and a cutoff of 300 Ry for the expansion of the electron density in plane waves. The auxiliary density matrix method with the cFIT auxiliary basis set has been used to accelerate hybrid functional calculations.[78] Thermodynamic ionization levels has been calculated by using the following expression:[79]

$$\varepsilon(q/q') = \frac{E[X^q]-E[X^{q'}]}{q'-q} + \frac{E^q_{corr} - E^{q'}_{corr}}{q'-q} - \varepsilon_{VB}$$

where $E[X^q]$ are the energies of self-trapped or defect systems in the different state of charge q, ε_{VB} is the valence band of the pristine system, and E^q_{corr} are finite size supercell corrections for charged defects. TILs were corrected by applying Makov–Payne corrections by using the static dielectric tensor of $(BA)_4AgBiBr_8$, i.e., $\varepsilon_{xx} \approx \varepsilon_{yy}$ = 6.8, ε_{zz} = 3.6, estimated by using the approach of Umari et al.[80] PL emission energies have been calculated by simulating vertical transitions between the excited (trapped) and the ground state potential energy surfaces of the defects at the excited state equilibrium geometry.

■ ASSOCIATED CONTENT

Supporting Information

The Supporting Information is available free of charge at https://pubs.acs.org/doi/10.1021/acs.chemmater.1c01182.

Optical microscope images of the 2D perovskite crystals, high-wavenumber regions of the Raman spectra, single crystals structure details, thermograms, HR-TEM images and TEM EDX data, thin film XRD patterns, thin films cross-section SEM images, AFM topography images, DLS spectra, calculated dipole moments of the organic cations, diffuse reflectance and PL spectra, and further computational details (PDF)

The cif file of the $(PEA)_4AgBiBr_8$ compound single crystal structure (CIF)

■ AUTHOR INFORMATION

Corresponding Authors

Daniele Meggiolaro − *Computational Laboratory for Hybrid/Organic Photovoltaics (CLHYO), Istituto CNR di Scienze e Tecnologie Chimiche "Giulio Natta" (CNR-SCITEC), 06123 Perugia, Italy*; Email: daniele.meggiolaro@cnr.it

Marcello Righetto − *Department of Physics and Astronomy, University College London, London WC1E 6BT, United Kingdom*; Email: m.righetto@ucl.ac.uk

Teresa Gatti − *Center for Materials Research, Justus Liebig University, 35392 Giessen, Germany; Institute of Physical Chemistry, Justus Liebig University, 35392 Giessen, Germany*; orcid.org/0000-0001-5343-8055; Email: teresa.gatti@phys.chemie.uni-giessen.de

Authors

Fabian Schmitz − *Center for Materials Research, Justus Liebig University, 35392 Giessen, Germany; Institute of Physical Chemistry, Justus Liebig University, 35392 Giessen, Germany*

Jonas Horn − *Center for Materials Research and Institute of Applied Physics, Justus Liebig University, 35392 Giessen, Germany*

https://doi.org/10.1021/acs.chemmater.1c01182
Chem. Mater. 2021, 33, 4688−4700

Nicola Dengo − *Department of Chemical Sciences, University of Padova, 35131 Padova, Italy*
Alexander E. Sedykh − *Center for Materials Research, Justus Liebig University, 35392 Giessen, Germany; Institute of Inorganic and Analytical Chemistry, Justus Liebig University, 35392 Giessen, Germany;* orcid.org/0000-0003-2650-5173
Jonathan Becker − *Center for Materials Research, Justus Liebig University, 35392 Giessen, Germany; Institute of Inorganic and Analytical Chemistry, Justus Liebig University, 35392 Giessen, Germany*
Elena Maiworm − *Institute of Physical Chemistry, Justus Liebig University, 35392 Giessen, Germany*
Péter Bélteky − *Interdisciplinary Excellence Centre, Department of Applied and Environmental Chemistry, University of Szeged, H-6720 Szeged, Hungary*
Ákos Kukovecz − *Interdisciplinary Excellence Centre, Department of Applied and Environmental Chemistry, University of Szeged, H-6720 Szeged, Hungary;* orcid.org/0000-0003-0716-9557
Silvia Gross − *Department of Chemical Sciences, University of Padova, 35131 Padova, Italy; Interdepartmental Centre Giorgio Levi Cases for Energy Economics and Technology, University of Padova, 35131 Padova, Italy;* orcid.org/0000-0003-1860-8711
Francesco Lamberti − *Department of Chemical Sciences, University of Padova, 35131 Padova, Italy; Interdepartmental Centre Giorgio Levi Cases for Energy Economics and Technology, University of Padova, 35131 Padova, Italy;* orcid.org/0000-0003-1720-8038
Klaus Müller-Buschbaum − *Center for Materials Research, Justus Liebig University, 35392 Giessen, Germany; Institute of Inorganic and Analytical Chemistry, Justus Liebig University, 35392 Giessen, Germany*
Derck Schlettwein − *Center for Materials Research and Institute of Applied Physics, Justus Liebig University, 35392 Giessen, Germany*

Complete contact information is available at: https://pubs.acs.org/10.1021/acs.chemmater.1c01182

Notes

The authors declare no competing financial interest.

■ ACKNOWLEDGMENTS

T.G. thanks the European Commission for financial support through the H2020 FET-PROACTIVE-EIC-07-2020 project LIGHT-CAP (Project No. 101017821) and the Verband der Chemischen Industrie e.V. for financial support through the "Fonds der Chemischen Industrie". D.S. acknowledges financial support by Deutsche Forschungsgemeinschaft (Schl. 340/21-3 and GRK 2204).

■ REFERENCES

(1) Green, M. A.; Ho-Baillie, A.; Snaith, H. J. The Emergence of Perovskite Solar Cells. *Nat. Photonics* **2014**, *8*, 506−514.
(2) Stranks, S. D.; Eperon, G. E.; Grancini, G.; Menelaou, C.; Alcocer, M. J. P.; Leijtens, T.; Herz, L. M.; Petrozza, A.; Snaith, H. J. Electron-Hole Diffusion Lengths Exceeding 1 Micrometer in an Organometal Trihalide Perovskite Absorber. *Science (Washington, DC, U. S.)* **2013**, *342* (6156), 341−344.
(3) Wehrenfennig, C.; Eperon, G. E.; Johnston, M. B.; Snaith, H. J.; Herz, L. M. High Charge Carrier Mobilities and Lifetimes in Organolead Trihalide Perovskites. *Adv. Mater.* **2014**, *26*, 1584−1589.
(4) Green, M.; Dunlop, E.; Hohl-Ebinger, J.; Yoshita, M.; Kopidakis, N.; Hao, X. Solar Cell Efficiency Tables (Version 57). *Prog. Photovoltaics* **2021**, *29* (1), 3−15.
(5) Li, J.; Cao, H.-L.; Jiao, W.-B.; Wang, Q.; Wei, M.; Cantone, I.; Lü, J.; Abate, A. Biological Impact of Lead from Halide Perovskites Reveals the Risk of Introducing a Safe Threshold. *Nat. Commun.* **2020**, *11* (1), 310.
(6) Zhang, S.; Han, G. Intrinsic and Environmental Stability Issues of Perovskite Photovoltaics. *Prog. Energy* **2020**, *2* (2), 22002.
(7) Kim, M.; Alfano, A.; Perotto, G.; Serri, M.; Dengo, N.; Mezzetti, A.; Gross, S.; Prato, M.; Salerno, M.; Rizzo, A.; Sorrentino, R.; Cescon, E.; Meneghesso, G.; Di Fonzo, F.; Petrozza, A.; Gatti, T.; Lamberti, F. Moisture Resistance in Perovskite Solar Cells Attributed to a Water-Splitting Layer. *Commun. Mater.* **2021**, *2* (1), 6.
(8) Kangsabanik, J.; Sugathan, V.; Yadav, A.; Yella, A.; Alam, A. Double Perovskites Overtaking the Single Perovskites: A Set of New Solar Harvesting Materials with Much Higher Stability and Efficiency. *Phys. Rev. Mater.* **2018**, *2* (5), 55401.
(9) Jin, Z.; Zhang, Z.; Xiu, J.; Song, H.; Gatti, T.; He, Z. A Critical Review on Bismuth and Antimony Halides Based Perovskites and Derivatives for Photovoltaic Applications: Recent Advances and Challenges. *J. Mater. Chem. A* **2020**, *8*, 16166−16188.
(10) Schmitz, F.; Guo, K.; Horn, J.; Sorrentino, R.; Conforto, G.; Lamberti, F.; Brescia, R.; Drago, F.; Prato, M.; He, Z.; Giovanella, U.; Cacialli, F.; Schlettwein, D.; Meggiolaro, D.; Gatti, T. Lanthanide-Induced Photoluminescence in Lead-Free Cs 2 AgBiBr 6 Bulk Perovskite: Insights from Optical and Theoretical Investigations. *J. Phys. Chem. Lett.* **2020**, *11* (20), 8893−8900.
(11) Fabini, D. H.; Seshadri, R.; Kanatzidis, M. G. The Underappreciated Lone Pair in Halide Perovskites Underpins Their Unusual Properties. *MRS Bull.* **2020**, *45* (6), 467−477.
(12) Righetto, M.; Meggiolaro, D.; Rizzo, A.; Sorrentino, R.; He, Z.; Meneghesso, G.; Sum, T. C.; Gatti, T.; Lamberti, F. Coupling Halide Perovskites with Different Materials: From Doping to Nanocomposites, beyond Photovoltaics. *Prog. Mater. Sci.* **2020**, *110*, 100639.
(13) Zhang, Z.; Liang, Y.; Huang, H.; Liu, X.; Li, Q.; Chen, L.; Xu, D. Stable and Highly Efficient Photocatalysis with Lead-Free Double-Perovskite of Cs2AgBiBr6. *Angew. Chem., Int. Ed.* **2019**, *58* (22), 7263−7267.
(14) Liu, G.; Wu, C.; Zhang, Z.; Chen, Z.; Xiao, L.; Qu, B. Ultraviolet-Protective Transparent Photovoltaics Based on Lead-Free Double Perovskites. *Sol. RRL* **2020**, *4* (5), 2000056.
(15) Peng, Y.; Huq, T. N.; Mei, J.; Portilla, L.; Jagt, R. A.; Occhipinti, L. G.; MacManus-Driscoll, J. L.; Hoye, R. L. Z.; Pecunia, V. Lead-Free Perovskite-Inspired Absorbers for Indoor Photovoltaics. *Adv. Energy Mater.* **2021**, *11* (1), 2002761.
(16) Pecunia, V.; Occhipinti, L. G.; Chakraborty, A.; Pan, Y.; Peng, Y. Lead-Free Halide Perovskite Photovoltaics: Challenges, Open Questions, and Opportunities. *APL Mater.* **2020**, *8* (10), 100901.
(17) Pan, W.; Wu, H.; Luo, J.; Deng, Z.; Ge, C.; Chen, C.; Jiang, X.; Yin, W.-J.; Niu, G.; Zhu, L.; Yin, L.; Zhou, Y.; Xie, Q.; Ke, X.; Sui, M.; Tang, J. Cs2AgBiBr6 Single-Crystal X-Ray Detectors with a Low Detection Limit. *Nat. Photonics* **2017**, *11* (11), 726−732.
(18) Xing, G.; Wu, B.; Wu, X.; Li, M.; Du, B.; Wei, Q.; Guo, J.; Yeow, E. K. L.; Sum, T. C.; Huang, W. Transcending the Slow Bimolecular Recombination in Lead-Halide Perovskites for Electroluminescence. *Nat. Commun.* **2017**, *8* (1), 14558.
(19) Giovanni, D.; Ramesh, S.; Righetto, M.; Melvin Lim, J. W.; Zhang, Q.; Wang, Y.; Ye, S.; Xu, Q.; Mathews, N.; Sum, T. C. The Physics of Interlayer Exciton Delocalization in Ruddlesden−Popper Lead Halide Perovskites. *Nano Lett.* **2021**, *21* (1), 405−413.
(20) Katan, C.; Mercier, N.; Even, J. Quantum and Dielectric Confinement Effects in Lower-Dimensional Hybrid Perovskite Semiconductors. *Chem. Rev.* **2019**, *119* (5), 3140−3192.
(21) Connor, B. A.; Leppert, L.; Smith, M. D.; Neaton, J. B.; Karunadasa, H. I. Layered Halide Double Perovskites: Dimensional Reduction of Cs2AgBiBr6. *J. Am. Chem. Soc.* **2018**, *140* (15), 5235−5240.

(22) Jana, M. K.; Janke, S. M.; Dirkes, D. J.; Dovletgeldi, S.; Liu, C.; Qin, X.; Gundogdu, K.; You, W.; Blum, V.; Mitzi, D. B. Direct-Bandgap 2D Silver−Bismuth Iodide Double Perovskite: The Structure-Directing Influence of an Oligothiophene Spacer Cation. *J. Am. Chem. Soc.* **2019**, *141* (19), 7955−7964.
(23) Ortiz-Cervantes, C.; Carmona-Monroy, P.; Solis-Ibarra, D. Two-Dimensional Halide Perovskites in Solar Cells: 2D or Not 2D? *ChemSusChem* **2019**, *12* (8), 1560−1575.
(24) Yao, Y.; Kou, B.; Peng, Y.; Wu, Z.; Li, L.; Wang, S.; Zhang, X.; Liu, X.; Luo, J. (C3H9NI)4AgBiI8: A Direct-Bandgap Layered Double Perovskite Based on a Short-Chain Spacer Cation for Light Absorption. *Chem. Commun.* **2020**, *56* (21), 3206−3209.
(25) Wang, X.; Li, K.; Xu, H.; Ali, N.; Wang, Y.; Shen, Q.; Wu, H. Synthesis of Large Two-Dimensional Lead-Free Bismuth−Silver Double Perovskite Microplatelets and Their Application for Field-Effect Transistors. *Chem. Commun.* **2020**, *56*, 7917−7920.
(26) Martin-Garcia, B.; Spirito, D.; Biffi, G.; Artyukhin, S.; Bonaccorso, F.; Krahne, R. Phase Transitions in Low-Dimensional Layered Double Perovskites: The Role of the Organic Moieties. *J. Phys. Chem. Lett.* **2021**, *12* (1), 280−286.
(27) Zhang, F.; Lu, H.; Tong, J.; Berry, J. J.; Beard, M. C.; Zhu, K. Advances in Two-Dimensional Organic−Inorganic Hybrid Perovskites. *Energy Environ. Sci.* **2020**, *13* (4), 1154−1186.
(28) Khalfin, S.; Bekenstein, Y. Advances in Lead-Free Double Perovskite Nanocrystals, Engineering Band-Gaps and Enhancing Stability through Composition Tunability. *Nanoscale* **2019**, *11* (18), 8665−8679.
(29) Cao, D. H.; Stoumpos, C. C.; Farha, O. K.; Hupp, J. T.; Kanatzidis, M. G. 2D Homologous Perovskites as Light-Absorbing Materials for Solar Cell Applications. *J. Am. Chem. Soc.* **2015**, *137* (24), 7843−7850.
(30) Kentsch, R.; Scholz, M.; Horn, J.; Schlettwein, D.; Oum, K.; Lenzer, T. Exciton Dynamics and Electron−Phonon Coupling Affect the Photovoltaic Performance of the Cs2AgBiBr6 Double Perovskite. *J. Phys. Chem. C* **2018**, *122* (45), 25940−25947.
(31) Li, X.; Fu, Y.; Pedesseau, L.; Guo, P.; Cuthriell, S.; Hadar, I.; Even, J.; Katan, C.; Stoumpos, C. C.; Schaller, R. D.; Harel, E.; Kanatzidis, M. G. Negative Pressure Engineering with Large Cage Cations in 2D Halide Perovskites Causes Lattice Softening. *J. Am. Chem. Soc.* **2020**, *142* (26), 11486−11496.
(32) Yuan, W.; Niu, G.; Xian, Y.; Wu, H.; Wang, H.; Yin, H.; Liu, P.; Li, W.; Fan, J. In Situ Regulating the Order−Disorder Phase Transition in Cs2AgBiBr6 Single Crystal toward the Application in an X-Ray Detector. *Adv. Funct. Mater.* **2019**, *29* (20), 1900234.
(33) Guijarro, A.; Vergés, J. A.; San-Fabián, E.; Chiappe, G.; Louis, E. Herringbone Pattern and CH−π Bonding in the Crystal Architecture of Linear Polycyclic Aromatic Hydrocarbons. *ChemPhysChem* **2016**, *17* (21), 3548−3557.
(34) Gatti, T.; Brambilla, L.; Tommasini, M.; Villafiorita-Monteleone, F.; Botta, C.; Sarritzu, V.; Mura, A.; Bongiovanni, G.; Zoppo, M. D. Near IR to Red Up-Conversion in Tetracene/Pentacene Host/Guest Cocrystals Enhanced by Energy Transfer from Host to Guest. *J. Phys. Chem. C* **2015**, *119* (31), 17495.
(35) Nicolini, T.; Famulari, A.; Gatti, T.; Martí-Rujas, J.; Villafiorita-Monteleone, F.; Canesi, E. V.; Meinardi, F.; Botta, C.; Parisini, E.; Meille, S. V.; Bertarelli, C. Structure-Photoluminescence Correlation for Two Crystalline Polymorphs of a Thiophene-Phenylene Co-Oligomer with Bulky Terminal Substituents. *J. Phys. Chem. Lett.* **2014**, *5* (13), 2171.
(36) Liu, Y.; Siron, M.; Lu, D.; Yang, J.; dos Reis, R.; Cui, F.; Gao, M.; Lai, M.; Lin, J.; Kong, Q.; Lei, T.; Kang, J.; Jin, J.; Ciston, J.; Yang, P. Self-Assembly of Two-Dimensional Perovskite Nanosheet Building Blocks into Ordered Ruddlesden−Popper Perovskite Phase. *J. Am. Chem. Soc.* **2019**, *141* (33), 13028−13032.
(37) Xu, Y.; Wang, M.; Lei, Y.; Ci, Z.; Jin, Z. Crystallization Kinetics in 2D Perovskite Solar Cells. *Adv. Energy Mater.* **2020**, *10* (43), 2002558.
(38) Quintero-Bermudez, R.; Gold-Parker, A.; Proppe, A. H.; Munir, R.; Yang, Z.; Kelley, S. O.; Amassian, A.; Toney, M. F.; Sargent, E. H. Compositional and Orientational Control in Metal Halide Perovskites of Reduced Dimensionality. *Nat. Mater.* **2018**, *17* (10), 900−907.
(39) Zuo, C.; Scully, A. D.; Tan, W. L.; Zheng, F.; Ghiggino, K. P.; Vak, D.; Weerasinghe, H.; McNeill, C. R.; Angmo, D.; Chesman, A. S. R.; Gao, M. Crystallisation Control of Drop-Cast Quasi-2D/3D Perovskite Layers for Efficient Solar Cells. *Commun. Mater.* **2020**, *1* (1), 33.
(40) Wang, J.; Luo, S.; Lin, Y.; Chen, Y.; Deng, Y.; Li, Z.; Meng, K.; Chen, G.; Huang, T.; Xiao, S.; Huang, H.; Zhou, C.; Ding, L.; He, J.; Huang, J.; Yuan, Y. Templated Growth of Oriented Layered Hybrid Perovskites on 3D-like Perovskites. *Nat. Commun.* **2020**, *11* (1), 582.
(41) Pratap, S.; Schlipf, J.; Bießmann, L.; Müller-Buschbaum, P. Hierarchical Structures from Nanocrystalline Colloidal Precursors within Hybrid Perovskite Thin Films: Implications for Photovoltaics. *ACS Appl. Nano Mater.* **2020**, *3* (12), 11701−11708.
(42) Yang, J.; Xiong, S.; Song, J.; Wu, H.; Zeng, Y.; Lu, L.; Shen, K.; Hao, T.; Ma, Z.; Liu, F.; Duan, C.; Fahlman, M.; Bao, Q. Energetics and Energy Loss in 2D Ruddlesden−Popper Perovskite Solar Cells. *Adv. Energy Mater.* **2020**, *10* (23), 2000687.
(43) Meggiolaro, D.; Mosconi, E.; Proppe, A. H.; Quintero-Bermudez, R.; Kelley, S. O.; Sargent, E. H.; De Angelis, F. Energy Level Tuning at the MAPbI3 Perovskite/Contact Interface Using Chemical Treatment. *ACS Energy Lett.* **2019**, *4* (9), 2181−2184.
(44) Bekenstein, Y.; Dahl, J. C.; Huang, J.; Osowiecki, W. T.; Swabeck, J. K.; Chan, E. M.; Yang, P.; Alivisatos, A. P. The Making and Breaking of Lead-Free Double Perovskite Nanocrystals of Cesium Silver−Bismuth Halide Compositions. *Nano Lett.* **2018**, *18* (6), 3502−3508.
(45) Schmitz, A.; Schaberg, L. L.; Sirotinskaya, S.; Pantaler, M.; Lupascu, D. C.; Benson, N.; Bacher, G. Fine Structure of the Optical Absorption Resonance in Cs2AgBiBr6 Double Perovskite Thin Films. *ACS Energy Lett.* **2020**, *5* (2), 559−565.
(46) Palummo, M.; Berrios, E.; Varsano, D.; Giorgi, G. Optical Properties of Lead-Free Double Perovskites by Ab Initio Excited-State Methods. *ACS Energy Lett.* **2020**, *5* (2), 457−463.
(47) Zelewski, S. J.; Urban, J. M.; Surrente, A.; Maude, D. K.; Kuc, A.; Schade, L.; Johnson, R. D.; Dollmann, M.; Nayak, P. K.; Snaith, H. J.; Radaelli, P.; Kudrawiec, R.; Nicholas, R. J.; Plochocka, P.; Baranowski, M. Revealing the Nature of Photoluminescence Emission in the Metal-Halide Double Perovskite Cs2AgBiBr6. *J. Mater. Chem. C* **2019**, *7* (27), 8350−8356.
(48) Schade, L.; Wright, A. D.; Johnson, R. D.; Dollmann, M.; Wenger, B.; Nayak, P. K.; Prabhakaran, D.; Herz, L. M.; Nicholas, R.; Snaith, H. J.; Radaelli, P. G. Structural and Optical Properties of Cs2AgBiBr6 Double Perovskite. *ACS Energy Lett.* **2019**, *4* (1), 299−305.
(49) Righetto, M.; Lim, S. S.; Giovanni, D.; Lim, J. W. M.; Zhang, Q.; Ramesh, S.; Tay, Y. K. E.; Sum, T. C. Hot Carriers Perspective on the Nature of Traps in Perovskites. *Nat. Commun.* **2020**, *11* (1), 2712.
(50) Righetto, M.; Privitera, A.; Fortunati, I.; Mosconi, D.; Zerbetto, M.; Curri, M. L.; Corricelli, M.; Moretto, A.; Agnoli, S.; Franco, L.; Bozio, R.; Ferrante, C. Spectroscopic Insights into Carbon Dot Systems. *J. Phys. Chem. Lett.* **2017**, *8* (10), 2236−2242.
(51) Righetto, M.; Minotto, A.; Bozio, R. Bridging Energetics and Dynamics of Exciton Trapping in Core−Shell Quantum Dots. *J. Phys. Chem. C* **2017**, *121* (1), 896−902.
(52) Kasha, M. Characterization of Electronic Transitions in Complex Molecules. *Discuss. Faraday Soc.* **1950**, *9* (0), 14−19.
(53) Li, B.; Brosseau, P. J.; Strandell, D. P.; Mack, T. G.; Kambhampati, P. Photophysical Action Spectra of Emission from Semiconductor Nanocrystals Reveal Violations to the Vavilov Rule Behavior from Hot Carrier Effects. *J. Phys. Chem. C* **2019**, *123* (8), 5092−5098.
(54) Perdew, J. P.; Burke, K.; Ernzerhof, M. Generalized Gradient Approximation Made Simple. *Phys. Rev. Lett.* **1996**, *77*, 3865−3868.
(55) Grimme, S.; Antony, J.; Ehrlich, S.; Krieg, H. A Consistent and Accurate Ab Initio Parametrization of Density Functional Dispersion Correction (DFT-D) for the 94 Elements H-Pu. *J. Chem. Phys.* **2010**, *132* (15), 154104.

https://doi.org/10.1021/acs.chemmater.1c01182
Chem. Mater. 2021, 33, 4688−4700

(56) Hybertsen, M. S.; Louie, S. G. Electron Correlation in Semiconductors and Insulators: Band Gaps and Quasiparticle Energies. *Phys. Rev. B: Condens. Matter Mater. Phys.* **1986**, *34* (8), 5390−5413.
(57) Onida, G.; Reining, L.; Rubio, A. Electronic Excitations: Density-Functional versus Many-Body Green's-Function Approaches. *Rev. Mod. Phys.* **2002**, *74* (2), 601−659.
(58) Righetto, M.; Giovanni, D.; Lim, S. S.; Sum, T. C. The Photophysics of Ruddlesden-Popper Perovskites: A Tale of Energy, Charges, and Spins. *Appl. Phys. Rev.* **2021**, *8* (1), 11318.
(59) Perdew, J. P.; Ernzerhof, M.; Burke, K. Rationale for Mixing Exact Exchange with Density Functional Approximations. *J. Chem. Phys.* **1996**, *105*, 9982−9985.
(60) Li, S.; Luo, J.; Liu, J.; Tang, J. Self-Trapped Excitons in All-Inorganic Halide Perovskites: Fundamentals, Status, and Potential Applications. *J. Phys. Chem. Lett.* **2019**, *10* (8), 1999−2007.
(61) Smith, M. D.; Karunadasa, H. I. White-Light Emission from Layered Halide Perovskites. *Acc. Chem. Res.* **2018**, *51* (3), 619−627.
(62) Febriansyah, B.; Neo, C. S. D.; Giovanni, D.; Srivastava, S.; Lekina, Y.; Koh, T. M.; Li, Y.; Shen, Z. X.; Asta, M.; Sum, T. C.; Mathews, N.; England, J. Targeted Synthesis of Trimeric Organic−Bromoplumbate Hybrids That Display Intrinsic, Highly Stokes-Shifted, Broadband Emission. *Chem. Mater.* **2020**, *32* (11), 4431−4441.
(63) Kahmann, S.; Tekelenburg, E. K.; Duim, H.; Kamminga, M. E.; Loi, M. A. Extrinsic Nature of the Broad Photoluminescence in Lead Iodide-Based Ruddlesden−Popper Perovskites. *Nat. Commun.* **2020**, *11* (1), 2344.
(64) Febriansyah, B.; Giovanni, D.; Ramesh, S.; Koh, T. M.; Li, Y.; Sum, T. C.; Mathews, N.; England, J. Inducing Formation of a Corrugated, White-Light Emitting 2D Lead-Bromide Perovskite via Subtle Changes in Templating Cation. *J. Mater. Chem. C* **2020**, *8* (3), 889−893.
(65) Krause, L.; Herbst-Irmer, R.; Sheldrick, G. M.; Stalke, D. Comparison of Silver and Molybdenum Microfocus X-Ray Sources for Single-Crystal Structure Determination. *J. Appl. Crystallogr.* **2015**, *48* (1), 3−10.
(66) Sheldrick, G. M. {it SHELXT} {–} Integrated Space-Group and Crystal-Structure Determination. *Acta Crystallogr., Sect. A: Found. Adv.* **2015**, *71* (1), 3−8.
(67) Sheldrick, G. M. Crystal Structure Refinement with {\it SHELXL}. *Acta Crystallogr., Sect. C: Struct. Chem.* **2015**, *71* (1), 3−8.
(68) Müller, P. Practical Suggestions for Better Crystal Structures. *Crystallogr. Rev.* **2009**, *15* (1), 57−83.
(69) Thorn, A.; Dittrich, B.; Sheldrick, G. M. Enhanced Rigid-Bond Restraints. *Acta Crystallogr., Sect. A: Found. Crystallogr.* **2012**, *68* (4), 448−451.
(70) Fernández Garrillo, P. A.; Grévin, B.; Chevalier, N.; Borowik, Ł. Calibrated Work Function Mapping by Kelvin Probe Force Microscopy. *Rev. Sci. Instrum.* **2018**, *89* (4), 43702.
(71) Giannozzi, P.; Baroni, S.; Bonini, N.; Calandra, M.; Car, R.; Cavazzoni, C.; Ceresoli, D.; Chiarotti, G. L.; Cococcioni, M.; Dabo, I.; Dal Corso, A.; de Gironcoli, S.; Fabris, S.; Fratesi, G.; Gebauer, R.; Gerstmann, U.; Gougoussis, C.; Kokalj, A.; Lazzeri, M.; Martin-Samos, L.; Marzari, N.; Mauri, F.; Mazzarello, R.; Paolini, S.; Pasquarello, A.; Paulatto, L.; Sbraccia, C.; Scandolo, S.; Sclauzero, G.; Seitsonen, A. P.; Smogunov, A.; Umari, P.; Wentzcovitch, R. M. QUANTUM ESPRESSO: A Modular and Open-Source Software Project for Quantum Simulations of Materials. *J. Phys.: Condens. Matter* **2009**, *21* (39), 395502.
(72) Marini, A.; Hogan, C.; Grüning, M.; Varsano, D. Yambo: An Ab Initio Tool for Excited State Calculations. *Comput. Phys. Commun.* **2009**, *180* (8), 1392−1403.
(73) Godby, R. W.; Needs, R. J. Metal-Insulator Transition in Kohn-Sham Theory and Quasiparticle Theory. *Phys. Rev. Lett.* **1989**, *62* (10), 1169−1172.
(74) VandeVondele, J.; Krack, M.; Mohamed, F.; Parrinello, M.; Chassaing, T.; Hutter, J. Quickstep: Fast and Accurate Density Functional Calculations Using a Mixed Gaussian and Plane Waves Approach. *Comput. Phys. Commun.* **2005**, *167* (2), 103−128.
(75) Adamo, C.; Barone, V. Toward Reliable Density Functional Methods without Adjustable Parameters: The PBE0Model. *J. Chem. Phys.* **1999**, *110* (13), 6158−6170.
(76) Goedecker, S.; Teter, M.; Hutter, J. Separable Dual-Space Gaussian Pseudopotentials. *Phys. Rev. B: Condens. Matter Mater. Phys.* **1996**, *54* (3), 1703−1710.
(77) VandeVondele, J.; Hutter, J. Gaussian Basis Sets for Accurate Calculations on Molecular Systems in Gas and Condensed Phases. *J. Chem. Phys.* **2007**, *127* (11), 114105.
(78) Guidon, M.; Hutter, J.; VandeVondele, J. Auxiliary Density Matrix Methods for Hartree-Fock Exchange Calculations. *J. Chem. Theory Comput.* **2010**, *6* (8), 2348−2364.
(79) Van de Walle, C. G.; Neugebauer, J. First-Principles Calculations for Defects and Impurities: Applications to III-Nitrides. *J. Appl. Phys.* **2004**, *95*, 3851−3879.
(80) Umari, P.; Pasquarello, A. Ab Initio Molecular Dynamics in a Finite Homogeneous Electric Field. *Phys. Rev. Lett.* **2002**, *89* (15), 157602.

https://doi.org/10.1021/acs.chemmater.1c01182
Chem. Mater. 2021, 33, 4688−4700

Supporting Information for:

Large cation engineering in two-dimensional silver-bismuth bromide double perovskites

Fabian Schmitz, Jonas Horn, Nicola Dengo, Alexander E. Sedykh, Jonathan Becker, Elena Maiworm, Péter Bélteky, Ákos Kukovecz, Silvia Gross, Francesco Lamberti, Klaus Müller-Buschbaum, Derck Schlettwein, Daniele Meggiolaro, Marcello Righetto, Teresa Gatti

Table of Contents

- AFM topography scans of spin-coated thin films of $(iBA)_4AgBiBr_8$ and $(HA)_4AgBiBr_8$ 2D monolayers double perovskites 2D monolayers double perovskites (Figure S19)
- WF of $(RA)_4AgBiBr_8$ as a function of the calculated dipole moment of the organic cations RA^+ (Figure S20)
- Diffuse reflectance spectra of the four hydrothermally synthesized $(RA)_4AgBiBr_8$ 2D monolayer double perovskites crystalline powders (Figure S21)
- PL spectra of the four hydrothermally synthesized $(RA)_4AgBiBr_8$ 2D monolayer double perovskite thin films (Figure S22)
- PL spectra of the $(iBA)_4AgBiBr_8$ and $(BA)_4AgBiBr_8$ hydrothermally synthesized 2D monolayer double perovskites crystalline powders (Figure S23)
- Integrated PL values for the $(RA)_4AgBiBr_8$ series under 3.29 eV excitation (Table S2)
- G_0W_0 band gap convergence of $(BA)_4AgBiBr_8$ vs computational setup (Table S3)
- $(BA)_4AgBiBr_8$ BSE spectrum convergence vs number of k-points in BZ (Figure S24)

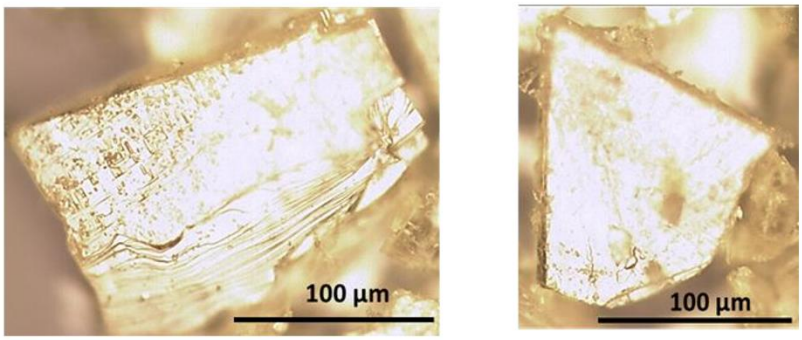

Figure S1. Optical microscope images of a prototypical crystal of 2D $(RA)_4AgBiBr_8$ compound that evidence the platelet-like structure and crystal growth along the (001) plane.

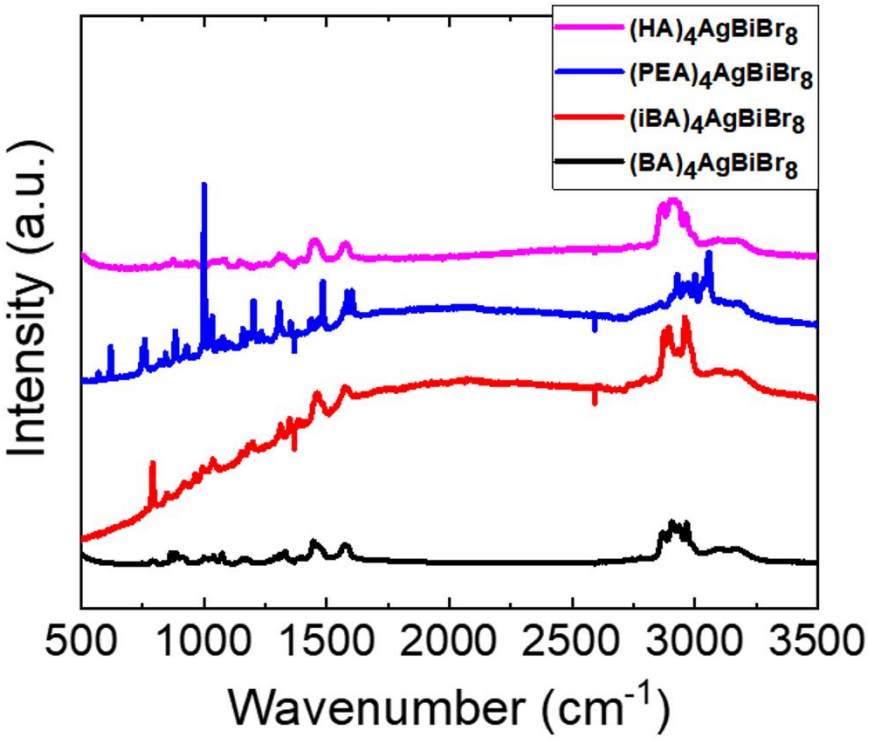

Figure S2. High wavenumbers region of the Raman spectra of the four $(RA)_4AgBiBr_8$ compounds.

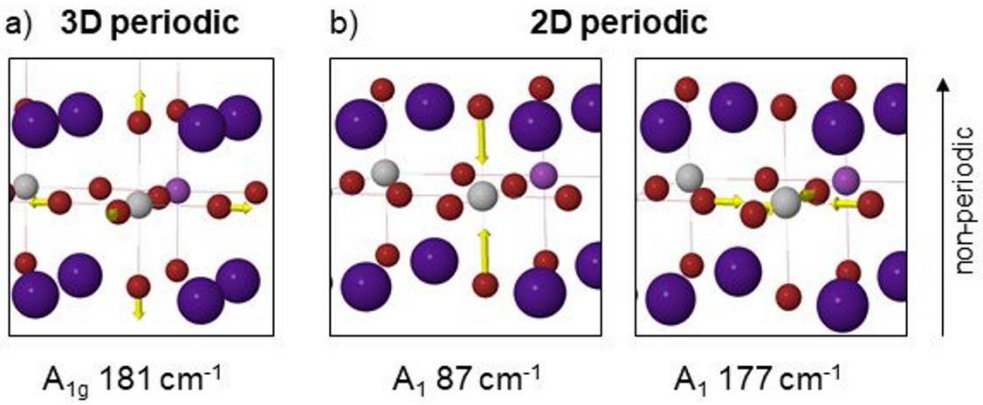

Figure S3. Vibrational modes and relative frequencies associated to symmetric stretching of the Ag-Br octahedra in a) 3D bulk $Cs_2AgBiBr_6$ and b) in a single layer of $Cs_2AgBiBr_6$ where the periodicity is interrupted in the direction perpendicular to the inorganic layer. By interrupting the periodicity in one direction a decoupling of the stretching mode to Br displacements perpendicular and parallel to the plane is observed. The stretching modes perpendicular to the plane occur at lower frequencies (87 cm^{-1}) than in-plane stretching (177 cm^{-1}). Based on this model, a softening of the Raman active modes involving metal-Br stretching is expected moving from 3D bulk to 2D double perovskites. Vibrational modes have been calculated at the PBE level by selectively displacing six Br ions in the Ag-Br octahedra.

Table S1. Crystal data and structure refinement for $(PEA)_4AgBiBr_8$

CCDC No	2031528	
Empirical formula	C_{32} H_{48} Ag Bi Br_8 N_4	
Formula weight	1444.87	
Temperature	100(2) K	
Wavelength	0.71073 Å	
Crystal system	Triclinic	
Space group	$P\bar{1}$	
Unit cell dimensions	a = 11.4661(5) Å	α= 106.6140(16)°.
	b = 11.5138(5) Å	β= 99.6956(16)°.
	c = 17.0237(8) Å	γ = 90.0802(16)°.
Volume	2119.93(17) $Å^3$	
Z	2	
Density (calculated)	2.264 Mg/m^3	
Absorption coefficient	12.174 mm^{-1}	
F(000)	1356	
Crystal size	0.136 x 0.135 x 0.044 mm^3	
Theta range for data collection	1.804 to 28.281°.	
Index ranges	$-15 \leq h \leq 15$, $-15 \leq k \leq 15$, $-22 \leq l \leq 22$	
Reflections collected	86176	
Independent reflections	10539 [R(int) = 0.0639]	
Completeness to theta = 25.242°	100.0 %	
Absorption correction	Semi-empirical from equivalents	
Refinement method	Full-matrix least-squares on F^2	
Data / restraints / parameters	10539 / 1412 / 560	
Goodness-of-fit on F^2	1.122	
Final R indices [I>2σ(I)]	R1 = 0.0548, wR2 = 0.1013	
R indices (all data)	R1 = 0.0745, wR2 = 0.1080	
Largest diff. peak and hole	2.321 and -3.255 $e.Å^{-3}$	

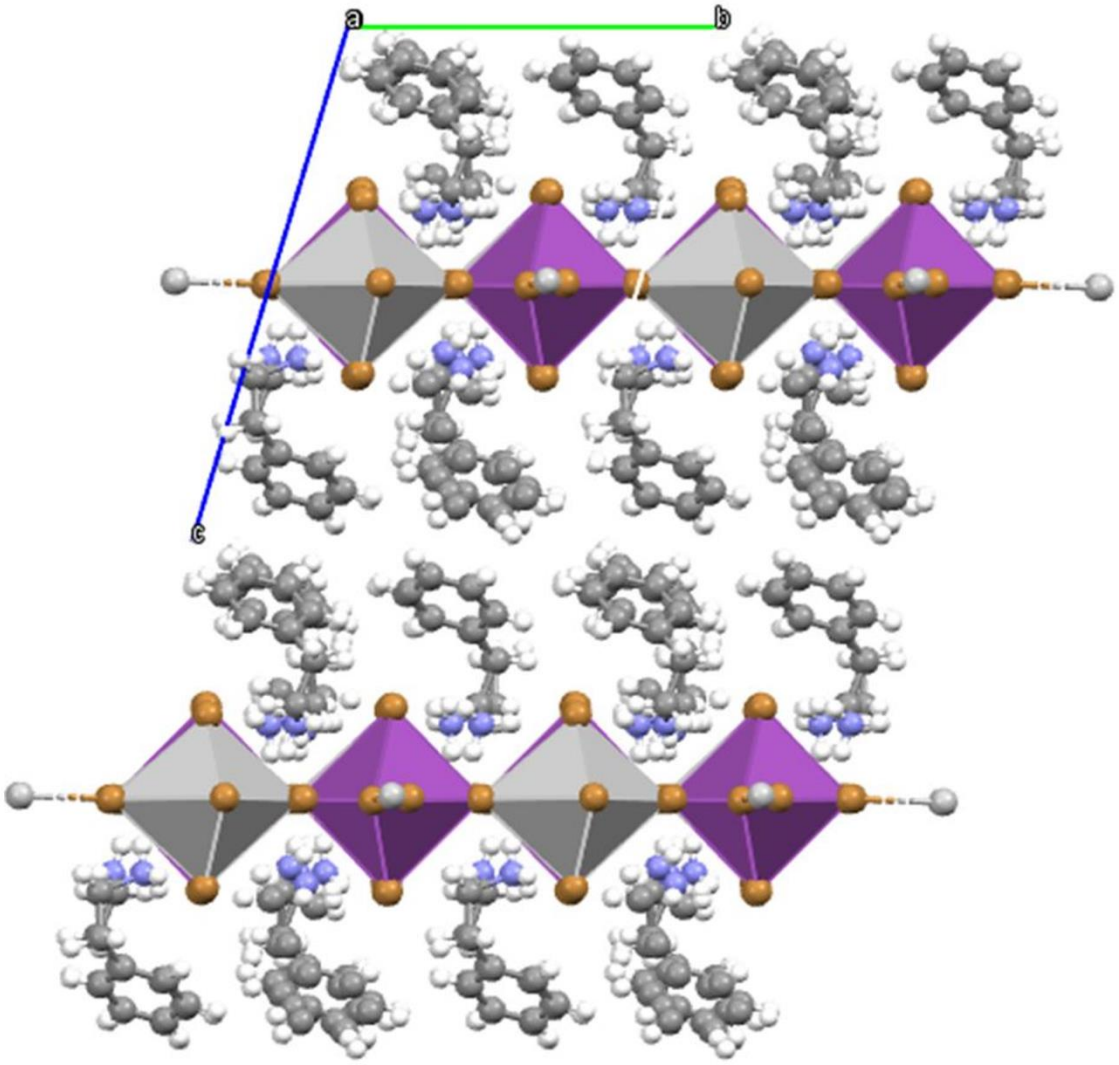

Figure S4. Details of the single crystal structure of $(PEA)_4AgBiBr_8$: view along the a-axis.

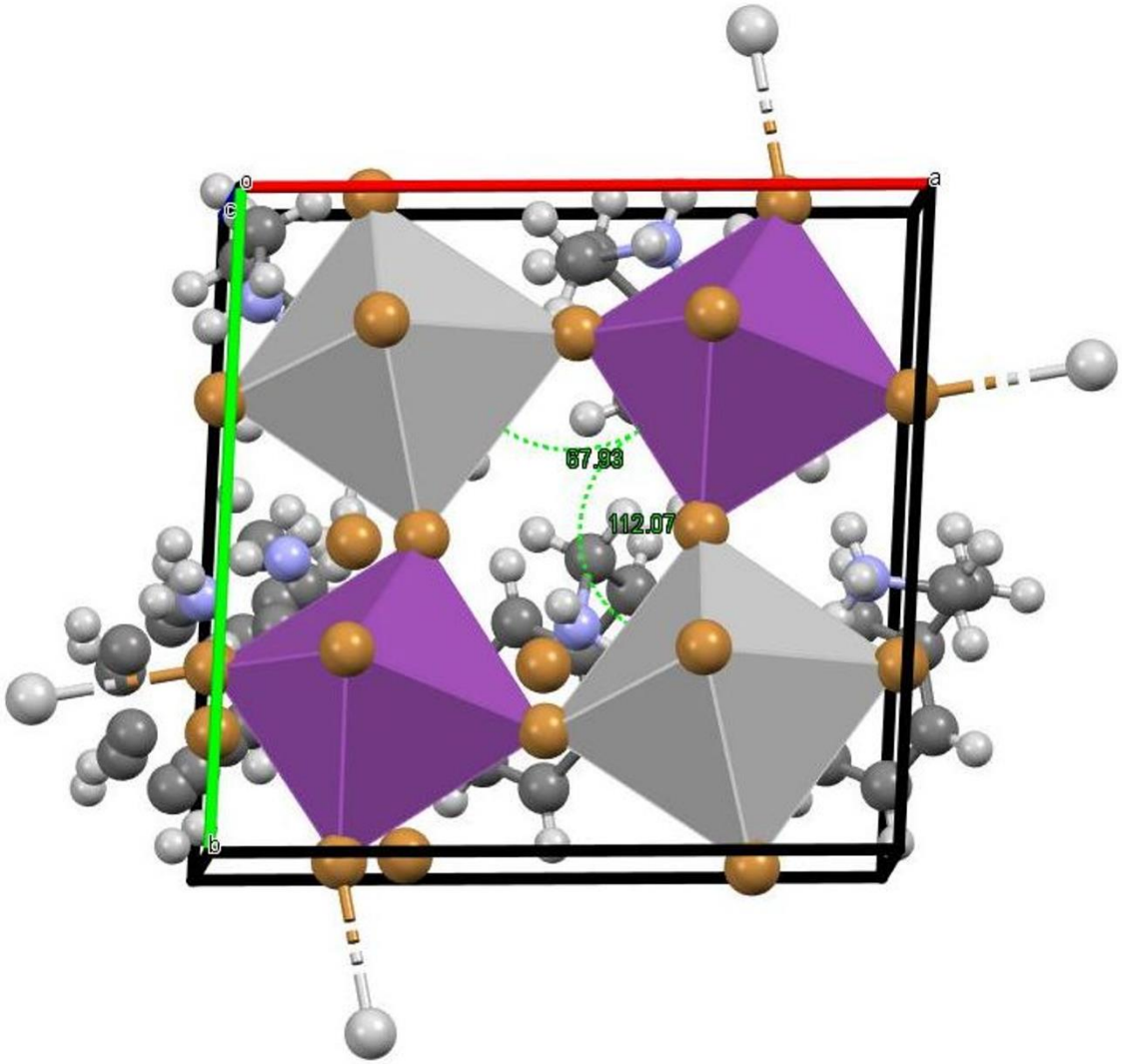

Figure S5. Details of the single crystal structure of $(PEA)_4AgBiBr_8$: view along the c-axis with indications of the value of dihedral angles between two adjacent Ag-Br_6 and Bi-Br_6 octahedra.

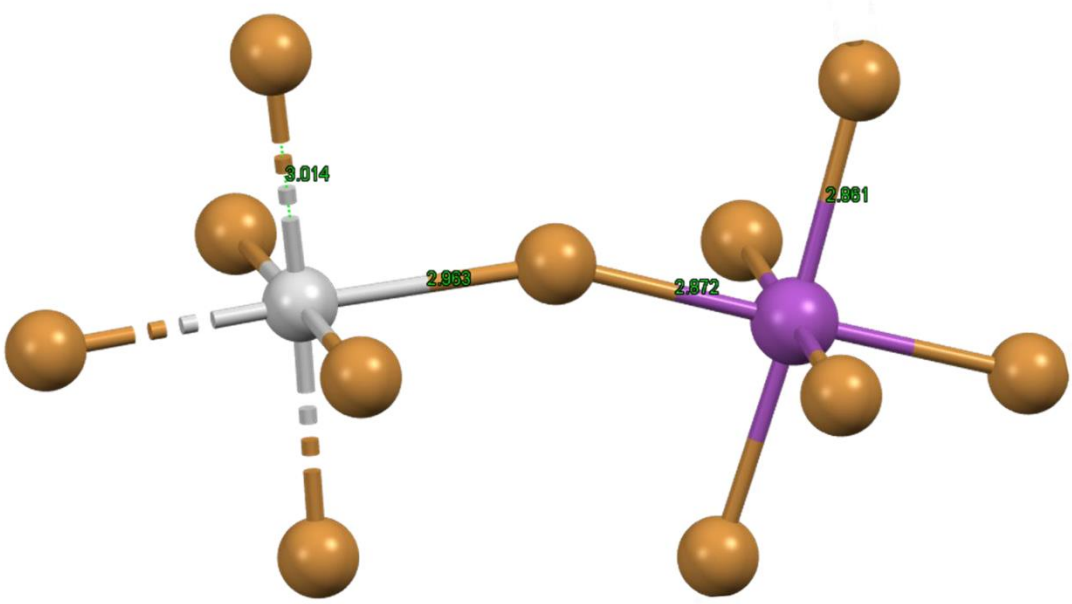

Figure S6. Details of the single crystal structure of $(PEA)_4AgBiBr_8$: two adjacent Ag-Br_6 and Bi-Br_6 octahedra with indicated the relative bond distances.

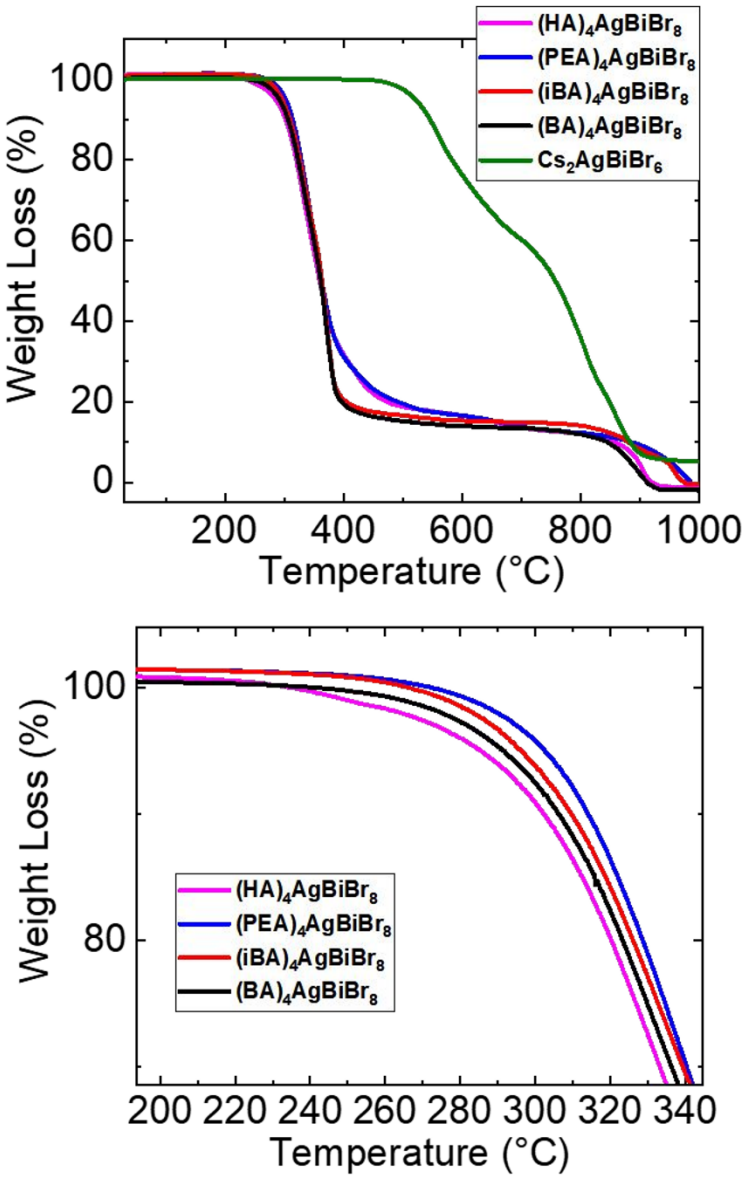

Figure S7. Thermograms of the four $(XA)_4AgBiBr_8$ compounds and of the of the reference 3D double perovskite $Cs_2AgBiBr_6$ (top graphs), with detail on decomposition onsets (bottom graphs).

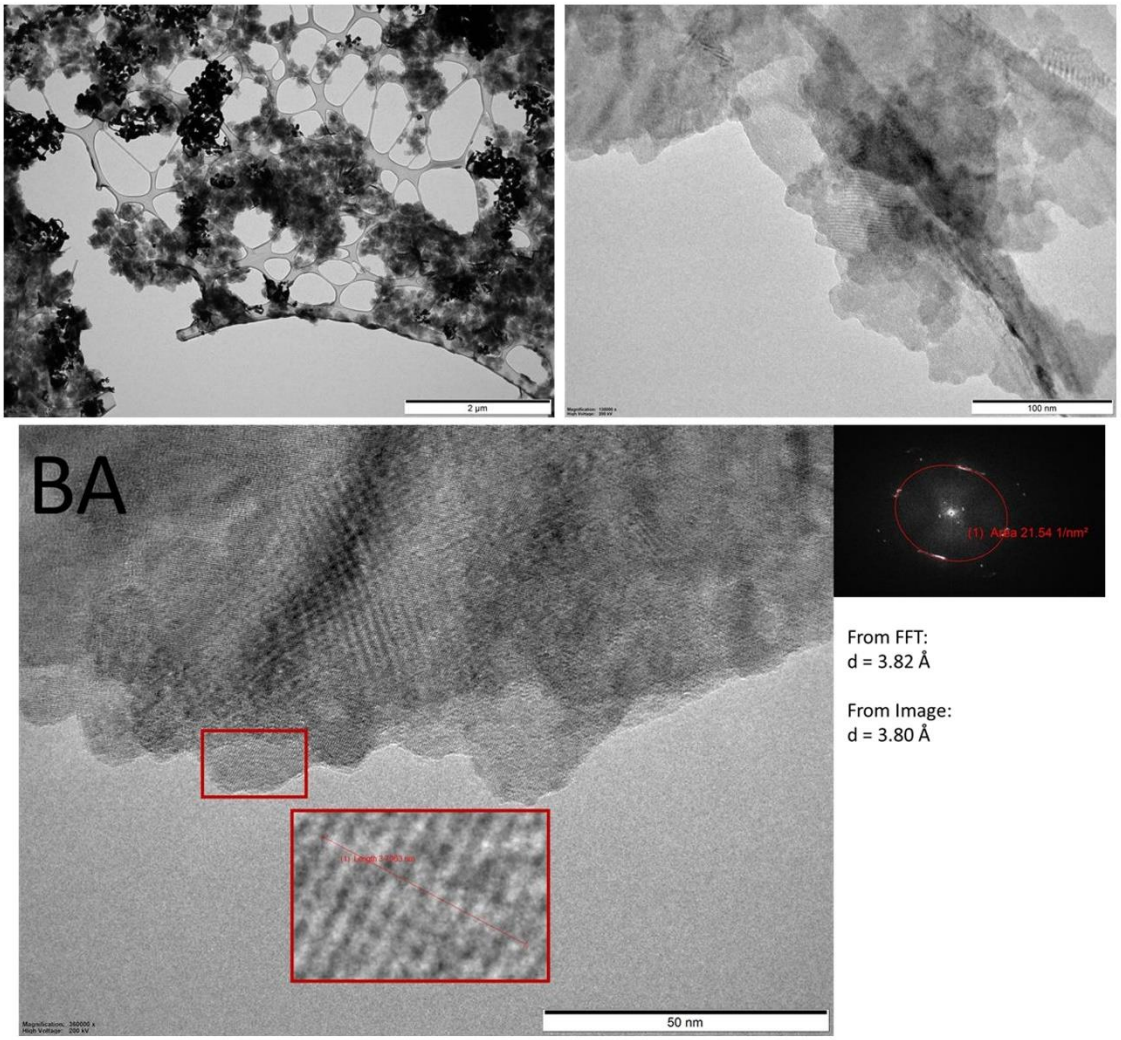

Figure S8. Representative HR-TEM images of hydrothermally synthesized $(BA)_4AgBiBr_8$ with details on repetitive structures and associated distance (calculated both manually and through FFT).

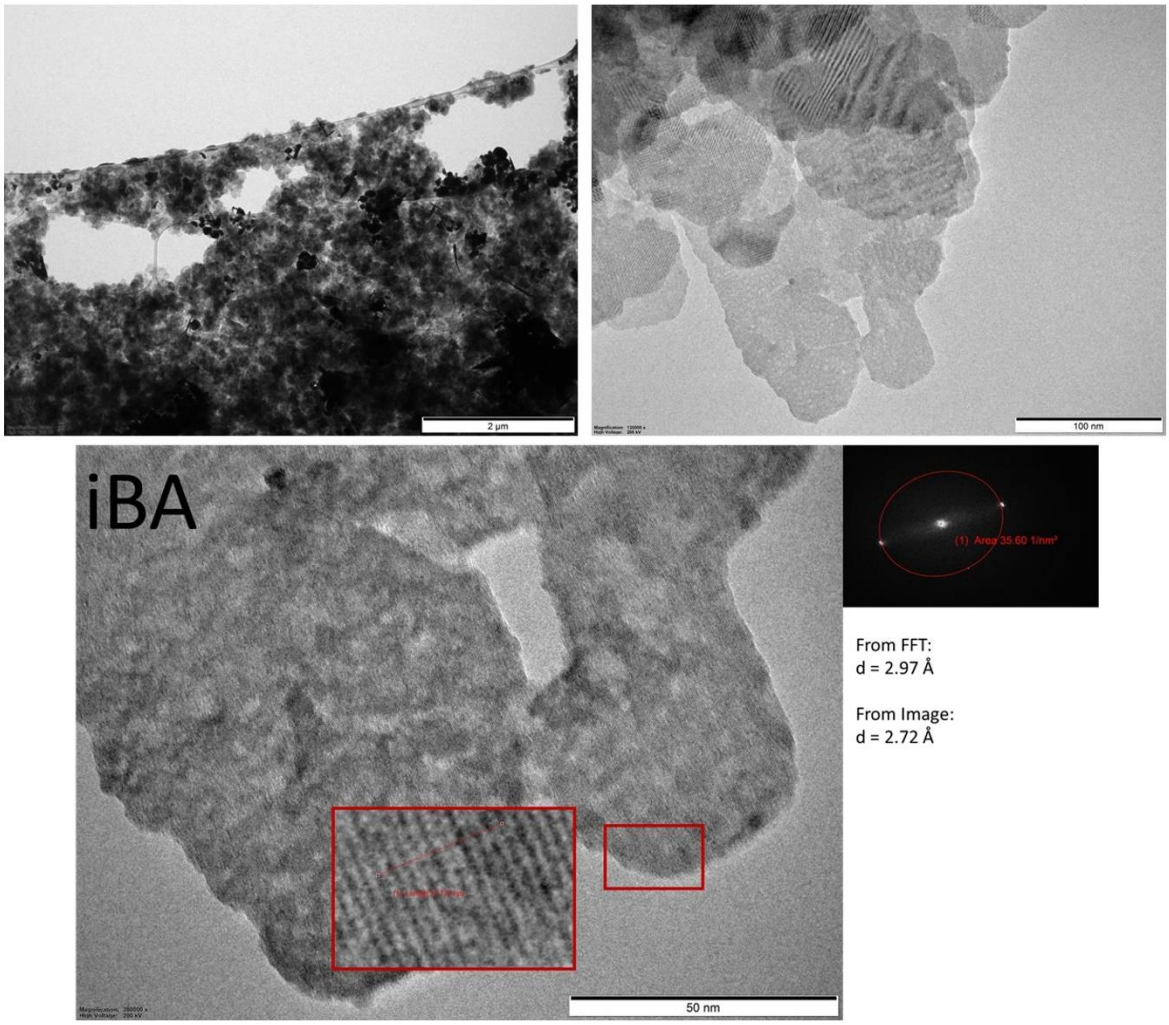

Figure S9. Representative HR-TEM images of hydrothermally synthesized $(iBA)_4AgBiBr_8$ with details on repetitive structures and associated distance (calculated both manually and through FFT).

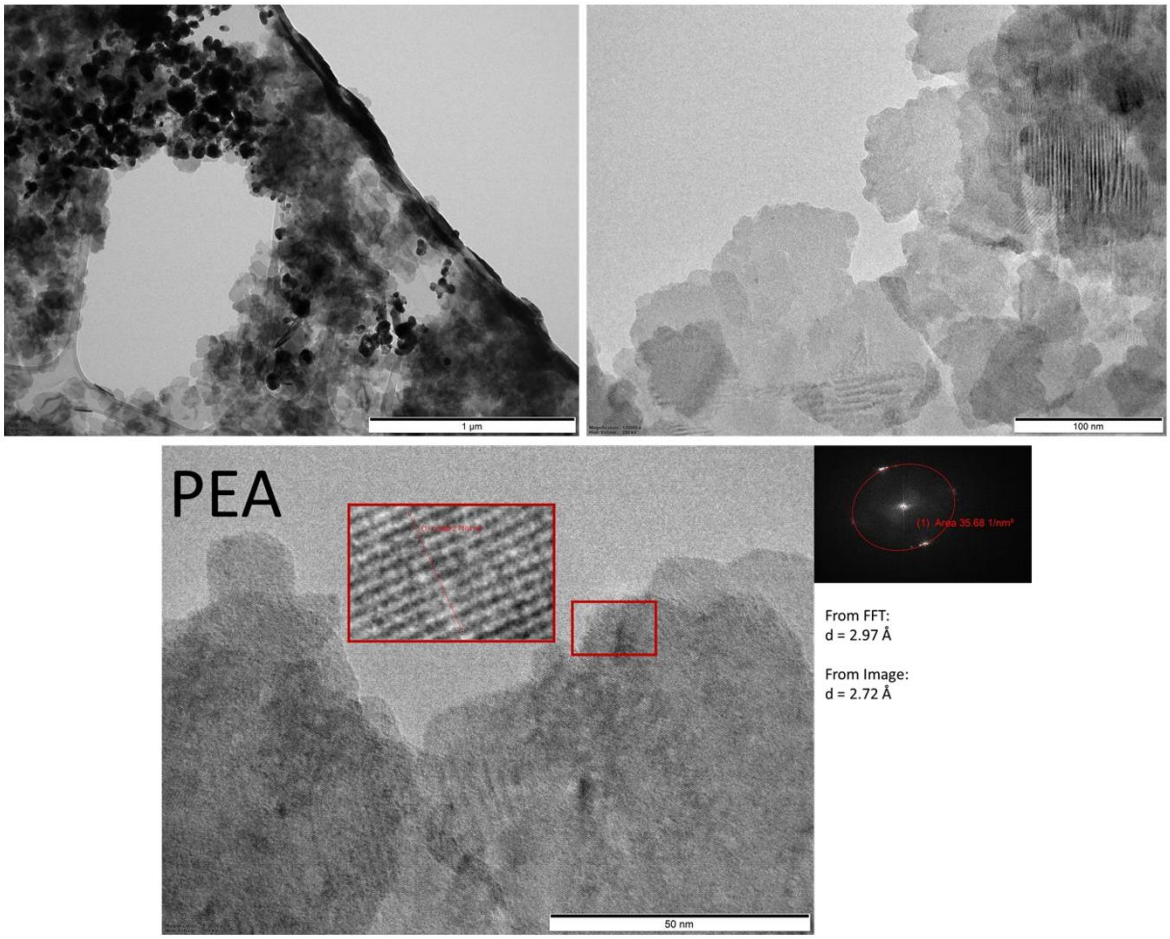

Figure S10. Representative HR-TEM images of hydrothermally synthesized $(PEA)_4AgBiBr_8$ with details on repetitive structures and associated distance (calculated both manually and through FFT).

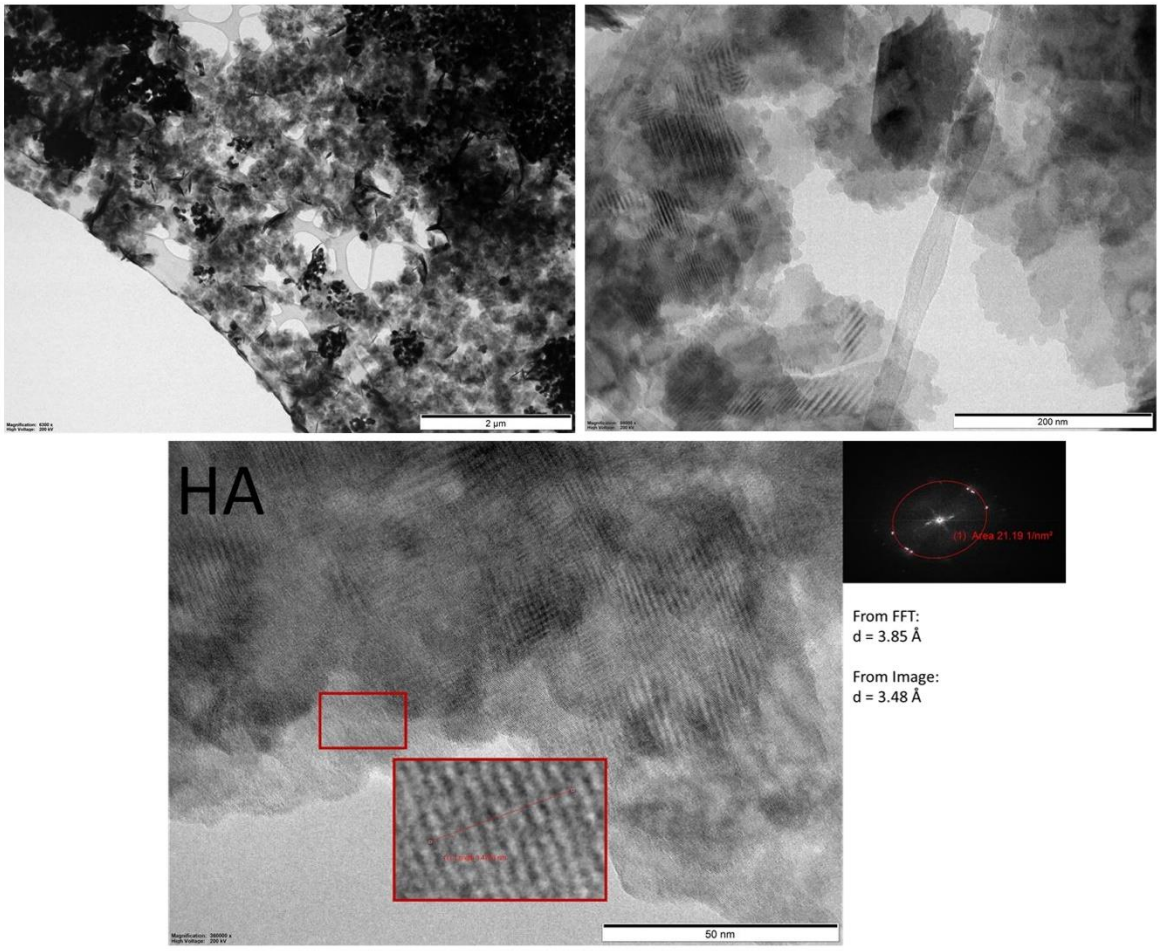

Figure S11. Representative HR-TEM images of hydrothermally synthesized $(HA)_4AgBiBr_8$ with details on repetitive structures and associated distance (calculated both manually and through FFT).

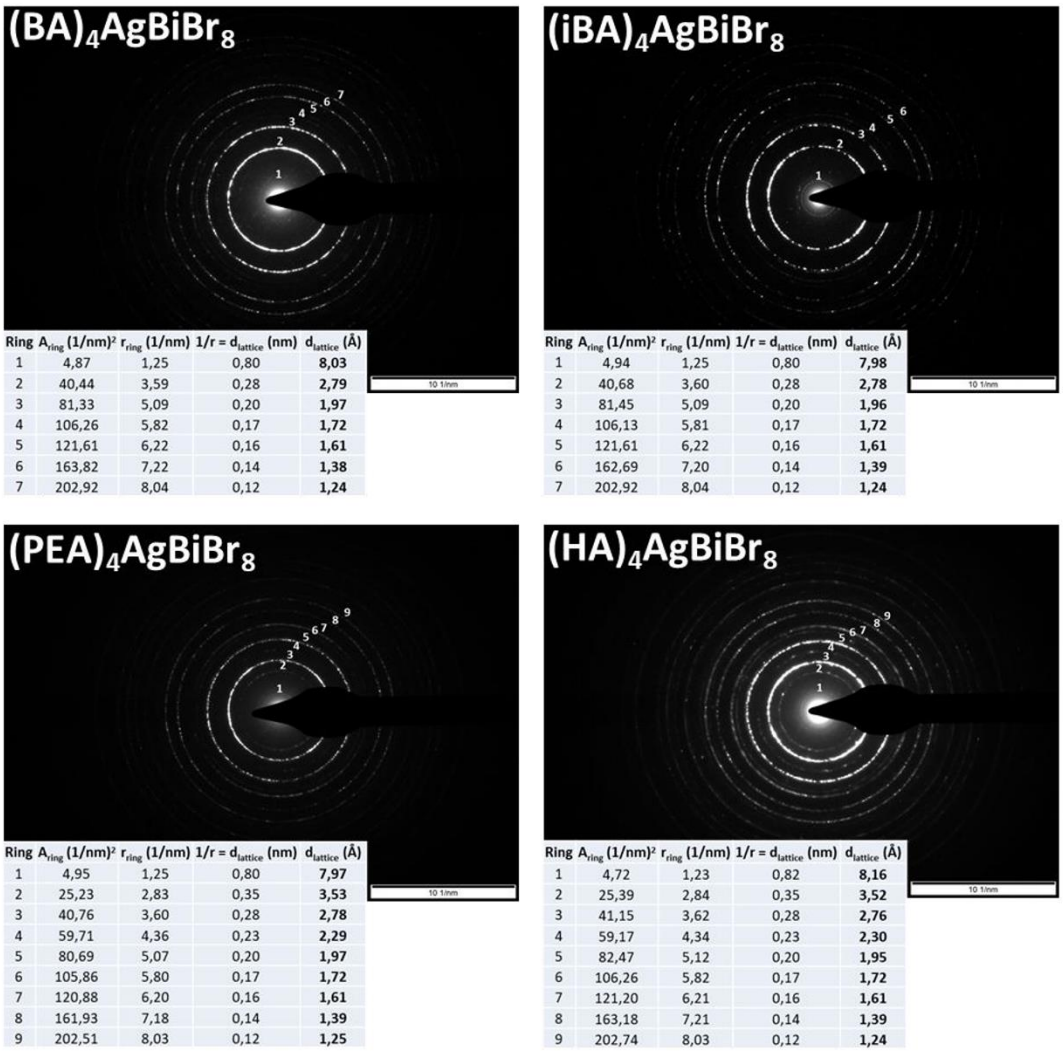

Ring	A_{ring} (1/nm)²	r_{ring} (1/nm)	$1/r = d_{lattice}$ (nm)	$d_{lattice}$ (Å)
1	4,87	1,25	0,80	**8,03**
2	40,44	3,59	0,28	**2,79**
3	81,33	5,09	0,20	**1,97**
4	106,26	5,82	0,17	**1,72**
5	121,61	6,22	0,16	**1,61**
6	163,82	7,22	0,14	**1,38**
7	202,92	8,04	0,12	**1,24**

Ring	A_{ring} (1/nm)²	r_{ring} (1/nm)	$1/r = d_{lattice}$ (nm)	$d_{lattice}$ (Å)
1	4,94	1,25	0,80	**7,98**
2	40,68	3,60	0,28	**2,78**
3	81,45	5,09	0,20	**1,96**
4	106,13	5,81	0,17	**1,72**
5	121,61	6,22	0,16	**1,61**
6	162,69	7,20	0,14	**1,39**
7	202,92	8,04	0,12	**1,24**

Ring	A_{ring} (1/nm)²	r_{ring} (1/nm)	$1/r = d_{lattice}$ (nm)	$d_{lattice}$ (Å)
1	4,95	1,25	0,80	**7,97**
2	25,23	2,83	0,35	**3,53**
3	40,76	3,60	0,28	**2,78**
4	59,71	4,36	0,23	**2,29**
5	80,69	5,07	0,20	**1,97**
6	105,86	5,80	0,17	**1,72**
7	120,88	6,20	0,16	**1,61**
8	161,93	7,18	0,14	**1,39**
9	202,51	8,03	0,12	**1,25**

Ring	A_{ring} (1/nm)²	r_{ring} (1/nm)	$1/r = d_{lattice}$ (nm)	$d_{lattice}$ (Å)
1	4,72	1,23	0,82	**8,16**
2	25,39	2,84	0,35	**3,52**
3	41,15	3,62	0,28	**2,76**
4	59,17	4,34	0,23	**2,30**
5	82,47	5,12	0,20	**1,95**
6	106,26	5,82	0,17	**1,72**
7	121,20	6,21	0,16	**1,61**
8	163,18	7,21	0,14	**1,39**
9	202,74	8,03	0,12	**1,24**

Figure S12. SAED patterns of the four hydrothermally synthesized $(XA)_4AgBiBr_8$ with relative average lattice parameters.

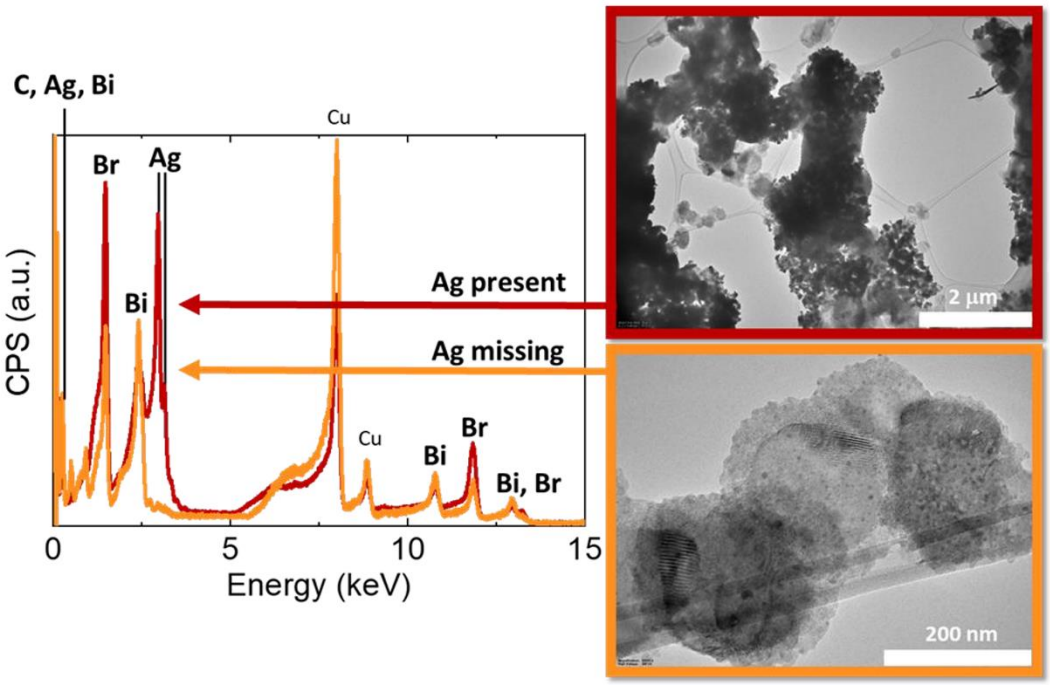

Figure S13. TEM EDX analysis of the hydrothermally synthesized $(BA)_4AgBiBr_8$ crystalline sample, showing the existence of two different regions characterized by the presence and absence of Ag atoms (the Cu signal stems from the TEM grid).

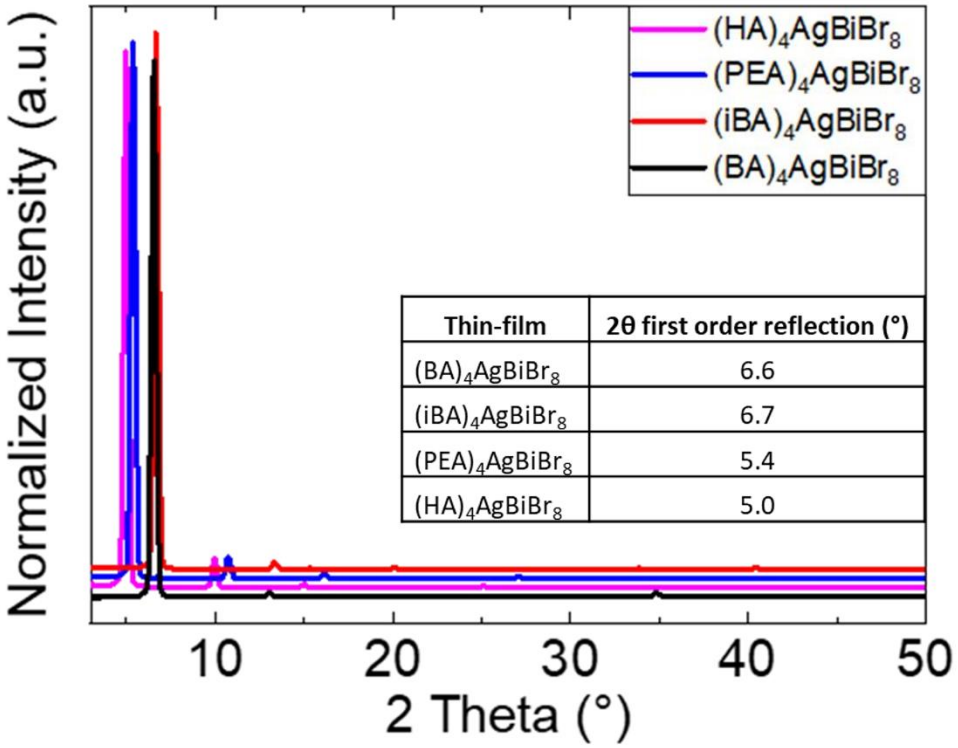

Thin-film	2θ first order reflection (°)
$(BA)_4AgBiBr_8$	6.6
$(iBA)_4AgBiBr_8$	6.7
$(PEA)_4AgBiBr_8$	5.4
$(HA)_4AgBiBr_8$	5.0

Figure S14. Thin film XRD patterns of spin-coated thin films of the four $(XA)_4AgBiBr_8$ 2D monolayers double perovskites. The inset table reports the exact value of the maximum in the first order (001) reflections. The average crystallite size for the four thin films, calculated by applying the Scherrer equation to the first order reflection, results to be 24.4 ± 0.3 nm.

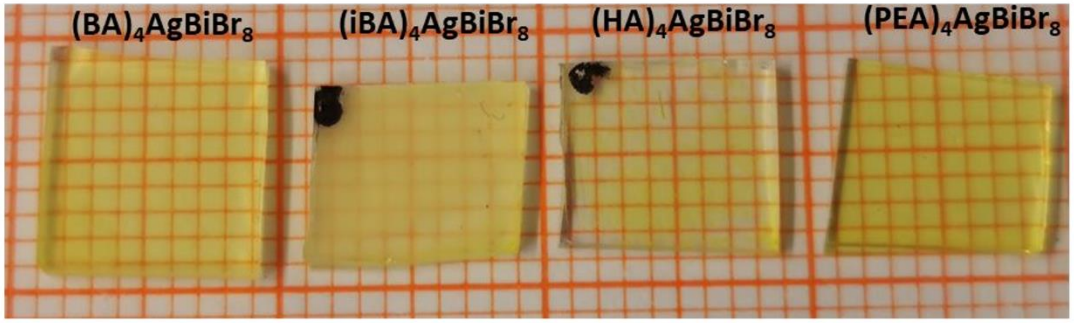

Figure S15. Photos of the thin films obtained from the four $(XA)_4AgBiBr_8$ 2D monolayers double perovskites on glass slides that show their visual appearance.

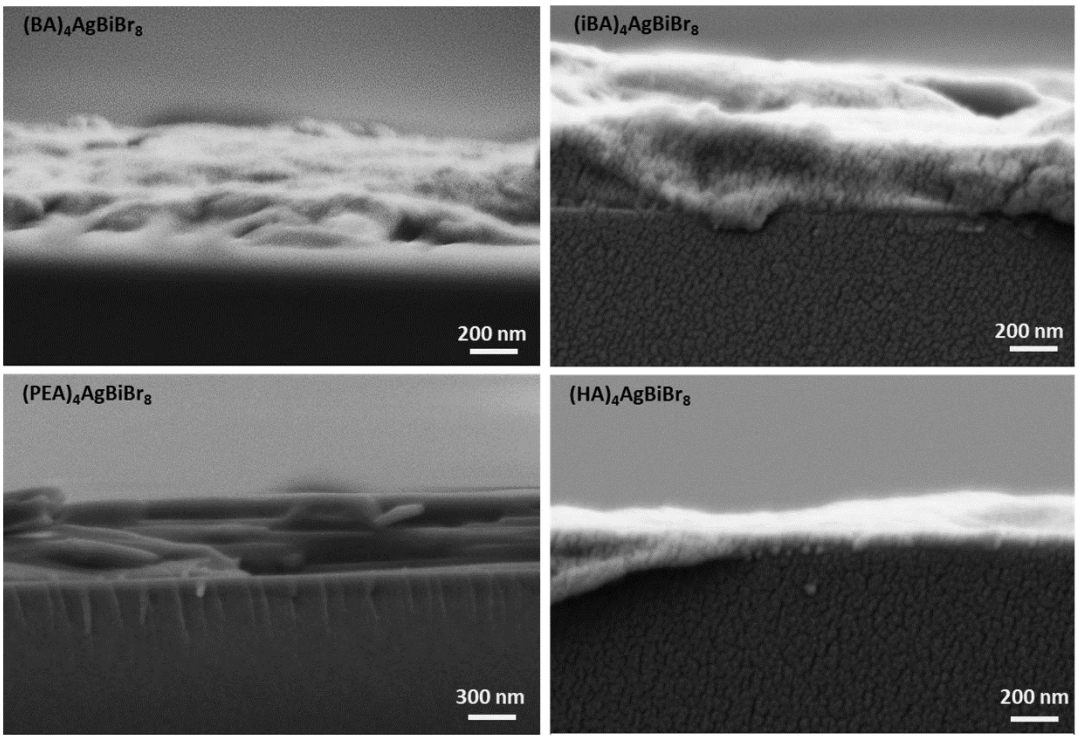

Figure S16. Cross-section SEM images of spin-coated thin films of the four $(XA)_4AgBiBr_8$ 2D monolayers double perovskites.

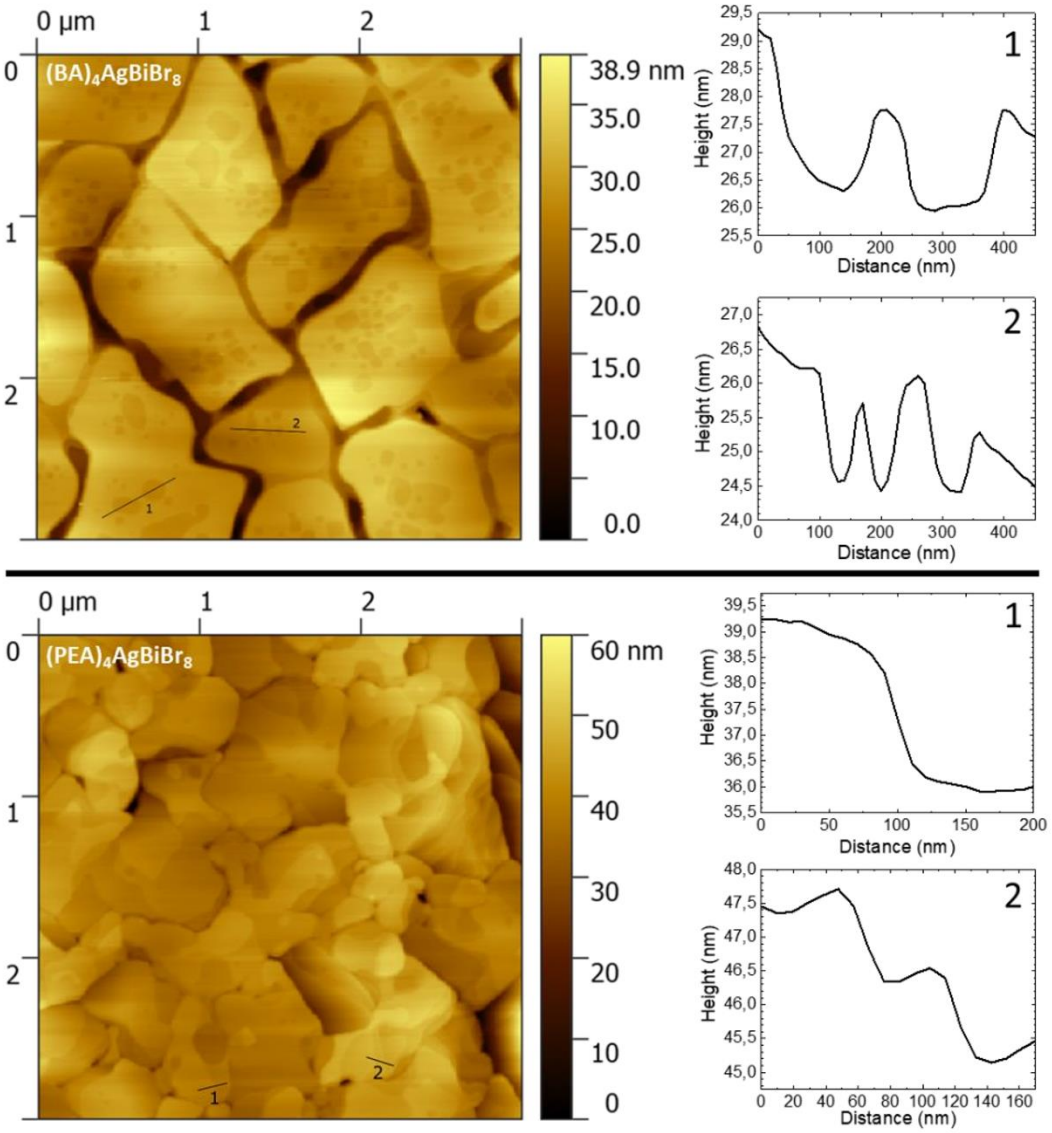

Figure S17. AFM topography images of spin coated thin films of $(BA)_4AgBiBr_8$ (top) and $(PEA)_4AgBiBr_8$ (bottom) with representative cross-section height profiles.

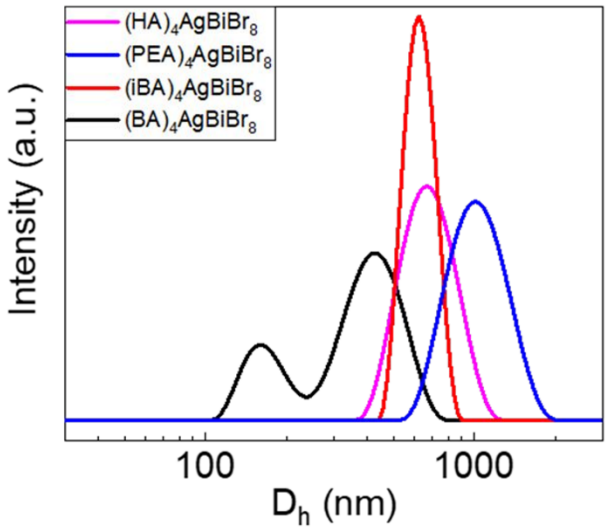

Figure S18. DLS size distributions of the DMF solutions used for processing the four $(XA)_4AgBiBr_8$ 2D monolayers double perovskites into thin films.

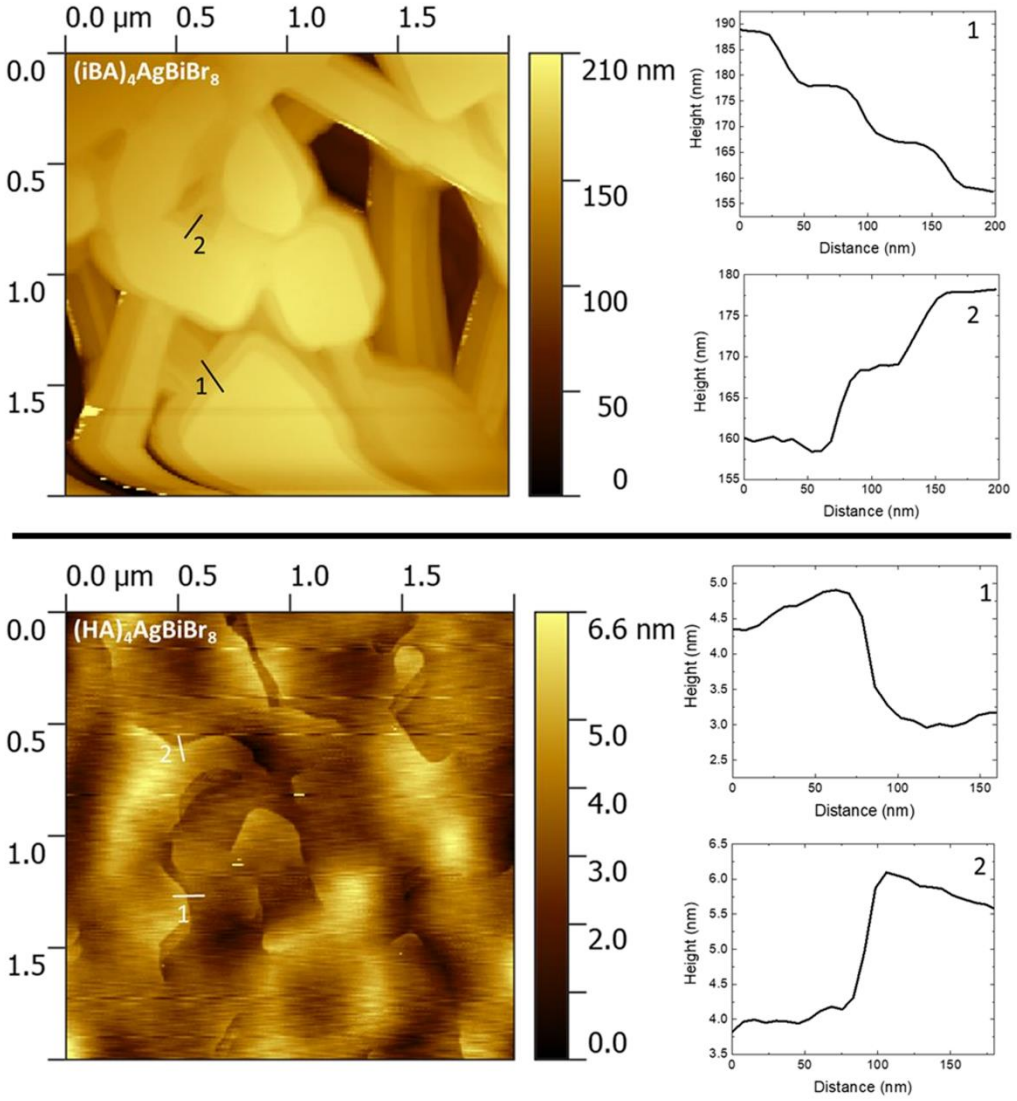

Figure S19. AFM topography images of spin coated thin films of (iBA)4AgBiBr8 (top) and (HA)4AgBiBr8 (bottom) with representative cross-section height profiles.

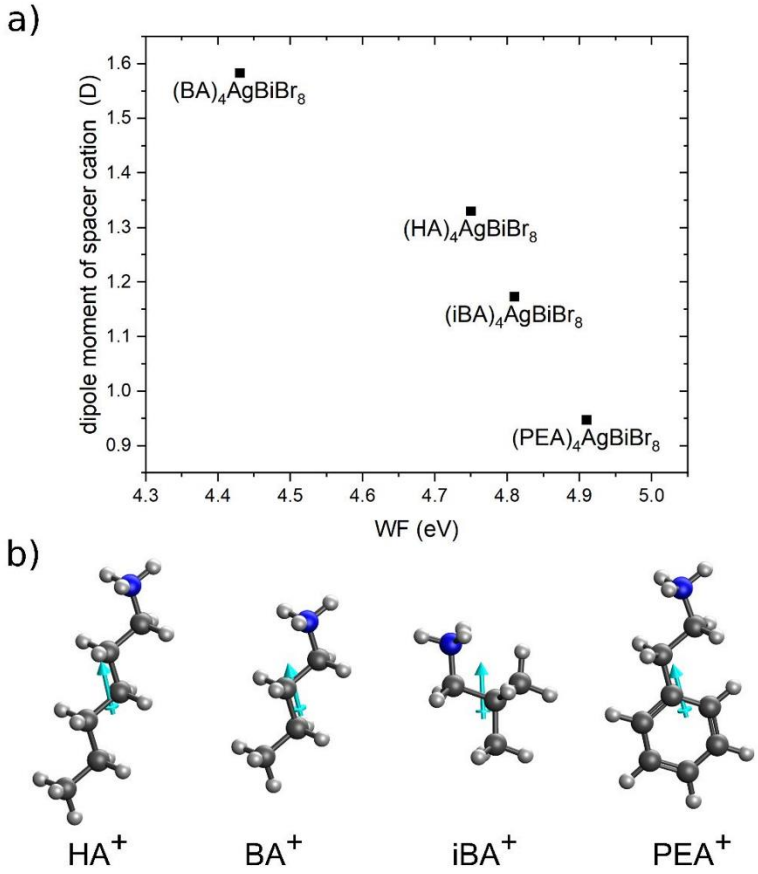

Figure S20. a) WF of $(RA)_4AgBiBr_8$ as a function of the calculated dipole moment of the organic cations RA^+ shown in b).

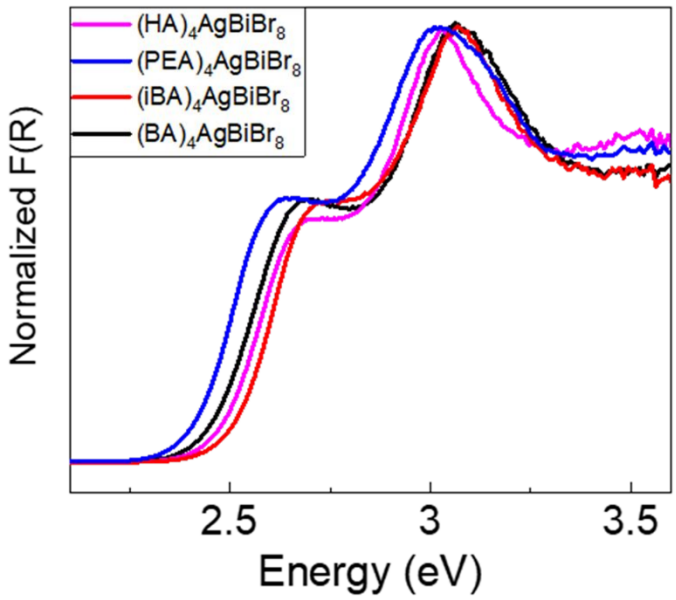

Figure S21. Normalized diffuse reflectance spectra (Kubelka – Munk function vs. energy) of the four hydrothermally synthesized $(RA)_4AgBiBr_8$ 2D monolayers double perovskites crystalline powders.

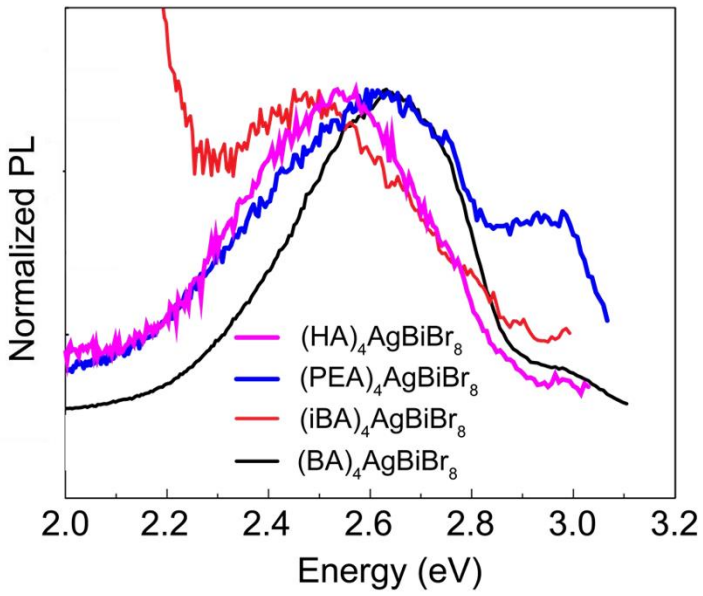

Figure S22. Normalized PL spectra of the four $(RA)_4AgBiBr_8$ 2D monolayers double perovskites thin films.

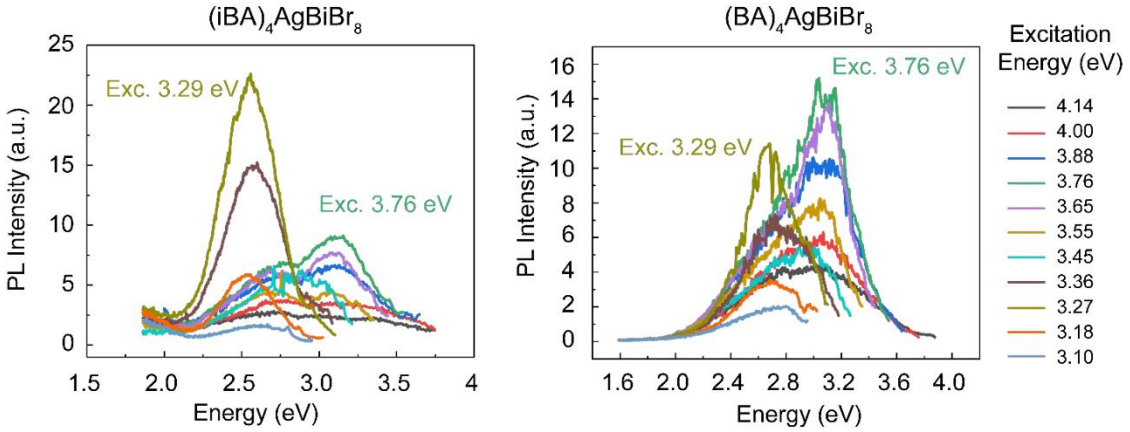

Figure S23. PL spectra of the $(iBA)_4AgBiBr_8$ and $(BA)_4AgBiBr_8$ hydrothermally synthesized 2D monolayer double perovskites crystalline powders

Table S2. Integrated PL values for the $(RA)_4AgBiBr_8$ series under 3.29 eV excitation

Compound	Integrated PL (a.u.)	Comparison with iBA
$(BA)_4AgBiBr_8$	1.4×10^{10}	0.65
$(iBA)_4AgBiBr_8$	2.2×10^{10}	-
$(PEA)_4AgBiBr_8$	3×10^{9}	0.13
$(HA)_4AgBiBr_8$	8×10^{9}	0.37

Table S3. Energy gaps vs computational setup in G_0W_0 calculations of $(BA)_4AgBiBr_8$. The k-grid in the BZ was reduced to 2x2x1 in order to perform the tests. Based on results in the Table the following computational setup has been set in G_0W_0 calculations: k-grid 4x4x1, EXX cutoff 30 Ry, dielectric matrix cutoff 3 Ry, total number of bands in dielectric matrix and correlation energy has been further increased to 2560.

Computational setup	E_g (eV)
Exchange cutoff *vs* HF gap	
20 Ry	7.72
30 Ry	8.21
40 Ry	8.20
Dielectric matrix cutoff *vs* band gap	
(fixed EXX cutoff = 20 Ry; total number of bands 512)	
1 Ry	4.48
2 Ry	4.38
3 Ry	4.35
Total number of bands *vs* band gap	
(fixed EXX cutoff = 20 Ry; Dielectric matrix cutoff = 1 Ry)	
512	4.48
1024	3.51
1536	3.33
2048	3.27

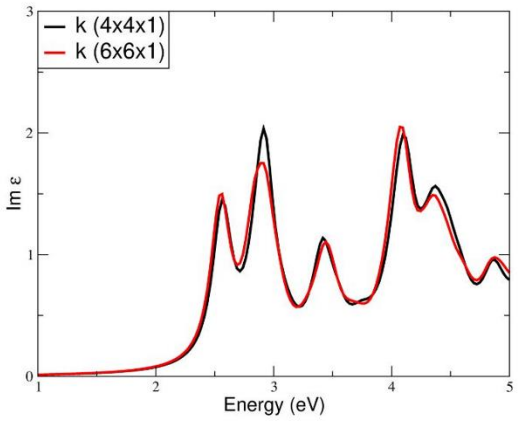

Figure S24. BSE spectra of $(BA)_4AgBiBr_8$ calculated for two different k-point grids, i.e. 4x4x1 and 6x6x1, and by using the scissor operator (1.56 eV). Computational parameters: BSE exchange (screening) cutoff of 30 Ry (3 Ry), 20 occupied / 20 unoccupied bands; screening: exchange (dielectric matrix) cutoff of 30 Ry (3 Ry), 2560 total bands.

4.4 Publication 3

Tuning the optical properties of 2D monolayer silver-bismuth bromide double perovskite by halide substitution

Authors: **Fabian Schmitz**, Raphael Neisius, Jonas Horn, Joachim Sann, Derck Schlettwein, Marina Gerhard, Teresa Gatti

A combination of the Goldschmidt tolerance factor and the radius ratio of Bi^{3+} have shown that double perovskite iodides tend to be elusive which is why they are far less reported than respective bromides or chlorides.[233] Therefore, the 3D double perovskite $Cs_2AgBiBr_6$ has not been prepared as an iodide, yet, but only a partial halide substitution towards $Cs_2AgBiBr_{6-x}I_x$ *via* anion exchange has been successfully performed, providing a decreasing bandgap with increasing I^- ratio.[131] 2D AgBi-based double perovskites utilizing the spacer cations propylammonium[234] (PA) and 5,5'-diylbis(aminoethyl)-[2,2'-bithiophene][173] (AE2T) have been reported to be prepared as pure iodides in single crystals and thin films which possess bandgaps of 1.87 eV (PA) and 2.00 eV (AE2T). However, no mixed halide 2D double perovskite had been prepared before this work.

Thus, **publication 3** focuses on the gradual halide substitution in $(BA)_4AgBiBr_{8-x}I_x$ (x = 0, 1, 2, 3, 4) thin films to finely tune the material's optical properties. The halide ratios of the resulting thin films are confirmed to match the precursor stoichiometries *via* quantitative XPS analysis and using GIXRD, the presence of a single phase is confirmed. While homogeneous thin films can be observed for $(BA)_4AgBiBr_8$, a progressive increase of nanostructuring, and roughness with increasing I^- content as well as a reduction of surface coverage for x = 3, 4 are observed using SEM and AFM imaging. Also, the absorption edge of $(BA)_4AgBiBr_{8-x}I_x$ redshifts for enhanced x values as probed by UV-Vis absorption spectroscopy. The material's emissive spectra match the one observed in **publication 2** for x = 0, and for higher I^- contents (x = 2, 3, 4) an additional emissive feature at 2.9 eV emerges, indicating strong emission from a free exciton. While $(BA)_4AgBiBr_8$ is characterized by high stability under ambient conditions, a blueshift of the absorption edge as well as the formation of bismuth- and bromide-rich are observed after aging for several days under ambient conditions *via* UV-Vis absorption spectroscopy and SEM-EDX, respectively.

In conclusion, this work provides the first report of 2D mixed halide AgBi-based double perovskites. It further reveals that adjusting the Br^-/I^- ratio offers precise control over the material's optical features. The tunability is accompanied by limited stability due to phase segregation under ambient conditions that have already been observed for mixed halide LHPs[235] and which will need to be the focus for future work on 2D mixed halide double perovskites. An additional 2D AgBi-based iodide perovskite has been reported after the publication of this work.[236]

In addition to the *General Contributions*, all samples that were analyzed within this work were prepared by me. I performed SEM, SEM-EDX, UV-Vis absorption spectroscopy, thin film GIXRD, and AFM, including the respective data processing.

OPEN ACCESS
IOP Publishing
Nanotechnology
Nanotechnology **33** (2022) 215706 (12pp)
https://doi.org/10.1088/1361-6528/ac54df

Tuning the optical properties of 2D monolayer silver-bismuth bromide double perovskite by halide substitution

Fabian Schmitz[1,2], Raphael Neisius[1], Jonas Horn[2,3], Joachim Sann[1,2], Derck Schlettwein[2,3], Marina Gerhard[4,*] and Teresa Gatti[1,2,5,*]

[1] Institute of Physical Chemistry, Justus Liebig University, Heinrich-Buff-Ring 17, 35392 Giessen, Germany
[2] Center for Materials Research, Justus Liebig University, Heinrich-Buff-Ring 17, 35392 Giessen, Germany
[3] Institute of Applied Physics, Justus Liebig University, Heinrich Buff Ring 16, 35392 Giessen, Germany
[4] Faculty of Physics and Materials Science Center, Philipps-Universität Marburg, Renthof 7a, Marburg D-35032, Germany
[5] Centre of Excellence ENSEMBLE 3 sp. z o.o., Wolczynska 133, Warsaw, 01-919, Poland

E-mail: marina.gerhard@physik.uni-marburg.de and teresa.gatti@phys.chemie.uni-giessen.de

Received 17 December 2021, revised 4 February 2022
Accepted for publication 14 February 2022
Published 4 March 2022

Abstract

Silver-bismuth double perovskites are promising replacement materials for lead-based ones in photovoltaic (PV) devices due to the lower toxicity and enhanced stability to environmental factors. In addition, they might even be more suitable for indoor PV, due to the size of their bandgap better matching white LEDs emission. Unfortunately, their optoelectronic performance does not reach that of the lead-based counterparts, because of the indirect nature of the band gap and the high exciton binding energy. One strategy to improve the electronic properties is the dimensional reduction from the 3D to the 2D perovskite structure, which features a direct band gap, as it has been reported for 2D monolayer derivates of $Cs_2AgBiBr_6$ obtained by substituting Cs^+ cations with bulky alkylammonium cations. However, a similar dimensional reduction also brings to a band gap opening, limiting light absorption in the visible. In this work, we report on the achievement of a bathochromic shift in the absorption features of a butylammonium-based silver-bismuth bromide monolayer double perovskite through doping with iodide and study the optical properties and stability of the resulting thin films in environmental conditions. These species might constitute the starting point to design future sustainable materials to implement as active components in indoor photovoltaic devices used to power the IoT.

Supplementary material for this article is available online

Keywords: silver-bismuth double perovskite, 2D perovskite, mixed-halide perovskite, lead-free perovskite

(Some figures may appear in colour only in the online journal)

1. Introduction

Lead halide perovskites received tremendous attention in the last decade due to their outstanding optoelectronic properties that make them suitable materials to be employed in the next generation of low-cost photovoltaic (PV) devices. However, the toxicity of the contained lead in combination with the

* Authors to whom any correspondence should be addressed.

Table 1. Stoichiometric amounts of precursors used for the preparation of $(BA)_4AgBiBr_{8-x}I_x$ (with $x = 0, 1, 2, 3, 4$) thin films.

Perovskite formula	AgBr (mg mmol^{-1})	AgI (mg mmol^{-1})	$BiBr_3$ (mg mmol^{-1})	BiI_3 (mg mmol^{-1})	$C_4H_{12}NBr$ (mg mmol^{-1})
$(BA)_4AgBiBr_8$	23.5/0.125	/	56.1/0.125	/	77.0/0.5
$(BA)_4AgBiBr_7I$	/	29.3/0.125	56.1/0.125	/	77.0/0.5
$(BA)_4AgBiBr_6I_2$	/	29.3/0.125	37.2/0.08	24.8/0.04	77.0/0.5
$(BA)_4AgBiBr_5I_3$	/	29.3/0.125	18.8/0.04	48.9/0.08	77.0/0.5
$(BA)_4AgBiBr_4I_4$	/	29.3/0.125	/	73.7/0.125	77.0/0.5

limited stability against heat, moisture and air impede a broad commercialization [1]. In several approaches the substitution of Pb^{2+} was performed with other bivalent cations such as Sn^{2+} or Ge^{2+} to maintain the good optoelectronic properties by substitution with cations of similar electronic configuration [2, 3]. However, due to their preference of the oxidized states (Sn^{4+} or Ge^{4+}) their environmental stability is further decreased. To expand the possible substitution options the usual bivalent cation was substituted with equal amounts of monovalent cations such as Cu^{+}, Ag^{+} and Na^{+} and trivalent cations such as Bi^{3+}, Sb^{3+} and In^{3+} [4, 5]. This approach forms a new perovskite class, known as double perovskite with the general formula $A_2B^{+}B^{3+}X_6$, which differ from the originated structure by the alternating occupation of the octahedral cavities with mono- and trivalent cations. Being these compounds generally characterized by higher band gaps compared to those of the bivalent perovskites due to preferential lattice stabilization as bromides, they might be more suitable to harvest the light coming from artificial lighting sources like white light emitting diodes (WLED) compared to the standard solar radiation, thus being suitable for use in indoor PV (optimum bandgap for indoor PV applications is in the range 1.9–2.0 eV, therefore far from the optimum one for outdoor that is between 1.1 and 1.4 eV) [6, 7].

Despite the high variety of prepared double perovskites, it has not been possible up to-now to reach the high optoelectronic performance of the lead-based ones. Several features of the 3D double perovskites limit their performance in optoelectronic devices, such as the indirect nature of their band gap, the high exciton binding energy and the low charge carrier lifetimes [8–10]. One possible approach to solve this issue is the dimensional reduction of the 3D bulk material towards the purely bidimensional form (precisely the monolayer one), which has been shown by calculations to provide direct band-gap species [11, 12]. To practically perform this structural modification, it is necessary to substitute the A^{+} cation in the 3D lattice with bulky primary ammonium cations, forming organic bilayers in between adjacent all-inorganic 2D planes in the so-called Ruddlesden–Popper phases [13–15]. However, together with a transition from an indirect to a direct bandgap, also an undesired bandgap opening takes place after production of the 2D monolayer double perovskites, which brings the material light absorption features in hypsochromic direction, thus also compromising possible use in indoor PV.

In this work we report on iodide doping [16–19] in a Ruddlesden–Popper 2D monolayer silver-bismuth bromide double perovskite featuring butylammonium cations as organic spacers, named from now on with its formula $(BA)_4AgBiBr_8$, as a valuable strategy to achieve a red shift and broadening of the main absorption peak, which might make the resulting material more suitable for WLED light harvesting. We furthermore examine the structural properties and stability to prolonged illumination of the resulting thin films, trying to define the real potential of a similar low-toxicity material for use as active layer in indoor PV. While the formation of stable pure iodides for double perovskite structures has resulted elusive up to now [20], the mixing strategy might represent an alternative opportunity for the obtainment of comparable optical features, once the proper structural features for lattice stabilization have been identified.

2. Materials and methods

All the double perovskite precursors, namely $BiBr_3$(99%), CsBr (99.9%), AgBr (99.5%) were purchased from Alfa Aesar. N-butylammonium bromide was purchased from Sigma Aldrich, as well as were the solvents. $BiBr_3$ was stored in a glovebox due to moisture sensitivity and AgBr in dark due to light sensitivity. AgI was synthesized by dissolving 1.447 g (8.518 mmol) of $AgNO_3$ and 1.418 g (8.542 mmol) of KI in 10 ml of demineralized water each, leaving the two resulting solutions to stir for 1 h at room temperature. Mixing of the two solutions led to precipitation of a yellow solid, that was filtered and dried at 120 °C in an oven over night. The obtained yellow powder was stored in the dark. BiI_3 was prepared by mixing solutions of $Bi(NO_3)_3 \cdot 5H_2O$ (1.656 g, 3.414 mmol) and KI (1.695 g, 10.21 mmol) in diluted HNO_3 (10 ml each). A black solid precipitated, which was filtered, washed with water and dried in oven at 120 °C.

2.1. Preparation of $(BA)_4AgBiBr_{8-x}I_x$ (with $x = 0, 1, 2, 3, 4$) thin films

While in the past we employed an hydrothermal synthesis method to produce crystalline $(BA)_4AgBiBr_8$ and then with the resulting material we performed thin film fabrication through re-dissolution in dimethylformamide (DMF) [13], for the partial substitution of bromide ions in the metal-halide octahedra with iodides this method is not suitable, because it is normally conducted in excess of the halide (Br^{-} in this case) in hydrobromic acid solutions. Therefore, a solvent procedure was adopted, dissolving stoichiometric amounts of the AgBr, AgI, $BiBr_3$, BiI_3 and n-butylammonium bromide in DMF. The solvent procedure was first applied for the synthesis of

$(BA)_4AgBiBr_8$ to test its suitability to provide the pure compound directly in thin film form and then to synthesize the iodide-doped species. The amounts which are given in table 1 were weighed, dissolved in 500 μl DMF and stirred overnight. All suspensions were heated up to 70 °C–80 °C to fully dissolve the precursors. In case of $(BA)_4AgBiBr_5I_3$ and $(BA)_4AgBiBr_4I_4$, which did not fully dissolve, 500 μl and 1000 μl of DMF respectively were added to complete the dissolution. These solutions varied in color from yellow to red-orange in relation to the dissolved iodide amounts, as shown in figure S1 (available online at stacks.iop.org/NANO/33/215706/mmedia) in the Supporting Information (S.I.). The solutions of the iodide doped double perovskite were directly used for thin film preparation on fluorine-doped tin oxide (FTO) transparent conductive substrates. The FTO-substrates were prepared by washing in an ultrasonic bath in demineralized water, ethanol and isopropanol for 5 min each. After drying, they were further cleaned for 15 min in an UV-Ozone Cleaner. The preparation of the thin films was performed in a glove box in an argon atmosphere by spin-coating. Therefore, the FTO-substrates were placed in the spin-coater and 35 μl of the chosen perovskite solutions were added, followed by spin-coating at 4000 rpm for 40 s (acceleration of 200 rpm s^{-1}). Finally, the deposited films were heated at 100 °C for 4 min on a hotplate (also in the glovebox). Figure 1(b) shows the visual appearance of the obtained thin films for the different Br/I stoichiometries.

2.2. Characterization of $(BA)_4AgBiBr_{8-x}I_x$ (with x = 0, 1, 2, 3, 4) thin films

UV–visible absorption measurements of thin films were carried out on an Agilent 8453 UV–vis spectrometer. Scanning electron microscopy (SEM) was performed on a Zeiss Merlin instrument at a working potential of 3 kV. Energy-dispersive x-ray (EDX) spectroscopy was performed on the same instrument at a working potential of 10 kV, an electron beam current of 3 nA and a X-Max 50 Silicon Drift Detector with 50 mm^2 active area and polymer window was used. Grazing incidence X-ray diffraction (GIXRD) was performed in a range of 3°–70° (0.05° step size, 0.014° s^{-1} scan speed) with a PANalytical B.V. X'Pert Pro diffractometer using Cu Kα1 radiation. The diffraction patterns were measured along the 2θ axis with a grazing incidence of $\omega = 0.5°$. X-ray photoelectron spectroscopy (XPS) measurements were conducted with a PHI 5000 VersaProbe II Scanning ESCA Microprobe (Physical Electronics) with monochromatized Al Kα X-ray source in high power mode (beam size 1300 μm × 100 μm, X-ray power: 100 W). Time steps of 50 ms, a step size of 0.2 eV and an analyzer pass energy of 46.95 eV were used for measuring the detail spectra. The sample surface was charge neutralized with slow electrons and argon ions, and the pressure was in the range from 10^{-7} Pa to 10^{-6} Pa during the measurement. Data analysis was performed using the CasaXPS software [21]. Atomic force microscopy (AFM) and Kelvin probe force microscopy (KPFM) were carried out using an AIST NT Vacuscope 1000 microscope operated below 10^{-6} mbar with SPARK 350 Pt -coated AFM probes excited at the resonant frequency of around 330 kHz. The work function was obtained by measuring the contact potential difference between probe and sample via FM-KPFM at an AC amplitude of 2 V at around 1 kHz. The probe work function was referenced by obtaining the contact potential difference of the probe to a freshly cleaved highly oriented pyrolytic graphite (ZYB, MikroMasch) with a known work function of 4.6 eV previous before and after each measurement. For time-resolved photoluminescence (TR-PL) spectroscopy, the samples were mounted in a microscopy cryostat (CryoVac) and cooled with liquid nitrogen. As excitation wavelength 380 nm was chosen, corresponding to the frequency-doubled output (760 nm) of a Titanium:Sapphire laser (Spectra Physics) with a repetition rate of 80 MHz and a pulse duration of ca. 100 fs. The average excitation power was approximately 1 mW. In order to suppress the excitation laser, several long-pass filters with a cut-off wavelength between 395 and 400 nm were placed in the detection path. The data was recorded with a synchroscan streak camera (Hamamatsu, C6860) and corrected by underground and spectral sensitivity of the detection system. Time-integrated PL spectra were obtained from the time-resolved streak camera data by summing up the intensity over all rows of the images. Note that the PL in all samples decayed almost entirely in the observed time window of 2 ns.

3. Results and discussion

The partial substitution of bromide ions with iodides within the metal halide octahedra of a perovskite structure to obtain mixed halide perovskites is a very common strategy to achieve a red shift of the absorption, due to the resulting bandgap reduction [22]. Unfortunately it is not always successful in providing pure mixed phases, but it often results in phase-segregation within thin films, providing domains of the sole bromide-rich phase separated by domains of the sole iodide-one [23, 24]. This phenomenon is not usually seen on freshly-prepared films, but can take place after exposure to light and/or other environmental factors. However, very recently it has been shown that, while in 3D perovskites this is a huge drawback for photo-active layers stability, in 2D perovskites the dimensional reduction might play a beneficial role in suppressing phase segregation [25, 26].

For this reason, we were prompted to attempt iodide substitution in previously reported lead-free $(BA)_4AgBiBr_8$ (figure 1(a)) [11, 13], a crystalline compound which was produced through hydrothermal synthesis, by mixing the inorganic bromide precursors and butylamine in hydrobromic acid solutions, and then re-dissolved in DMF to fabricate very homogeneous thin films via spin-coating. Unfortunately, a similar two-step procedure going through the hydrothermal product appeared unsuitable to the specific task that we were aiming at, namely the partial bromide substitution with iodide. This is due to the fact that the initial synthetic step is carried out in excess bromide ions (in concentrated aqueous HBr) and thus possibly compromising the incorporation of the iodide ions in the crystal lattice of the 2D double

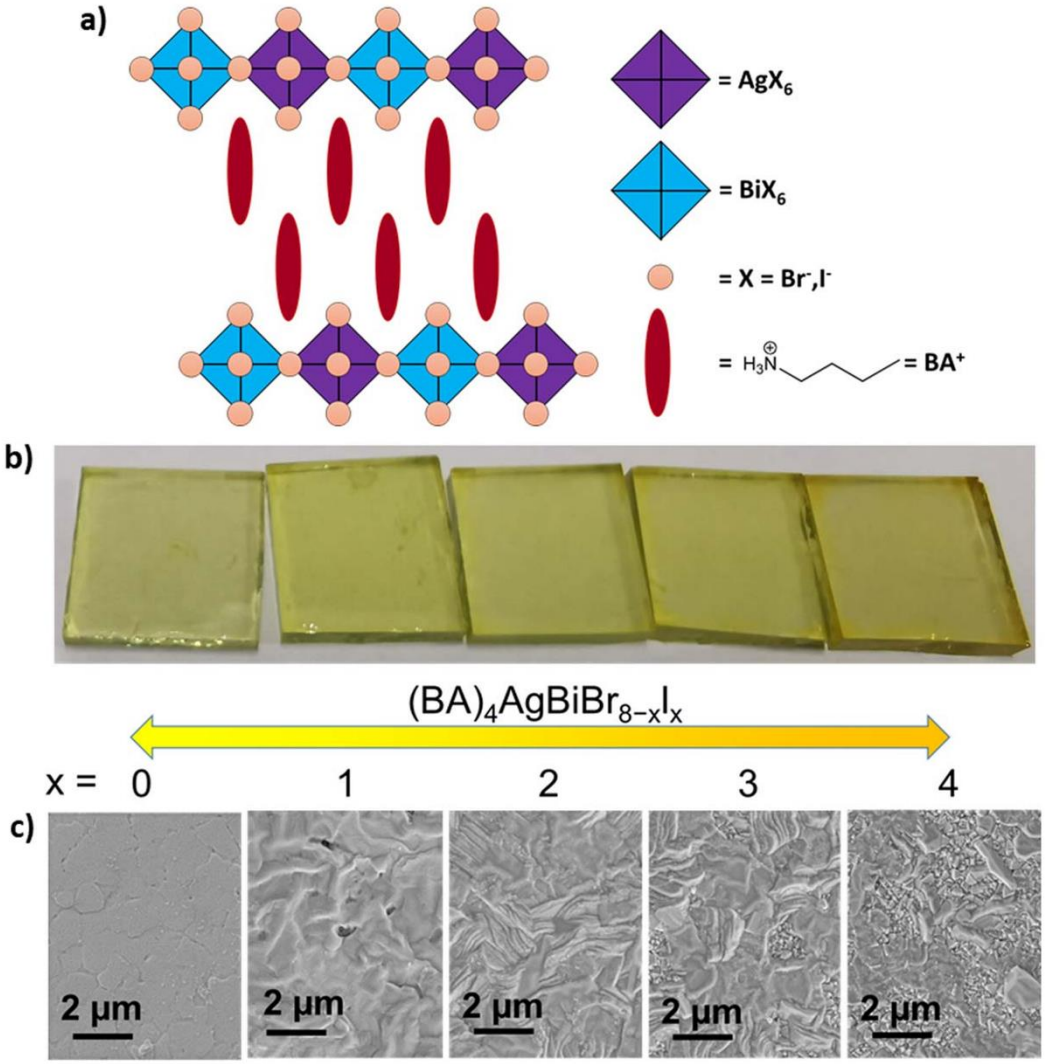

Figure 1. (a) Sketch of the structure of 2D monolayer silver-bismuth halide double perovskites of formula $(BA)_4AgBiBr_{8-x}I_x$ (with $x = 0$, 1, 2, 3, 4) studied in this work. (b) Macroscopic aspect and (c) top-view SEM images of the resulting spin-coated thin films on FTO substrates.

perovskite. The preparation of two rare cases of pure iodides of 2D monolayers double perovskites was reported recently employing bifunctional ammonium cations (thus in a Dion-Jacobson conformation) [20, 27, 28], also operating in excess iodide in aqueous HI, but, to the best of our knowledge, no cases of mixed bromide/iodide of this type have been reported in the literature up to now. To be sure to introduce the right relative amount of the two halides in the mixed species, we chose to proceed through a one-step process starting from different relative stoichiometric amounts of AgI, $BiBr_3$, BiI_3 and $C_4H_{12}NBr$ all dissolved in DMF and directly spin-coated on top transparent substrates to obtain thin films suitable for structural, optical and stability analysis (see details in the Materials and Methods section). In this way, we were able to prepare and study four different mixed bromide-iodide 2D-monolayer double perovskite samples, with increasing Br/I ratios, ranging from 7:1 to 6:2, 5:3 and 4:4. However, given the limited solubility of BiI_3 in DMF, for the two highest iodide ratios we were forced to increase dilution in the precursor solutions, which resulted anyway darker than the others, already pre-announcing the possibility to achieve red-shift in the thin films prepared starting from them (see figure S1 in the S.I. for pictures of these solutions and figure 1(b) for that of the resulting films on FTO). On the other hand, all our attempts to prepare the pure iodide compound $(BA)_4AgBiI_8$, both hydrothermally in concentrated aqueous HI and following the procedure for direct thin film preparation discussed before (with AgI, BiI_3 and $C_4H_{12}NI$ in DMF), failed. It might be possible that such a compound is unstable, as many other double perovskite iodides are [20].

The as-prepared thin films of $(BA)_4AgBiBr_{8-x}I_x$ (with $x = 1$, 2, 3, 4) were studied through GIXRD and the resulting diffractograms were compared to that of a thin film of pure $(BA)_4AgBiBr_8$ also prepared through the one-step procedure

(i.e. without previous preparation of the crystalline compound through hydrothermal synthesis), to probe the existence of one or more crystalline phases. The obtained GIXRD data for the thin films of $(BA)_4AgBiBr_7I$, $(BA)_4AgBiBr_6I_2$, $(BA)_4AgBiBr_5I_3$ and $(BA)_4AgBiBr_4I_4$ are reported in figure S2 of the S.I. At all the examined iodide contents, the GIXRD patterns of the $(BA)_4AgBiBr_{1-x}I_x$ thin films show an intense (001)-reflex at almost 6.6°, which is nearly identical to that of the reference $(BA)_4AgBiBr_8$ thin film (figure S1(a)). In samples with $x \geqslant 2$, another weak reflex at 13.2° appears, which is most likely the second order reflex of the (001) dominant scattering feature. For all compounds therefore, the crystalline phase is identical to that of $(BA)_4AgBiBr_8$ and no side phases could be detected, allowing us to exclude the occurrence of phase-separation of an iodide-rich phase during the thin-film production process. However, by increasing bromide-iodide substitution, the shape of the dominant (001)-reflex becomes progressively broader, likely indicating the formation of smaller crystallites in the thin films (see figure S1(b)). In addition, since all reflexes are identified as (001)-reflexes or its multiples, an ordered layer structure parallel to the substrate is suggested.

The SEM images of the iodide-doped and reference $(BA)_4AgBiBr_8$ thin films are reported in figure 1(c) (the macroscopic appearance of the same thin films as results to the naked eye is reported for the sake of clarity in figure 1(b), from which it can be noticed how the yellow color of the pure bromide reference becomes darker with increasing amounts of iodide substitution). While pure $(BA)_4AgBiBr_8$ forms a very uniform and homogeneous film on the FTO substrate, the progressive increase in iodide content seems to affect the homogeneity of the layer. The microstructure of $(BA)_4AgBiBr_7I$ reveals the presence of a layer mostly parallel to the substrate and with relatively good coverage of this last one, although in comparison with that of $(BA)_4AgBiBr_8$ appears to be more disordered and featuring a few small pinholes. For $(BA)_4AgBiBr_6I_2$ the SEM image shows an increased nano-structuring in the layer, as edges of packed layers are clearly visible. This trend in nano-structuring and reduced surface coverage continues with $(BA)_4AgBiBr_5I_3$ and $(BA)_4AgBiBr_4I_4$ and is further confirmed by AFM (see figure S6(a)). The reduced coverage of the substrate is most likely due to the higher dilution applied to the precursor solution for $(BA)_4AgBiBr_5I_3$ and $(BA)_4AgBiBr_4I_4$ due to the reduced DMF solubility of BiI_3 compared to that of $BiBr_3$, as mentioned earlier. Such inhomogeneity prevented us from obtaining exact film thicknesses from SEM cross-sections. However, the film thicknesses of the thin films with high coverage ($x = 0$, 1) show values around 440 nm, while the thickness of the $x = 2$ film is significantly reduced to circa 100 nm, as can be inferred from figure S3.

To validate that the 2D monolayer double perovskite thin films have the same compositions that were given by the particular precursor solution composition, XPS analysis was performed, to compare the atomic ratios of Ag, Bi, Br and I, that can be calculated by their respective XPS spectra (see table S1 for a summary of all the calculated atomic ratios).

The XPS spectra in the Br and I region, reported in figures 2(a) and (b) respectively, show that the intensity of the Br 3d spectrum decreases with increasing iodide substitution (here indicated as x) while the intensity of the I $3d_{5/2}$ spectrum increases with increasing x and shows no signal at $x = 0$, meaning that the reference $(BA)_4AgBiBr_8$ perovskite contains no iodide as solely bromide precursors were used for its preparation (table 1). Furthermore, the direct comparison of the calculated bromide and iodide contents reported in figure 2(c) proves that the halide ratios match the corresponding precursor compositions. For what concerns the metallic components in the thin films, namely Bi and Ag, it is important to note that while the Bi 4f spectrum did only change slightly in intensity for any halide ratio (figure S5(b)) the intensity of the Ag 3d spectrum underwent larger changes across the different substitution stoichiometry, which cannot be anyway reconnected to the iodide-bromide ratio trends. In general, a Bi:Ag ratio of around 2:1 for each halide composition (see table S1) was detected, although equimolar amounts of Ag and Bi were used as precursors. These results are in agreement with our former evidences, indicating the presence of Ag-depleted regions in crystalline $(BA)_4AgBiBr_8$ powder samples as resulted by EDX analysis carried out during transmission electron microscopy (TEM) imaging [13]. Additionally, we performed EDX measurements within the SEM to gain further insight into the bulk composition of the thin films, since XPS is a surface sensitive technique. However, due to the higher penetration depth of EDX with respect to XPS, only thick and homogeneous films ($x = 0$, 1, 2) provided reliable results on their atomic ratios (see table S2), while for the $x = 3$, 4 samples most of the signal could be assigned to the substrate. The calculated ratios of bromide and iodide which are plotted in figure S4 are in good accordance to the ratios calculated from the XPS measurements and the precursor ratios shown in table 1. Furthermore, elemental maps obtained from EDX, which are depicted in figure 6 (*vide infra*), show homogeneous distributions of bromide and iodide across the thin film for low iodide contents ($x = 1$) and only small inhomogeneities for increased iodide contents ($x = 2$).

The $(BA)_4AgBiBr_{8-x}I_x$ thin films with progressively increasing substitution of bromide anions with iodide have been studied through UV–vis absorption spectroscopy to precisely evaluate the change in their optical absorbance. The resulting UV–vis spectra are reported in figure 3(a) and effectively demonstrate the progressive bathochromic shift of the optical absorption as a function of augmented iodide-bromide substitution. Since the film thickness and morphology is likely varying too, as we could detect from SEM, we normalized the spectra at their absorbance minimum in the area between 370 and 400 nm, to be able to compare relative variations in the peak intensities and shapes. The strong and relatively narrow peak with a maximum at 410 nm (~3 eV) in the pure bromide thin film is consistent with what was observed previously by us and by other authors [11, 13]. This transition is of apparent excitonic type and has been reported to feature a large contribution of the light-triggered charge transfer from Ag-d to Bi-s/Bi-p orbitals. Still, its exact nature, particularly in a highly confined space as that of a 2D monolayer structure, is subject of debate and it is well far

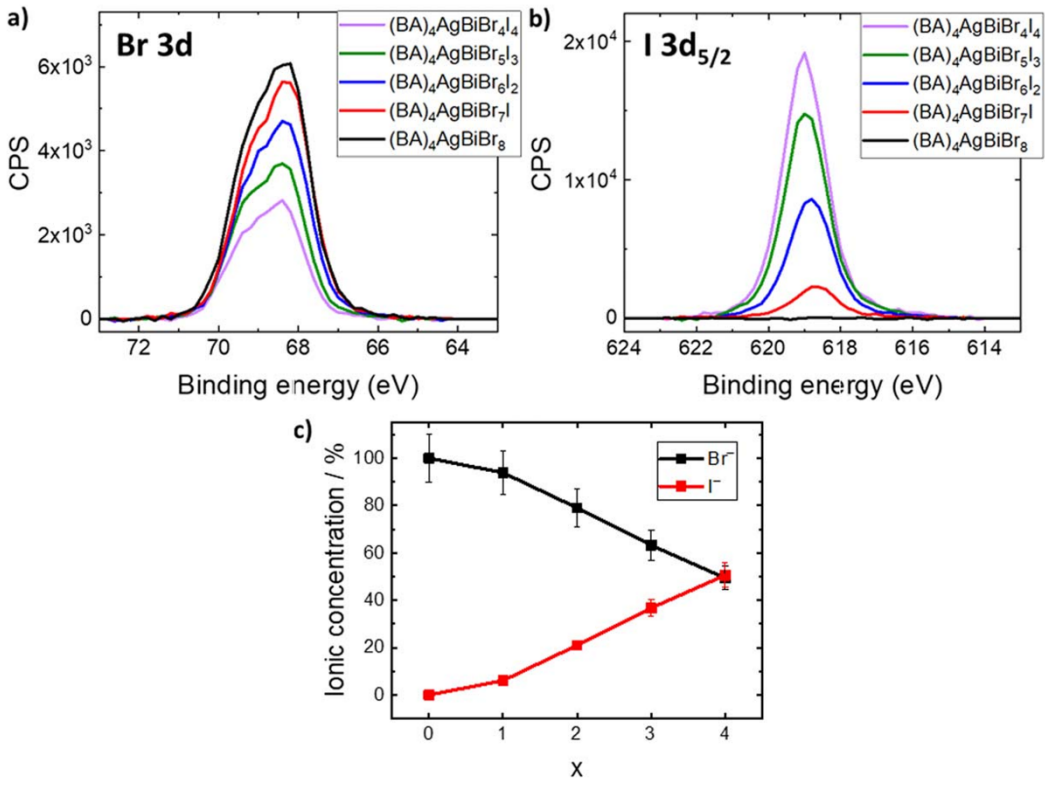

Figure 2. Details of the XPS spectra of the $(BA)_4AgBiBr_{8-x}I_x$ ($x = 0, 1, 2, 3, 4$) thin films: (a) Br 3d region and (b) I $3d_{5/2}$ region. (c) Halide ions ratio variation in the corresponding films (the error bars include a relative error of 10% for each estimated concentration value).

from our intentions to provide a full explanation for it in the present work. What anyway appears to be perfectly clear is that by increasing the alloying percentage with iodide, this peak decreases in intensity, broadens and shifts its maximum towards longer wavelengths [up to 454 nm (~2.7 eV) in the species with the highest iodide/bromide ratio, namely $(BA)_4AgBiBr_4I_4$], as desired.

This shift might result from the partial participation of iodide atoms orbitals to the states involved in the edge optical transition, or to changes in the lattice constant following partial bromide replacement with iodide, this also perhaps related to a different orientation of the octahedra in the inorganic sheets in comparison to the situation in the pure $(BA)_4AgBiBr_8$ [11]. The beneficial effect of iodide substitution on the band edge absorption bathochromic shifting is therefore well proven from these measurements. Still, the nature of the involved transitions and the reason for peak broadening are difficult to determine: very recently, Kanatzidis and coworkers reported for pure iodide 2D monolayer Ag–Bi double perovskites with small cyclic diammonium cations that an electronic transition from I-5p states in the valence band maximum to I-5p/ Bi-6p states in the conduction band minimum could better explain band edge absorption, when iodide is involved as the halide in this type of compounds [27]. Unfortunately, the absorption spectra of thin films of these compounds are not reported in their work, but only the Kubelka–Munk transformations applied on the diffuse reflectance spectra of the powder species, not allowing a good comparison of the shape of this absorption with that measured for the here reported films. Nevertheless, it appears that also in their materials a rather broad absorption without pronounced exciton resonance characterizes the band edge features, as it is in the present case. Whether this broadening is a sign of decreased exciton confinement in these iodide-enriched materials [15, 29], is hard to clarify at this stage and remains subject of future investigations: what we can anticipate here is that, if this would be the case, it might have a beneficial effect on the charge transport properties that could favor photocurrent generation in suitable light-conversion architectures.

The optoelectronic properties of the mixed iodide-bromide 2D monolayer silver-bismuth double perovskite thin films have been further studied by PL spectroscopy. The room-temperature PL spectra of the thin-films obtained from laser excitation at 380 nm (~3.26 eV) are reported in figure 3(b). In earlier work, we have identified this excitation energy as the one giving the highest PL response for the reference $(BA)_4AgBiBr_8$ material [13]. Moreover, as demonstrated in figure 3(a), this energy provides excitation well above the band gap for all investigated samples. The PL response of the pure bromide thin film confirms previous observations [11, 13], i.e. a relatively broad and weak emission centered at around 470 nm is recorded, likely due to a trap-assisted radiative recombination. In the present case, this emission appears also perhaps broader (larger full weight half maximum) than in precedent reports, featuring a tail which could derive from a self-trapped exciton

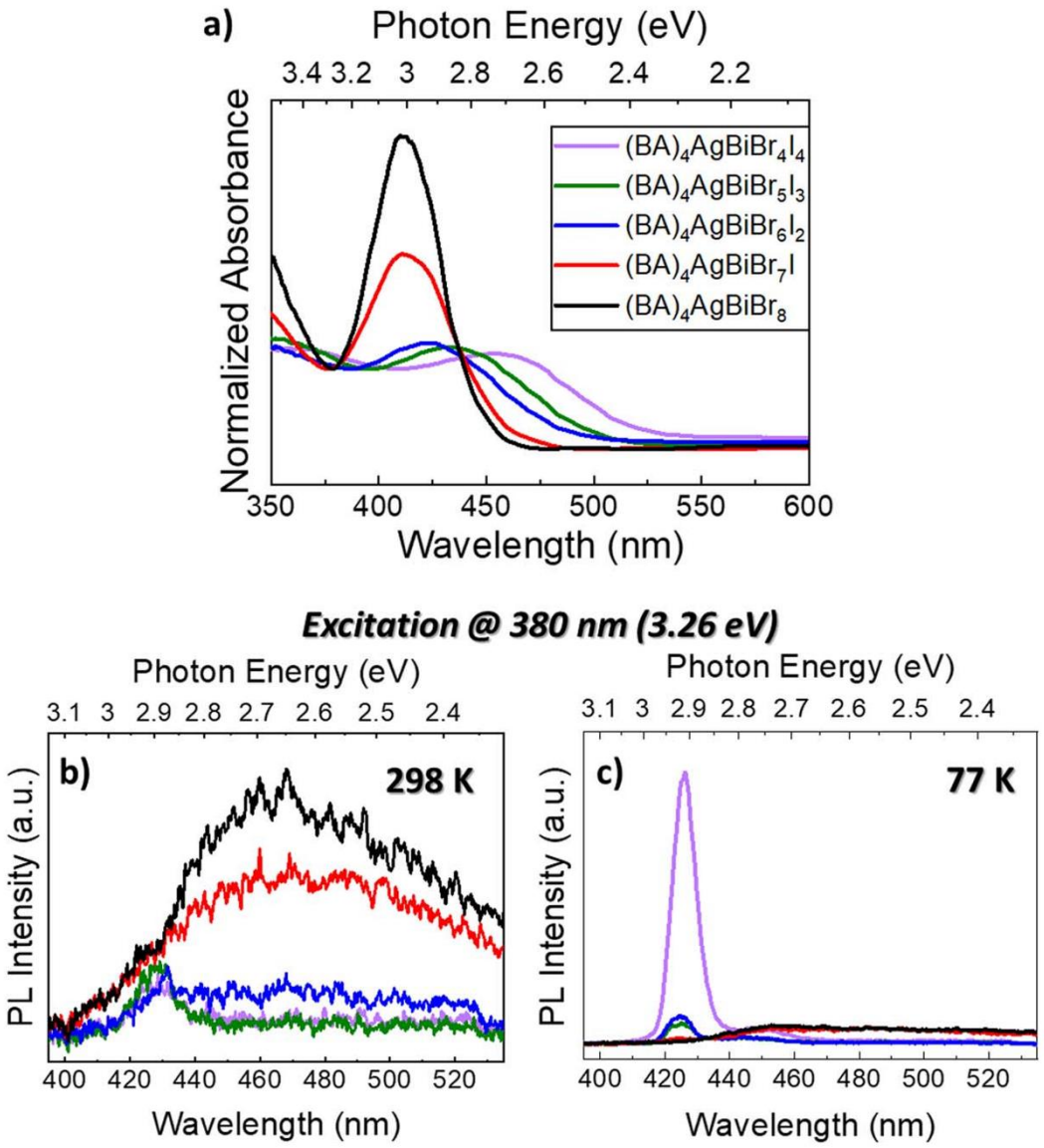

Figure 3. Optical properties of the $(BA)_4AgBiBr_{8-x}I_x$ ($x = 0, 1, 2, 3, 4$) thin films: (a) UV–visible absorption and PL spectra measured at (b) room temperature (298 K) and (c) at 77 K ($\lambda_{exc} = 380$ nm, $E_{exc} = 3.26$ eV). The color/sample legend is reported only in the first graph for the sake of clarity.

(STE) contribution [30], by us seen up to now in a well-defined manner only for an isomeric compound in which the n-butyl ammonium cations were completely replaced by iso-butylammonium in the 2D monolayer double perovskite lattice [13]. The effect of iodide-bromide substitution on the PL behavior of the thin films is peculiar and points out at possible re-adjustments of the lattice, which however do not apparently affect the spacing between the 2D layers but mostly the inorganic nanosheets conformation, as we could not detect them through GIXRD (figure S2). The broad trap-mediated PL of the $(BA)_4AgBiBr_8$ thin film progressively decreases and, in the samples with higher iodide content, namely $(BA)_4AgBiBr_5I_3$ and $(BA)_4AgBiBr_4I_4$, a new feature emerges at shorter wavelength/higher energies (around 425 nm/2.9 eV), which is very narrow (linewidth ~100 nm) and becomes more intense after lowering the temperature to 77 K (figure 3(c)). A quantitative comparison of this signature between different temperatures and different iodine concentrations is not possible due to the sample inhomogeneity, which lead to a varying contribution of the feature around 425 nm across the studied thin films. Moreover, the intensity of the signature decreased after longer illumination with the laser. Nevertheless, a clear trend towards higher intensities at lower temperature and higher iodine concentration is observed. In the data recorded for the $(BA)_4AgBiBr_4I_4$ sample (lilac line), the intensity of this peak at low temperature becomes almost 10 times higher than

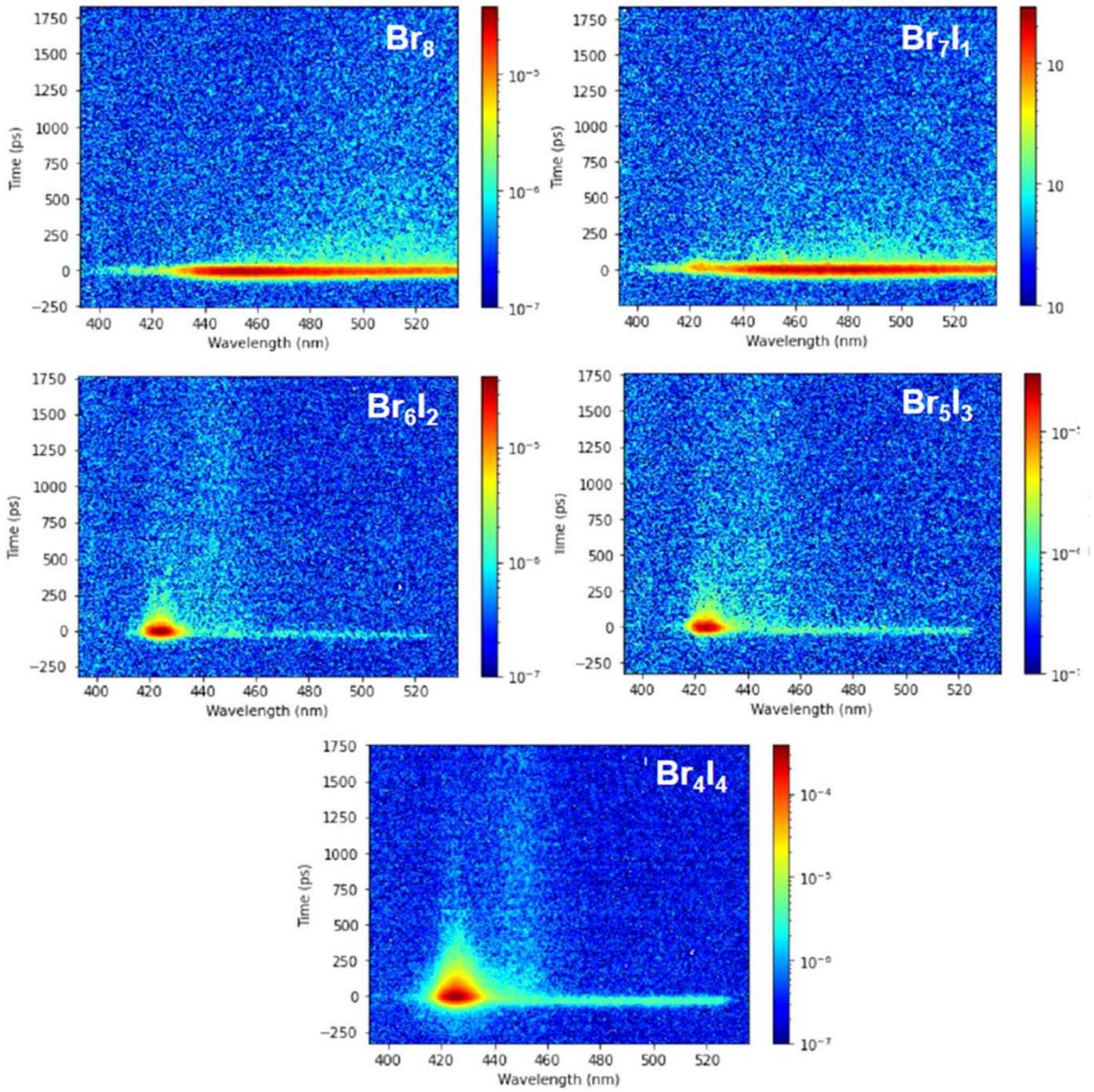

Figure 4. PL decays for the $(BA)_4AgBiBr_{8-x}I_x$ ($x = 0, 1, 2, 3, 4$) thin films measured at 77 K ($\lambda_{exc} = 380$ nm, $E_{exc} = 3.26$ eV).

in $(BA)_4AgBiBr_5I_3$ and $(BA)_4AgBiBr_6I_2$ (green and blue line) and indicates strong emission from a presumable free exciton [15], which to the best of our knowledge was never seen before in this type of double perovskites. In this spectrum, a minor contribution at longer wavelengths coming from the trap-mediated recombination typical of the pure bromide system can also be recognized (see figure 3(a)).

We further examined the PL decays of the thin films at 77 K: figure 4 reports three dimensional maps of the PL wavelength/PL decay time/PL intensity correlation, from which it can be qualitatively inferred that the emergence of the pure excitonic emission give rise to longer PL lifetimes, the longest ones clearly evident in the $(BA)_4AgBiBr_4I_4$ sample. A more precise quantification of the PL decay is given in the TR-PL spectra in figure S4, in which a fitting has been carried out: typically, two contributions are present, a short one on the order of 20 ps and a longer one between 100 and 250 ps, with the longest time constant coming from some longer-lived emission of the broad signature for the $(BA)_4AgBiBr_8$ and $(BA)_4AgBiBr_7I_1$ samples and from the feature at 425 nm in the other samples. An even shorter contribution emerging from the broad emission peaking around 470 nm could not be fit adequately, as it decayed within the instrument response time. Such a short decay could originate from a high number or non-radiative decay channels introduced by defects. The longer PL decay of the 425 nm

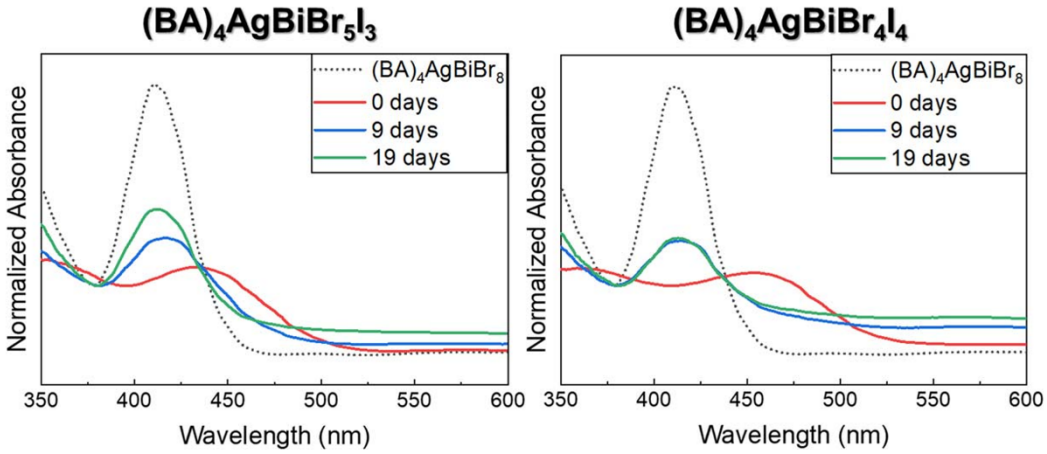

Figure 5. UV–visible absorption spectra for unencapsulated $(BA)_4AgBiBr_5I_3$ and $(BA)_4AgBiBr_4I_4$ thin films at different times during progressive ageing indoor at 60% relative humidity. The spectrum of the as-prepared $(BA)_4AgBiBr_8$ thin film is also reported for the sake of comparison.

emission on the other hand indicates the presence of domains with a considerably lower defect density (much brighter, but small in volume, so that they do not appear clearly in absorption and in GIXRD), in which photogenerated excitons or charges can travel for relatively long distances across the inorganic lattice before they recombine radiatively or non-radiatively [31]. A similar scenario might prospect improved photocurrent generation in the system, once better control over these low-defects density domains is achieved, which would be beneficial for photovoltaic applications.

To examine how iodide doping affects the electronic structure of the perovskite and to provide a basis for an appropriate choice of contact materials, we performed KPFM analysis on thin films (figure S6(b)) and compared the perovskite's work function (WF) at varying degrees of iodide content ($x = 0$, 1, 2, 4, figure S6(c)). While the pristine perovskite ($x = 0$) showed a WF of ~4.95 eV (see figure S7(c)), an upward shift to ~4.80 eV was detected when a small amount of iodide was incorporated ($x = 1$). The WF was shifted even further for the sample with the highest iodide content ($x = 4$), but showed a broadened distribution with a maximum at ~4.66 eV and a shoulder at ~4.60 eV. This can be explained by an inhomogeneous distribution of iodide across the perovskite surface and/or by an inhomogeneous orientation of the perovskite crystals relative to the substrate, which can lead to differently strong interactions of the tip with monolayer edges. Such differences in orientation were detected in the AFM images in figure S6(a), speaking in favor of at least partial relevance of this explanation. Interestingly, for $x = 2$, topologically homogeneous areas were seen in AFM that showed spots of ~500 nm diameter with significantly lowered WF. These result in a broad WF distribution in this sample, with a maximum at the same energy as the undoped pure bromide perovskite and another weaker local maximum at ~4.57 eV, a similar energy as the aforementioned shoulder of (BA)4AgBiBr4I4. We, therefore, conclude that for $x = 2$ a separation of bromide- and iodide-rich phases might have an influence, whereas iodide is homogeneously distributed even at the surface at $x = 1$. The WF of 4.95 eV determined in the present series for $(BA)_4AgBiBr_8$ ($x = 0$) significantly deviates from a previously reported value of 4.42 eV [13]. This difference was caused by characteristically different ways of film preparation. When measuring the WF of a thin film obtained from hydrothermally pre-synthesized $(BA)_4AgBiBr_8$ subsequently dissolved in DMF for spin coating, as in [13], as part of the present series, we confirmed the previously reported WF for such film (see figure S7). Since both $(BA)_4AgBiBr_8$ films show similar morphology, we assign this difference in WF to differences in surface termination when the metal halide and butylammonium halide precursors are directly dissolved in DMF and casted in the present series as opposed to direct precipitation from $(BA)_4AgBiBr_8$ crystalline precursors as in [13]. Good opportunities of tuning the contact formation with charge extraction layers by appropriate surface termination are, thereby, indicated.

To evaluate the environmental stability of the mixed iodide-bromide 2D monolayer Ag–Bi perovskite thin films, we exposed the two samples with the more pronounced red shift of the absorption edge, namely $(BA)_4AgBiBr_5I_3$ and $(BA)_4AgBiBr_4I_4$, to prolonged ageing. The shelf-life test was carried out by maintaining the films for a maximum of 19 days in air at a relative humidity of 60% under standard day/night illumination conditions on a bench within the laboratory (no coverage) and measuring the absorption spectra after 9 and 19 days. The results are shown in figure 5: the spectra for both the samples appear to regain the features of the pure bromide reference compound (shown as dotted line in the figures for comparison), although they do not recover completely the same intensity in the excitonic transition.

We believe that what we observe here is a progressive loss of iodide most likely in the form of volatile I_2 [20, 32] (easily undergoing sublimation in standard environmental conditions) and consequent rearrangement of the crystal lattice, as arguable from the top-view SEM images reported in figure S9. This process is undoubtedly accelerated in the

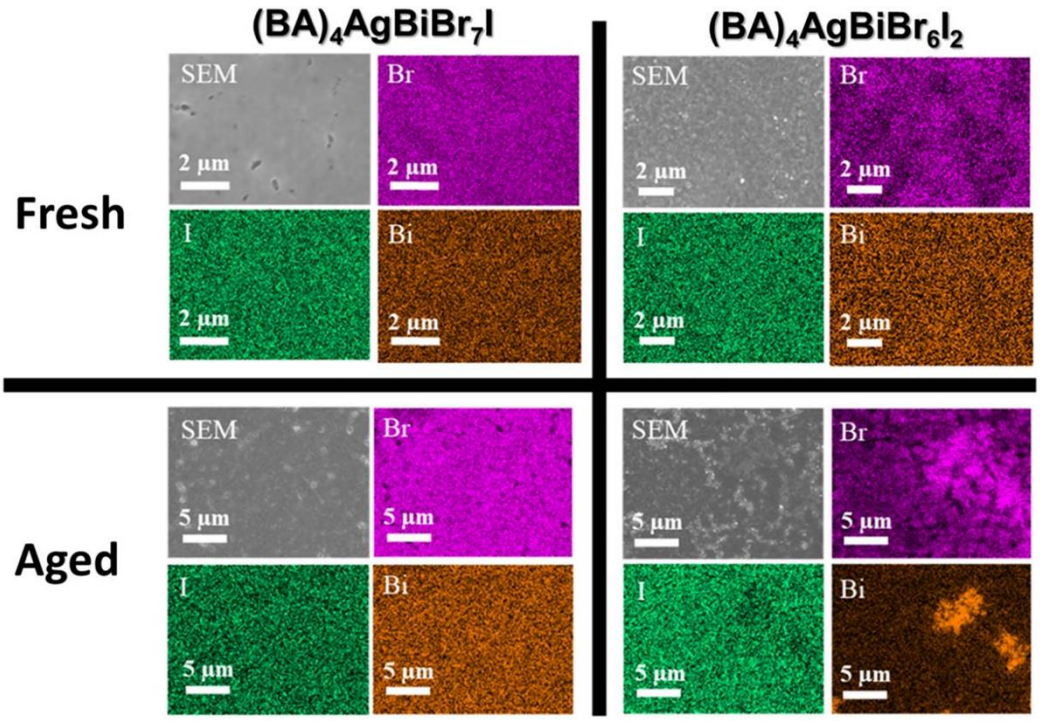

Figure 6. Elemental maps of bromide, iodide and bismuth distribution for $(BA)_4AgBiBr_7I$ (left) and $(BA)_4AgBiBr_6I_2$ (right) thin films that were freshly prepared (top) and underwent prolonged ageing (bottom) as obtained by EDX. SEM images of the measured areas are depicted in the respective top left corner for the sake of clarity.

presence of light, heat and/or humidity, which trigger decomposition by generating surface defects that promote iodine release [32]. The relatively thin and pinhole-rich films for these two bromide-compositions (see figure 1(c)), likely forming as the result of the higher dilution in the precursor solutions that we were forced to employ, offers undoubtedly more surface sites for the occurrence of similar degradation pathways. The influence of light in this process is further suggested by the progressive disappearance of the free exciton PL signal under prolonged laser excitation (1–2 min times, data not shown).

The iodide loss can be indeed verified from samples with x values up to 2 from EDX analysis (see table S2). Additionally, GIXRD measurements on aged samples (see figures S2(c), (d)) show that in thin films with high iodide content ($x = 2, 3, 4$) a reflex at 12.0°, that could not be observed in freshly prepared samples, appears and is particularly intense for the $(BA)_4AgBiBr_4I_4$ aged sample. Although elemental maps measured by EDX (figure 6) show agglomerations of bismuth and bromide in the aged $(BA)_4AgBiBr_6I_2$ sample, this new XRD reflex could not be assigned to $BiBr_3$ or to any other used precursor. Elemental maps further show a homogeneous distribution of silver (see figure S10) for freshly prepared as well as aged samples, while the iodide content decreases slightly at locations of increased bismuth and bromide co-localization in the aged $(BA)_4AgBiBr_6I_2$ thin film. On the other hand, $(BA)_4AgBiBr_7I$ thin film presents a homogeneous distribution for all elements, in freshly prepared samples as well as in degraded samples. Therefore, we assume that the aforementioned newly appearing reflex has to be assigned to a yet unknown Bi- and Br-rich side phase which forms upon degradation.

4. Conclusion

In this work we report, to the best of our knowledge, the first study on the production of mixed halide thin films of a 2D monolayer silver-bismuth double perovskite and study their optical properties, aiming at providing first hints on their potential utilization as light absorber in the future generation of low-cost, environmentally friendly photovoltaic devices to power the IoT. We unravel very interesting insights from the study of these double perovskite materials, which could represent a valuable alternative to the use of the mono-halide counterparts, which particularly for the case of pure iodides, having the most promising expected bandgap, have only very rarely been isolated and characterized, due to a lack of lattice stability [20]. For increasing proportions of iodide alloying in a reference bromide phase, we observe a progressive bathochromic shift of the absorption edge which brings to cover an always larger part of the typical emission spectrum of a WLED lamp. We also provide evidence for the emergence of domains with a higher radiative yield likely due to lower amounts of defects, which could have a positive impact on the generation of free charges following light absorption, to be

collected as a photocurrent in suitably arranged photovoltaic architectures.

Since the environmental stability of these materials under prolonged exposure to light and air humidity results still very limited, we envisage the possibility to further boost the robustness of these systems by performing organic layer engineering: in the present preliminary study we made use of a very simple alkylammonium cation, but in our previous work we have already demonstrated that in the pure bromide structure the use of an aromatic cation brings to a stabilization of the lattice through the establishment of further van der Waals interactions within the organic double layer [13] and it has also been reported for mixed halide phases of lead-based perovskites by other groups [18, 26].

A limitation that still has to be faced for prospecting good efficiency in PV devices regards the obtainment of a preferential vertical orientation with respect to a substrate, which would favor the removal of the photo-generated free charges in the 2D perovskite by means of adjacent charge extracting layers. To allow access to this crystalline configuration, different methods have been reported to be employed during thin film processing, such as the hot casting method and the additive assisted crystallization [33], which should be thoroughly explored in future work. As in this study we have revealed first hints of the tendency towards a vertical arrangement of the most iodide-enriched thin films, we can guess that we are moving in the right direction to enable an optimal morphology for this scope after further optimization of the layer casting method. All these further studies will be very useful to allow the actual future utilization of these highly promising material platforms in sustainable solar cells or other optoelectronic devices.

Acknowledgments

T G would like to acknowledge financial support of the European commission through the H2020 FET-PROACTIVE-EIC-07-2020 project LIGHT-CAP (project number 101017821) and of the Deutsche Forschungsgemeinschaft (DFG, German Research Foundation) through the project GA 3052/1-1. T G also thanks the ENSEMBLE3-Centre of Excellence for nanophotonics, advanced materials and novel crystal growth-based technologies project (GA No. MAB/2020/14) carried out within the International Research Agendas programme of the Foundation for Polish Science co-financed by the European Union under the European Regional Development Fund and the European Union's Horizon 2020 research and innovation programme Teaming for Excellence (GA. No. 857543) for support of this work. M G thanks Prof Martin Koch for his support and access to experimental equipment.

Data availability statement

All data that support the findings of this study are included within the article (and any supplementary files).

ORCID iDs

Derck Schlettwein https://orcid.org/0000-0002-3446-196X
Teresa Gatti https://orcid.org/0000-0001-5343-8055

References

[1] Li J, Cao H-L, Jiao W-B, Wang Q, Wei M, Cantone I, Lü J and Abate A 2020 Biological impact of lead from halide perovskites reveals the risk of introducing a safe threshold *Nat. Commun.* **11** 310
[2] Ju M-G, Dai J, Ma L and Zeng X C 2017 Lead-free mixed tin and germanium perovskites for photovoltaic application *J. Am. Chem. Soc.* **139** 8038–43
[3] Chiara R, Morana M and Malavasi L 2021 Germanium-based halide perovskites: materials, properties, and applications *Chempluschem* **86** 879–88
[4] Pecunia V, Occhipinti L G, Chakraborty A, Pan Y and Peng Y 2020 Lead-free halide perovskite photovoltaics: challenges, open questions, and opportunities *APL Mater.* **8** 100901
[5] Jin Z, Zhang Z, Xiu J, Song H, Gatti T and He Z 2020 A critical review on bismuth and antimony halide based perovskites and their derivatives for photovoltaic applications: recent advances and challenges *J. Mater. Chem.* A **8** 16166–88
[6] Peng Y, Huq T N, Mei J, Portilla L, Jagt R A, Occhipinti L G, MacManus-Driscoll J L, Hoye R L Z and Pecunia V 2021 Lead-free perovskite-inspired absorbers for indoor photovoltaics *Adv. Energy Mater.* **11** 2002761
[7] Pecunia V, Occhipinti L G and Hoye R L Z 2021 Emerging indoor photovoltaic technologies for sustainable internet of things *Adv. Energy Mater.* **11** 2100698
[8] Longo G, Mahesh S, Buizza L R V, Wright A D, Ramadan A J, Abdi-Jalebi M, Nayak P K, Herz L M and Snaith H J 2020 Understanding the performance limiting factors of $Cs_2AgBiBr_6$ double-perovskite solar cells *ACS Energy Lett.* **5** 2200–7
[9] Schmitz F *et al* 2020 Lanthanide-induced photoluminescence in lead-free $Cs_2AgBiBr_6$ bulk perovskite: insights from optical and theoretical investigations *J. Phys. Chem. Lett.* **11** 8893–900
[10] Schade L *et al* 2019 Structural and optical properties of $Cs_2AgBiBr_6$ double perovskite *ACS Energy Lett.* **4** 299–305
[11] Connor B A, Leppert L, Smith M D, Neaton J B and Karunadasa H I 2018 Layered halide double perovskites: dimensional reduction of $Cs_2AgBiBr_6$ *J. Am. Chem. Soc.* **140** 5235–40
[12] Jana M K, Janke S M, Dirkes D J, Dovletgeldi S, Liu C, Qin X, Gundogdu K, You W, Blum V and Mitzi D B 2019 Direct-bandgap 2D silver–bismuth iodide double perovskite: the structure-directing influence of an oligothiophene spacer cation *J. Am. Chem. Soc.* **141** 7955–64
[13] Schmitz F *et al* 2021 Large cation engineering in two-dimensional silver–bismuth bromide double perovskites *Chem. Mater.* **33** 4688–700
[14] Zheng Y, Niu T, Ran X, Qiu J, Li B, Xia Y, Chen Y and Huang W 2019 Unique characteristics of 2D Ruddlesden–Popper (2DRP) perovskite for future photovoltaic application *J. Mater. Chem.* A **7** 13860–72
[15] Righetto M, Giovanni D, Lim S S and Sum T C 2021 The photophysics of Ruddlesden-Popper perovskites: a tale of energy, charges, and spins *Appl. Phys. Rev.* **8** 11318
[16] Righetto M, Meggiolaro D, Rizzo A, Sorrentino R, He Z, Meneghesso G, Sum T C, Gatti T and Lamberti F 2020 Coupling halide perovskites with different materials: from

doping to nanocomposites, beyond photovoltaics *Prog. Mater Sci.* **110** 100639
[17] Li C, Wei J, Sato M, Koike H, Xie Z-Z, Li Y-Q, Kanai K, Kera S, Ueno N and Tang J-X 2016 Halide-substituted electronic properties of organometal halide perovskite films: direct and inverse photoemission studies *ACS Appl. Mater. Interfaces* **8** 11526–31
[18] Zanetta A *et al* 2021 Manipulating color emission in 2D hybrid perovskites by fine tuning halide segregation: a transparent green emitter *Adv. Mater.* **34** 2105942
[19] Bonomi S, Galinetto P, Patrini M, Romani L and Malavasi L 2021 Optical and structural property tuning in physical vapor deposited bismuth halides Cs3Bi2(I1–*x*Br*x*)9 ($0 \leqslant x \leqslant 1$) *Inorg. Chem.* **60** 14142–50
[20] Vishnoi P, Seshadri R and Cheetham A K 2021 Why are double perovskite iodides so rare? *J. Phys. Chem.* C **125** 11756–64
[21] Fairley N *et al* 2021 Systematic and collaborative approach to problem solving using x-ray photoelectron spectroscopy *Appl. Surf. Sci. Adv.* **5** 100112
[22] Zarick H F, Soetan N, Erwin W R and Bardhan R 2018 Mixed halide hybrid perovskites: a paradigm shift in photovoltaics *J. Mater. Chem.* A **6** 5507–37
[23] Chen Z, Brocks G, Tao S and Bobbert P A 2021 Unified theory for light-induced halide segregation in mixed halide perovskites *Nat. Commun.* **12** 2687
[24] Knight A J, Borchert J, Oliver R D J, Patel J B, Radaelli P G, Snaith H J, Johnston M B and Herz L M 2021 Halide segregation in mixed-halide perovskites: influence of a-site cations *ACS Energy Lett.* **6** 799–808
[25] Cho J, Mathew P S, DuBose J T and Kamat P V 2021 Photoinduced halide segregation in Ruddlesden–Popper 2D mixed halide perovskite films *Adv. Mater.* **33** 2105585
[26] Mathew P S, DuBose J T, Cho J and Kamat P V 2021 Spacer cations dictate photoinduced phase segregation in 2D mixed halide perovskites *ACS Energy Lett.* **6** 2499–501
[27] Li X, Traoré B, Kepenekian M, Li L, Stoumpos C C, Guo P, Even J, Katan C and Kanatzidis M G 2021 Bismuth/silver-based two-dimensional iodide double and one-dimensional Bi perovskites: interplay between structural and electronic dimensions *Chem. Mater.* **33** 6206–16
[28] Bi L-Y, Hu Y-Q, Li M-Q, Hu T-L, Zhang H-L, Yin X-T, Que W-X, Lassoued M S and Zheng Y-Z 2019 Two-dimensional lead-free iodide-based hybrid double perovskites: crystal growth, thin-film preparation and photocurrent responses *J. Mater. Chem.* A **7** 19662–7
[29] Giovanni D, Ramesh S, Righetto M, Melvin Lim J W, Zhang Q, Wang Y, Ye S, Xu Q, Mathews N and Sum T C 2021 The physics of interlayer exciton delocalization in Ruddlesden–Popper lead halide perovskites *Nano Lett.* **21** 405–13
[30] Li S, Luo J, Liu J and Tang J 2019 Self-trapped excitons in all-inorganic Halide Perovskites: fundamentals, status, and potential applications *J. Phys. Chem. Lett.* **10** 1999–2007
[31] Liang M *et al* 2021 Free carriers versus self-trapped excitons at different facets of Ruddlesden–Popper two-dimensional lead halide perovskite single crystals *J. Phys. Chem. Lett.* **12** 4965–71
[32] Wu W-Q, Rudd P N, Ni Z, Van Brackle C H, Wei H, Wang Q, Ecker B R, Gao Y and Huang J 2020 Reducing surface halide deficiency for efficient and stable iodide-based perovskite solar cells *J. Am. Chem. Soc.* **142** 3989–96
[33] Zhao X, Liu T and Loo Y-L 2022 Advancing 2D perovskites for efficient and stable solar cells: challenges and opportunities *Adv. Mater.* **34** 2105849

Supporting Information for:

Tuning the optical properties of 2D monolayer silver-bismuth bromide double perovskite by halide substitution

Fabian Schmitz,[1,2] Raphael Neisius,[1] Jonas Horn,[2,3] Joachim Sann,[1,2] Derck Schlettwein,[2,3] Marina Gerhard,[4] Teresa Gatti[1,2]

[1] Institute of Physical Chemistry, Justus Liebig University, Heinrich-Buff-Ring 17, 35392 Giessen, Germany

[2] Center for Materials Research, Justus Liebig University, Heinrich-Buff-Ring 17, 35392 Giessen, Germany

[3] Institute of Applied Physics, Justus Liebig University, Heinrich Buff Ring 16, 35392 Giessen, Germany

[4] Faculty of Physics and Materials Science Center, Philipps-Universität Marburg, Renthof 7a, Marburg D-35032, Germany

Table of Contents

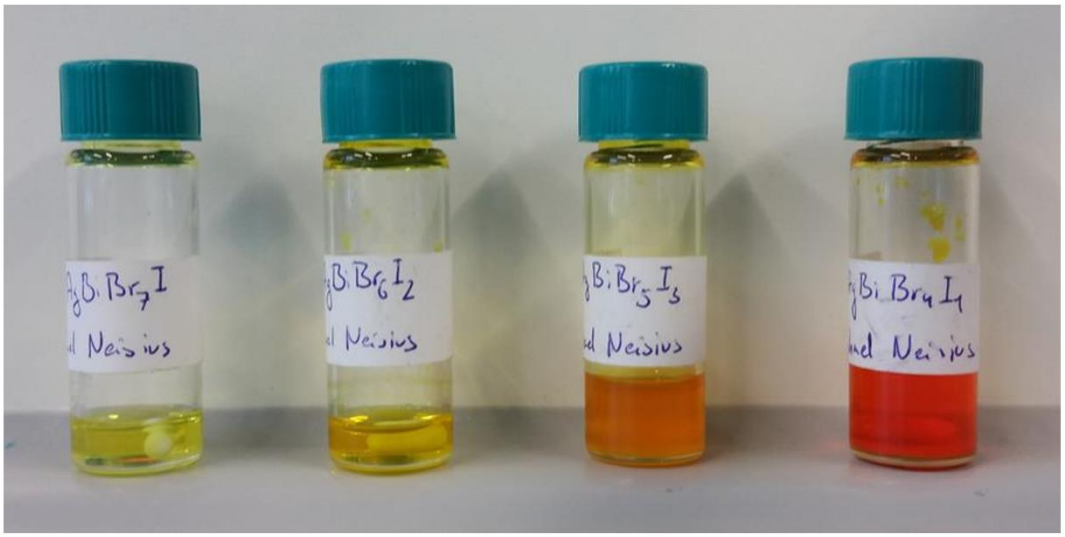

Figure S1. Pictures of the DMF solutions used for the preparation of the $(BA)_4AgBiBr_{8-x}I_x$ (with x = 1,2,3,4) thin films. From left to right: $(BA)_4AgBiBr_7I$, $(BA)_4AgBiBr_6I_2$, $(BA)_4AgBiBr_5I_3$ and $(BA)_4AgBiBr_4I_4$

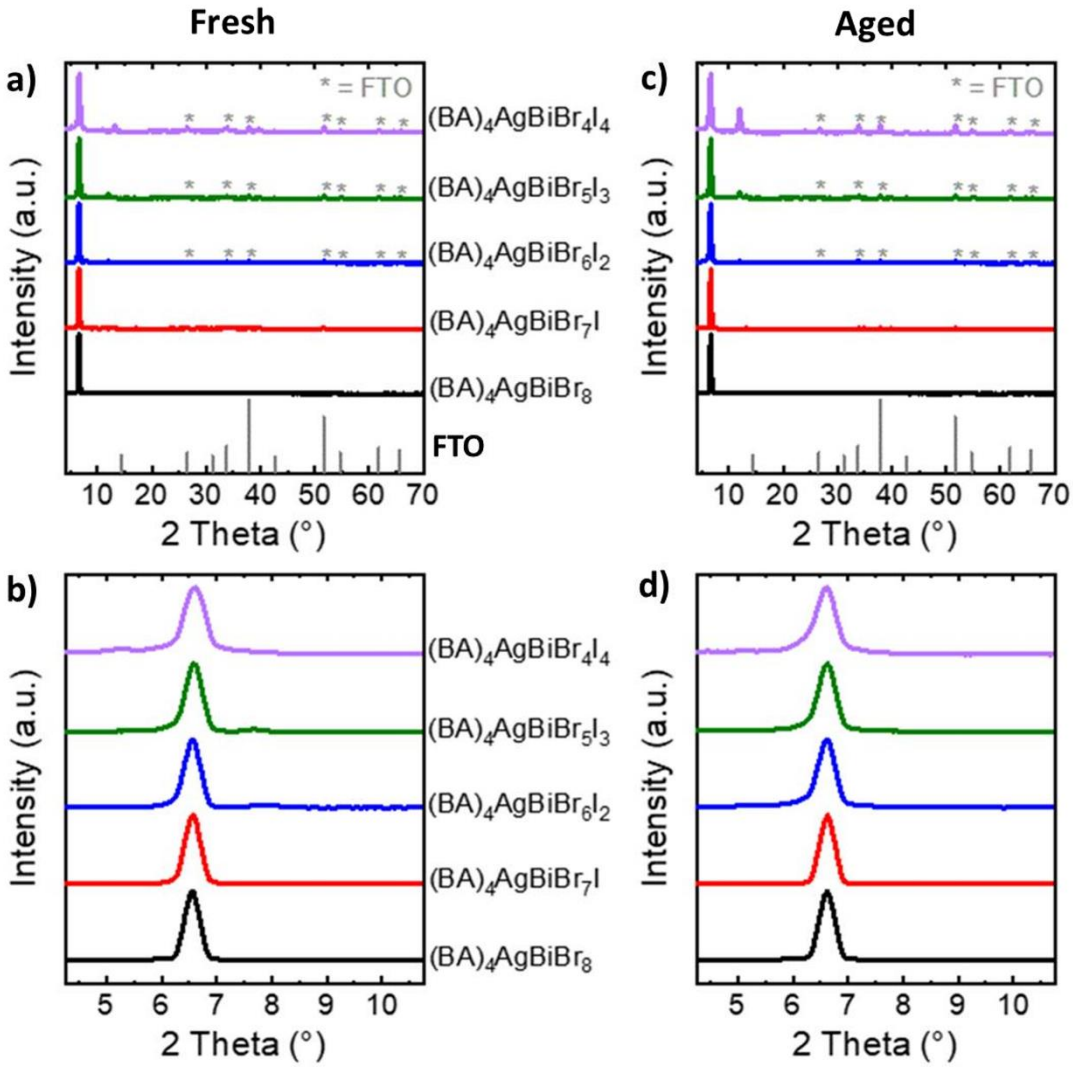

Figure S2. GIXRD patterns for the $(BA)_4AgBiBr_{8-x}I_x$ (with x = 1,2,3,4) thin films and for the reference thin film of $(BA)_4AgBiBr_8$ on FTO substrates: a) Freshly prepared samples and c) aged samples (9 days). Zoom on the (001)-reflex: b) Freshly prepared samples and d) aged samples (9 days).

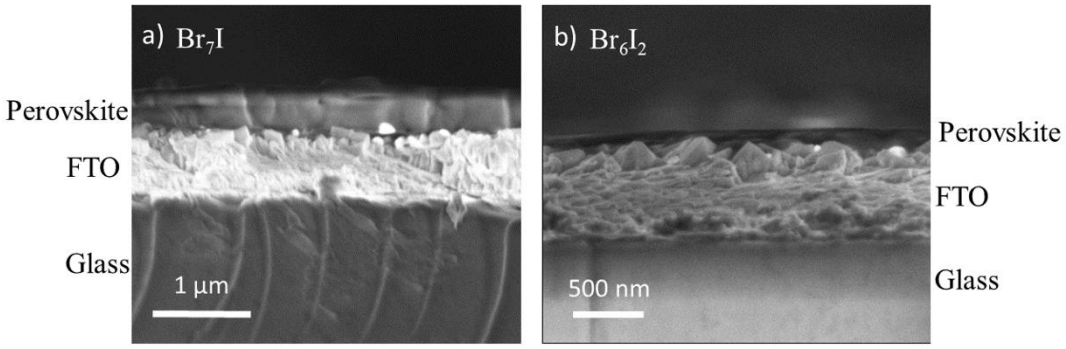

Figure S3. SEM cross-section images of a) $(BA)_4AgBiBr_7I$ and b) $(BA)_4AgBiBr_6I_2$ thin films prepared on FTO covered glass.

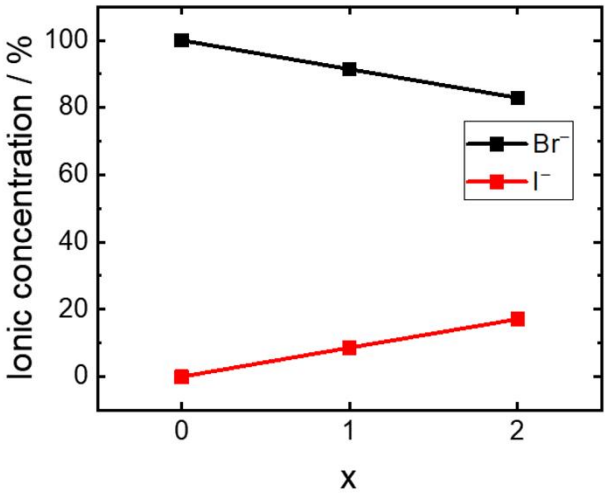

Figure S4. Relative bromide and iodide ratio of $(BA)_4AgBiBr_{8-x}I_x$ for x = 0,1,2 calculated through EDX measurements.

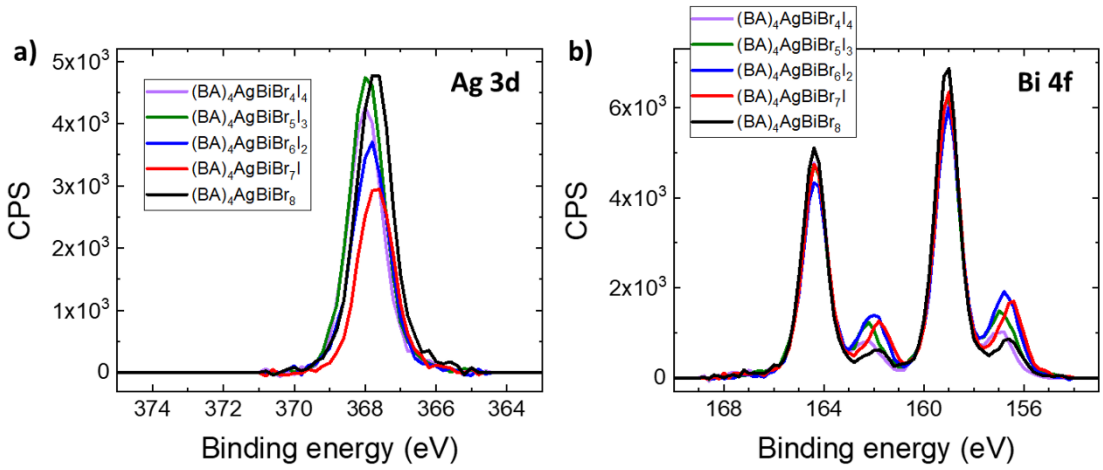

Figure S5. Details of the XPS spectra of the $(BA)_4AgBiBr_{8-x}I_x$ (x = 0,1,2,3,4) thin films: a) Ag 3d region and b) Bi 4f region.

Table S1. Summary of XPS data for $(BA)_4AgBiBr_{8-x}I_x$ (x = 0,1,2,3,4) thin films. Iodide and bromide atomic percentages are highlighted for each film, which were used to build the graph in Figure 2c

x	Peak Name	Peak Position (eV)	Peak Area	At%
0	I 3d5	615.6	-1.5	0
	Br 3d	68.2	280.1	80
	Ag 3d	367.8	141.9	8
	Bi 4f	159.0	377.8	12
1	I 3d5	618.8	86.8	5
	Br 3d	68.4	253.9	77
	Ag 3d	367.6	84.6	5
	Bi 4f	159.0	399.1	14
2	I 3d5	618.8	308.7	17
	Br 3d	68.4	212.5	64
	Ag 3d	367.8	105.3	6
	Bi 4f	159.0	397.2	14
3	I 3d5	619.0	530.0	29
	Br 3d	68.4	166.4	50
	Ag 3d	368.0	133.4	7
	Bi 4f	159.0	390.3	13
4	I 3d5	619.0	673.6	40
	Br 3d	68.4	121.6	39
	Ag 3d	368.0	118.3	7
	Bi 4f	159.0	363.2	14

Table S2. Calculated atomic ratios from EDX measurements of $(BA)_4AgBiBr_{8-x}I_x$ (x = 0,1,2) thin films. Iodide and bromide atomic percentages are highlighted for each film.

x	Species	At% (fresh samples)	At% (aged samples)
0	I	-	-
	Br	83	80
	Ag	9	11
	Bi	8	10
1	I	7	3
	Br	75	76
	Ag	8	10
	Bi	9	11
2	I	14	6
	Br	68	69
	Ag	9	11
	Bi	9	14

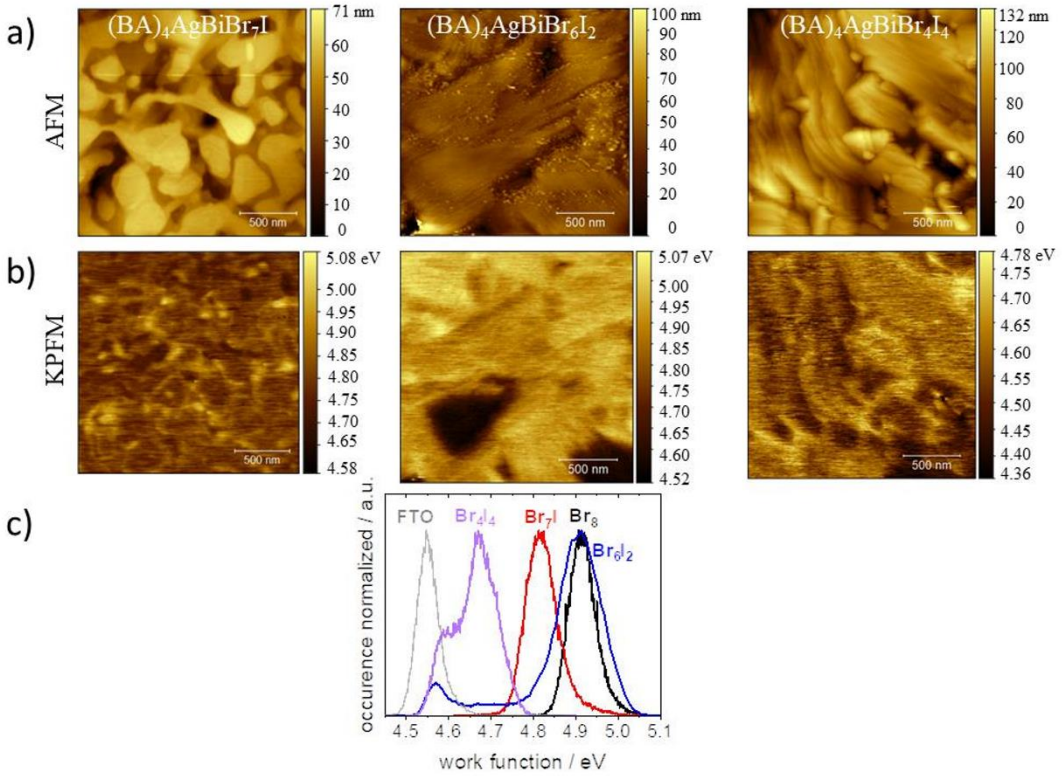

Figure S6. a) AFM images of $(BA)_xAgBiBr_{8-x}I_x$ (x = 1,2,4) and b) KPFM images of the respective areas. c) Distribution of respective Fermi energies. Distributions for bare FTO and for $(BA)_4AgBiBr_8$ reference film are also provided for the sake of comparison.

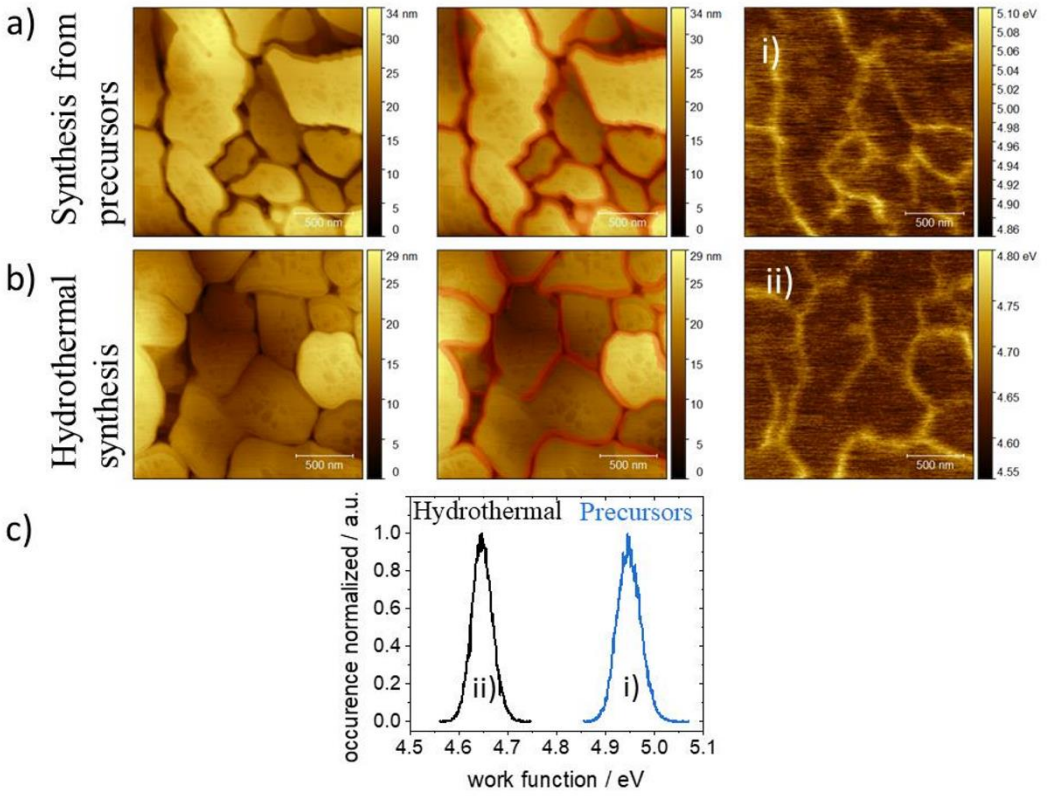

Figure S7. AFM image (left), masked grains to determine the Fermi energy (middle) and KPFM image (right) from thin films of a) $(BA)_4AgBiBr_8$ prepared from precursors dissolved in DMF as described in the experimental section and b) hydrothermally pre-synthesized $(BA)_4AgBiBr_8$ powder which was then dissolved in DMF to cast the thin film. c) Fermi energy distribution of a) (blue, i) and b) (black, ii).

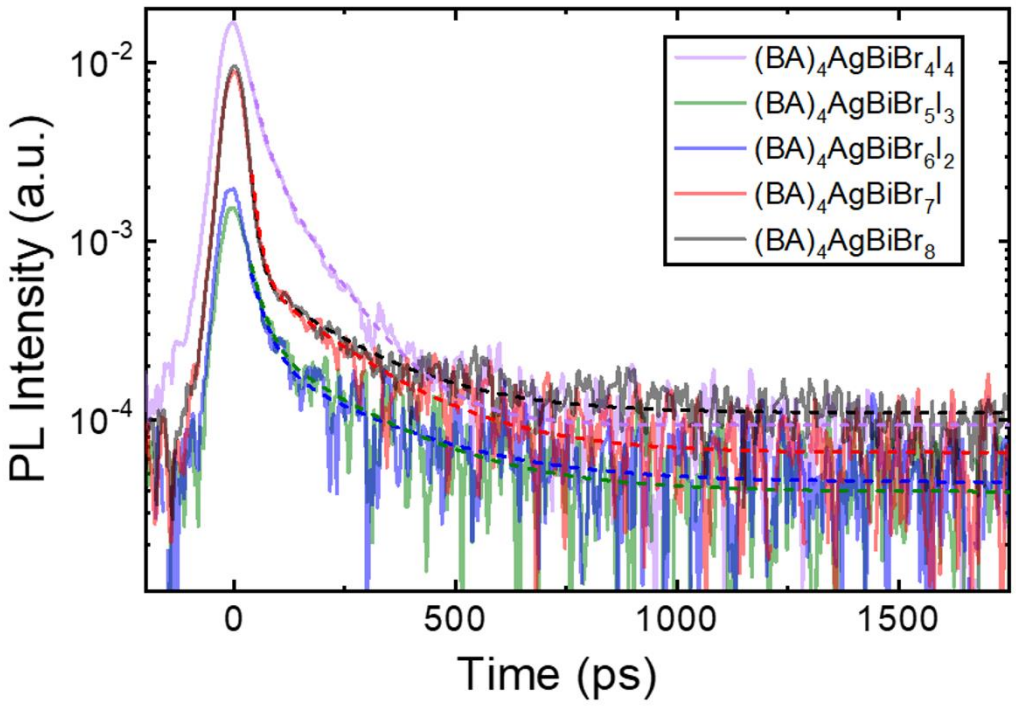

Figure S8. TR-PL decays for $(BA)_4AgBiBr_{8-x}I_x$ (x = 0,1,2,3,4) thin films measured at 77 K with associated fittings. The fitting of the TR-PL decays was carried out omitting the first 40 ps to exclude any influence of the instrument´s response function on the decay dynamics.

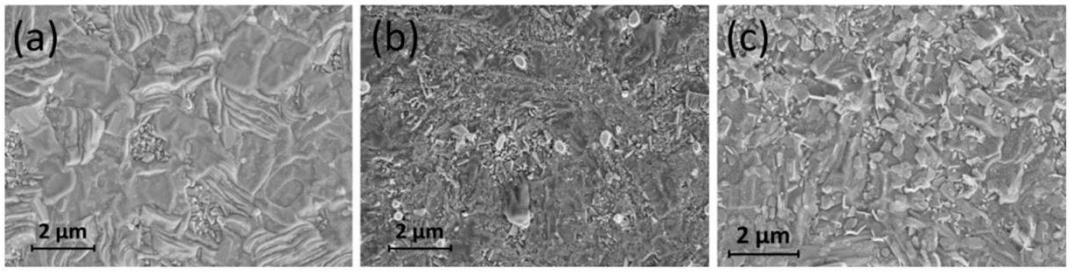

Figure S9. Top-view SEM images of a $(BA)_4AgBiBr_5I_3$ thin film undergoing progressive ageing: a) as-prepared, b) after 9 days and c) after 19 days air and light exposure.

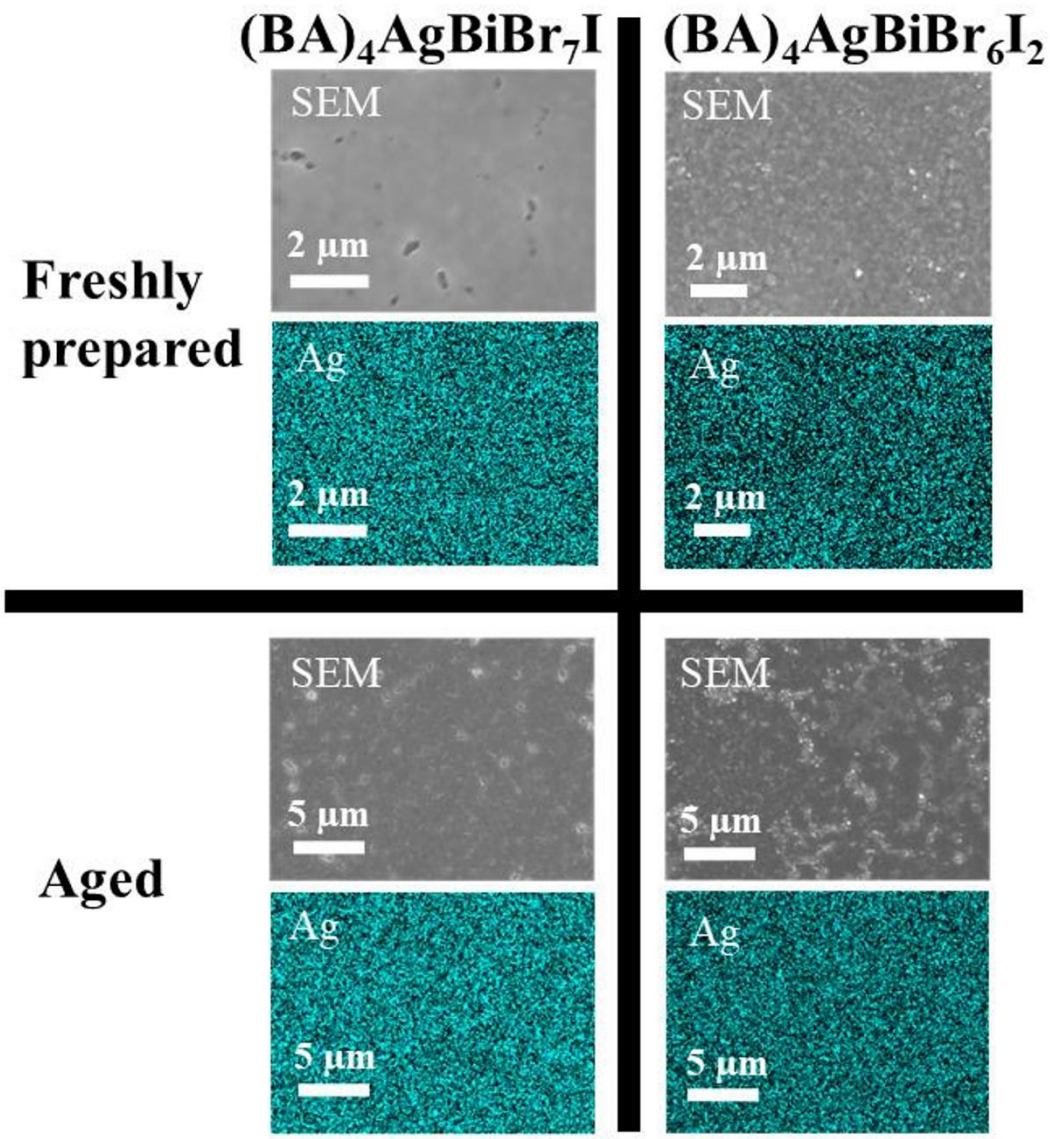

Figure S10. Elemental maps of silver content for $(BA)_4AgBiBr_7I$ (left) and $(BA)_4AgBiBr_6I_2$ (right) thin films that were freshly prepared (top) and aged (bottom) obtained by EDX. SEM images of the measured areas are also depicted on top of each map.

4.5 Publication 4

Co-Authorship with considerable contribution:

The Non-Innocent Role of Hole Transporting Materials in Perovskite Solar Cells

Authors: Francesco Lamberti, **Fabian Schmitz**, Wei Chen, Zhubing He, Teresa Gatti

The fabrication of benchmark perovskite solar cells relies not only on finely adjusting the perovskite composition and controlling the thin film crystallization but also on the choice of the optimum charge-selective transport materials. Regarding HTMs, spiro-OMeTAD is one of the most used materials, especially when in aiming for devices with PCEs of more than 25%.[66,237] However, the expensive spiro-OMeTAD – in more detail, its hygroscopic dopants which are necessary for optimum performance - is also reported to cause perovskite degradation, thus hampering the longevity of PSCs. Therefore, this work elaborates on promising alternative HTMs that show the potential to overcome the drawbacks of spiro-OMeTAD. These include strategies like the application of dopant-free HTMs, inorganic HTMs, and smart HTMs. Another option to save material and deposition costs is to entirely omit the HTM and fabricate HTM-free PSCs. The publication gives an overview of various pathways to create HTM-free PSCs, discusses differences in the electronic structure compared to the n-i-p architecture, and summarizes back electrode materials that are suited to be applied in HTM-free PSCs. HTM-free PSCs based on $Cs_2AgBiBr_6$ have been fabricated and analyzed in **publications 4** and **6**.

To this publication, I contributed the chapter “4 HTM-Free PSCs”.

REVIEW

Solar RRL

www.solar-rrl.com

The Non-Innocent Role of Hole-Transporting Materials in Perovskite Solar Cells

Francesco Lamberti, Fabian Schmitz, Wei Chen, Zhubing He,* and Teresa Gatti**

The race to the future generation of low-cost photovoltaic devices continuously takes on added momentum with the appearance of novel practical solutions for the fabrication of perovskite solar cells (PSCs), a paradigm technology for ultracheap light-to-electricity conversion. Much has been done in the past few years toward defining standard protocols for the assessment of their efficiency and stability, aiming at achieving a worldwide consensus on the issue, that will allow reliable reporting of new data. While this is undoubtedly a step ahead toward commercialization of these devices, it also often triggers researchers to test record architectures using benchmark configurations, mainly for what regards the ancillary layers that extract electrical charges from the photoexcited perovskite. In particular, the mostly used hole-transporting material (HTM) is the small-molecule spiro-OMeTAD, which is also well known to be the origin of PSC degradation after prolonged operation. Herein, it is aimed to remark the huge impact of the HTM on PSC performance, recalling major issues associated with the conventional spiro-based one and providing an overview of state-of-the-art alternatives. Finally, possible scenarios for the future development of smart HTMs are also envisioned, as charge-extracting layers, with a real active role in ensuring PSC operational stability.

1. Introduction

Spiro-OMeTAD (2,2′,7,7′-tetrakis[*N*,*N*-di(4-methoxyphenyl)amino]-9,9′-spirobifluorene, from now on simply Spiro) is the most used and applied hole-transporting material (HTM) in perovskite solar cells (PSCs). The reason is straightforward: after opportune formulation (i.e., addition of 4-*tert*-butylpyridine, tBP, and lithium bis(trifluoromethylsulfonyl)-imide, LiTFSI, as dopants/additives), the planar PSCs normally achieve the highest power conversion efficiencies (PCEs) at lab scale (up to 24%).[1] However, this result is strongly overestimated when compared with the long-term stability of the device: it has been already largely proved by several works that the necessary doping of the organic material augments the hygroscopic character of the layer, thus favoring moisture uptake from the atmosphere and subsequent perovskite film decomposition.[2,3] Combined with its notable cost (nowadays slightly decreasing due to the presence of more producers on the market),[4,5] we can assert that Spiro is only a model/benchmark HTM useful for lab-scale PSC production and testing. This is a pity indeed, because it possesses all the properties required for a good performing HTM: the high glass transition temperature due to the Spiro-type bond, the smooth film morphology that it forms, the relative simple processing, the electrochemical stability, the optical transparency in the visible window, the amorphous nature, the optimal band alignment with the perovskite valence band, and the chemical compatibility with dopants. Despite these very promising properties therefore, the high costs and very low inherent hole conductivity hugely reduce the possible commercialization of Spiro-based PSCs and force scientists to identify new avenues for obtaining long-term stability and for simplifying device processing methods.

F. Lamberti
Department of Chemical Sciences
University of Padova
via Marzolo 1, 35131 Padova, Italy
E-mail: francesco.lamberti@unipd.it

F. Lamberti
Interdepartmental Centre Giorgio Levi Cases for Energy Economics and Technology
University of Padova
via Marzolo 9, 35131 Padova, Italy

The ORCID identification number(s) for the author(s) of this article can be found under https://doi.org/10.1002/solr.202100514.

DOI: 10.1002/solr.202100514

F. Schmitz, T. Gatti
Center for Materials Research
Justus Liebig University Giessen
Heinrich Buff Ring 17, 35392 Giessen, Germany
E-mail: teresa.gatti@phys.chemie.uni-giessen.de

W. Chen, Z. He
Department of Materials Science and Engineering, Shenzhen Key Laboratory of Full Spectral Solar Electricity Generation (FSSEG)
Southern University of Science and Technology
Xueyuan Rd. 1088, 518055 Shenzhen, China
E-mail: hezb@sustech.edu.cn

ADVANCED SCIENCE NEWS
www.advancedsciencenews.com

Solar RRL
www.solar-rrl.com

After proper molecular structure engineering through the introduction of methoxy groups, allowing to reach the ideal melting temperature (≈121 °C),[6] the subsequent engineering of the Spiro-HTM formulation underwent two different routes: reducing the effect of the environment by replacing the additives (e.g., with cobalt-based complexes[7]) and optimizing the energy matching with the perovskite films.[8] Beyond these experimental strategies, other organic compounds were adopted as HTMs, such as poly(3,4-ethenedioxythiophene):poly(styrenesulfonate) (PEDOT:PSS), the most implemented HTM in inverted and flexible PSC architectures due to its very low processing temperature,[9] polytriarylamine (PTAA), going from 16.2%[10] up to 20.2%[11] PCE in few years, or (poly[(9,9-dioctyl-fluorenyl-2,7-diyl)-co- (4,4′-(*N*-(4-secbutylphenyl) diphenylamine)]) (TFB)[12] with the overall goal to diminish electrical hysteresis and improve the conductivity of the HTM without the use of any dopants. In addition, HTM–perovskite interface tuning through 2D/3D engineering also allowed to open up new perspectives for remarkable device stability improvement and elimination of dopants from the hole-extracting layer.[13]

At the same time, inorganic semiconductors, mainly oxides, were applied to both inverted and direct architectures: materials like NiO_x,[14] CuI,[15] CuO_x,[16] V_2O_x,[17] MoO_x,[18] MoS_2,[19] CuSCN[20] became competitors of Spiro-based HTMs. The use of inorganic semiconductors prevents the chemical degradation occurring in organic HTMs after light soaking and prolonged use. In particular, detrimental effects of nitrogen, oxygen, and moisture were proven to be effective when organic HTMs were used.[21,22] In a recent paper, some of us also showed that instability can be due to a direct action of the additives in a classical Spiroformulation: oxygen soaking coupled to the contemporary presence of tBP and LiTFSI, fundamental for achieving the highest conductivity in Spirolayers, ultimately causes a dedoping process with the formation of a pyridinium cation (see the next paragraph for more details).[23] However, inorganic HTMs do not guarantee to date the same conductivities and ease of processing of organic molecules: are we thus at a dead end? How can we exploit the benefits of organic HTMs without neglecting the long-term stability that is vital for commercialization within the design of next-generation HTMs? In this Review, we want to highlight the most recent efforts reported in the literature that display unique properties for HTMs able to provide both a functional and an active role in the device fortune, that is, emphasizing the "noninnocent" role of HTMs in PSCs. Leveraging on Spiro-based HTMs intrinsic limitations, we will review the most innovative alternatives, starting from dopant-free and fully inorganic HTMs, to then discuss even more promising possibilities, such as those deriving from HTMs-free carbon-based PSCs (C-PSCs) and "smart" HTMs that display intriguing properties able to actively cope with specific stability issues (**Figure 1**).

2. Dopant-Free HTMs for PSCs

As discussed previously, the need to use LiTFSI as the dopant to trigger the oxidation of Spiro-based HTM formulations[24] has been shown to be a key issue for device stability, due the hygroscopic quality of the finally obtained layer, causing an undesirable water uptake from the atmosphere that ultimately reaches the perovskite photon absorber, causing its degradation toward the high-bandgap metal halide precursors.[25] While much attention has been addressed to the role of this ionic additive in influencing PSC stability, less was known until few years ago about the possible influence of the second major additive in the Spiro-HTM formulation, namely, the small organic molecule *t*BP. This additive is generally assumed to provide considerable help in reaching the optimal HTM morphology on top of the perovskite layer, permitting good pinhole passivation. In contrast, it is used in large excess with respect to Spiro-molecules in the HTM blend (about three times more) and it has a very high boiling point (197 °C), excluding the possibility that it leaves the layer after casting through evaporation. In 2019, some of us fully demonstrated, following previous reports that hinted at the same conclusion but did not fully explain the mechanism behind,[3,26] that such additives have indeed the ability to cause progressive dedoping of Spiro-HTMs, thus altering the charge transport properties.[27] To investigate this ageing process, we used electron spin resonance (ESR) spectroscopy, a technique very sensitive to the presence of unpaired radicals in samples and of their surrounding environment. Being the doped Spiro-molecule, a radical cation, we could very nicely follow the decay of its ESR signal

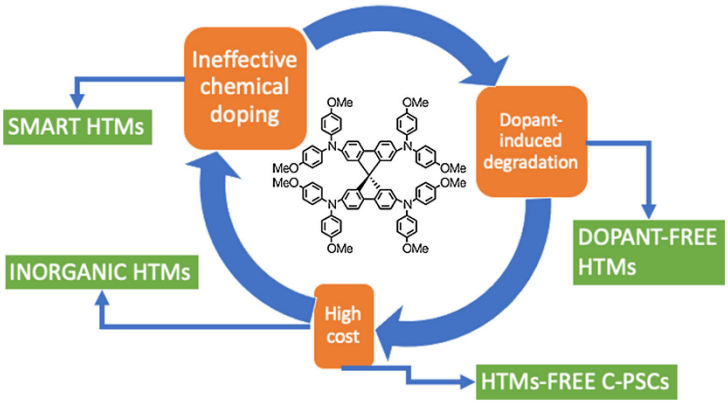

Figure 1. Main drawbacks associated with Spiro-OMeTAD HTMs for PSCs and possible solutions to circumvent them examined in this Review.

ADVANCED SCIENCE NEWS
www.advancedsciencenews.com

Solar RRL
www.solar-rrl.com

in different conditions (**Figure 2**a). With the help of Raman spectroscopy then, we were able to unequivocally identify the existence of pyridinium ions as the residual products existing in the Spiro:LiTFSI:*t*BP mixture after the ESR signal of the Spiro radical cation completely disappeared (Figure 2b). Based on these evidences, we proposed a dedoping mechanism for $Spiro^+$ molecules that pass through the formation of an unstable *t*BP radical cation, which then further reacts with another $Spiro^+$ species to produce a *t*-butylpyridinium adduct (Figure 2c).

It is evident from all the earlier discussed aspects that doping of small-molecule-based HTMs cannot most likely represent an adoptable solution in future commercialized PSCs. In this sense, many efforts from chemists and materials scientists have been addressed in the past few years at developing other small molecules that can extract and transport holes efficiently without requiring a doping step (dopant-free HTMs). Molecular engineering has provided a plethora of new structures exploiting different strategies to improve hole mobility such as donor–acceptor (D–A) alternation or extended π-conjugation. This specific topic has been anyway thoroughly addressed in other seminal reviews—we address the reader interested in understanding more of this particular aspect.[28,29] Here, we will just report some peculiar and very recent examples that might constitute the bases for next improvements in the field.

Some of us reported recently on new small-molecule structures characterized by an advanced and very accurate design, able to address multiple requirements and functions for an ideal dopant-free molecular HTM to be used in inverted PSC architectures.[30] In **Figure 3**a, such a design strategy is highlighted, showing that together with the unmissable hole transport properties, dipole moment tuning (which can induce self-doping and built-in potential to boost charge extraction—more on this topic is discussed in Section 5), appropriate π-stacking (to improve charge mobility), and ability to passivate perovskite surface defects are additional powerful features installed in the newly developed molecules (namely, MPA-BTI and MPA-BTTI). With similar compounds, p–i–n devices reached a remarkable maximum PCE of 21.17%, with negligible hysteresis and superior stability under prolonged illumination. A further step is the development of similar structures, brought to the synthesis of dendritic derivatives like the ones shown in Figure 3b.[31] Here, the central acceptor moiety is decorated with either diphenylamine, carbazole, or diphenylamine-/carbazole-mixed dendrons that act as the donor components. With these dendrimers, structures which are located in the middle between small molecules and polymers, excellent HTM film morphology was achieved, allowing good interfacial contacts with the overlaying perovskite layer and providing PCEs above 20%, with exceptionally ultrahigh fill factor (FF) values.

The most recent trends in small-molecule-based dopant-free HTMs have shown evergrowing attention in the direction of always more complex chemical engineering, with remarkable reports on species able to conduct multisite defect healing at the perovskite/HTM interface, allowing application in solar modules,[32] to adopt face-on orientation on the perovskite surfaces to provide high hole mobilities[33,34] or tune aggregation states and intermolecular interactions depending on peripheral substituents that influence PCE and device stability,[35,36] also in inverted PSCs.[37]

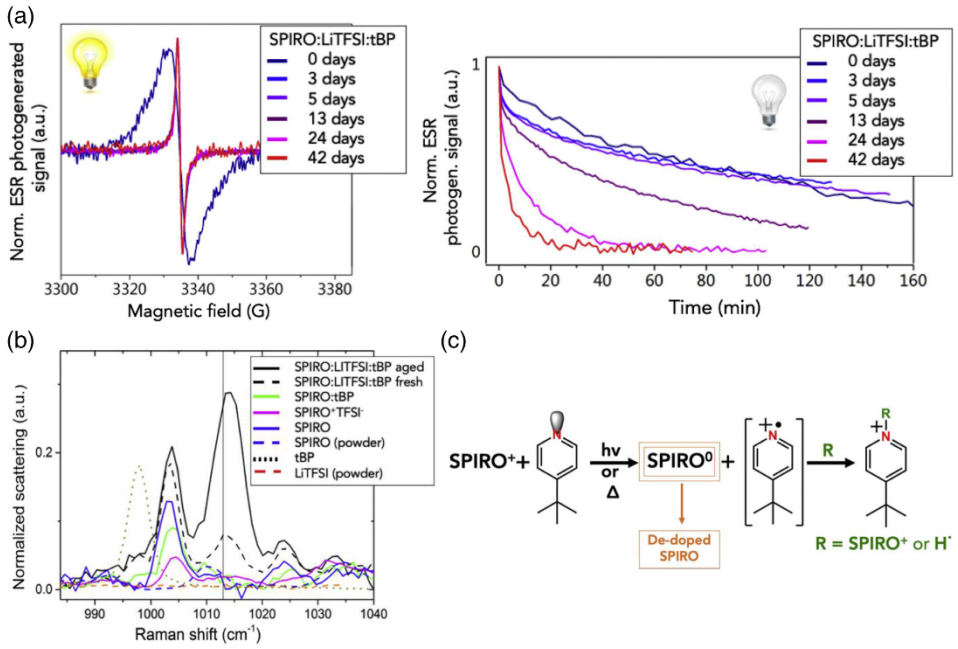

Figure 2. Spiro-OMeTAD dedoping process triggered by the *t*BP additive. a) ESR investigation of the dedoping process. b) Raman spectra of the aged samples showing the presence of an intense pyridinium ion signal. c) Proposed mechanism for dedoping. Reproduced with permission.[27] Copyright 2019, Elsevier Inc.

ADVANCED SCIENCE NEWS
www.advancedsciencenews.com

Solar RRL
www.solar-rrl.com

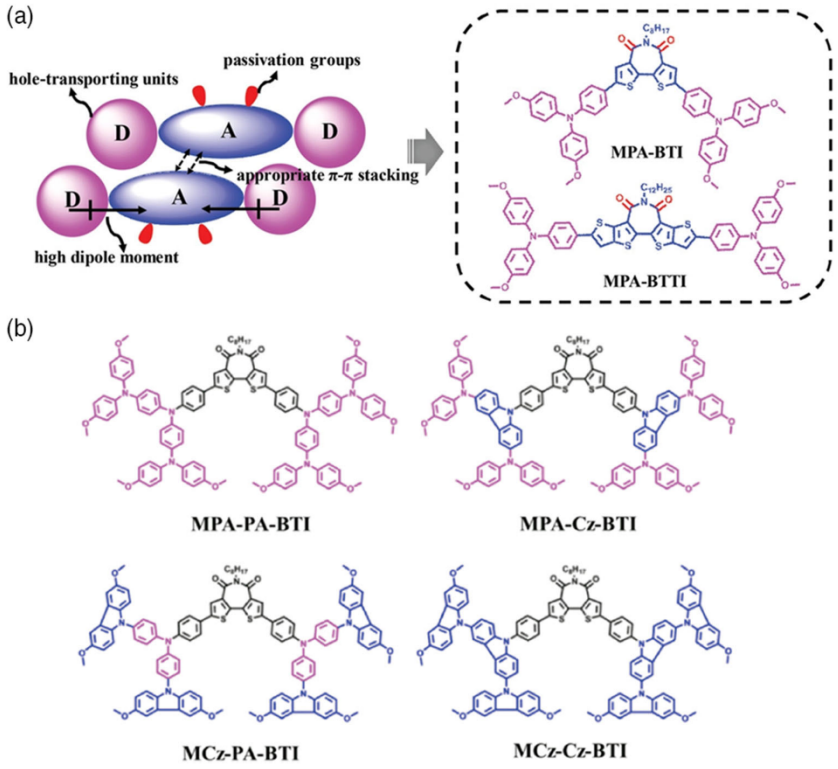

Figure 3. Emerging dopant-free small-molecule HTMs for inverted PSCs. a) Molecular design principle for D-A-D dopant-free molecular HTMs with reinforced π-stacking, high dipole moment, and perovskite passivation ability. Reproduced with permission.[30] Copyright 2019, Wiley-VCH. b) Structures of D-A-D dopant-free dendritic HTMs. Adapted with permission.[31] Copyright 2020, Science China Press and Springer-Verlag GmbH.

An alternative strategy to overcome the dopant-related bottleneck is to resort to composite materials as HTMs. This approach can rely on the choice of a suitable matrix, which is perhaps already a good organic HTM, in which fillers like nanomaterials or small molecules are inserted, that have a positive influence on the overall conductivity of the matrix and thus somehow act as dopants, even if they do not hold the previously discussed drawbacks of classical ones, like lithium salts. For example, nanocarbon species like carbon nanotubes (CNTs) or graphene-based materials (GBMs) can be selected for the role of conducting fillers, when their optimal dispersion within HTM matrix is attainable. In this way, HTMs which normally perform worse than Spiro in terms of overall PCE they allow to deliver, like poly(3-hexylthiophene) (P3HT), can be endowed with augmented transport properties. P3HT composites containing CNTs as HTMs in direct-architecture PSCs were first proposed by Wang and coworkers[38] and characterized by significantly reduced charge recombination at the interface with the perovskite layer compared with bare P3HT, which consequently provided higher PCEs due to improved open-circuit voltage (V_{OC}) and FF. In 2016 then, some of us reported on the use of highly homogeneous P3HT composite HTMs with organic functionalized CNTs and GBMs, where the optimized concentration of carbon nanostructures to ensure the best dispersibility in the polymer matrix was determined by applying a sedimentation-based separation (SBS) process before HTM deposition, thus eliminating all major aggregates that can act as sources of charge recombination within the thin layer.[39] With these HTMs, both efficiency and long-term stabilities of the resulting PSCs were improved compared with the use of pristine P3HT. As the organic functionalization in this blend approach seemed to have a significant role in defining the final quantity of well-dispersed nanocarbons within the polymer phase after application of the SBS process, we further investigated the effect of different functionalization moieties able to establish supramolecular interactions with the P3HT matrix and, more specifically, with either the lateral alkyl chains or the thiophene-based polymeric backbone (**Figure 4**a).[40] From this systematic screening of functionalized GBM derivatives, two composites resulted in having the higher stabilized concentrations of fillers in the polymer blend after SBS and those were namely the derivatives bearing aryl-bithiophene and aryl-hexyloxy moieties, which were consequently tested for the role of HTMs in n–i–p solar devices in comparison with pure P3HT and Spiro-based HTMs. As the performance of the two types of composites in PSCs resulted in being significantly different, with the derivative containing the bithiophene functionalities providing lower PCEs (even lower than bare P3HT) as a consequence of reduced short-circuit

ADVANCED SCIENCE NEWS
www.advancedsciencenews.com

Solar RRL
www.solar-rrl.com

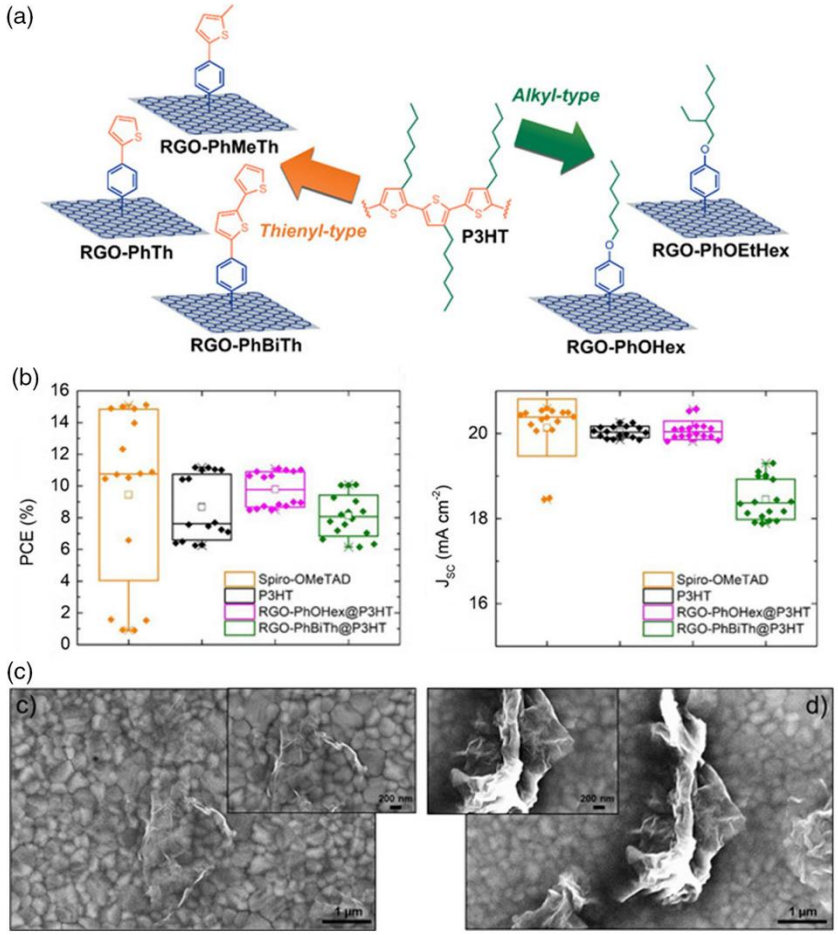

Figure 4. Use of organic-functionalized reduced graphene oxide (RGO) fillers in a P3HT matrix for the construction of composite HTMs. a) Different functionalities address supramolecular interactions with the semiconducting polymer matrix and allow to obtain high concentrations of the carbon nanostructure in a polymer blend without the concomitant formation of aggregates. b) PSC performance is strongly affected by the type of functionality covalently attached to RGO. c) Lower PCEs and J_{SC} in bithiophene-functionalized RGO/P3HT HTMs are due to self-aggregation of the RGO flakes (right SEM image) that generate short circuits within the charge-extracting layer, ultimately affecting charge recombination. In contrast, the presence of hexyl moieties on the nanocarbon favors flat disposition of the sheets in the polymer matrix, allowing improved hole extraction and transport across the HTM. Adapted with permission.[40] Copyright 2018, Wiley-VCH.

current densities (J_{SC}, Figure 4b), we investigated the morphology and electrical properties of the perovskite/HTM interface by means of scanning electron microscopy (SEM) and impedance spectroscopy. In this way, we were able to evidence increased charge recombination occurring in this down-performing HTM case, due to the self-crumpling of the GBM flakes within the polymer matrix (Figure 4c), generating local short circuits that funnel back to the perovskite and the extracted holes. In contrast, the presence of hexyl chains on the GBM filler seems to favor the smooth displacement of the nanocarbon sheets within the P3HT HTM, favoring charge extraction and transport.

The versatility of P3HT to host nanofillers of various natures, together with its relatively low price, high hydrophobicity, and ease of processability/film-forming ability, has stimulated several other attempts to design and prepare innovative polymer composite HTMs to improve PSC performance and stability. Xu and coworkers reported on three different types of P3HT composite HTMs tested in n–i–p device configuration.[41–43] In the first work, they prepared P3HT/phtalocyanine nanowire composites tuning the ratio between the two components to achieve a modulation of both HTM energy levels and hole mobility (**Figure 5**a).[41] With these composite HTMs, better efficiency was obtained in as-prepared PSCs compared with the use of pristine P3HT as HTM and, more strikingly, also remarkable long-term stability resulted for devices kept unencapsulated in high-humidity conditions (Figure 5a). In another work, the same group reported a similar blending approach between P3HT and a highly hydrophobic Lewis acid small molecule, namely,

ADVANCED SCIENCE NEWS
www.advancedsciencenews.com

Solar RRL
www.solar-rrl.com

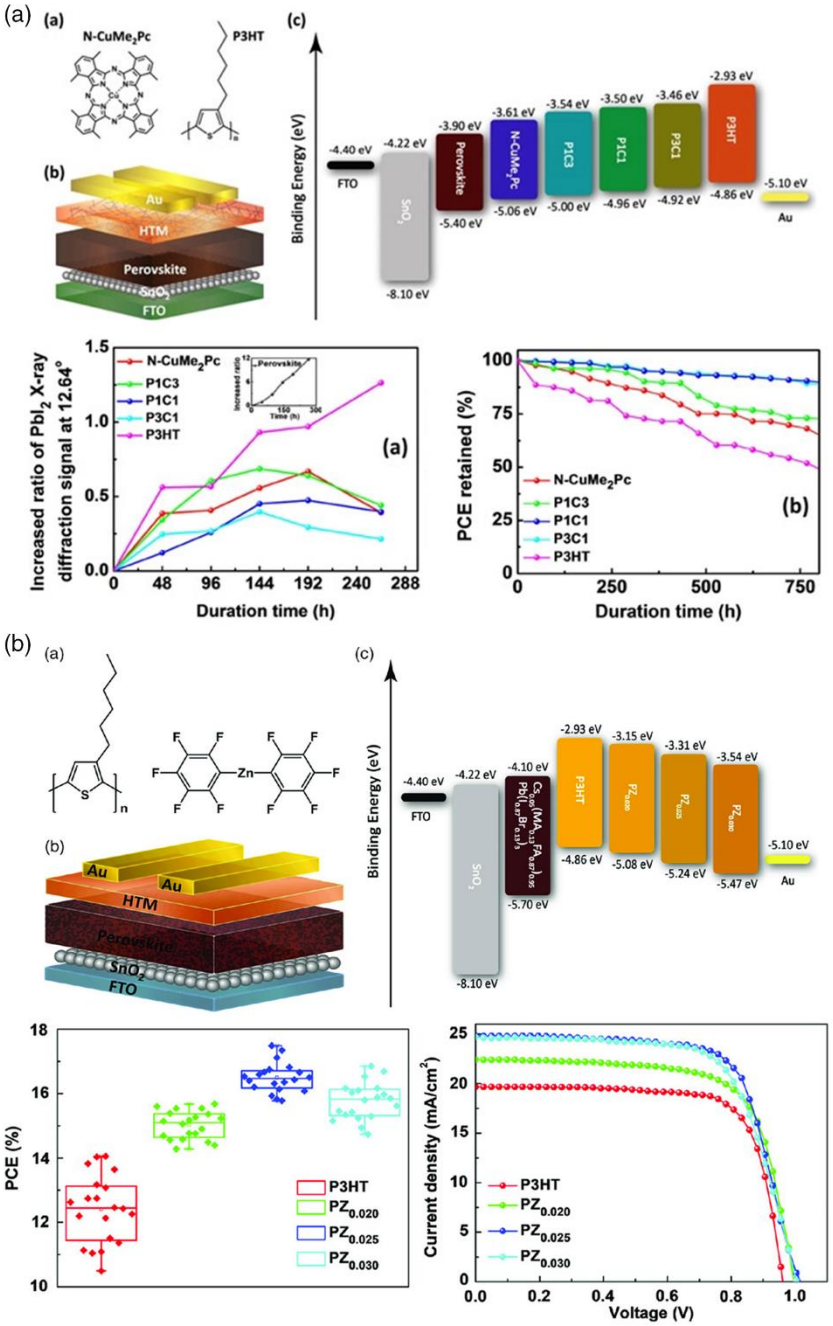

Figure 5. Examples of P3HT composite HTMs with different small molecules acting as highly hydrophobic dopants. a) P3HT composite HTMs with copper(II) phtalocyanine (*N*-CuMe$_2$Pc) nanowires at different polymer:nanowire ratios (P1C3, P1C1, P3C1) are used in direct-architecture PSCs, providing interesting environmental stability profiles compared with the use of the sole pristine polymer. Reproduced with permission.[41] Copyright 2018, Wiley-VCH. b) P3HT composite HTMs with a bis(pentafluorophenyl)zinc Lewis acid at different dopant concentrations providing improved performance in n–i–p devices compared with pristine P3HT. Reproduced with permission.[42] Copyright 2019, Wiley-VCH.

ADVANCED SCIENCE NEWS
www.advancedsciencenews.com

Solar RRL
www.solar-rrl.com

bis(pentafluorophenyl)zinc, to achieve doping of the polymer and consequently higher PCEs in PSCs as a consequence of improved hole mobility and hole extraction ability (Figure 5b).[42]

Finally, it should be mentioned that the mixing of p-type semiconducting polymers with phtalolocyanines into composite HTM structures has provided also other interesting results in terms of PSC performance enhancement. P3HT composites with either Zn or Cu phtalocyanines were used recently to, respectively, improve efficiency in carbon-based PSCs[44] (see discussion on these particular devices in Section 4) and deliver outstanding FF values and thermal stabilities in large-area nanostructured PSCs.[45] In a p–i–n configuration, poly(3,4-ethylenedioxythiophene):polystyrenesulfonate (PEDOT:PSS) composites with Cu phtalocyanines as HTMs delivered a maximum PCE above 17% with high FF, due to excellent hole extraction capability and improved perovskite crystallization on top of the composite layer.[46]

3. Inorganic HTMs for PSCs

A huge number of works discussing the integration of inorganic HTMs in PSCs are present in literature.[47–49] The reason for this wide interest in similar layers/materials is certainly related to the numerous inorganic compounds that can be applied for this role, their relative ease of processing through versatile technologies (spin coating, spray coating, thermal evaporation, electrospraying), the low cost associated with high-abundant raw materials, and the inherent hydrophobic nature of many of them, which prospects good device stability. In addition, further benefits can be derived by the interfacing of inorganic HTM layers with organic ones, enabling higher levels of control of the hole-extracting properties.[50] Particular mention should be given to bidimensional transition metal dichalcogenides (2D TMDs), whose use in HTMs has been thoroughly discussed in a recent review.[51] For this reason, in this brief overview, we will highlight only the last remarkable results concerning the use of inorganic HTMs, trying to give emphasis to the functional role of the HTM layer itself with respect to the overall device performance.

The mostly used materials are the ones belonging to the copper family: CuO_x, CuSCN, CuI. Historically, they were first extensively applied to dye-sensitized solar cells (DSSCs)[52] and then (as occurred many times in PSC history, directly derived from DSSC research) applied also to PSCs. Researchers active in the field are indeed very lucky: copper is a wonderful element because it is abundant on Earth and does not show any major safety issue for humans and the environment (for this reason it is considered as a noncritical raw material),[53] so, most likely, next-generation solar devices will be realized, exploiting copper-based compounds and other noncritical transition metals like iron or manganese.[54] Copper materials are economical and chemically stable, with proper energy levels for alignment with perovskite photoactive layers and optimal transmittance. In particular, copper oxides, CuO_x, different from the other species of the family, have a very narrow bandgap and thanks to its p-conductivity it has been extensively used for the so-called all-oxide solar cells,[54,55] in which it acts as the absorbing layer. However, hole conductivity is not so high, forcing researchers to adopt doping strategies when preparing such solar devices. In the perovskite field, however, these materials are generally used in the pristine form. The first example of Cu_2O as HTM in a PSC provided about 9% PCE[56]: cuprous oxide was deposited by magnetron sputtering, a methodology that allows fine tuning of the oxygen percentage in the prepared thin film but, conversely, does not allow to obtain the highest crystallinities required for high FFs. For these limitations, copper oxide-based PSCs have generally very low efficiencies (below 10%).[48] More suitable for perovskite photovoltaics (PV) is copper iodide, CuI, because it has good solubility in organic solvents (thus making it a perfect candidate for replacing Spiro or as a dopant replacing hygroscopic LiTFSI[57]), a good hole mobility (up to 20 $cm^2 V^{-1} s^{-1}$),[58] and a high bandgap (3.1 eV) acting as the blocking layer for interfacial charge recombination. However, also in this case, the obtainable PCE does not exceed 10% due to lower V_{OC} values than those provided using Spiro as reference, although FF is higher.[59] To the best of our knowledge, however, there is only one example in which an engineered CuI HTM allowed to reach almost 20% PCE[60]: in this work Ye et al., by exploiting molecular engineering, realized for the first time a p-type semiconductor including thiourea in the CuI structure, increasing the PCE from 14.6% to 19.9%. The authors explained this result by an ongoing perovskite trap passivation conducted by the thiourea additives.

The main character in the copper family is undoubtedly copper thiocyanate, CuSCN, that displays all the good properties of a suitable HTM for PSCs[61]: decent hole mobility due to the quasimolecular structure given by the pseudohalide SCN^-,[62] high bandgap (3.4–3.9 eV), p-type character (work function [WF] of 5.2 eV), hydrophobic nature and good solubility in organic solvents (mainly sulfides) and aqueous ammonia.[63] In this latter case, researchers demonstrate the possibility of integrating CuSCN in a water environment, paving the way to scalable manufacturing of PSCs using mild solvents and obtaining a remarkable PCE of 17.5%. In addition, CuSCN filmability is very straightforward due to its lamellae-like structure, bringing reduced surface roughness. CuSCN can well be combined with other 2D materials like graphene. Arora et al. achieved 20% PCE in a standard-architecture PSC in which the CuSCN layer was wet processed: by the addition of a thin layer of RGO between CuSCN and top-contact gold electrode, the performance of the device remained almost unchanged after 1000 h of continuous illumination at 60° (**Figure 6**a).[64] The high potential of this compound is demonstrated also by the emerging attempts of CuSCN engineering: in an early article,[65] Yang et al. optimized the interface between perovskite and CuSCN by the addition of an organic aromatic compound that facilitates hole extraction: in this way, the resulting device showed remarkable long-term stability (86% of initial PCE after 200 days). Similarly, Xu and coworkers reported a CuSCN/conjugated polymer multilayer HTM structure to achieve 21.7% certified PCE in a direct-architecture PSC and high light and moisture stability.[66]

Another promising example of copper-based HTM is copper phthalocyanine (CuPc), that recently was applied to standard-architecture PSCs using Au as top electrode[67]: in this remarkable work, the researchers found that by conducting a postannealing step at 85 °C, the recombination at the HTM/perovskite interface strongly diminishes due to Au doping of the CuPc layer that favors the dissolution of cracks in between grains, as shown in the SEM image (Figure 6b). The thermal

ADVANCED SCIENCE NEWS
www.advancedsciencenews.com

Solar RRL
www.solar-rrl.com

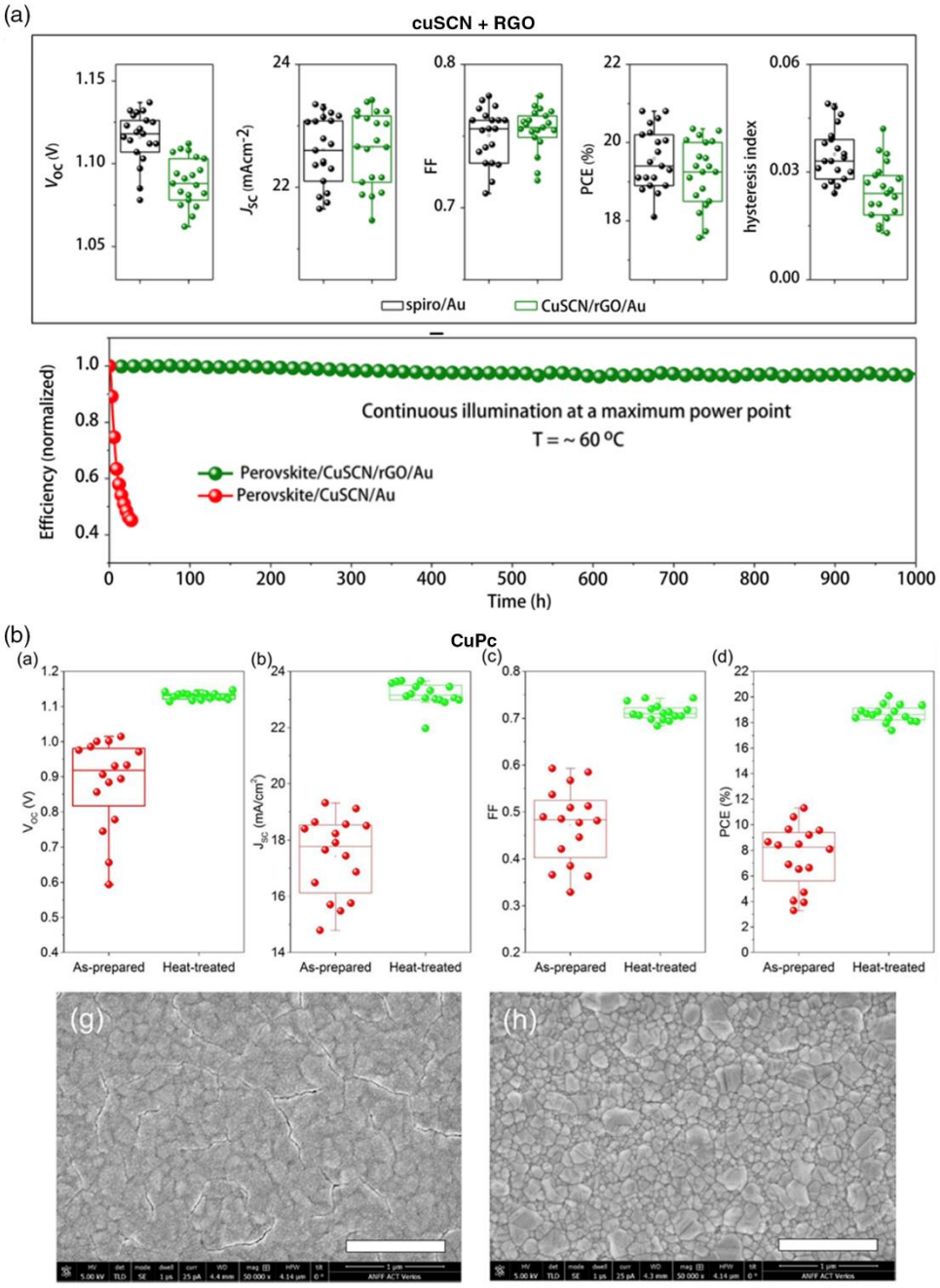

Figure 6. To-date, best-performance examples of PSCs containing copper-based HTMs. a) Long-term stability of a PSC containing a CuSCN/RGO HTM. Adapted with permission.[64] Copyright 2017, The Authors, some rights reserved; exclusive licensee American Association for the Advancement of Science. b) Effect of heat treatment on a CuPc HTM-based PSC. Adapted with permission.[67] Copyright 2018, American Chemical Society.

ADVANCED SCIENCE NEWS
www.advancedsciencenews.com

Solar RRL
www.solar-rrl.com

stability is thus hugely increased, showing almost unchanged performances after 2000 h at 85 °C.

Another example of very popular inorganic HTMs is nickel oxide, NiO. The compound is a notable candidate for replacing organic HTMs having intrinsic p-character with good hole mobility ($2.8\ cm^2\ V^{-1}\ s^{-1}$),[68] excellent transparency, optical bandgap (3.6–4 eV),[69] and valence band values in agreement with perovskite configuration, facilitating hole extraction and electron blocking.[70] It can be processed by exploiting different strategies, like sol–gel, electrodeposition, spray and spin coating, sputtering, pulsed laser deposition, and more. His fortune derives from the very-low hygroscopic and acidic nature and for this reason it is widely applied to inverted p–i–n devices. Although remarkable PCEs were reached (20%),[71–73] its use is not so extensive, and the main reason can be ascribed to the toxicity of nickel. Comprehensive detailed reviews are available in literature for further reading.[74,75]

Over the past several years, some of us have systematically investigated the optimization of NiO_x HTMs via both doping and surface passivation strategies, by which we have achieved over 22% efficiency for inverted PSCs with low-temperature-processed NiO_x-based HTMs.[76] It is well established that stoichiometric NiO is insulating, which results in increased recombination and reduced hole extraction. The conductivity of NiO_x can be increased by extrinsic dopants with shallower acceptor levels. In 2017, we demonstrated that Cs could be an effective dopant for significantly improving the conductivity and enhancement of device performances.[70] We have obtained a best efficiency over 19% based on $MAPbI_3$ perovskites. However, these Cs-doped NiO_x HTMs were prepared by a sol–gel solution method, which required high-temperature post-annealing (270 °C), limiting its application on flexible substrates and increasing the fabrication costs. To avoid high-temperature processing, we developed NiO_x nanoparticles ink recipe to prepare the NiO_x HTMs at low temperatures (<150 °C). We achieved over 18% PCE for the devices with NiO_x nanoplatelets (NPs) HTMs and $MAPbI_3$ perovskites.[77,78] To further improve performance, Cu-doped NiO_x NPs were prepared, thus increasing HTM conductivity and tailoring hole concentration and WF. The possible mechanism of Cu doping was comprehensively investigated, and the best efficiency for small-area, large-area, and flexible devices was over 20%, 18%, and 17%, respectively.[79] At a later stage, another molecular doping strategy for NiO_x with F6TCNNQ was developed, allowing to achieve over 20.8% efficiency for NiO_x-based inverted PSCs, which was the highest reported efficiency in that period.[80] More recently, we attempted the use of alkali chlorides as interfacial modifiers at the NiO_x/perovskite interfaces.[81] The role of the alkali chlorides in passivating the perovskite defects was explored experimentally and theoretically. After alkali chloride modification, the V_{OC} and PCE of the resulting inverted PSCs were significantly improved, with best PCE close to 21%.

For concluding this section on inorganic HTMs, we highlight the last works exploiting 2D TMD HTMs[51,82] exceeding the 20% PCE threshold. 2D WS_2 was applied in p–i–n devices by Liu et al.,[83] exploiting its ultrahigh hole mobility and its capability of driving high-quality epitaxial growth of the perovskite thin film, thus achieving about 21% PCE. At the same time, 2D MoS_2 flakes were adopted also in an inverted PSC in which, as in the previous example, the chalcogenides guided the anisotropic growth of the perovskite, allowing the device to reach 20.55% PCE with no hysteresis.[84] The last example that is noteworthy to highlight concerns the use of a not common HTM like MnS: like copper, manganese represents one of the noncritical metals that makes sense to try to exploit and engineer. In a recent work,[85] Chen et al. showed the possibility of retaining 90% of the initial PCE (≈20%) in a very humid environment (80% relative humidity: RH) for 1000 h, using the suboptimal perovskite methylammonium lead iodide and MnS HTM.

4. HTM-Free PSCs

A drastic, yet simple solution to overcome the drawbacks as well as the high costs of an HTM is to spare it entirely and deposit the back electrode directly on top of the perovskite layer. However, when using metallic electrodes, this method reveals new problems for the PSC performance. For example in case of the often used silver electrodes,[86–89] those limits are a large energy mismatch between the perovskite's valence band maximum (VBM) and the electrode's WF,[90] as well as the formation of silver halides at the perovskite/electrode interface, leading to a degradation of the perovskite layer itself.[91–94] Gold, another commonly used electrode material, has been observed to also negatively affect PSC performances due to ion migration of gold particles into the perovskite layer,[95] as well as the formation of gold halide complexes.[96] Furthermore, both HTMs and metal electrodes take up a large part of PSC material costs. **Figure 7** shows that eliminating the HTM and substituting a gold electrode by an abundant, easily processable material can drastically reduce the material cost of PSCs.[97]

Carbon-based materials can work as metal electrode/HTM substitutes, as they show WFs comparable with that of gold (5.1 eV),[90] are chemically inert toward the perovskite layer, and, due to the typical thickness of carbon electrodes (CEs) of several micrometers, they protect the perovskite layer from humidity, increasing the environmental stability of PSCs.[98–101] Still, there are several factors that suppress PSC efficiencies when CEs are applied that have to be targeted to boost the performance of carbon-based PSCs (C-PSCs). Those are the

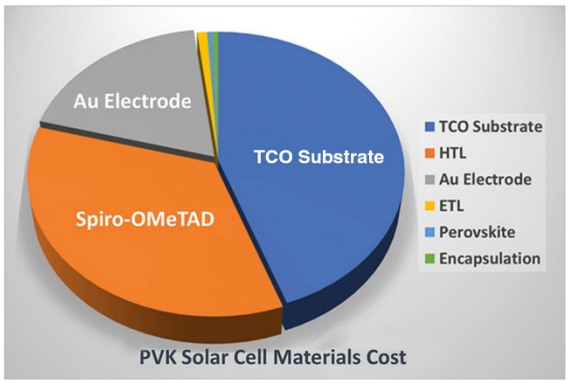

Figure 7. Relative material costs of separate PSC components. Adapted with permission.[97] Copyright 2020, Wiley-VCH.

ADVANCED SCIENCE NEWS
www.advancedsciencenews.com

Solar RRL
www.solar-rrl.com

deposition-caused inhomogeneous contact of the CE with the perovskite layer, that reduces the interfacial charge transfer,[100,102,103] as well as the anisotropic conductivity of graphene/graphite layers, characterized by low resistance along the 2D plane of individual graphene sheets but high resistance in the perpendicular direction.[102–105] CEs also lack the reflectivity of metal electrodes, which means that the thickness of a perovskite layer in a C-PSC has to be increased for it to absorb the same amount of photons as it would do when a metal electrode is applied.[98,106] Approaches to improve the perovskite/CE energy-level mismatch either aim at the heterogeneous incorporation of hole-extracting materials with a VBM lower than the CEs' WF[99,107] or at the modification of the perovskite's VBM at the perovskite/CE interface.[98,108]

The latter approach was adopted by Zhong and coworkers, post-treating a $CsPbI_2Br$ perovskite film surface with hexyltrimethylammonium bromide (HTAB), which decreased the energy offset between the perovskite and the CE from 0.70 eV in the pristine perovskite to 0.32 eV in the HTAB-treated one, as shown in **Figure 8**a.[98] This lowered energy mismatch increased the V_{OC} from 1.13 V for the pristine perovskite to 1.20 V for the HTAB-treated perovskite in C-PSCs. The HTAB-treated film additionally shows suppressed defect-induced charge carrier recombination and increased hydrophobicity, leading to devices that maintained 90% of their initial PCE over 330 h at 40–60% humidity and temperature of 85 °C. The HTAB-treated PSCs showed an average PCE of 13.9%. Chen et al. conducted a perovskite post-treatment on $MAPbI_3$ and $FAPbI_3$ (where MA is methylammonium and FA is formamidinium) using another long alkyl chain ammonium halide, namely, pentafluorophenylethylammonium iodide (F5PEAI), to create a passivating 2D perovskite phase at the perovskite/CE interface.[101] As shown in Figure 8b, they were able to increase the V_{OC} of their post-treated PSCs from 0.92 and 0.96 V for the nontreated PSCs to 0.98 V and 1.02 V for $MAPbI_3$ (PCE: 16.24%) and $FAPbI_3$ (PCE: 17.47%), respectively.

A similar approach was further adopted by Wu et al. to passivate a $MAPbI_3$ perovskite layer with phenethyl ammonium iodide (PEAI) that increased the films' hydrophobicity, smoothened the perovskite surface, increased the interface area, and lowered the defect concentration.[99] In combination with a copper phtalocyanine(CuPc)-modified CE, they were able to build PSCs with a maximum PCE of 13.41% that maintained 93% of their initial efficiency for 300 h (30% humidity, 70 °C). CuPc was integrated into the CE to lower the energy offset between the perovskite's VBM and the electrode's WF, while at the same time blocking the electron transfer from perovskite to electrode due the high-energy CBM of CuPc. In this direction, Liu and coworkers resorted to a CuPc modifier to increase the hole extraction from the perovskite to a CE but deposited it as a separate layer on top of $CsPbI_2Br$ perovskite film to build C-PSCs with a maximum PCE of 11.04%.[109] Gong et al. increased the VBM of $CsPbBr_3$ not by surface post-treatment but by adding small amounts of tetra-bisphenol A (TBBPA) in the bulk of the perovskite layer to enhance the hole extraction capability into the CE.[108] In addition, the TBBPA-treated perovskite was characterized by larger grain sizes and fewer trap states than the unmodified one, resulting in PSCs achieving a maximum efficiency of 9.82%.

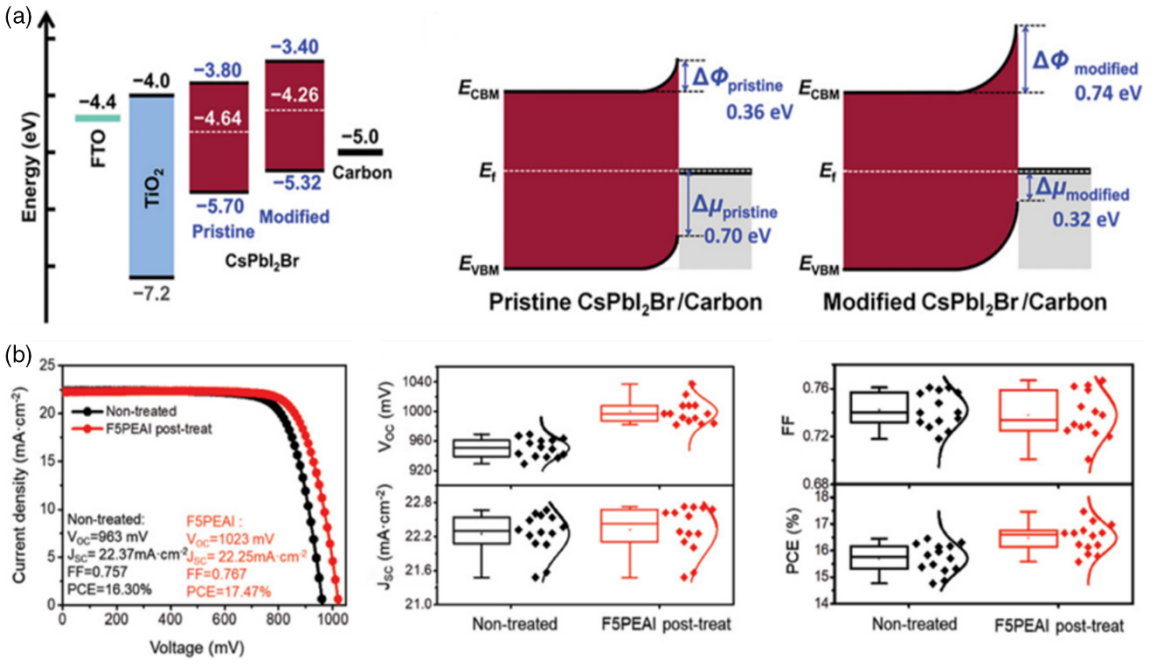

Figure 8. a) Energy diagram of a C-PSC incorporating a pristine $CsPbI_2$ photoactive layer in comparison with a HTAB-post-treated $CsPbI_2$ one. Adapted with permission.[98] Copyright 2021, Wiley-VCH. b) C-PSCs performances comparing pristine $FAPbI_3$ (black) and F5PEAI-post-treated $FAPbI_3$ (red) perovskite layers. Reproduced with permission.[101] Copyright 2021, Wiley-VCH.

ADVANCED SCIENCE NEWS
www.advancedsciencenews.com

Solar RRL
www.solar-rrl.com

The major goal of the previously discussed perovskite and CE modifications is to lower the energy mismatch at the perovskite/CE interface. In addition, these modifications are accompanied by enhanced optoelectronic properties, for example, reduced charge carrier recombination, which result in increased C-PSC performances. In contrast to those examples, Lin et al. suggested a new C-PSC device design that is based on the idea of a perovskite layer that is not entirely p or n doped due to PbI_2 or MAI excess, respectively, but consists of two separate parts, one of which is n doped while the other one is p doped.[106] A similar active-layer architecture creates a built-in field that encourages the charge separation and suppresses recombination. From their simulations, they concluded that an optimal $MAPbI_3$ perovskite layer would consist of a 400 nm-thick n-doped and a 700 nm-thick p-doped layer with doping concentrations of 10^{15} and 10^{19} cm^{-3}, respectively. An optimized C-PSC from such a perovskite layer could reach a theoretical PCE of 25.07%.

While the modified perovskite layers in C-PSCs are used to achieve a more efficient hole extraction that positively affects device PCEs, the efficiency-suppressing factors related to the suboptimal conductivity of CEs as well as their typically improvable small contact area with the perovskite photoactive layer are other issues that have to be seriously tackled. Chu et al. tried to face these bottlenecks by depositing a CE consisting of carbon black nanoparticles and carbon fibers (CFs) onto a $MAPbI_3$ perovskite layer to build a device that achieved a maximum PCE of 14.1% due to good conductivity and high perovskite/CE contact area.[100] In addition, they conducted a Mott–Schottky analysis and determined that nanosized noncontact areas do not hinder the hole extraction from the perovskite into the CE as they are overcome by a driving force of the built-in field originating from the band offset at the perovskite/electrode interface. In contrast, macrosized noncontact areas significantly suppress the hole extraction. The group of Huang improved the contact area using a mixture of CNTs and CFs as the CE to incorporate additional highly conductive pathways within this last one.[102] C-PSCs containing this electrode material and $MAPbI_3$ as the photoactive layer showed a maximum PCE of 11.80%, outperforming C-PSCs prepared with electrodes consisting of pure CNTs or CFs.

CEs can be prepared either through high-temperature or through low-temperature fabrication procedures (for a detailed review on the topic, we address the reader to very recent and complete reviews[110,111]). For the former fabrication approach, all layers of the solar cells except the perovskite ones are prepared in separate high-temperature steps and finally the temperature-sensitive photoactive perovskite is incorporated into a mesoporous buffer layer which separates the CE from the electron-transporting layer (see **Figure 9**).[112]

In contrast, low-temperature fabrication of the carbon back electrode allows to adopt a layer-by-layer method in which the CE can be deposited through different low-temperature procedures. In contrast to metal electrode deposition, which is an energy-demanding vacuum-assisted fabrication, those CE deposition methods are not only scalable for high-throughput industrial fabrication but, due to the low-temperature processability, they also require less energy to be processed and thereby are less cost intensive. In addition, the high abundancy of carbon (CEs have been derived from a variety of plants and biomasses [113–115]) lowers the production cost even further. Wu et al. demonstrated a procedure to not only deposit a dense carbon back electrode via electrospray printing but also to fabricate an entire solar cell using this method, as shown in **Figure 10**.[97] In comparison with doctor-bladed CEs, these electrosprayed CEs, consisting of a mixture of carbon black nanoparticles and graphite, showed a lower sheet resistance due to denser films and lower average carrier lifetimes, indicating faster hole extraction originating from an increased interfacial charge transfer. PSCs containing the electrosprayed electrodes showed a PCE of 14.41%, which was significantly higher than that of PSCs with doctor-bladed ones (11.14%). Furthermore, the possibility to fabricate entire C-PSCs through solution-based low-temperature processes opens up interesting perspectives for the manufacturing of flexible PSCs.[107,116,117] A preliminary example in this direction was reported recently by Que and coworkers, who built

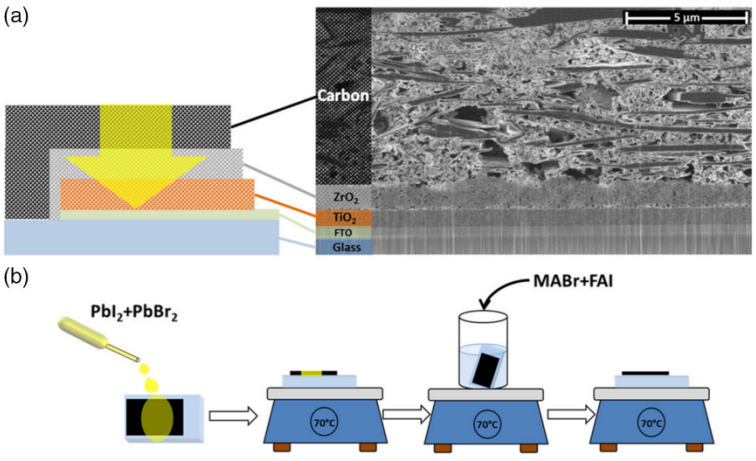

Figure 9. a) Sketch and SEM cross section of a high-temperature-fabricated C-PSC. The perovskite is incorporated through the porous layers as the last fabrication step, depicted by the yellow arrow in (a). b) Two-step perovskite deposition in which the porous layers of the cell are first soaked with PbI_2 and $PbBr_2$ solution and later the cell is dipped into a solution of MABr and FAI. Reproduced with permission.[112] Copyright 2021, Wiley-VCH.

ADVANCED SCIENCE NEWS
www.advancedsciencenews.com

Solar RRL
www.solar-rrl.com

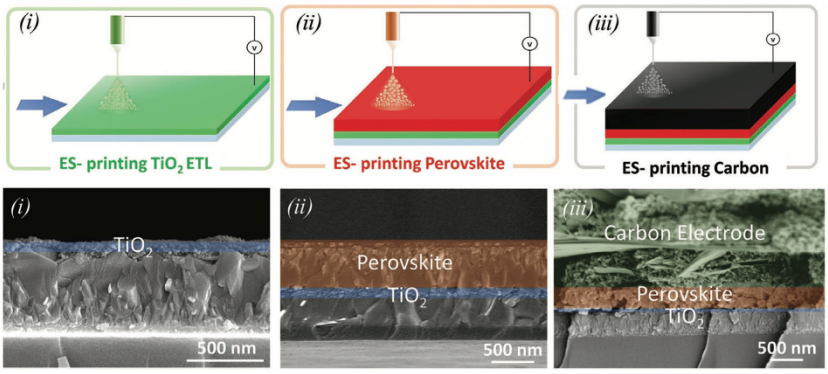

Figure 10. Layer-by-layer electrospray fabrication of entire C-PSCs. Reproduced with permission.[97] Copyright 2020, Wiley-VCH.

flexible $MAPbI_3$-based C-PSCs with doctor-bladed CEs on flexible polyethylene naphthalate/ITO substrates that showed a maximum PCE of 11.53% and retained 69% of their initial efficiency after 2000 bending cycles (2 mm bending radius).[118]

To construct well-performing large active area solar cells, Chen et al. chose a modular PSC architecture glass/FTO/SnO_2/$Cs_{0.05}(FA_{0.85}MA_{0.15})_{0.95}Pb(I_{0.85}Br_{0.15})_3$/CE as well as a glass/FTO/CE charge collector which they pressed onto the PSC by contacting both CEs.[105] This modular architecture enhanced the lateral conductivity of the back electrode and enabled the fabrication of 1 cm^2 active-area PSC with a maximum PCE of 11.2%. The authors also compared the performance of three CE materials like graphene, carbon nanocoils, and multiwalled CNTs (MWCNTs) and found that MWCNTs outperformed the other materials in terms of hole extraction ability, perovskite/CE band alignment, electrical conductivity, and thermal stability.

A different approach to deposit the CE is to prefabricate it and to then transfer it onto the PSC. For this procedure the contact of the perovskite/CE interface is increased by applying pressure on the cell. Such a preparation method was demonstrated by the group of Lee, who constructed a separate hybrid graphene/dry-spun CNT CE and then deposited it on the solar cell using a laminator.[104] Their $MAPbI_3$-based PSCs that incorporated also a Spiro-OMeTAD HTM showed a maximum PCE of 15.36% and maintained 86% of the initial PCE after 500 h (25 °C, 50% humidity) due to the presence of the highly hydrophobic CE. Teixeira et al. used separately fabricated transferable CEs to demonstrate a direct comparison of different electrodes on PSCs.[119] This was achieved by first fabricating and measuring PSCs with gold electrodes. Those electrodes were removed again, CEs were transferred onto that same PSCs, and finally the PSCs were measured with exchanged electrodes (the PSC incorporated the HTM Spiro-OMeTAD). The PSCs with CEs showed a maximum of 89% of the PCE that was obtained originally with the gold electrode.

It is important to mention that CEs are not only applied in high-performing lead-based PSCs but also in their lead-free counterparts in which the highly toxic Pb is substituted with less toxic metals. In general, lead-free PSCs achieve efficiencies that cannot be compared with those of the lead-based counterparts, and this results in relatively low PCEs also when CEs are introduced. Panneerselvam and Angaiah built lead-free C-PSCs based on $MASnI_3$ on which they deposited CEs that incorporated either Cu_2AgInS_4 (CAIS) or $Cu_2AgInSe_4$ (CAISe) nanoparticles to increase the CEs' hole extraction capability.[120] C-PSCs with the CAIS-modified CE achieved a PCE of 4.24% in comparison with 2.69% of C-PSCs that incorporated an unmodified CE. Another example of lead-free perovskite materials is the highly stable all-inorganic double-perovskite $Cs_2AgBiBr_6$ that was used as the photoactive layer by the group of Tang to prepare highly sustainable C-PSCs.[121] These solar cells showed a maximum PCE of 2.57% for Li^+-doped $Cs_2AgBiBr_6$, which is not far from the maximum efficiencies of around 3% obtained from analogous PSCs based on this material using metal electrodes.[122]

It is important to remind that there are also ways to fabricate HTM-free PSCs other than applying CEs. Song et al. showed such an example by replacing a CE with a screen-printed electrode consisting of indium tin oxide (ITO) nanoparticles.[123] Due to the increased light reflectance of ITO as well as its lower WF, which enhances hole extraction, tin-based PSCs' PCE can be increased from 5.4% when the ITO nanoparticle electrode is used in comparison with 3.0% with a CE.

5. Smart HTMs for PSCs

Up to now we have discussed the most recent opportunities offered by newly developed HTMs that can substitute Spiro-OMeTAD for the role of hole transporters without featuring the same instability problems related to the presence of the added dopants. As it is anyway also well recognized, to ensure PSC stability, it is necessary to delay or suppress any other decomposition pathway triggered by environmental factors such as, primarily, atmospheric humidity but also heat and excess irradiation. To cope with these second major issues, the incorporation of a protective function within the HTM, particularly for direct-architecture devices, can be considered a smart approach to overcome device instability. In addition, for both direct n–i–p and inverted p–i–n configurations, other aspects may become relevant, such as the effect of light on organic HTMs, thus calling for optically engineered species to improve overall performances, or solvent orthogonality issues, requiring the deposition of stable

ADVANCED SCIENCE NEWS
www.advancedsciencenews.com

Solar RRL
www.solar-rrl.com

redissolution layers. In this paragraph, we will extend the discussion to these aspects in relation to the design of novel "smart" HTMs and, for logistic reasons, we will start with examining the latter cases of optically engineered and solubility engineered HTM in PSCs.

The idea that photoexcited or electrically induced configurations of molecular or polymeric constituents of an organic HTM can have a huge impact in determining device performance has recently emerged. The formation of properly oriented electric dipole layers at the HTM/perovskite interface can result in improved charge extraction and reduced charge recombination, thus providing overall better PCEs. This concept was first explored by Hu and coworkers in 2016, reporting on the beneficial effect of photoinduced dipoles in thieno[3,4-b]thiophene-alt-benzodithiophene (PTB7) polymeric HTM on the performance of direct-architecture PSCs.[124] When compared with crystalline P3HT, the amorphous PTB7 was found to be able to undergo partial alignment of optically generated dipoles under the influence of the device's built-in potential. By carrying out magneto-photocurrent measurements under the influence of an external electric field, they proved that the presence of these dipoles partially suppresses the recombination of the photogenerated charge carriers in the bulk of the perovskite layer. Following this interesting concept, the group of Park engineered the optical features of HTM layer in a p–i–n PSC (where the HTM is the first layer to absorb the incoming light) by designing organic molecules that have a high transition dipole moment at the excited state and can be processed as an interlayer between NiO_x HTM and the perovskite absorber.[125] Their structures can undergo keto-enol tautomerism that causes an excited-state intramolecular proton transfer (ESIPT) process to take place after light absorption, as shown in **Figure 11**a. This transient structural variation is accompanied a change in dipole moment and polarizability, which can be further tuned by adding electron donor or acceptor moieties to the main molecular scaffold. By applying this concept, the authors achieved interesting results in terms of PCEs, with considerably reduced interfacial charge recombination in the resulting PSCs, as well as improved photostability due to the UV-blocking properties of the wisely engineered molecular HTMs. The same group also very recently reported an update to this strategy, by further developing the idea to achieve not only control over the excited-state polarizability of the HTMs but also over their aggregation properties, which drive charge transport in organic semiconductors-based layers.[126] The structure of the designed compounds is shown in Figure 11b, together with a scheme depicting the effect of the oriented excited-state dipoles within an inverted PSC architecture. The two molecules have a D–A character, with a triarylamine donor and an imidazole-based acceptor moiety. The second derivative (DNI) features an extended π-conjugation which favors intermolecular interactions in the solid state between adjacent molecules to boost aggregation and charge mobility, as demonstrated through grazing-incidence X-ray diffraction and hole mobility measurements. Overall, the synergy between the dipolar and aggregation effects led to improved charge extraction at the perovskite/HTM interface and prolonged stability of the devices kept in air at room temperature and under intense illumination. The generation of an electric dipole layer that increases the built-in potential in a PSC and thus causes the improvement of the overall performance can also be achieved by implementing smart doping of an organic HTM. A recent example reported by Kim and coworkers demonstrates the validity of this approach using a D–A-conducting polymer HTM with high doping capability by means of a tetrafluoro-tetracyanoquinodimethane (F4-TCNQ) interfacial dopant in direct-architecture PSC.[127] The establishment of the dipole layer and its entity was demonstrated by conducting Kelvin probe force microscopy measurements to track the WF variation, originating as a consequence of effective doping. The devices containing similar interfacial-doped HTMs provided better J_{SC} and FF compared with the un-doped reference, pointing out at increased hole extraction efficiency. In inverted PSC architectures, with generally lower efficiencies compared with direct ones, polymer-based HTMs such as PEDOT:PSS, PTAA, and Poly-TPD are widely used, either alone or in composite structures with other hole-extracting materials.[128–130] These HTMs result in good morphological properties and high efficiency, but inferior reproducibility and stability, in particular when dopants are needed for high-performance devices. As compared with polymer HTMs, small-molecular HTMs exhibit chemical structural tunability, design flexibility, and high purity. Unfortunately, their application in p–i–n configurations is hindered by their potential partial redissolution during the subsequent deposition of the perovskite layer from mixtures of highly polar solvents (DMF/DMSO). Even if this redissolution is sometimes minimal due to relatively good solvent orthogonality, it might be enough to diminish the HTM layer quality. A beneficial approach to improve the solvent stability of molecular HTMs used in inverted configurations is to resort to crosslinking strategies that can be activated once the HTM has been deposited, thus making it completely insoluble. In the past few years, some examples of this method have appeared in the literature, in which small-molecule HTMs were endowed with crosslinking ability, by conducting tailored modifications of their original structure with the introduction of a polymerizable functional group such as simple ethylene, as shown in **Figure 12**.[131–134] The effective crosslinking process can be then activated through different methods. In the first example reported by Hsu and coworkers, a *N*,*N*′-bis(tolyl)-*N*,*N*′-bis(vinylphenyl)-1,1′-biphenyl-4,4′-diamine (DVTPD) HTM was used, that can undergo simple thermally induced crosslinking of the styryl groups at 180 °C (Figure 12a), forming a robust film on top of a VO_2 electron blocking layer.[131] With this highly stabilized HTM structure and a top electron transporting layer (ETL) based on an ionic fullerene, they achieved maximum PCE of 18.8% and prolonged device stability in high humidity conditions. In another similar case, Getautis and coworkers reported on the use of cost-effective enamine-based cross-linkable HTMs, as the one shown in Figure 12c, in p–i–n PSC configuration, achieving a promising PCE of 18.14%.[133] Here, the crosslinking process was thermally initiated at 231 °C, which was identified after conducting an accurate thermal characterization of the newly synthesized HTM through differential scanning calorimetry and thermogravimetric analysis. Tremblay et al. designed a photocrosslinkable HTM based on a bis(triarylamine) molecule bearing cinnamate side chains[132]: photocrosslinking is a potentially more advantageous process with respect to thermally induced crosslinking, as it does not require high temperature (>150 °C) and thus can be conducted at ambient temperature also on plastic substrates.

ADVANCED SCIENCE NEWS
www.advancedsciencenews.com

Solar RRL
www.solar-rrl.com

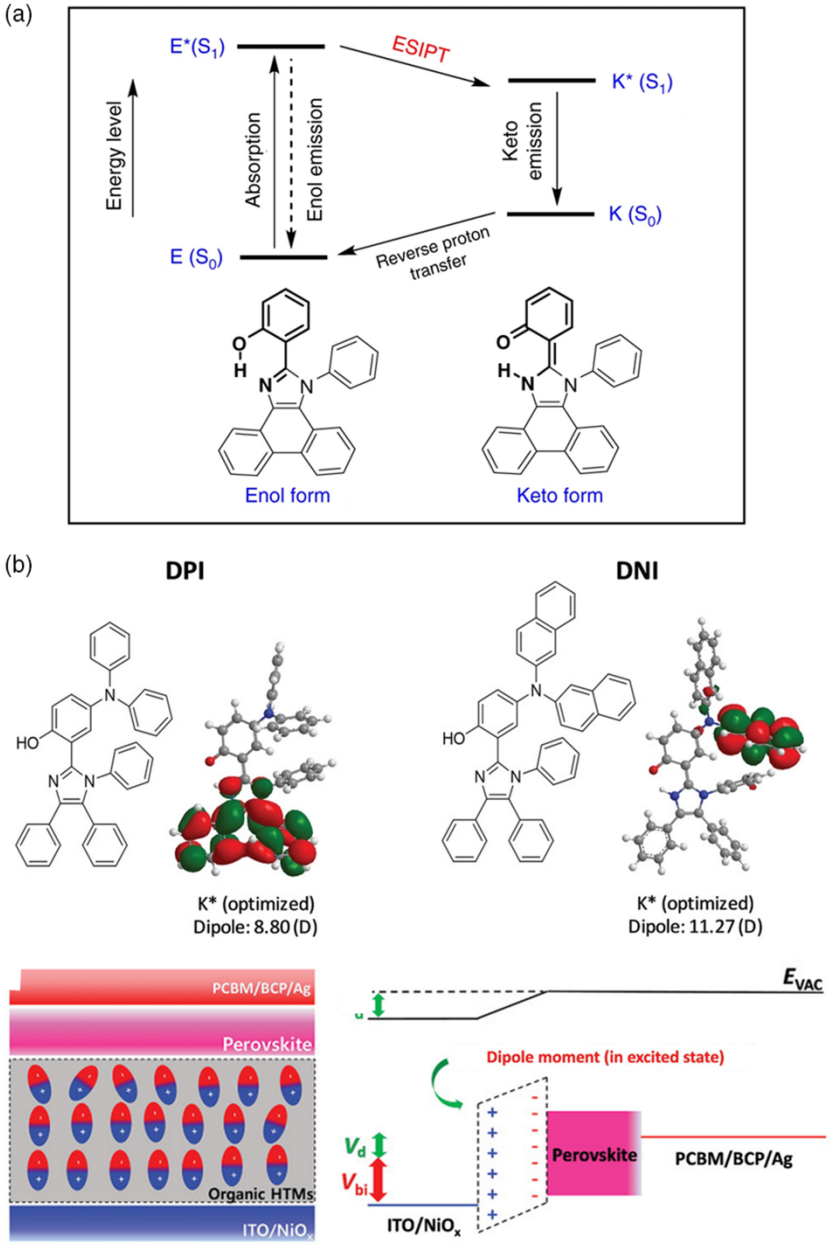

Figure 11. Emerging smart molecular HTMs for optically engineered hole extraction layers in PSCs. a) Basic molecular structure of these HTMs with illustration of the ESIPT process that drives the change in excited-state dipole moment. Reproduced under the terms of the Creative Commons CC BY License.[125] Copyright 2018, The Author(s). Published by Springer Nature. b) D-A structures with improved excited-state dipole moment and solid-state self-aggregation properties. Adapted with permission.[126] Copyright 2020, Wiley-VCH.

With a similar approach, the authors achieved a stable, dopant-free HTM, whose performance in inverted PSCs was found to be perfectly comparable with that achieved using a doped poly-TPD HTM.

Crosslinkable HTMs can also be considered valuable alternatives for direct-architecture n–i–p PSCs, being based on 3D network structures where a high density of charge-transport channels can be achieved, together with good thermal and

ADVANCED SCIENCE NEWS
www.advancedsciencenews.com

Solar RRL
www.solar-rrl.com

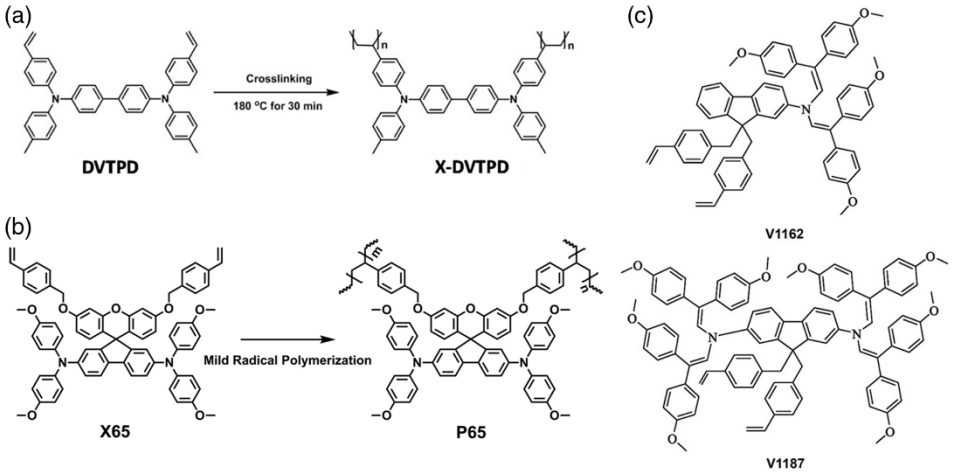

Figure 12. Examples of crosslinkable small-molecule HTMs for PSCs. a) A thermally crosslinkable *N,N′*-bis(tolyl)-*N,N′*-bis(vinylphenyl)-1,1′-biphenyl-4,4′-diamine (DVTPD) HTM used in an inverted PSC. Reproduced with permission.[131] Copyright 2018, American Chemical Society. b) A spiro[fluorene-9,9′-xanthene]-3′,6′-diol-based, crosslinked polymer, obtained through a mild free-radical polymerization as a dopant-free HTM for n–i–p-type PSCs. Reproduced under the terms of the Creative Commons CC BY License.[134] Copyright 2020, The Authors. Published by ELSEVIER B.V. and Science Press. c) Molecular structures of two enamine-based crosslinkable HTMs used in p–i–n devices. Reproduced with permission.[133] Copyright 2020, Wiley-VCH.

mechanical durability. In this regard, Sun and coworkers recently reported on the use of a novel spiro[fluorene-9,9′-xanthene]-3′,6′-diol-based crosslinked polymer (Figure 12b), obtained through mild free-radical polymerization as a dopant-free HTM for n–i–p-type PSCs.[134] With a similar HTM they achieved PCEs slightly lower than those obtained with a classically doped Spiro-based HTM (17.7% vs 19%) but a remarkably higher stability in high-humidity conditions, most likely ensured by the improved hydrophobicity of the layer following crosslinking.

Other remarkable crosslinking approaches reported in the past two years by different groups regard the incorporation of fluorine moieties within a crosslinkable and dopant-free small-molecule HTM to further boost hydrophobicity of the charge-extracting layer and target defect-passivating interactions with the perovskite surface,[135] the use of electropolymerization to induce in situ formation of polyamine-based dopant-free HTMs for inverted PSCs,[136] and the in situ thermal conversion of solution-processable xanthate precursors into the corresponding insoluble glycol-derivatized poly(1,4-phenylenevinylene) HTMs with different hydrophilicity profiles influencing final device performance.[137]

The insertion of an interfacial layer between the perovskite and the HTM or the HTM and the top metal electrode has been shown in other cases to be advantageous for reducing charge recombination in PSCs,[138,139] also through the passivation of surface defects in the semiconductor.[140–142] Engineering of the perovskite/HTM interface at the molecular level has even allowed Seo and coworkers to achieve outstanding PSC performance (a PCE of 22.7%) and stability, using a pristine, undoped P3HT HTM,[143] which normally provides relatively low PCEs (10–15%,[39,144] slightly better ones if doped[145,146]). The concomitant perovskite surface passivation with a quasi-2D perovskite layer and the supramolecular hydrophobic interaction of this last one with the lateral chains of the P3HT HTM created the right conditions to form a highly oriented, self-assembled semiconducting polymer layer with very high hole mobility. If the passivation layer is based on a highly hydrophobic material, further protection from humidity-driven decomposition can be achieved.[147] This was the case, for example, in the work of Chaudhary et al.,[148] where a solution-processable poly (4-vinylpyridine) film was used to passivate the perovskite surface, through the coordination of the pyridine moieties to undercoordinated lead atoms on the surface of the perovskite light absorber. Similarly, Prabakar and coworkers used two highly hydrophobic, dopant-free, donor–π–acceptor semiconducting polymer HTMs containing thiophene residues, able to passivate surface defects on the perovskite photoactive layer and to fabricate standard-architecture PSCs with good efficiency and environmental stability.[149]

A notable emerging direction in the field of smart HTM development that deserves to be reminded in this Review is undoubtedly the implementation of self-assembled monolayers (SAMs) at the interface between the HTM itself and the perovskite layer in inverted PSCs, similarly as it was done in the past for electron-transporting layers in direct-architecture devices.[150] The first example of a SAM HTM implemented in a p–i–n PSC was reported in 2018 by the groups of Getautis and Albrecht using a dopant-free small-molecule HTM functionalized with phosphonic groups able to directly bind to the transparent conductive oxide (TCO) surface.[151] More recent reports have described the use of carboxylic acid-decorated species for anchoring to the TCO,[152] as well as the systematic study of the effect of different anchoring groups on the final device PCE and stability.[153] However, the most remarkable achievement of a similar strategy is the incorporation into tandem solar cells, allowing

ADVANCED SCIENCE NEWS
www.advancedsciencenews.com

Solar RRL
www.solar-rrl.com

considerable simplification and high versatility of device architecture design: with the SAM HTM approach indeed, Albrecht and coworkers were able to fabricate both CIGSe/perovskite[154] and silicon/perovskite monolithic solar cells[155] with very high efficiencies and environmental stability. As discussed along this entire Review, the improvement of hydrophobicity at the level of the HTM has often provided good opportunities to obtain PSCs with interesting stability profiles with respect to the exposure to ambient moisture or even to excess humidity. In contrast, it is necessary to highlight here that hydrophobic materials/additives/functional groups are only a "passive" way to hinder the income of water molecules across a PSC, so as to avoid their contact with the highly water-sensitive photoactive perovskite layer. Similar hydrophobic HTMs might be therefore able to ensure such a blocking effect only until they do not start to degrade themselves, thus not being anymore able to act as a barrier for humidity. A different perspective could be offered by the development of HTMs that have the capability of "actively" transforming water into unharmful or even beneficial species, which ultimately boost the overall PSC performance. In this regard, some of us have recently reported on the incorporation of a water-splitting active layer as the HTM in n–i–p PSCs.[156] Endowing an HTM with water oxidation and reduction properties is indeed a very peculiar and potentially disruptive approach to solve the problem of water-driven perovskite decomposition, which might even lead to the realization of compact photovoltaic technologies able to generate at the same time both electricity and hydrogen as a solar fuel. Our proof-of-concept water-splitting active HTM was realized by incorporating CuSCN nanoplatelets (CuSCN-NPs, a transmission electron microscopy (TEM) image is shown in **Figure 13**a, together with an estimation of the average diameter obtained through dynamic light scattering, DLS) into P3HT matrix, producing a nanocomposite in which both the components have hole-transport properties. In this blend, a hole transfer process between the inorganic nanofillers and the semiconducting polymer host is detected through ESR spectroscopy (here the signal of the P3HT polaron is considerably increased in the presence of the blended CuSCN-NPs, see Figure 13b). The ability to conduct both water oxidation (at the composite valence band) and reduction (at the CuSCN Fermi level) was demonstrated by conducting electrochemical studies on the CuSCN@P3HT composite and by comparing

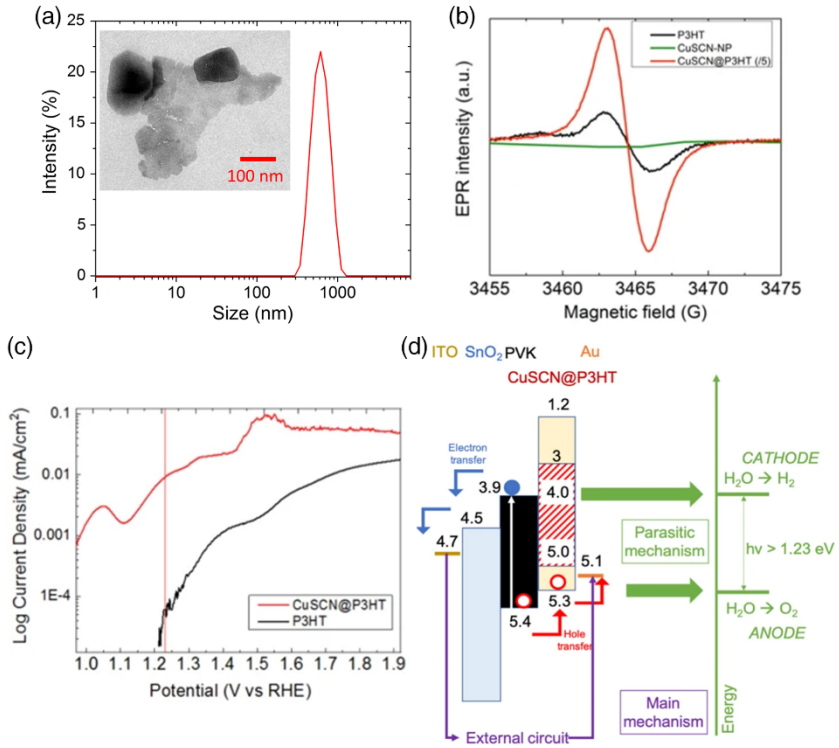

Figure 13. A water-splitting "active" CuSCN@P3HT composite HTM transforms harmful water molecules into hydrogen and oxygen. This last one further promotes the in situ p-doping of P3HT, improving the charge transport properties of the layer during PSC operation in high-humidity conditions. a) CuSCN-NPs used as nanofillers for a P3HT HTM matrix (TEM image and DLS spectrum). b) ESR spectra of the composite HTM, highlighting the considerably greater polaronic response of P3HT in the presence of the inorganic nanofillers. c) Linear sweep voltammetry curves (anodic region) of the CuSCN@P3HT composite HTM and neat P3HT, highlighting the current contribution of the two different materials at 1.23 V. d) Working mechanism of a water-splitting HTM-endowed direct-architecture PSC, in which the parasitic mechanism occurring within the HTM itself promotes the generation of both hydrogen and oxygen molecules from incoming moisture. Reproduced under the terms of the Creative Commons CC BY 4.0 License.[156] Copyright 2021, The Authors. Published by Springer Nature.

them with results obtained on pristine P3HT: in Figure 13c, the anodic regime is shown, where a remarkable difference in current response between the composite and the neat P3HT film is well visible at 1.23 V, the minimal potential required to promote water oxidation. Also, at the cathodic side (not shown), a clear contribution to water reduction in the presence of CuSCN was detected. The additional peculiarity of a similar "active" HTM resides in the fact that the in situ-generated oxygen molecules can act as p-dopants for the P3HT phase (as shown through Kelvin probe experiments in which an evident downshifting of the WF is found), improving the charge transport properties of this last one during device operation in RH > 80%: it was indeed in such conditions and not in "dry" ones that the potential of this water-splitting active HTM was revealed, allowing to achieve a stable (and even slightly improved) PCE in standard PSCs over a 1 month time storage in a water-saturated atmosphere. In Figure 13d, the occurrence of a water-splitting process within the HTM is conjectured to make use of a part of the photocurrent generated by the solar cell (through the there-defined "main mechanism") to install a "parasitic mechanism" able to promote the generation of oxygen and hydrogen molecules, being the right energetics for both reactions available within the layer itself.

6. Conclusions and Outlook

Within this contribution, we wanted to highlight new scenarios in the development and application of smart HTMs for PSCs. We started from an experimental and highly validated evidence that supports the closing of the first PSC era, represented by high-performance devices with a limited shelf-life and reflecting the impossibility of producing commercial items exploiting the very popular Spiro-based HTM, whose golden age appears to have reached a definitive end. For this reason, researchers have learnt how to resort to new inorganic and organic HTMs, by exalting their noninnocent role to guarantee similar peak performances of Spiro-based devices that also prolong long-term stability, thus closing the gap for industrial scale-up. Within this scenario, we believe that a species like CuSCN will become the new main character of upcoming PSC research, thanks to its chemical stability in high humidity conditions and its optimal electronic properties. However, there are some issues in the processing as the solubility in sulfide was demonstrated to be a problem for the underneath perovskite layer, so that miniaturization (as done in our P3HT-CuSCN composite HTM work[156]) can perhaps fix this issue. In addition, the inspiration of the experienced organic chemists will help the community in the development of new molecules able to replace Spiro at lower costs of production and without the need for additional dopants. These new small molecules are already under development and are characterized by an extremely sophisticated structural design and highly optimized electronic properties. Finally, there is the possibility of completely cutting the HTM layer, thus notably simplifying device architectures, by resorting to the so-called HTM-free C-PSCSs, that use CEs having both the quality of hole acceptors and real top electrodes. Apart for the essential benefit in terms of economic savings that results from the elimination of the highly expensive gold electrode, the use of carbon-based layers can improve PSC stability and, after proper interface engineering with the perovskite layer, can open perspectives for application in tandem solar cells, devices in which the number of layers is undoubtedly an issue to be tightly monitored.[157] In addition, drastic cost reduction paves the way to new opportunities for similar ultracheap photovoltaic technologies, such as the ever-growing need for viable power sources to be applied in the internet of things (IoT) field.

All these intriguing possibilities require versatile and reproducible processing that actual lab-scale methodology does not allow. For this reason, there is the need of exploring new and even not yet considered approaches for thin-film photovoltaics production, such as for instance spray coating[158] and sputtering,[159] that can overcome, in principle, the intrinsic limitation of CuSCN processing, opening the way for the new (and ultimate) era of PSC development: the industrialization.

Acknowledgements

T.G. acknowledges the financial support of the European Commission through the H2020 FET-PROACTIVE-EIC-07-2020 project LIGHT-CAP (no. 101017821), of the Deutsche Forschungsgemeinschaft (DFG) (project GA 3052/1-1) and Fonds der Chemischen Industrie (Verband der Chemischen Industrie e.V.). F.S. and T.G. further thank the DFG for the RTG 2204 "Substitute materials for sustainable energy technologies." Z.H. acknowledges support from the National Natural Science Foundation of China (NSFC) (nos. 61775091 and U2001216), Science, Technology and Innovation Commission of Shenzhen Municipality (no. JCYJ20180504165851864), and the Shenzhen Key Laboratory Project (no. ZDSYS201602261933302). F.L. acknowledges "Centro Levi Cases" of University of Padova for financial support (AMONRA project).

Open Access Funding provided by Universita degli Studi di Padova within the CRUI-CARE Agreement.

Conflict of Interest

The authors declare no conflict of interest.

Keywords

dopant-free hole-transporting materials, hole-transporting materials, inorganic materials, perovskite solar cells, smart materials

Received: July 8, 2021
Revised: August 2, 2021
Published online: August 19, 2021

[1] M. Jeong, I. W. Choi, E. M. Go, Y. Cho, M. Kim, B. Lee, S. Jeong, Y. Jo, H. W. Choi, J. Lee, J.-H. Bae, S. K. Kwak, D. S. Kim, C. Yang, *Science (80-.).* **2020**, *369*, 1615.
[2] Z. Hawash, L. K. Ono, Y. Qi, *Adv. Mater. Interfaces* **2018**, *5*, 1700623.
[3] E. Kasparavicius, A. Magomedov, T. Malinauskas, V. Getautis, *Chem. – A Eur. J.* **2018**, *24*, 9910.
[4] L. Hajikhanmirzaei, H. Shahroosvand, B. Pashaei, G. D. Monache, M. K. Nazeeruddin, M. Pilkington, *J. Mater. Chem. C* **2020**, *8*, 6221.
[5] A. T. Murray, J. M. Frost, C. H. Hendon, C. D. Molloy, D. R. Carbery, A. Walsh, *Chem. Commun.* **2015**, *51*, 8935.
[6] L. Calió, S. Kazim, M. Grätzel, S. Ahmad, *Angew. Chem., Int. Ed.* **2016**, *55*, 14522.

[7] J. H. Noh, N. J. Jeon, Y. C. Choi, M. K. Nazeeruddin, M. Grätzel, S. Il Seok, *J. Mater. Chem. A* **2013**, *1*, 11842.
[8] Z. Hawash, L. K. Ono, Y. Qi, *Adv. Mater. Interfaces* **2018**, *5*, 1700623.
[9] W. Han, G. Ren, J. Liu, Z. Li, H. Bao, C. Liu, W. Guo, *ACS Appl. Mater. Interfaces* **2020**, *12*, 49297.
[10] W. S. Yang, J. H. Noh, N. J. Jeon, Y. C. Kim, S. Ryu, J. Seo, S. I. Seok, *Science (80-.)*. **2015**, *348*, 1234.
[11] Y. Deng, X. Zheng, Y. Bai, Q. Wang, J. Zhao, J. Huang, *Nat. Energy* **2018**, *3*, 560.
[12] D. Yang, T. Sano, Y. Yaguchi, H. Sun, H. Sasabe, J. Kido, *Adv. Funct. Mater.* **2019**, *29*, 1807556.
[13] G. Grancini, C. Roldán-Carmona, I. Zimmermann, E. Mosconi, X. Lee, D. Martineau, S. Narbey, F. Oswald, F. De Angelis, M. Graetzel, M. K. Nazeeruddin, *Nat. Commun.* **2017**, *8*, 15684.
[14] J. W. Jung, C.-C. Chueh, A. K.-Y. Jen, *Adv. Mater.* **2015**, *27*, 7874.
[15] M. Huangfu, Y. Shen, G. Zhu, K. Xu, M. Cao, F. Gu, L. Wang, *Appl. Surf. Sci.* **2015**, *357*, 2234.
[16] W. Sun, Y. Li, S. Ye, H. Rao, W. Yan, H. Peng, Y. Li, Z. Liu, S. Wang, Z. Chen, L. Xiao, Z. Bian, C. Huang, *Nanoscale* **2016**, *8*, 10806.
[17] H. Peng, W. Sun, Y. Li, S. Ye, H. Rao, W. Yan, H. Zhou, Z. Bian, C. Huang, *Nano Res.* **2016**, *9*, 2960.
[18] H. Sung, N. Ahn, M. S. Jang, J.-K. Lee, H. Yoon, N.-G. Park, M. Choi, *Adv. Energy Mater.* **2016**, *6*, 1501873.
[19] E. Singh, K. S. Kim, G. Y. Yeom, H. S. Nalwa, *ACS Appl. Mater. Interfaces* **2017**, *9*, 3223.
[20] N. Arora, M. I. Dar, A. Hinderhofer, N. Pellet, F. Schreiber, S. M. Zakeeruddin, M. Grätzel, *Science (80-.)*. **2017**, *358*, 768.
[21] R. S. Sanchez, E. Mas-Marza, *Sol. Energy Mater. Sol. Cells* **2016**, *158*, 189.
[22] A. Di Carlo, F. Matteocci, S. Razza, M. Mincuzzi, F. Di Giacomo, S. Casaluci, D. Gentilini, T. M. Brown, A. Reale, F. Brunetti, A. D'Epifanio, S. Licoccia, in *14th IEEE Int. Conf. Nanotechnology*, IEEE, Piscataway, NJ **2014**, pp. 70–74.
[23] F. Lamberti, T. Gatti, E. Cescon, R. Sorrentino, A. Rizzo, E. Menna, G. Meneghesso, M. Meneghetti, A. Petrozza, L. Franco, *Chem* **2019**, *5*, 1806.
[24] A. Abate, D. J. Hollman, J. Teuscher, S. Pathak, R. Avolio, G. D'Errico, G. Vitiello, S. Fantacci, H. J. Snaith, *J. Am. Chem. Soc.* **2013**, *135*, 13538.
[25] G. Ren, W. Han, Y. Deng, W. Wu, Z. Li, J. Guo, H. Bao, C. Liu, W. Guo, *J. Mater. Chem. A* **2021**, *9*, 4589.
[26] A. Magomedov, E. Kasparavičius, K. Rakstys, S. Paek, N. Gasilova, K. Genevičius, G. Juška, T. Malinauskas, M. K. Nazeeruddin, V. Getautis, *J. Mater. Chem. C* **2018**, *6*, 8874.
[27] F. Lamberti, T. Gatti, E. Cescon, R. Sorrentino, A. Rizzo, E. Menna, G. Meneghesso, M. Meneghetti, A. Petrozza, L. Franco, *Chem* **2019**, *5*, 1806.
[28] X. Yin, Z. Song, Z. Li, W. Tang, *Energy Environ. Sci.* **2020**, *13*, 4057.
[29] K. Rakstys, C. Igci, M. K. Nazeeruddin, *Chem. Sci.* **2019**, *10*, 6748.
[30] Y. Wang, W. Chen, L. Wang, B. Tu, T. Chen, B. Liu, K. Yang, C. W. Koh, X. Zhang, H. Sun, G. Chen, X. Feng, H. Y. Woo, A. B. Djurišić, Z. He, X. Guo, *Adv. Mater.* **2019**, *31*, 1902781.
[31] W. Chen, Y. Wang, B. Liu, Y. Gao, Z. Wu, Y. Shi, Y. Tang, K. Yang, Y. Zhang, W. Sun, X. Feng, F. Laquai, H. Y. Woo, A. B. Djurišić, X. Guo, Z. He, *Sci. China Chem.* **2021**, *64*, 41.
[32] M. K. Nazeeruddin, C. Liu, C. Igci, Y. Yang, O. A. Syzgantseva, M. A. Syzgantseva, K. Rakstys, H. Kanda, N. Shibayama, B. Ding, X. Zhang, V. Jankauskas, Y. Ding, S. Dai, P. Dyson, *Angew. Chem., Int. Ed.* **2021**, https://doi.org/10.1002/anie.202107774.
[33] K. Rakstys, S. Paek, P. Gao, P. Gratia, T. Marszalek, G. Grancini, K. T. Cho, K. Genevicius, V. Jankauskas, W. Pisula, M. K. Nazeeruddin, *J. Mater. Chem. A* **2017**, *5*, 7811.
[34] Q. Fu, Z. Xu, X. Tang, T. Liu, X. Dong, X. Zhang, N. Zheng, Z. Xie, Y. Liu, *ACS Energy Lett.* **2021**, *6*, 1521.
[35] C. Igci, S. Paek, K. Rakstys, H. Kanda, N. Shibayama, V. Jankauskas, C. Roldán-Carmona, H. Kim, A. M. Asiri, M. K. Nazeeruddin, *Sol. RRL* **2020**, *4*, 2000173.
[36] J. Wang, X. Wu, Y. Liu, T. Qin, K. Zhang, N. Li, J. Zhao, R. Ye, Z. Fan, Z. Chi, Z. Zhu, *Adv. Energy Mater.* **2021**, 2100967.
[37] J. Yuan, Y. Chen, X. Liu, S. Xue, *ACS Appl. Energy Mater.* **2021**, *4*, 5756.
[38] M. Cai, V. T. Tiong, T. Hreid, J. Bell, H. Wang, *J. Mater. Chem. A* **2015**, *3*, 2784.
[39] T. Gatti, S. Casaluci, M. Prato, M. Salerno, F. Di Stasio, A. Ansaldo, E. Menna, A. Di Carlo, F. Bonaccorso, *Adv. Funct. Mater.* **2016**, *26*, https://doi.org/10.1002/adfm.201602803.
[40] T. Gatti, F. Lamberti, P. Topolovsek, M. Abdu-Aguye, R. Sorrentino, L. Perino, M. Salerno, L. Girardi, C. Marega, G. A. Rizzi, M. A. Loi, A. Petrozza, E. Menna, *Sol. RRL* **2018**, *2*, 1800013.
[41] Q. Hu, E. Rezaee, Q. Dong, H. Shan, Q. Chen, L. Wang, B. Liu, J.-H. Pan, Z.-X. Xu, *Sol. RRL* **2019**, *3*, 1800264.
[42] Q. Hu, E. Rezaee, M. Li, Q. Chen, C. Li, S. Cai, H. Shan, Z.-X. Xu, *Sol. RRL* **2020**, *4*, 1900340.
[43] J. Wang, Q. Hu, M. Li, H. Shan, Y. Feng, Z.-X. Xu, *Sol. RRL* **2020**, *4*, 2000109.
[44] Y. Liu, B. He, J. Duan, Y. Zhao, Y. Ding, M. Tang, H. Chen, Q. Tang, *J. Mater. Chem. A* **2019**, *7*, 12635.
[45] J. Peng, D. Walter, Y. Ren, M. Tebyetekerwa, Y. Wu, T. Duong, Q. Lin, J. Li, T. Lu, M. A. Mahmud, O. L. C. Lem, S. Zhao, W. Liu, Y. Liu, H. Shen, L. Li, F. Kremer, H. T. Nguyen, D.-Y. Choi, K. J. Weber, K. R. Catchpole, T. P. White, *Science (80-.)*. **2021**, *371*, 390.
[46] J.-M. Wang, Z.-K. Wang, M. Li, K.-H. Hu, Y.-G. Yang, Y. Hu, X.-Y. Gao, L.-S. Liao, *ACS Appl. Mater. Interfaces* **2017**, *9*, 13240.
[47] J. Chen, N.-G. Park, *J. Phys. Chem. C* **2018**, *122*, 14039.
[48] R. Singh, P. K. Singh, B. Bhattacharya, H.-W. Rhee, *Appl. Mater. Today* **2019**, *14*, 175.
[49] L. C. Palilis, M. Vasilopoulou, A. Verykios, A. Soultati, E. Polydorou, P. Argitis, D. Davazoglou, A. R. bin Mohd Yusoff, M. K. Nazeeruddin, *Adv. Energy Mater.* **2020**, *10*, 2000910.
[50] Y. Hou, X. Du, S. Scheiner, D. P. McMeekin, Z. Wang, N. Li, M. S. Killian, H. Chen, M. Richter, I. Levchuk, N. Schrenker, E. Spiecker, T. Stubhan, N. A. Luechinger, A. Hirsch, P. Schmuki, H.-P. Steinrück, R. H. Fink, M. Halik, H. J. Snaith, C. J. Brabec, *Science (80-.)*. **2017**, *358*, 1192.
[51] L. C. Palilis, M. Vasilopoulou, A. Verykios, A. Soultati, E. Polydorou, P. Argitis, D. Davazoglou, A. R. bin Mohd Yusoff, M. K. Nazeeruddin, *Adv. Energy Mater.* **2020**, *10*, 2000910.
[52] V. Sugathan, E. John, K. Sudhakar, *Renew. Sustain. Energy Rev.* **2015**, *52*, 54.
[53] T. Gatti, F. Lamberti, R. Mazzaro, I. Kriegel, D. Schlettwein, F. Enrichi, N. Lago, E. Di Maria, G. Meneghesso, A. Vomiero, S. Gross, *Adv. Energy Mater.* **2021**, 2101041.
[54] T. Gatti, F. Lamberti, R. Mazzaro, I. Kriegel, D. Schlettwein, F. Enrichi, N. Lago, E. Di Maria, G. Meneghesso, A. Vomiero, S. Gross, *Adv. Energy Mater.* **2021**, 2101041.
[55] P. Dalle Feste, M. Crisci, F. Barbon, F. Tajoli, M. Salerno, F. Drago, M. Prato, S. Gross, T. Gatti, F. Lamberti, *Appl. Sci.* **2021**, *11*, 2016.
[56] B. A. Nejand, V. Ahmadi, S. Gharibzadeh, H. R. Shahverdi, *ChemSusChem* **2016**, *9*, 302.
[57] P. Wang, J. Zhang, Z. Zeng, R. Chen, X. Huang, L. Wang, J. Xu, Z. Hu, Y. Zhu, *J. Mater. Chem. C* **2016**, *4*, 9003.
[58] N. Yamada, R. Ino, H. Tomura, Y. Kondo, Y. Ninomiya, *Adv. Electron. Mater.* **2017**, *3*, 1700298.
[59] J. A. Christians, R. C. M. Fung, P. V. Kamat, *J. Am. Chem. Soc.* **2014**, *136*, 758.

[60] S. Ye, H. Rao, Z. Zhao, L. Zhang, H. Bao, W. Sun, Y. Li, F. Gu, J. Wang, Z. Liu, Z. Bian, C. Huang, *J. Am. Chem. Soc.* **2017**, *139*, 7504.
[61] F. Matebese, R. Taziwa, D. Mutukwa, *Materials (Basel)*. **2018**, *11*, 2592.
[62] J. E. Jaffe, T. C. Kaspar, T. C. Droubay, T. Varga, M. E. Bowden, G. J. Exarhos, *J. Phys. Chem. C* **2010**, *114*, 9111.
[63] N. Wijeyasinghe, A. Regoutz, F. Eisner, T. Du, L. Tsetseris, Y.-H. Lin, H. Faber, P. Pattanasattayavong, J. Li, F. Yan, M. A. McLachlan, D. J. Payne, M. Heeney, T. D. Anthopoulos, *Adv. Funct. Mater.* **2017**, *27*, 1701818.
[64] N. Arora, M. I. Dar, A. Hinderhofer, N. Pellet, F. Schreiber, S. M. Zakeeruddin, M. Grätzel, *Science (80-.)*. **2017**, *358*, 768.
[65] I. S. Yang, S. Lee, J. Choi, M. T. Jung, J. Kim, W. I. Lee, *J. Mater. Chem. A* **2019**, *7*, 6028.
[66] C. Liu, L. Zhang, Y. Li, X. Zhou, S. She, X. Wang, Y. Tian, A. K. Y. Jen, B. Xu, *Adv. Funct. Mater.* **2020**, *30*, 1908462.
[67] T. Duong, J. Peng, D. Walter, J. Xiang, H. Shen, D. Chugh, M. Lockrey, D. Zhong, J. Li, K. Weber, T. P. White, K. R. Catchpole, *ACS Energy Lett.* **2018**, *3*, 2441.
[68] M. Tyagi, M. Tomar, V. Gupta, *Anal. Chim. Acta* **2012**, *726*, 93.
[69] N. M. Hosny, *Polyhedron* **2011**, *30*, 470.
[70] W. Chen, F.-Z. Liu, X.-Y. Feng, A. B. Djurišić, W. K. Chan, Z.-B. He, *Adv. Energy Mater.* **2017**, *7*, 1700722.
[71] F. Xie, C.-C. Chen, Y. Wu, X. Li, M. Cai, X. Liu, X. Yang, L. Han, *Energy Environ. Sci.* **2017**, *10*, 1942.
[72] S. Yue, K. Liu, R. Xu, M. Li, M. Azam, K. Ren, J. Liu, Y. Sun, Z. Wang, D. Cao, X. Yan, S. Qu, Y. Lei, Z. Wang, *Energy Environ. Sci.* **2017**, *10*, 2570.
[73] Y. Wu, F. Xie, H. Chen, X. Yang, H. Su, M. Cai, Z. Zhou, T. Noda, L. Han, *Adv. Mater.* **2017**, *29*, 1701073.
[74] D. Di Girolamo, F. Di Giacomo, F. Matteocci, A. G. Marrani, D. Dini, A. Abate, *Chem. Sci.* **2020**, *11*, 7746.
[75] S. Sajid, A. M. Elseman, H. Huang, J. Ji, S. Dou, H. Jiang, X. Liu, D. Wei, P. Cui, M. Li, *Nano Energy* **2018**, *51*, 408.
[76] W. Chen, B. Han, Q. Hu, M. Gu, Y. Zhu, W. Yang, Y. Zhou, D. Luo, F.-Z. Liu, R. Cheng, R. Zhu, S.-P. Feng, A. B. Djurišić, T. P. Russell, Z. He, *Sci. Bull.* **2021**, *66*, 991.
[77] W. Chen, L. Xu, X. Feng, J. Jie, Z. He, *Adv. Mater.* **2017**, *29*, 1603923.
[78] W. Chen, G. Zhang, L. Xu, R. Gu, Z. Xu, H. Wang, Z. He, *Mater. Today Energy* **2016**, *1–2*, 1.
[79] W. Chen, Y. Wu, J. Fan, A. B. Djurišić, F. Liu, H. W. Tam, A. Ng, C. Surya, W. K. Chan, D. Wang, Z.-B. He, *Adv. Energy Mater.* **2018**, *8*, 1703519.
[80] W. Chen, Y. Zhou, L. Wang, Y. Wu, B. Tu, B. Yu, F. Liu, H.-W. Tam, G. Wang, A. B. Djurišić, L. Huang, Z. He, *Adv. Mater.* **2018**, *30*, 1800515.
[81] W. Chen, Y. Zhou, G. Chen, Y. Wu, B. Tu, F.-Z. Liu, L. Huang, A. M. C. Ng, A. B. Djurišić, Z. He, *Adv. Energy Mater.* **2019**, *9*, 1803872.
[82] D. Tiwari, O. S. Hutter, G. Longo, *J. Phys. Energy* **2021**, *3*, 034010.
[83] X. Liu, Y. Cheng, B. Tang, Z. G. Yu, M. Li, F. Lin, S. Zhang, Y.-W. Zhang, J. Ouyang, H. Gong, *Nano Energy* **2020**, *71*, 104556.
[84] G. Tang, P. You, Q. Tai, A. Yang, J. Cao, F. Zheng, Z. Zhou, J. Zhao, P. K. L. Chan, F. Yan, *Adv. Mater.* **2019**, 1807689.
[85] X. Li, J. Yang, Q. Jiang, H. Lai, S. Li, Y. Tan, Y. Chen, S. Li, *J. Mater. Chem. A* **2019**, *7*, 7065.
[86] A. D. Taylor, Q. Sun, K. P. Goetz, Q. An, T. Schramm, Y. Hofstetter, M. Litterst, F. Paulus, Y. Vaynzof, *Nat. Commun.* **2021**, *12*, 1.
[87] X. L. Trinh, H. C. Kim, *Energy Reports* **2020**, *6*, 1297.
[88] D. Chen, S. Pang, W. Zhu, H. Zhang, L. Zhou, F. He, J. Chang, Z. Lin, H. Xi, J. Zhang, C. Zhang, Y. Hao, *J. Nanomater.* **2018**, *2018*, https://doi.org/10.1155/2018/4012850.
[89] L. Lin, C. Gu, J. Zhu, Q. Ye, E. Jiang, W. Wang, M. Liao, Z. Yang, Y. Zeng, J. Sheng, W. Guo, B. Yan, P. Gao, J. Ye, Y. Zhu, *J. Mater. Sci.* **2019**, *54*, 7789.
[90] H. B. Michaelson, *J. Appl. Phys.* **1977**, *48*, 4729.
[91] K. Domanski, J. P. Correa-Baena, N. Mine, M. K. Nazeeruddin, A. Abate, M. Saliba, W. Tress, A. Hagfeldt, M. Grätzel, *ACS Nano* **2016**, *10*, 6306.
[92] C. Besleaga, L. E. Abramiuc, V. Stancu, A. G. Tomulescu, M. Sima, L. Trinca, N. Plugaru, L. Pintilie, G. A. Nemnes, M. Iliescu, H. G. Svavarsson, A. Manolescu, I. Pintilie, *J. Phys. Chem. Lett.* **2016**, *7*, 5168.
[93] H. Li, R. Yang, C. Wang, Y. Wang, H. Chen, H. Zheng, D. Liu, T. Zhang, F. Wang, P. Gu, J. Wu, Z. D. Chen, P. Zhang, S. Li, *IEEE J. Photovoltaics* **2019**, *9*, 1081.
[94] S. Svanström, T. J. Jacobsson, G. Boschloo, E. M. J. Johansson, H. Rensmo, U. B. Cappel, *ACS Appl. Mater. Interfaces* **2020**, *12*, 7212.
[95] S. Cacovich, L. Ciná, F. Matteocci, G. Divitini, P. A. Midgley, A. Di Carlo, C. Ducati, *Nanoscale* **2017**, *9*, 4700.
[96] N. N. Shlenskaya, N. A. Belich, M. Grätzel, E. A. Goodilin, A. B. Tarasov, *J. Mater. Chem. A* **2018**, *6*, 1780.
[97] C. Wu, K. Wang, Y. Jiang, D. Yang, Y. Hou, T. Ye, C. S. Han, B. Chi, L. Zhao, S. Wang, W. Deng, S. Priya, *Adv. Funct. Mater.* **2021**, *31*, 1.
[98] G. Zhang, P. Xie, Z. Huang, Z. Yang, Z. Pan, Y. Fang, H. Rao, X. Zhong, *Adv. Funct. Mater.* **2021**, *2011187*, 1.
[99] Y. Wu, S. Wang, T. Ouyang, W. Li, M. Chen, Y. Lu, P. Qi, Y. Tang, *Nanotechnology* **2021**, *32*, https://doi.org/10.1088/1361-6528/abe891.
[100] Q. Q. Chu, Z. Sun, B. Ding, K. sik Moon, G. J. Yang, C. P. Wong, *Nano Energy* **2020**, *77*, 105110.
[101] X. Chen, Y. Xia, Q. Huang, Z. Li, A. Mei, Y. Hu, T. Wang, R. Cheacharoen, Y. Rong, H. Han, *Adv. Energy Mater.* **2021**, https://doi.org/10.1002/aenm.202100292.
[102] M. Guo, J. Liu, Y. Yuan, Z. Zhang, S. Yin, J. Leng, N. Huang, *J. Photochem. Photobiol. A Chem.* **2020**, *403*, 112843.
[103] R. Chen, Y. Feng, C. Zhang, M. Wang, L. Jing, C. Ma, J. Bian, Y. Shi, *J. Mater. Chem. C* **2020**, *8*, 9262.
[104] M. Tian, C. Y. Woo, J. W. Choi, J. Y. Seo, J. M. Kim, S. H. Kim, M. Song, H. W. Lee, *ACS Appl. Mater. Interfaces* **2020**, *12*, 54806.
[105] R. Chen, Y. Feng, L. Jing, M. Wang, H. Ma, J. Bian, Y. Shi, *J. Mater. Chem. C* **2021**, *9*, 3546.
[106] L. Lin, P. Li, Z. Kang, H. Xiong, Y. Chen, Q. Yan, L. Jiang, Y. Qiu, *Adv. Theory Simulations* **2021**, *4*, 1.
[107] S. He, L. Qiu, D. Y. Son, Z. Liu, E. J. Juarez-Perez, L. K. Ono, C. Stecker, Y. Qi, *ACS Energy Lett.* **2019**, *4*, 2032.
[108] Z. Gong, B. He, J. Zhu, X. Yao, S. Wang, H. Chen, Y. Duan, Q. Tang, *Sol. RRL* **2021**, *5*, 1.
[109] X. Zhang, J. Yang, L. Xie, X. Lu, X. Gao, J. Gao, L. Shui, S. Wu, J. M. Liu, *Dye. Pigment.* **2021**, *186*, 109024.
[110] D. Bogachuk, S. Zouhair, K. Wojciechowski, B. Yang, V. Babu, L. Wagner, B. Xu, J. Lim, S. Mastroianni, H. Pettersson, A. Hagfeldt, A. Hinsch, *Energy Environ. Sci.* **2020**, *13*, 3880.
[111] F. Yang, L. Dong, D. Jang, B. Saparov, K. C. Tam, K. Zhang, N. Li, C. J. Brabec, H.-J. Egelhaaf, *Adv. Energy Mater.* **2021**, 2101219.
[112] S. Alon, M. Sohmer, C. S. Pathak, I. Visoly-Fisher, L. Etgar, *Sol. RRL* **2021**, *5*, 2100028.
[113] H. Liu, Y. Xie, P. Wei, W. Wang, H. Chen, C. Geng, Y. Qiang, *J. Alloys Compd.* **2020**, *842*, 155851.
[114] S. Pitchaiya, N. Eswaramoorthy, M. Natarajan, A. Santhanam, V. Asokan, V. Madurai Ramakrishnan, B. Rangasamy, S. Sundaram, P. Ravirajan, D. Velauthapillai, *Sci. Rep.* **2020**, *10*, 1.

[115] S. S. Mali, H. Kim, J. V. Patil, C. K. Hong, *ACS Appl. Mater. Interfaces* **2018**, *10*, 31280.
[116] V. Babu, R. Fuentes Pineda, T. Ahmad, A. O. Alvarez, L. A. Castriotta, A. Di Carlo, F. Fabregat-Santiago, K. Wojciechowski, *ACS Appl. Energy Mater.* **2020**, *3*, 5126.
[117] Q. Luo, H. Ma, Q. Hou, Y. Li, J. Ren, X. Dai, Z. Yao, Y. Zhou, L. Xiang, H. Du, H. He, N. Wang, K. Jiang, H. Lin, H. Zhang, Z. Guo, *Adv. Funct. Mater.* **2018**, *28*, 1.
[118] H. Xie, X. Yin, Y. Guo, D. Liu, T. Liang, G. Wang, W. Que, *Nanotechnology* **2020**, *32*, https://doi.org/10.1088/1361-6528/abcf70.
[119] C. O. Teixeira, L. Andrade, A. Mendes, *J. Power Sources* **2020**, *479*, 1.
[120] P. Panneerselvam, S. Angaiah, *New J. Chem.* **2021**, *45*, 423.
[121] J. Li, J. Duan, J. Du, X. Yang, Y. Wang, P. Yang, Y. Duan, Q. Tang, *ACS Appl. Mater. Interfaces* **2020**, *12*, 47408.
[122] B. Wang, N. Li, L. Yang, C. Dall'agnese, A. K. Jena, S. I. Sasaki, T. Miyasaka, H. Tamiaki, X. F. Wang, *J. Am. Chem. Soc.* **2021**, *143*, 2207.
[123] D. Song, L. Y. Hsu, C.-M. Tseng, E. W.-G. Diau, *Mater. Adv.* **2021**, *2*, 754.
[124] M. Ahmadi, Y.-C. Hsiao, T. Wu, Q. Liu, W. Qin, B. Hu, *Adv. Energy Mater.* **2017**, *7*, 1601575.
[125] S. A. Ok, B. Jo, S. Somasundaram, H. J. Woo, D. W. Lee, Z. Li, B.-G. Kim, J. H. Kim, Y. J. Song, T. K. Ahn, S. Park, H. J. Park, *Nat. Commun.* **2018**, *9*, 4537.
[126] B. Jo, H. Park, E. Kamaraj, S. Lee, B. Jung, S. Somasundaram, G. G. Jeon, K.-T. Lee, N. Kim, J. H. Kim, B.-G. Kim, T. K. Ahn, S. Park, H. J. Park, *Adv. Funct. Mater.* **2021**, *31*, 2007180.
[127] J. Park, S. E. Yoon, J. Lee, D. R. Whang, S. Y. Lee, S. J. Shin, J. M. Han, H. Seo, H. J. Park, J. H. Kim, B.-G. Kim, *Adv. Funct. Mater.* **2020**, *30*, 2001560.
[128] X. Lin, D. Cui, X. Luo, C. Zhang, Q. Han, Y. Wang, L. Han, *Energy Environ. Sci.* **2020**, *13*, 3823.
[129] W. Chen, K. Li, Y. Wang, X. Feng, Z. Liao, Q. Su, X. Lin, Z. He, *J. Phys. Chem. Lett.* **2017**, *8*, 591.
[130] Q. Hu, W. Chen, W. Yang, Y. Li, Y. Zhou, B. W. Larson, J. C. Johnson, Y.-H. Lu, W. Zhong, J. Xu, L. Klivansky, C. Wang, M. Salmeron, A. B. Djurišić, F. Liu, Z. He, R. Zhu, T. P. Russell, *Joule* **2020**, *4*, 1575.
[131] C.-C. Chang, J.-H. Tao, C.-E. Tsai, Y.-J. Cheng, C.-S. Hsu, *ACS Appl. Mater. Interfaces* **2018**, *10*, 21466.
[132] M.-H. Tremblay, K. Schutt, Y. Zhang, J. Lim, Y.-H. Lin, J. H. Warby, S. Barlow, H. J. Snaith, S. R. Marder, *Sustain. Energy Fuels* **2020**, *4*, 190.
[133] D. Vaitukaitytė, A. Al-Ashouri, M. Daškevičienė, E. Kamarauskas, J. Nekrasovas, V. Jankauskas, A. Magomedov, S. Albrecht, V. Getautis, *Sol. RRL* **2021**, *5*, 2000597.
[134] L. Wang, F. Zhang, T. Liu, W. Zhang, Y. Li, B. Cai, L. He, Y. Guo, X. Yang, B. Xu, J. M. Gardner, L. Kloo, L. Sun, *J. Energy Chem.* **2021**, *55*, 211.
[135] J. Wu, M. Hu, L. zhang, G. Song, Y. Li, W. Tan, Y. Tian, B. Xu, *Chem. Eng. J.* **2021**, *422*, 130124.
[136] J.-Y. Shao, B. Yu, Y.-D. Wang, Z.-R. Lan, D. Li, Q. Meng, Y.-W. Zhong, *ACS Appl. Energy Mater.* **2020**, *3*, 5058.
[137] K. Rakstys, M. Stephen, J. Saghaei, H. Jin, M. Gao, G. Zhang, K. Hutchinson, A. Chesman, P. L. Burn, I. Gentle, P. E. Shaw, *ACS Appl. Energy Mater.* **2020**, *3*, 889.
[138] H. Kwon, J. W. Lim, J. Han, L. N. Quan, D. Kim, E.-S. Shin, E. Kim, D.-W. Kim, Y.-Y. Noh, I. Chung, D. H. Kim, *Nanoscale* **2019**, *11*, 19586.
[139] H. Zhu, Y. Ren, L. Pan, O. Ouellette, F. T. Eickemeyer, Y. Wu, X. Li, S. Wang, H. Liu, X. Dong, S. M. Zakeeruddin, Y. Liu, A. Hagfeldt, M. Grätzel, *J. Am. Chem. Soc.* **2021**, *143*, 3231.
[140] J. Luo, J. Xia, H. Yang, H. A. Malik, F. Han, H. Shu, X. Yao, Z. Wan, C. Jia, *Nano Energy* **2020**, *70*, 104509.
[141] Z. Li, B. H. Jo, S. J. Hwang, T. H. Kim, S. Somasundaram, E. Kamaraj, J. Bang, T. K. Ahn, S. Park, H. J. Park, *Adv. Sci.* **2019**, *6*, 1802163.
[142] B. Wang, F. Wu, S. Bi, J. Zhou, J. Wang, X. Leng, D. Zhang, R. Meng, B. Xue, C. Zong, L. Zhu, Y. Zhang, H. Zhou, *J. Mater. Chem. A* **2019**, *7*, 23895.
[143] E. H. Jung, N. J. Jeon, E. Y. Park, C. S. Moon, T. J. Shin, T.-Y. Yang, J. H. Noh, J. Seo, *Nature* **2019**, *567*, 511.
[144] F. Di Giacomo, S. Razza, F. Matteocci, A. D'Epifanio, S. Licoccia, T. M. Brown, A. Di Carlo, *J. Power Sources* **2014**, *251*, 152.
[145] N. Yaghoobi Nia, M. Bonomo, M. Zendehdel, E. Lamanna, M. M. H. Desoky, B. Paci, F. Zurlo, A. Generosi, C. Barolo, G. Viscardi, P. Quagliotto, A. Di Carlo, *ACS Sustain. Chem. Eng.* **2021**, *9*, 5061.
[146] N. Y. Nia, F. Matteocci, L. Cina, A. Di Carlo, *ChemSusChem* **2017**, *10*, 3854.
[147] M. Kim, S. G. Motti, R. Sorrentino, A. Petrozza, *Energy Environ. Sci.* **2018**, *11*, 2609.
[148] B. Chaudhary, A. Kulkarni, A. K. Jena, M. Ikegami, Y. Udagawa, H. Kunugita, K. Ema, T. Miyasaka, *ChemSusChem* **2017**, *10*, 2473.
[149] P. J. S. Rana, R. K. Gunasekaran, S. H. Park, V. Tamilavan, S. Karuppanan, H.-J. Kim, K. Prabakar, *J. Phys. Chem. C* **2019**, *123*, 8560.
[150] P. Topolovsek, F. Lamberti, T. Gatti, A. Cito, J. M. Ball, E. Menna, C. Gadermaier, A. Petrozza, *J. Mater. Chem. A* **2017**, *5*, 11882.
[151] A. Magomedov, A. Al-Ashouri, E. Kasparavičius, S. Strazdaite, G. Niaura, M. Jošt, T. Malinauskas, S. Albrecht, V. Getautis, *Adv. Energy Mater.* **2018**, *8*, 1801892.
[152] E. Aktas, N. Phung, H. Köbler, D. A. González, M. Méndez, I. Kafedjiska, S.-H. Turren-Cruz, R. Wenisch, I. Lauermann, A. Abate, E. Palomares, *Energy Environ. Sci.* **2021**, *14*, 3976.
[153] E. Li, C. Liu, H. Lin, X. Xu, S. Liu, S. Zhang, M. Yu, X.-M. Cao, Y. Wu, W.-H. Zhu, *Adv. Funct. Mater.* **2021**, 2103847.
[154] A. Al-Ashouri, A. Magomedov, M. Roß, M. Jošt, M. Talaikis, G. Chistiakova, T. Bertram, J. A. Márquez, E. Köhnen, E. Kasparavičius, S. Levcenco, L. Gil-Escrig, C. J. Hages, R. Schlatmann, B. Rech, T. Malinauskas, T. Unold, C. A. Kaufmann, L. Korte, G. Niaura, V. Getautis, S. Albrecht, *Energy Environ. Sci.* **2019**, *12*, 3356.
[155] A. Al-Ashouri, E. Köhnen, B. Li, A. Magomedov, H. Hempel, P. Caprioglio, J. A. Márquez, A. B. Morales Vilches, E. Kasparavicius, J. A. Smith, N. Phung, D. Menzel, M. Grischek, L. Kegelmann, D. Skroblin, C. Gollwitzer, T. Malinauskas, M. Jošt, G. Matič, B. Rech, R. Schlatmann, M. Topič, L. Korte, A. Abate, B. Stannowski, D. Neher, M. Stolterfoht, T. Unold, V. Getautis, S. Albrecht, *Science (80-.).* **2020**, *370*, 1300 LP.
[156] M. Kim, A. Alfano, G. Perotto, M. Serri, N. Dengo, A. Mezzetti, S. Gross, M. Prato, M. Salerno, A. Rizzo, R. Sorrentino, E. Cescon, G. Meneghesso, F. Di Fonzo, A. Petrozza, T. Gatti, F. Lamberti, *Commun. Mater.* **2021**, *2*, 6.
[157] M. De Bastiani, A. J. Mirabelli, Y. Hou, F. Gota, E. Aydin, T. G. Allen, J. Troughton, A. S. Subbiah, F. H. Isikgor, J. Liu, L. Xu, B. Chen, E. Van Kerschaver, D. Baran, B. Fraboni, M. F. Salvador, U. W. Paetzold, E. H. Sargent, S. De Wolf, *Nat. Energy* **2021**, *6*, 167.
[158] S. Sansoni, M. De Bastiani, E. Aydin, E. Ugur, F. H. Isikgor, A. Al-Zahrani, F. Lamberti, F. Laquai, M. Meneghetti, S. De Wolf, *Adv. Mater. Technol.* **2020**, *5*, https://doi.org/10.1002/admt.201901009.
[159] K. K. Wang, Z. Z. Wu, C. J. Peng, K. P. Wang, B. Cheng, C. L. Song, G. R. Han, Y. Liu, *Sol. Energy Mater. Sol. Cells* **2015**, *143*, 198.

Francesco Lamberti obtained his Ph.D. in material sciences and engineering from the University of Padova in 2011. After studying electrochemical biosensors on optically transparent electrodes, he moved to the Italian Institute of Technology (IIT) in Milano, working in the group of Dr. Annamaria Petrozza on the development of perovskite solar cells. Currently, he holds a research position at the University of Padova focusing on thin-film processing for emerging photovoltaics exploiting ultrasonic spraying system.

Zhu-Bing He obtained his Ph.D. in physics and materials science from City University of Hong Kong in 2009. He joined as an associate professor in the Department of Materials Science and Engineering of Southern University of Science and Technology in 2012, after working as a research scientist to develop HIT photovoltaics in industry. Currently, he focuses on interface science and engineering in solar conversion topics, especially high-efficient hybrid and heterojunction solar cells, spectrum splitting and accumulation of solar photons via nanophotonics, and heat transfer in fluid and phase-change materials.

Teresa Gatti holds a master's degree in chemistry from the University of Bologna, Italy (2008) and a Ph.D. in materials engineering from Politecnico di Milano, Italy (2014). After postdoctoral activities at the Department of Chemical Sciences of the University of Padova (Italy), since 2019, she has been a group leader at the Center for Materials Research of the Justus Liebig University Giessen (Germany). Her research interests cover the production, processing, and application in optoelectronic devices of different emerging semiconducting materials, with special attention to species based on noncritical elements and featuring low-environmental impact.

4.6 Publication 5

High Open-Circuit Voltage $Cs_2AgBiBr_6$ Carbon-Based Perovskite Solar Cells via Green Processing of Ultrasonic Spray-Coated Carbon Electrodes from Waste Tire Sources

Authors: **Fabian Schmitz**,* Nicolò Lago,* Luca Fagiolari, Julian Burkhart, Andrea Cester, Andrea Polo, Mirko Prato, Gaudenzio Meneghesso, Silvia Gross, Federico Bella, Francesco Lamberti, Teresa Gatti

*equal contributions as first authors

Most reported $Cs_2AgBiBr_6$-based solar cells possess the regular n-i-p architecture, including an HTM and a metal electrode, often spiro-OMeTAD and gold.[31,37,103,109] The substitution of both layers by a single carbon layer not only dislodges the harmful influence of the former towards the perovskite layer[90,91,238,239] but also strongly reduces the device material and fabrication costs.[240–242] Detailed information about the utilization, the advantages, and the resulting device architectures of carbon electrodes in HTM-free PSCs is shown in the aforementioned chapter "4 HTM-Free PSCs" of **publication 4**. HTM-free $Cs_2AgBiBr_6$-based PSCs with carbon electrodes had already been reported[96,97,99] but since those works were comparative studies in which alkali metals[96] and ionic liquids[99] were introduced into $Cs_2AgBiBr_6$ or $Cs_2AgBiBr_6$ thin films were capped with a polymethyl methacrylate (PMMA) layer,[97] neither elaborated the absent HTM's and electrode's effect on the device performance.

Publication 6 presents the deposition of additive-free carbon electrodes *via* ultrasonic (US) spray-coating of carbon black particles, dispersed in isopropanol (IPA), to fabricate $Cs_2AgBiBr_6$-based solar cells. The carbon black powder for the electrodes is won from 5-year-old waste tires that are ground into pieces of a few centimeters in diameter, treated in H_2SO_4, and then pyrolyzed to obtain particles with an average size of 150 nm. J-V curves of the solar cells reveal a record V_{OC} of 1.293 V. However, its low J_{SC} of 0.5 mA/cm² and poor FF (0.3) result in only 0.19% PCE. To investigate whether those parameters originate from the CBE's low conductivity, a fluorine doped tin oxide (FTO) covered glass substrate is pressed onto the CBE to improve its lateral conductivity. Indeed, the resultant J-V curve possesses enhanced J_{SC} (0.75 mA/cm²) and FF (0.39) while maintaining a high V_{OC} (1.28 V), leading to an increased PCE (0.37%). Furthermore, the solar cells with US spray-coated CBEs are compared with solar cells utilizing screen-printed CBEs. For the screen-printing process, polyvinylpyrrolidone is added to the carbon black dispersion to increase its viscosity. Both CBE deposition methods, USSC and screen-printing, result in almost equal PCEs for the respective solar cells which proves that the former can compete with the latter. Applying the Mott-Gurney model on the current density-voltage (*J-V*) curve, measured under dark conditions, and a modified Sokel-Hughes model on the *J-V* curve, measured under illumination, explains that the high V_{OC} originates from a strong built-in field caused by the presence of an electric dipole at the

perovskite/CBE interface and that the high series resistance of the CBE (8 kΩ) is the reason for the solar cell's low FF.

In conclusion, this work presents an end-of-waste approach to fabricate low-cost, non-toxic "green" $Cs_2AgBiBr_6$ solar cells. The devices possess a record V_{OC} that has not been reported before. Further work must be put into the improvement of the CBE's conductivity which has been identified as the FF-hampering factor, both empirically and through theoretical modelling. In general, their low cost, abundance, inert character towards perovskite thin films, and easy processability have made carbon electrodes alternatives to metal electrodes not only for ($Cs_2AgBiBr_6$) PSCs,[94,243,244] but also for silicon photovoltaics.[245–247]

Nicolò Lago and I contributed equally as the first authors to this publication. Nicolò Lago performed the electrical characterization of the solar cells and created the draft regarding this analysis. I contributed to the introduction, as well as the sample preparation and analysis, including composing the draft about it.

High Open-Circuit Voltage $Cs_2AgBiBr_6$ Carbon-Based Perovskite Solar Cells via Green Processing of Ultrasonic Spray-Coated Carbon Electrodes from Waste Tire Sources

Fabian Schmitz[+,[a, b]] Nicolò Lago[+,[c]] Lucia Fagiolari,[[d]] Julian Burkhart,[[a]] Andrea Cester,[[c]] Andrea Polo,[[c]] Mirko Prato,[[e]] Gaudenzio Meneghesso,[[c, f]] Silvia Gross,[[f, g]] Federico Bella,*[[d]] Francesco Lamberti,*[[f, g]] and Teresa Gatti*[[a, b, d]]

Costs and toxicity concerns are at the center of a heated debate regarding the implementation of perovskite solar cells (PSCs) into commercial products. The first bottleneck could be overcome by eliminating the top metal electrode (generally gold) and the underlying hole transporting material and substituting both with one single thick layer of conductive carbon, as in the so-called carbon-based PSCs (C-PSCs). The second issue, related to the presence of lead, can be tackled by resorting to other perovskite structures based on less toxic metallic components. An interesting case is that of the double perovskite $Cs_2AgBiBr_6$, which at present still lacks the outstanding optoelectronic performances of the lead-based counterparts but is very stable to environmental factors. In this work, the processing of carbon electrodes onto $Cs_2AgBiBr_6$-based C-PSCs was reported, starting from an additive-free isopropanol ink of a carbon material obtained from the hydrothermal recycling of waste tires and employing a high-throughput ultrasonic spray coating method in normal environmental conditions. Through this highly sustainable approach that ensures a valuable step from an end-of-life to an end-of-waste status for used tires, devices were obtained delivering a record open circuit voltage of 1.293 V, which might in the future represent ultra-cheap solutions to power the indoor Internet of Things ecosystem.

Introduction

Lead-based perovskite solar cells (PSCs) experienced a decade of tremendous progress, with power conversion efficiency (PCE) starting at 3.8% in 2009[1] and reaching >25%[2,3] nowadays, due to favorable properties such as high absorption coefficients,[4] defects tolerance,[5] and charge carrier mobility.[6] Additionally, the solution-based preparation of perovskite thin films is rather cost-effective as it requires low temperatures, small amounts of material, and several high-throughput processes, such as roll-to-roll[7,8] and spray-coating[9,10] deposition, can be implemented for their production. However, to complete a direct architecture PSC, a hole transporting material (HTM) as well as a back electrode are required, to achieve efficient devices. HTMs such as the commonly employed 2,2′,7,7′-tetrakis-(*N*,*N*-di-4-methoxyphenylamino)-9,9′-spirobifluorene (spiro-OMeTAD) as well as metal electrodes were identified to play crucial roles in the degradation process of PSCs.[11–14] Furthermore, established HTMs and metallic (mostly gold or silver) electrodes are not only expensive,[15] but the latter are additionally non-abundant materials and have to be deposited through non-scalable vacuum-assisted processes. An

[a] *F. Schmitz,[+] J. Burkhart, Dr. T. Gatti*
Institute of Physical Chemistry
Justus Liebig University
Heinrich-Buff-Ring 17, 35392 Giessen (Germany)
E-mail: teresa.gatti@phys.chemie.uni-giessen.de
[b] *F. Schmitz,[+] Dr. T. Gatti*
Center for Materials Research
Justus Liebig University
Heinrich-Buff-Ring 17, 35392 Giessen (Germany)
[c] *Dr. N. Lago,[+] Prof. A. Cester, A. Polo, Prof. G. Meneghesso*
Department of Information Engineering
University of Padova
Via Gradenigo 6/B, 35131 Padova (Italy)
[d] *Dr. L. Fagiolari, Prof. F. Bella, Dr. T. Gatti*
Department of Applied Science and Technology
Politecnico di Torino
C.so Duca degli Abruzzi 24, 10129 Torino (Italy)
E-mail: federico.bella@polito.it
[e] *Dr. M. Prato*
Materials Characterization Facility
Istituto Italiano di Tecnologia
Via Morego 30, 16163 Genova (Italy)
[f] *Prof. G. Meneghesso, Prof. S. Gross, Dr. F. Lamberti*
Center "Giorgio Levi Cases" for Energy Economics and Technology
Via Marzolo 9, 35131 Padova (Italy)
[g] *Prof. S. Gross, Dr. F. Lamberti*
Department of Chemical Sciences
University of Padova
Via Marzolo 1, 35131 Padova (Italy)
E-mail: francesco.lamberti@unipd.it
[+] *These two authors contributed equally to this work.*

Supporting information for this article is available on the WWW under https://doi.org/10.1002/cssc.202201590

This publication is part of a Special Collection highlighting "The Latest Research from our Board Members". Please visit the Special Collection at chemsuschem.org/collections.

approach that is emerging in the last few years to overcome these drawbacks is to utilize carbon materials,[16] for example carbon black,[17] graphene,[18] or carbon nanotubes,[18,19] as combined HTM and electrode in one single layer. These layers are generally defined as carbon electrodes (CEs) and the resulting photovoltaic devices are named carbon-based PSCs (C-PSCs). CEs are not known to play any role in perovskite degradation and were shown to have an encapsulating effect on PSCs due to their hydrophobicity that can increase device lifetimes.[20,21] Notably, the utilization of CEs as substitution for other HTMs or metal electrodes enables drastic cost reduction for PSC production, due to the high abundancy of carbon (which can even be extracted and processed from waste)[22] and the applicability in solution-based high-throughput processes such as spray-coating.[18,23,24]

Despite their outstanding optoelectronic properties, lead-based PSCs lack environmental stability[25] and present environmental and human risks due to the high toxicity of the lead component.[26] While the substitution of lead(II) with tin(II) or germanium(II) tackles the material toxicity, these elements' tendency to oxidize still significantly hinders device stability.[27] A material that combines both low toxicity and high environmental stability is the double perovskite (DP) $Cs_2AgBiBr_6$, in which the divalent Pb^{2+} is substituted with equimolar amounts of monovalent Ag^+ and trivalent Bi^{3+}. However, due to many sub-optimal properties, such as its large indirect bandgap,[28–30] fast surface charge carrier recombination,[31] and strong electron-phonon coupling and exciton binding energy,[32] the maximum PCEs achieved from PSCs with $Cs_2AgBiBr_6$ as a single absorber rarely exceed 2.8%. Still, a calculated maximum PCE of 7.92% for PSCs based on pristine $Cs_2AgBiBr_6$ underlines the material's large unexploited potential.[33] On the other hand, it is also true that the silver component in this DP is somewhat suffering from scarcity issues.[34] While there might be alternatives to this DP based on more abundant elements, current research on "lead-free" perovskites or perovskite-inspired compounds is very much focusing on it, given its excellent environmental stability and current good level of knowledge about how to produce high-quality thin films from solution processing, making it a sort of benchmark to carry out fundamental and applied studies on this category of materials.[35–37]

Although the indirect bandgap of $Cs_2AgBiBr_6$ is reported as 2–2.2 eV,[28–30] PSCs based on this material have been characterized by open-circuit voltages (V_{OC}) that, to the best of our knowledge, are close to or, in one single case, equal to the 1.2 V threshold.[38] Furthermore, those high values could only be achieved when the DP itself or some interfaces within the device were modified by, for example, substituting the organic HTM with an inorganic CuO_2 layer (1.198 V),[39] doping the perovskite with Li^+ (1.177 V),[40] making use of polymethyl methacrylate (PMMA) as a passivating capping layer between perovskite and a CE (1.180 V),[41] or by capping the perovskite layer with a 2D/3D mixed perovskite phase (1.18 V).[42] All these approaches aimed at improving the energy level alignment at the perovskite/HTM interface, which emphasizes its crucial role for boosting the V_{OC}. The V_{OC} of PSCs that are based on unmodified $Cs_2AgBiBr_6$ has been mostly lower than 1.1 V[9,42,43] and has only surpassed this value when Cu_2O was applied as an HTM[39] or when CEs were used,[40,41] as it could also be observed for lead-based PSCs.[44]

C-PSCs based on the DP have yet been reported only three times: originally, Li et al. achieved a PCE of 1.77% and a 1.119 V V_{OC} for pristine $Cs_2AgBiBr_6$, which could be further improved to 2.57% and 1.177 V by doping the perovskite with small amounts of Li^+.[40] Later, the same authors found that the addition of a thin passivating layer of PMMA enhances the PSC performances of pristine $Cs_2AgBiBr_6$ (2.25%, 1.180 V).[41] Finally, Shao and co-workers have improved the PCE and V_{OC} of $Cs_2AgBiBr_6$-based C-PSCs from 1.73% and 1.13 V to 2.22% and 1.20 V, respectively, by introducing 1-butyl-1-methylpyrrolidinium chloride (BMPyrCl) into the perovskite structure to pin bromide ions, thus inhibiting their migration towards the interface with the CE.[45] In all cases, for the CEs, commercial carbon paste was employed, deposited on the DP photoactive layer from concentrated chlorobenzene (CB) dispersions through screen printing or blade coating.

Herein, we employ ultrasonic (US) spray-coating for the deposition on top of $Cs_2AgBiBr_6$ thin films of additive-free CEs processed from isopropanol (iPA), a green and low-boiling-point solvent, which provides stable to re-aggregation colloidal suspensions of a carbon black like material obtained from the recycling of waste tires.

Considering the big environmental concerns that end-of-life tires abandoned in open fields all over the world are raising, the production of carbon black from them is highly pursued already by many companies worldwide.[46,47] This process, as of today, can only be carried out employing a pyrolysis step at 1500 °C on pre-treated tires;[48] therefore, it is of the utmost importance to find applications for the resulting raw materials that ensure a proper payback of the energy consumed for their production. The demonstration of valuable uses from this waste tire-derived conductive materials is, however, still ongoing at a low technology readiness research level, with examples mostly in the field of energy storage.[48] In optoelectronics, there are, however, no cases reported up to now, to the best of our knowledge.

From the C-PSCs based on the DP absorber and waste tires-derived CE, we obtain a record V_{OC} of 1.293 V, which is the highest reported until now for similar device architectures. Although PCEs remain overall lower than 1%, due to poor fill factor (FF) and short-circuit current density (J_{SC}), the highly sustainable approach that we report for both the CE component preparation and processing will constitute an interesting proof-of-concept from which starts the future realization of better-performing, environmentally friendly lead-free C-PSCs. In particular, we demonstrate a valuable end-of-waste (EoW) for used tires, which will serve as a further model of the possibility to effectively implement a circular economy.

Experimental Section

All solvents were purchased from Sigma-Aldrich and used without further purification. $Cs_2AgBiBr_6$ crystalline powder was hydrothermally synthesized as described in our earlier publication.[49] Powder X-ray diffraction (P-XRD) analysis was carried out through a Panalytical X'Pert MRD Pro diffractometer, equipped with a Cu K_α X-ray source and a curved graphite secondary monochromator. Thermogravimetric analysis (TGA) was performed with a TG 209 F3 Tarsus instrument by Netzsch. X-ray photoelectron spectroscopy (XPS) measurements were conducted with a PHI 5000 VersaProbe II Scanning ESCA Microprobe (Physical Electronics) with monochromatized Al K_α X-ray source in high power mode (beam size 1300 μm × 100 μm, X-ray power: 100 W). Time steps of 50 ms, a step size of 0.2 eV, and an analyzer pass energy of 46.95 eV were used for measuring the detail spectra. The sample surface was charge neutralized with slow electrons and argon ions, and the pressure was in the range from 10^{-7} to 10^{-6} Pa during the measurement. Data analysis was performed using the CasaXPS software. Raman spectroscopy was performed on a Bruker Senterra instrument using a 514 nm laser excitation source. The powder sample was displaced over a silicon slide and then analyzed. Dynamic light scattering (DLS) and Zeta potential (ZP) measurements were carried on a Malvern Zetasizer Nano-ZS device. Grazing incidence X-ray diffraction (GIXRD) measurements were performed in a range of 3–70° (0.05° step size, 0.014° s^{-1} scan speed) with a PANalytical B.V. X'Pert Pro diffractometer using CuK_α1 radiation. The diffraction patterns were measured along the 2θ axis with a grazing incidence of $\omega =$ 0.5°. The sheet resistance of the pure CEs was measured with a four-point probe system (Ossila) controlled by a dedicated software (Ossila Sheet Resistance v2.0.3.3). Scanning electron microscopy (SEM) images were acquired on a Zeiss Merlin instrument operating at a working potential of 20 kV. To calculate the specific surface area, argon physisorption measurements were conducted with an automated gas adsorption station Autosorb iQ2 by Quantachrome Instruments at 87 K by using a cryostat (CryoSync). Prior to the measurements, the samples were degassed in vacuum at 120 °C for 12 h. The surface area was determined using the Brunauer–Emmet–Teller (BET) method as implemented in ASiQwin Version 4.0 from Quantachrome Corporation.

Preparation of the carbon powder from waste tires

A 5-year used car tire (model Powergy, Pirelli) was washed with water, mechanically reduced into crumbs (diameter: 2–2.5 cm) with a high-speed grinder, and subsequently soaked in concentrated H_2SO_4. Temperature was raised up to 125 °C, and the batch was kept warm overnight to yield sulfonated tire rubber. After 15 h, the heating plate was switched off, and the mixture was allowed to reach room temperature. The carbon-based product was filtered and washed twice with deionized water. Of note, the H_2SO_4 solution was re-used seven more times for the same process on other samples before being discarded. The sulfonated tire rubber was dried in the fume hood and then transferred into a tube furnace for the pyrolysis process, which took place under flowing N_2 with a ramp rate of 1 °C min^{-1} up to 450 °C, followed by a 2 °C min^{-1} ramp up to 1500 °C.

C-PSCs fabrication and characterization

$Cs_2AgBiBr_6$ crystalline powder was dissolved in dimethyl sulfoxide (DMSO) in a glovebox under an argon inert atmosphere to obtain a 0.5 M precursor solution left stirring for several hours. Commercial pre-patterned substrates from Solaronix, composed of glass covered by fluorine-doped tin oxide (FTO) and a TiO_2 compact layer, were used for the preparation of planar solar cells. Before PSC preparation, the substrates were heated at 450 °C for 45 min. Substrates were consecutively treated in the UV ozone cleaner for 15 min before being transferred into the glove box. Next, 50 μL precursor solution were spread across the substrate before spin-coating at 4000 rpm for 40 s and finally annealing at 285 °C for 5 min, to prepare $Cs_2AgBiBr_6$ thin films as depicted in Figure 2a. The substrates were then transferred into a ND-SP Mini ultrasonic US spray-coater (Nadetech, Spain) to deposit the CEs under ambient atmosphere. A 0.1 mg mL^{-1} colloidal ink for the CE deposition was prepared by dispersing the carbon powder in iPA by ultrasonication for 15 min (3 s on, 3 s off). The substrates were masked to optimize the electrode shapes (active area 0.14 cm^2), put onto a hotplate, and heated to 100 °C. US spray-coating was conducted with a flow rate of 8.00 mL h^{-1} at a speed of 100.0 mm min^{-1} for 50 and 100 cycles to deposit CEs with a thickness of circa 4 and 8 μm, respectively. The exact pattern followed for the spray deposition is depicted for the sake of clarity in Figure S2 of the Supporting Information. To screen-print CEs, both an iPA- and a CB-based precursor paste were used. The former was prepared by first dissolving 400 mg polyvinylpyrrolidone (PVP, $M = 58000$ g mol^{-1}) in 2 mL iPA, while for the latter 240 mg PMMA ($M = 996000$ g mol^{-1}) was dissolved in 2 mL CB, as a first step. Then, within each mixture further 100 mg of the carbon black powder was dispersed through ball milling for 3 h.

C-PSCs performance was assessed performing current density–voltage (J–V) scans both under dark and under illumination. As a light source, we used a high-power chip-on-board white LED array with an emitting area of 4 cm^2 to guarantee a stable and uniform light spot and a fine tuning of the light intensity for prolonged times. In agreement with the International Electrochemical Commission standard IEC 60904-7-2019, the LED intensity was calibrated at 1 sun for each sample by means of external-quantum-efficiency (EQE) measurements to account for the spectral mismatch between the LED spectrum and the reference spectrum AM1.5G.

Results and Discussion

The carbon-based material used in this work for the preparation of C-PSCs CEs was obtained from a 5-year used car tire. As described in detail in the Experimental Section, tire crumbs were attacked by a re-usable H_2SO_4 solution, washed with water, and pyrolyzed at 1500 °C (Figure 1a). XPS analysis carried out on the synthesized carbon material (Figure 1b) shows the presence of a dominant component from π-conjugated carbon atoms (C=C, graphitic carbon), with minor contributions associated to carbon-based defects and carbon-oxygen species like hydroxyls or epoxides and carbonyls.[50,51] However, these last ones are almost negligible as the oxygen in the sample is only of a few at%. The material appears to be rather defects-rich from Raman analysis (Figure S1a), since the I_D/I_G ratio is slightly higher than 1 (1.09) and allows for an estimation of the graphitic crystallite sizes (L_a) in the material through the Ferrari/Robertson relationship for disordered and amorphous carbon ($I_D/I_G \propto L_a^2$) to be around 1.04 nm.[52,53] Thermal and structural analysis of the carbon powder were carried out and are also shown in Figure S1 in the Supporting Information. From TGA, an overall thermal stability in air of up to 400 °C can be assessed (Figure S1b), thus making this carbon powder a suitable component for thermally stable CEs in C-PSCs. From P-XRD (Figure S1c), a broad peak around $2\theta = 27°$ and a weaker peak

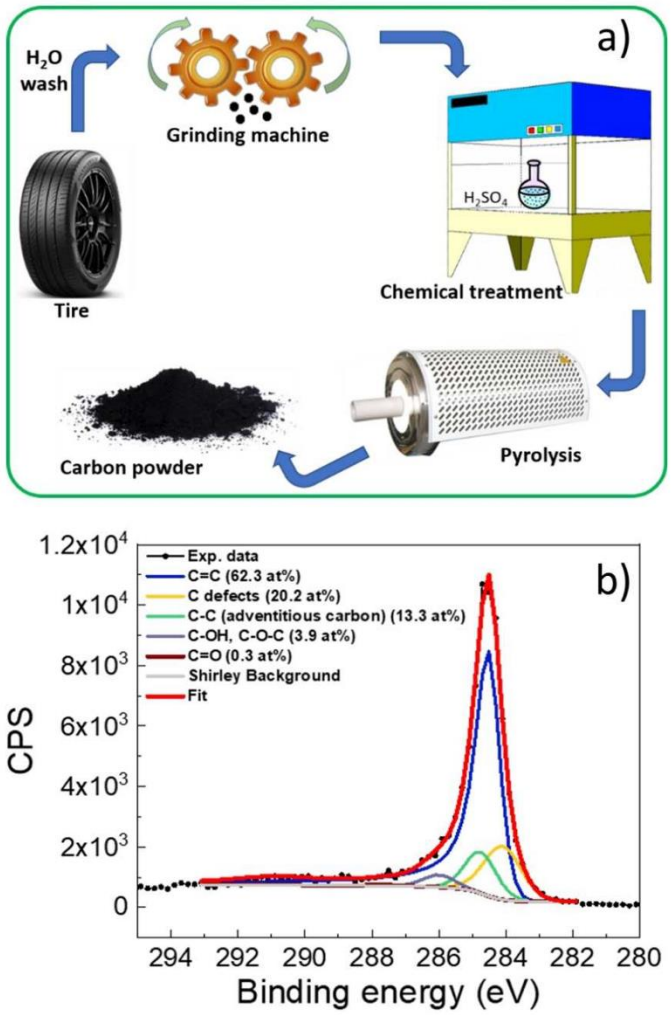

Figure 1. (a) Schematic representation of the process applied for the preparation of the carbon-based material employed as CE component for C-PSCs in the present work, starting from waste tires. (b) XPS spectrum of the C 1 s region of the obtained carbon material.

at $2\theta = 44^\circ$ are detectable, indicating the disordered nature and, overall, the low graphitization of the carbon sheets in the powder sample, respectively. We also calculated the *R* value, that is, the peak height divided by the background at the position of the peak. An *R* value equal to 3.18 was obtained, indicating that the pyrolytic process led to a carbon material bearing a large fraction of parallel graphene layers.[54]

C-PSCs were fabricated by first processing the $Cs_2AgBiBr_6$ DP on the top of compact TiO_2 electron transporting layer (ETL) grown onto transparent FTO glass substrates (as schematized in Figure 2a). The procedure was carried out under an inert atmosphere starting from the pre-synthesized perovskite crystalline powder, as described in the Experimental Section. The obtainment of phase-pure $Cs_2AgBiBr_6$ thin films on the TiO_2 substrates is proved by the GIXRD patterns, reported in Figure S3 (no reflexes of the $Cs_3Bi_2Br_9$ side phase are detected). The films show a compact morphology from top-view SEM images (Figure S4a), with average grain sizes of 340 nm. The perovskite layer thickness was further examined by looking at the cross-section SEM images, reported in Figure S4b. The perovskite film growth on compact TiO_2 shows an average thickness of 220 nm.

To deposit CEs via common methods such as blade coating or screen-printing, the precursor paste must be composed not only of the carbon material itself, but also of polymer additives that assure a certain viscosity to the paste for effective deposition. These additives do not only limit the adjustment of the CE thickness but can also negatively affect the conductivity due to the insulating character of commonly utilized polymer binders. In contrast, the precursor for US spray deposition can

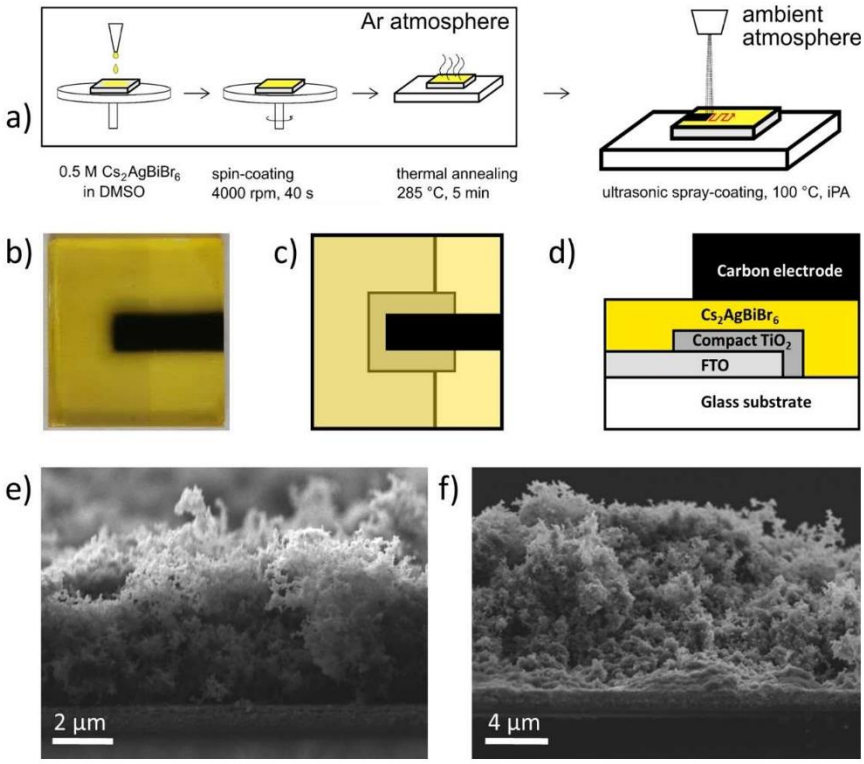

Figure 2. (a) Schematic representation of the preparation process for $Cs_2AgBiBr_6$ based C-PSCs via spin-coating (perovskite layer) and US spray-coating (CE). (b) Picture of the resulting device and (c, d) sketch of the overall architecture from top and cross-section view, respectively. SEM cross-section images of (e) 4 µm and (f) 8 µm-thick CE deposited on top of FTO/TiO_2/$Cs_2AgBiBr_6$ architectures.

consist of the sole carbon material, if these can be dispersed efficiently in a solvent medium, and the thickness of deposited CEs can be finely tuned by a variation of the number of spraying cycles (Figure 2e, f). To proceed with US spray coating, a dispersion of the carbon material in iPA was prepared using tip sonication. A concentration high enough to deposit as much material as possible during the process was chosen to reduce the duration of this step (0.1 mg mL^{-1}). By analyzing the 0.1 mg mL^{-1} carbon dispersion in iPA through DLS (Figure S5), average sizes of 150 nm were found for the dispersed particles and ZP resulted to be around values of −30 mV, indicating negatively charged particles and a good colloidal stability in the additive-free ink. This is surely an advantage for the use in the US spray deposition process, as this lasts for relatively long times and it is necessary to have in the instrument liquid reservoir a suspension that does not undergo precipitation, which would be noxious for the proper functioning of the instrument (clogging of the needle by agglomerated particles could block the process).

The thickness of spray-coated CEs is likely to linearly depend on the number of cycles repeated by the US spray-coater along the defined pattern (see Figure S2 for the exact pattern used). While 50 cycles provided a thickness of around 4 µm for the deposited CE, additional 50 cycles created an 8 µm thick one, as it can be inferred from SEM cross-section images depicted in Figure 2e, f, respectively. Furthermore, the 4 µm-thick CE shows a pronounced aerogel-like morphology, with high porosity, in which the carbon black particles have only small contact to each other. The fact that the CEs could easily be removed from the perovskite by scratching (which is why the CE thicknesses were not measurable by profilometry) supports this observation. While the upper part of the 8 µm-thick CE resembles the same low-density agglomeration as the 4 µm one, the bottom part in direct contact with the perovskite layer has a significantly increased density, which we assume is the result of a collapse of the porous structure due to the electrode own weight and ensures good perovskite/CE contact. In order to obtain an estimation of the specific surface area in the US spray-coated CE, we performed argon physisorption measurements on the carbon black powder (being technically impossible to measure it directly on the deposited electrodes, due to the too low masses). From the application of the BET method, we obtain a surface area for this material of 40 m^2 g^{-1} (see Figure S6). Using this value, we can infer a maximum CE surface area for the 8 µm-thick layer of around 500 cm^2, when considering only the pure powder with no aggregation due to structure collapse. On the other hand, if we had an ideally compact electrode, the overall surface area would be only the

top one (i.e., in this case 0.5 cm^2). With these two extreme cases in mind, we can presume that the 4 μm layer's surface area is close to the calculated maximum value for it (250 cm^2) due to its aerogel-like morphology, while the 8 μm-thick layer must have a lower surface area than the thinner one due to its dense bottom part (thus between 500 and 0.5 cm^2).

The resulting photovoltaic devices were characterized as described in the Experimental Section. First, EQE measurements were performed in order to precisely determine J_{SC} complying with the AM1.5G standard reference. As reported in Figure 3a, the EQE spectrum of a prototypical cell is comprised between 300 and 560 nm, compatible with a bandgap of around 2.2 eV, and two dominant peaks at 366 nm (3.39 eV) and 438 nm (2.83 eV) are visible. Although the contribution at lower energies can be safely ascribed to the photo-generation of charge carriers directly in the $Cs_2AgBiBr_6$ film (maximum absorption of the excitonic feature of $Cs_2AgBiBr_6$ onto compact TiO_2 is located at 438 nm, see Figure S7) the high energy contribution can be tentatively associated to charge photo-generation and separation at the perovskite/TiO_2 interface (TiO_2 energy gap is 3.2 eV).[55] Figure 3b shows the *J–V* characteristics of the best cell performed under dark (red solid line) and under 1 sun illumination (solid blue line) from which a record V_{OC} of 1.293 V is detected. Despite the high V_{OC}, a low PCE (0.19%) results, due to a poor FF (0.3). However, it is important to point out that the here presented C-PSCs feature an active area (0.14 cm^2) that is roughly four times bigger than that used for the champion $Cs_2AgBiBr_6$-based C-PSC present in literature[45] (PCE = 2.2%, active are = 0.04 cm^2). From *J–V* curves recorded under dark, it is possible to notice that the cells do not present shunts and short-circuit paths between FTO and the CE, indicating that this is not the reason for such a low FF.

To understand whether the carbon layer itself is responsible for such low FF, we attempted further engineering of the top contact by gently displacing a clean FTO substrate on top of the CE (the relative EQE spectra are shown in Figure S8 for the sake of completeness). In this way, we obtained the *J–V* curve in Figure 3b (dashed black line), from which an improved efficiency results with respect to the sample with the sole CE as top contact (0.37%). The relevant figures of merit under investigation are the V_{OC} and the FF, because the J_{SC} is hugely dependent on the sample. The outcomes (V_{OC} = 1.28 V, FF = 0.39) show that the compression of the carbon layer given by the FTO electrode strongly affects the conductivity of the top contact CE (i.e., by importantly reducing the contact resistance), thus boosting the FF value, whereas the V_{OC} remains almost unchanged. Therefore, we can safely assume that the carbon layer allows to obtain high V_{OC}, but the top contact architecture needs to be further optimized in order to provide a state-of-the-art photocurrent. In addition, it is clear that the main reason for the low FF is to be identified in the sub-optimal conductivity across the CE and not in the DP absorber itself.

To further verify that the strong PCE limitations that we have encountered are not deriving from the specific US spray coating processing method utilized for the CE, we prepared analogous C-PSCs by depositing the CE via screen-printing, thus resorting to a more conventional approach for the preparation of similar devices.[14] To do this, we could not resort to the relatively diluted ink used for US spray coating but had to prepare a viscous paste of the carbon material in iPA, for which the addition of a polymer binder was strictly necessary (see details in the Experimental Section). We also prepared a second reference CE employing CB as the dispersing medium, which is a better dispersant for the carbon material than iPA, as well as being the solvent normally used to process CEs on top of perovskites, but at the same time is also more toxic and thus less sustainable for industrial processing. Also in this case, we were forced to add a polymer to the mixture to have the suitable viscosity for screen-printing. In contrast to the US spray coated CEs, the SEM cross-sections of the screen-printed CE (see Figure S9) are characterized by a homogeneous and dense morphology in which several single carbon black nanoparticles are observable as well as a thickness of around 2 μm for the iPA-based and 3 μm for the CB-based paste. The increased density is due to the addition of the binders, which work as a glue between carbon black particles, while the film thickness is almost only influenced by the precursor viscosity. Representative *J–V* characteristics obtained for these two types of C-PSCs

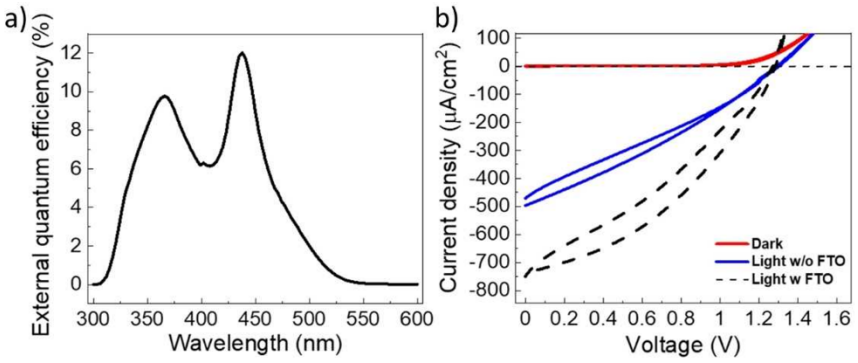

Figure 3. (a) EQE measurement, performed under 1 sun light intensity, from which the calibration value of J_{SC} is extracted. (b) *J–V* characteristics of the cell performed under dark (solid red line), light (solid blue line), and light with another FTO electrode gently displaced on top of CE (dashed black line) conditions.

based on screen-printed CEs are reported in Figure S10. While for the device whose top contact was deposited from CB, PCE is comparable (0.18%) to that obtained from the US spray coating processed one, but with a better FF (0.51), most likely due to higher conductivity in the carbon layer, and slightly lower V_{OC} (1.18 V), for the one screen-printed from the iPA-based paste efficiency drops considerably (0.03%), due to very low J_{SC} and FF. Overall, we can conclude that the US spray coating is a fully comparable method to state-of-the-art ones for the processing of CEs, while at the same time allowing for the use of additive-free inks in non-toxic solvents. Furthermore, when trying to resort to a commercial carbon paste (used as received) to prepare reference devices, we could never obtain suitable *J–V* curves (V_{OC} always below 1 V and S-shapes, which do not allow proper FF evaluation), and for this reason we do not show them here as valuable comparisons for our US spray-coated CEs.

To deeper investigate the performance of the carbon layer used in this study, we performed sheet resistance (R_{sheet}) measurements of the CEs spray coated over a glass substrate. From this characterization, we extracted average value of $R_{sheet} = 2.2\ k\Omega\ square^{-1}$, from which we can estimate the resistivity of the CE to be $\rho = 17\ m\Omega\ m$. This high value of resistivity (compared to $2 \cdot 10^{-5}\ m\Omega\ m$ of gold) produces the important parasitic series resistance that limits carrier extraction, explaining the shape and FF of the curve in Figure 3b. In addition, by looking at the EQE data on samples with and without the additional FTO (Figure S8), we can observe that the addition of FTO improves only the high-frequency contribution to the spectrum (the one related to the TiO_2/perovskite interface), thus confirming the idea that the perovskite/carbon layer interface is not affected by the extra FTO and that, reasonably, the external compression improves the photoelectrons collection by boosting the adhesion of the perovskite layer to the underlying TiO_2 ETL. This result is in agreement with some recent calculations in which a 20% higher stiffness was found for the fully inorganic $Cs_2AgBiBr_6$ perovskite with respect to the classical organic–inorganic methylammonium–lead-iodide perovskite.[56]

Within this scenario, the main question still to be answered is how to correlate the high V_{oc} value found for the C-PSCs based on US spray coated CEs with the device architecture. One possible explanation can be obtained by analyzing the performance of the devices under dark conditions: in this way, the eventual presence of electrical dipoles at the perovskite/CE interface can be studied through the application of proper modelling. Therefore, in order to understand the energy level alignment between the CE and $Cs_2AgBiBr_6$, we performed dark *J–V* measurement from −1.5 to +1.5 V. Figure 4a highlights the rectifying behavior of our cells that displays a strong asymmetry between positive and negative voltages, indicating the formation of a strong built-in potential (V_{bi}) formed within the $Cs_2AgBiBr_6$ layer. Accordingly, the current density under dark

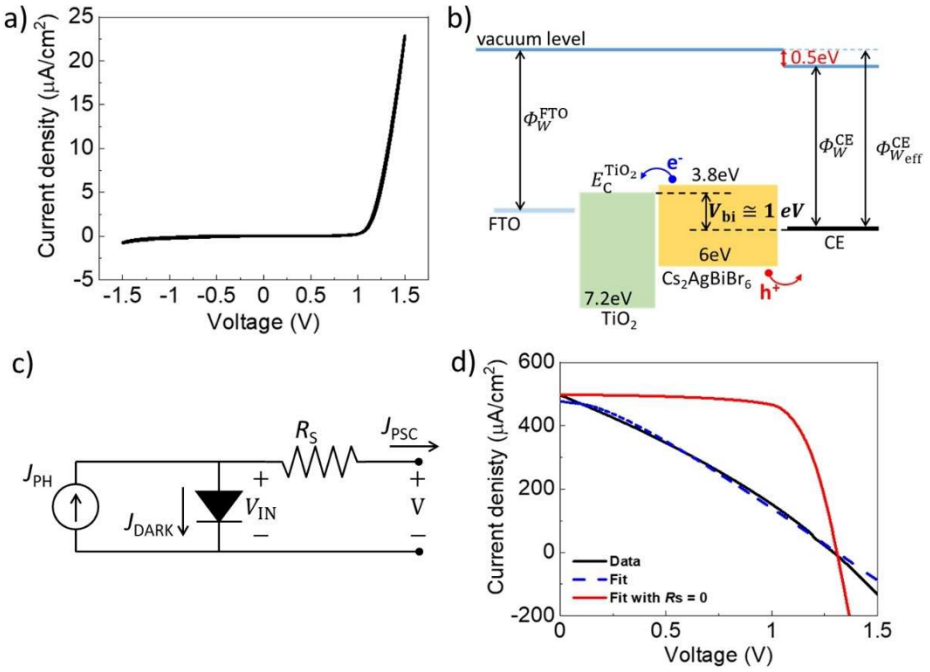

Figure 4. (a) *J–V* characteristics of a C-PSC based on a US spray coated CE from −1.5 to 1.5 V measured under dark conditions. (b) Proposed energy band diagram for the FTO/TiO_2/$Cs_2AgBiBr_6$/CE architecture under flat-band conditions. Valence and conduction bands values for the perovskite are average values according to literature.[40,43,63,64] (c) Lumped equivalent circuit model of the tested PSCs under illumination. (d) Comparison between under illumination *J–V* data and our model: the black solid line is the measured current; the blue dotted line is the numerical fitting applying the model; the red solid line is a model simulation with $R_S = 0\ \Omega$.

conditions (J_{DARK}) can be described by the Mott–Gurney model [Eq. (1)]:[57]

$$J_{DARK}\ [V] = \frac{9}{8}\varepsilon_r\varepsilon_0\mu\frac{(V - V_{bi})^2}{L^3} \quad (1)$$

Where ε_0 is the vacuum permittivity, $\varepsilon_r = 6.1$ is the $Cs_2AgBiBr_6$ relative permittivity,[58] μ is the carrier mobility, and L is the thickness of the perovskite layer, which is 220 nm in our samples (estimated from SEM cross section images in Figure 2e, f).

Equation (1) can be applied to the data in Figure 4a, leading to the estimation of V_{bi} as well as the carrier mobility (in the order of 10^{-6}–10^{-5} $cm^2 V s^{-1}$). Neglecting the voltage drop on the TiO_2 layer and on the $TiO_2/Cs_2AgBiBr_6$ interface, V_{bi} is defined as [Eq. (2)]:

$$V_{bi} = \Phi^{CE}_{W_{eff}} - E^{TiO_2}_C \quad (2)$$

where $E^{TiO_2}_C$ is the conduction band of TiO_2, and $\Phi^{CE}_{W_{eff}}$ is the effective work function of the CE. From *J–V* curve under dark, we measured $V_{bi} = 1$ V and, assuming $E^{TiO_2}_C \cong 4$ eV,[55,59] we can estimate $\Phi^{CE}_{W_{eff}} = V_{bi} + E^{TiO_2}_C = 5$ eV.

For CEs, a work function of $\Phi^{CE}_W \cong 4.5$ eV is typically reported,[60] indicating the presence of an electric dipole at the $Cs_2AgBiBr_6$/CE interface ($\approx$0.5 eV) that contributes to explain the high V_{OC} found in our cells. Figure 4b shows the proposed scenario that justifies the experimental data. However, it is already known from literature that such inorganic double perovskite allows to generally obtain high V_{OC} (1.20 V is the record value as of today to the best of our knowledge, obtained not on the pure double perovskite but after the addition of the ionic liquid BMPyrCl to pin bromide ions),[45] and the reasons are normally ascribed to the very good alignment between the perovskite and the HTM. In addition, recent relevant literature further asserts that V_{bi} itself is the main cause of a high V_{OC};[61] therefore, even considering the band alignment between the CE and the double perovskite valence/conduction band in our architecture, we can further confirm the validity of our previous discussion.

To further support our findings, we developed a qualitative model to describe the obtained *J–V* characteristics. As sketched in Figure 4c, the PSC current (J_{PSC}) of an illuminated device is given by two contributions (namely, the photo-generated current J_{PH} minus the dark current J_{DARK}):

$$J_{PSC}\ [V] = J_{PH}\ [V_{IN}] - J_{DARK}\ [V_{IN}] \quad (3)$$

Where V_{IN} is the internal C-PSC voltage that differs from the applied potential V by the voltage drop across the series resistance R_S [i.e., $V_{IN} = V - R_S J_{PSC}(V)$]. In our modelling, R_S is a lumped parameter used to describe the distributed resistivity of the extracting contacts, thus avoiding the complexity of finite element computation.[62]

J_{PH} can be describe by a modified Sokel–Hughes model,[65] particularly suited for materials with low conductivity. Furthermore, based on the band diagram in Figure 4b, we can assume that the TiO_2 layer acts as a selective contact for electrons, thus J_{PH} can be written as Equation (4):

$$J_{PH}\ [V_{IN}] = qGL\left[\frac{1}{1 - \exp\left(\frac{V_{IN} - V_{FB}}{k_B T/q}\right)} + \frac{k_B T/q}{V_{IN} - V_{FB}}\right] \quad (4)$$

where q is the electrons charge, k_B the Boltzmann constant, T the absolute temperature in K, G is the photo-generation rate of free charges, and V_{FB} is the quasi-flat band voltage corresponding to the condition of zero electric-field in the bulk of the $Cs_2AgBiBr_6$ layer, and, ideally, we can assume that $V_{OC} = V_{FB}$.

Figure 4d shows the resulting fitting of experimental applying the model already described, allowing the estimation of the photocurrent parameters $G = 1.4 \times 10^{20}$ $cm^{-3} s^{-1}$ (a value in agreement with the methyl ammonium lead iodide perovskite)[66] and $V_{FB} = 1.3$ V.

Notably, the flat-band voltage is larger than the V_{bi} estimated by *J–V* measurements under dark conditions. This is consistent with previous findings showing that, under illumination, the accumulation of mobile ions at the anode and cathode interfaces increases the internal electric field;[67] therefore, higher flat-band voltages are expected under illumination explaining the high V_{OC} in our cells.

The proposed model also highlights the importance of the resistivity of the extracting contacts described by the in-series lumped resistance R_S, which we calculated to be around 8 kΩ. Such resistance is the main contribution responsible for the low FF of our cells. In fact, we can use our model to simulate an ideal scenario by setting $R_S = 0\ \Omega$ (without changing the previously fitted parameters) and the performance of the cell would drastically improve. In particular, from our simulation we can estimate an ideal FF as high as 76%, pointing out the need of improving the conductivity of selective contacts to increase the performance of $Cs_2AgBiBr_6$-based cells and architectures.

Conclusions

In this work, we describe the ultrasonic (US) spray deposition of carbon electrodes (CEs) on top of $Cs_2AgBiBr_6$-based carbon perovskite solar cells (C-PSCs) employing a highly sustainable ink, containing a carbon black like material obtained from the recycling of waste tires, thus also implementing a virtuous concept of the circular economy. In this way, we both ensure a suitable end-of-waste for a highly environmentally cumbersome end-of-life product and, given the proposed use in renewable energy harvesting devices, we also prospect an effective payback of the energy necessary to produce such electrode material.

From the resulting devices, we achieve a very high open-circuit voltage (the current record for PSCs containing this double perovskite light absorber, to the best of our knowledge), while the other figures of merit still lag behind the state-of-the-

art for analogous architectures prepared by others through more classical blade coating or screen-printing methods. These approaches, however, always resort to toxic solvents and polymeric additives, which are completely avoided in the present work. On the other hand, electrical conductivity in the US spray-coated CEs will require improvement through the possible addition of conductive additives like carbon nanotubes or graphene, which will be the subject of future investigations aimed at increasing the overall power conversion efficiency. Similar C-PSC devices, with relatively modest performances but extremely low costs of production and toxicity issues, might have an actual economic impact for powering many of the technological items belonging to the burgeoning Internet of Things ecosystem.[35,68]

Acknowledgements

T. G. would like to acknowledge financial support of the European commission through the H2020 FET-PROACTIVE-EIC-07-2020 project LIGHT-CAP (project number 101017821) and of the Deutsche Forschungsgemeinschaft (DFG, German Research Foundation) through the project GA 3052/1-1. N. L. and A. C. thank financial support of the Italian project "Bifacial Efficient Solar cell Technology with 4 terminal architecture for Utility scale" – BEST4U (PONARS01_00519). Open Access funding enabled and organized by Projekt DEAL.

Conflict of Interest

The authors declare no conflict of interest.

Data Availability Statement

The data that support the findings of this study are available from the corresponding author upon reasonable request.

Keywords: carbon electrodes · lead-free · perovskite solar cells · photovoltaics · sustainable chemistry

[1] A. Kojima, K. Teshima, Y. Shirai, T. Miyasaka, *J. Am. Chem. Soc.* **2009**, *131*, 6050–6051.
[2] J. J. Yoo, G. Seo, M. R. Chua, T. G. Park, Y. Lu, F. Rotermund, Y. K. Kim, C. S. Moon, N. J. Jeon, J. P. Correa-Baena, V. Bulović, S. S. Shin, M. G. Bawendi, J. Seo, *Nature* **2021**, *590*, 587–593.
[3] J. Jeong et al., *Nature* **2021**, *592*, 381–385.
[4] S. De Wolf, J. Holovsky, S. J. Moon, P. Löper, B. Niesen, M. Ledinsky, F. J. Haug, J. H. Yum, C. Ballif, *J. Phys. Chem. Lett.* **2014**, *5*, 1035–1039.
[5] J. Kang, L. W. Wang, *J. Phys. Chem. Lett.* **2017**, *8*, 489–493.
[6] L. M. Herz, *ACS Energy Lett.* **2017**, *2*, 1539–1548.
[7] K. Hwang, Y. S. Jung, Y. J. Heo, F. H. Scholes, S. E. Watkins, J. Subbiah, D. J. Jones, D. Y. Kim, D. Vak, *Adv. Mater.* **2015**, *27*, 1241–1247.
[8] N. L. Chang, A. W. Y. Ho-Baillie, D. Vak, M. Gao, M. A. Green, R. J. Egan, *Sol. Energy Mater. Sol. Cells* **2018**, *174*, 314–324.
[9] N. Daem, J. Dewalque, F. Lang, A. Maho, G. Spronck, C. Henrist, P. Colson, S. D. Stranks, R. Cloots, *Solar RRL* **2021**, *5*, 2100422.
[10] A. T. Barrows, A. J. Pearson, C. K. Kwak, A. D. F. Dunbar, A. R. Buckley, D. G. Lidzey, *Energy Environ. Sci.* **2014**, *7*, 2944–2950.
[11] Z. Hawash, L. K. Ono, Y. Qi, *Adv. Mater. Interfaces* **2018**, *5*, 1700623.
[12] N. N. Shlenskaya, N. A. Belich, M. Grätzel, E. A. Goodilin, A. B. Tarasov, *J. Mater. Chem. A* **2018**, *6*, 1780–1786.
[13] F. Lamberti, T. Gatti, E. Cescon, R. Sorrentino, A. Rizzo, E. Menna, G. Meneghesso, M. Meneghetti, A. Petrozza, L. Franco, *Chem* **2019**, *5*, 1806–1817.
[14] F. Lamberti, F. Schmitz, W. Chen, Z. He, T. Gatti, *Solar RRL* **2021**, *5*, 2100514.
[15] L. Hajikhanmirzaei, H. Shahroosvand, B. Pashaei, G. D. Monache, M. K. Nazeeruddin, M. Pilkington, *J. Mater. Chem. C* **2020**, *8*, 6221–6227.
[16] L. Fagiolari, F. Bella, *Energy Environ. Sci.* **2019**, *12*, 3437–3472.
[17] Q. Q. Chu, Z. Sun, B. Ding, K. sik Moon, G. J. Yang, C. P. Wong, *Nano Energy* **2020**, *77*, 105110.
[18] R. Chen, Y. Feng, L. Jing, M. Wang, H. Ma, J. Bian, Y. Shi, *J. Mater. Chem. C* **2021**, *9*, 3546–3554.
[19] M. Guo, J. Liu, Y. Yuan, Z. Zhang, S. Yin, J. Leng, N. Huang, *J. Photochem. Photobiol. A* **2020**, *403*, 112843.
[20] Y. Wu, S. Wang, T. Ouyang, W. Li, M. Chen, Y. Lu, P. Qi, Y. Tang, *Nanotechnology* **2021**, *32*, 225701.
[21] G. Zhang, P. Xie, Z. Huang, Z. Yang, Z. Pan, Y. Fang, H. Rao, X. Zhong, *Adv. Funct. Mater.* **2021**, *31*, 2011187.
[22] H. Liu, Y. Xie, P. Wei, W. Wang, H. Chen, C. Geng, Y. Qiang, *J. Alloys Compd.* **2020**, *842*, 155851.
[23] C. Zhang, S. Wang, H. Zhang, Y. Feng, W. Tian, Y. Yan, J. Bian, Y. Wang, S. Jin, S. M. Zakeeruddin, M. Grätzel, Y. Shi, *Energy Environ. Sci.* **2019**, *12*, 3585–3594.
[24] C. Wu, K. Wang, Y. Jiang, D. Yang, Y. Hou, T. Ye, C. S. Han, B. Chi, L. Zhao, S. Wang, W. Deng, S. Priya, *Adv. Funct. Mater.* **2021**, *31*, 2006803.
[25] M. Li, H. Li, J. Fu, T. Liang, W. Ma, *J. Phys. Chem. C* **2020**, *124*, 27251–27266.
[26] P. Su, Y. Liu, J. Zhang, C. Chen, B. Yang, C. Zhang, X. Zhao, *J. Phys. Chem. Lett.* **2020**, *11*, 2812–2817.
[27] M. Wang, W. Wang, B. Ma, W. Shen, L. Liu, K. Cao, S. Chen, W. Huang, in *Lead-Free Perovskite Materials for Solar Cells*, Springer Singapore, **2021**.
[28] E. T. McClure, M. R. Ball, W. Windl, P. M. Woodward, *Chem. Mater.* **2016**, *28*, 1348–1354.
[29] K. Z. Du, W. Meng, X. Wang, Y. Yan, D. B. Mitzi, *Angew. Chem. Int. Ed.* **2017**, *56*, 8158–8162; *Angew. Chem.* **2017**, *129*, 8270–8274.
[30] F. Igbari, R. Wang, Z. K. Wang, X. J. Ma, Q. Wang, K. L. Wang, Y. Zhang, L. S. Liao, Y. Yang, *Nano Lett.* **2019**, *19*, 2066–2073.
[31] D. Bartesaghi, A. H. Slavney, M. C. Gélvez-Rueda, B. A. Connor, F. C. Grozema, H. I. Karunadasa, T. J. Savenije, *J. Phys. Chem. C* **2018**, *122*, 4809–4816.
[32] R. Kentsch, M. Scholz, J. Horn, D. Schlettwein, K. Oum, T. Lenzer, *J. Phys. Chem. C* **2018**, *122*, 25940–25947.
[33] C. N. Savory, A. Walsh, D. O. Scanlon, *ACS Energy Lett.* **2016**, *1*, 949–955.
[34] G. Schileo, G. Grancini, *J. Mater. Chem. C* **2021**, *9*, 67–76.
[35] Y. Peng, T. N. Huq, J. Mei, L. Portilla, R. A. Jagt, L. G. Occhipinti, J. L. MacManus-Driscoll, R. L. Z. Hoye, V. Pecunia, *Adv. Energy Mater.* **2021**, *11*, 2002761.
[36] V. Pecunia, L. G. Occhipinti, A. Chakraborty, Y. Pan, Y. Peng, *APL Mater.* **2020**, *8*, 100901.
[37] Z. Jin, Z. Zhang, J. Xiu, H. Song, T. Gatti, Z. He, *J. Mater. Chem. A* **2020**, *8*, 16166–16188.
[38] J. Li, X. Meng, Z. Wu, Y. Duan, R. Guo, W. Xiao, Y. Zhang, Y. Li, Y. Shen, W. Zhang, G. Shao, *Adv. Funct. Mater.* **2022**, *32*, 2112991.
[39] B. Xiao, Y. Tan, Z. Yi, Y. Luo, Q. Jiang, J. Yang, *ACS Appl. Mater. Interfaces* **2021**, *13*, 37027–37034.
[40] J. Li, J. Duan, J. Du, X. Yang, Y. Wang, P. Yang, Y. Duan, Q. Tang, *ACS Appl. Mater. Interfaces* **2020**, *12*, 47408–47415.
[41] J. Li, F. Yan, P. Yang, Y. Duan, J. Duan, Q. Tang, *Solar RRL* **2021**, *6*, 2100791.
[42] M. T. Sirtl, R. Hooijer, M. Armer, F. G. Ebadi, M. Mohammadi, C. Maheu, A. Weis, B. T. van Gorkom, S. Häringer, R. A. J. Janssen, T. Mayer, V. Dyakonov, W. Tress, T. Bein, *Adv. Energy Mater.* **2022**, *12*, 2103215.
[43] E. Greul, M. L. Petrus, A. Binek, P. Docampo, T. Bein, *J. Mater. Chem. A* **2017**, *5*, 19972–19981.
[44] Q. Q. Chu, B. Ding, Q. Qiu, Y. Liu, C. X. Li, C. J. Li, G. J. Yang, B. Fang, *J. Mater. Chem. A* **2018**, *6*, 8271–8279.
[45] J. Li, X. Meng, Z. Wu, Y. Duan, R. Guo, W. Xiao, Y. Zhang, Y. Li, Y. Shen, W. Zhang, G. Shao, *Adv. Funct. Mater.* **2022**, *32*, 2112991.
[46] K. Formela, *Adv. Ind. Eng. Polym. Res.* **2021**, *4*, 209–222.
[47] S. Dabic-Miletic, V. Simic, S. Karagoz, *Environ. Sci. Pollut. Res. Int.* **2021**, *28*, 68053–68070.
[48] C. Sathiskumar, S. Karthikeyan, *Sustain. Mater. Technol.* **2019**, *22*, e00125.

[49] F. Schmitz, K. Guo, J. Horn, R. Sorrentino, G. Conforto, F. Lamberti, R. Brescia, F. Drago, M. Prato, Z. He, U. Giovanella, F. Cacialli, D. Schlettwein, D. Meggiolaro, T. Gatti, *J. Phys. Chem. Lett.* **2020**, *11*, 8893–8900.
[50] K. Ganesan, S. Ghosh, N. Gopala Krishna, S. Ilango, M. Kamruddin, A. K. Tyagi, *Phys. Chem. Chem. Phys.* **2016**, *18*, 22160–22167.
[51] D. J. Morgan, *C* **2021**, *7*, 51, https://www.mdpi.com/journal/carbon.
[52] A. C. Ferrari, J. Robertson, *Phys. Rev. B* **2000**, *61*, 14095–14107.
[53] D. B. Schuepfer, F. Badaczewski, J. M. Guerra-Castro, D. M. Hofmann, C. Heiliger, B. Smarsly, P. J. Klar, *Carbon* **2020**, *161*, 359–372.
[54] P. Puech, A. Dabrowska, N. Ratel-Ramond, G. L. Vignoles, M. Monthioux, *Carbon* **2019**, *147*, 602–611.
[55] H. Fan, Z. Yang, X. Ren, M. Yin, F. Gao, S. Liu, *AIP Adv.* **2016**, *6*, 15314.
[56] L. Dong, S. Sun, Z. Deng, W. Li, F. Wei, Y. Qi, Y. Li, X. Li, P. Lu, U. Ramamurty, *Comput. Mater. Sci.* **2018**, *141*, 49–58.
[57] N. F. Mott, R. W. Gurney, in *Electronic Processes in Ionic Crystals*, Clarendon Press, **1948**.
[58] P. R. Varadwaj, *Nanomater.* **2020**, *10*, 973.
[59] J. Fujisawa, T. Eda, M. Hanaya, *Chem. Phys. Lett.* **2017**, *685*, 23–26.
[60] A. Ilie, A. Hart, A. J. Flewitt, J. Robertson, W. I. Milne, *J. Appl. Phys.* **2000**, *88*, 6002–6010.
[61] O. J. Sandberg, J. Kurpiers, M. Stolterfoht, D. Neher, P. Meredith, S. Shoaee, A. Armin, *Adv. Mater. Interfaces* **2020**, *7*, 2000041.
[62] M. W. Denhoff, N. Drolet, *Sol. Energy Mater. Sol. Cells* **2009**, *93*, 1499–1506.
[63] C. Wu, Q. Zhang, Y. Liu, W. Luo, X. Guo, Z. Huang, H. Ting, W. Sun, X. Zhong, S. Wei, S. Wang, Z. Chen, L. Xiao, *Adv. Sci.* **2018**, *5*, 1700759.
[64] M. Pantaler, K. T. Cho, V. I. E. Queloz, I. García Benito, C. Fettkenhauer, I. Anusca, M. K. Nazeeruddin, D. C. Lupascu, G. Grancini, *ACS Energy Lett.* **2018**, *3*, 1781–1786.
[65] R. Sokel, R. C. Hughes, *J. Appl. Phys.* **1982**, *53*, 7414–7424.
[66] T. S. Sherkar, C. Momblona, L. Gil-Escrig, J. Ávila, M. Sessolo, H. J. Bolink, L. J. A. Koster, *ACS Energy Lett.* **2017**, *2*, 1214–1222.
[67] F. Ebadi, M. Aryanpour, R. Mohammadpour, N. Taghavinia, *Sci. Rep.* **2019**, *9*, 11962.
[68] V. Pecunia, L. G. Occhipinti, R. L. Z. Hoye, *Adv. Energy Mater.* **2021**, *11*, 2100698.

Manuscript received: August 19, 2022
Revised manuscript received: September 7, 2022
Accepted manuscript online: September 8, 2022

ChemSusChem

Supporting Information

High Open-Circuit Voltage $Cs_2AgBiBr_6$ Carbon-Based Perovskite Solar Cells via Green Processing of Ultrasonic Spray-Coated Carbon Electrodes from Waste Tire Sources

Fabian Schmitz[+], Nicolò Lago[+], Lucia Fagiolari, Julian Burkhart, Andrea Cester, Andrea Polo, Mirko Prato, Gaudenzio Meneghesso, Silvia Gross, Federico Bella,* Francesco Lamberti,* and Teresa Gatti*

Table of Contents

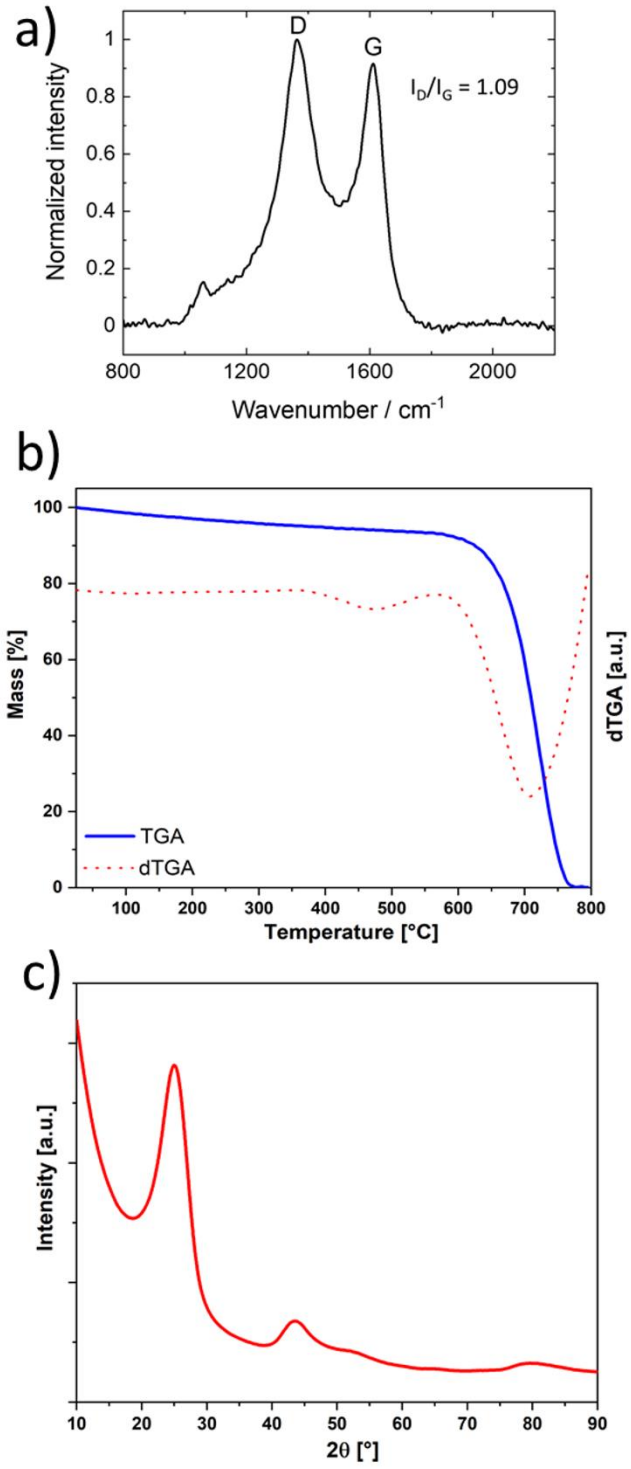

Figure S1. a) Raman plot, b) TGA thermogram and c) P-XRD trace for tire-derived carbon black.

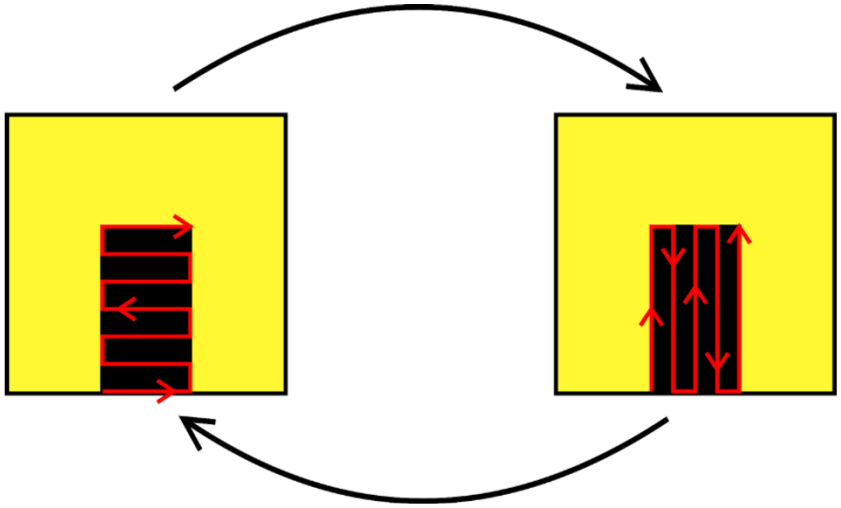

Figure S2. CE US deposition pattern on top of the FTO/TiO_2/$Cs_2AgBiBr_6$ direct PSC architecture.

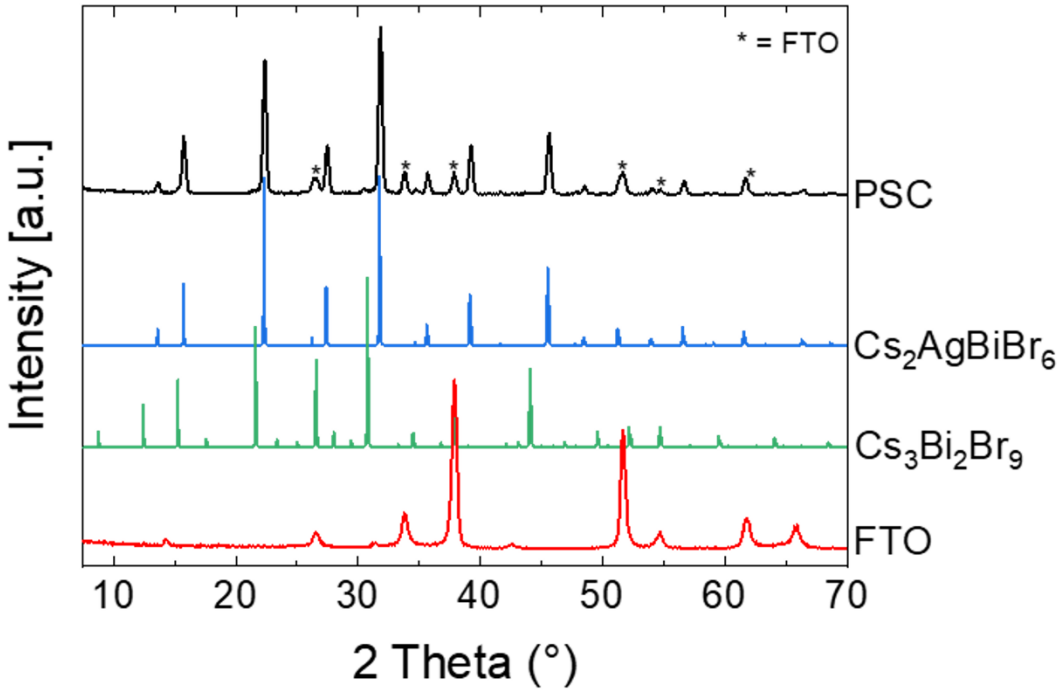

Figure S3. GIXRD pattern of the FTO/TiO_2/$Cs_2AgBiBr_6$/CE C-PSC. The measured GIXRD pattern for the FTO substrate and the theoretical patterns of the $Cs_2AgBiBr_6$ double perovskite and of the typical side-phase $Cs_3Bi_2Br_9$ are also reported for the sake of comparison, showing that no side phase is present (or at least detectable) in the solar cell architecture.

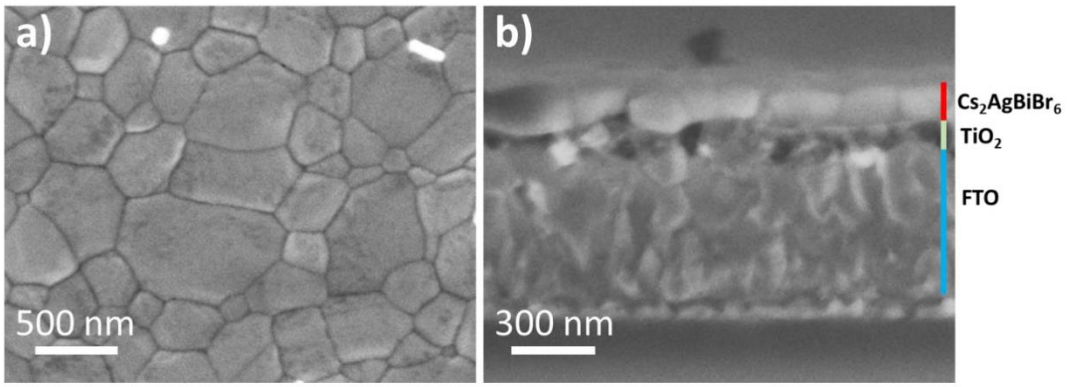

Figure S4. Top-view a) and cross-section b) SEM images of the $Cs_2AgBiBr_6$ double perovskite thin film processed on top of a FTO/compact TiO_2 substrate.

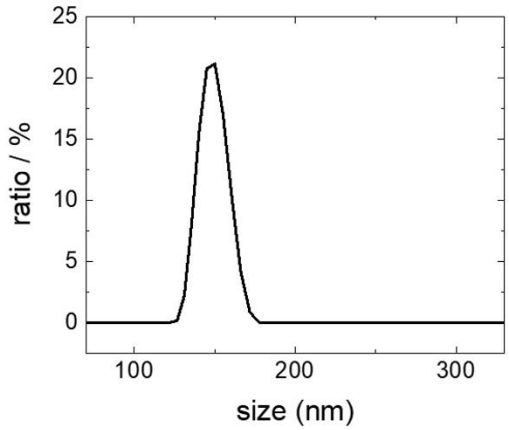

Figure S5. DLS spectrum of the 0.1 mg/mL carbon ink in iPA prepared after tip-sonication and used for US spray coating.

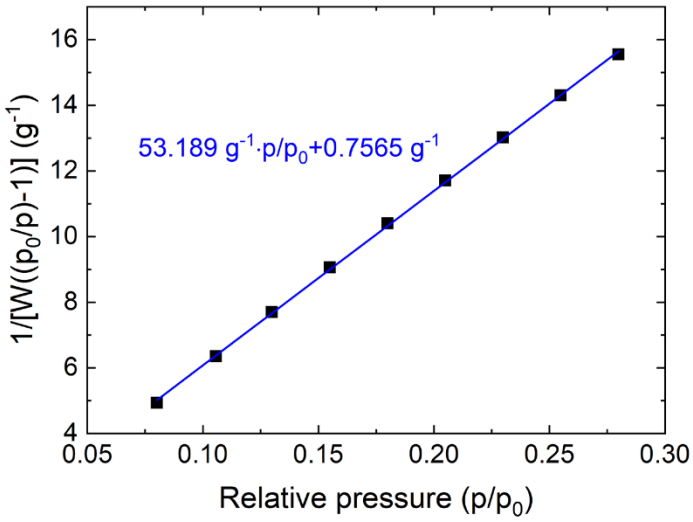

Figure S6. Argon physisorption measurements (black dots) and BET fit (blue) to calculate the specific surface area of the carbon black powder.

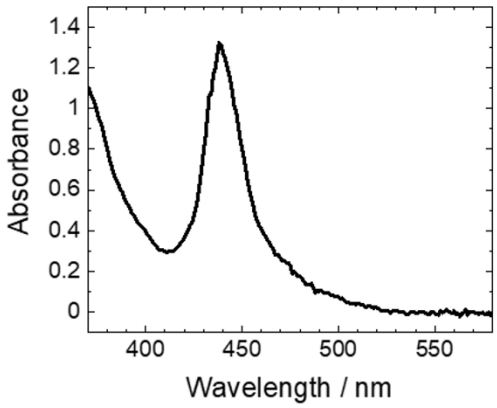

Figure S7. UV-visible absorption spectrum of the FTO/TiO_2/$Cs_2AgBiBr_6$ junction.

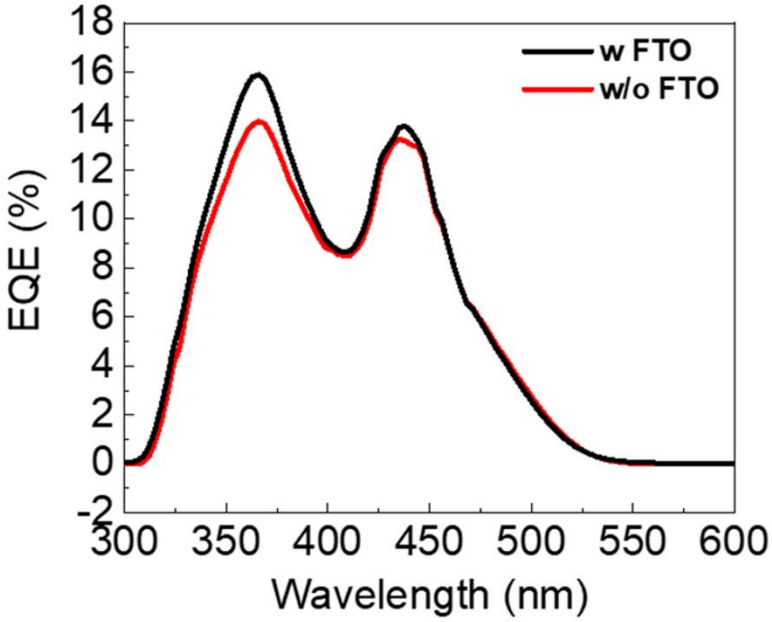

Figure S8. EQE spectra of a FTO/TiO2/$Cs_2AgBiBr_6$/CE C-PSC with and without application of a clean FTO electrode on top of the CE.

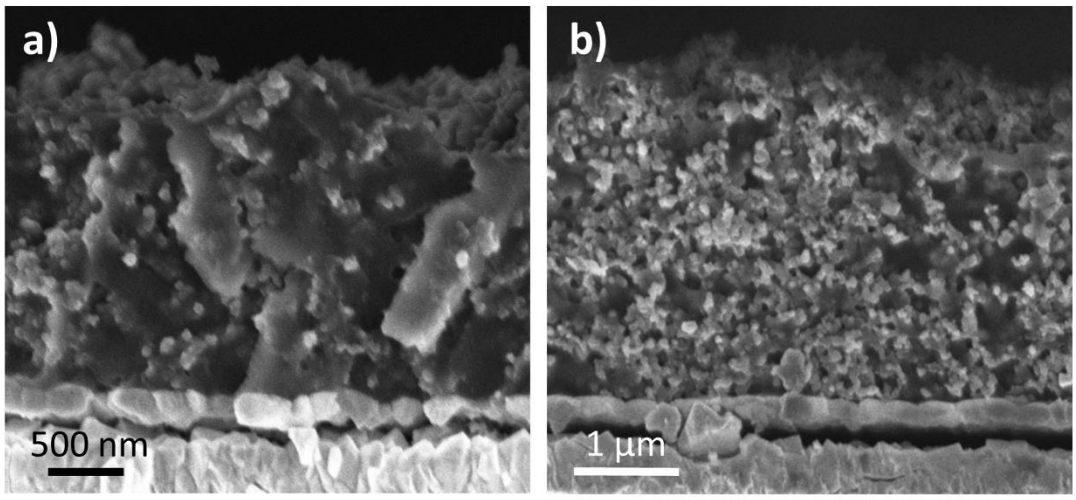

Figure S9. SEM cross-section images of C-PSCs based on screen-printed CEs prepared from a) iPA/PVP/carbon paste and b) CB/PMMA/carbon paste.

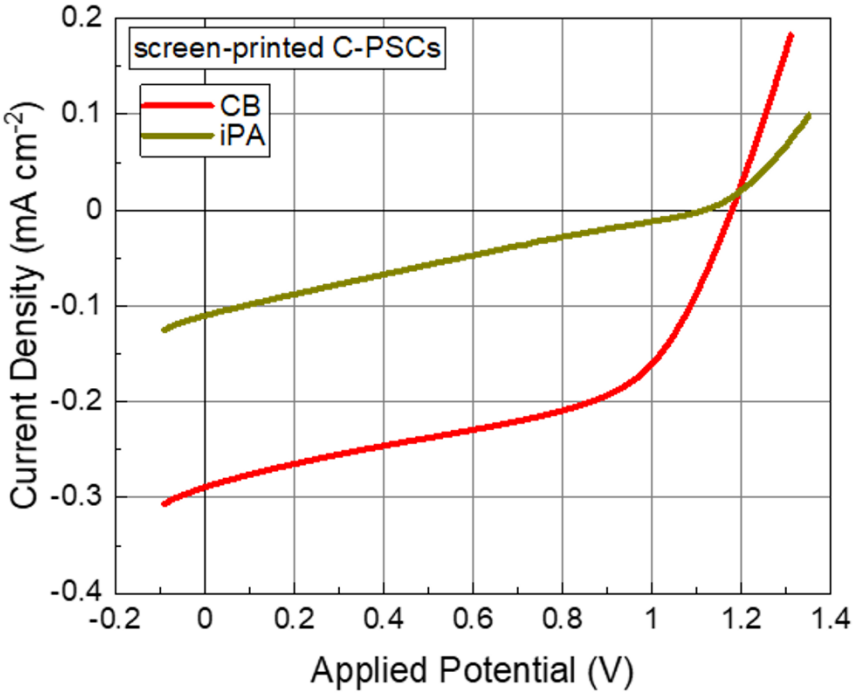

Figure S10. Prototypical J-V characteristics for C-PSCs based on screen-printed CEs prepared from iPA and CB pastes.

4.7 Publication 6

Heavy pnictogens-based perovskite-inspired materials: sustainable light-harvesters for indoor photovoltaics

Authors: **Fabian Schmitz**, Ribhu Bhatia, Francesco Lamberti, Simone Meloni, Teresa Gatti

Their easy bandgap tunability results in the enormous utility of LHPs as light-harvesting materials under any given spectral conditions. For example, LHPs find application in solar cells that power satellites or spacecrafts[248,249] and which must, unlike terrestrial devices, resist harsh, unfiltered radiation. Furthermore, besides single junction solar cells, they are also used in tandem solar cells.[250–252] Thus, it is no surprise that LHPs can also be designed to harvest light from indoor illumination, stemming from white light-emitting diodes (WLEDs), fluorescent lamps, or diffuse sunlight.[253–257] Most prominently, indoor photovoltaics could be used to charge battery-powered, remote Internet of Things (IoT) devices.[184,258] However, since many indoor IoT devices are, unlike outdoor photovoltaics, frequently handled by workers or touched by customers, e.g., smart supermarket labels, the presence of toxic lead can pose a high risk for human health. Lead-free alternative materials could strongly reduce the health hazards of such devices.

Publication 6 reviews lead-free perovskite-inspired materials (PIMs) for application in indoor photovoltaics, with a detailed focus on recent progress (at the time when the work was published) on the pnictogen-based PIMs $Cs_2AgBiBr_6$, $Cs_3Sb_2I_{9-x}Cl_x$, and BiOI. PIMs are materials that possess a similar electronic character as LHPs although their ionic structure deviates from the perovskite structure. Accordingly, this work first elaborates on the ionic and electronic structures of LHPs, especially the bandgap tunability and defect tolerance of LHPs, as well as the conditions under which indoor photovoltaics are operated. Those properties are then compared with theoretical calculations of the described PIMs in the theoretical background part. Finally, the status quo of the research for each PIM is described in detail in their respective chapters, describing synthesis routes, and the progress of photovoltaics based on those three materials. Not only applications are reviewed for indoor light harvesters but also the latest studies on solar cells made from $Cs_2AgBiBr_6$, $Cs_3Sb_2I_{9-x}Cl_x$, and BiOI, as well as strategies that show the potential to boost the performance of indoor photovoltaics such as bandgap engineering.

To this review, my co-authors contributed the chapters “II. Theoretical Background”, “IV. Emerging PIMs: The case of the BiOI oxyhalide”, and “V. Emerging PIMs: The case of $Cs_3Sb_2I_{9-x}Cl_x$”. I wrote the remaining chapters of the review and managed the combination of all contributions to one consistent review.

APL Energy REVIEW pubs.aip.org/aip/ape

Heavy pnictogens-based perovskite-inspired materials: Sustainable light-harvesters for indoor photovoltaics

Cite as: APL Energy 1, 021502 (2023); doi: 10.1063/5.0161023
Submitted: 7 June 2023 • Accepted: 11 August 2023 •
Published Online: 31 August 2023

Fabian Schmitz,[1] Ribhu Bhatia,[2] Francesco Lamberti,[3] Simone Meloni,[2,a)] and Teresa Gatti[1,4,b)]

AFFILIATIONS

[1] Center for Materials Research, Justus Liebig University, Heinrich-Buff-Ring 17, 35392 Giessen, Germany
[2] Department of Chemical and Pharmaceutical Sciences, Università di Ferrara, Via Luigi Borsari 46, I-44121 Ferrara, Italy
[3] Department of Chemical Sciences, University of Padova, via Marzolo 1, 35131 Padova, Italy
[4] Department of Applied Science and Technology, Politecnico di Torino, C.so Duca degli Abruzzi 24, 10129 Torino, Italy

[a)] **E-mail:** simone.meloni@unife.it
[b)] **Author to whom correspondence should be addressed:** teresa.gatti@polito.it

ABSTRACT

The need for self-powered electronics is progressively growing in parallel with the flourishing of the Internet of Things (IoT). Although batteries are dominating as powering devices, other small systems, such as piezoelectric, thermoelectric, and photovoltaic systems, are attracting attention. These last ones can be adapted from their classical outdoor configuration to work preferentially under indoor illumination, i.e., by harvesting the spectrum emitted by LEDs and/or fluorescent lamps. However, crystalline silicon, the classical photovoltaic material for solar panels, has a bandgap not suitable for ensuring good efficiency with such spectra. With wider bandgaps, other semiconductors can come into play for this task. Still, the materials of choice, having to be integrated within households, should also satisfy the criterion of non-toxicity and maintain low-cost production. While lead-based halide perovskites cannot represent a valuable solution for this scope, due to the strong environmental and health concerns associated with the presence of Pb, analogous compounds based on the heaviest pnictogens, i.e., bismuth and antimony, could work as sustainable light-harvesters for indoor photovoltaic devices. In this Review, we focus on reporting the most recent developments of three compounds of this class: The double perovskite $Cs_2AgBiBr_6$ is first chosen as a model system for the other two, which are emerging perovskite-inspired materials, namely, $Cs_3Sb_2I_{9-x}Cl_x$ and bismuth oxyiodide. We show the potential of these semiconductors to play a crucial role in the future market of self-powering IoT devices, which will become a large class of devices in the electronics industry in the upcoming years.

I. INTRODUCTION

The development of the Internet of Things (IoT) is booming as the number of interconnected smart devices implemented in healthcare,[1] buildings,[2] factories,[3] vehicles,[4] cities,[5] and a plethora of other areas is continuously increasing. While in 2022 around 13×10^9 smart devices were estimated to exist, prognoses show that this number will more than double by 2030, with an expected amount of 30×10^9 smart devices connected to the IoT. Powering such an enormous number of remote devices is a crucial aspect since the usage of batteries poses several challenges, e.g., regular check of their power levels requiring maintenance, thus increasing their operational costs. As many IoT devices find a use for indoor applications, indoor photovoltaics (IPVs) (i.e., solar cells that harvest light emitted from white light LED—WLED—or fluorescent lamps—FL-illumination) offer a possibility to continuously supply those devices with power when indoor light (and also diffuse light from the external environment) is on.[6] Outdoor photovoltaics (OPVs) harvest the solar spectrum, which is reduced by atmospheric absorption losses and therefore subject to the Shockley–Queisser (SQ) limit that postulates a bandgap of 1.34 eV for an optimum power conversion efficiency (PCE) of around 33%, as depicted in Fig. 1.[7] In contrast,

APL Energy REVIEW pubs.aip.org/aip/ape

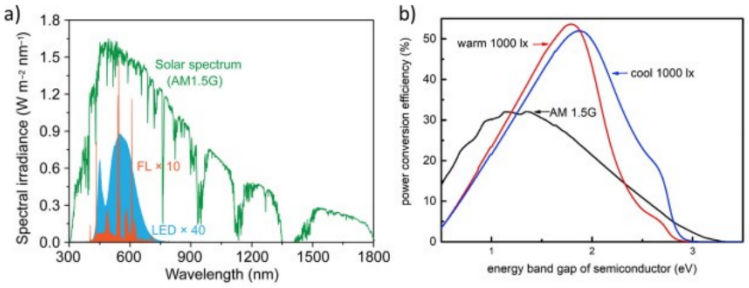

FIG. 1. (a) Comparison of WLED, FL, and AM 1.5G solar spectrum. (b) Dependence between light-harvester's bandgap and maximum achievable PCE for solar and WLED spectra. Reproduced with permission from Jarosz, Marczyński, and Signerski, Mater. Sci. Semicond. Process. **107**, 104812 (2020). Copyright 2020 Elsevier.

single-junction IPVs can exhibit a calculated maximum PCE of ~51%–68% for bandgaps between around 1.7 and 2 eV due to the vastly different emission spectra of WLEDs and FLs in comparison to the sun spectrum (Fig. 1).[8–11] The discrepancy of those values originates from the nonuniformity of indoor light sources, e.g., whether they are calculated for warm or cold LEDs.[10] Still, this shows that IPVs are not only able to surpass PCEs of OPVs but also that IPV solar absorbers need to possess much larger bandgaps to achieve such efficiencies. Additionally, indoor light sources provide light intensities of around 200 lux for living room environments and up to around 1000–2000 lux for bright light environments, e.g., office spaces or stores, in which IPVs are irradiated by a power density of around 0.5–3 W/m^2.[9,12,13] This power density is four orders of magnitude lower than for typical working conditions of OPVs (1000 W/m^2). For example, the PCE of crystalline silicon solar cells drastically decreases when they are operated, not under outdoor but, under indoor conditions due to the silicon bandgap of 1.1 eV and increased Shockley–Read–Hall recombination at low power irradiation.[14,15]

An alternative but promising class of light-harvesting materials to silicon are metal-halide perovskites (MHPs) owing to their advantageous optoelectronic properties, such as high charge carrier mobilities,[16] long charge carrier diffusion lengths,[17] high defect tolerance, low exciton binding energy,[18] and high absorption coefficients, that enable the use of device film thicknesses below 1 μm. When they are utilized as OPVs, perovskite photovoltaics (PPVs) reach competing PCEs to silicon solar cells.[19] Classical MHPs possess the stoichiometry ABX_3, where the A-site is occupied by an organic or inorganic monovalent cation like methylammonium (MA), formamidinium (FA), or Cs^+, the B-site is occupied by Pb^{2+}, and X is a halide (I^-, Br^- or Cl^-). What contrasts these materials from many other semiconductors and makes them particularly suitable for IPVs is that their bandgap can be adjusted by halide tuning, i.e., the bandgap increases with decreasing anion size from iodide to chloride.[20–22] This bandgap versatility in MHP materials made it possible for indoor perovskite photovoltaics (IPPVs) to surpass the 30% and rarely even the 40% PCE threshold.[23–27] For example, the authors of the work of Dong *et al.* fabricated an IPPV with an indoor efficiency of 40.24% under 1000 lux FL illumination by modifying a perovskite layer with the botanic antioxidant tomato lycopene, which additionally protected the thin films against oxygen and humidity and therefore increased their stability.[25] Moreover, the authors of the work of He *et al.* were able to achieve 40.1% indoor efficiency for ~3 W/m^2 WLED (2700 K) irradiation by incorporating guanidinium into their perovskite and additionally passivating the perovskite's surface with 2-(4-methoxyphenyl)ethylamine hydrobromide to reduce nonradiative recombination.[27]

Another favorable feature of PPVs is their solution-processability at low temperatures, which not only suppresses their processing costs but also enables the fabrication of flexible substrates.[28,29] The latter can either be a practical necessity for many IoT devices or serve as an opportunity to realize creative designs.[30] However, PPVs tend to degrade under the influence of high temperatures, under ultraviolet light, and when they are in contact with water or oxygen, thus, in a humid atmosphere.[31–33] This instability of PPVs usually causes a significant decrease in the initial PCE after several days or a few weeks, which is why often perovskite films are shielded from moisture and oxygen by protective interface layers or entire devices are encapsulated to increase their lifetimes to several weeks or even few months.[25,34] It is important to note that stability tests for PPVs are usually performed under harsh conditions to simulate their usage as OPVs. Since indoor conditions are much gentler, e.g., involve lower working temperatures and UV irradiation, IPPVs will have enhanced device lifetimes in comparison to OPVs. Still, a requirement to reliably power IoT devices is that IPPVs sustain their PCE during their entire life cycles. This allows one to limit operational costs to control the charge level of batteries, guaranteeing IoT operatively in the dark hours, and manual replacement, if discharged. Furthermore, high-efficiency PPVs contain lead, which displays toxicity to the human body on exposure, hence representing a serious hazard for users in case of leakage, especially for use in any indoor IoT as well as in wearable devices.[35] Apart from exposition issues, the lead content also introduces questions and challenges regarding the end of life or recycling of such devices.[35]

As a result, there is a broad variety of materials in which lead has been substituted by less toxic elements to exploit the structure's favorable properties while reducing their toxicity.[38] Of all lead-free perovskite materials, tin-based PPVs show the highest efficiencies but still suffer from low stabilities due to the hardly suppressible oxidation of Sn^{2+} to Sn^{4+} in ambient atmosphere because of its very low redox potential of 0.15 V.[39,40] As a consequence, additional focus

APL Energy REVIEW pubs.aip.org/aip/ape

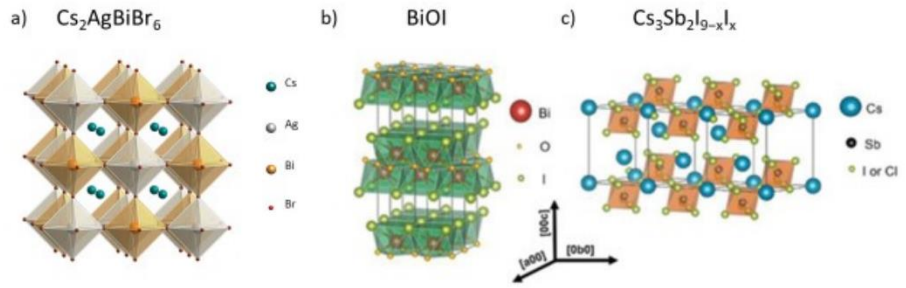

FIG. 2. Structures of the three heavy pnictogen-based perovskite and PIMs discussed in this review: (a) $Cs_2AgBiBr_6$ [reproduced with permission from Slavney *et al.*, J. Am. Chem. Soc. **138**(7), 2138–2141 (2016). Copyright 2016 American Chemical Society], (b) BiOI, and (c) $Cs_3Sb_2I_{9-x}Cl_x$ [Reproduced with permission from Peng *et al.*, Adv. Energy Mater. **11**(1), 2002761 (2021). Copyright 2021 Wiley].

had been set on the investigation of more stable lead-free perovskite materials. One of the earliest, and therefore also one of the most frequently explored materials, is the inorganic double perovskite (DP) $Cs_2AgBiBr_6$, whose structure is depicted in Fig. 2(a). In the following chapters, a general overview of its semiconducting properties, as well as a detailed summary of the most recent photovoltaic (PV) research, is given. However, due to its sub-optimal optoelectronic properties, as well as the issue of scarcity regarding the incorporated Ag, interest broadened toward other materials that no longer possess the perovskite structure but are still closely related to it, to benefit from its advantageous optoelectronic properties. Such materials are classified as perovskite-inspired materials (PIMs). There has been a special interest in materials based on heavy-pnictogen cations such as Bi^{3+} and Sb^{3+} in the form of halides or oxyhalides, e.g., bismuth oxyiodide (BiOI) and $Cs_3Sb_2I_{9-x}Cl_x$, depicted in Figs. 2(b) and 2(c),[37] that possess a similar electronic structure as Pb^{2+}. A crucial feature of lead-halide perovskites is the antibonding valence band maximum (VBM), originating from the Pb(6s)–X(*n*p) antibonding hybridization, while the conduction band minimum (CBM) is attributed to bond-like hybridization among Pb(6p) orbitals, though there is no actual consensus in the literature on this latter point. Thus, the formation of some of the most energetically favorable defects, e.g., such as halide or lead vacancies, characterized by dangling bonds of the complementary element forming the inorganic framework, results in states located deeply in the VB or CB.

It can be observed that, for the example of $MAPbI_3$, the Pb 5p state is located close to the CBM. Therefore, Pb antisite defects, besides other intrinsic defects such as iodide vacancies, will be created either inside of the CB or slightly below the CBM, the so-called "shallow defects" [see Fig. 3(b)].[41–44] As a result, electrons trapped in such defects require only low energy, close to or below the thermal energy at room temperature (≈25 meV), to overcome the energy barrier between the shallow trap and CBM (charge transition level) to be released. The formation of shallow hole defects works analogously, due to the energetic proximity between VBM and I 5p states, as depicted in Fig. 3(b).[44] Thus, charge carriers in trap states are likely to be released into the respective bands, which is why such materials are described as defect tolerant.

In contrast, binary II-VI, III-V, or group IV semiconductors tend to form a bonding VBM and an antibonding CBM that lead to the formation of trap states lying deep inside of the bandgap [Fig. 3(a)]. This leads to the formation of defect states deep within the bandgap. Accordingly, charge carriers trapped in such deep defect states require large energies, far above the thermal energy at room temperature, to be released back into the respective bands. Therefore, nonradiative recombination is far more likely to take

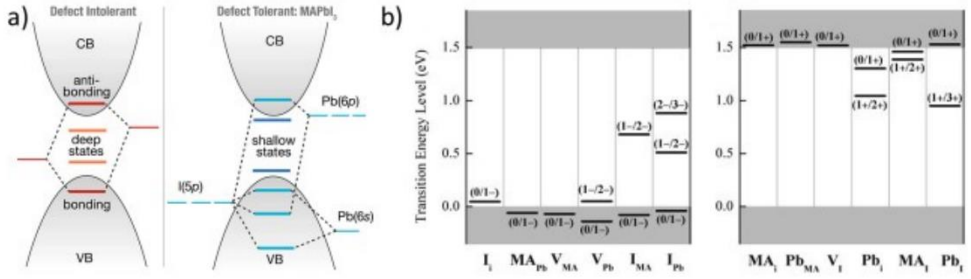

FIG. 3. (a) Electronic structure comparison of typical binary semiconductors (left) and a lead iodide perovskite (right). Reproduced with permission from Brandt *et al.*, Chem. Mater. **29**(11), 4667–4674 (2017). Copyright 2017 American Chemical Society. (b) Depiction of transition energy levels of point defects. Left: Intrinsic acceptors. Right: Intrinsic donors. Reproduced with permission from Yin, Shi, and Yan, Appl. Phys. Lett. **104**(6), 063903 (2014). Copyright 2014 AIP Publishing LLC.

APL Energy REVIEW pubs.aip.org/aip/ape

place for charge carriers trapped in deep defect states than in shallow defect states.[41,42] It is important to note that, even though there is a close structural relation between lead-halide perovskites (LHPs) and PIMs, the described formation of the electronic structure of the former cannot be fully transferred to the latter. For example, the degree of order of $[BiBr_6]^{3-}$ and $[AgBr_6]^{5-}$ octahedra in $Cs_2AgBiBr_6$ strongly affects its electronic band structure, which does not play any role for LHPs due to the presence of solely lead-halide octahedra in those materials. Moreover, the presence of Ag^+ as well as Bi^{3+} to substitute Pb^{2+} increases the number of intrinsic defect types and will be discussed further in Sec. II (Fig. 5). The electronic structures of all three PIMs of interest for this review are described in more detail in Sec. II.

High defect tolerance is a key factor in why materials possessing LHP-like electronic structures are well suited to be applied as IPVs. Even at low-intensity indoor illumination, and therefore low concentrations of excited charge carriers, LHPs and PIMs achieve comparably high power conversion efficiencies due to the nature of shallow traps.[27,45] Additionally, in those materials, defect concentrations can be reduced by passivating strategies and controlled crystal growth, as will be described in the following sections. This is an advantage over semiconductors like Si suffering from increased nonradiative recombination at low intensities due to the presence of deep trap states.

The double perovskite is here considered as a model compound in the field of heavy pnictogen-based lead-free PIMs and is further discussed in Sec. III to provide a general overview of the advantages and disadvantages of its use in IPV devices. The other two, BiOI and $Cs_3Sb_2I_{9-x}Cl_x$, are emerging species in the field, with high potential for use in low-cost, low-toxicity IPV. Overviews of recent research about BiOI are given in Sec. IV and about $Cs_3Sb_2I_{9-x}Cl_x$ in Sec. V.

Bi and Sb are elements from the 15th group of the periodic table, also known as group 5A, meaning that they share the same group as As, which is famous for its high toxicity in its pure form as well as in its compounds. They belong to the family of pnictogens as nitrogen (they are the "heaviest" ones in the group) and indeed this specific nomenclature refers to the suffocating action of pure N_2 gas (from ancient Greek: πνίγω "to choke" and gen, "generator"). Since the goal of applying Bi and Sb in IPVs is the reduction of the biological hazard in case the devices get damaged and start to leak, an assessment of the toxicity of those elements is crucial. While the high toxicity of lead has been broadly investigated due to its vast utilization and abundance through the last several millennia, the biological hazards that stem from Sb and Bi exposition are far less explored. Bi is known to cause neurological dysfunction when humans are exposed to small doses periodically over a long time or large doses within a short time as it was observed for patients that ingested Bi-based medication.[46–48] However, Bi has a toxic intake level of 15 g in comparison with a 1 mg toxic intake level for Pb for a 70 kg human.[49] This underlines the drastically reduced intoxication risk when Pb is substituted with Bi in IPVs. In contrast to Bi, the toxic intake level of Sb is far lower (37 mg for a 70 kg human) but still more than an order of magnitude larger than that of Pb.[50] For details about the consequences of Sb intoxication, its potential carcinogenicity, and interferences with the metabolism of sugars and lipids, we refer the reader to recent literature reviews.[51,52]

Apart from toxicity aspects, both Bi and Sb, unlike Pb, are included in the critical raw material (CRM) list of the European Commission (Bi since 2017, Sb since its establishment in 2011). The CRM incorporates materials that are characterized by economic importance in industry and technology, are non-substitutable, and are characterized by a high supply risk. In comparison to the estimated ultimately available 20 000 Mt of lead, the scarcity of Sb and Bi is further underlined by their far lower estimated availabilities of 100 and 20 Mt, respectively.[53] Additionally, in 2016, 58% of the globally used lead was won from recycling,[54] while in 2021 these values were just 20% for Sb and 0% for Bi.[53] This drastically reduces the global warming potential (GWP) of lead (1.3 kg CO_2-eq per kg) in contrast to Sb (12.9 CO_2-eq per kg) and Bi (58.9 CO_2-eq per kg).[54] Still, the potential global recycling rates for Sb and Bi are 55% and 48%, respectively, which could drastically decrease their GWP in the future.[53] Therefore, the route, in our opinion, is to find new experimental strategies for replacing both critical and toxic materials by using domestic (i.e., European) elements that would strongly diminish our dependence on imports:[55] For Bi, for instance (but the argument can be easily generalized to other critical materials), one must take into account that it is mainly extracted in Vietnam and China and the recycling processes are too complex and expensive.[56] This is of course only one part of the problem: At the early stages of life of IoT devices, as we are currently, the aim is to create a robust demand for these technologies and the only way to do so is to make them reliable by the realization of well-performing devices. The first steps in perovskites adoption for IPV started from the use of well-known toxic elements (such as lead, arsenide, and cadmium),[57] then research moved to attempt the implementation of a greener technology by resorting to atoxic but relatively scarce elements that can provide sufficient performance. In summary, the choice of a metal utilized in a light-harvesting material is a balancing act between its scarcity and performance and we cannot ignore this argument from the perspective of a more general and progressive advance in the field.

As the focus of this review lies specifically on recent advances in the research on MHPs and PIMs like $Cs_2AgBiBr_6$, BiOI, and $Cs_3Sb_2I_{9-x}Cl_x$ and their potential as indoor light-harvesting materials, for further information about other PIM-based IPVs, we refer the readers to the reviews of Ünlü *et al.*[58] and Huang *et al.*,[59] providing more in-depth and complete overviews.

II. THEORETICAL BACKGROUND

Descriptors, like the nature (direct or indirect) of the electronic bandgap E_g, carrier mobilities and lifetimes, defect tolerance, absorption coefficient (α), the photoluminescence quantum efficiency (PLQE)(η), effective mass, static polaron binding energy, and Fröhlich electron–phonon coupling (EPC), are commonly used to identify material for photovoltaic applications. Density functional theory (DFT) has established itself as a powerful technique for first-principles investigations of solids for PV and optoelectronic devices, which can help establish the origin of these characteristics for pnictogens. Among the others, theoretical calculations and simulations have been performed on Sn-based perovskites, double perovskites, and other potentially defect-tolerant compounds ($A_3B_2X_9$, ABZ_2, binary halides, and V–VI–VII materials), which have been identified as suitable alternatives to lead-based MHPs.[59]

DPs are a promising class of materials of formula $A_2B'B''X_6$, with B' monovalent and B'' trivalent metal cations. $A_2B'B''X_6$ was

APL Energy REVIEW pubs.aip.org/aip/ape

already considered in the early days of research on metal-halide perovskites for PV applications to eliminate Pb. Numerous combinations of A, B′, B″, and X have been identified to be structurally and thermodynamically stable; however, **$Cs_2AgBiBr_6$ *emerged as a reference system***. $Cs_2AgBiBr_6$ is appealing for its optoelectronic properties, 3D structure, long carrier lifetimes, and low carrier effective mass as LHPs and also higher stability and nontoxicity.

An important limitation of $Cs_2AgBiBr_6$ for OPVs is its relatively large bandgap, 2.18 eV. However, recently it was shown that this can be reduced by hydrogenation of the sample, achieving a record 1.64 eV low value.[60] This led to a corresponding high 6.37% power conversion efficiency. First-principles calculations revealed that the doping is interstitial, with three possible positions, denominated H_1(in), H_2(in), and H_3(in). This results in bonding states between H-1*s* and nearby cation orbitals. Depending on the interstitial site occupied by hydrogen atoms, one could obtain a wide [coupling between H_1(in)-1*s*, Br-4*p* and Ag-4*d*], narrow [coupling between H_2(in)-1*s*, Br-4*p* and Bi-6*p*], or a flat band [H_3(in)-1*s* and Br-4*p*] (see Fig. 4).

Additionally, device simulation of solar cells based on standard $Cs_2AgBiBr_6$ revealed that the optimization of the SnO_2/absorber interface can boost the cell's PCE to more than 14%.[61] These findings suggest that the fundamental structural, optical, and electronic properties of $Cs_2AgBiBr_6$, on-purpose doping, which was not of great help in LHPs, and absorber/hole transport layer (HTL) interface must be better understood at an atomistic level to improve the efficiency of PIMs. In the following, we present a systematic review of theoretical results on the reference $Cs_2AgBiBr_6$ double perovskite. First, the structure–property relation and stability of $Cs_2AgBiBr_6$ are emphasized. Next, the fundamental optical and electronic properties, e.g., absorption and emission, followed by electron–phonon coupling and the effect of defects on the properties of the material are discussed.

Let us first focus on the relation between the $Cs_2AgBiBr_6$ structure and the fundamental optoelectronic properties of the material. At room temperature (RT), the stable crystalline phase of this double perovskite (lattice constant 11.7 Å) belongs to the Fm3m cubic space group.[62] The ordered structure consists of alternating corner-sharing $[AgBr_6]^{5-}$ and $[BiBr_6]^{3-}$ octahedra forming a three-dimensional *checkboard*, with Cs^+ being centered at the cavities. The corresponding Ag–Br/Bi–Br and Ag–Br–Bi bonds all maintain a 90° or 180° angle, and the bond length for Ag–Br and Bi–Br is comparable (2.804–2.828 Å). The shorter metal-halide distance to the corresponding lead-halide perovskite (3.18 Å) is an indication of the stronger B-X bonds at the basis of the improved stability of the $Cs_2AgBiBr_6$ framework.[63] However, there exists a relative mismatch between ionic radii (1.15 and 1.03 Å for Ag^+ and Bi^{3+}, respectively) and the electronegativity (1.93 and 2.02 for Ag^+ and Bi^{3+}, respectively) of the two metals. A consequence of such a mismatch is the volume variation and distortion/tilting of octahedra (mainly associated with bond lengths and bond angles) on exposure to external stimuli like temperature or pressure (mentioned later in this section). This has a significant effect on the electronic structure and consequently on the optoelectronic properties of the perovskites.[64]

Concerning the electronic structure, $Cs_2AgBiBr_6$ VBM and CBM are very different from ordinary metal-halide perovskites. In this double perovskite, VBM and CBM are made of Ag-4d, Bi-6s, and Br-4p, and Ag-5s, Bi-6p, and Br-4s orbitals, respectively.[65–67] VBM is

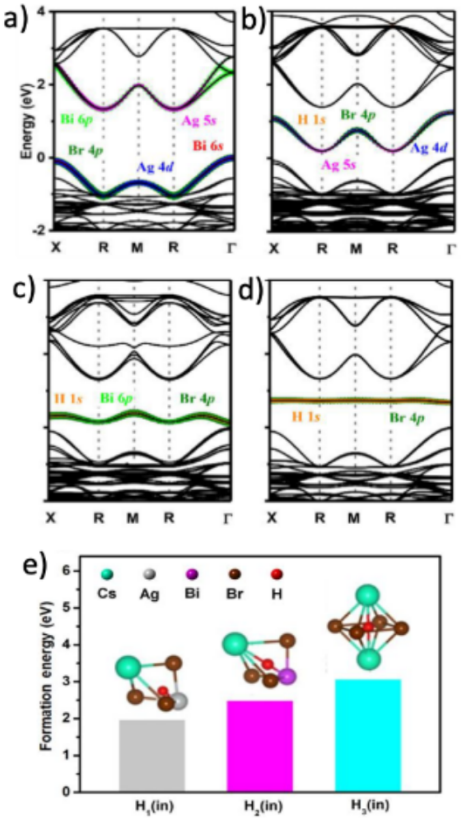

FIG. 4. (a) Band structure of a pure $Cs_2AgBiBr_6$ DP (host); (b)–(d) band structures of $Cs_2AgBiBr_6$ in the presence of hydrogen interstitial. Red, light green, blue, pink, dark green, and orange curves correspond to Bi 6s, Bi 6p, Ag 4d, Ag 5s, Br 4p, and H 1s orbitals, respectively; (e) H1(in), H2(in), H3(in) represent different sites occupied by of the interstitial hydrogen in the $[AgBr_6]^{5-}$ and $[BiBr_6]^{3-}$ octahedra, respectively. Reproduced with permission from Zhang *et al.*, Nat. Commun. **13**(1), 3397 (2022). Copyright 2022 Author(s), licensed under a Creative Commons Attribution 4.0 License.

dominated by an antibonding hybridization between Ag-4d and Br-4p, with a minor contribution from antibonding Bi-6s and Br-4p. CBM mainly consists of a mixture of Bi-6p orbitals, Bi-6p and Br-4p antibonding states, and Ag-5s, Br-4p bonding states. At variance with ordinary halide perovskites, $Cs_2AgBiBr_6$ presents an indirect bandgap. The presence of $[AgBr_6]^{5-}$ and $[BiBr_6]^{3-}$ in the framework raises the question of whether in the $Cs_2AgBiBr_6$ structure, these octahedra are alternated or random. Octahedra order/disorder significantly affects the optoelectronic properties, including bandgaps, lattice distortion, defects, and carrier mobility, and can therefore be used to manipulate light absorption.

The first-principles calculation presented in the work of Yang *et al.* revealed enhanced light absorption in the visible and

APL Energy REVIEW pubs.aip.org/aip/ape

near-infrared region on moving from an ordered, i.e., alternated $[AgBr_6]^{5-}$ and $[BiBr_6]^{3-}$ octahedral structure, to partially disordered to completely random ones, as depicted in Fig. 12(b). Depending on the degree of disorder, changes in the band structure from indirect to pseudodirect and band shrinkage by 1–1.5 eV were observed.[68] Unfortunately, calculations also revealed that such a random structure and the ensuing improved band structure were possible only if $Cs_2AgBiBr_6$ was synthesized by quenching from temperatures beyond 1200 K, which greatly limit practical applications. Exposing $Cs_2AgBiBr_6$ to high pressures appears to be another alternative to manipulate the material's properties. For instance, the authors of the work of Fu *et al.* computed the bandgap and structural evolution of the system for P values in the experimental range.[69] Consistent with their experimental findings, a decrease in the bandgap with increasing pressure in the 1 atm–12 GPa range is observed for the cubic phase. However, a more complex trend of bandgap evolution is observed for the tetragonal phase. In this case, the bandgap decreases from 2.84 to 2.74 eV in the 1 atm to 6 GPa pressure range, followed by an increase to 3.01 eV for pressures beyond 6 GPa. Furthermore, a semiconductor-to-metallic transition is reported at ~20 GPa in the work of Islam *et al.*[70] Such bandgap evolutions are attributed to the pressure-induced symmetry breaking of $[AgBr_6]^{5-}$ and $[BiBr_6]^{3-}$ octahedra. In other words, pressure induces tilting of octahedra, the soft mode in perovskites, leading to orbital interactions resulting in the evolution of the bandgap.

Let us now focus on the stability of $Cs_2AgBiBr_6$ and summarize theoretical results, shedding some light on its superior stability. Two parameters must be considered: (i) the tolerance factor—here we highlight the more accurate formulation recently proposed,

$$\tau = r_A/r_B - n_A\left(n_A - \frac{\frac{r_A}{r_B}}{\ln\left(\frac{r_A}{r_B}\right)}\right)$$

with r_A, r_B, n_A being ionic radii and oxidation state of A and B ion, respectively, and (ii) the octahedral factor,

$$\mu = r_B/r_X,$$

where r_X is the ionic radius of the X ion. Both factors are commonly used to evaluate the structural stability of ABX_3 perovskites. Typically, a perovskite is structurally and thermodynamically stable when $\mu < 4.18$ and $0.44 \leq \tau \leq 0.9$, and both conditions are essentially met by $Cs_2AgBiBr_6$, which presents a $\tau = 0.56 - 0.60$ and a $\mu = 4.07 - 4.21$. The work of Chapa *et al.* provided evidence of mechanical stability of $Cs_2AgBiBr_6$ via DFT calculations, while the thermodynamic stability was confirmed by Zhang and coworkers.[71,72] They evaluated the decomposition energies of possible decomposition pathways like CsBr, AgBr, Cs_2AgBr_3, $CsAgBr_2$, and $Cs_3Bi_2Br_9$ via first-principles calculations and all the values they obtained appear to be positive and higher than 20 meV, suggesting a high thermodynamic stability of $Cs_2AgBiBr_6$.

Concerning the properties of $Cs_2AgBiBr_6$ affecting its performance, the bandgap is certainly the most relevant intrinsic property for a light-harvesting material because a precise knowledge of E_g helps to predict the PV maximum efficiency under given illumination conditions, e.g., within the Shockley–Queisser (SQ) framework. Here, one assumes that all the incident light with energy larger than E_g is absorbed. However, in real materials, there is a non-negligible transmission of photons with energies greater than the bandgap. $Cs_2AgBiBr_6$ has an indirect bandgap with reported values spanning a large energy range, from 1.95 to 2.25 eV.[66,73] Within the SQ formalism, these values would allow for theoretical photocurrents and PCEs under AM 1.5G illumination conditions between 17 mA/cm^2 and a PCE of 25% for E_g = 1.9 eV, and 6 mA/cm^2 and a PCE of 12% for E_g = 2.5 eV. These values are very optimistic concerning the more realistic spectroscopic limited maximum efficiency (SLME) of 7.9%, estimated based on first-principles calculations, which consider the calculated shape of the absorption spectrum and nonradioactive recombination. This discrepancy suggests that a thorough theoretical analysis of the optical properties is needed when screening materials for PV applications.[74,75]

A typical $Cs_2AgBiBr_6$ absorption spectrum can be seen in Fig. 5(a). There is high absorption below 340 nm (3.6 eV), a strong feature at around 440 nm (2.8 eV), and weak absorption at lower energy. The high absorption is attributed to the vertical transition, and the direct bandgap, while the strong feature observed in the spectra is still under debate; finally, the long tail toward low energies indicates the absorption due to the indirect bandgap. It should be noted that the sharp peak at 440 nm corresponding to 2.8 eV contributes more than 20% of the overall light absorption of $Cs_2AgBiBr_6$ perovskite. Peaks at high energies, which are of limited interest for OPVs, are very relevant for indoor applications, and understanding their origin may help optimize present materials or develop newer ones. Some speculations for the origin of the sharp peak include excitonic absorption, charge transfer-like transition between Ag and Bi/Br orbitals, or localized Bi 6s-6p transitions. Even though experimental investigations favor the latter to be the cause of this observed absorption peak, there is no theoretical evidence supporting this claim.[76]

The photoluminescence (PL) yield of $Cs_2AgBiBr_6$ was reported to be in a very low range from 0.01% to 0.08% for an excitation density comparable to one sun, while the decay of the PL intensity is rather slow, indicating long-living charge carriers.[77] This strengthens the interest of the community as these characteristics are promising for efficient extraction of charge carriers. The PL spectrum is broad and shows a Stokes shift [Fig. 5(a)], which is also confirmed by Baranowski and co-workers, who reported a ≃500 meV shift between PL and PLE spectra.[78] This Stokes shift is attributed to a strong electron–phonon coupling, a relevant phenomenon affecting PV cells' efficiency, discussed in detail below. This conjecture was confirmed by comparing phonon energies as obtained from Raman spectra with corresponding values obtained from DFT calculations.[78] Nevertheless, the origin of the PL emission is still debated. The work of Baranowski *et al.* provided evidence that the PL peak results from spatially localized color centers, which can be either intrinsic self-trapping of exciton/carriers or defects.[78]

PL results are associated with mechanisms—electron–phonon coupling (EPC) and polaronic effects on carrier mobility—which critically affect the efficiency of $Cs_2AgBiBr_6$-based PV devices. Let us focus first on the former phenomenon, EPC, i.e., the scattering of moving electrons by longitudinal optical (LO) phonons, when atoms move parallel to the phonon propagation direction, or transverse optical (TO) phonons when atoms move in the plane

APL Energy REVIEW pubs.aip.org/aip/ape

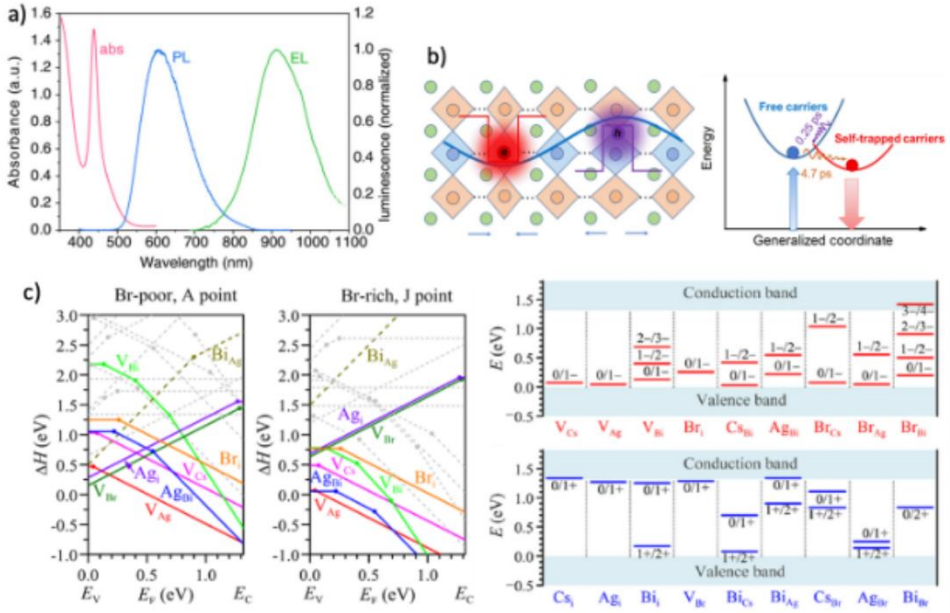

FIG. 5. Optical, transport, and defect properties of $Cs_2AgBiBr_6$. (a) Absorption and emission spectra of $Cs_2AgBiBr_6$ (here, abs stands for absorption, PL for photoluminescence, and EL for electroluminescence). Reproduced with permission from W. Tress and M. T. Sirtl, Sol. RRL **6**(2), 2100770 (2022). Copyright 2022 Author(s), licensed under a Creative Commons Attribution 4.0 License. (b), left: Schematic of the self-trapping mechanism of charge carriers by acoustic phonons or deformation potential. The dots between adjacent perovskite octahedra represent the lattice units omitted for the sake of simplicity. This panel shows that the deformation of the lattice results in a localizing potential for holes and electrons. This localizing potential controls the dynamics of charge carriers: Trapping and de-trapping of holes and electrons follows the dynamics of phonons responsible for the formation of the localizing potential wells. (b), right: Schematic of the energy diagram for carrier self-trapping. Free electrons in the conduction band are energetically driven to localizing potential, where they remain trapped. Reproduced with permission from Wu *et al.*, Sci. Adv. **7**(8), eabd3160 (2021). Copyright 2021 Author(s), licensed under a Creative Commons Attribution 4.0 License. (c), left: Point defect formation energies, ΔH(eV), of intrinsic defects in $Cs_2AgBiBr_6$ as a function of the Fermi level, E_F, at representative Br-rich and Br-poor conditions. Defects with very high ΔH values are shown by the dashed lines. (c), right: Calculated transition energy for intrinsic acceptors (top) and intrinsic donors (bottom). Reproduced with permission from Xiao *et al.*, ChemSusChem **9**(18), 2628–2633 (2016). Copyright 2016 Wiley.

orthogonal to their propagation direction. Broadly speaking, the carrier–optical phonon interactions affect the carrier's mobility while the carrier–acoustic phonon interactions influence the thermal properties of materials, like thermal conductivity and thermal expansion coefficient. For instance, for halide perovskites, it has been pointed out that low thermal conductivity can lead to a temperature rise in an operating device and cause stability issues. The resulting large thermal expansion can give rise to thermal strain and stress,[81] possibly mitigated by a self-protecting mechanism recently proposed.[82]

On the other hand, perovskites are susceptible to local distortion by charge carriers leading to the formation of polarons. A polaron is a quasiparticle formed because of conduction electrons (or holes) interacting with their self-induced polarization in the polar semiconductor or ionic crystal. This is expected to be especially important in the case of soft and potentially polar systems, like ordinary and double perovskites. Polarons can be classified according to the degree of the spatial localization of the carrier. One distinguishes between small when it is localized within a single site, or large, when it involves several lattice sites, polarons. Herz and co-workers showed that for traditional perovskites (like methyl ammonium lead iodide—MAPI—or formamidinium lead iodide—FAPI), at room temperature, charge carrier scattering is dominated by the coupling between carriers and longitudinal optical (LO) phonons rather than interaction with acoustic phonons or from ionized impurities.[83] Within the Fröhlich model (which addresses electrons in ionic crystals or polar semiconductors and considers the long-range interaction between an electron and a polar optical phonon mode under the continuum approximation), the strength of this carrier–LO phonon interactions is characterized by Fröhlich polaron coupling constant α, such that

$$\alpha = \frac{2\pi q^2}{h}\left(\frac{1}{\varepsilon_{\text{inf}}} - \frac{1}{\varepsilon_0}\right)\sqrt{\frac{\pi m^*}{h\omega_{LO}}},$$

where q is the elementary charge, h is the Planck constant, ε_{inf} and ε_0 are the dielectric constant at infinite and zero frequency, respectively, m^* is the effective mass of the electron or hole, and ω_{LO} is the frequency of the dominant phonon. For conventional ionic

APL Energy REVIEW pubs.aip.org/aip/ape

inorganic semiconductors, the Fröhlich coupling constant is significantly smaller than unity, while the same adopts values of ~1 to 2 for electrons and holes in MAPI, respectively. These values are considered to be "intermediate" for traditional halide perovskites,[84] giving rise to polarons that can limit charge carrier's mobility in MAPI.[85] However, first-principles calculations presented in the work of Steele *et al.* on $Cs_2AgBiBr_6$ revealed α_e and α_h values of 2.54 and 2.0, respecctively.[86] Similar values (2.68 and 2.52 for electrons and holes, respectively) have been reported in the work of Wu *et al.*[79] Using the Feynman–Osaka formula, the same group estimated polaron mobilities to be equal to ~27 (e) and 33 (h) cm^2/s V for electrons (e) and holes (h), respectively. These values are much lower than those observed for selected LHPs, e.g., $CH_3NH_3PbBr_3$, showing mobilities of μ_e ~150 (e) and μ_h ~79 (h) $cm^2/s\ V^{-1}$, while $CsPbBr_3$ shows mobilities of μ_e ~ 48 and μ_h ~42 $cm^2/s\ V^{-}$.[187] These results suggested that only Fröhlich coupling may not be responsible for such a large difference in carrier mobility between the Bi-based double perovskite and LHP. This prompted investigations on the role of the deformation potential: local lattice deformations produced by an electron/hole carrier induce changes in the band structure localizing it in a small polaron. When electron–phonon interaction strength is above a given threshold, a transition from free-carriers to a self-trapped state is observed.[88] Following Toyozawa, self-trapping by charge-induced deformation potential can be assessed by a factor, *g*, that in the case of cubic lattices reads

$$g = \Xi 2m/6\hbar 2Ca, \quad (1)$$

where Ξ is the deformation potential, *m* is the bare electron effective mass, *C* is the elastic constant, and *a* is the lattice parameter.[89] For $Cs_2AgBiBr_6$, the authors of the work of Wu *et al.* reported values of 0.87 and 0.89 for electrons and holes, respectively.[79] Values very close to unity indicate the possibility of self-trapping of both charge carriers in small polarons with a coherent length comparable with the lattice parameter, ~11.2 Å. They speculate that both optical phonons (Fröhlich coupling) and acoustic phonons (deformation potential) synergistically contribute to the electron–phonon scattering mechanism in $Cs_2AgBiBr_6$. In other words, electron and hole carriers in $Cs_2AgBiBr_6$ are first localized by optical phonons and then self-trapped by acoustic phonons, which further localize the charge carriers [Fig. 5(b)].

Beyond electron–phonon coupling, which has proven to be an important aspect determining the transport properties in $Cs_2AgBiBr_6$, it is imperative to understand the role of defects, their stability, hence abundance according to thermodynamics, and their effect on the properties of materials at a fundamental level: This may allow achieving highly efficient optoelectronic devices. Concerning defects, one usually distinguishes between point defects (i.e., vacancies, interstitials, and antisites), line defects (i.e., dislocations), plane defects (i.e., surfaces and grain boundaries), and bulk defects (i.e., voids or precipitates). One of the reasons for the success of lead-based MHPs is their high defect tolerance, i.e., that the presence of defects does not result in deep defect states, defect-induced localized electronic states with energy close to the middle of the bandgap that, according to the Shockley–Read–Hall theory, induce nonradiative recombination [see Fig. 3(b)]. This defect tolerance is attributed to the strong antibonding coupling between Pb s and halide p orbitals for the VB, and Pb p and halide s ones for the CB.[90] $Cs_2AgBiBr_6$ DP exhibits lower defect tolerance owing to the presence of two B-site metal ions. The authors of the work of Xiao *et al.* computed the formation enthalpies and thermodynamic transition energy levels of typical point defects (vacancies, cation-on-anion antisites, anion-on-cation antisites, and interstitial) in $Cs_2AgBiBr_6$ under representative Br-poor and Br-rich conditions [Fig. 5(c)].[80] They concluded that even in Ag-rich conditions, Ag vacancies are the most easily formed defects. Ag vacancies, however, are shallow and do not deteriorate optoelectronic performance, like Pb vacancies in $MAPbI_3$ (see Fig. 3). The dominant deep-level acceptor defects include Ag_{Bi}, Bi_{Ag} antisites, and V_{Bi}. They suggested that the formation of deep defects can be significantly suppressed by synthesizing the materials under a Br-poor/Bi-rich growth condition, which was deemed necessary for PV and other optoelectronic applications of $Cs_2AgBiBr_6$. Similar conclusions were reported in the work of Li *et al.*[91] However, in addition to identifying Ag_{Bi}, Bi_{Ag} antisites, and V_{Bi}, the authors also identified halogen vacancy V_{Br} as a deep-level defect. It is worth remarking that defects seem to be very sensitive to the synthesis environment of $Cs_2AgBiBr_6$.

Though experimental works have identified some of the detrimental defects mentioned above and developed strategies to passivate them, the charge carrier trapping mechanism is unclear. Recently, the authors of the work of Liu *et al.* implemented machine learning methods, DFT calculations, and nonadiabatic molecular dynamics (NA-MD) to investigate the recombination mechanism in defective $Cs_2AgBiBr_6$ induced by negative V_{Br}.[92] The distribution of excess charge between the metal atoms close to the vacancy was identified to be at the basis of the deep trap state. According to their calculations, the electrons from the vacancy are first localized on the adjacent (to the vacancy) Bi atom and then are shared with the neighboring Ag atom. This charge transfer transforms the trap state from shallow to deep. The same authors also proposed a strategy to mitigate this effect. Doping the system with indium, and replacing the Ag involved in the trap with In, prevents the delocalization of charge responsible for deep trapping (Fig. 6). The work of She *et al.* revealed another mechanism for the mitigation properties of indium: The longer In–Bi bond and the relatively weaker hybridization of the In-p and Bi-p orbitals prevent the formation of deep traps.[93]

We conclude this part on $Cs_2AgBiBr_6$ mentioning that, so far, investigation of trapping and recombination at surfaces and grain boundaries in this material is still lacking. It is worth remarking that in the case of LHPs, it was shown that often trapping and recombination of charge carriers occurs at grain boundaries and surfaces[94] and more specifically interfaces between the perovskite and (HTL)/electron transport layer (ETL). Hence, theoretical research on these extended defects is especially important for progress of the field.

***Bismuth oxyiodide* (*BiOI*)**, a PIM composed of elements from the V, VI, and VII groups has recently gained popularity as a potential candidate for PV thanks to its 10^4 cm^{-1} absorption coefficients in the visible wavelength range.[59] BiOI, belonging to a tetragonal structure with space group *P4/nmm*, is composed of a layer of $(Bi_2O_2)^{2+}$ slabs interleaved by a double layer of I, forming –I–Bi–O–O–Bi–I– slabs stacked along the c-axis held together by nonbonding van der Waals interactions [Fig. 7(a)]. As a result of such a structural configuration, an electric field is developed between the $(Bi_2O_2)^{2+}$ and

APL Energy REVIEW pubs.aip.org/aip/ape

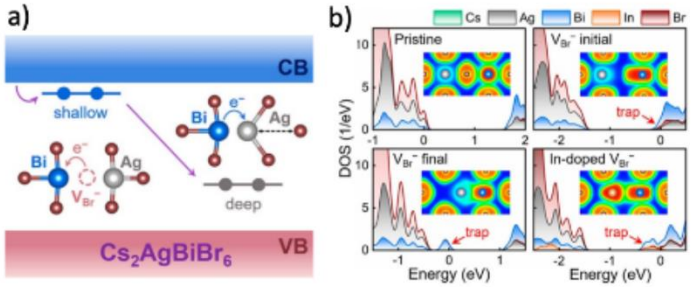

FIG. 6. (a) Mechanism of sharing of the electrons trapped in a bromide vacancy. The electron is initially accepted in a Bi orbital and then shared with Ag. This brings to a sizable and local distortion of the lattice transforming the shallow into a deep trap state. (b) Element-projected density of states (DOSs) in pristine and In-doped $Cs_2AgBiBr_6$. The insets show the electron localization function (ELF) maps around the vacancy sites. Red and blue indicate ELF values of 1 and 0, respectively. This panel shows that indium prevents the formation of deep trap states. Reproduced with permission from Liu *et al.*, J. Phys. Chem. Lett. **13**(16), 3645–3651 (2022). Copyright 2022 American Chemical Society.

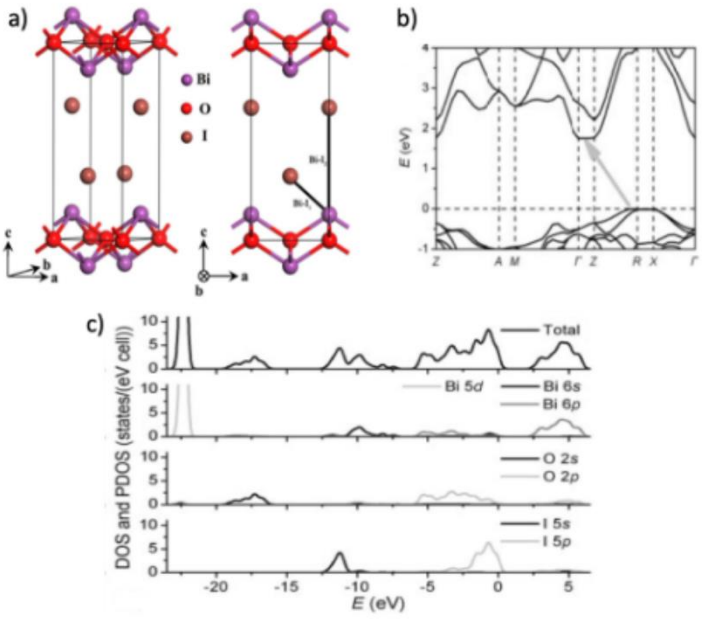

FIG. 7. (a) Crystal structure of BiOI. BiOI is a 2D material made of BiO layers intercalated by I ions. (b) BiOI band structure. The arrow highlights the indirect nature of the bandgap. (c) Total density of states (DOS) and individual atomic contributions to it (PDOS) of BiOI. This shows that the valence band maximum mostly comes from I 5s and 5p orbitals, while the conduction band minimum mostly arises from Bi 5s and 6d. Reproduced with permission from W. L. Huang and Q. Zhu, Comput. Mater. Sci. **43**(4), 1101–1108 (2008). Copyright 2008 Elsevier.

two I^- layers. A prior research, assessing the performance of BiOI as a photocatalyst, reported improved photocatalytic activity due to effective electron–hole charge carrier separation by this built-in electric field.[95] This mechanism of charge separations is appealing also for PV applications, but, no reported theoretical studies have explored the influence[96] of this intrinsic property on charge carrier dynamics in BiOI for PV applications. Furthermore, like other heavy pnictogens-based semiconductors, an important limitation of BiOI for OPV is its wide indirect bandgap of ≈2 eV [Fig. 7(b)]. While the indirect nature is still a problem for IPV, its relatively large bandgap

APL Energy REVIEW pubs.aip.org/aip/ape

value is optimal for indoor light harvesting owing to the spectra of indoor light sources being blue-shifted compared to the AM 1.5G spectrum, as shown in Fig. 1.[37]

It is useful to analyze the electronic structure of BiOI in comparison with that of lead-based perovskites, where the valence 6s orbitals of Pb^{2+} hybridize with the halide p orbitals to form a pair of bonding and antibonding states within the upper VB. The empty valence Pb p orbitals also hybridize with the anion s orbitals to form the antibonding state at the CBM. In addition, the high spin–orbit coupling results in a further decrease in bandgap.[84] The combination of these effects is at the basis of the formation of only/predominantly shallow trap states in lead-halide perovskites, a key characteristic for high PV performance materials (see Sec. I for more details). BiOI shares several characteristics with the electronic structure of these last ones, as band edges are predicted to have an antibonding orbital character. In particular, the VBM is predominantly made of I-5p orbitals hybridizing with Bi-6s ones with some contribution from O-2p states. The CBM is mainly made of Bi-6s, with contributions from s and p orbitals of I and O [Fig. 7(c)]. This raises hope that BiOI is *defect tolerant*.

One of the first relevant computational and experimental works on BiOI has indeed found that the material is tolerant to vacancy and antisite defects. To understand the tolerance of BiOI to intrinsic point defects, the authors of the work of Hoye *et al.* calculated the formation energy as a function of Fermi energy of V_{Bi}, V_O, and V_I vacancies, and O_I, I_O, Bi_O, Bi_I, O_{Bi}, I_{Bi} antisite defects.[97] The authors concluded that owing to their low formation energies, V_{Bi}, O_I, and V_I were the prevalent defects under I-rich conditions, while V_I and O_I prevail under Bi-rich conditions (Fig. 8). Other defects had significantly higher formation energies ($\Delta H_{D,q} > 1$ eV), implying that they had much lower equilibrium concentrations and can likely be neglected. It should be noted that all the defects were shallow because their charge transition levels were either inside or close to the band edges. They also reported a high (relative) dielectric constant of 45, which typically means effective screening of charged defects, consequently leading to a low trapping probability. This provides the theoretical rationale for the defect tolerance of BiOI.

These conclusions were challenged by the authors of the work of Brandt *et al.*, who investigated the decay time of charge carriers in a series of materials, including BiOI and SbSeI pnictogens, by time-resolved PL (TRPL).[41] They found that the carrier lifetimes of explored pnictogens were hundreds of nanoseconds shorter with respect to carrier lifetimes observed in $CH_3NH_3PbI_3$. These results suggest defect tolerance as assessed by thermodynamic transition energy level may be an insufficient heuristic to judge the suitability of a material for PV applications. Additionally, photoinduced current transient spectroscopy measurements performed in the work of Huq *et al.*[98] showed that BiOI films have deep traps located at 0.3 and 0.6 eV from the band edges, which were not identified in the calculations.

The authors of the work of Ganose *et al.*[43] remarked on the defect tolerance challenge in wider bandgap semiconductors. Here, we report some criteria that have been proposed in the literature and that theoretical research may in screening to help address the defect tolerance challenge in wider bandgap semiconductors. The authors of the work of Ganose *et al.* proposed enhancing ionic (vibrational) contributions to the static dielectric constant, exploiting, for example, spontaneous electric polarization, like in SbSI possessing a Curie temperature of 291 K, or flexibility of the framework, like in MHPs. Therefore, the authors of the work of Brandt *et al.*[41] themselves proposed additional screening criteria for the selection of materials that are likely to exhibit a long carrier lifetime. The first criterion stems from the heuristic observation that there is a correlation between the symmetry of the crystal structure's low effective masses and long lifetimes (>660 ns), such as double perovskite $Cs_2AgBiBr_6$, among the materials considered here. The second criterion is the importance of the choice of anion for a given cation. As already mentioned in the Introduction, one of the reasons for the defect tolerance of MHPs is the formation of antibonding orbitals at the valence band edge. The conclusion of the work of Brandt *et al.* is that the energy mismatch between Bi(6s) and I(5p) orbitals makes their hybridization insufficient to achieve good defect tolerance.

A comment is in order about theoretical research on defects and related electronic states. The apparent mismatch between calculations, which reveal no likely defects associated with such deep gap states, and experimental results from the work of Brandt *et al.* and, especially, that of Huq *et al.* can be due to several facts. First, defect calculations are typically performed in the zero-temperature approximation, i.e., after creating the defect, the atomistic structure of the sample is either held fixed at the perfect crystalline structure or relaxed to the nearest local minimum. A limited number of studies, mostly devoted to lead-based MHPs, have shown that the finite temperature structure of the defect can significantly differ from the one obtained within the standard zero-temperature approximation.[99,100] Moreover, at finite temperature, the structure can significantly change from charge state to charge state, a phenomenon strongly affecting the nature of defect states that is overlooked in the zero-temperature approximation. The mismatch between computational results and that presented in the work of Huq *et al.* is not necessarily due to artifacts resulting from the simulation protocol but might also be due to processes that have not been investigated, so far. For example, for LHPs, on which research has been more intense, it was found that interstitial iodide, a shallow defect in the bulk, may become a trap state at grain boundaries.[94] Finally, the analysis of shallow or deep gap states focuses on the equilibrium abundance of defects. This, however, disregards nonequilibrium effects, i.e., defect abundance beyond their thermodynamic value: Once formed during film deposition, typically a nonequilibrium process, annihilation might be too slow for defect concentration to achieve its equilibrium value, possibly resulting in the observed deep gap state. Thus, despite the significant progress made in this field, systematic theoretical research is needed to address defect tolerance in BiOI, which might also help identify heuristic criteria for selecting novel PV materials.

The search for lead-free PIM alternatives has focused on elements with electronic configurations analogous to lead in LHPs as well as a crystal structure based on corner-sharing $[PbX_6]^{4-}$ octahedra. Indeed, the defect tolerance of the latter has been linked to the high symmetry of these structures and the ionic–covalent bonding arising from the stable ns^2 configuration of the Pb^{2+} cations hybridizing with halide anions.[90] Both antimony and bismuth formally fit this criterion as their valence ns^2 electrons hybridize with halide anion orbitals to form a similar electronic structure. Antimony-based compounds are more appealing due to their

APL Energy REVIEW pubs.aip.org/aip/ape

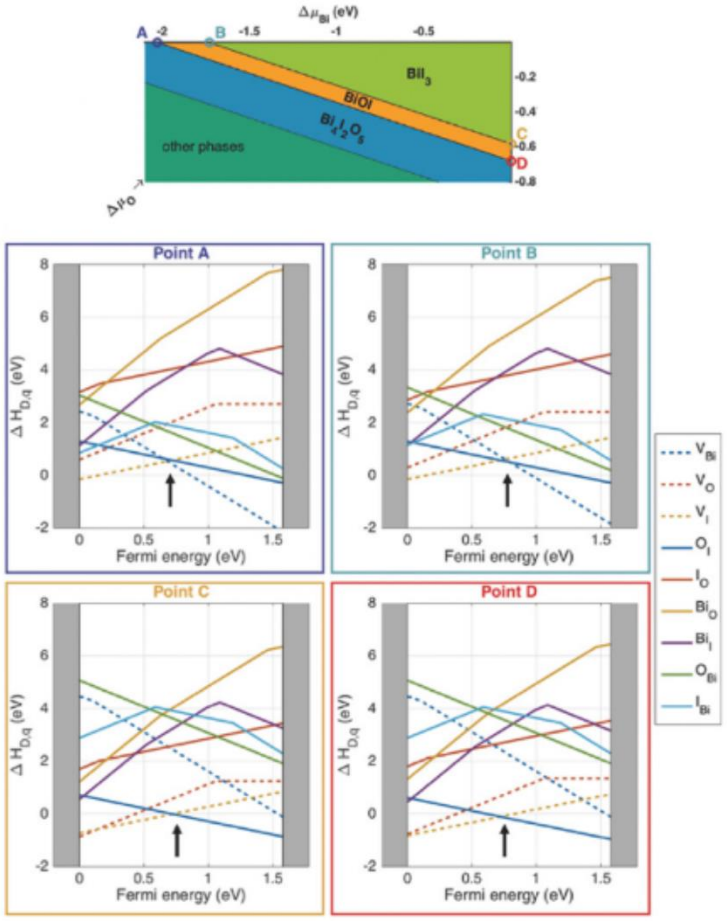

FIG. 8. Top: Phase diagram of the Bi–O–I system, showing the stability region of BiOI as well as phases with close equilibrium conditions. Bottom: Formation energy of intrinsic point defects in BiOI at the four extremes in the phase-stable region for BiOI. These diagrams allow one to identify the most likely defects in the various thermodynamic conditions as a function of the fermi energy of the system. Points A and B correspond to I-rich growth conditions, whereas points C and D correspond to Bi-rich conditions. Adapted with permission from Hoye *et al.*, Adv. Mater. **29**(36), 1702176 (2017). Copyright 2017 Author(s), licensed under a Creative Commons Attribution 4.0 License.

appreciably smaller exciton binding energy (~100 meV range) compared to the bismuth-based counterparts (~300 to 400 meV), promising a higher PCE.[101] However, due to the +3-oxidation state of Sb, it is not possible to directly substitute it in ABX_3 materials. Instead, a defect-ordered $A_3B_2X_9$ perovskite can be formed, with A^+: MA^+, FA^+, Rb^+, K^+, Cs^+; B^{3+}: Sb^{3+}; X^-: Cl^-, Br^-, I^-. This can be thought of as $A_3B_2(\cdot)X_9$, in which every third metal cation in ABX_3 is substituted for a vacancy, $(\cdot)$. Systems with $A_3B_2X_9$ composition can arrange in the structure of a different kind and often form 0D materials of the kind shown in Fig. 9(a), consisting of isolated bioctahedral $[B_2X_9]^{3-}$ groups alternating with A^+-site cations.

The band structure of such systems is rather flat, implying high effective masses of charge carriers, hence reduced mobility and limited efficiency.[84] However, this effective mass can be reduced by tuning the A-site or X-site ions to stabilize the corresponding 2D structure [Fig. 9(a)], possessing better electronic characteristics. In particular, smaller A cations favor the formation of the 2D phase over the 0D one [Fig. 9(c)].[102] For example, according to numerous reports, $MA_3Sb_2I_9$ (ionic radius ~180 pm) forms in the 0D phase whereas $(NH_4)_3Sb_2I_9$, $Rb_3Sb_2I_9$, and $K_3Sb_2I_9$ (ionic radius ~150 pm) in the 2D polymorph. It is worth noting that the 0D and 2D phases of Cs^+ (ionic radius 167 pm) have similar formation energies, and which polymorph is formed depends on the synthesis conditions.

APL Energy REVIEW pubs.aip.org/aip/ape

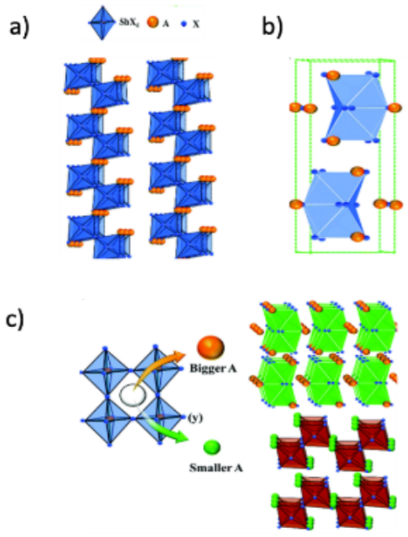

FIG. 9. (a) Layered (2D) structure of $A_3Sb_2X_9$. (b) (0D), face-sharing fused bioctahedron dimer structure of $A_3Sb_2X_9$; (c) schematic representation showing the impact of the A cation having a different ionic radius: A bigger A cation (X) results in the 0D dimer structure and a smaller A (y) one in the 2D layered structure phase. Adapted with permission from Nie *et al.*, Energy Environ. Sci. **13**(8), 2363–2385 (2020). Copyright 2020 Royal Society of Chemistry.

The 2D $A_3B_2X_9$ phases can be stabilized by alloying halides, I with Br or Cl, favoring a change in the structure from face- (0D phase) to corner-sharing $[BX_6]^{3-}$ octahedra (2D phase). For instance, the authors of the work of Mie *et al.* obtained 0D to a 2D structure transition via fractional substitution of iodide with chloride in $Cs_3Sb_2I_9$ (leading to $Cs_3Sb_2I_{9-x}Cl_x$) with a low-temperature, solution-based deposition process.[103]

2D $Cs_3Sb_2I_9$ has attracted significant interest owing to its lowest bandgap, among its other halide derivatives ($Cs_3Sb_2Cl_9$, $Cs_3Sb_2Br_9$), which results in potentially higher performance of OPV due to higher absorption coefficient at 1.5 AM conditions ($>10^5$ cm^{-1}). However, similar to LHPs, $Cs_3Sb_2X_{9-\alpha}Y_\alpha$ possesses a compositional tunable bandgap, which makes this material very interesting for IPV applications. DFT band structure calculations showed that the VBM of 2D $Cs_3Sb_2I_9$ is composed of mixed I *p* and Sb s orbitals, whereas CBM is mainly derived from Sb *p* states [Fig. 10(a)].[104] It is rather interesting to note that this band structure strongly mimics the 2D layered (N = 4) lead-halide counterpart (Cs_2PbI_4), where the VBM consists of hybridized filled Pb-6s and I-5p orbitals, while the CBM mainly consists of empty Pb-6p orbitals [Figs. 10(c) and 10(d)].[105,106] Thus, one expects 2D $Cs_3Sb_2I_9$ to deliver similar structural characteristics and optoelectronic properties to its lead-based counterpart. The 2D $Cs_3Sb_2I_9$ does not only display a lower direct bandgap of ~2 eV but also shows improved band dispersion compared to its 0D counterpart, which, on the contrary, has a much larger indirect bandgap of 2.4 eV [Fig. 10(b)]. Furthermore, it has been verified by the space charge limited current (SCLC) that 2D $Cs_3Sb_2I_9$ thin films have a hole mobility of 6.81 $cm^2/V\ s^{-1}$, which is almost double that in 0D polymorph, which is also indicative of the reduced carrier effective mass in the case of the 2D phase.

Despite the positive aspects highlighted above, theoretical studies of defect properties by Saparov and co-workers have suggested the presence of dominant deep-level defects in 2D $Cs_3Sb_2I_9$.[104] Out of the studied intrinsic point defects, like cation vacancies (V_{Cs}, V_{Sb}), iodide interstitial (I_i), Cs on Sb cation substitution (Cs_{Sb}), anion-on-cation antisites (I_{Cs}, I_{Sb}), iodide vacancy (V_I), cation interstitial (Cs_i, Sb_i), Sb on Cs substitution (Sb_{Cs}), and cation-on-anion antisite substitution (Cs_I, Sb_I), the thermodynamically dominant defects are V_{Cs}, I_i, I_{Sb}, Cs_i, and V_I; among these, only Cs_i and V_{Cs} produce shallow levels, whereas I_i, I_{Sb}, and V_I produce deep levels according to the calculated charge transition levels.

These defects have also been considered responsible for the limited stability of both 0D and 2D polymorphs of $Cs_3Sb_2I_9$ to humidity, air, heat, and light.[107] The authors identified the loss of iodine from the system as the prime reason for the degradation of the $Cs_3Sb_2I_9$ system. Unfortunately, no theoretical explanation has yet been provided to help devise strategies to counteract this phenomenon. Finally, mild fabrication conditions favor the formation of 0D $Cs_3Sb_2I_9$, while to obtain the 2D polymorph, specialized techniques, such as thermal evaporation or treatments at temperatures ≥230 °C, must be used.[108]

Halide alloying is proposed to overcome some of the limitations of $Cs_3Sb_2I_9$ without impairing the intriguing characteristics of the material. According to theoretical investigations of Park and Hong, 33% Cl substitution in $Cs_3Sb_2I_9$ leads to formation of stable 2D $Cs_3Bi_2I_6Cl_3$ and was accompanied by 0.22 eV bandgap reduction compared to 0D $Cs_3Bi_2I_9$.[109] While reduction of the bandgap is neither important nor desirable for IPV, the authors of the work of Jiang *et al.* also reported that partial replacement of iodide with chloride in the $Cs_3Sb_2I_9$ lattice suppresses the formation of the 0D phase.[110] The previous observations were supported by Peng and co-workers, who reported a PCE of 2.15% for high-quality 2D $Cs_3Sb_2Cl_xI_{9-x}$ films.[101] However, none of the theoretical calculations report the composition–structure–optical property relations specifically for $Cs_3Sb_2I_{9-x}Cl_x$ PV cells. However, a recent theoretical study carried out by Pradhan *et al.* showed that a minimal (two atoms per formula structure) substitution of Br in $Cs_3Sb_2Cl_9$, $Cs_3Sb_2Cl_7Br_2$, led to an indirect (2.28 eV)-to-direct (2.17 eV) bandgap transition.[111] The splitting of p-states of halides and Sb just above the Fermi level induced by change in the terminal Cl/Br–Sb–Cl/Br bond angle is observed to be the primary reason for transition of the band from an indirect to direct type with Br substitution. Hence, halide alloying does appear to be an effective strategy to obtain high-quality 2D structures and, henceforth, materials that can deliver high PCE. Despite the progress, the still limited efficiency raises numerous questions about charge transport between the material and the HTL/ETL. Hence, extensive and systematic theoretical research is important for the progress of this field.

III. HEAVY PNICTOGEN-BASED PEROVSKITES AND PIMs: THE MODEL CASE OF THE $Cs_2AgBiBr_6$ DP

In the frame of the three PIMs discussed within this review, the ionic structure of the $Cs_2AgBiBr_6$ DP is undoubtedly the closest to the original ABX_3 perovskite structure. In this material, the

APL Energy REVIEW pubs.aip.org/aip/ape

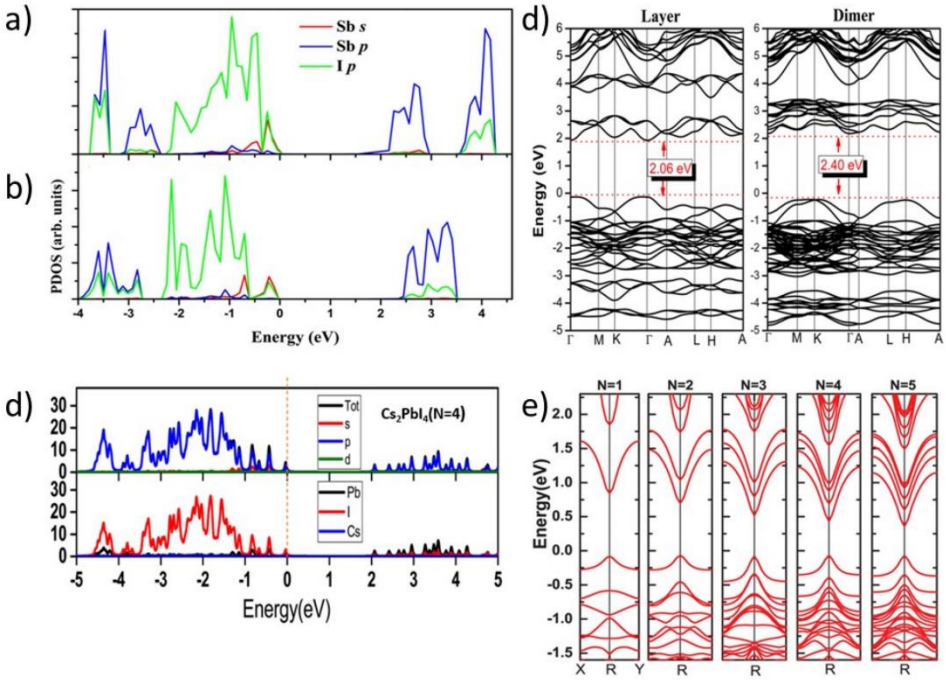

FIG. 10. Partial density of states (PDOSs) of (a) layered and (b) dimer modifications of $Cs_3Sb_2I_9$, respectively. (c) In the panel, the corresponding band structures are shown. Adapted with permission from Saparov *et al.*, Chem. Mater. **27**(16), 5622–5632 (2015). Copyright 2015 Author(s), licensed under a Creative Commons Attribution 4.0 License. (d) PDOSs of Cs_2PbI_4 (N = 4); (e) calculated band structures of Cs_2PbI_4(*N* = 1–4). Reproduced with permission from L. Zhang and W. Liang, J. Phys. Chem. Lett. **8**(7), 1517–1523 (2017). Copyright 2017 American Chemical Society.

divalent Pb^{2+} cations on the B-site are substituted by a (theoretically) equal ratio of monovalent Ag^+ and trivalent Bi^{3+} cations, to form a perovskite-like structure in which $[AgBr_6]^{5-}$ and $[BiBr_6]^{3-}$ octahedra are arranged in an alternating fashion [see Fig. 2(a)]. Accordingly, this material and materials in which analogous substitutions are performed are named DPs or elpasolites. As $Cs_2AgBiBr_6$ is a fully inorganic DP and Ag^+ and Bi^{3+} are very inert cations, this material is generally characterized by high stability to environmental conditions. In contrast to its lead-containing counterparts, $Cs_2AgBiBr_6$ possesses an indirect bandgap that is reported to be between 2 and 2.2 eV.[66,112,113] Although this bandgap energy is only slightly exceeding the optimum value for IPVs (see Fig. 1), its indirect character and other optoelectronic properties of this material, like the strong electron–phonon coupling (described in detail in Sec. II),[114,115] and the fast surface carrier recombination,[116] prevent it from achieving large PCEs as a light-harvesting material in PPVs. Still, since $Cs_2AgBiBr_6$ is one of the earliest PIMs investigated,[36] extensive research on this material can serve as the basis to synthesize and characterize related PIMs, which can help overcome the efficiency-hampering features of $Cs_2AgBiBr_6$. For this reason, we summarize here relevant information about the state-of-the-art research progress on $Cs_2AgBiBr_6$, to show from which of these findings other PIMs can benefit. It is important to note that, in the vast majority of reports that studied $Cs_2AgBiBr_6$ as light-harvesting material, the PV devices were not characterized under indoor but rather under outdoor irradiation. Still, $Cs_2AgBiBr_6$ IPVs will benefit from investigations about the material's crystallization behavior, its optoelectronic properties, or the dependence of its bandgap on the structure. Moreover, research on entire solar cells will support the investigation on IPVs, owing to $Cs_2AgBiBr_6$'s suitable bandgap for the scope. For example, recently, some of us reported on a "green" $Cs_2AgBiBr_6$-based solar cell architecture by substituting the gold back electrode and HTL with a single layer of carbon black that was obtained from upcycled 5-year-old used car tires and deposited by ultrasonic spray-coating from atoxic isopropanol with no additives (Fig. 11).[117] This approach of utilizing an end-of-waste material, in conjunction with a sustainable PIM as a light-absorber, drastically reduces production costs and toxicity concerns for devices expected to operate within households and at the same time enables the fabrication of solar cells with exceptionally high open-circuit voltages (V_{OC}).

$Cs_2AgBiBr_6$ is prepared analogously to its lead counterparts from solution, e.g., via spin-coating,[118,119] by evaporation, even single-source evaporation,[120] or by pulsed laser deposition (PLD).[121] The first critical step to creating well-performing PVs is to fabricate homogeneous, pinhole-free perovskite thin films

APL Energy REVIEW pubs.aip.org/aip/ape

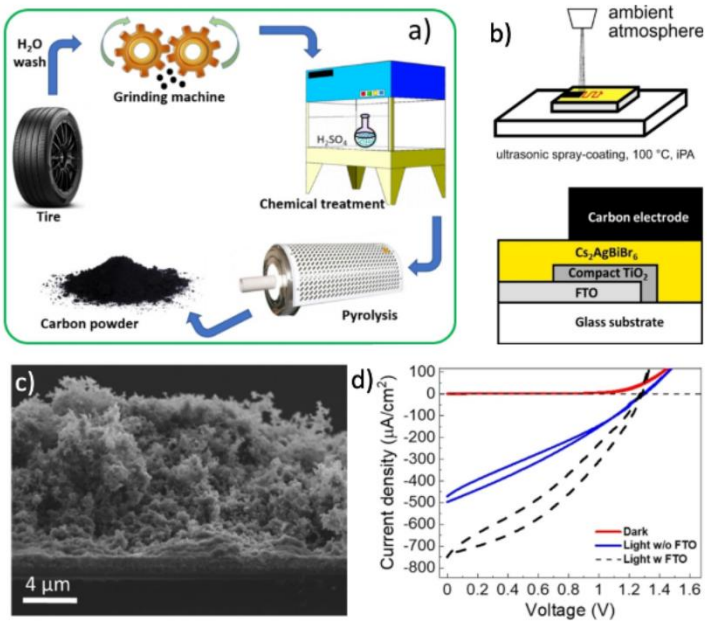

FIG. 11. (a) Process for the production of an end-of-waste carbon black powder from waste tires. (b) Schematic of the ultrasonic spray-coating method used to deposit the carbon electrode on $Cs_2AgBiBr_6$ solar cells. (c) Cross-section scanning electron microscope image of the resulting solar cell. (d) Current density–voltage characteristics of the device in dark, light, and after application of gentle pressure on top of the carbon electrode with a conductive glass slide. Adapted with permission from Schmitz *et al.*, ChemSusChem **15**(22), e202201590 (2022). Copyright 2022 Author(s), licensed under a Creative Commons Attribution 4.0 License.

that feature large grain sizes, thus reducing the number of grain boundaries, which serve as dominant nonradiative recombination sites and as main channels for ion transport.[122] To reduce this degradation-inducing ion diffusion during long-term operation,[123] the authors of the work of Li *et al.* added the ionic liquids 1-butyl-1-methylpyrrolidinium chloride (BMPyrCl) and 1-butyl-3-methylpyridinium chloride (BMPyCl) to interact with the Br^- ions, pinning them in the perovskite structure.[124] This drastically improved the resulting device long-term stability.

Moreover, control over the PIMs crystallization process is crucial to fabricate high-quality thin films. The grain growth and homogeneity of PIM thin films can either be positively affected by introducing additives, such as thiourea (TU),[118] formamidinium acetate,[119] an (HBr)-assisted synthesis,[125] or by covering the ETL with methylammonium chloride before spin-coating $Cs_2AgBiBr_6$.[126] The latter does not only enhance the crystallization but also reduces trap-assisted recombination by facilitating the electron extraction from the perovskite to the ETL.[126] A more fundamental method to enhance the film quality is to perform solvent engineering. The authors of the work of Abdelsamie *et al.* were able to obtain detailed insights into the crystallization process when antisolvent dropping was performed during the spin-coating process, using *in situ* spectroscopy and *in situ* grazing incidence wide-angle x-ray scattering (GIWAXS).[125] They found that antisolvent dropping increased the film homogeneity by inducing instantaneous supersaturation and crystallization of the wet film. Furthermore, not only does antisolvent dropping require a hot casting but also the dropping time within a narrow window is critical to creating pinhole-free films.

Since the bandgap of $Cs_2AgBiBr_6$ is too large even to achieve an optimum PCE in IPVs, various options to decrease it have been investigated. Analogous to lead-based perovskites, ionic substitution, especially anion exchange, is a promising attempt to tune the bandgap. In this regard, substituting Br^- by I^- would reduce the material's bandgap. Simulations by the authors of the work of Alla *et al.* indicate that Cs_2AgBiI_6 could reach up to ~29% PCE in combination with suited ETL and HTL in OPVs. Despite this, pure Cs_2AgBiI_6 has not found use in real devices due to its unstable nature.[127] On the contrary, a partial substitution of Br^- by I^- via anion exchange utilizing methylammonium iodide (MAI) during post-treatment to fabricate $CsAgBiBr_{6-x}I_x$ ($0 \le x \le 4$) thin films led to a bandgap reduction by up to 0.3 eV for an iodide content of $x = 4$ [Fig. 12(a)].[128] Shifting the bandgap toward larger values is also possible by substituting Br^- with Cl^- instead of I^-. The authors of the work of Ahn *et al.* showed this for their mechanochemically synthesized $CsAgBiBr_{6-x}Cl_x$ ($0 \le x \le 6$) powders, gradually blue-shifting the material's absorption as well as emission spectra with increasing Cl^- content.[129] Interestingly, Raman spectral analyses pointed out

APL Energy REVIEW pubs.aip.org/aip/ape

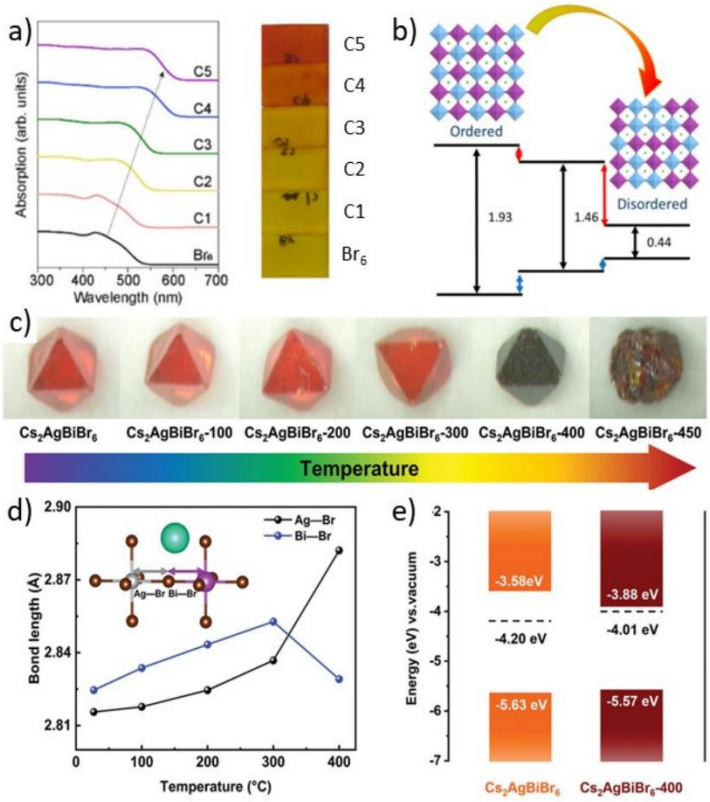

FIG. 12. (a) Bandgap tuning through halide exchange via MAI post-treatment. Adapted with permission from Wu *et al.*, ChemSusChem **14**(20), 4507–4515 (2021). Copyright 2021 Wiley. (b) Schematic bandgap dependency on the degree of disorder in the $[BiBr_6]^{3-}$ and $[AgBr_6]^{5-}$ octahedra for $Cs_2AgBiBr_6$. Reproduced with permission from Yang, Zhang, and Wei, J. Phys. Chem. Lett. **9**, 31–35 (2018). Copyright 2018 American Chemical Society. (c) Color of single crystals as well as (d) Ag–Br and Bi–Br bond lengths for varying annealing temperatures, and (e) effect of 400 °C annealing temperature on VB, CB, and Fermi energy. Reproduced with permission from Zhang *et al.*, Small **18**(24), 2201943 (2022). Copyright 2022 Wiley.

that the formation of Br^--rich and Cl^--rich octahedra is preferred rather than a homogeneous alloy.[130] Not only the anionic but also the cationic substitution of Bi^{3+} can have an impact on the bandgap. The incorporation of Sb^{3+} on the Bi^{3+} site can lead to a reduction of the bandgap.[131] However, Sb^{3+} hardly substitutes Bi^{3+} except when utilizing a mechanochemical or a spray-drying synthesis that allows up to 40% of Sb^{3+} substitution.[131]

As mentioned in Sec. II, composition alternation is not a necessity to tune the material's bandgap. Due to the special property of $Cs_2AgBiBr_6$, containing a mixture of two different B-site octahedra, a variation of their structural arrangement, too, strongly influences its bandgap. First-principles calculations show that the large indirect bandgap that is typically observed for $Cs_2AgBiBr_6$ exists due to the highly ordered structure of alternating $[BiBr_6]^{3-}$ and $[AgBr_6]^{5-}$ octahedra.[68,132] However, as soon as antisite-type defects are created, changing the ordered structure to a disordered one, not only does the bandgap decrease gradually with the degree of disorder, reaching a minimum of 0.44 eV for a fully disordered structure,[68] as it is depicted in Fig. 12(b), but also the bandgap character changes from indirect to direct[132] or pseudodirect.[68] Since the energy difference per mixed cation site between the ordered and disordered $Cs_2AgBiBr_6$ is quite large with a value of 0.141 eV, most reported thin films and single crystals possess the ordered structure and therefore the unwanted large indirect bandgap.

The authors of the work of Zhang *et al.* proved this theoretical model experimentally by annealing a $Cs_2AgBiBr_6$ single crystal at various temperatures. They observed a shift in UV–vis absorption spectra and photoluminescence spectra as well as a coherent change of the single crystal color from red to black at 400 °C, depicted in Fig. 12(c), that corresponded with a bandgap reduction from 2.05 to 1.69 eV.[133] Lower temperatures from room temperature up to 300 °C did not induce any change in optical properties and an

APL Energy REVIEW pubs.aip.org/aip/ape

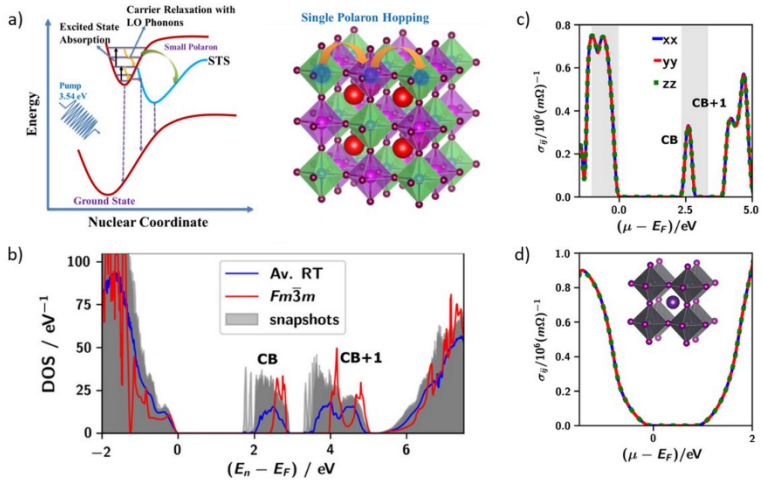

FIG. 13. (a) Polaron hopping mechanism in $Cs_2AgBiBr_6$: Excited carriers relax via coupling with longitudinal optical (LO) phonons. Distortion of the soft $Cs_2AgBiBr_6$ lattice triggers acoustic phonons in which the carriers are self-trapped. This ultrafast trapping process favors the polaron hopping transport. Reproduced with permission from Tailor *et al.*, J. Phys. Chem. Lett. **14**(3), 730–736 (2023). Copyright 2023 American Chemical Society. (b) Comparison of $Cs_2AgBiBr_6$ DOS at T = 0 K and room temperature, (c) electrical conductivity tensors calculated for T = 300 K for $Cs_2AgBiBr_6$ and for (d) $CsPbI_3$. Reproduced with permission from J. Gebhardt and C. Elsässer, Phys. Status Solidi B **259**(8), 2200124 (2022). Copyright 2022 Wiley.

annealing temperature of 450 °C led to the decomposition of the material, which follows the thermal stability limit of 410 °C, reported by Dakshinamurthy and Sudakar.[134] For the 400 °C annealed single crystal, a large change of Ag–Br and Bi–Br bond lengths occurred, shown in Fig. 12(d), that could not be attributed to temperature-induced lattice expansion but was explained by the formation of Ag_{Bi} and Bi_{Ag} antisite defects.[133] As a result, those antisite defects broaden the band edges, change the energy levels of VBM and CBM, which could be observed by x-ray photon spectroscopy measurements, and therefore decrease the bandgap [Fig. 12(e)].

Finally, a hydrogenation of $Cs_2AgBiBr_6$ thin films, resulting from interstitial doping with atomic hydrogen atoms, also strongly affects their bandgap.[60,61] Using this method, the group of Sui was able to reduce the bandgap from 2.18 to 1.64 eV, to create $Cs_2AgBiBr_6$ OPVs with a record PCE of 6.37%.[60] They also observed that the hydrogenation treatment improved the material's charge carrier concentration, mobility, and lifetime. Numerical simulations show that an optimization of the ETL toward a $SnO/ZnO_{0.4}S_{0.6}$ double ETL system as well as an increased $Cs_2AgBiBr_6$ film thickness could increase the OPV PCE to 14.23% and a PCE of 15.61% at a lower intensity of 40 mW/cm^2, which hints at the perspective use of this architecture in IPVs.

Besides the optimum band alignment between $Cs_2AgBiBr_6$ and ETL as well as HTL, respectively, and the width of the bandgap, its character, followed by other intrinsic optoelectronic properties have deeply been investigated to reveal the reason for its weak PV performance of $Cs_2AgBiBr_6$. Recent electrochemical analyses such as temperature-dependent electrochemical spectroscopy,[136] temperature-dependent ac conductivity analysis,[115] and field-effect transistor measurements[122] revealed that the dominant conduction mechanism in this material is thermally activated polaron hopping, which is depicted in Fig. 13(a). Additionally, Gebhardt and Elsässer used a self-energy-corrected DFT method to investigate the electronic structure of $Cs_2AgBiBr_6$ in which they emphasized that the inclusion of structural dynamics broadened the CB and therefore decreased the indirect bandgap, an aspect, which many calculations neglect but is crucial for an accurate description of its electronic structure, as shown in Fig. 13(b).[135] Furthermore, they debated the low DOS in CB, as well as the absence of states between the CB and the next band CB + 1, is the cause of the low conductivity of $Cs_2AgBiBr_6$, since charge extraction in photovoltaics does not only rely on charge carriers that occupy the band edges. While the conductivity in the VB of $Cs_2AgBiBr_6$ [Fig. 13(c)] is like that of $CsPbI_3$ [Fig. 13(d)], its CB conductivity is significantly lower, which results in PCEs for $Cs_2AgBiBr_6$ that are an order of magnitude lower than those of LHP solar cells.

In summary, these investigations show that there are unexploited aspects of $Cs_2AgBiBr_6$ for PVs, which is contrasted by its unfavorable intrinsic optoelectronic properties. Still, the detailed analyses of this material can pave the way for related PIMs that, by clever design, can overcome the limits of $Cs_2AgBiBr_6$.

IV. EMERGING PIMs: THE CASE OF THE BiOI OXYHALIDE

The BiOI oxyhalide PIM is at the forefront of many different research efforts, trying to implement it both in (I)PV[6] and also in photoelectrochemical systems for the solar-driven splitting of water to produce hydrogen or for the reduction of CO_2.[137] Bi- and Sb-based chalcohalides are also investigated for similar

APL Energy REVIEW pubs.aip.org/aip/ape

purposes. Although we do not discuss them here, we want to address the reader with another interesting and very recent review on the topic.[138]

The BiOI semiconductor has a layered structure [see Fig. 2(b)], with layers being held together by weak van der Waals forces along the *c*-axis, analogous to its sister halide species like BiI_3 and Ag_3BiI_6. Although the 2D structure is not generally considered favorable for light-induced charge separation processes, this issue could become almost irrelevant when a semiconductor growth strategy has been properly developed to induce the orientation of the *c*-axis parallel to the substrate (and thus to the ETL and HTL). The authors of the work of Crovetto *et al.* have reported a detailed analysis of the three sister bismuth halide semiconductors (i.e., BiOI, BiI_3, and Ag_3BiI_6) in terms of electronic properties, thin film growth, and PV performance in single-junction solar cells.[139] All three of them have common features, such as the low to moderate temperature suitable for their synthesis [here carried out through oxy(iodization) of metallic precursors], the optimal bandgaps for top absorbers in tandem solar cells, and a relatively deep VB. However, this survey shows that texture control, i.e., crystals' orientation, could only be achieved partially for BiOI and BiI_3, with the former showing overall the best PV parameters, with a maximum PCE of 0.66%.

The first consistent contribution to making the PV performance obtained from BiOI-based solar cells competitive with other emerging semiconductors has been given in the work of Hoye *et al.* in 2017.[97] In this milestone work, the authors have investigated all-inorganic devices with configuration ITO|NiO_x|BiOI|ZnO|Al [Fig. 14(b)], in which the BiOI photoabsorber layer was grown by chemical vapor transport (CVT), a process with excellent perspectives for industrialization. The thus produced BiOI layers resulted to be very stable under standard environmental conditions (20–25 °C ambient temperature, 46%–67% relative humidity, and standard laboratory illumination) without any encapsulation, as shown by the x-ray diffraction (XRD) patterns measured over 197 days [Fig. 14(a)]. The stability was confirmed by a direct comparison within entire PV architectures with a classical LHP, i.e., MAPI. While the latter is well known for its strong sensitivity to moisture, causing a progressive PCE decay within a few minutes of operation, the BiOI-based devices were found to maintain their initial performance for up to 3 days [Fig. 14(c)]. Although the best PCE values were lower than 2%, an impressive external quantum efficiency (EQE) of 80% was measured, thanks to the densely packed morphology of the NiO_x HTL and BiOI layers. In addition, the first evidence of the better suitability of this semiconductor for PV operation under low-intensity illumination comes from the observed trend in Fill Factor (FF) reported in Fig. 14(c): This figure of merit is indeed at its maximum at the lowest tested light intensity. The observation agrees with the trends in shunt and series resistances, indicating an increase in photogenerated carrier recombination when carrier densities rise, at elevated light intensity.

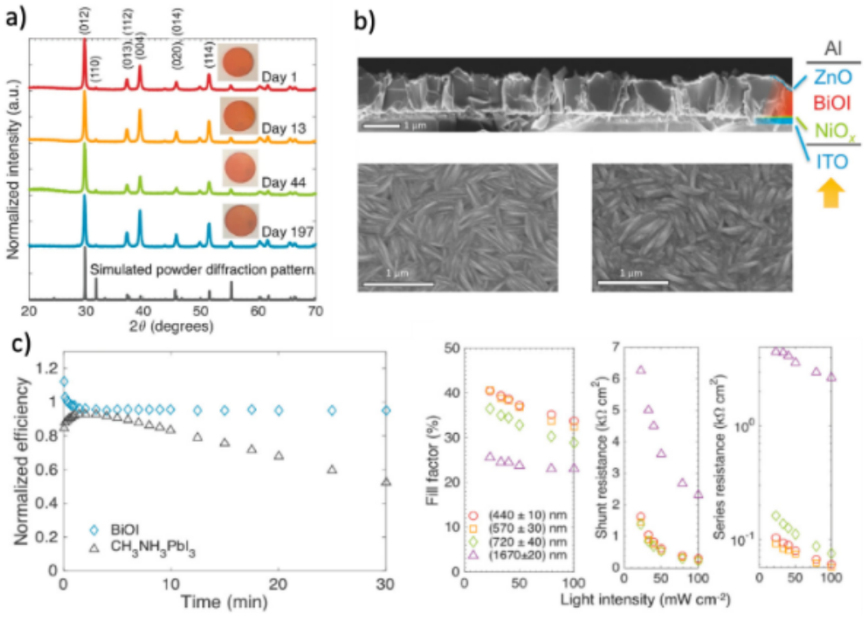

FIG. 14. Characterization of CVT BiOI thin films and solar devices. (a) Long-term stability of the CVT BiOI films as determined by x-ray diffraction on films kept in air for a prolonged time. (b) Solar cell architecture as seen by cross-section SEM image and BiOI film morphology as seen in top-view SEM images (left: sole BiOI; right: ZnO further grown onto BiOI). (c) Performance of BiOI and $CH_3NH_3PbI_3$ devices over time under constant 1 sun illumination (left) and effect of light intensity onto cell parameters (right). Adapted with permission from Hoye *et al.*, Adv. Mater. **29**(36), 1702176 (2017). Copyright 2017 Author(s), licensed under a Creative Commons Attribution 4.0 License.

APL Energy REVIEW pubs.aip.org/aip/ape

The same group achieved a preferential orientation along the *c*-axis with higher control over the BiOI layer. This allowed a shift of the V_{OC} from 0.7 to 0.9 V, which is near the calculated theoretical limit of 1.34 V.[140] Tuning of the orientation was possible thanks to the variation of operative conditions used for CVT: In a nucleation-dominated regime, the *c*-axis orientation results are favored [Fig. 15(b)] compared to a grain-growth dominated one, in which *a*/*b*-axis orientation is preferred [Fig. 15(a)]. This morphological change has a direct influence on solar cell performance, as shown in Figs. 15(c) and 15(d) with higher V_{OC} measured in devices featuring the absorber in preferential *c*-axis orientation. However, this arrangement is detrimental to charge extraction, as clearly shown by the concomitant decrease in current density [Fig. 15(c) and 15(e)], as the ETL and HTL are not directly connected with the higher mobility crystal planes. The authors concluded that for the specific case of (I)PV applications, a combination of *a*/*b*-axis and *c*-axis oriented platelets might be necessary within the photoactive layer. Alternatively, a back-contact architecture may be explored using *c*-axis oriented BiOI. From this last orientation, other applications might benefit, for example, field-effect transistors.[141]

Recently, there has been a growing interest in demonstrating the use of solution-processing methods to fabricate films of BiOI suitable for PV. Soga and co-workers have pioneered the successive ionic layer adsorption and reaction (SILAR) method carried out on a spin-coating platform (previously SILAR was reported only through dip-coating) as a simple and "green" technique to prepare BiOI thin films suitable for PV.[141] In this first contribution, 300 nm thick films of BiOI on FTO were obtained by applying 30 reactive cycles of SILAR employing water solutions of $Bi(NO_3)_3 \bullet 5H_2O$ and KI as the alternatively-deposited precursors, although no indications of annealing treatment are provided. The films were used in dye-sensitized solar cell-like configurations as photoanodes with a liquid iodide/triiodide electrolyte couple, delivering very low PCE (0.05%). Improvements in device performance were obtained by applying a 100 °C 1 h annealing treatment in air on the spin-SILAR deposited films, reaching a PCE of slightly more than 0.1%.[142]

The most remarkable and recent result obtained from solution-processing of BiOI is undoubtedly the one presented in work of Feeney *et al.*, in which solar cells with the same all-inorganic architecture as the one employed in the work of Hoye *et al.* were fabricated uniquely resorting to solution-based deposition of both the BiOI photoactive layer and the NiO_x HTL and ZnO ETL.[143] Here, the authors have resorted to the templated conversion of bismuth iodide thin films through hydrolysis in a methanol/water bath, in a low-temperature (<100 °C), carbon-free iterative process, which is depicted in Fig. 16(a). In detail, they first spin-coated BiI_3 solution onto substrates that were annealed, afterward. Then, they submerged the films in a 1:1 mixture of methanol and water to convert the BiI_3 to BiOI and then rinsed it two times in pure methanol, before drying the thin films at 100 °C [Fig. 16(a)]. The nickel oxide HTL was instead prepared via sol–gel, while the ZnO ETL was obtained from direct spin-coating deposition of ZnO nanoparticles. In similar solar cells, the PCE was strongly influenced by the number of BiOI layers (and partially by that of the ETL), with a peak performance at three layers of around 0.7% [Fig. 16(a)]. In the attempt to exploit the effect of a preferential *a*/*b*-axis orientation in the BiOI film, the authors further examined the effect of using sodium iodate as a templating agent and dopant in the hydrolysis bath. Figure 16(b) shows the effect of this treatment, with a relevant improvement happening only at 0.5 mM concentration of the iodate template, allowing partial vertical deposition of the BiOI grains within the films, which favors charge extraction. In this configuration, PCE

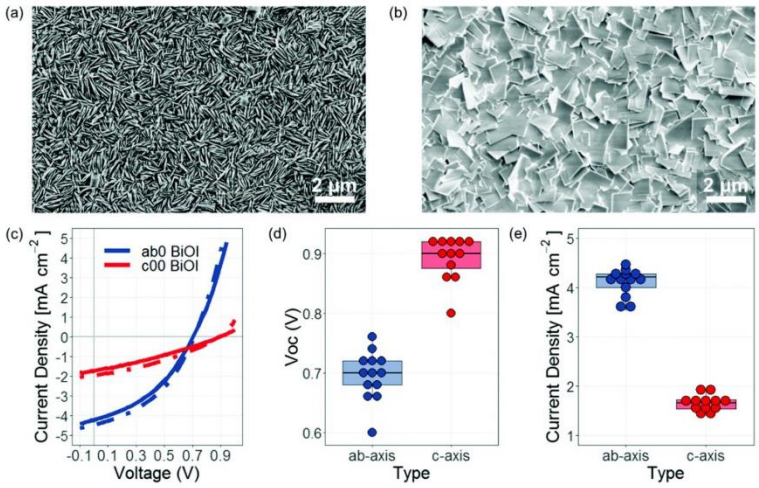

FIG. 15. Effect of controlled orientation of BiOI films on PV parameters. Morphology of thin film photo-absorbers having preferential (a) *a*/*b*-axis and (b) *c*-axis orientation. (c)–(e) PV data for the differently oriented films. Reproduced with permission from Jagt *et al.*, J. Mater. Chem. C **8**(31), 10791–10797 (2020). Copyright 2020 Author(s), licensed under a Creative Commons Attribution 3.0 Unported License.

APL Energy REVIEW pubs.aip.org/aip/ape

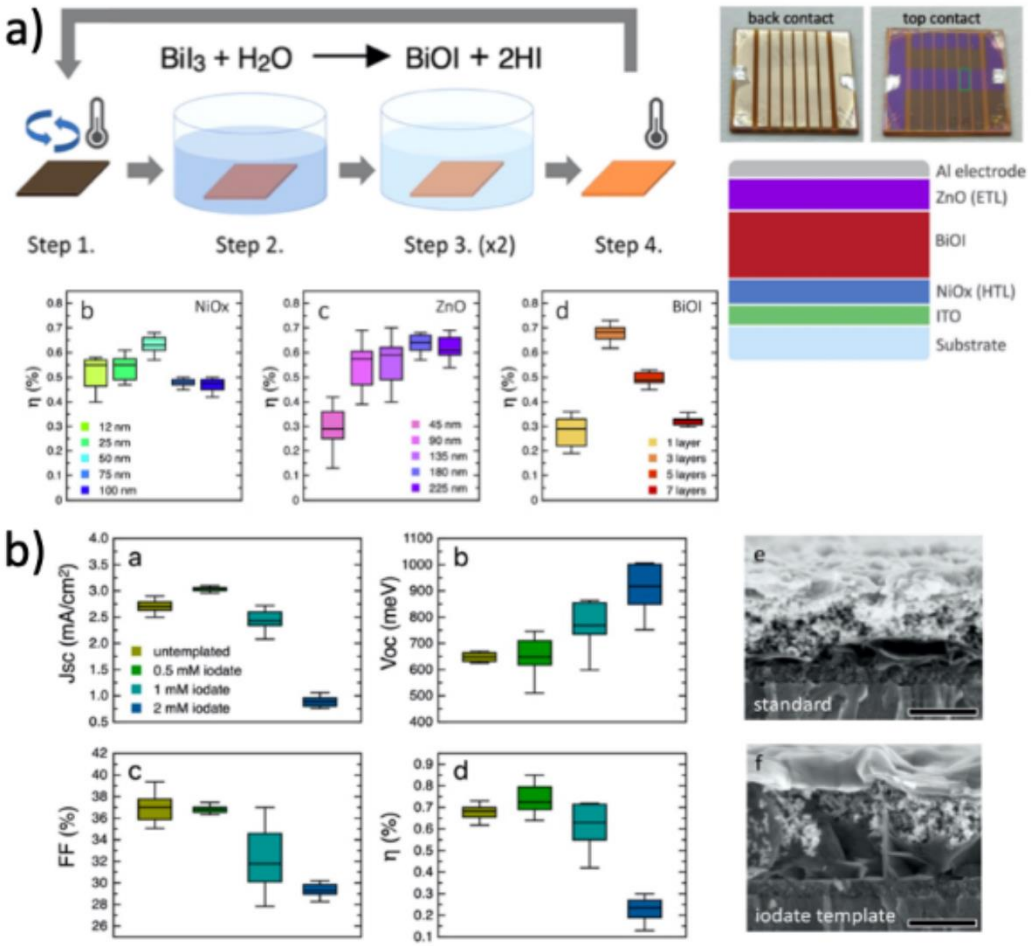

FIG. 16. Solution-processed BiOI thin films and devices. (a) Sketch of the deposition solution-based method, device architecture, and device characteristics at different thicknesses of the HTL, ETL, and photo-absorber. (b) Effect of iodate treatment on the device performance and crystalline grain orientation. Adapted with permission from Feeney *et al.*, Nanotechnology **34**, 305404 (2023). Copyright 2023 Author(s), licensed under a Creative Commons Attribution 4.0 License.

shifted to an average of 0.75%, thanks to the improvement in current density.

Ultimately, studies on bandgap tuning in BiOI might also allow to improve (I)PV performance of this material: Although the bandgap is optimal for indoor conditions, some slight changes might still allow it to reach better match with the spectrum of LEDs, for example. Moreover, narrowing the gap might pave the way for utilization of this material in outdoor applications. For the moment, very few reports have studied this issue and mostly about the use of the material as a photo(electro)catalyst: Zhang and Zhang have reported iodine self-doping of BiOI,[144] while the authors of the work of Ren *et al.* have studied the effect of defects engineering by acting on oxygen vacancies.[145] These are undoubtedly valuable approaches, but likely they require a better rationalization for use in solar cells.

V. EMERGING PIMs: THE CASE OF $Cs_3Sb_2I_{9-x}Cl_x$

Considering antimony, when Sb replaces the Pb^{2+} cation in a metal-halide structure, being its stable cation trivalent, the resultant basic unit is of the form SbX_6^{3-}. The tridimensional shape is an octahedron, where the halides are coordinated by the A^+ cation, providing a PIM with a particular dimensionality and structure. $A_3B_2X_9$ usually crystallizes into zero-dimensional (0D) or two-dimensional (2D) species [for comparison, the $A_2B^IB^{III}X_6$ DP is a tridimensional—3D—species, see Fig. 2(a)].

APL Energy REVIEW pubs.aip.org/aip/ape

In particular, the fully inorganic $Cs_3Sb_2I_9$ PIM shows either a 0D dimeric form or a layer-shaped 2D one. Colloidal nanocrystals of this compound possess deeper defect levels compared to the lead-based counterparts, thus affecting electronic properties and requiring tight control over the defect's chemistry.[146] The 2D form has an optical bandgap of 2.05 eV and it is known for being notably stable in ambient conditions compared to $MAPbI_3$. Colloidal $Cs_3Sb_2I_9$ nanocrystals are synthesized in a 2D structure with a high absorption coefficient, making them a valuable candidate for perovskite light absorbers. The substitution of the A^+ cation with other alkali metals like K or Rb creates other interesting light absorbers that were previously reviewed.[147]

The solution-processed PIM forms the 0D structure, whereas the 2D form is obtained only when a solid or gas reaction takes place. The authors of the work of Saparov *et al.*[104] determined a bandgap of 2.05 eV, an absorption coefficient of 105 cm^{-1}, and an ionization potential of 5.6 eV. However, the high number of defects that form in both cases hugely affects the PV performances, thus providing a general PCE not higher than 1% in OPV architectures.[108] Furthermore, the high binding energy and the presence of an indirect bandgap of 2.5 eV cause low photocurrents.[148] In addition, it is worth mentioning that some recent studies have shown the possibility of tuning the optical bandgap exploiting high pressure: Narrowing of bandgap takes place from the initial 2.05 eV value to 1.36 eV, with proved recrystallization of the lattice.[149,150] These studies demonstrate that a similar strategy can be useful for successful bandgap tuning of 2D structures.

For this reason, halide doping strategies have been applied, to improve optoelectronic properties of the $A_3Sb_2I_9$ PIM. One of these strategies resorts to the use of an HCl treatment. Cl^- anions are suspected to suppress the formation of Sb–I–Sb clusters, thus improving the crystallization process. In an important work, Zhou and co-workers demonstrated that, by incorporating a discrete amount of chloride into the methylammonium (MA) antimony iodide PIM ($MA_3Sb_2I_9$), a stabilized high-quality 2D layered phase film forms: By proper calculations, it is possible to demonstrate that chloride inclusion energetically favors the 2D layered phase with respect to the 0D dimeric phase, thus corroborating the experimental evidence (Fig. 17). This modification provides a PCE of more than 2% (2.15%–2.17% stabilized efficiency), that was the record for the time.[110] In the same period, the authors of the work of Umar *et al.*[151] proposed an antisolvent engineering methodology for stabilizing the planar phase, by adding a chloride additive like HCl, achieving a best PCE of 1.2%, probably lower due to the fast crystallization that produced smaller grains (not bigger than 50 nm).

For increasing the size of crystalline domains, chemical additives were employed, such as N-Methyl-2-pyrrolidone (NMP), thiourea (TU), and bis(trifluoromethane)sulfonimide lithium (the well-known LiTFSI used for 2,2′,7,7′-Tetrakis[N,N-di(4-methoxyphenyl)amino]-9,9′-spirobifluorene (SPIRO-OMeTAD) HTLs p-doping). These compounds have the ability to form complexes with the trivalent antimony cation, thus retarding the perovskite formation process through the so-called "intramolecular exchange:" The authors of the work of Yang *et al.*[152] applied lithium bis(trifluoromethane)sulfonimide (LiTFSI) to $MA_3Sb_2I_{9-x}Cl_x$ films, reaching 3.34% PCE value and retaining 90% of the initial PCE after storing the solar cells under ambient conditions for 1400 h (Fig. 18). This result is very relevant, since the MA-based Sb(III)

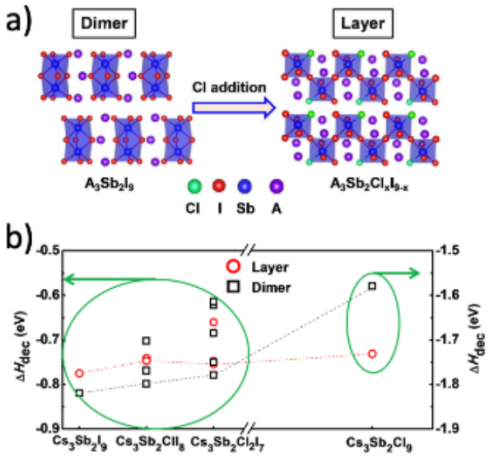

FIG. 17. Effect of chloride addition to dimeric/layered structural transition in Sb(III)-based PIMs. Reproduced with permission from Jiang *et al.*, J. Am. Chem. Soc. **140**(3), 1019–1027 (2018). Copyright 2018 American Chemical Society.

PIM usually suffers from chemical instability due to the presence of humidity, with respect to the all-inorganic sister species previously discussed.

TU and NMP are used for their capability of acting as Lewis bases as it is commonly reported for LHPs.[153] The presence of an intermediate complex [formed from the reaction with the Lewis acid, i.e., the Sb(III) halides] decreases the formation rate constant and thus also the rate of crystallization. However, the use of Lewis adduct phases is usually applied to organic–inorganic perovskites like MA or FA Pb perovskite.[154–156] The authors of the work of Singh *et al.*[157] for the first time used the methodology with the full inorganic Sb-based PIM, by selectively adding either TU or NMP, achieving notable efficiencies (more than 1.5%), substantially given by increase in the photocurrent (3.5 vs 2.5 mA cm^2 for the control sample). The authors indicate that this improved efficiency originated from diminished charge carrier recombination, as confirmed by PL measurements and EQE analysis. However, the NMP additive is more effective than TU because the latter makes the films more vulnerable to environmental stress.

However, TU addition is beneficial for obtaining a tuned morphology. The orientation of crystals on the substrate surface indeed strongly affects the efficiency[158] of solar cells when 2D layers are considered. For this reason, several efforts were made in forcing vertical growth: In a very recent report,[159] 2D $Cs_3Sb_2I_{9-x}Cl_x$ film with (201) preferential orientation was realized. In this work, the authors added TU to the precursor solution and, thanks to the C=S group in this molecule, the crystallization dynamics were regulated so that the (201) orientation could be achieved instead of the unwanted (001) orientation, providing a stabilized efficiency of about 2.2%. In another relevant work,[160] 3,9-bis(2-methylene-(3-(1,1-dicyanomethylene)indanone))-5,5,11,11-tetrakis (4-hexylphenyl)dithieno[2,3-d:2′,3′-d′]-s-indaceno[1,2-b:5,6-b′]dithiophene, usually abbreviated as ITIC additive, was used both as

APL Energy REVIEW pubs.aip.org/aip/ape

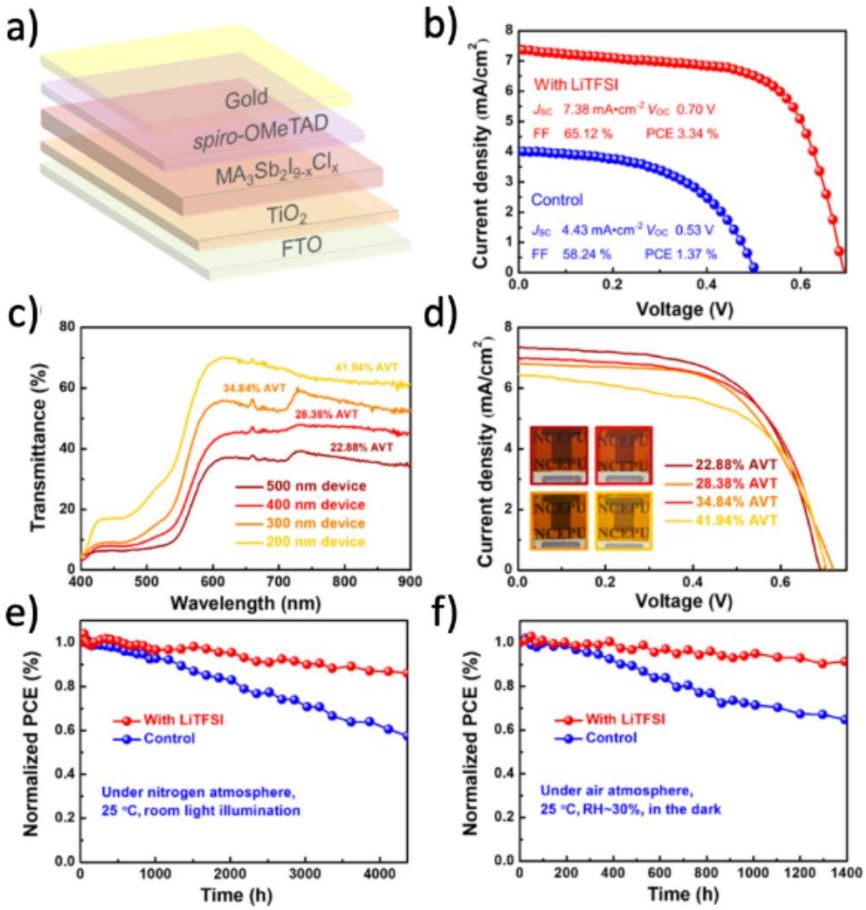

FIG. 18. LiTSI addition to $MA_3Sb_2I_{9-x}Cl_x$ PIM and OPV stability tests. Adapted with permission from Yang *et al.*, ACS Appl. Mater. Interfaces **12**(14), 17062–17069 (2020). Copyright 2020 American Chemical Society.

Lewis base and as a complimentary ETL for an antimony-based PIM to improve both the quality and the spectral coverage of the light-absorber film. The resulting solar cells (with the architecture ITO/PEDOT:PSS/$Cs_3Sb_2I_9$/ITIC/PCBM/Ca) showed the highest reported efficiency so far, to the best of our knowledge, i.e., 3.25%.

The compositional manipulation of $Cs_3Sb_2I_9$ to realize a reproducible 0D to 2D structural conversion, while preventing the formation of the preferential in-plane orientation, commonly obtained by solution-based low-temperature routes involving a mixture of halides (chloride and iodide), is a relevant result reported in a recent study of Peng *et al.*[101] In this contribution, the active layer is composed of a sandwich structure ($Cs_3Sb_2Cl_3I_6$/$Cs_3Sb_2I_9$) that allows obtaining unoriented perovskite films that provide superior EQEs. The consequence of this outcome is that layered all-inorganic Sb halides could potentially deliver higher PV performances by aligning their perovskite sheets in the out-of-plane direction as it usually occurs in layered LHPs.[161]

VI. CONCLUSIONS

In this Review, we combine discussion on theoretical background and experimental results to provide an up-to-date overview of the potential for application in IPV of three representative PIMs, which are the DP $Cs_2AgBiBr_6$, here considered as a model system for pnictogens-based species, BiOI, and $Cs_3Sb_2I_{9-x}Cl_x$. Although the current (I)PV performance of these semiconductors is still rather low (PCEs rarely above 5%), their bandgaps (in particular

APL Energy REVIEW pubs.aip.org/aip/ape

the ones of the two latter PIMs) are close to the optimum value of 1.9 eV, with EQE spectra in devices matching very well the emission spectra of WLEDs and FLs. Ideal IPV cell efficiencies have been estimated to have the potential to reach maximum values around 40% (but only slightly more than 10% for the Ag–Bi DP).[6] Those numbers justify the need for more thorough investigations to be carried out in the future on performance optimization in these materials, which will be achieved through a better understanding of their defects physics as well as their structural and morphological arrangements when deposited as thin films. For example, in this Review, we described how doping of such materials can on the one hand tune the bandgap toward optimum values and on the other also improve properties such as carrier mobility and lifetime, i.e., for hydrogenated $Cs_2AgBiBr_6$.[60] Therefore, we believe that further research on this process will improve the efficiency of PIMs as indoor light-harvesters, eventually.

However, this cannot be seen as the only advantage to investigate the implementation of BiOI and $Cs_3Sb_2I_{9-x}Cl_x$ in light energy harvesting devices. Perhaps, the biggest advantage is deriving from the good level of sustainability characteristics of these PIMs, based on low-toxicity elements like the heaviest pnictogens Sb and Bi, which contrasts with that of other emerging semiconductors of the same family, i.e., the LHPs. The purchase criticality of the former compared to the latter is currently more pronounced, but there are very optimistic perspectives for an increased recycling rate, which will certainly be sought if demonstration for technological and, consequently, industrial utility is achieved. In the end, silicon, the main protagonist of the semiconductor industry, is also listed among CRMs, but this does not prevent its widespread implementation in a wide range of applications for which semiconductors are necessary.

The current requirements for more sustainable energy harvesters, which can also be produced at low costs and undergo ease of recovery *postmortem*, calls for a collective effort involving materials scientists, physicists, and engineers toward the identification of the most promising semiconductors, taking into consideration the many aspects discussed above. We believe that for the two emerging PIMs discussed here, by taking inspiration from what has been previously learned for the more studied $Cs_2AgBiBr_6$, it will be possible to achieve excellent results in terms of device efficiency within the next 5–10 years, whereas the environmental stability is already a well-recognized asset. In this way, we soon expect to have IPV devices to power our IoT systems within households and other private or public spaces and also perhaps within "delicate" environments, such as those connected to agriculture and farming, based on these and other similar materials, which will contribute to close the loop between energy efficiency and sustainability of production and operation.

ACKNOWLEDGMENTS

T.G. would like to acknowledge the financial support provided by the European Commission through the H2020 FET-PROACTIVE-EIC-07-2020 project LIGHT-CAP (Grant No. G.A. 101017821), by the European Research Council through the ERC StG project JANUS BI (Grant No. G.A. 101041229), and by the Deutsche Forschungsgemeinschaft (DFG, German Research Foundation) through the project Grant No. GA 3052/1-1. T.G. acknowledges the support of the Justus Liebig University Giessen through the Herbert-Stolzenberg-Preis for research 2022.

AUTHOR DECLARATIONS

Conflict of Interest

The authors have no conflicts to disclose.

Author Contributions

Fabian Schmitz: Conceptualization (lead); Data curation (equal); Formal analysis (equal); Funding acquisition (lead); Investigation (equal); Methodology (equal); Project administration (equal); Resources (lead); Supervision (equal); Validation (equal); Writing – original draft (equal); Writing – review & editing (equal). **Ribhu Bhatia**: Data curation (equal); Formal analysis (equal); Investigation (equal); Methodology (equal); Project administration (equal); Writing – original draft (equal); Writing – review & editing (equal). **Francesco Lamberti**: Data curation (equal); Formal analysis (equal); Investigation (equal); Methodology (equal); Project administration (equal); Writing – original draft (equal); Writing – review & editing (equal). **Simone Meloni**: Conceptualization (lead); Data curation (equal); Formal analysis (equal); Funding acquisition (lead); Investigation (equal); Methodology (equal); Project administration (lead); Resources (lead); Supervision (equal); Validation (equal); Writing – original draft (equal); Writing – review & editing (equal). **Teresa Gatti**: Conceptualization (lead); Funding acquisition (lead); Investigation (equal); Methodology (equal); Project administration (lead); Resources (lead); Supervision (equal); Validation (equal); Writing – original draft (equal); Writing – review & editing (equal).

DATA AVAILABILITY

Data sharing is not applicable to this article as no new data were created or analyzed in this study.

REFERENCES

[1]S. Zeadally and O. Bello, "Harnessing the power of internet of things based connectivity to improve healthcare," Internet Things **14**, 100074 (2021).
[2]X. Gao, P. Pishdad-Bozorgi, D. R. Shelden, and S. Tang, "Internet of things enabled data acquisition framework for smart building applications," J. Constr. Eng. Manage. **147**(2), 04020169 (2021).
[3]H. Pei Breivold, "Towards factories of the future: Migration of industrial legacy automation systems in the cloud computing and internet-of-things context," Enterp. Inf. Syst. **14**(4), 542–562 (2020).
[4]E. Twahirwa, J. Rwigema, and R. Datta, "Design and deployment of vehicular internet of things for smart city applications," Sustainability **14**(1), 176 (2021).
[5]D. P. Abreu, K. Velasquez, M. Curado, and E. Monteiro, "A resilient internet of things architecture for smart cities," Ann. Telecommun. **72**(1–2), 19–30 (2017).
[6]V. Pecunia, L. G. Occhipinti, and R. L. Z. Hoye, "Emerging indoor photovoltaic technologies for sustainable internet of things," Adv. Energy Mater. **11**(29), 2100698 (2021).
[7]S. Rühle, "Tabulated values of the Shockley-Queisser limit for single junction solar cells," Sol. Energy **130**, 139–147 (2016).
[8]M. J. Wu, C. C. Kuo, L. S. Jhuang, P. H. Chen, Y. F. Lai, and F. C. Chen, "Bandgap engineering enhances the performance of mixed-cation perovskite materials for indoor photovoltaic applications," Adv. Energy Mater. **9**(37), 1901863 (2019).

[9]J. K. W. Ho, H. Yin, and S. K. So, "From 33% to 57%—An elevated potential of efficiency limit for indoor photovoltaics," J. Mater. Chem. A **8**(4), 1717–1723 (2020).
[10]G. Jarosz, R. Marczyński, and R. Signerski, "Effect of band gap on power conversion efficiency of single-junction semiconductor photovoltaic cells under white light phosphor-based LED illumination," Mater. Sci. Semicond. Process. **107**, 104812 (2020).
[11]A. Saha, K. A. Haque, and M. Z. Baten, "Performance evaluation of single-junction indoor photovoltaic devices for different absorber bandgaps under spectrally varying white light-emitting diodes," IEEE J. Photovoltaics **10**(2), 539–545 (2020).
[12]H. K. H. Lee, Z. Li, J. R. Durrant, and W. C. Tsoi, "Is organic photovoltaics promising for indoor applications?," Appl. Phys. Lett. **108**(25), 253301 (2016).
[13]B. Li, B. Hou, and G. A. J. Amaratunga, "Indoor photovoltaics, the next big trend in solution-processed solar cells," InfoMat **3**(5), 445–459 (2021).
[14]N. H. Reich, W. G. J. H. M. van Sark, and W. C. Turkenburg, "Charge yield potential of indoor-operated solar cells incorporated into product integrated photovoltaic (PIPV)," Renewable Energy **36**(2), 642–647 (2011).
[15]M. Freunek, M. Freunek, and L. M. Reindl, "Maximum efficiencies of indoor photovoltaic devices," IEEE J. Photovoltaics **3**(1), 59–64 (2013).
[16]C. Wehrenfennig, G. E. Eperon, M. B. Johnston, H. J. Snaith, and L. M. Herz, "High charge carrier mobilities and lifetimes in organolead trihalide perovskites," Adv. Mater. **26**(10), 1584–1589 (2014).
[17]S. D. Stranks, G. E. Eperon, G. Grancini, C. Menelaou, M. J. P. Alcocer, T. Leijtens, L. M. Herz, A. Petrozza, and H. J. Snaith, "Electron-hole diffusion lengths exceeding 1 micrometer in an organometal trihalide perovskite absorber," Science **342**(6156), 341–344 (2013).
[18]A. Miyata, A. Mitioglu, P. Plochocka, O. Portugall, J. T. W. Wang, S. D. Stranks, H. J. Snaith, and R. J. Nicholas, "Direct measurement of the exciton binding energy and effective masses for charge carriers in organic-inorganic tri-halide perovskites," Nat. Phys. **11**(7), 582–587 (2015).
[19]N.R.E.L. (NREL), Best Research Efficiency, Http://Www.Nrel.Gov/Ncpv/Images/Efficiency_Chart.Jpg, 2016.
[20]L. Protesescu, S. Yakunin, M. I. Bodnarchuk, F. Krieg, R. Caputo, C. H. Hendon, R. X. Yang, A. Walsh, and M. V. Kovalenko, "Nanocrystals of cesium lead halide perovskites ($CsPbX_3$, X = Cl, Br, and I): Novel optoelectronic materials showing bright emission with wide color gamut," Nano Lett. **15**(6), 3692–3696 (2015).
[21]V. K. Ravi, G. B. Markad, and A. Nag, "Band edge energies and excitonic transition probabilities of colloidal $CsPbX_3$ (X = Cl, Br, I) perovskite nanocrystals," ACS Energy Lett. **1**(4), 665–671 (2016).
[22]S. Meloni, G. Palermo, N. Ashari-Astani, M. Grätzel, and U. Rothlisberger, "Valence and conduction band tuning in halide perovskites for solar cell applications," J. Mater. Chem. A **4**(41), 15997–16002 (2016).
[23]M. Wang, Q. Wang, J. Zhao, Y. Xu, H. Wang, X. Zhou, S. Yang, Z. Ci, and Z. Jin, "Low-trap-density $CsPbX_3$ film for high-efficiency indoor photovoltaics," ACS Appl. Mater. Interfaces **14**(9), 11528–11537 (2022).
[24]M. Li, C. Zhao, Z.-K. Wang, C.-C. Zhang, H. K. H. Lee, A. Pockett, J. Barbé, W. C. Tsoi, Y.-G. Yang, M. J. Carnie, X.-Y. Gao, W.-X. Yang, J. R. Durrant, L.-S. Liao, and S. M. Jain, "Interface modification by ionic liquid: A promising candidate for indoor light harvesting and stability improvement of planar perovskite solar cells," Adv. Energy Mater. **8**(24), 1801509 (2018).
[25]C. Dong, X.-M. Li, C. Ma, W.-F. Yang, J.-J. Cao, F. Igbari, Z.-K. Wang, and L.-S. Liao, "Lycopene-based bionic membrane for stable perovskite photovoltaics," Adv. Funct. Mater. **31**(25), 2011242 (2021).
[26]R. Cheng, C.-C. Chung, H. Zhang, F. Liu, W.-T. Wang, Z. Zhou, S. Wang, and A. B. Djurišic, "Tailoring triple-anion perovskite material for indoor light harvesting with restrained halide segregation and record high efficiency beyond 36%," Adv. Energy Mater. **9**(38), 1901980 (2019).
[27]X. He, J. Chen, X. Ren, L. Zhang, Y. Liu, J. Feng, J. Fang, K. Zhao, and S. F. Liu, "40.1% record low-light solar-cell efficiency by holistic trap-passivation using micrometer-thick perovskite film," Adv. Mater. **33**(27), 2100770 (2021).
[28]Z. Saki, M. M. Byranvand, N. Taghavinia, M. Kedia, and M. Saliba, "Solution-processed perovskite thin-films: The journey from lab- to large-scale solar cells," Energy Environ. Sci. **14**(11), 5690–5722 (2021).
[29]Y. Hu, T. Niu, Y. Liu, Y. Zhou, Y. Xia, C. Ran, Z. Wu, L. Song, P. Müller-Buschbaum, Y. Chen, and W. Huang, "Flexible perovskite solar cells with high power-per-weight: Progress, application, and perspectives," ACS Energy Lett. **6**(8), 2917–2943 (2021).
[30]K. Wojciechowski and D. Forgács, "Commercial applications of indoor photovoltaics based on flexible perovskite solar cells," ACS Energy Lett. **7**(10), 3729–3733 (2022).
[31]K. O. Brinkmann, J. Zhao, N. Pourdavoud, T. Becker, T. Hu, S. Olthof, K. Meerholz, L. Hoffmann, T. Gahlmann, R. Heiderhoff, M. F. Oszajca, N. A. Luechinger, D. Rogalla, Y. Chen, B. Cheng, and T. Riedl, "Suppressed decomposition of organometal halide perovskites by impermeable electron-extraction layers in inverted solar cells," Nat. Commun. **8**, 13938 (2017).
[32]D. Zhang, D. Li, Y. Hu, A. Mei, and H. Han, "Degradation pathways in perovskite solar cells and how to meet international standards," Commun. Mater. **3**, 58 (2022).
[33]D. Di Girolamo, M. I. Dar, D. Dini, L. Gontrani, R. Caminiti, A. Mattoni, M. Graetzel, S. Meloni, and S. Meloni, "Dual effect of humidity on cesium lead bromide: Enhancement and degradation of perovskite films," J. Mater. Chem. A **7**(19), 12292–12302 (2019).
[34]B. Li and W. Zhang, "Improving the stability of inverted perovskite solar cells towards commercialization," Commun. Mater. **3**, 65 (2022).
[35]C.-H. Chen, S.-N. Cheng, L. Cheng, and Z.-K. Wang, "Toxicity, leakage, and recycling of lead in perovskite photovoltaics," Adv. Energy Mater. **13**, 2204144 (2023).
[36]A. H. Slavney, T. Hu, A. M. Lindenberg, and H. I. Karunadasa, "A bismuth-halide double perovskite with long carrier recombination lifetime for photovoltaic applications," J. Am. Chem. Soc. **138**(7), 2138–2141 (2016).
[37]Y. Peng, T. N. Huq, J. Mei, L. Portilla, R. A. Jagt, L. G. Occhipinti, J. L. MacManus-Driscoll, R. L. Z. Hoye, and V. Pecunia, "Lead-free perovskite-inspired absorbers for indoor photovoltaics," Adv. Energy Mater. **11**(1), 2002761 (2021).
[38]S. T. Thornton, G. Abdelmageed, R. F. Kahwagi, and G. I. Koleilat, "Progress towards lead-free, efficient, and stable perovskite solar cells," J. Chem. Technol. Biotechnol. **97**(4), 810–829 (2022).
[39]W.-F. Yang, J.-J. Cao, C. Dong, M. Li, Q. S. Tian, Z. K. Wang, and L. S. Liao, "Suppressed oxidation of tin perovskite by Catechin for eco-friendly indoor photovoltaics," Appl. Phys. Lett. **118**(2), 023501 (2021).
[40]J. Cao, Y.-H. Lou, W.-F. Yang, K.-L. Wang, Z.-H. Su, J. Chen, C.-H. Chen, C. Dong, X.-Y. Gao, and Z.-K. Wang, "Multifunctional potassium thiocyanate interlayer for eco-friendly tin perovskite indoor and outdoor photovoltaics," Chem. Eng. J. **433**(3), 133832 (2022).
[41]R. E. Brandt, J. R. Poindexter, P. Gorai, R. C. Kurchin, R. L. Z. Hoye, L. Nienhaus, M. W. B. Wilson, J. A. Polizzotti, R. Sereika, R. Žaltauskas, L. C. Lee, J. L. Macmanus-Driscoll, M. Bawendi, V. Stevanović, and T. Buonassisi, "Searching for 'defect-tolerant' photovoltaic materials: Combined theoretical and experimental screening," Chem. Mater. **29**(11), 4667–4674 (2017).
[42]Y. M. Lee, I. Maeng, J. Park, M. Song, J. H. Yun, M. C. Jung, and M. Nakamura, "Comprehensive understanding and controlling the defect structures: An effective approach for organic-inorganic hybrid perovskite-based solar-cell application," Front. Energy Res. **6**, 128 (2018).
[43]A. M. Ganose, D. O. Scanlon, A. Walsh, and R. L. Z. Hoye, "The defect challenge of wide-bandgap semiconductors for photovoltaics and beyond," Nat. Commun. **13**(1), 4715 (2022).
[44]W. J. Yin, T. Shi, and Y. Yan, "Unusual defect physics in $CH_3NH_3PbI_3$ perovskite solar cell absorber," Appl. Phys. Lett. **104**(6), 063903 (2014).
[45]C. Y. Chen, J. H. Chang, K. M. Chiang, H. L. Lin, S. Y. Hsiao, and H. W. Lin, "Perovskite photovoltaics for dim-light applications," Adv. Funct. Mater. **25**(45), 7064–7070 (2015).
[46]C. Borbinha, F. Serrazina, M. Salavisa, and M. Viana-Baptista, "Bismuth encephalopathy—A rare complication of long-standing use of bismuth subsalicylate," BMC Neurol. **19**(1), 212 (2019).
[47]P. T. Reynolds, K. C. Abalos, J. Hopp, and M. E. Williams, "Bismuth toxicity: A rare cause of neurologic dysfunction," Int. J. Clin. Med. **3**(1), 46–48 (2012).
[48]M. F. Gordon, R. I. Abrams, D. B. Rubin, W. B. Barr, and D. D. Correa, "Bismuth subsalicylate toxicity as a cause of prolonged encephalopathy with myoclonus," Mov. Disord. **10**(2), 220–222 (1995).
[49]R. Wang, H. Li, and H. Sun, "Bismuth: Environmental pollution and health effects," in *Encyclopedia of Environmental Health* (Elsevier, 2019), pp. 415–423.

[50]S. Sundar and J. Chakravarty, "Antimony toxicity," Int. J. Environ. Res. Public Health **7**(12), 4267–4277 (2010).
[51]C. J. Boreiko and T. G. Rossman, "Antimony and its compounds: Health impacts related to pulmonary toxicity, cancer, and genotoxicity," Toxicol. Appl. Pharmacol. **403**, 115156 (2020).
[52]A. Periferakis, A. Caruntu, A. T. Periferakis, A. E. Scheau, I. A. Badarau, C. Caruntu, and C. Scheau, "Availability, toxicology and medical significance of antimony," Int. J. Environ. Res. Public Health **19**(8), 4669 (2022).
[53]T. Henckens, "Scarce mineral resources: Extraction, consumption and limits of sustainability," Resour., Conserv. Recycl. **169**, 105511 (2021).
[54]G. Schileo and G. Grancini, "Lead or no lead? Availability, toxicity, sustainability and environmental impact of lead-free perovskite solar cells," J. Mater. Chem. C **9**(1), 67–76 (2021).
[55]T. Gatti, F. Lamberti, R. Mazzaro, I. Kriegel, D. Schlettwein, F. Enrichi, N. Lago, E. Di Maria, G. Meneghesso, A. Vomiero, and S. Gross, "Opportunities from doping of non-critical metal oxides in last generation light-conversion devices," Adv. Energy Mater. **11**(31), 2101041 (2021).
[56]E. Deady, C. Moon, K. Moore, K. M. Goodenough, and R. K. Shail, "Bismuth: Economic geology and value chains," Ore Geol. Rev. **143**, 104722 (2022).
[57]A. Babayigit, A. Ethirajan, M. Muller, and B. Conings, "Toxicity of organometal halide perovskite solar cells," Nat. Mater. **15**(3), 247–251 (2016).
[58]F. Ünlü, M. Deo, S. Mathur, T. Kirchartz, and A. Kulkarni, "Bismuth-based halide perovskite and perovskite-inspired light absorbing materials for photovoltaics," J. Phys. D: Appl. Phys. **55**(11), 113002 (2022).
[59]Y. T. Huang, S. R. Kavanagh, D. O. Scanlon, A. Walsh, and R. L. Z. Hoye, "Perovskite-inspired materials for photovoltaics and beyond-from design to devices," Nanotechnology **32**(13), 132004 (2021).
[60]Z. Zhang, Q. Sun, Y. Lu, F. Lu, X. Mu, S.-H. Wei, and M. Sui, "Hydrogenated $Cs_2AgBiBr_6$ for significantly improved efficiency of lead-free inorganic double perovskite solar cell," Nat. Commun. **13**(1), 3397 (2022).
[61]T. I. Alanazi, "Design and device numerical analysis of lead-free $Cs_2AgBiBr_6$ double perovskite solar cell," Crystals **13**(2), 267 (2023).
[62]W. Ning, J. Bao, Y. Puttisong, F. Moro, L. Kobera, S. Shimono, L. Wang, F. Ji, M. Cuartero, S. Kawaguchi, S. Abbrent, H. Ishibashi, R. de Marco, I. A. Bouianova, G. A. Crespo, Y. Kubota, J. Brus, D. Y. Chung, L. Sun, W. M. Chen, M. G. Kanatzidis, and F. Gao, "Magnetizing lead-free halide double perovskites," Sci. Adv. **6**(45), eabb5381 (2020).
[63]G. Feng, Y. Qin, C. Ran, L. Ji, L. Dong, and W. Li, "Structural evolution and photoluminescence properties of a 2D hybrid perovskite under pressure," APL Mater. **6**(11), 114201 (2018).
[64]H. Lei, D. Hardy, and F. Gao, "Lead-free double perovskite $Cs_2AgBiBr_6$: Fundamentals, applications, and perspectives," Adv. Funct. Mater. **31**(49), 2105898 (2021).
[65]X. G. Zhao, J. H. Yang, Y. Fu, D. Yang, Q. Xu, L. Yu, S. H. Wei, and L. Zhang, "Design of lead-free inorganic halide perovskites for solar cells via cation-transmutation," J. Am. Chem. Soc. **139**(7), 2630–2638 (2017).
[66]E. T. McClure, M. R. Ball, W. Windl, and P. M. Woodward, "Cs_2AgBiX_6 (X = Br, Cl): New visible light absorbing, lead-free halide perovskite semiconductors," Chem. Mater. **28**(5), 1348–1354 (2016).
[67]M. R. Filip, S. Hillman, A. A. Haghighirad, H. J. Snaith, and F. Giustino, "Band gaps of the lead-free halide double perovskites $Cs_2BiAgCl_6$ and $Cs_2BiAgBr_6$ from theory and experiment," J. Phys. Chem. Lett. **7**(13), 2579–2585 (2016).
[68]J. Yang, P. Zhang, and S.-H. Wei, "Band structure engineering of $Cs_2AgBiBr_6$ perovskite through order–disordered transition: A first-principle study," J. Phys. Chem. Lett. **9**, 31–35 (2018).
[69]R. Fu, Y. Chen, X. Yong, Z. Ma, L. Wang, P. Lv, S. Lu, G. Xiao, and B. Zou, "Pressure-induced structural transition and band gap evolution of double perovskite $Cs_2AgBiBr_6$ nanocrystals," Nanoscale **11**(36), 17004–17009 (2019).
[70]M. N. Islam, J. Podder, T. Saha, and P. Rani, "Semiconductor to metallic transition under induced pressure in $Cs_2AgBiBr_6$ double halide perovskite: A theoretical DFT study for photovoltaic and optoelectronic applications," RSC Adv. **11**(39), 24001–24012 (2021).
[71]W. A. C. Pamodani Wanniarachchi, H. Eidsvag, T. Arunasalam, P. Ravirajan, D. Velauthapillai, and P. Vajeeston, "$Cs_2AgBiBr_6$ as a mixed anion perovskites for photovoltaic applications: A first-principle study," Mater. Today: Proc. **64**(5), 1783–1788 (2022).
[72]D. Han, T. Zhang, M. Huang, D. Sun, M. H. Du, and S. Chen, "Predicting the thermodynamic stability of double-perovskite halides from density functional theory," APL Mater. **6**(8), 084902 (2018).
[73]Z. Li, S. R. Kavanagh, M. Napari, R. G. Palgrave, M. Abdi-Jalebi, Z. Andaji-Garmaroudi, D. W. Davies, M. Laitinen, J. Julin, M. A. Isaacs, R. H. Friend, D. O. Scanlon, A. Walsh, and R. L. Z. Hoye, "Bandgap lowering in mixed alloys of $Cs_2Ag(Sb_xBi_{1-x})Br_6$ double perovskite thin films," J. Mater. Chem. A **8**(41), 21780–21788 (2020).
[74]W. Tress and M. T. Sirtl, "$Cs_2AgBiBr_6$ double perovskites as lead-free alternatives for perovskite solar cells?," Sol. RRL **6**(2), 2100770 (2022).
[75]L. Yu and A. Zunger, "Identification of potential photovoltaic absorbers based on first-principles spectroscopic screening of materials," Phys. Rev. Lett. **108**(6), 068701 (2012).
[76]Y. Bekenstein, J. C. Dahl, J. Huang, W. T. Osowiecki, J. K. Swabeck, E. M. Chan, P. Yang, and A. P. Alivisatos, "The making and breaking of lead-free double perovskite nanocrystals of cesium silver–bismuth halide compositions," Nano Lett. **18**(6), 3502–3508 (2018).
[77]R. L. Z. Hoye, L. Eyre, F. Wei, F. Brivio, A. Sadhanala, S. Sun, W. Li, K. H. L. Zhang, J. L. MacManus-Driscoll, P. D. Bristowe, R. H. Friend, A. K. Cheetham, and F. Deschler, "Fundamental carrier lifetime exceeding 1 μs in $Cs_2AgBiBr_6$ double perovskite," Adv. Mater. Interfaces **5**(15), 1800464 (2018).
[78]S. J. Zelewski, J. M. Urban, A. Surrente, D. K. Maude, A. Kuc, L. Schade, R. D. Johnson, M. Dollmann, P. K. Nayak, H. J. Snaith, P. Radaelli, R. Kudrawiec, R. J. Nicholas, P. Plochocka, and M. Baranowski, "Revealing the nature of photoluminescence emission in the metal-halide double perovskite $Cs_2AgBiBr_6$," J. Mater. Chem. C **7**(27), 8350–8356 (2019).
[79]B. Wu, W. Ning, Q. Xu, M. Manjappa, M. Feng, S. Ye, J. Fu, S. Lie, T. Yin, F. Wang, T. W. Goh, P. C. Harikesh, Y. K. E. Tay, Z. X. Shen, F. Huang, R. Singh, G. Zhou, F. Gao, and T. Chien Sum, "Strong self-trapping by deformation potential limits photovoltaic performance in bismuth double perovskite," Sci. Adv. **7**(8), eabd3160 (2021).
[80]Z. Xiao, W. Meng, J. Wang, and Y. Yan, "Thermodynamic stability and defect chemistry of bismuth-based lead-free double perovskites," ChemSusChem **9**(18), 2628–2633 (2016).
[81]T. Handa, T. Yamada, M. Nagai, and Y. Kanemitsu, "Phonon, thermal, and thermo-optical properties of halide perovskites," Phys. Chem. Chem. Phys. **22**(45), 26069–26087 (2020).
[82]N. Phung, A. Mattoni, J. A. Smith, D. Skroblin, H. Köbler, L. Choubrac, J. Breternitz, J. Li, T. Unold, S. Schorr, C. Gollwitzer, I. G. Scheblykin, E. L. Unger, M. Saliba, S. Meloni, A. Abate, and A. Merdasa, "Photoprotection in metal halide perovskites by ionic defect formation," Joule **6**(9), 2152–2174 (2022).
[83]A. D. Wright, L. R. V. Buizza, K. J. Savill, G. Longo, H. J. Snaith, M. B. Johnston, and L. M. Herz, "Ultrafast excited-state localization in $Cs_2AgBiBr_6$ double perovskite," J. Phys. Chem. Lett. **12**(13), 3352–3360 (2021).
[84]R. L. Z. Hoye, J. Hidalgo, R. A. Jagt, J. Correa-Baena, T. Fix, and J. L. MacManus-Driscoll, "The role of dimensionality on the optoelectronic properties of oxide and halide perovskites, and their halide derivatives," Adv. Energy Mater. **12**(4), 2100499 (2022).
[85]M. Sendner, P. K. Nayak, D. A. Egger, S. Beck, C. Müller, B. Epding, W. Kowalsky, L. Kronik, H. J. Snaith, A. Pucci, and R. Lovrincic, "Optical phonons in methylammonium lead halide perovskites and implications for charge transport," Mater. Horiz. **3**(6), 613–620 (2016).
[86]J. A. Steele, P. Puech, M. Keshavarz, R. Yang, S. Banerjee, E. Debroye, C. W. Kim, H. Yuan, N. H. Heo, J. Vanacken, A. Walsh, J. Hofkens, and M. B. J. Roeffaers, "Giant electron–phonon coupling and deep conduction band resonance in metal halide double perovskite," ACS Nano **12**(8), 8081–8090 (2018).
[87]K. Miyata, D. Meggiolaro, M. T. Trinh, P. P. Joshi, E. Mosconi, S. C. Jones, F. De Angelis, and X. Zhu, "Large polarons in lead halide perovskites," Sci. Adv. **3**(8), e1701217 (2017).
[88]H. Sumi and Y. Toyozawa, "Urbach-martienseen rule and exciton trapped momentarily by lattice vibrations," J. Phys. Soc. Jpn. **31**(2), 342–358 (1971).
[89]Y. Toyozawa, "Self-trapping of an electron by the acoustical mode of lattice vibration. I," Prog. Theor. Phys. **26**(1), 29–44 (1961).
[90]J. Kang and L. W. Wang, "High defect tolerance in lead halide perovskite $CsPbBr_3$," J. Phys. Chem. Lett. **8**(2), 489–493 (2017).

[91]T. Li, X. Zhao, D. Yang, M. Du, and L. Zhang, "Intrinsic defect properties in halide double perovskites for optoelectronic," Phys. Rev. Appl. **10**(1), 041001 (2018).
[92]D. Liu, C. M. Perez, A. S. Vasenko, and O. V. Prezhdo, "Ag–Bi charge redistribution creates deep traps in defective $Cs_2AgBiBr_6$: Machine learning analysis of density functional theory," J. Phys. Chem. Lett. **13**(16), 3645–3651 (2022).
[93]Y. She, Z. Hou, O. V. Prezhdo, and W. Li, "Identifying and passivating killer defects in Pb-free double $Cs_2AgBiBr_6$ perovskite," J. Phys. Chem. Lett. **12**(43), 10581–10588 (2021).
[94]J. Park, J. Calbo, Y. K. Jung, L. D. Whalley, and A. Walsh, "Accumulation of deep traps at grain boundaries in halide perovskites," ACS Energy Lett. **4**(6), 1321–1327 (2019).
[95]W.-W. Dai and Z.-Y. Zhao, "Electronic structure and optical properties of BiOI as a photocatalyst driven by visible light," Catalysts **6**(9), 133 (2016).
[96]W. L. Huang and Q. Zhu, "Electronic structures of relaxed BiOX (X = F, Cl, Br, I) photocatalysts," Comput. Mater. Sci. **43**(4), 1101–1108 (2008).
[97]R. L. Z. Hoye, L. C. Lee, R. C. Kurchin, T. N. Huq, K. H. L. Zhang, M. Sponseller, L. Nienhaus, R. E. Brandt, J. Jean, J. A. Polizzotti, A. Kursumović, M. G. Bawendi, V. Bulović, V. Stevanović, T. Buonassisi, and J. L. MacManus-Driscoll, "Strongly enhanced photovoltaic performance and defect physics of air-stable bismuth oxyiodide (BiOI)," Adv. Mater. **29**(36), 1702176 (2017).
[98]T. N. Huq, L. C. Lee, L. Eyre, W. Li, R. A. Jagt, C. Kim, S. Fearn, V. Pecunia, F. Deschler, J. L. Macmanus-driscoll, and R. L. Z. Hoye, "Electronic structure and optoelectronic properties of bismuth oxyiodide robust against percent-level iodine-, oxygen-, and bismuth-related surface defects," Adv. Funct. Mater. **30**(13), 1909983 (2020).
[99]M. L. Agiorgousis, Y. Sun, H. Zeng, and S. Zhang, "Strong covalency-induced recombination centers in perovskite solar cell material $CH_3NH_3PbI_3$," J. Am. Chem. Soc. **136**(41), 14570–14575 (2014).
[100]M. Yavari, F. Ebadi, S. Meloni, S. Wang, T. C. Yang, S. Sun, H. Schwartz, Z. Wang, B. Niesen, J. Durantini, P. Rieder, K. Tvingstedt, T. Buonassisi, W. C. H. Choy, A. Filippetti, T. Dittrich, S. Olthof, J.-P. Correa-Baena, and W. Tress, "How far does the defect tolerance of lead-halide perovskites range? The example of Bi impurities introducing efficient recombination centers," J. Mater. Chem. A **7**(41), 23838–23853 (2019).
[101]Y. Peng, F. Li, Y. Wang, Y. Li, R. L. Z. Hoye, L. Feng, K. Xia, and V. Pecunia, "Enhanced photoconversion efficiency in cesium-antimony-halide perovskite derivatives by tuning crystallographic dimensionality," Appl. Mater. Today **19**, 100637 (2020).
[102]R. Nie, R. R. Sumukam, S. H. Reddy, M. Banavoth, and S. I. Seok, "Lead-free perovskite solar cells enabled by hetero-valent substitutes," Energy Environ. Sci. **13**(8), 2363–2385 (2020).
[103]J. Mei, M. Liu, P. Vivo, and V. Pecunia, "Two-dimensional antimony-based perovskite-inspired materials for high-performance self-powered photodetectors," Adv. Funct. Mater. **31**(50), 2106295 (2021).
[104]B. Saparov, F. Hong, J.-P. Sun, H.-S. Duan, W. Meng, S. Cameron, I. G. Hill, Y. Yan, and D. B. Mitzi, "Thin-film preparation and characterization of $Cs_3Sb_2I_9$: A lead-free layered perovskite semiconductor," Chem. Mater. **27**(16), 5622–5632 (2015).
[105]C. M. M. Soe, G. P. Nagabhushana, R. Shivaramaiah, H. Tsai, W. Nie, J. C. Blancon, F. Melkonyan, D. H. Cao, B. Traoré, L. Pedesseau, M. Kepenekian, C. Katan, J. Even, T. J. Marks, A. Navrotsky, A. D. Mohite, C. C. Stoumpos, and M. G. Kanatzidis, "Structural and thermodynamic limits of layer thickness in 2D halide perovskites," Proc. Natl. Acad. Sci. U. S. A. **116**(1), 58–66 (2019).
[106]L. Zhang and W. Liang, "How the structures and properties of two-dimensional layered perovskites $MAPbI_3$ and $CsPbI_3$ vary with the number of layers," J. Phys. Chem. Lett. **8**(7), 1517–1523 (2017).
[107]T. D. Chonamada, A. B. Dey, and P. K. Santra, "Degradation studies of $Cs_3Sb_2I_9$: A lead-free perovskite," ACS Appl. Energy Mater. **3**(1), 47–55 (2020).
[108]A. Singh, K. M. Boopathi, A. Mohapatra, Y. F. Chen, G. Li, and C. W. Chu, "Photovoltaic performance of vapor-assisted solution-processed layer polymorph of $Cs_3Sb_2I_9$," ACS Appl. Mater. Interfaces **10**(3), 2566–2573 (2018).
[109]J.-G. Park and K.-H. Hong, "Dual-site compositional engineering of bismuth-based halide perovskites for stable and efficient lead-free solar cells," J. Phys. Chem. C **125**(24), 13138–13145 (2021).
[110]F. Jiang, D. Yang, Y. Jiang, T. Liu, X. Zhao, Y. Ming, B. Luo, F. Qin, J. Fan, H. Han, L. Zhang, and Y. Zhou, "Chlorine-incorporation-induced formation of the layered phase for antimony-based lead-free perovskite solar cells," J. Am. Chem. Soc. **140**(3), 1019–1027 (2018).
[111]A. Pradhan, M. K. Jena, and S. L. Samal, "Understanding of the band gap transition in $Cs_3Sb_2Cl_{9-x}Br_x$: Anion site preference-induced structural distortion," ACS Appl. Energy Mater. **5**(6), 6952–6961 (2022).
[112]F. Igbari, R. Wang, Z. K. Wang, X. J. Ma, Q. Wang, K. L. Wang, Y. Zhang, L. S. Liao, and Y. Yang, "Composition stoichiometry of $Cs_2AgBiBr_6$ films for highly efficient lead-free perovskite solar cells," Nano Lett. **19**(3), 2066–2073 (2019).
[113]K. Z. Du, W. Meng, X. Wang, Y. Yan, and D. B. Mitzi, "Bandgap engineering of lead-free double perovskite $Cs_2AgBiBr_6$ through trivalent metal alloying," Angew. Chem., Int. Ed. **56**(28), 8158–8162 (2017).
[114]R. Kentsch, M. Scholz, J. Horn, D. Schlettwein, K. Oum, and T. Lenzer, "Exciton dynamics and electron-phonon coupling affect the photovoltaic performance of the $Cs_2AgBiBr_6$ double perovskite," J. Phys. Chem. C **122**(45), 25940–25947 (2018).
[115]N. K. Tailor, S. K. Saini, P. Yadav, M. Kumar, and S. Satapathi, "Elucidating polaron dynamics in $Cs_2AgBiBr_6$ double perovskite," J. Phys. Chem. Lett. **14**(3), 730–736 (2023).
[116]D. Bartesaghi, A. H. Slavney, M. C. Gélvez-Rueda, B. A. Connor, F. C. Grozema, H. I. Karunadasa, and T. J. Savenije, "Charge carrier dynamics in $Cs_2AgBiBr_6$ double perovskite," J. Phys. Chem. C **122**(9), 4809–4816 (2018).
[117]F. Schmitz, N. Lago, L. Fagiolari, J. Burkhart, A. Cester, A. Polo, M. Prato, G. Meneghesso, S. Gross, F. Bella, F. Lamberti, and T. Gatti, "High open-circuit voltage $Cs_2AgBiBr_6$ carbon-based perovskite solar cells via green processing of ultrasonic spray-coated carbon electrodes from waste tire sources," ChemSusChem **15**(22), e202201590 (2022).
[118]L. Zhang, Y. Xu, P. Niu, M. Lyu, H. Lu, and J. Zhu, "Regulating film crystallization kinetics with thiourea additive in $Cs_2AgBiBr_6$ solar cells," J. Phys. D: Appl. Phys. **56**(7), 075501 (2023).
[119]A. Yang, L. Zhang, Y. Xu, Q. Wang, M. Lyu, H. Lu, and J. Zhu, "V_{OC} over 1.2 V for $Cs_2AgBiBr_6$ solar cells based on formamidinium acetate additive," J. Mater. Sci.: Mater. Electron. **33**(23), 18758–18767 (2022).
[120]H. Peng, P. Fan, Z. Zheng, S. Chen, and G. Liang, "Phase-controlled strategy for high-quality single-source vapor-deposited $Cs_2AgBiBr_6$ thin films," ACS Appl. Energy Mater. **5**(12), 15058–15068 (2022).
[121]N. Rodkey, S. Kaal, P. Sebastia-luna, Y. A. Birkhölzer, M. Ledinsky, F. Palazon, H. J. Bolink, and M. Morales-Masis, "Pulsed laser deposition of $Cs_2AgBiBr_6$: From mechanochemically synthesized powders to dry, single-step deposition," Chem. Mater. **33**(18), 7417–7422 (2021).
[122]Z. Li, S. P. Senanayak, L. Dai, G. Kusch, R. Shivanna, Y. Zhang, D. Pradhan, J. Ye, Y. Huang, H. Sirringhaus, R. A. Oliver, N. C. Greenham, R. H. Friend, and R. L. Z. Hoye, "Understanding the role of grain boundaries on charge-carrier and ion transport in $Cs_2AgBiBr_6$ thin films," Adv. Funct. Mater. **31**(49), 2104981 (2021).
[123]M. Ghasemi, L. Zhang, J. Yun, M. Hao, D. He, P. Chen, Y. Bai, T. Lin, M. Xiao, A. Du, M. Lyu, and L. Wang, "Dual-ion-diffusion induced degradation in lead-free $Cs_2AgBiBr_6$ double perovskite solar cells," Adv. Funct. Mater. **30**(42), 2002342 (2020).
[124]J. Li, X. Meng, Z. Wu, Y. Duan, R. Guo, W. Xiao, Y. Zhang, Y. Li, Y. Shen, W. Zhang, and G. Shao, "Pinning bromide ion with ionic liquid in lead-free $Cs_2AgBiBr_6$ double perovskite solar cells," Adv. Funct. Mater. **32**(25), 2112991 (2022).
[125]M. Abdelsamie, K. Cruse, N. Tamura, G. Ceder, and C. M. Sutter-Fella, "Impact of processing conditions on the film formation of lead-free halide double perovskite $Cs_2AgBiBr_6$," J. Mater. Chem. A **10**(37), 19868–19880 (2022).
[126]J. Duan, Y. Yang, J. Tang, H. Wan, G. Ma, L. Shen, J. Zhang, H. Wang, and H. Zhou, "MACl enhanced electron extraction in all-inorganic $Cs_2AgBiBr_6$ perovskite photovoltaics," Chem. Commun. **59**(9), 1173–1176 (2023).
[127]M. Alla, V. Manjunath, E. Choudhary, M. Samtham, S. Sharma, P. A. Shaikh, M. Rouchdi, and B. Fares, "Evaluating the potential of lead-free non-toxic Cs_2BiAgI_6-based double perovskite solar cell," Phys. Status Solidi A **220**(2), 2200642 (2023).
[128]H. Wu, A. Erbing, M. B. Johansson, J. Wang, C. Kamal, M. Odelius, and E. M. J. Johansson, "Mixed-halide double perovskite Cs_2AgBiX_6 (X = Br, I) with tunable optical properties via anion exchange," ChemSusChem **14**(20), 4507–4515 (2021).

[129]C. W. Ahn, J. H. Jo, J. S. Choi, Y. H. Hwang, I. W. Kim, and T. H. Kim, "Heteroanionic lead-free double-perovskite halides for bandgap engineering," Adv. Eng. Mater. **25**(1), 2201119 (2023).
[130]A. C. Dakshinamurthy, M. Gupta, B. R. K. Nanda, and C. Sudakar, "Anionic alloying in hybrid halide $Cs_2AgBiBr_{6-x}Cl_x$ double perovskites: Is it true alloying or preferential occupation of halide ions in MX_6 octahedra," J. Phys. Chem. C **127**(3), 1588–1597 (2023).
[131]S. Yoon, B. Fett, A. Frebel, S. Kroisl, B. Herbig, M. Widenmeyer, B. Balke, G. Sextl, K. Mandel, and A. Weidenkaff, "Sb-substituted $Cs_2AgBiBr_6$—As much as it could Be?—Influence of synthesis methods on Sb-substitution level in $Cs_2AgBiBr_6$," Energy Technol. **10**(8), 2200197 (2022).
[132]M. A. Hadi, N. Islam, and J. Podder, "Indirect to direct band gap transition through order to disorder transformation of $Cs_2AgBiBr_6$ via creating anti-site defects for optoelectronic and photovoltaic applications," RSC Adv. **12**(24), 15461–15469 (2022).
[133]Y. Zhang, Y. Song, Y. Lu, Z. Zhang, Y. Wang, Y. Yang, Q. Dong, Y. Yu, P. Qin, and F. Huang, "Thermochromic $Cs_2AgBiBr_6$ single crystal with decreased band gap through order-disorder transition," Small **18**(24), 2201943 (2022).
[134]A. C. Dakshinamurthy and C. Sudakar, "Photoinduced degradation of thermally stable $Cs_2AgBiBr_6$ double perovskites by micro-Raman studies," Mater. Adv. **3**(14), 5813–5817 (2022).
[135]J. Gebhardt and C. Elsässer, "The electronic structure of $Cs_2AgBiBr_6$ at room temperature," Phys. Status Solidi B **259**(8), 2200124 (2022).
[136]N. K. Tailor, N. Parikh, P. Yadav, and S. Satapathi, "Dielectric relaxation and polaron hopping in $Cs_2AgBiBr_6$ halide double perovskites," J. Phys. Chem. C **126**(24), 10199–10208 (2022).
[137]V. Andrei, R. A. Jagt, M. Rahaman, L. Lari, V. K. Lazarov, J. L. Macmanus-driscoll, R. L. Z. Hoye, and E. Reisner, "Long-term solar water and CO_2 splitting with photoelectrochemical BiOI–$BiVO_4$ tandems," Nat. Mater. **21**, 864–868 (2022).
[138]Y. C. Choi and R. Nie, "Heavy pnictogen chalcohalides for efficient, stable, and environmentally friendly solar cell applications," Nanotechnology **34**(14), 142001 (2023).
[139]A. Crovetto, A. Hajijafarassar, O. Hansen, B. Seger, I. Chorkendorff, and P. C. K. Vesborg, "Parallel evaluation of the BiI_3, BiOI, and Ag_3BiI_6 layered photoabsorbers," Chem. Mater. **32**(8), 3385–3395 (2020).
[140]R. A. Jagt, T. N. Huq, K. M. Börsig, D. Sauven, L. C. Lee, J. L. Macmanus-driscoll, and R. L. Z. Hoye, "Controlling the preferred orientation of layered BiOI solar absorbers," J. Mater. Chem. C **8**(31), 10791–10797 (2020).
[141]A. A. Putri, A. A. Abuelwafa, S. Kato, N. Kishi, and T. Soga, "A simple spin-assisted SILAR of bismuth oxyiodide films preparation for photovoltaic application," SN Appl. Sci. **2**(1), 119 (2020).
[142]R. M. Matiur, A. A. Abuelwafa, A. A. Putri, S. Kato, N. Kishi, and T. Soga, "Annealing effects on structural and photovoltaic properties of the dip-SILAR-prepared bismuth oxyhalides (BiOI, $Bi_7O_9I_3$, Bi_5O_7I) films," SN Appl. Sci. **3**(2), 138 (2021).
[143]T. Feeney, G. Aygur, T. Nguyen, S. Farooq, J. Mendes, H. Tuohey, D. E. Gómez, E. Della Gaspera, and J. van Embden, "Solution processed bismuth oxyiodide (BiOI) thin films and solar cells," Nanotechnology **34**, 305404 (2023).
[144]X. Zhang and L. Zhang, "Electronic and band structure tuning of ternary semiconductor photocatalysts by self doping: The case of BiOI," J. Phys. Chem. C **114**(42), 18198–18206 (2010).
[145]X. Ren, J. Yao, L. Cai, J. Li, X. Cao, Y. Zhang, B. Wang, and Y. Wei, "Band gap engineering of BiOI via oxygen vacancies induced by graphene for improved photocatalysis," New J. Chem. **43**(3), 1523–1530 (2019).
[146]J. Pal, S. Manna, A. Mondal, S. Das, K. V. Adarsh, and A. Nag, "Colloidal synthesis and photophysics of $M_3Sb_2I_9$ (M = Cs and Rb) nanocrystals: Lead-free perovskites," Angew. Chem., Int. Ed. **56**(45), 14187–14191 (2017).
[147]A. S. Thomas, "A review on antimony-based perovskite solar cells," Equilib. J. Chem. Eng. **6**(2), 75 (2022).
[148]J.-P. Correa-Baena, L. Nienhaus, R. C. Kurchin, S. S. Shin, S. Wieghold, N. T. Putri Hartono, M. Layurova, N. D. Klein, J. R. Poindexter, A. Polizzotti, S. Sun, M. G. Bawendi, and T. Buonassisi, "*A*-site cation in inorganic $A_3Sb_2I_9$ perovskite influences structural dimensionality, exciton binding energy, and solar cell performance," Chem. Mater. **30**(11), 3734–3742 (2018).
[149]T. Geng, Z. Ma, Y. Chen, Y. Cao, P. Lv, N. Li, and G. Xiao, "Bandgap engineering in two-dimensional halide perovskite $Cs_3Sb_2I_9$ nanocrystals under pressure," Nanoscale **12**(3), 1425–1431 (2020).
[150]D. Samanta, S. P. Chaudhary, B. Ghosh, S. Bhattacharyya, G. Shukla, and G. D. Mukherjee, "Pressure-induced emission enhancement and bandgap narrowing: Experimental investigations and first-principles theoretical simulations on the model halide perovskite $Cs_3Sb_2Br_9$," Phys. Rev. B **105**(10), 104103 (2022).
[151]F. Umar, J. Zhang, Z. Jin, I. Muhammad, X. Yang, H. Deng, K. Jahangeer, Q. Hu, H. Song, and J. Tang, "Dimensionality controlling of $Cs_3Sb_2I_9$ for efficient all-inorganic planar thin film solar cells by HCl-assisted solution method," Adv. Opt. Mater. **7**(5), 1801368 (2019).
[152]Y. Yang, C. Liu, M. Cai, Y. Liao, Y. Ding, S. Ma, X. Liu, M. Guli, S. Dai, and M. K. Nazeeruddin, "Dimension-controlled growth of antimony-based perovskite-like halides for lead-free and semitransparent photovoltaics," ACS Appl. Mater. Interfaces **12**(14), 17062–17069 (2020).
[153]I. Wharf, T. Gramstad, R. Makhija, and M. Onyszchuk, "Synthesis and vibrational spectra of some lead(II) halide adducts with O-, S- and N-donor atom ligands," Can. J. Chem. **54**(21), 3430–3438 (1976).
[154]J.-W. Lee, Z. Dai, C. Lee, H. M. Lee, T.-H. Han, N. De Marco, O. Lin, C. S. Choi, B. Dunn, J. Koh, D. Di Carlo, J. H. Ko, H. D. Maynard, and Y. Yang, "Tuning molecular interactions for highly reproducible and efficient formamidinium perovskite solar cells via adduct approach," J. Am. Chem. Soc. **140**(20), 6317–6324 (2018).
[155]N. Ahn, D.-Y. Son, I.-H. Jang, S. M. Kang, M. Choi, and N.-G. Park, "Highly reproducible perovskite solar cells with average efficiency of 18.3% and best efficiency of 19.7% fabricated via Lewis base adduct of lead(II) iodide," J. Am. Chem. Soc. **137**(27), 8696–8699 (2015).
[156]J.-W. Lee, H.-S. Kim, and N.-G. Park, "Lewis acid–base adduct approach for high efficiency perovskite solar cells," Acc. Chem. Res. **49**(2), 311–319 (2016).
[157]A. Singh, S. Najman, A. Mohapatra, Y.-J. Lu, C. Hanmandlu, C.-W. Pao, Y.-F. Chen, C. S. Lai, and C.-W. Chu, "Modulating performance and stability of inorganic lead-free perovskite solar cells via Lewis-pair mediation," ACS Appl. Mater. Interfaces **12**(29), 32649–32657 (2020).
[158]X. Zhao, T. Liu, A. B. Kaplan, C. Yao, and Y.-L. Loo, "Accessing highly oriented two-dimensional perovskite films via solvent-vapor annealing for efficient and stable solar cells," Nano Lett. **20**(12), 8880–8889 (2020).
[159]J. Li, Y. Lv, H. Han, J. Xu, and J. Yao, "Two-dimensional $Cs_3Sb_2I_{9-x}Cl_x$ film with (201) preferred orientation for efficient perovskite solar cells," Materials **15**(8), 2883 (2022).
[160]A. Singh, P.-T. Lai, A. Mohapatra, C.-Y. Chen, H.-W. Lin, Y.-J. Lu, and C. W. Chu, "Panchromatic heterojunction solar cells for Pb-free all-inorganic antimony based perovskite," Chem. Eng. J. **419**, 129424 (2021).
[161]H. Tsai, W. Nie, J.-C. Blancon, C. C. Stoumpos, R. Asadpour, B. Harutyunyan, A. J. Neukirch, R. Verduzco, J. J. Crochet, S. Tretiak, L. Pedesseau, J. Even, M. A. Alam, G. Gupta, J. Lou, P. M. Ajayan, M. J. Bedzyk, M. G. Kanatzidis, and A. D. Mohite, "High-efficiency two-dimensional Ruddlesden–Popper perovskite solar cells," Nature **536**(7616), 312–316 (2016).

4.8 Publication 7

Improved hole extraction and band alignment via interface modification in HTM-free Ag/Bi double perovskite solar cells

Authors: **Fabian Schmitz**, Ribhu Bhatia, Julian Burkhart, Pascal Schweitzer, Marco Allione, Jaime Gallego, Piotr Piotrowski, Jakub Cajzl, Piotr Paszke, Gour Mohan Das, Dorota A. Pawlak, Federico Bella, Derck Schlettwein, Francesco Lamberti, Simone Meloni, Teresa Gatti

While lead-halide-based perovskites have experienced rapid and continuous improvement of PCE within a decade of research, the temporary maximum PCE achieved with a $Cs_2AgBiBr_6$-based perovskite solar cell has been 4.23% (using an organic dye as additional absorber material),[259] reported in 2021 and since then languished. Apart from a strong improvement in 2022 of the PCE towards 6.37% due to the incorporation of interstitial hydrogen into the elpasolite structure,[37] the record PCE from 2021 has not been exceeded. In comparison, calculations of the theoretically maximum achievable PCE of pure $Cs_2AgBiBr_6$ have proposed values ranging from 6.68%[260] to 14.23%.[120–122] Thus, new strategies must be applied to exhaust this material's unexploited potential. In 2022, Sirtl *et al*. reported on boosting the PCE of $Cs_2AgBiBr_6$ by utilizing a 2D/3D surface modification using phenethylammonium (PEA) that enhanced the perovskite's band alignment towards the hole transport layer.

In **publication 7**, a similar 2D/3D surface modification is applied to $Cs_2AgBiBr_6$ thin films by treating them with various concentrations of BA dissolved in isopropanol. Using this attempt as well as the HTM-free solar cell architecture from **publication 5**, the work aims to improve the solar cells' PCE by not only enhancing the valence band alignment towards the carbon black electrode but also by improving the carbon electrode's selectivity due to 2D/3D modifications elevated conduction band level. BA has been chosen since in **publication 2** it was observed that 2D monolayered BA thin films possess a more homogeneous and smoother surface as well as a lower work function than PEA thin films. First, the presence of the 2D/3D modification is proved by a combination of and surface-sensitive analyses. The materials' valence and conduction band edges as well as their Fermi level are obtained via XPS and KPFM, respectively. By combining these values with the reported bandgap of the 2D perovskite, the band alignment between $Cs_2AgBiBr_6$ and its surface modification is depicted. Solar cell measurements show that the 2D/3D modification enhances the PCE to an optimum when a concentration of 0.05 M BA in isopropanol is applied to the $Cs_2AgBiBr_6$ thin films. Furthermore, density functional theory (DFT) calculations suggest that the presence of multiple stacks of 2D perovskite on top of $Cs_2AgBiBr_6$ increases the latter's density of states for holes close to the 2D/3D interface. Thus, the probability of extracting holes into the back

electrode is increased, explaining the enhanced solar cell performances for the 2D/3D modified perovskite.

This work continues the research that was performed on **publication 5** and incorporates the findings of **publication 2**. The work depicts a concept to enhance the PCE of HTM-free $Cs_2AgBiBr_6$ solar cells by applying a mixed 2D/3D surface modification that improves the perovskite's band alignment and selectivity towards the carbon back electrode. A direct comparison with regular architecture 2D/3D modified solar cells, comprising the HTM Spiro-OMeTAD and gold back electrodes demonstrates that the HTM-free solar cells achieve comparable PCEs. Therefore, the presented 2D/3D modification allows the fabrication of low-cost and "green" lead-free perovskite solar cells with PCEs that have been further improved in comparison to **publication 5**.

In addition to the *General Contributions*, all samples that were analyzed within this work were prepared by my student Julian Burkhart under my supervision and by me. I performed thin film GIXRD, UV-Vis absorption spectroscopy, SEM, current-voltage measurements of solar cells, electrochemical impedance spectroscopy, external and internal quantum efficiency measurements, contact angle measurements, and diffuse reflectance infrared Fourier transform spectroscopy (DRIFT), including the respective data processing.

RESEARCH ARTICLE

Solar RRL
www.solar-rrl.com

Improved Hole Extraction and Band Alignment via Interface Modification in Hole Transport Material-Free Ag/Bi Double Perovskite Solar Cells

Fabian Schmitz, Ribhu Bhatia, Julian Burkhart, Pascal Schweitzer, Marco Allione, Jaime Gallego, Piotr Piotrowski, Jakub Cajzl, Piotr Paszke, Gour Mohan Das, Dorota A. Pawlak, Federico Bella, Derck Schlettwein, Francesco Lamberti,* Simone Meloni,* and Teresa Gatti**

Within one decade, lead halide perovskite solar cells have reached power conversion efficiencies (PCEs) compatible with that of silicon solar cells. While in the beginning, they suffered from short device lifetimes, those have also been strongly improved over time. However, their content of toxic lead still poses a risk of environmental pollution and human health on exposure. The double perovskite (DP) $Cs_2AgBiBr_6$ offers the potential to be a lead-free alternative light-harvesting material. Herein, the fabrication of hole transport material (HTM)-free $Cs_2AgBiBr_6$-based solar cells is presented, in which the DP surface is modified via a *n*-butylammonium posttreatment to create a 2D/3D mixed interface. Additionally, the commonly utilized metal electrode and HTM are substituted with a carbon black back electrode (CBE) consisting of up-cycled biowaste. Through the 2D/3D interface modification, charge recombination is suppressed, and band alignment is improved at the perovskite/CBE interface. Additionally, density functional theory calculations reveal that an increasing 2D modification thickness enhances the probability for holes in $Cs_2AgBiBr_6$ to be located close to the perovskite/CBE interface, further supporting their extraction. Overall, the PCE of the HTM-free solar cells is improved through the implementation of a low-cost and end-of-waste fabrication strategy.

1. Introduction

As the global energy demand is continuously increasing, renewable energies have gained large importance, since fossil fuels are limited, are a health hazard due to air pollution, and are the major source of global greenhouse gas emissions, resulting in anthropogenic global warming.[1,2] Since solar energy is the most abundant energy source on earth,[3] photovoltaics (PV) have the potential to play a crucial role in saturating the world's increasing energy demand.

Among several available absorbers for PV, hybrid organic–inorganic lead halide perovskites (LHPs) have attracted significant attention in recent years due to their combined features of large absorption coefficients,[4,5] high charge carrier lifetimes[6–10] and mobilities,[10,11] high defect tolerance,[11,12] as well as a convenient bandgap tunability.[4,13,14] Those properties enabled the fabrication of highly efficient PVs not only for outdoor,[5–8,10,13]

F. Schmitz, J. Burkhart, P. Schweitzer, J. Gallego, D. Schlettwein, T. Gatti
Center for Materials Research
Justus Liebig University
Heinrich-Buff-Ring 17, 35392 Giessen, Germany
E-mail: fabian.schmitz@phys.chemie.uni-giessen.de;
teresa.gatti@phys.chemie.uni-giessen.de

R. Bhatia, S. Meloni
Department of Chemical and Pharmaceutical Sciences
Università of Ferrara
Via Luigi Borsari 46, I-44121 Ferrara, Italy
E-mail: simone.meloni@unife.it

P. Schweitzer, D. Schlettwein
Institute of Applied Physics
Justus Liebig University
Heinrich-Buff-Ring 16, 35392 Giessen, Germany

The ORCID identification number(s) for the author(s) of this article can be found under https://doi.org/10.1002/solr.202300965.

DOI: 10.1002/solr.202300965

M. Allione, F. Bella, T. Gatti
Department of Applied Science and Technology
Politecnico di Torino
C.so Duca degli Abruzzi 24, 10129 Torino, Italy

P. Piotrowski, J. Cajzl, P. Paszke, G. Mohan Das, D. A. Pawlak
Centre of Excellence ENSEMBLE3 sp. z o. o.
Wólczyńska 133, 01-919 Warsaw, Poland

F. Lamberti
Department of Chemical Sciences
University of Padova
Via Marzolo 1, 35131 Padova, Italy
E-mail: francesco.lamberti@unipd.it

F. Lamberti
Department of Information Engineering
University of Padova
Via Gradenigo 6a, 35131 Padova, Italy

ADVANCED SCIENCE NEWS
www.advancedsciencenews.com

Solar RRL
www.solar-rrl.com

but also for indoor applications,[15–17] under which they achieved power conversion efficiencies (PCEs) of up to 26.1%[18] and 41.2%,[19] respectively. However, lead harbors a health hazard,[20,21] which especially limits the application possibilities of LHPs.

When the divalent lead is substituted from the ABX_3 perovskite structure by stoichiometric amounts[22] of monovalent silver and trivalent bismuth, the elpasolite (broadly named double perovskite (DP)) $Cs_2AgBiBr_6$ is formed, a material that possesses high environmental stability[23–25] and drastically reduced toxicity, in comparison to LHPs.[26] Like LHPs, this DP features long charge carrier lifetimes[27–29] and can easily be solution-processed.[30–32] Yet, the PCEs of solar cells that are based on pristine $Cs_2AgBiBr_6$ as sole light-harvesting material have not exceeded 2.81%[33] due to a large indirect bandgap,[23,32,34] strong electron–phonon coupling,[31,35,36] short electron diffusion length,[37,38] and an unfavorable polaron-hopping transport mechanism.[28,39,40] Also, the role of the $Cs_2AgBiBr_6$ crystallization to form thin films for well-performing solar cells is still not understood: thin films of pristine $Cs_2AgBiBr_6$ with comparable thicknesses and homogeneities result in reported solar cells with PCEs ranging from below 1% to above 2% despite equal solar cell architectures.[38,41–49] Sirtl et al. revealed in their work that low selectivity of the hole transport material (HTM) supports recombination and therefore hampers the solar cell performance, due to insufficient band alignment, i.e., the absence of an electron barrier between perovskite and HTM.[50] Thus, they exposed a critical bottleneck of $Cs_2AgBiBr_6$-based solar cells. One common strategy to tackle the low selectivity and improve the band alignment between perovskite layers and HTM (and electron transport layers (ETLs) in inverted solar cells) is creating a two-dimensional (2D) perovskite interlayer.[46,51,52] When the dimensionality of a perovskite crystal is reduced from three-dimensional (3D) to 2D, it undergoes quantum confinement that increases its bandgap with decreasing layer thickness.[53–55] In detail, the valence band maximum (VBM) is slightly elevated and the conduction band minimum (CBM) is strongly elevated. When the 2D layer is utilized as an interlayer between the perovskite layer and the HTM, the high CBM level serves as an energy barrier that suppresses the injection of excited electrons from the perovskite layer into the HTM.[52,56] However, the VBM and CBM elevation of a 2D interlayer can not only improve the band alignment between perovskite and HTM but also allow the removal of the HTM to fabricate HTM-free perovskite solar cells. In the latter case, the 2D interlayer adopts the HTM's purpose of blocking electron extraction into the back electrode and improving the valence band (VB) alignment toward the back electrode. The schematic band diagrams of a $Cs_2AgBiBr_6$ solar cell with HTM as well as of HTM-free solar cells with and without a 2D perovskite layer are depicted in **Figure 1**. While the removal of the HTM causes increased recombination at the back electrode in a pure $Cs_2AgBiBr_6$ solar cell (Figure 1b), the presence of a 2D layer (Figure 1c) will improve the selectivity and the band alignment toward the back electrode. Thereby, the 2D modification adopts the function of the HTM.

Dimensional reduction from 3D to 2D has already been reported for $Cs_2AgBiBr_6$ by introducing large organic cations to substitute Cs.[57–60] Furthermore, Sirtl et al. carried out a post-treatment of $Cs_2AgBiBr_6$ thin films with phenethylammonium (PEA) bromide solution in which PEA substituted Cs in the top layers, thus forming a 2D capping layer.[46] Accordingly, the 2D-modified surface of the perovskite films enhanced the VB alignment and the selectivity toward the HTM 2,2′,7,7′-tetrakis-(*N*,*N*-di-4-methoxyphenylamino)-9,9′-spirobifluorene (Spiro-OMeTAD) which resulted in improved solar cells. The transformation of the upper layers of 3D perovskite thin films into 2D capping layers via ion exchange within a 2-step spin-coating process represents a commonly applied strategy for hybrid organic–inorganic LHPs.[51,61–64] We present the modification of $Cs_2AgBiBr_6$ with n-butylammonium (BA) to form a 2D capping layer and its application in HTM-free perovskite solar cells. BA was chosen to substitute Cs since in previous work, thin films of the 2D monolayered perovskite $(BA)_4AgBiBr_8$ (full substitution of Cs with BA) were characterized by enhanced homogeneity as well as a strongly differing work function in comparison to $(PEA)_4AgBiBr_8$.[58]

In this work, we thoroughly investigate the extent of conversion from $Cs_2AgBiBr_6$ toward a mixed 2D/3D phase when treating $Cs_2AgBiBr_6$ with different concentrations of BABr precursor solutions. Through a combination of structural, optical, and

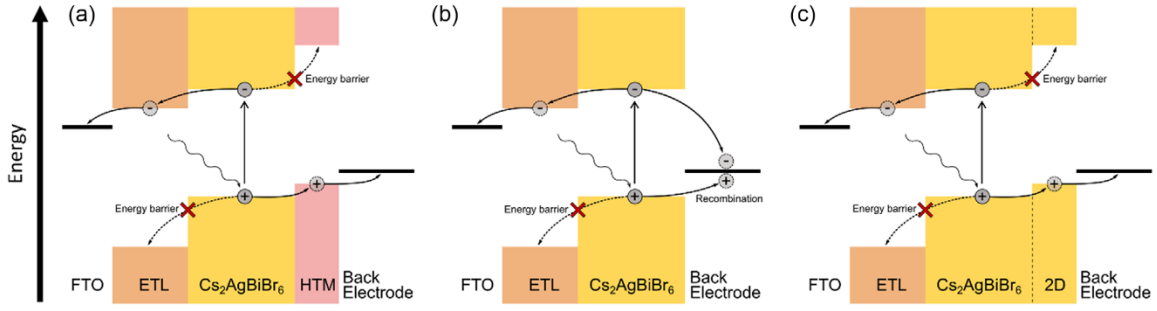

Figure 1. Schematic band diagrams of $Cs_2AgBiBr_6$ solar cell architectures. a) Classical n-i-p architecture in which $Cs_2AgBiBr_6$ is sandwiched between ETL and HTM, e.g., TiO_2 and Spiro-OMeTAD, respectively. The HTM creates an energy barrier for electrons and the band alignment favors the hole drift toward the back electrode. b) HTM-free $Cs_2AgBiBr_6$ solar cell. No energy barrier prevents the recombination of electrons and holes at the back electrode. c) 2D/3D surface modified $Cs_2AgBiBr_6$ solar cell. The 2D perovskite functions like an HTM, elevating the VBM slightly and the CBM strongly as will be shown in this work.

ADVANCED SCIENCE NEWS
www.advancedsciencenews.com

Solar RRL
www.solar-rrl.com

electrochemical analysis, we reveal the processes leading to enhanced PCEs in 2D/3D-modified $Cs_2AgBiBr_6$ PVs and identify the best conditions for carrying out such modification. Simulations were performed to validate some hypotheses on the effect of $(BA)_4AgBiBr_8$. In particular, we focused on the effect of the concentration of BABr precursor solutions. Additionally, we combined the 2D surface modification with the application of a carbon-based electrode (CBE) to substitute both the HTM and the metal electrode. Through the introduction of a 2D interlayer between $Cs_2AgBiBr_6$ and CBE, we introduce both an additional energy barrier for electrons to suppress recombination at the perovskite/CBE interface and an improved band alignment to enhance the hole injection into the CBE. We remark once more that the objective of this work is not to obtain the most efficient $Cs_2AgBiBr_6$-based PV devices, which are typically obtained with a gold electrode, a Spiro-OMeTAD HTM, etc. Rather, we aim at making a step forward in the direction of cheap devices, by replacing altogether two expensive components of DP PV with alternative components, CBE and 2D modification of the 3D $Cs_2AgBiBr_6$ film. Moreover, not only will the utilization of CBEs and the removal of the HTM drastically reduce the material and fabrication costs of solar cells[65,66] but the carbon black in our CBE was even obtained from hazelnut shells, an industrial waste product. Thus, the presented solar cells serve as an end-of-waste design for low-toxic, low-cost perovskite solar cells.

2. Results and Discussion

$Cs_2AgBiBr_6$ thin films were fabricated by spin-coating in an argon-filled glovebox as described in the Experimental Section. The perovskite layers were deposited onto mesoporous TiO_2 (see Figure S1, Supporting Information) since it was reported to enable enhanced charge collection compared to compact TiO_2.[38,50] To create 2D/3D mixed perovskites, the $Cs_2AgBiBr_6$ thin films were covered with BABr, dissolved in isopropanol at various concentrations (0.01, 0.05, and 0.1 M), spin-coated, and then left to dry overnight inside the glovebox. A sketch of the preparation process is depicted in **Figure 2**. For the sake of readability, samples treated with 0.01, 0.05, and 0.1 M BABr solution will be abbreviated as 0.01, 0.05, and 0.1 M, respectively, throughout the report. We remark that our focus is the effect of the 2D posttreatment, particularly, the 2D/3D mixed perovskite in conjunction with a CBE which is obtained from byproducts of other (agricultural/food) industries. The devices fabricated and used in this work, including the reference devices based on the HTM Spiro-OMeTAD and a gold back electrode, are not optimized to achieve top efficiencies, e.g., adding passivating agents regularly used in the literature, or adopting careful deposition methods (see, for example, ref. [67] and references cited therein). This is in line with the objective of exploring approaches to develop PV for markets requiring very low-cost devices.[68]

We performed grazing-incidence X-ray diffraction (GIXRD) measurements on the thin films, as shown in **Figure 3**a, to detect the formation of a 2D phase within the $Cs_2AgBiBr_6$ thin film. For all thin films, the reflections of the 3D perovskite $Cs_2AgBiBr_6$ can be observed. Their shapes and positions are not affected by the BABr treatment, and no side phases are created due to this process. This also underlines that after the BABr treatment, bulk $Cs_2AgBiBr_6$ is still the dominant material in the thin films. While no differences between the pure 3D DP thin film and the 0.01 M one can be detected, a weak reflection at around 4.5° appears for the 0.05 M thin film, which can be correlated to the bilayer 2D phase $(BA)_2CsAgBiBr_7$.[57] For the 0.1 M film, the intensity of this reflection strongly increases. Additionally, a second reflection at 6.1° appears which can be attributed to BABr residues that are still present on the thin film's surface. Interestingly, no reflections of the monolayer phase can be observed in either sample, which would appear at 6.5°.[57,58] It

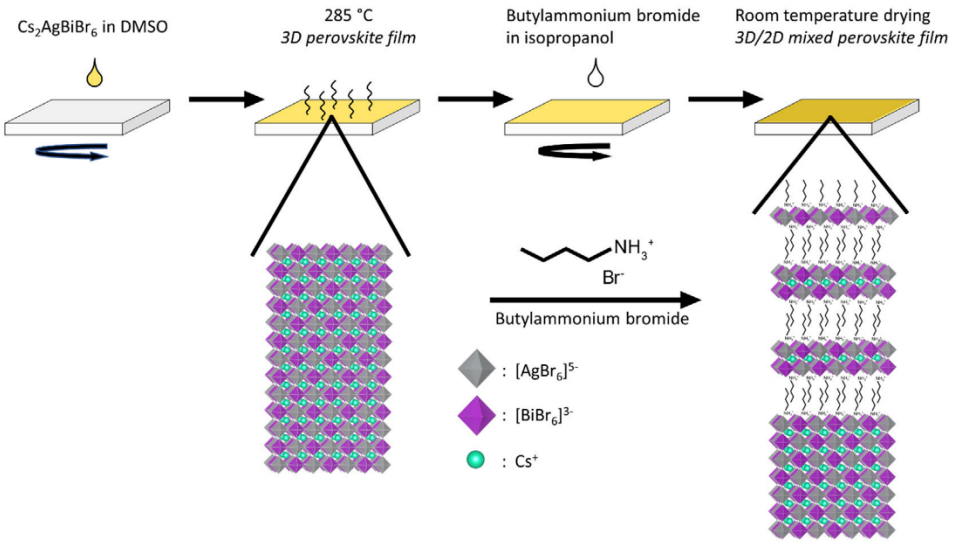

Figure 2. Schematic representation of the process used to produce 2D/3D interfaces in $Cs_2AgBiBr_6$ thin films.

ADVANCED SCIENCE NEWS
www.advancedsciencenews.com

Solar RRL
www.solar-rrl.com

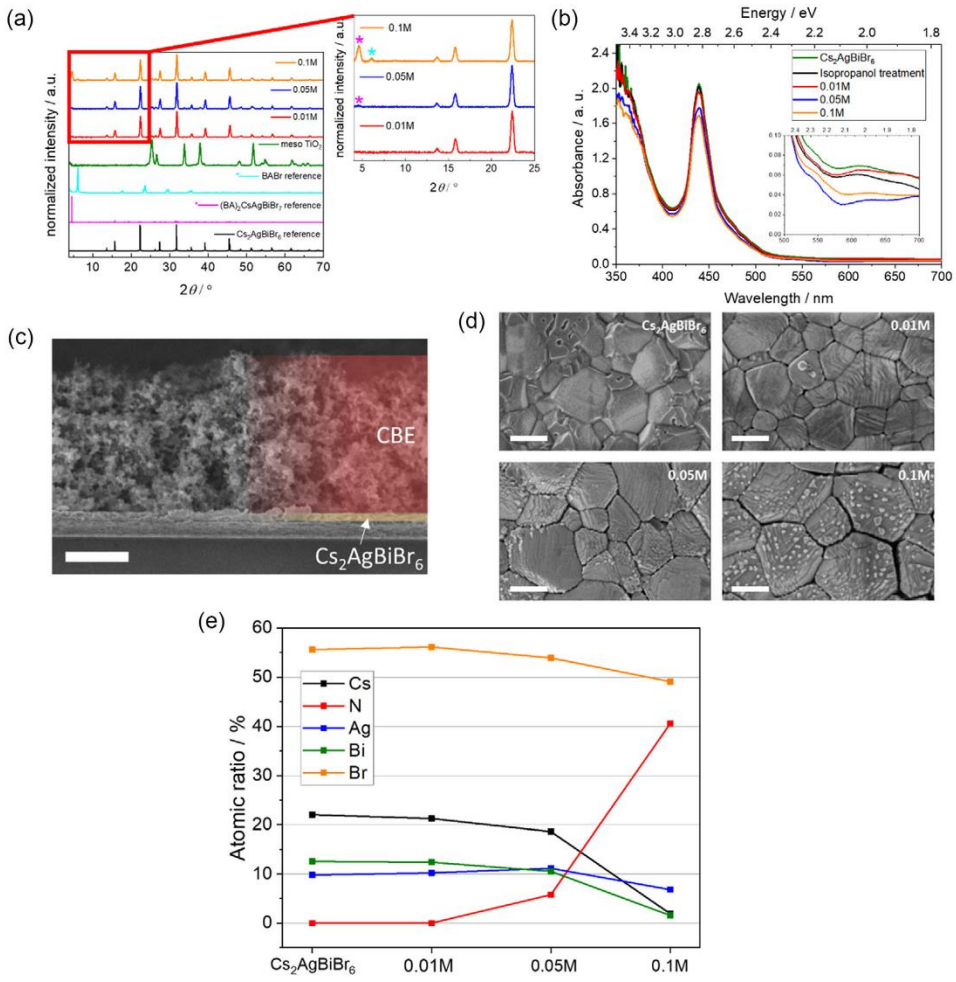

Figure 3. Physicochemical characterization of the 2D/3D-modified $Cs_2AgBiBr_6$ thin films at different BABr concentrations. a) GIXRD diffractograms of the 2D/3D-modified thin films, with zoom on low angles region. b) UV–vis absorption spectra of the 2D/3D-modified thin films, of the reference and a reference film treated with only isopropanol. c) Cross-section SEM of a $Cs_2AgBiBr_6$ solar cell (scale is 2 µm). d) Top-view SEM images of the 2D/3D-modified thin films and the reference DP film. Top-view SEM scales are 200 nm, each. e) Surface elemental composition as measured through XPS on the reference and modified films.

is important to note that the missing reflection for 0.01 M does not rule out the formation of nonperiodic 2D phases with lower or higher inorganic slab thicknesses due to the character of X-ray diffraction (XRD) in which reflections can only occur when periodicity is present.

The transmission UV–visible (UV–vis) absorption spectra of all samples, depicted in Figure 3b, possess the typical shape of $Cs_2AgBiBr_6$ that is characterized by a resonant absorption feature at 448 nm and whose origins are still debated in the literature.[31,69] The overall absorbance decreases with increasing concentration of the BABr solution. We attribute this behavior to the enhanced conversion of 3D $Cs_2AgBiBr_6$ into 2D phases as observed by GIXRD which leaves less $Cs_2AgBiBr_6$ to absorb. To verify that the $Cs_2AgBiBr_6$ was lost due to conversion into 2D phases and not to its dissolution in isopropanol from the BABr solution treatment, we performed the same treatment with pure isopropanol (without BABr addition). Since the spectra before and after this control treatment do not differ and the perovskite layer thicknesses are independent of the 2D modification (see Figure S2, Supporting Information), we assume the absorbance loss to solely stem from enhanced 3D/2D conversion.

2D perovskites feature an increased hydrophobicity due to the incorporation of organic ions.[70–72] As a consequence, 2D surface-modified 3D perovskites have been reported to better withstand humid conditions, due to their enhanced surface hydrophobicity.[73,74] Even though DP films typically show no such problems of chemical instability, changes in wettability by subsequent coatings will have consequences for contact

ADVANCED SCIENCE NEWS
www.advancedsciencenews.com

Solar RRL
www.solar-rrl.com

formation. To investigate this effect on the $Cs_2AgBiBr_6$ thin films after BABr treatment, we performed contact angle measurements which are shown in Figure S3 in the Supporting Information. The contact angle of the pure $Cs_2AgBiBr_6$ thin film with water is 18°, whereas the contact angle for all 2D-modified thin films is increased to 51°–52° due to the hydrophobicity of the BA. Although we observed the formation of increased amounts of the bilayer phase with increasing BABr concentration from GIXRD, the contact angle is independent of the amount of 2D phase that was formed. Therefore, we assume that the perovskite layer's surface is either already transformed into 2D phase for 0.01 M or the surface of $Cs_2AgBiBr_6$ is covered with BA^+ ions which enhance the thin film hydrophobicity. An increased BABr concentration then leads to further phase transition of bulk $Cs_2AgBiBr_6$ at the surface and progressing into the film (see Figure 2).

In Figure 3c, a cross-section scanning electron microscopy (SEM) image of a $Cs_2AgBiBr_6$ solar cell with a CBE is depicted. The perovskite layer has a thickness of around 200 nm (yellow) and the CBE has a thickness of around 4 µm (red). Cross-section SEM images of the 2D/3D-modified $Cs_2AgBiBr_6$ layers are shown in Figure S2 in the Supporting Information. Independent of the 2D/3D modification, the perovskite layers possess thicknesses of around 200 nm. Top-view SEM images of the pure $Cs_2AgBiBr_6$ thin film and the different modifications, shown in Figure 3d and S4 (Supporting Information), give information about the surface morphology as well as about the extent of BABr residues that remain on the thin films after the treatment, respectively. For the pure $Cs_2AgBiBr_6$, an almost pinhole-free homogeneous film can be observed, that consists of 100–300 nm large grains. When the 0.01 M BABr treatment is conducted, few BABr residues (dark regions in Figure S4, Supporting Information) can be found on the film surface and the perovskite grains are now characterized by a terrace-like morphology, that was already observed for thin films of pure 2D layered DPs.[58] This terrace-like character is even more pronounced for 0.05 and 0.1 M, which follows the enhanced transformation from $Cs_2AgBiBr_6$ into a 2D phase with increased BABr concentration. Because of both the increased contact angle of 0.01 M and the presence of the terrace-like structure, we assume that the phase transformation already takes place on the perovskite surface, despite missing evidence in GIXRD. Furthermore, for 0.05 M, small grains start to grow on top of the perovskite grains. The amount and size of those small grains drastically increase for the 0.1 M sample. We exclude recrystallization of $Cs_2AgBiBr_6$ due to the isopropanol posttreatment as the origin of the smaller grains, since they cannot be observed for 0.01 M. However, due to the intense reflection that we observed from GIXRD analysis, we link those grains to the further growth of the 2D $(BA)_2CsAgBiBr_7$. It is important to note that the coverage of the perovskite films by BABr residues (Figure S4, Supporting Information) drastically increases with the BABr concentration during the posttreatment of the $Cs_2AgBiBr_6$ thin films. We expect the contamination to be BABr residues due to the presence of a BABr reflection in GIXRD for 0.1 M. These residues could not be removed by an additional washing step with isopropanol after BABr treatment.

We analyzed the surface compositions of the BABr-treated samples using X-ray photoelectron spectroscopy (XPS), as shown in Figure 3e. The elemental composition of the unmodified $Cs_2AgBiBr_6$ matches its sum formula. No difference in composition can be observed for 0.01 M. However, an analysis of the elemental core levels of Cs, Ag, Bi, and Br, shown in Figure S5 (Supporting Information), reveals a binding energy shift of −0.1 eV from $Cs_2AgBiBr_6$ toward 0.01 M. Such shifts stem from the increased electron densities of those elements due to the presence of the organic spacer cations and, therefore, are additional proof of the 2D phase formation and their tight binding with the 3D phases in 0.01 M thin films.[75] Furthermore, for 0.05 M, small amounts of nitrogen can be detected (see also Figure S6, Supporting Information) while the composition of the other elements still equals the stoichiometry of $Cs_2AgBiBr_6$ within the significance of this method. The formation of large quantities of 2D phase, i.e., $(BA)_2CsAgBiBr_7$, would cause a decrease in Cs concentration. Thus, most of the XPS-detectable material is $Cs_2AgBiBr_6$, as the relatively weak $(BA)_2CsAgBiBr_7$ reflection in GIXRD suggests. Still, we report an enhanced binding energy shift in the core level spectra of −0.2 eV for Ag, Bi, and Br, and of −0.35 eV for Cs that underlines the enhanced phase transformation from $Cs_2AgBiBr_6$ into 2D phases. Furthermore, upward-shifted core level energies, equaling increased electron densities, amount to passivated ions. For 0.1 M, the concentrations of Cs, Ag, and Bi strongly decrease while the concentration of Br only decreases slightly, and the concentration of N drastically increases to almost equal that of Br. This matches the observations from GIXRD and SEM that the surface of the thin film is covered by BABr residues. Furthermore, the high Cs, Ag, Bi, and Br concentrations, and the relatively low N concentration for the 0.05 M film, detected via surface-sensitive XPS analysis, reveal that the amount of BABr residues is far lower than the SEM images make it appear.

To further prove the presence of BA in the material, we performed infrared (IR) spectroscopy on $Cs_2AgBiBr_6$ and 2D/3D-modified thin films, as well as on a reference substrate that was not covered with a perovskite thin film, depicted as Fourier-transformed IR (FTIR) spectra in Figure S7 (Supporting Information). While the spectra of $Cs_2AgBiBr_6$ and the reference substrate show no differences, for 0.05 and 0.1 M, the absorbance at high wavenumbers gradually increases with a maximum at 2950 cm^{-1} which can be attributed to C-H stretching vibration due to the increasing amount of BA in the samples. For 0.01 M, only a weak signal at 2950 cm^{-1} can be observed due to the much lower BA content compared to 0.05 and 0.1 M.

We compared high-resolution transmission electron microscopy (HRTEM) cross-sections of a $Cs_2AgBiBr_6$ and a 0.05 M thin film (Figure S8a,c, Supporting Information), respectively. Like in the SEM cross-sections (Figure S2, Supporting Information), the 2D modification is not distinctly observable for 0.05 M. However, to investigate the loss of 3D phase at the thin film surface, we conducted energy dispersive X-ray spectroscopy (EDX) across both thin films, as shown in Figures S8b,d (Supporting Information). As expected, the $Cs_2AgBiBr_6$ thin film showed a constant elemental distribution along the entire cross-section. In contrast, for 0.05 M, we observed a decay of Cs concentration toward the thin film surface while the Bi concentration stayed constant. We associate this behavior with the formation of

ADVANCED SCIENCE NEWS
www.advancedsciencenews.com

Solar RRL
www.solar-rrl.com

Cs-poor 2D perovskite phases comparable to the XPS elemental analysis (see Figure 3e).

Furthermore, we investigated the 2D modifications' impact on the perovskite's electronic structure, i.e., its VBM, CBM, and Fermi energy E_F, via XPS and Kelvin probe force microscopy (KPFM). We prepared the respective perovskite layers on fluorine-doped tin oxide (FTO)-covered glass substrates for this. The atomic force microscopy (AFM) as well as the related KPFM images of $Cs_2AgBiBr_6$ are shown in **Figure 4**a,b, respectively. KPFM and AFM of 0.01, and 0.05 M, are shown in Figure S9 in the Supporting Information. The high amount of insulating BABr residues on the 0.1 M surface prevents an AFM analysis and, therefore, a detailed and reliable analysis of the perovskite layer's Fermi energy. The AFM images match the observed homogeneity and grain sizes from the SEM images. Figure 4c shows that the average E_F, obtained from KPFM analysis, increases from $Cs_2AgBiBr_6$ (4.31 eV) to 0.01 M (4.48 eV), and finally 0.05 M (4.65 eV) with increasing 2D modification penetration depth.

To gather further information on how the 2D modification affects the perovskite/CBE band alignment, we performed XPS measurements. The energetic shift of the elemental core levels has already been discussed in a previous section. The valence shell energies as well as the extracted VB offsets toward E_F are depicted in Figure S10 in the Supporting Information. It can be observed that the energetic difference between VBM and E_F is slightly reduced from pure $Cs_2AgBiBr_6$ (0.75 eV) toward 0.01 M (0.65 eV) and strongly reduced for 0.05 M (0.40 eV). The absolute VBM-E_F discrepancies as well as their enhancement for $Cs_2AgBiBr_6$ and 0.01 M are similar to the values found by Sirtl et al. for their PEA 2D modification.[46] In contrast, we report a strongly improved band alignment for 0.05 M. Using the E_F values from our KPFM analysis as well as an average literature bandgap of 2 eV for $Cs_2AgBiBr_6$ and a bandgap of 2.96 eV for the 2D bilayer[57] that is the dominant phase according to our GIXRD analysis, we created a band diagram of our $Cs_2AgBiBr_6$, 0.01 and 0.05 M thin films. In Figure 4d, the investigated samples' VBM, CBM, and vacuum energy levels are depicted relative to their

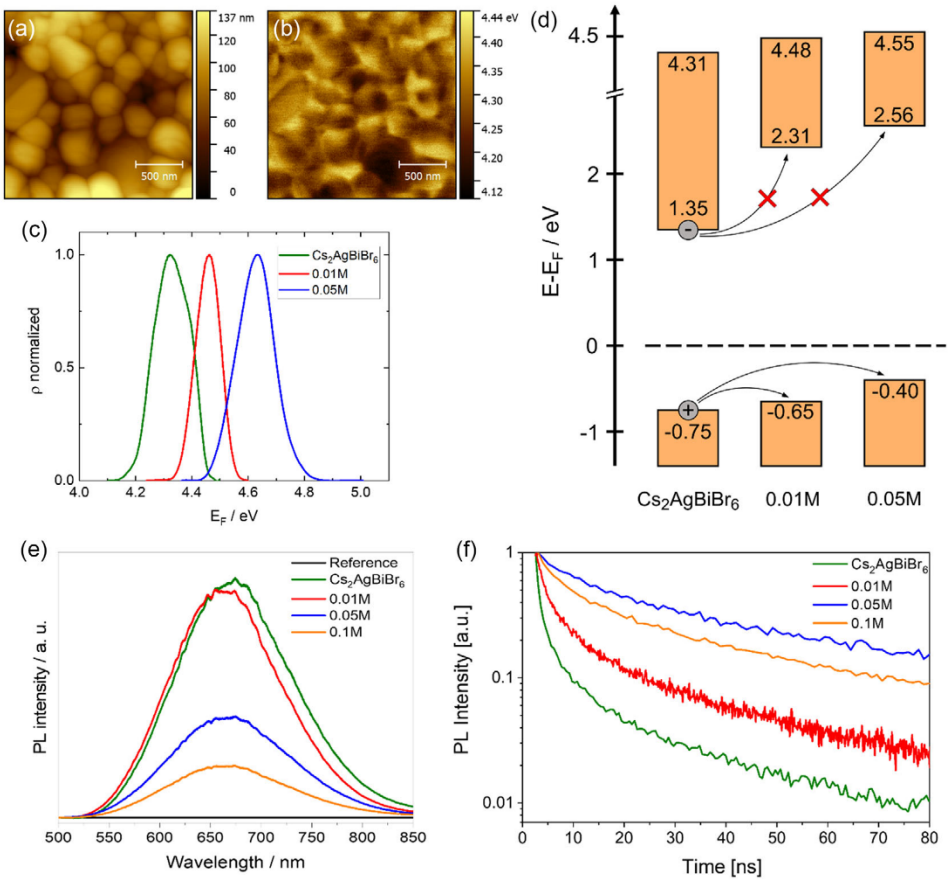

Figure 4. a) AFM and b) KPFM images of $Cs_2AgBiBr_6$. c) Work function distribution, calculated from KPFM images. d) Sketched band alignment between $Cs_2AgBiBr_6$, and 0.01 M, or 0.05 M, respectively. e,f) PL characterization of 2D/3D-modified $Cs_2AgBiBr_6$ thin films and the reference one. e) SSPL and f) TRPL spectra recorded at room temperature ($\lambda_{exc} = 405$ nm).

ADVANCED SCIENCE NEWS
www.advancedsciencenews.com

Solar RRL
www.solar-rrl.com

respective E_F. A band diagram with absolute values is shown in Figure S11 (Supporting Information). Furthermore, the energetic difference between E_F and CBM decreases from $Cs_2AgBiBr_6$ toward 0.05M, as observable in Figure 4d.

To further elucidate the surface-passivating effects of the mixed 2D/3D phase, we investigated the 2D modifications' effects on the photoluminescence (PL) of the perovskite thin films. Steady-state PL of thin films is depicted in Figure 4e. Pure $Cs_2AgBiBr_6$ and the 2D/3D-modified samples feature a PL maximum at 673 nm, which is characteristic of $Cs_2AgBiBr_6$, usually recognized as the indirect bandgap slow emission from the excited state that is responsible for the shallow absorption at 650 nm (Figure 3b, inset graph).[69] The absolute intensity of this emission peak decreases with increasing thickness of the 2D modification. We assume this behavior to be caused by the introduction of new oscillation modes, originating from the mixed 2D/3D perovskite, that affect the dynamics of the population of the red-shifted excited state, and therefore enhance the carrier relaxation modes by a nonradiative recombination mechanism. It is important to highlight that the red window of the absorption spectrum is not accountable for the overall optoelectronic performance, but only the high-energy excitonic peak (Figure 3b) significantly contributes to the photoabsorption. The photocurrent of the different solar cells does not decrease but increases, as discussed in a later section of this report. Consequently, a faster dissociation of excited states would also explain suppressed emission and, therefore, improved solar cell efficiency.

Time-resolved PL (TRPL) decay curves are depicted in Figure 4f. To extract information about charge carrier lifetimes, the curves were fitted with the triple exponential function:

$$I(t) = \sum A_i \exp(-t/\tau_i)\,(i = 1, 2, 3) \quad (1)$$

with A_i being the respective component's amplitude, and τ_i its respective lifetime.[29,76] The extracted parameters are shown in Table S1 (Supporting Information). While the fast and intermediate lifetimes τ_1 and τ_2 are reported to correspond to trap and surface state emission, the slow component τ_3 allows an estimation of the material's fundamental charge carrier lifetime since it was reported that around 80% of the charge carriers emit via the long-lived recombination process.[29,76] A comparison of τ_3 for $Cs_2AgBiBr_6$ and the 2D/3D-modified thin films reveals that τ_3 increases from pure $Cs_2AgBiBr_6$ (40 ns) to 0.01 M (59 ns) and 0.05 M (182 ns), while it decreases again for 0.1 M (165 ns).

However, it is important to note that the relative carrier population of the three recombination processes is unknown. To obtain the correct charge carrier lifetime, the PL quantum yield of the distinct processes must be considered.

The CBEs of this work's HTM-free $Cs_2AgBiBr_6$ solar cells consisted of carbon black powder which was obtained from a pyrolytic process using hazelnut shell waste, via a procedure that is described in an earlier work.[77] As described in detail in the Experimental Section, the carbon black was ball-milled in a polyvinylpyrrolidone (PVP) solution in isopropanol for several hours to fabricate a viscous paste which is depicted in Figure S1b (Supporting Information). The back electrodes were then deposited onto the perovskite thin films via screen-printing and consecutive thermal annealing. PVP was added to the paste to increase its viscosity (rheometric details shown in Figure S12, Supporting Information) and optimize the screen-printing deposition: while a too-low viscosity leads to smearing of the electrodes directly after their deposition, a too-high viscosity results in agglomerations and inhomogeneities of the electrodes. Reference solar cells were fabricated by first depositing Spiro-OMeTAD on the perovskite thin films via spin-coating, followed by electron-beam deposition of gold electrodes. Details of the Spiro-OMeTAD and gold electrode deposition procedures can be found in the Experimental Section.

Current density–voltage (J–V) curves of the solar cells that were prepared, as depicted in Figure S1a (Supporting Information), were measured under AM 1.5G irradiation. In **Figure 5**a, the parameters of multiple CBE solar cells consisting of pure $Cs_2AgBiBr_6$ as well as of the 2D-modified thin films are depicted. The application of a 2D modification of the $Cs_2AgBiBr_6$ perovskite film is expected to suppress the interfacial recombination between the perovskite layer and CBE due to defect passivation.[46,51,52] Also, the band alignment between perovskite and CBE can be improved due to an increased VB energy when the 2D modification is applied (Figure 4d). Accordingly, a change in solar cell parameters can be associated with the different treatments of the $Cs_2AgBiBr_6$ thin film. For 0.01 M, the average open-circuit voltage (V_{OC}) and fill factor (FF) are close to that of pure $Cs_2AgBiBr_6$ but its short-circuit current density (J_{SC}) is increased, which leads to a 7% improvement of the average PCE compared to $Cs_2AgBiBr_6$. For 0.05 M, the average J_{SC}, V_{OC}, and FF are further enhanced in comparison with pure $Cs_2AgBiBr_6$ and 0.01 M, and the average and record PCEs of 0.05 M improve by 38% and 57%, respectively, compared to $Cs_2AgBiBr_6$. Using this modification, we also achieved a record V_{OC} of 1.25 V within all CBE solar cells in this work. The enhanced PCEs of 0.05 M solar cells stem from the improved VB alignment toward the CBE which results in improved J_{SC} as well as the formation of a high-lying CBM, creating an energy barrier that suppresses recombination at the perovskite CBE interface, thus enhancing the CBE's selectivity (see Figure 4d). However, the PCE does not further improve with increasing concentration of the BABr solution. Although the average V_{OC} of 0.1 M is further enhanced, their J_{SC} strongly decreases due to the insulating character of the organic double layers in between the large number of 2D layers (see Figure 3a).

Furthermore, we compared the performances of the HTM-free CBE solar cells with solar cells consisting of Spiro-OMeTAD and gold. The J–V characteristics of the respective best-performing solar cells for 0.05 M are shown in Figure 5b. While the CBE device achieves a higher V_{OC}, the gold electrode device possesses a better FF. We assume the origin of the high V_{OC} to be attributed to the presence of an electric dipole at the perovskite/CBE interface, as we reported on devices with similar CBE solar cells, in a previous work.[77] Surprisingly, the current densities of both electrodes show almost no differences although the CBE's resistivity is six orders of magnitude higher than that of gold. This leads to comparable PCEs and J_{SC}s for the record devices of both top electrode types, implying that the CBE is not the efficiency-hampering bottleneck for those devices.

We performed electrochemical impedance spectroscopy (EIS) on $Cs_2AgBiBr_6$, 0.01, and 0.05 M solar cells, shown in Figure 5c, to analyze the origin of the increased solar cell performances.

ADVANCED SCIENCE NEWS
www.advancedsciencenews.com

Solar RRL
www.solar-rrl.com

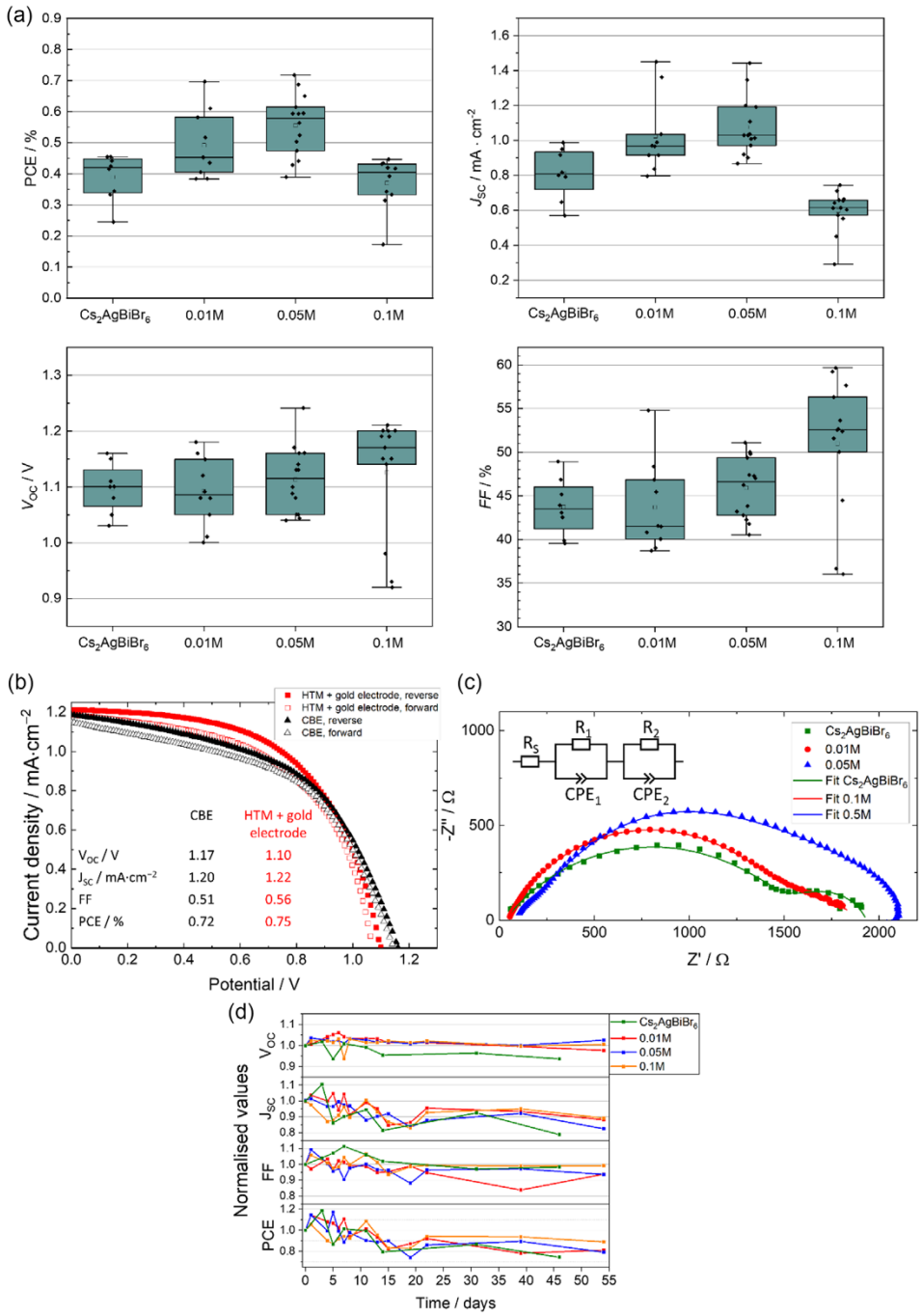

Figure 5. 2D/3D-modified $Cs_2AgBiBr_6$ solar cells characterization. a) Statistics on relevant figures of merits for HTM-free solar cells containing a CBE top electrode. b) *J–V* characteristics for 0.05 M-modified devices containing either a CBE top electrode or Spiro-OMeTAD HTM and gold electrode. c) EIS characterization on pristine and 2D/3D-modified $Cs_2AgBiBr_6$ solar cells containing a Spiro-OMeTAD HTM and a gold top electrode. d) Variations in relevant figures of merit for HTM-free solar cells containing a CBE top electrode over 54 days of storage in standard laboratory conditions.

ADVANCED SCIENCE NEWS
www.advancedsciencenews.com

Solar RRL
www.solar-rrl.com

The CBEs possess a resistivity ρ of 5.1 mΩ m (for comparison: $\rho_{gold} = 2.20 \cdot 10^{-5}$ mΩ m) obtained by measuring the sheet resistance of carbon electrodes that were deposited on insulating glass with a four-point-probe setup. Therefore, to obtain reliable and reproducible impedance spectra, we compared only $Cs_2AgBiBr_6$, 0.01, and 0.05 M devices with HTM and gold electrodes since the high resistivity of the carbon electrodes strongly affected the impedance spectra in the low-frequency regions. We applied an equivalent circuit model (ECM), as depicted in Figure 5c, that allows us to determine the recombination resistance as well as the selective contact resistance.[43] The former is expected to increase with increasing BABr concentration due to the defect-passivating properties of capping 2D modifications, whereas the latter is expected to decrease due to improved band alignment, as depicted in the scheme of Figure 1 and in Figure 4d. The ECM consists of a resistor R_S representing the resistance of the wires, contacts, and electrodes, one resistor R_1//constant phase element (CPE_1) circuit to model the selective contacts for low frequencies, as well as an R_2//CPE_2 circuit representing the interfacial recombination at high frequencies.[43] Parameters obtained by fitting the ECMs to the respective impedance spectra are shown in Table S2 in the Supporting Information. With increasing thickness of the 2D modification, the interfacial recombination resistance R_2 is increasing from 367 Ω ($Cs_2AgBiBr_6$) to 610 Ω (0.01 M) and 1760 Ω (0.05 M), in line with a strongly decreasing rate of recombination. These results agree with increased carrier lifetimes obtained from TRPL analyses we performed on the respective perovskite thin films and are also supported by the enhanced V_{OC} that causes the improvement of the shunt resistance values leading to FF value optimization of the 0.05 M solar cells. Additionally, the decreasing selective contact resistance R_1 with increasing 2D modification thickness corresponds with an enhanced charge carrier injection into the selective contacts from the perovskite layer. For the $Cs_2AgBiBr_6$ solar cells (1536 Ω), it is the largest and it reduces for 0.01 M (1284 Ω) and 0.05 M (409 Ω). This behavior results from the improved band alignment and selectivity of the 2D/3D-modified thin films (Figure 4d).

Since the 2D modification increased the thin films' hydrophobicity and passivated the material, we evaluated the evolution of solar cell parameters within several weeks, as shown in Figure 5d. While the $Cs_2AgBiBr_6$ solar cells already possess a long device lifetime, the 2D/3D modification further enhanced their longevity. Especially the 0.1 M devices retained close to 90% of their initial efficiency after 54 days. Their high conversion of 3D perovskite into 2D phases provides the best protection against efficiency losses in 0.1 M, which results in the highest long-term stability. However, since the PCEs in Figure 5d are normalized values, the 0.1 M solar cells still on average possess the lowest efficiencies of all solar cells discussed in this report.

To investigate the origin of the increased J_{SC} of the 0.01 and 0.05 M solar cells, we performed external quantum efficiency (EQE) determination, as shown in **Figure 6**a. The EQE of 0.01 and 0.05 M feature an absolute maximum at around 340 nm of ≈43% and a local maximum at around 440 nm of ≈32% and therefore possess close similarity to the absorbance spectra (Figure 3b) in their shape. In comparison, the spectra of $Cs_2AgBiBr_6$ possess a similar shape but their EQE is reduced by around 10% throughout the entire spectrum which is in accordance with the reduced J_{SC} of $Cs_2AgBiBr_6$ compared to 0.01, and 0.05 M solar cells (Figure 5a). At the 440 nm maximum, the EQE of all 2D-modified solar cells is slightly red-shifted in comparison to the $Cs_2AgBiBr_6$. Furthermore, the internal quantum efficiency (IQE) of the 2D-modified solar cells is drastically increased close to bandgap energies in comparison to $Cs_2AgBiBr_6$ (see Figure 6b). This behavior corresponds to an enhanced charge carrier extraction close to the band edges. It can best be observed by comparing $Cs_2AgBiBr_6$ and 0.1 M (see Figure 6b): while $Cs_2AgBiBr_6$ shows higher IQE at the 440 nm maximum, the IQE of 0.1 M is higher in the region between 450 and 520 nm, close to the bandgap. To compare the different behavior of IQE and EQE at bandgap wavelengths as well as sub-bandgap wavelengths, both are depicted for the 0.05 M solar cell in Figure 6c.

The viability of the 2D perovskite phase as an HTM has also been assessed via density functional theory (DFT) calculations. To investigate the effect of increasing number of 2D DP stacks, we calculated samples consisting of 3D/2D heterostructures made of 8 symmetric layers of 3D cubic DP ($Cs_2AgBiBr_6$) slab and a 2D ($(BA)_2CsAgBiBr_7$)) capping layer with growing number of layers (**Figure 7** - see Supporting Information Table S3 for detailed structural information). In particular, we considered four heterostructures containing 1, 2, 3, and 5 2D layers, dubbed hs1, hs2, hs3, and hs5, respectively. **Figure 8** presents the density of states (DOS) projected (pDOS) on the 3D, and organic and inorganic sublattices of 2D domains of the hs1 heterostructure. One notices that the VBM and close-by energy states are related

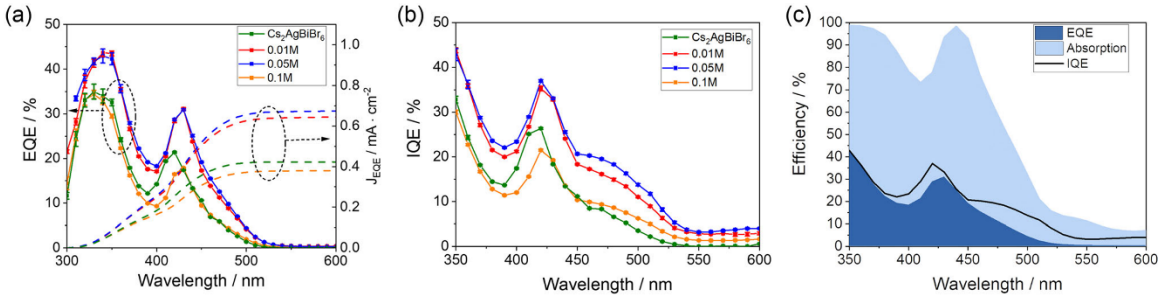

Figure 6. Quantum efficiencies of 2D/3D-modified $Cs_2AgBiBr_6$ solar cells with CBE. a) EQE (left *y*-axis, squares connected by solid curves) and integrated current densities (right *y*-axis, dotted curves). b) IQE, calculated using absorption spectra from Figure 3b. c) EQE (dark blue), IQE (light blue), and absorption (black curve) of 0.05 M in direct comparison.

ADVANCED SCIENCE NEWS
www.advancedsciencenews.com

Solar RRL
www.solar-rrl.com

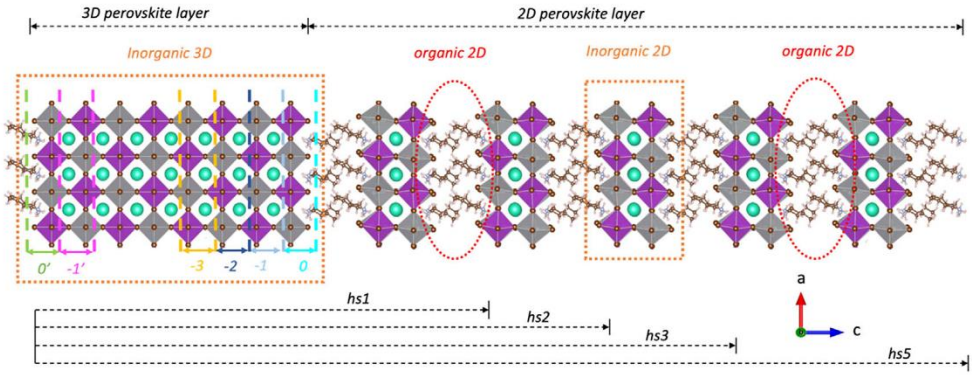

Figure 7. Slab models considered for DFT calculations. Divisions of 3D perovskite layer used to calculate npDOS for respective slabs. Periodic boundary conditions (PBC) applied along the direction perpendicular to the surface result in the creation of two equivalent 3D/2D interfaces.

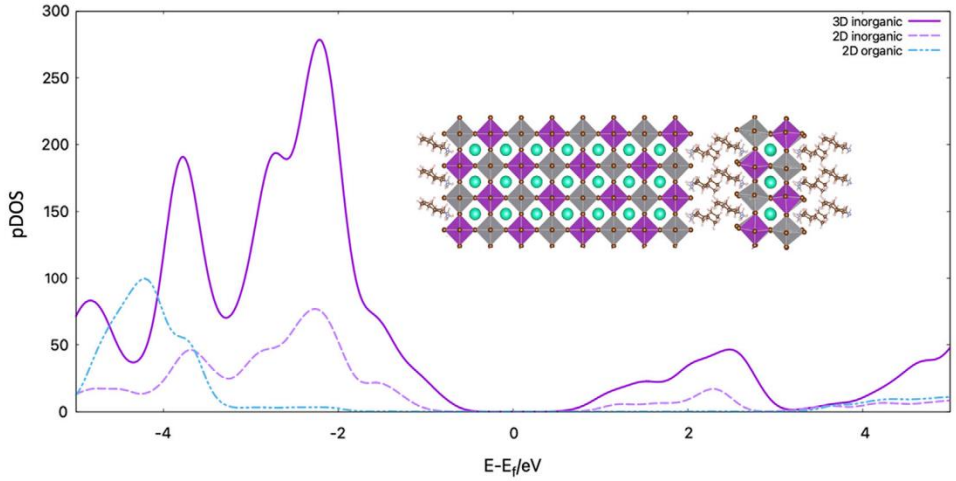

Figure 8. pDOS calculated for 3D/2D hs1.

to the 3D and the inorganic sublattice of the 2D DPs, which are in agreement with previous studies.[23,46,58,78] Similar results are found for the other heterostructures (Figure S13, Supporting Information).

To identify the microscopic origin of the enhanced charge extraction revealed by the increased IQE with BABr concentration up to 0.05 M, we computed the contribution of the various layers of Figure 7 of the 3D slab to the density of states (see Figure S14, Supporting Information). This contribution, expressed in percentage and denominated *normalized* pDOS (npDOS), is obtained by dividing pDOS relative to one 3D layer by (total) DOS and multiplying by 100. npDOS is set to zero in the region of the bandgap. One sees that for the single 2D bilayer (hs1), the contribution of the interface 3D layer (0) to the DOS at VBM and closer energies is the lowest among all the layers of the $Cs_2AgBiBr_6$ computational slab, with the largest contribution arising from the bulk-like layers (−3). This implies that for the hs1 sample, one has little probability of finding holes at the 3D/2D interface and their extraction is inefficient. The picture changes with the increase of the thickness of the 2D slab, with the contribution of the interface layer to the VBM growing steadily from 3 to, 10, to 16, to 26% for hs1, hs2, hs3, and hs5, respectively. A similar effect of a thicker 2D layer is observed up to 0.7 eV below the VBM. This increase in the contribution of the interface layer to VBM means that thermalized holes are closer to the interface, which makes their extraction easier as revealed in the experiments. We attribute to this phenomenon the increase of the IQE close to the bandgap energy (see Figure 6b).

However, experimental IQE shows a maximum at the bandgap for the 0.05 M solar cells. We attribute this phenomenon to two additional effects of the thickness of the 2D capping layer. First, the resistance of the 2D capping layer increases with its thickness, balancing the beneficial effect of the heterostructure in attracting holes at the interface. Moreover, 2D layer capping has also the effect of increasing the contribution of the interface 3D layer in the CBM (Figure S15, Supporting

ADVANCED SCIENCE NEWS
www.advancedsciencenews.com

Solar RRL
www.solar-rrl.com

Information), i.e., attracting electrons in the CB toward a region with higher concentration of holes. Thus, a longer residence time of holes at the interface due to the longer extraction time of the thicker 2D layer favors their recombination with electrons also present in this region. This leads to a reduction of the current density and, henceforth, PCE.

Experimental results from TRPL (Figure 4f) and EIS (Figure 5c) suggest that the 2D layers passivate defects and, here, we investigate the microscopic origin of this phenomenon. We considered the three most likely defects in bulk $Cs_2AgBiBr_6$:[79–83] bismuth antisite, and bismuth and bromide vacancies: Ag_{Bi}'', V_{Bi}''', and $V_{Br}^{\bullet}$, following the Kröger–Vink notation. We computed the relative energy of these defects as a function of their position along the slab (**Figure 9**a–c) for the 2D capping at various thicknesses. First and foremost, we notice that all defects (encircled in pink) are more stable when moved away from the interface layer. In other words, the effect of 2D capping is preventing any accumulation of defects at the $Cs_2AgBiBr_6$ surface, where, as shown before, we have an accumulation of holes and electrons and defects can promote recombination. Our simulations suggest that the *passivation* effect of 2D capping is, indeed, not passivation in the usual sense: here, the presence of 2D layers prevents the accumulation of defects at the 3D surface/interface. Concerning defect *passivation*, the thickness of the slab does not play any major role. We observe similar energy of defects versus position in the 3D slab for all heterostructures, regardless of the thickness of the 2D layer.

To further investigate the effect of defect passivation of the 2D capping, we performed analogous calculations for a 3D/Spiro-OMeTAD interface model. We also computed the relative energetics of $V_{Br}^{\bullet}$ and Ag_{Bi}'' defects as functions of position. At a variance with the 3D/2D system, we noticed that with Spiro-OMeTAD both defects are attracted to the interface layer (see Figure S16 in the supporting information). Even in the absence of any defect at the perovskite interface layer, a visual inspection of the minimum energy configuration clearly shows a more pronounced and prolonged (farther from the interface) distortion of the perovskite lattice with respect to the 2D/3D sample (compare Figure S17 and S18, Supporting Information). It is well known that tilting of $[AgBr_6]^{5-}$ and $[BiBr_6]^{3-}$ octahedra in the case of DPs affects its electronic structure and consequently the electronic properties.[24] Indeed, the pDOS of the interface layer of the defect-free 3D/Spiro-OMeTAD system (Figure S19, Supporting Information) shows some orbitals with energies deeper in the bandgap with respect to the 2D/3D case. These states can either result in trap-assisted recombination or simply slow down carrier dynamics. This effect is enhanced when $V_{Br}^{\bullet}$ and Ag_{Bi}'' defects are accumulated at the 3D/Spiro-OMeTAD interface, according to the driving force discussed above. This is illustrated by comparing the pDOS of the interface layer of the pristine and defected 3D/Spiro-OMeTAD system (Figure S20, Supporting Information), which shows additional states due to the defects appearing at the bottom of the CB for both types of defects.

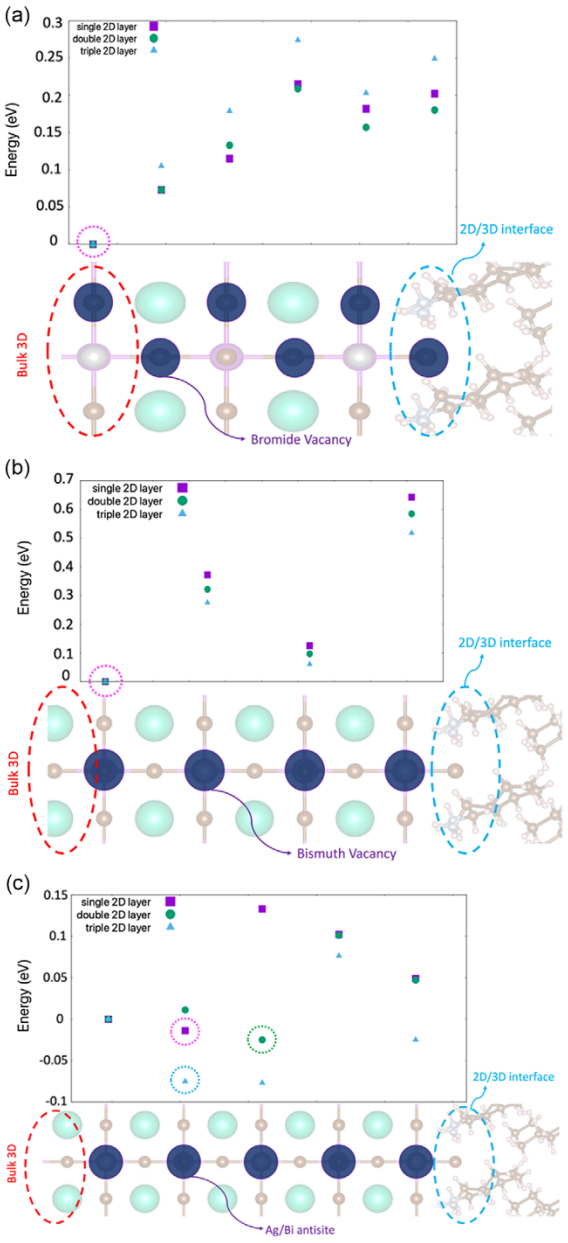

Figure 9. Energy versus position of a) bromide vacancy ($V_{Br}^{\bullet}$), b) bismuth vacancy (V_{Bi}'''), and c) antisite (Ag_{Bi}'') of hs1, hs2, and hs3. Dashed circles around symbols denote the state corresponding to the minimum energy defect position. Energies are arbitrarily shifted so that the value in the bulk position is zero. In each panel is reported a cartoon illustrating the portion of the 3D/2D computational sample illustrating the position of the corresponding defect.

ADVANCED SCIENCE NEWS
www.advancedsciencenews.com

Solar RRL
www.solar-rrl.com

3. Conclusion

In this work, we present the fabrication of low-cost HTM-free 2D/3D-modified DP solar cells via a treatment of $Cs_2AgBiBr_6$ thin films with n-butylammonium bromide solution in isopropanol, followed by the deposition of electrodes consisting of carbon black from up-cycled biowaste. The presence of the 2D/3D modification, consisting mainly of $(BA)_2CsAgBiBr_7$ bilayers, is experimentally confirmed, and its thickness is shown to depend on the concentration of the BABr solution. Using a combination of XPS and KPFM, we provide a band diagram, showing an improved VB alignment between $Cs_2AgBiBr_6$ and the CBE for 2D/3D-modified solar cells as well as a strongly increased CBM, leading to enhanced selectivity. Both effects are further confirmed via electrochemical characterization and result in improved J_{SC}, V_{OC}, FF, and PCE for HTM-free 2D/3D $Cs_2AgBiBr_6$ solar cells that were treated with 0.05 M BABr solution. DFT calculations, that simulate various numbers of $(BA)_2CsAgBiBr_7$ bilayers which are capping 3D $Cs_2AgBiBr_6$, reveal that the presence of 2D perovskite increases the 3D phase's DOS for holes at the 2D/3D interface and, therefore, enhances the hole extraction probability. The calculations are supported by an improved IQE for 2D/3D-modified solar cells close to their band edge.

This work demonstrates how the application of a 2D/3D modification enhances the PCE of HTM-free $Cs_2AgBiBr_6$ solar cells. The absence of an HTM and the substitution of the metal electrode not only strongly reduce the device costs, but also the application of the carbon electrode from up-cycled biowaste also represents a path toward "green" PV. Furthermore, the drawbacks of low selectivity and weak band alignment for HTM-free PVs are mitigated by the formation of the 2D/3D-mixed perovskite phase. Although our solar cells possess relatively low PCEs, which is a common problem for this material,[38,41–49] there are promising reports of highly improved $Cs_2AgBiBr_6$, i.e., by hydrogenating the material, that will benefit from applying our approach to further boost such technology.[84]

4. Experimental Section

Fabrication of 2D-Modified $Cs_2AgBiBr_6$ Thin Films: The preparation of $Cs_2AgBiBr_6$ thin films as well as their 2D modification were entirely performed in an argon-filled glovebox. First, $Cs_2AgBiBr_6$ powder, which was synthesized as described in previous work,[30] was dissolved in dimethyl sulfoxide (99.7+%, thermos scientific) to create a 0.5 mol L^{-1} precursor solution. The solution was stirred until the powder was fully dissolved. To deposit the $Cs_2AgBiBr_6$ thin film, a substrate (2×2 cm^2) was mounted onto a spin-coater, precursor solution (50 µL) was evenly spread across the substrate, and the substrate was rotated at 4000 rpm for 40 s (3 s acceleration time). Immediately after the spin-coating process, the substrate was transferred to a preheated 285 °C hot plate and annealed for 5 min. To prepare the 2D modification, we adapted the synthesis route from Sirtl et al.[46] The room-temperature $Cs_2AgBiBr_6$ thin films were again mounted onto a spin-coater, then n-butylammonium bromide (Aldrich) solution (100 µL, 0.01/0.05/0.1 mol L^{-1} in isopropanol) was evenly spread across the thin films, and they were rotated at 4000 rpm for 40 s. Afterward, the thin films were left to dry in the glovebox overnight.

Preparation of Solar Cells: FTO-covered glass substrates were etched as depicted in Figure S1a (Supporting Information) and cleaned by consecutive ultrasonication in demineralized water, acetone, and isopropanol for 15 min each. Then, the substrates were UV–ozone treated for 15 min and mounted on a spin-coater under an ambient atmosphere. They were covered with commercial compact TiO_2 precursor solution (70 µL, Solaronix), rotated at 5000 rpm for 30 s, and annealed for 1 h at 550 °C in air. For the preparation of the mesoporous TiO_2 layer, the substrates were again UV–ozone cleaned for 15 min and mounted on a spin-coater. They were covered with diluted (1:5 abs. ethanol) commercial mesoporous TiO_2 precursor solution (100 µL, Solaronix), rotated at 5000 rpm for 30 s, and then annealed at 475 °C for 30 min in air. Before the deposition of the $Cs_2AgBiBr_6$, the substrates were heated at 400 °C for 30 min to release water encapsulated in the TiO_2 scaffold. The substrates were then transferred into an argon-filled glove box and the perovskite layers were deposited as described above.

Deposition of CBE: The CBE precursor paste was prepared by first dissolving PVP (70 mg) in of isopropanol (2 mL). The solution was vigorously stirred overnight until the PVP was fully dissolved. Then, the viscous solution was mixed with carbon black (100 mg) that was synthesized via a process analogous to the one described in our previous work.[77] The mixture was ball-milled at 250 rpm for 3 h using two stainless steel balls (1 cm diameter) to create a homogeneous, viscous carbon paste (Figure S1b, Supporting Information). The CBEs were deposited via screen-printing (mesh size 80 T) and then annealed at 100 °C for 1 h.

Deposition of HTM and Gold Electrode: The HTM for the reference devices was deposited according to the literature.[46] To prepare the HTM precursor solution, Spiro-OMeTAD (73 mg) was dissolved in chlorobenzene (1 mL) in an argon-filled glove box. To this solution, 4-tert-butylpyridine (10 µL) and lithium bis(trifluoromethanesulfonyl) imide solution (30 µL, 170 mg dissolved in 1 mL acetonitrile) were added. The solution was spin-coated onto the perovskite layer at 1500 rpm for 45 s. Gold electrodes with 60 nm thickness were deposited via electron-beam physical vapor deposition.

Characterization: GIXRD measurements were performed with a PANalytical B.V. X'Pert Pro diffractometer using Cu Kα1 radiation. The instrument was operated at 40 kV and 40 mA, the step size was 0.05°, and the scan speed was 0.014° s^{-1}. The diffraction patterns were measured along the 2θ axis with a grazing incidence of $\omega = 0.5°$. Thin film absorption spectra were measured using a two-ray setup with a UVIKON XS from Schott Instruments. Contact angles were conducted with an OCA 20 from Dataphysics Instruments GmbH using demineralized water. SEM images were taken using a GeminiSEM 560 from Zeiss at a working potential of 1 kV. HRTEM images were taken using a Talos F200X from Thermo Scientific (Eindhoven, the Netherlands). The analysis was performed at an acceleration voltage of 200 kV. EDX was performed with a 4-quadrant EDX detector in STEM mode. Further instrument details as well as a description of the sample preparation are shown in the Supporting Information. XPS was performed with a PHI 5000 VersaProbe II Scanning ESCA Microprobe (Physical Electronics) with monochromatized Al Kα X-ray source in high power mode (beam size 1300 µm × 100 µm, X-ray power: 100 W). Time steps of 50 ms, a step size of 0.2 eV, and an analyzer pass energy of 46.95 eV were used for measuring the detail spectra. For every detailed region, 30 sweeps, or a P/N ratio equal to 180, were set. The sample surface was charge neutralized with slow electrons and argon ions, and the pressure was in the range from 10^{-7} Pa to 10^{-6} Pa during the measurement. Data analysis was performed using the CasaXPS software.[85] Diffuse reflectance infrared Fourier transform spectroscopy was performed with a Bruker alpha. The spectra were recorded in a range of 400–4000 cm^{-1} with a resolution of 2 cm^{-1}. AFM and KPFM were carried out using an AIST NT Vacuscope 1000 microscope operated below $5 \cdot 10^{-6}$ mbar with SPARK 350 Pt-coated AFM probes excited at the resonant frequency of around 300 kHz. An amplitude of 8.5 nm was chosen for the noncontact morphology scans in AC-mode operation. The work function was obtained by measuring the contact potential difference between the probe and sample via FM-KPFM at an AC amplitude of 2 V at around 1 kHz. The probe work function was referenced by obtaining the contact potential difference of the probe to a freshly cleaved highly oriented pyrolytic graphite (ZYB, MikroMasch) with a known work function of 4.6 eV before and after each measurement. Linear sweep voltammetry (J–V curves) was conducted with an IviumStat potentiostat from Ivium Technologies. Solar cells were

ADVANCED SCIENCE NEWS
www.advancedsciencenews.com

Solar RRL
www.solar-rrl.com

measured with a rate of 0.05 $V \cdot s^{-1}$. For irradiation, an LS0160 solar simulator from LOT-Oriel with an LSB521U 150 W xenon high-pressure arc lamp and an LSZ189 AM1.5 filter (both LOT-Oriel) was used. The power density was calibrated to 100 mW cm^{-2} using an ML-020VM pyranometer from ECO Instruments. All measured solar cells were masked (3×3 mm^2). EIS was performed with an SP-50e potentiostat from BioLogic. The spectra were taken at frequencies from 10 Hz to 1 MHz and were analyzed using the software RelaxIS (rhd instruments). The microphotoluminescence spectra were collected at room temperature on a LabRAM HR Evolution spectrometer (Horiba Jobin Yvon) equipped with an Olympus BXFM-ILHS confocal microscope working in backscattering geometry and Syncerity OE detector. Solid-state Cobolt Blues 25 laser was used as the excitation line at 473 nm with a beam power of 400 μW. Measurements were performed over the spectral range 500–850 nm and the signal was acquired with a 100× objective (NA = 0.9). The diameter of the confocal hole was 500 μm, and the diffraction grating was 300 lines/mm. For each spectrum, 5 acquisitions with an accumulation time of 1 s each were averaged. Spectra were smoothed and background-corrected where necessary. The fluorescence decay curves and fluorescence map measurements were performed on a MicroTime 200 confocal microscope (PicoQuant). As an excitation source, a 402 nm pulsed laser diode was used. The beam was directed via a dichroic mirror (Chroma ZT405rdc) into the Olympus IX71 microscope. Simultaneously, fluorescence emission passed the dichroic and was focused on a pinhole (size 30 μm). After the pinhole, the fluorescence light passed the 600 nm longpass filter (Thorlabs FEL0600) and was focused on the SPAD detector (Excelitas Technologies SPCM CD 3516 H). All measurements were performed using the SymPhoTime Software (PicoQuant). EQE measurements were conducted using a LSB551 1000 W xenon arc lamp, and a SpectraPro 2300i (Action) Monochromator. The spectra were measured using an IviumStat potentiostat from Ivium Technologies. Calibration on the incident photon number was done using an FDS100 silicon photodiode from Thorlabs. The IQE was calculated by dividing the EQE by the absorption of the respective thin films.

Simulations: Three computational samples were considered; sample 1) an eight-layer thick slab of $Cs_2AgBiBr_6$ oriented along the (001) crystallographic direction was prepared, and its geometry was optimized. On this, we deposited slabs of $(BA)_2AgBiBr_7$ with various layers of the material. Simulations are performed within PBC and the 3D and 2D slabs are combined so that the two 3D/2D interfaces are symmetric and there is no induced dipole moment (see Figure S15 in the Supporting Information); slabs 2 and 3) the thickness and the orientation of the $Cs_2AgBiBr_6$ slab along (001) direction were retained, however, the width was doubled along the (100) and (010) directions and its geometry was optimized. On this slab, we deposited the Spiro-OMeTAD molecule. While the $Cs_2AgBiBr_6$ slab is of the same dimensions for samples 2 and 3, the orientation of the HTM molecule differs. This approach is considered as no experimental data are available on the binding characteristics of Spiro-OMeTAD to DP surface. We refer to these different orientations as the different binding modes (see Figure S16, Supporting Information). Furthermore, one can have different surface/interface terminations in a crystallite in experimental samples. On the contrary, all our samples are symmetrically terminated. This is because computational samples are much smaller than experimental ones (few nanometers vs hundreds of nanometers to micrometers) and systematic asymmetries associated with different terminations likely, possibly introducing a dipole moment in the slab, may induce large electric fields. This likely induces artifacts in the computational results. Density functional calculations were performed within the Perdew–Burke–Ernzerhof generalized gradient approximation. Simulations were performed with the VASP code. Kohn–Sham orbitals were expanded on a planewave basis set with an energy cutoff of 400 eV. The interaction between valence electron and nuclei plus core electron was described within the projector augmented-wave formalism.[86,87] For the computational sample 1, the Brillouin zone has been sampled with $4 \times 4 \times 1$ K-points,[88] the latter figure referring to the (001) direction. For the other two computational samples, because of their larger size in the surface plane necessary to accommodate Spiro-OMeTAD, we used Γ-point sampling only. The suitability of this setup was validated by checking the convergence of total energy, bandgap, and atomic forces with respect to the parameters listed above.

Supporting Information

Supporting Information is available from the Wiley Online Library or from the author.

Acknowledgements

T.G. would like to acknowledge the financial support of the European Research Council through the ERC StG project JANUS BI (grant agreement no. [101041229]). This study was carried within the PINPOINT project funded by the European Union Next Generation EU within the PRIN 2022 PNRR program (D.D. del 14/09/2022 Ministero dell'Università e della Ricerca). This manuscript reflects only the authors' views and opinions and the Ministry cannot be considered responsible for them. P.P., J.C., P.P., G.D., and D. P. thank the ENSEMBLE^3 Project (MAB/2020/14) which is carried out within the International Research Agendas Programme (IRAP) of the Foundation for Polish Science cofinanced by the European Union under the European Regional Development Fund and Teaming Horizon 2020 program of the European Commission.

Conflict of Interest

The authors declare no conflict of interest.

Data Availability Statement

The data that support the findings of this study are available from the corresponding author upon reasonable request.

Keywords

carbon-based perovskite solar cells, hole transport material-free perovskite solar cells, interfacial engineering, lead-free perovskite solar cells, silver–bismuth double perovskites

Received: November 24, 2023
Revised: January 12, 2024
Published online:

[1] F. Perera, K. Nadeau, *N. Engl. J. Med.* **2022**, *386*, 2303.
[2] M. Höök, X. Tang, *Energy Policy* **2013**, *52*, 797.
[3] N. L. Panwar, S. C. Kaushik, S. Kothari, *Renewable Sustainable Energy Rev.* **2011**, *15*, 1513.
[4] A. W. Faridi, M. Imran, G. H. Tariq, S. Ullah, S. F. Noor, S. Ansar, F. Sher, *Ind. Eng. Chem. Res.* **2023**, *62*, 4494.
[5] Q. Jiang, Z. Chu, P. Wang, X. Yang, H. Liu, Y. Wang, Z. Yin, J. Wu, X. Zhang, J. You, *Adv. Mater.* **2017**, *29*, 1.
[6] J. Guo, B. Wang, D. Lu, T. Wang, T. Liu, R. Wang, X. Dong, T. Zhou, N. Zheng, Q. Fu, Z. Xie, X. Wan, G. Xing, Y. Chen, Y. Liu, *Adv. Mater.* **2023**, *35*, 1.
[7] B. Li, Y. Zhang, L. Zhang, L. Yin, *J. Power Sources* **2017**, *360*, 11.
[8] N. De Marco, H. Zhou, Q. Chen, P. Sun, Z. Liu, L. Meng, E. P. Yao, Y. Liu, A. Schiffer, Y. Yang, *Nano Lett.* **2016**, *16*, 1009.
[9] D. W. DeQuilettes, S. M. Vorpahl, S. D. Stranks, H. Nagaoka, G. E. Eperon, M. E. Ziffer, H. J. Snaith, D. S. Ginger, *Science* **2015**, *348*, 683.

[10] S. H. Turren-Cruz, M. Saliba, M. T. Mayer, H. Juárez-Santiesteban, X. Mathew, L. Nienhaus, W. Tress, M. P. Erodici, M. J. Sher, M. G. Bawendi, M. Grätzel, A. Abate, A. Hagfeldt, J. P. Correa-Baena, *Energy Environ. Sci.* **2018**, *11*, 78.
[11] H. Oga, A. Saeki, Y. Ogomi, S. Hayase, S. Seki, *J. Am. Chem. Soc.* **2014**, *136*, 13818.
[12] W. J. Yin, T. Shi, Y. Yan, *Appl. Phys. Lett.* **2014**, *104*, 063903.
[13] R. Prasanna, A. Gold-Parker, T. Leijtens, B. Conings, A. Babayigit, H. G. Boyen, M. F. Toney, M. D. McGehee, *J. Am. Chem. Soc.* **2017**, *139*, 11117.
[14] S. A. Kulkarni, T. Baikie, P. P. Boix, N. Yantara, N. Mathews, S. Mhaisalkar, *J. Mater. Chem. A* **2014**, *2*, 9221.
[15] K. L. Wang, Y. H. Zhou, Y. H. Lou, Z. K. Wang, *Chem. Sci.* **2021**, *12*, 11936.
[16] C. Polyzoidis, K. Rogdakis, E. Kymakis, *Adv. Energy Mater.* **2021**, *11*, 1.
[17] X. He, J. Chen, X. Ren, L. Zhang, Y. Liu, J. Feng, J. Fang, K. Zhao, S. F. Liu, *Adv. Mater.* **2021**, *33*, 2100770.
[18] Y. Zhao, F. Ma, Z. Qu, S. Yu, T. Shen, H. X. Deng, X. Chu, X. Peng, Y. Yuan, X. Zhang, J. You, *Science* **2022**, *377*, 531.
[19] K. L. Wang, H. Lu, M. Li, C. H. Chen, D. Bo Zhang, J. Chen, J. J. Wu, Y. H. Zhou, X. Q. Wang, Z. H. Su, Y. R. Shi, Q. S. Tian, Y. X. Ni, X. Y. Gao, S. M. Zakeeruddin, M. Grätzel, Z. K. Wang, L. S. Liao, *Adv. Mater.* **2023**, *35*, 1.
[20] A. Babayigit, A. Ethirajan, M. Muller, B. Conings, *Nat. Mater.* **2016**, *15*, 247.
[21] C. Chen, S. Cheng, L. Cheng, Z. Wang, *Adv. Energy Mater.* **2023**, *13*, 2204144.
[22] M. T. Sirtl, M. Armer, L. K. Reb, R. Hooijer, P. Dörflinger, M. A. Scheel, K. Tvingstedt, P. Rieder, N. Glück, P. Pandit, S. V. Roth, P. Müller-Buschbaum, V. Dyakonov, T. Bein, *ACS Appl. Energy Mater.* **2020**, *3*, 11597.
[23] E. T. McClure, M. R. Ball, W. Windl, P. M. Woodward, *Chem. Mater.* **2016**, *28*, 1348.
[24] H. Lei, D. Hardy, F. Gao, *Adv. Funct. Mater.* **2021**, *31*, 2105898.
[25] E. Greul, M. L. Petrus, A. Binek, P. Docampo, T. Bein, *J. Mater. Chem. A* **2017**, *5*, 19972.
[26] R. Wang, H. Li, H. Sun, *Encyclopedia of Environmental Health*, Elsevier, Amsterdam **2019**, p. 415.
[27] R. L. Z. Hoye, L. Eyre, F. Wei, F. Brivio, A. Sadhanala, S. Sun, W. Li, K. H. L. Zhang, J. L. MacManus-Driscoll, P. D. Bristowe, R. H. Friend, A. K. Cheetham, F. Deschler, *Adv. Mater. Interfaces* **2018**, *5*, 1800464.
[28] Z. Li, S. P. Senanayak, L. Dai, G. Kusch, R. Shivanna, Y. Zhang, D. Pradhan, J. Ye, Y. Huang, H. Sirringhaus, R. A. Oliver, N. C. Greenham, R. H. Friend, R. L. Z. Hoye, *Adv. Funct. Mater.* **2021**, *31*, 2104981.
[29] A. H. Slavney, T. Hu, A. M. Lindenberg, H. I. Karunadasa, *J. Am. Chem. Soc.* **2016**, *138*, 2138.
[30] F. Schmitz, K. Guo, J. Horn, R. Sorrentino, G. Conforto, F. Lamberti, R. Brescia, F. Drago, M. Prato, Z. He, U. Giovanella, F. Cacialli, D. Schlettwein, D. Meggiolaro, T. Gatti, *J. Phys. Chem. Lett.* **2020**, *11*, 8893.
[31] R. Kentsch, M. Scholz, J. Horn, D. Schlettwein, K. Oum, T. Lenzer, *J. Phys. Chem. C* **2018**, *122*, 25940.
[32] F. Igbari, R. Wang, Z. K. Wang, X. J. Ma, Q. Wang, K. L. Wang, Y. Zhang, L. S. Liao, Y. Yang, *Nano Lett.* **2019**, *19*, 2066.
[33] Z. Li, P. Wang, C. Ma, F. Igbari, Y. Kang, K. L. Wang, W. Song, C. Dong, Y. Li, J. Yao, D. Meng, Z. K. Wang, Y. Yang, *J. Am. Chem. Soc.* **2021**, *143*, 2593.
[34] K. Z. Du, W. Meng, X. Wang, Y. Yan, D. B. Mitzi, *Angew. Chem., - Int. Ed.* **2017**, *56*, 8158.
[35] J. A. Steele, P. Puech, M. Keshavarz, R. Yang, S. Banerjee, E. Debroye, C. W. Kim, H. Yuan, N. H. Heo, J. Vanacken, A. Walsh, J. Hofkens, M. B. J. Roeffars, *ACS Nano* **2018**, *12*, 8081.
[36] J. Leveillee, G. Volonakis, F. Giustino, *J. Phys. Chem. Lett.* **2021**, *12*, 4474.
[37] G. Longo, S. Mahesh, L. R. V. Buizza, A. D. Wright, A. J. Ramadan, M. Abdi-Jalebi, P. K. Nayak, L. M. Herz, H. J. Snaith, *ACS Energy Lett.* **2020**, *5*, 2200.
[38] D. Zhao, C. Liang, B. Wang, T. Liu, Q. Wei, K. Wang, H. Gu, S. Wang, S. Mei, G. Xing, *Energy Environ. Mater.* **2022**, *5*, 1317.
[39] N. K. Tailor, S. K. Saini, P. Yadav, M. Kumar, S. Satapathi, *J. Phys. Chem. Lett.* **2023**, *14*, 730.
[40] N. K. Tailor, N. Parikh, P. Yadav, S. Satapathi, *J. Phys. Chem. C* **2022**, *126*, 10199.
[41] L. Zhang, Y. Xu, P. Niu, M. Lyu, H. Lu, J. Zhu, *J. Phys. D: Appl. Phys.* **2023**, *56*, 075501.
[42] M. S. Shadabroo, H. Abdizadeh, M. R. Golobostanfard, *ACS Appl. Energy Mater.* **2021**, *4*, 6797.
[43] N. Daem, J. Dewalque, F. Lang, A. Maho, G. Spronck, C. Henrist, P. Colson, S. D. Stranks, R. Cloots, *Sol. RRL* **2021**, *5*, 2100422.
[44] X. Yang, Y. Chen, P. Liu, H. Xiang, W. Wang, R. Ran, W. Zhou, Z. Shao, *Adv. Funct. Mater.* **2020**, *30*, 2001557.
[45] P. Fan, H. Peng, Z. Zheng, Z. Chen, S. Tan, X. Chen, Y.-D. Luo, Z.-H. Su, J.-T. Luo, G.-X. Liang, *Nanomaterials* **2019**, *9*, 1760.
[46] M. T. Sirtl, R. Hooijer, M. Armer, F. G. Ebadi, M. Mohammadi, C. Maheu, A. Weis, B. T. van Gorkom, S. Häringer, R. A. J. Janssen, T. Mayer, V. Dyakonov, W. Tress, T. Bein, *Adv. Energy Mater.* **2022**, *12*, 2103215.
[47] A. Yang, L. Zhang, Y. Xu, Q. Wang, M. Lyu, H. Lu, J. Zhu, *J. Mater. Sci. Mater. Electron.* **2022**, *33*, 18758.
[48] H. Peng, P. Fan, Z. Zheng, S. Chen, G. Liang, *ACS Appl. Energy Mater.* **2022**, *5*, 15058.
[49] M. Pantaler, K. T. Cho, V. I. E. Queloz, I. García Benito, C. Fettkenhauer, I. Anusca, M. K. Nazeeruddin, D. C. Lupascu, G. Grancini, *ACS Energy Lett.* **2018**, *3*, 1781.
[50] M. T. Sirtl, F. Ebadi, B. T. van Gorkom, P. Ganswindt, R. A. J. Janssen, T. Bein, W. Tress, *Adv. Opt. Mater.* **2021**, *9*, 23.
[51] P. Chen, Y. Bai, S. Wang, M. Lyu, J. H. Yun, L. Wang, *Adv. Funct. Mater.* **2018**, *28*, 1.
[52] T. Zhang, M. Long, M. Qin, X. Lu, S. Chen, F. Xie, L. Gong, J. Chen, M. Chu, Q. Miao, Z. Chen, W. Xu, P. Liu, W. Xie, J. Bin Xu, *Joule* **2018**, *2*, 2706.
[53] Y. Hua, Y. Zhou, D. Hong, S. Wan, X. Hu, D. Xie, Y. Tian, *J. Phys. Chem. Lett.* **2019**, *10*, 7025.
[54] J. A. Sichert, Y. Tong, N. Mutz, M. Vollmer, S. Fischer, K. Z. Milowska, R. García Cortadella, B. Nickel, C. Cardenas-Daw, J. K. Stolarczyk, A. S. Urban, J. Feldmann, *Nano Lett.* **2015**, *15*, 6521.
[55] C. Ortiz-Cervantes, P. Carmona-Monroy, D. Solis-Ibarra, *ChemSusChem* **2019**, *12*, 1560.
[56] P. C. Huang, S. K. Huang, T. C. Lai, M. C. Shih, H. C. Hsu, C. H. Chen, C. C. Lin, C. H. Chiang, C. Y. Lin, K. Tsukagoshi, C. W. Chen, Y. P. Chiu, S. F. Tsay, Y. C. Wang, *Nano Energy* **2021**, *89*, 106362.
[57] B. A. Connor, L. Leppert, M. D. Smith, J. B. Neaton, H. I. Karunadasa, *J. Am. Chem. Soc.* **2018**, *140*, 5235.
[58] F. Schmitz, J. Horn, N. Dengo, A. E. Sedykh, J. Becker, E. Maiworm, P. Bélteky, Á. Kukovecz, S. Gross, F. Lamberti, K. Müller-Buschbaum, D. Schlettwein, D. Meggiolaro, M. Righetto, T. Gatti, *Chem. Mater.* **2021**, *33*, 4688.
[59] F. Schmitz, R. Neisius, J. Horn, J. Sann, D. Schlettwein, M. Gerhard, T. Gatti, *Nanotechnology* **2022**, *33*, 215706.
[60] R. Hooijer, A. Weis, A. Biewald, M. T. Sirtl, J. Malburg, R. Holfeuer, S. Thamm, A. A. Y. Amin, M. Righetto, A. Hartschuh, L. M. Herz, T. Bein, *Adv. Opt. Mater.* **2022**, *10*, 2200354.
[61] W. Sun, J. Zou, X. Wang, S. Wang, Y. Du, F. Cao, L. Zhang, J. Wu, P. Gao, *Nanoscale* **2021**, *13*, 14915.
[62] W. Shi, H. Ye, *J. Phys. Chem. Lett.* **2021**, *12*, 4052.

[63] Q. Zhou, L. Liang, J. Hu, B. Cao, L. Yang, T. Wu, X. Li, B. Zhang, P. Gao, *Adv. Energy Mater.* **2019**, *9*, 1.
[64] X. Wang, Y. Zhao, B. Li, X. Han, Z. Jin, Y. Wang, Q. Zhang, Y. Rui, *ACS Appl. Mater. Interfaces* **2022**, *14*, 22879.
[65] P. Kajal, B. Verma, S. G. R. Vadaga, S. Powar, *Glob. Chall.* **2022**, *6*, 2100070.
[66] N. L. Chang, A. W. Yi Ho-Baillie, P. A. Basore, T. L. Young, R. Evans, R. J. Egan, *Prog. Photovolt. Res. Appl.* **2017**, *25*, 390.
[67] M. Zhai, C. Chen, M. Cheng, *Sol. Energy* **2023**, *253*, 563.
[68] V. Pecunia, L. G. Occhipinti, R. L. Z. Hoye, *Adv. Energy Mater.* **2021**, *11*, 2100698.
[69] A. Schmitz, L. Leander Schaberg, S. Sirotinskaya, M. Pantaler, D. C. Lupascu, N. Benson, G. Bacher, *ACS Energy Lett.* **2020**, *5*, 559.
[70] M. H. Jung, *J. Mater. Chem. A* **2019**, *7*, 14689.
[71] T. L. Leung, I. Ahmad, A. A. Syed, A. M. C. Ng, J. Popović, A. B. Djurišić, *Commun. Mater.* **2022**, *3*, 1.
[72] E. S. Vasileiadou, B. Wang, I. Spanopoulos, I. Hadar, A. Navrotsky, M. G. Kanatzidis, *J. Am. Chem. Soc.* **2021**, *143*, 2523.
[73] H. Xu, G. Liu, X. Xu, S. Xu, L. Zhang, X. Chen, H. Zheng, X. Pan, *Sol. RRL* **2020**, *4*, 1.
[74] T. M. Koh, V. Shanmugam, X. Guo, S. S. Lim, O. Filonik, E. M. Herzig, P. Müller-Buschbaum, V. Swamy, S. T. Chien, S. G. Mhaisalkar, N. Mathews, *J. Mater. Chem. A* **2018**, *6*, 2122.
[75] C. Li, N. Zhang, P. Gao, *Mater. Chem. Front.* **2023**, *7*, 3797.
[76] Y. Yin, W. Tian, J. Leng, J. Bian, S. Jin, *J. Phys. Chem. Lett.* **2020**, *11*, 6956.
[77] F. Schmitz, N. Lago, L. Fagiolari, J. Burkhart, A. Cester, A. Polo, M. Prato, G. Meneghesso, S. Gross, F. Bella, F. Lamberti, T. Gatti, *Chem. Sustain. Energy Mater.* **2022**, *15*, e202201590.
[78] Y. Yao, B. Kou, Y. Peng, Z. Wu, L. Li, S. Wang, X. Zhang, X. Liu, J. Luo, *Chem. Commun.* **2020**, *56*, 3206.
[79] D. Liu, C. M. Perez, A. S. Vasenko, O. V. Prezhdo, *J. Phys. Chem. Lett.* **2022**, *13*, 3645.
[80] Z. He, Q. Tang, X. Liu, X. Yan, K. Li, D. Yue, *Energy Fuels* **2021**, *35*, 15005.
[81] Z. Xiao, W. Meng, J. Wang, Y. Yan, *Chem. Sustain. Energy Mater.* **2016**, *9*, 2628.
[82] T. Li, X. Zhao, D. Yang, M. Du, L. Zhang, *Phys. Rev. Appl.* **2018**, *10*, 041001.
[83] Y. She, H. Zhufeng, O. V. Prezhdo, W. Li, *J. Phys. Chem. Lett.* **2021**, *12*, 10581.
[84] Z. Zhang, Q. Sun, Y. Lu, F. Lu, X. Mu, S. Wei, M. Sui, *Nat. Commun.* **2022**, *13*, 1.
[85] N. Fairley, V. Fernandez, M. Richard-Plouet, C. Guillot-Deudon, J. Walton, E. Smith, D. Flahaut, M. Greiner, M. Biesinger, S. Tougaard, D. Morgan, J. Baltrusaitis, *Appl. Surf. Sci. Adv.* **2021**, *5*, 100112.
[86] J. P. Perdew, K. Burke, M. Ernzerhof, *Phys. Rev. Lett.* **1996**, *77*, 3865.
[87] G. Kresse, J. Hafner, *Phys. Rev. B* **1993**, *47*, 558.
[88] H. J. Monkhorst, J. D. Pack, *Phys. Rev. B* **1976**, *13*, 5188.

WILEY-VCH

Supporting Information

Improved hole extraction and band alignment *via* interface modification in HTM-free Ag/Bi double perovskite solar cells

Fabian Schmitz, *Ribhu Bhatia*, *Julian Burkhart*, *Pascal Schweitzer*, *Marco Allione*, *Jaime Gallego*, *Piotr Piotrowski*, *Jakub Cajzl*, *Piotr Paszke*, *Gour Mohan Das*, *Dorota A. Pawlak*, *Federico Bella*, *Derck Schlettwein*, *Francesco Lamberti*,* *Simone Meloni*,* *Teresa Gatti**

Table of contents

Characterization

To observe the sample layers cross section by means of transmission electron microscopy, we made use of a thin portion of the sample extracted and thinned using focused ion beam (FIB). To this purpose, we used a dual beam SEM-FIB machine combining a scanning electron microscope column with a Xe ion Plasma FIB column (Solaris X, Tescan, Brno, Czech Republic). Before starting the cutting process, a protective layer of material was deposited on the area of interest. The protecting material used was an alloy of Pt particles in an organic matrix, obtained by local decomposition of a Pt-containing precursor gas (Methyl cyclopentadienyl trimethyl platinum) locally injected in the machine vacuum chamber by a Gas injection nozzle placed close to the sample area of interest. To protect the sample upper layers from ion damage, we firstly deposited a thin (approx. 200 nm) layer of material by electron beam induced deposition (electron energy 2 keV, beam current around 3.3 nA), followed by a second thicker (about 2 mm) ion beam induced deposition (ion energy 10 keV, beam current of 250 pA). After this step, the small portion of sample under investigation was isolated by removing surrounding material using plasma FIB at 30 keV and different decreasing beam currents. The small Lamella-shaped portion of the sample (about 1-2 mm large, 15-18 mm long and reaching a depth of 5-8 mm in the device substrate) could be then detached from the substrate and, by means of a nanomanipulator, transferred to a standard TEM sample support grid. Here we performed final thinning of a small window of the lamella (about 5 mm large) until reaching good electron beam transparency for an observing electron beam of 5 keV (indicating a thickness usually well below 100 nm). We then performed a very gentle final polishing of both sides of the lamella using Xe ions accelerated by a lower 10 kV potential and with a current of only around 20 pA, in order to attenuate the thickness of the amorphized layer created by the surface damages caused by the impact of higher energy ions.

After the preparation of the thin sample cross-section, we observed a partial de-layering of the sample itself, creating a gap between the top and bottom layers of the device, splitting apart one of them.

We attribute this fact to an artifact of lamella preparation, being likely due to the stress locally induced by the deposition of the relatively thick Pt-based protective material and it does not seem to be present in the rest of the sample. Nevertheless, it seems not possible to extract a sample cross section without the addition of a protective layer, as ion beams and sample re-deposition would inevitably alter and damage the exposed portion of the device.

The samples thinned in this way could then be inserted into a TEM machine (Talos F200X, Thermo Scientific, Eindhoven, Netherland). This microscope can be used in standard parallel beam illumination configuration or in convergent beam illumination mode, using it as Scanning Transmission Electron Microscope (STEM). All analysis, in both modes, were performed using an electron acceleration voltage of 200 kV. The microscope is furthermore equipped with a 4 quadrant EDS detector which was used in combination with STEM configuration to obtain sample elemental maps, which were acquired, analyzed and plotted using the microscope embedded acquisition software (Velox, v. 3.6, Thermo Scientific, Eindhoven, Netherland).

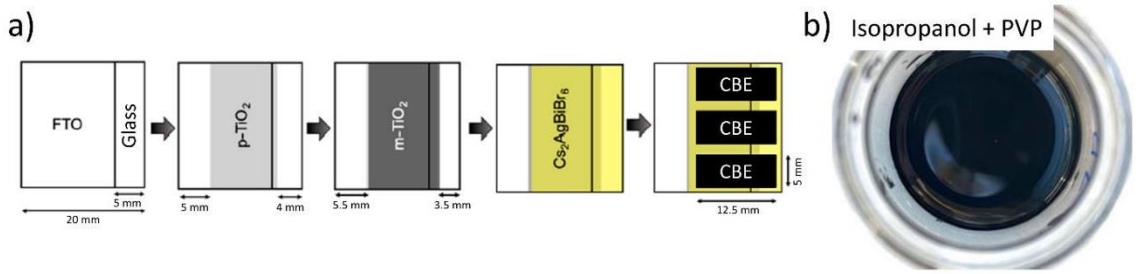

Figure S1. a) Patterning of solar cells. b) Carbon paste to fabricate CBEs through screen-printing.

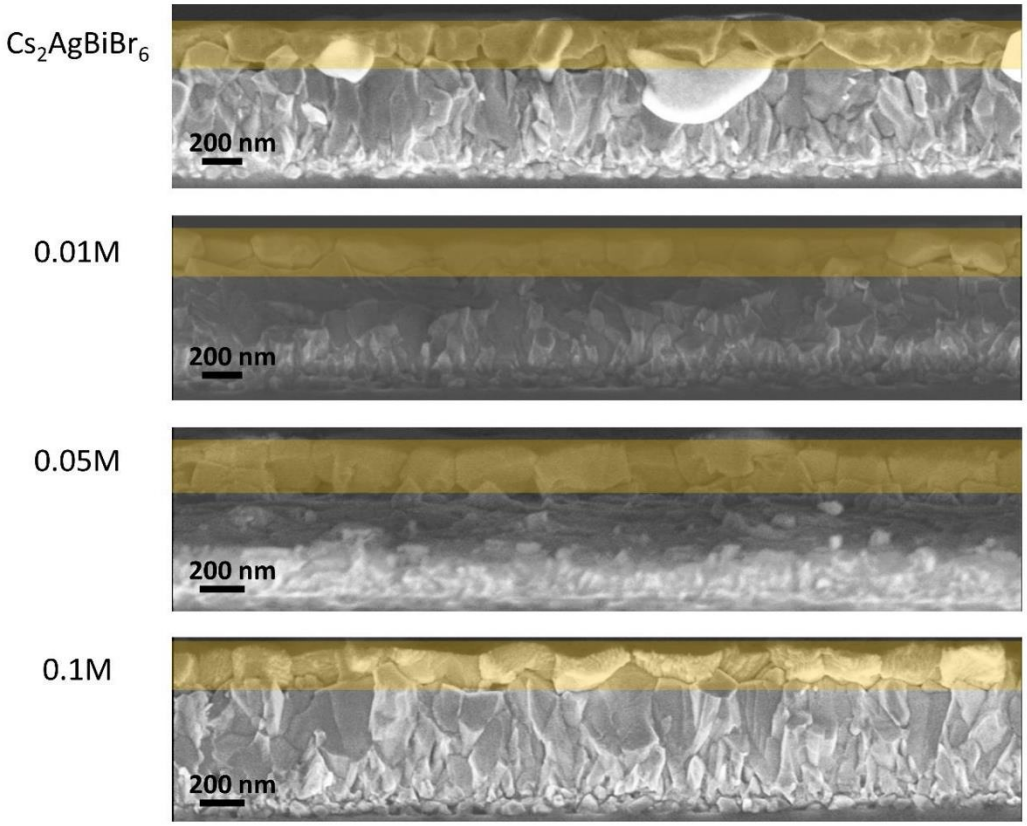

Figure S2. SEM cross-sections of $Cs_2AgBiBr_6$ and modified 2D/3D thin films. The perovskite layers are highlighted in yellow.

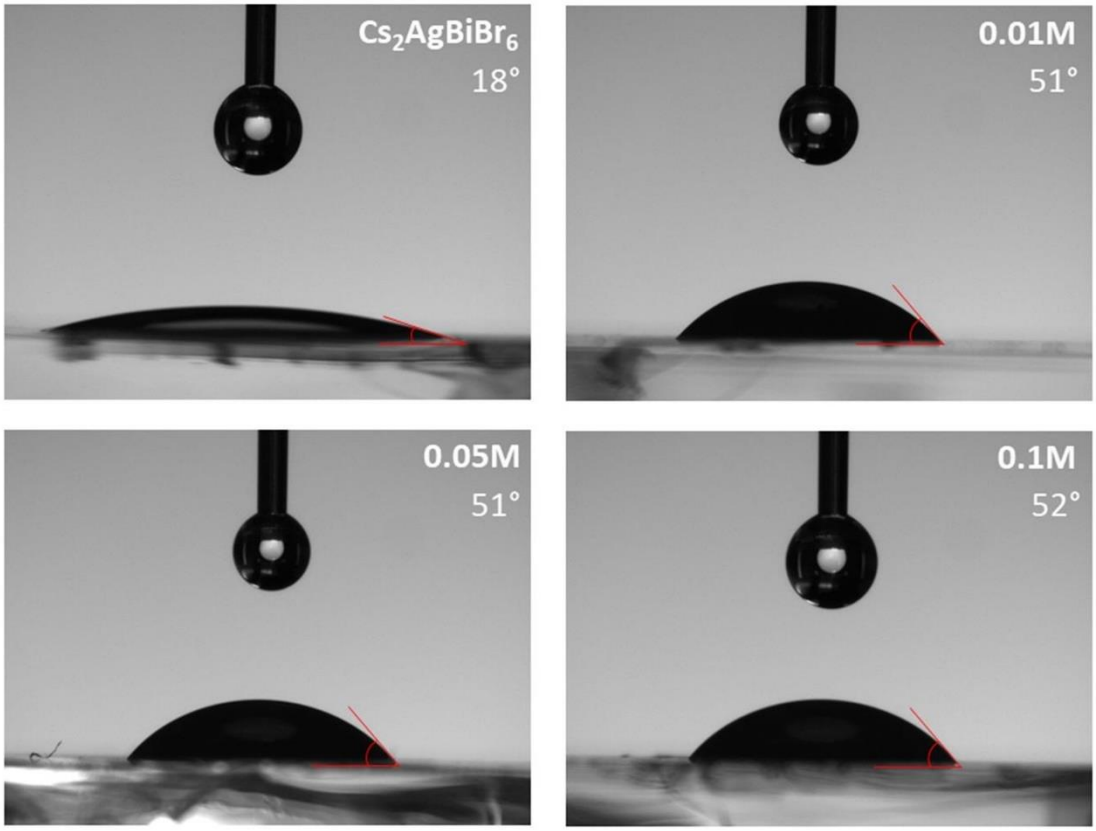

Figure S3. Contact-angle measurements.

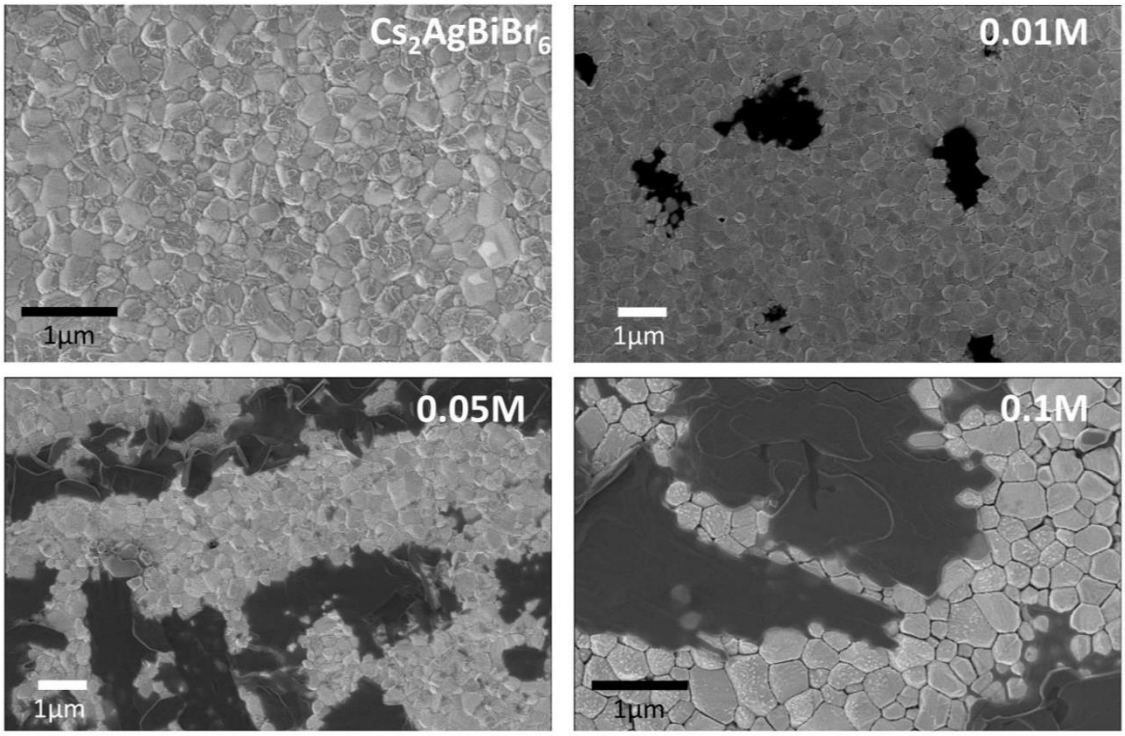

Figure S4. Overview of SEM images at high magnification on pristine and modified thin films.

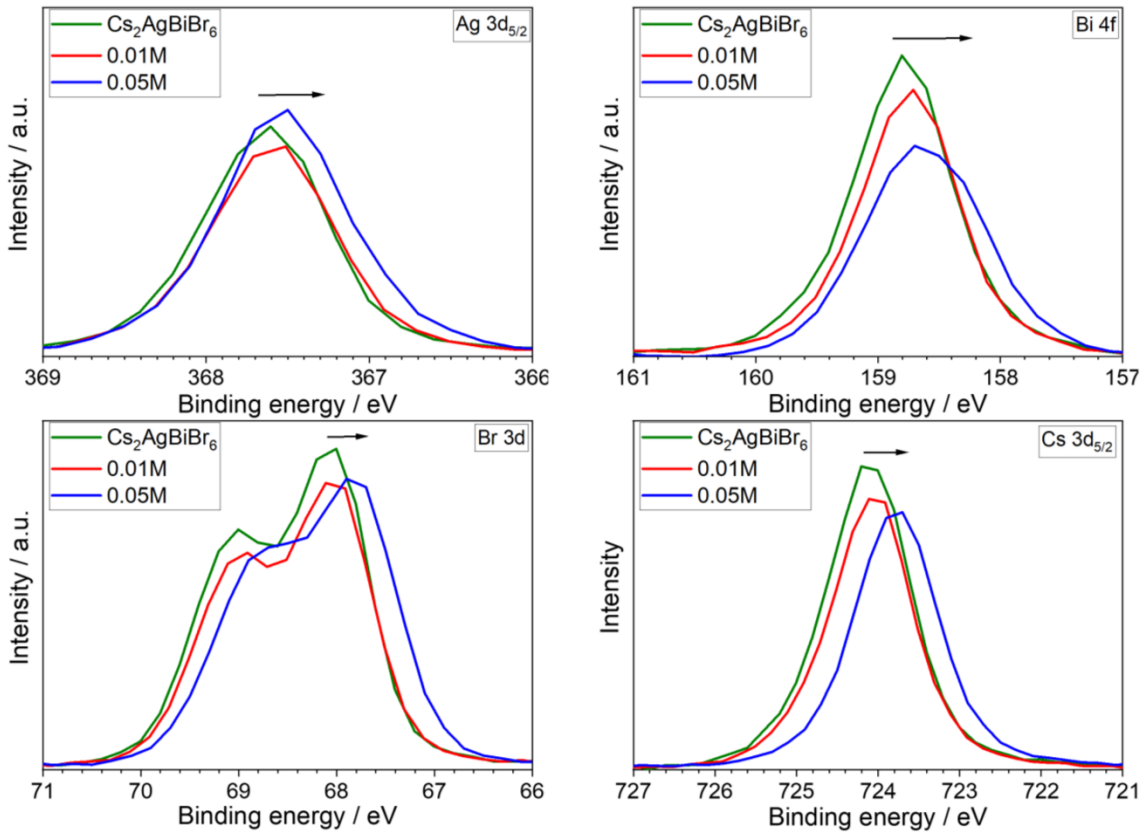

Figure S5. Core level energies from XPS.

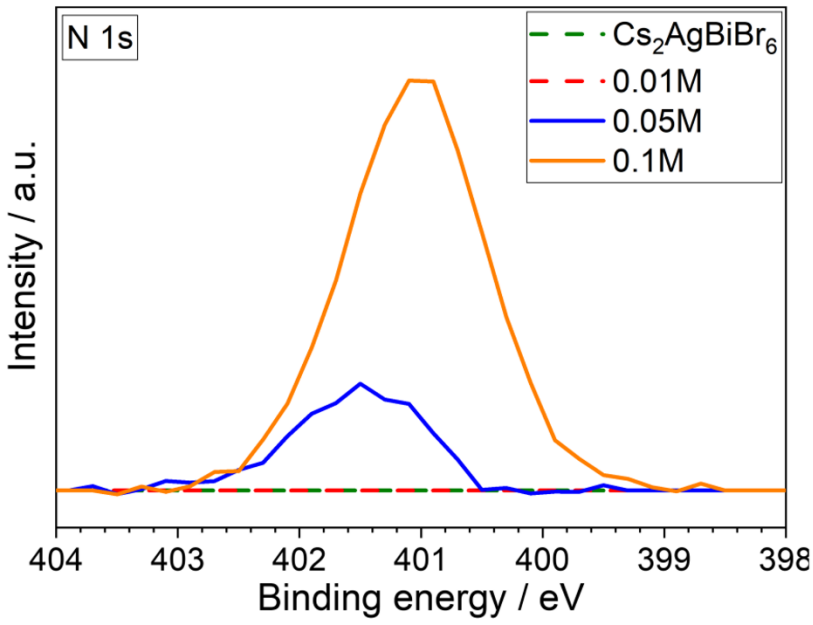

Figure S6. Nitrogen core level energies from XPS.

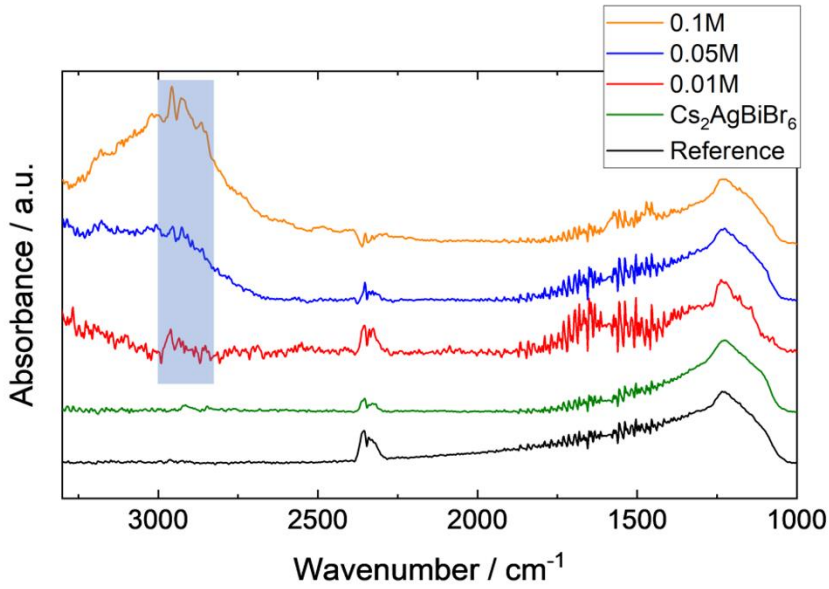

Figure S7. FTIR spectra of thin films of $Cs_2AgBiBr_6$ and the 2D/3D modified samples, as well as of a reference substrate. The specific region for C-H stretching vibrations is marked in blue.

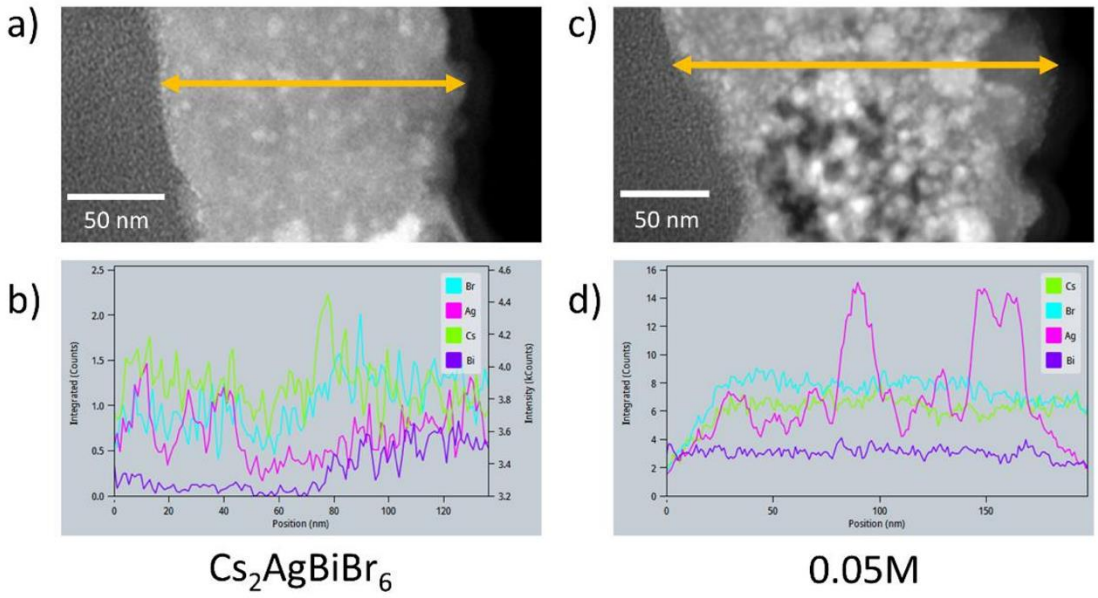

Figure S8. a,c) HRTEM images and b,d) EDX profiles of lamellae of the reference $Cs_2AgBiBr_6$ thin film and the 0.05M surface-modified one.). For the EDX of 0.05M, several agglomerations of Ag are observable. These agglomerations emerged during the measurements. The initial Ag distribution possessed a homogeneity like the other detected elements but with progressing measurement duration the agglomerations intensified, due to Ag(I) *in-situ* reduction to metallic Ag particles caused by the electron beam of the HRTEM.

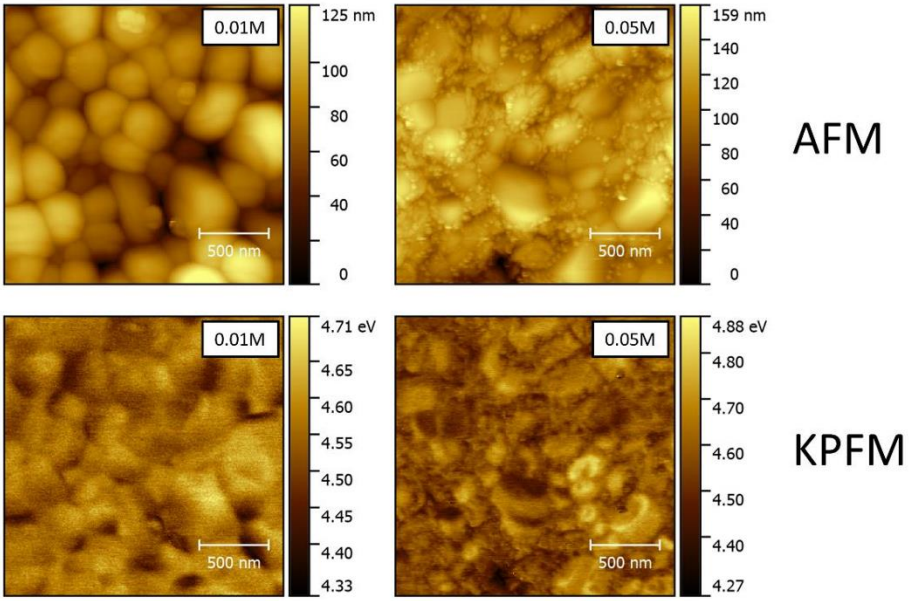

Figure S9. AFM and KPFM measurements of 0.01M, 0.05M, and 0.1M.

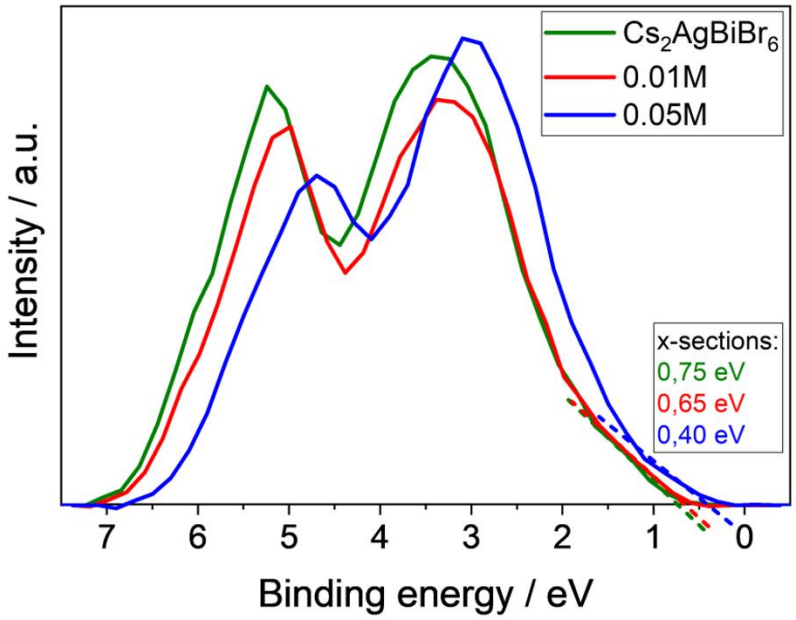

Figure S10. Zoom into the XPS valence shell spectra of $Cs_2AgBiBr_6$, 0.01M, and 0.05M.

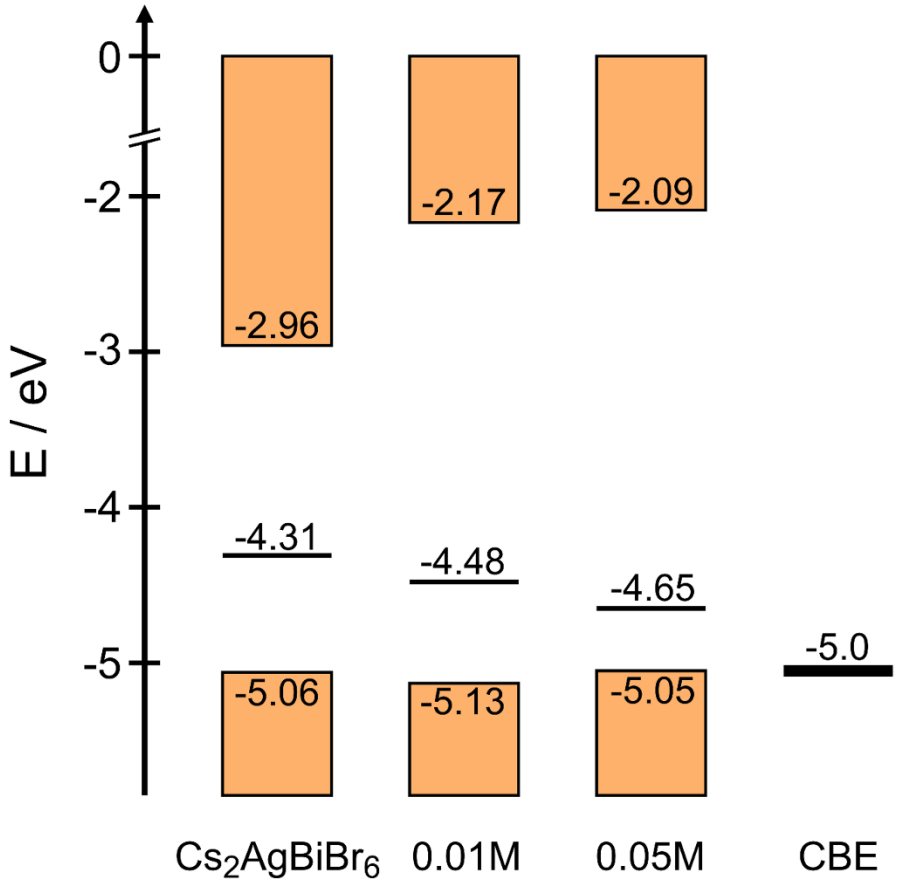

Figure S11. Band diagrams of $Cs_2AgBiBr_6$, 0.01M, and 0.05M. Energies are calculated against vacuum energy. CBE Fermi level was averaged from reported values.[1–5]

Table S1. Parameters, obtained from fitting the triple-exponential decay function $I(t) = \sum A_i \exp(-t/\tau_i)$ (i = 1, 2, 3) to the TRPL data.

	A_1	τ_1 / ns	A_2	τ_2 / ns	A_3	τ_3 / ns
$Cs_2AgBiBr_6$	64.85 (±2.25)	1 (±1)	0.466 (±0.008)	4 (±1)	0.0623 (±0.001)	40 (±1)
0.01M	3.17 (±0.04)	2 (±1)	0.388 (±0.005)	9 (±1)	0.100 (±0.001)	59 (±1)
0.05M	0.94 (±0.03)	4 (±1)	0.446 (±0.007)	36 (±1)	0.173 (±0.006)	182 (±5)
0.1M	1.85 (±0.15)	3 (±1)	0.351 (±0.018)	28 (±3)	0.117 (±0.013)	165 (±13)

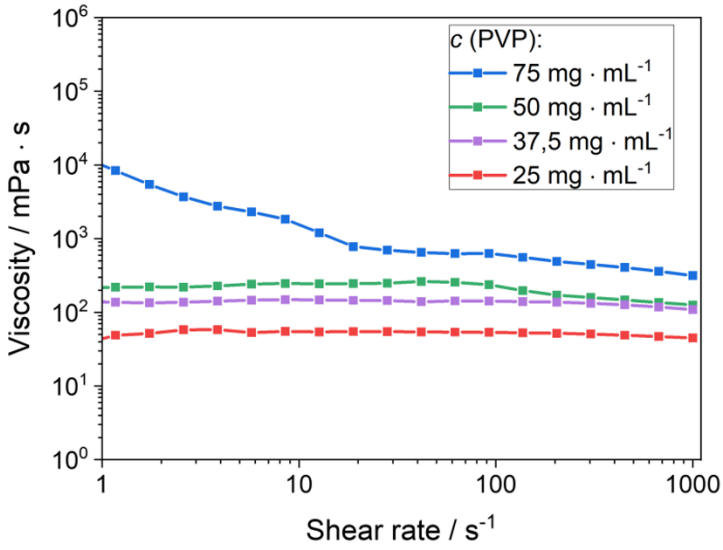

Figure S12. Viscosity depending on PVP concentration in isopropanol.

Table S2. Parameters from ECM fitting. The CPE impedance $\tilde{Z}$ can be calculated using the formula $\tilde{Z}(\omega) = \frac{1}{(j\omega)^{\alpha} C_{\alpha}}$.[6] Values in parentheses are the fit errors.

	R_S / Ω	R_1 / Ω	$C_{\alpha,1}$ / S·s$^{\alpha 1}$	α1	R_2 / Ω	$C_{\alpha,2}$ / S·s$^{\alpha 2}$	α2
$Cs_2AgBiBr_6$	30 (±4)	1536 (±14)	$1.7(\pm0.1)\cdot10^{-6}$	0.59 (±0.01)	367 (±23)	$1.8(\pm0.2)\cdot10^{-4}$	0.76 (±0.04)
0.01M	32 (±6)	1284 (±57)	$7.1(\pm0.5)\cdot10^{-7}$	0.75 (±0.01)	610 (±72)	$2.2(\pm0.3)\cdot10^{-4}$	0.39 (±0.02)
0.05M	75 (±2)	410 (±41)	$2.2(\pm0.3)\cdot10^{-6}$	0.99 (±0.02)	1760 (±36)	$6.3(\pm0.6)\cdot10^{-6}$	0.54 (±0.01)

Table S3. Geometry-optimized lattice parameters.

Lattice constant (Ang)	hs1	hs2	hs3	hs4
a	11.271	11.271	11.271	11.271
b	11.271	11.271	11.271	11.271
c	73.390	93.358	113.326	153.262

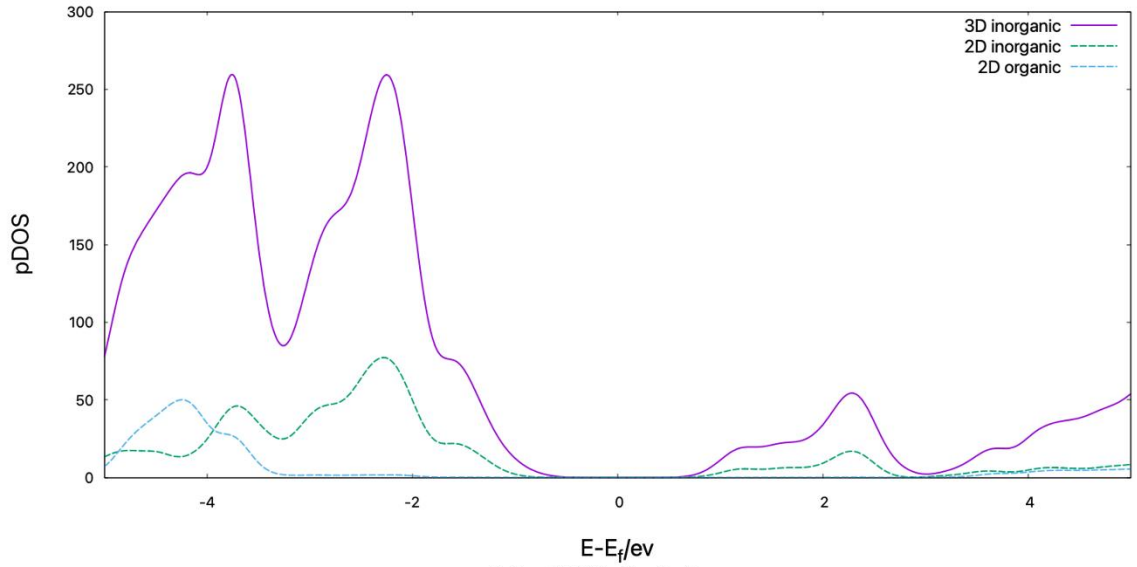

(a) pDOS for hs2

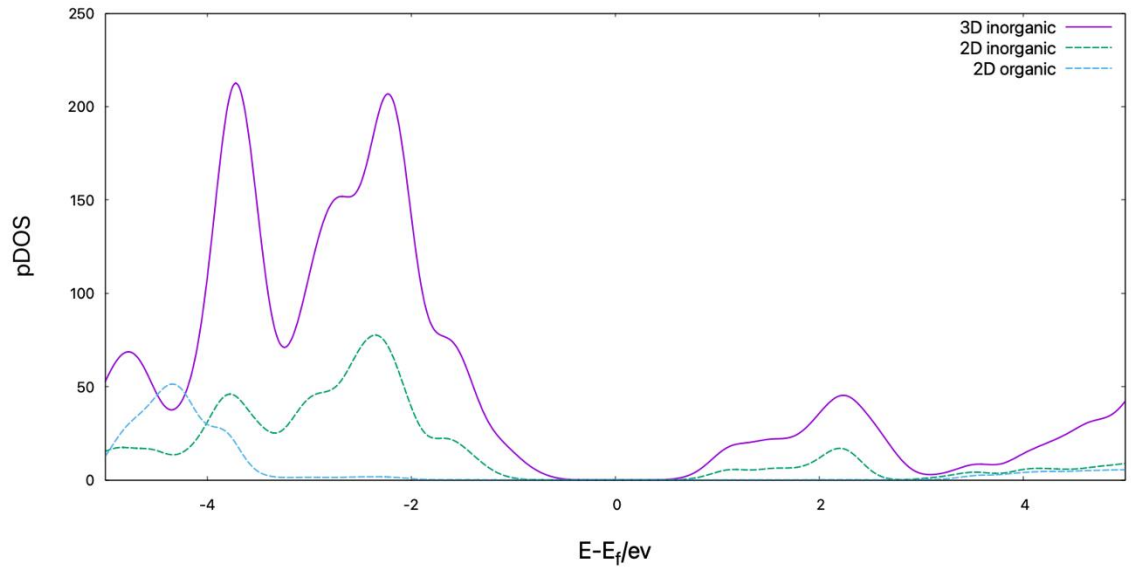

(b) pDOS for hs3

Figure S13. pDOS calculated for 3D/2D heterostructures a) hs2 and b) hs3.

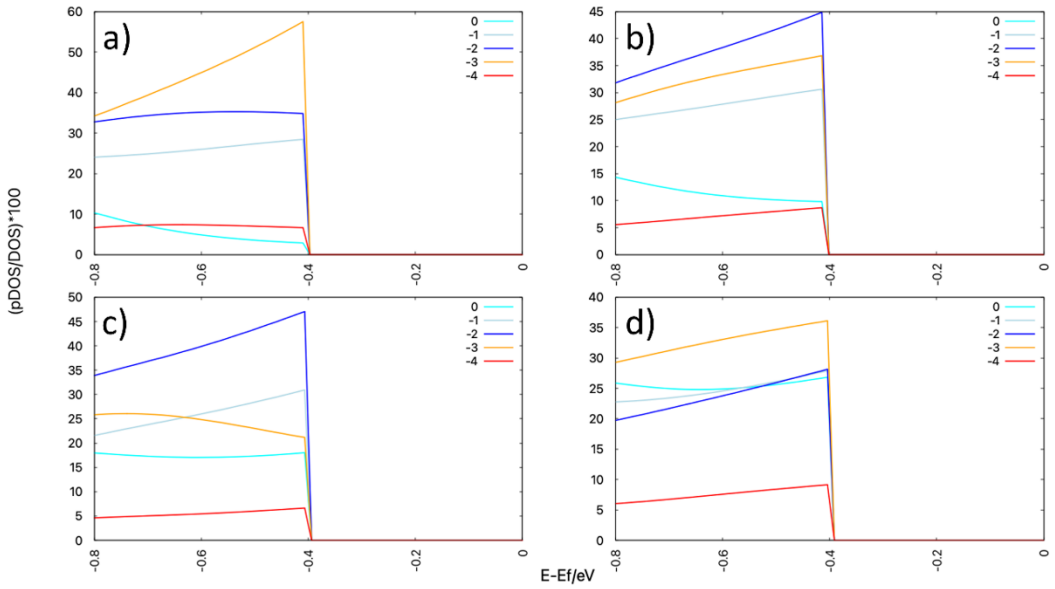

Figure S14. a-d) Contribution of npDOS of each sublayer to the VBM for hs1, hs2, hs3 and hs5 respectively

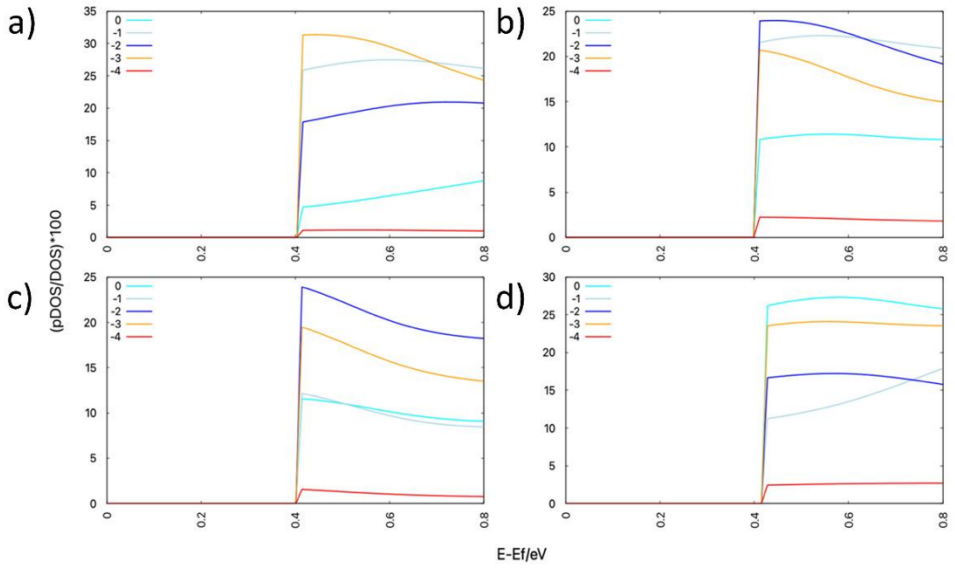

Figure S15. a-d) Contribution of npDOS of each sublayer to the CBM for hs1, hs2, hs3 and hs5 respectively.

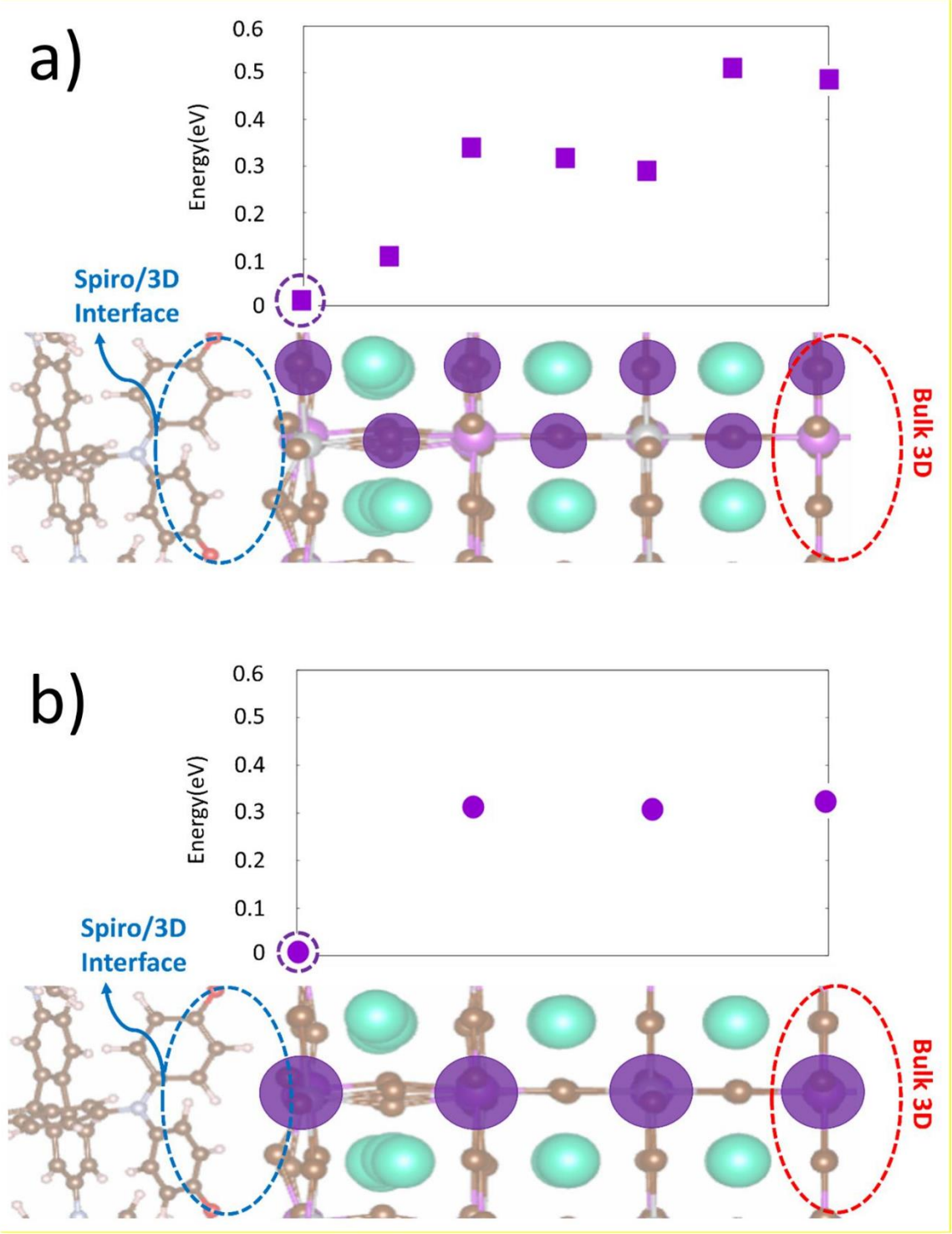

Figure S16. a) Defects energy vs position of a) bromide vacancy ($V_{Br}^{\bullet}$); b) Antisite (Ag_{Bi}'') in the case of 3D/Spiro-OMeTAD interface system. Dashed circles around symbols denote the state corresponding to the minimum energy defect position. Energies are arbitrarily shifted so that the value in the surface position is zero. In each panel is reported a cartoon illustrating the

portion of the 3D/2D computational sample illustrating the position of the corresponding defect.

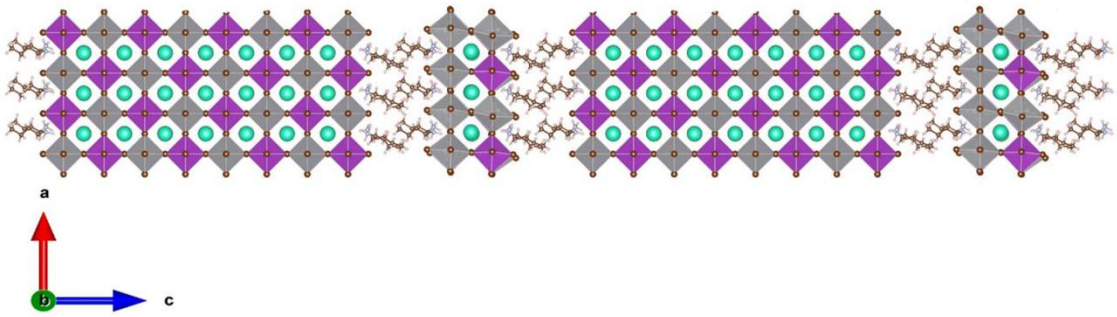

Figure S17. Symmetric 3D/2D interface with no induced dipole moment.

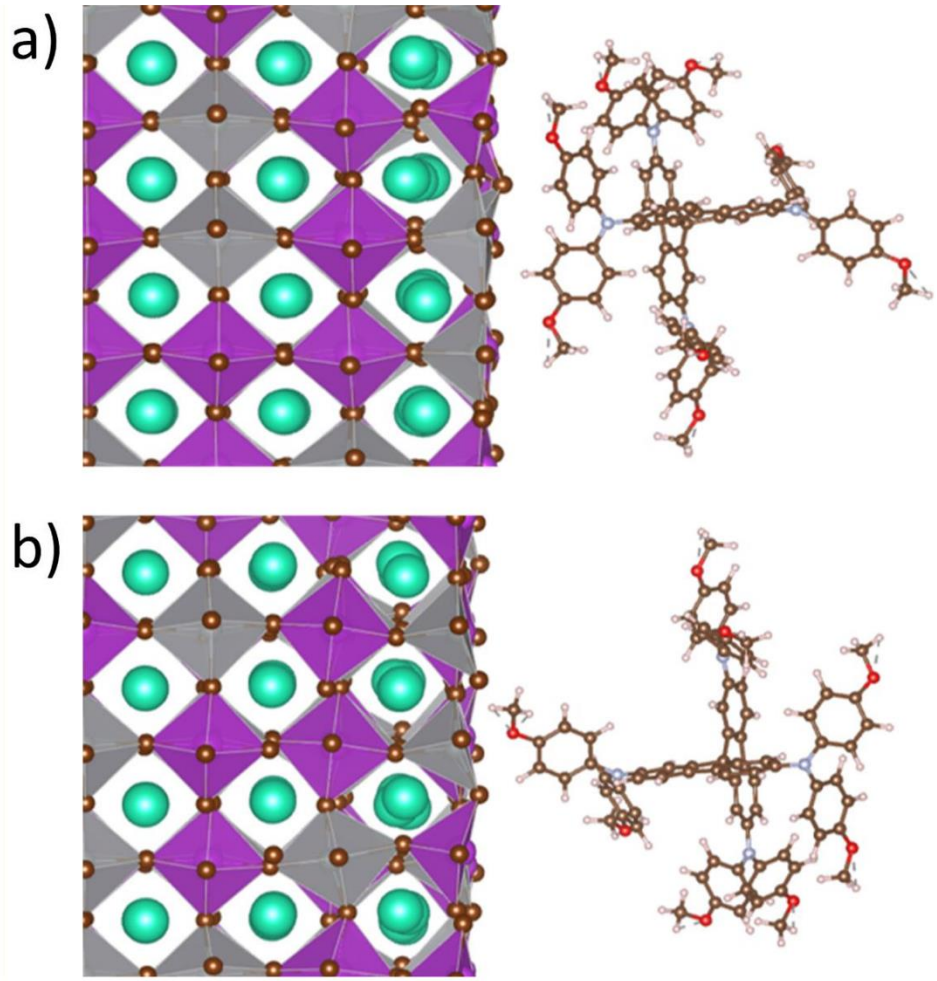

Figure S18. 3D/Spiro-OMeTAD samples. The panel a) and b) show the binding modes 1 and 2, respectively.

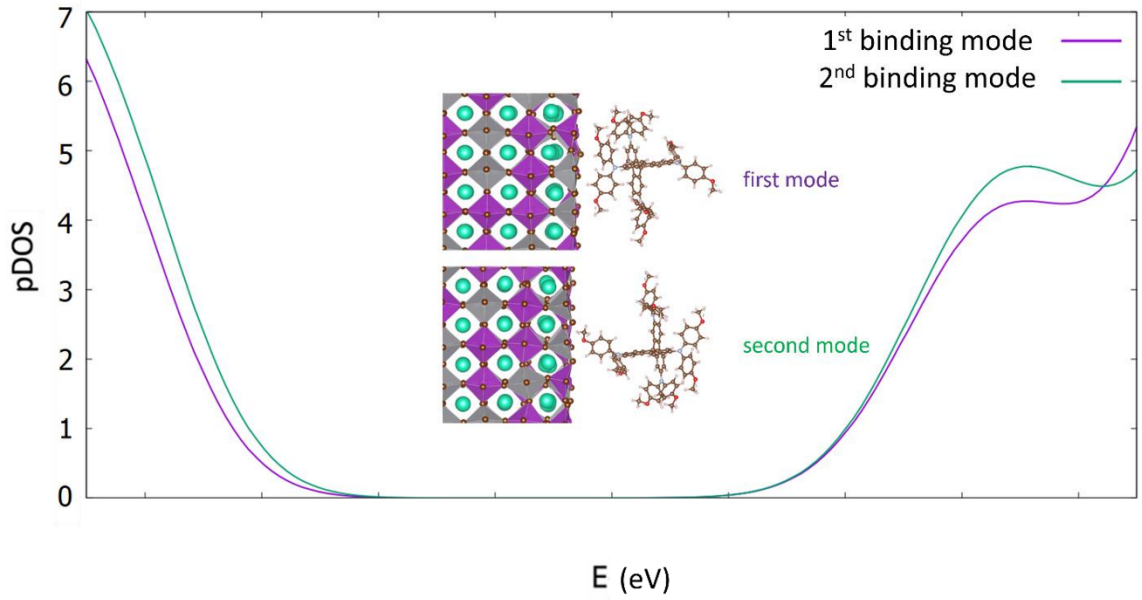

Figure S19. Calculated pDOS of the 3D/Spiro-OMeTAD for the two binding modes.

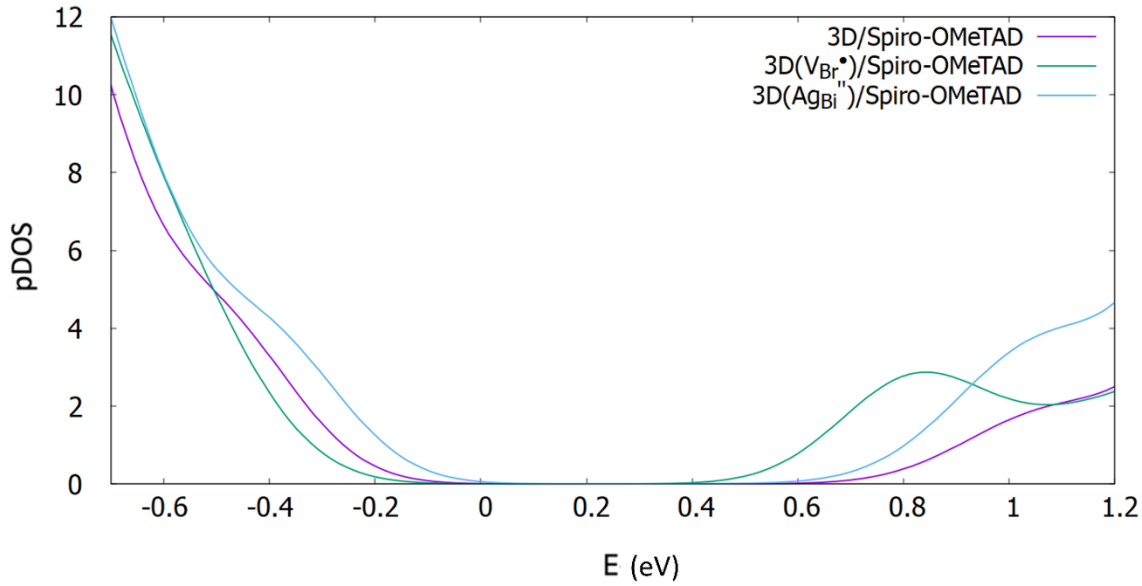

Figure S20. Calculated pDOS of the Spiro-OMeTAD/3D interface for pristine and defected systems respectively.

References

[1] Z. Ku, Y. Rong, M. Xu, T. Liu, H. Han, *Sci. Rep.* **2013**, *3*, DOI 10.1038/srep03132.
[2] M. Aftabuzzaman, C. Lu, H. K. Kim, *Nanoscale* **2020**, *12*, 17590.

[3] C. Zhou, S. Lin, *Sol. RRL* **2020**, *4*, 1.
[4] M. F. Don, P. Ekanayake, J. R. Jennings, H. Nakajima, C. M. Lim, *ACS Omega* **2022**, *7*, 22830.
[5] D. Bogachuk, B. Yang, J. Suo, D. Martineau, A. Verma, S. Narbey, M. Anaya, K. Frohna, T. Doherty, D. Müller, J. P. Herterich, S. Zouhair, A. Hagfeldt, S. D. Stranks, U. Würfel, A. Hinsch, L. Wagner, *Adv. Energy Mater.* **2022**, *12*, 1.
[6] S. Holm, T. Holm, Ø. G. Martinsen, *PLoS One* **2021**, *16*, 1.

5 Conclusions & Outlook

In summary, the work of this dissertation can be split into two main sections. First, several options have been established to tune the optical properties of the double perovskite $Cs_2AgBiBr_6$ through doping, through dimensional reduction, and then through the combination of dimensional reduction and halide substitution. Secondly, the topic was the fabrication and analysis of $Cs_2AgBiBr_6$-solar cells. Not only have devices been created that do not pose the toxicity concerns of LHPs, but also have low-cost and easily processable electrodes consisting of carbon black which was won from upcycled industry waste been applied to substitute the organic HTM and metal electrodes (often Spiro-OMeTAD and gold, respectively) of the regular PSC architecture.

Within this dissertation, successful doping of $Cs_2AgBiBr_6$ with the lanthanides europium and ytterbium which resulted in the occurrence of new emissive features has been demonstrated. The underlying mechanism of the newly introduced emission features was investigated and attributed to an effective energy transfer from $Cs_2AgBiBr_6$ towards the dopant for ytterbium and from trap emission for europium. Those differing emissive recombination mechanisms resulted in an additional very strong and weak PL signal, respectively.

Furthermore, $Cs_2AgBiBr_6$ has been dimensionally reduced to 2D monolayered materials by fully substituting cesium with one of four different large organic cations. The resulting materials possessed varying morphologies and emissive properties depending on the cation length, branching, or aromatic character when the materials were deposited as thin films. Thus, this work presents a material-by-design approach for 2D monolayered Ag-Bi double perovskites.

Also, partial bromide substitution with iodide of butylammonium-based 2D Ag-Bi double perovskites has been performed to finely tune the material's characteristic absorption and emission properties. The material has also been reported to suffer from phase segregation when the iodide content is 25% relative to the total halide content or higher.

Concerning PSCs, state-of-the-art research on HTM-free PSCs has been reviewed which mainly – but not exclusively – regards the utilization of back electrodes based on carbon materials like graphite, carbon nanotubes, carbon black, etc, and which substitutes both the HTM and metal electrodes. The topic is divided into the application of low-temperature and high-temperature processed carbon electrodes as well as the discussion of their bottlenecks and strategies to overcome them.

The HTM-free PSC design has been applied on $Cs_2AgBiBr_6$ thin films. To further apply a low-cost device strategy that relies on as few high-boiling point solvents as possible, ultrasonic spray-coating has been applied to deposit carbon electrodes from a carbon black dispersion in isopropanol. Additionally, the

carbon black was won from upcycled industry waste to employ an end-of-waste strategy and, therefore, enable the fabrication of “green”, low-cost, and non-toxic perovskite solar cells.

The successive step has been to further improve the established solar cell architecture, utilizing the application of a 2D/3D surface modification of $Cs_2AgBiBr_6$ thin films. This modification enhances both the perovskite’s selectivity and valence band alignment towards the carbon back electrode, thus boosting the solar cells’ PCE. Additional DFT calculations suggest that the presence of the 2D/3D modification enhances the extraction probability of holes close to the 3D/2D interface and passivates defects close to the perovskite/back electrode, at the same time.

Finally, also the possibilities of applying pnictogen-based perovskite-inspired materials in indoor photovoltaics to power the Internet of Things devices have been reviewed, particularly discussing state-of-the-art research on materials $Cs_2AgBiBr_6$, $Cs_3Sb_2I_{9-x}Cl_x$, and BiOI. To offer a complete overview of the research status, not only reports on fabricated and analyzed indoor photovoltaics have been summarized but also the potential of related research has been discussed, e.g., bandgap engineering to optimize materials for indoor illumination.

Further work on the PSCs prepared within this dissertation should include the assessment of factors that still suppress the devices’ PCEs. The comparison of regular architecture devices with HTM-free PSCs in **publications 5** and **7** revealed that both regular (HTM + gold electrode) and HTM-free PSCs possess similar J_{SC}, V_{OC}, *FF*, and PCE. Therefore, the application of the carbon electrodes does not seem to be the efficiency-hampering bottleneck. Other reports of HTM-free $Cs_2AgBiBr_6$ PSCs demonstrate PCEs of above 1%,[94,96,99] up to 1.78%[97] when a comparable architecture as in **publications 5** and **7** is used. Also, the homogeneity, thickness, and grain size distribution of the used $Cs_2AgBiBr_6$ thin films do almost not deviate from reported thin films[94] or even show fewer pin holes than those.[96,97]

Thus, the focus of further work should fall on the role of the ETM/$Cs_2AgBiBr_6$ interface. Inorganic oxide ETLs (like TiO_2 within this dissertation) have been reported to form deep trap states due to the presence of oxygen vacancies, hydroxyl groups, or contact-induced reconstruction.[261,262] Furthermore, also other ETLs, such as SnO, fullerene (C_{60}), CdS, SnO_2, or phenyl-C_{61}-butyric acid methyl ester (PCBM), have been utilized or suggested in literature to boost the PCE of $Cs_2AgBiBr_6$ PSCs due to their differing band alignment towards the perovskite and the TCO, respectively.[263–265]

Furthermore, the large bandgap of $Cs_2AgBiBr_6$ is well-suited for the application in indoor photovoltaics,[45,46] as discussed in **publication 6**. Thus, the solar cells that have been reported in **publications 5** and **7** should be analyzed under indoor illumination. However, unlike for the testing conditions of solar cells (AM 1.5G),[266,267] there is no protocol for the conditions under which to test indoor photovoltaics. Therefore, it is important to establish a test routine that allows the comparison of those devices with

devices reported in literature which have been tested and varying conditions.[268] The analysis of $Cs_2AgBiBr_6$ photovoltaics under low-intensity, large-bandgap indoor illumination has not been reported, yet, but PCEs of 10% and 20 % have been calculated to be theoretically achievable.[45,46] A test under such conditions and the evaluation of the double perovskite's response will bring new insights into its possible applicability for indoor photovoltaics.

6 Contributions to conferences

SPIE Optics + Photonics 2021

Oral contribution: “Light emission in doped and 2D silver-bismuth double perovskites”

Hybrid & Organic Photovoltaics HOPV 2022

Oran contribution: “High Open-Circuit Voltage $Cs_2AgBiBr_6$ Carbon-Based Perovskite Solar Cells Via Green Processing of Ultrasonic Spray-Coated Carbon Electrodes from Waste Tire Sources”

DPG Frühjahrstagung 2022

Oral contribution: “High Open-Circuit Voltage $Cs_2AgBiBr_6$ Carbon-Based Perovskite Solar Cells Via Green Processing of Ultrasonic Spray-Coated Carbon Electrodes from Waste Tire Sources”

E-MRS Fall Meeting 2023

Oral contribution: “Enhancing Stability and Band Alignment in $Cs_2AgBiBr_6$-based HTM Free Solar Cells by Applying a 2D Surface Modification”

Carbon Club 2023

Oral contribution: “Enhancing Stability and Band Alignment in $Cs_2AgBiBr_6$-based HTM Free Solar Cells by Applying a 2D Surface Modification”

7 Acknowledgments

Firstly, I want to thank Prof. Dr. Teresa Gatti for supervising my project and enabling this dissertation in the first place. Many fruitful discussions about my research, her support in writing all those papers, and the possibilities she offered me to participate in lots of conferences had a large influence on my work as a scientist and on me as a person. Especially, when I compare myself right now with the former me, when I just started the PhD. Although this time was shaken by one crisis after another, especially the cyber attack and the pandemic strongly affecting the everyday work, I hope that I also did a good job as the first PhD student in her work group. Grazie mille!

I also want to thank Prof. Dr. Derck Schlettwein for allowing me to perform a large share of my experiments in his labs. Since it took some time to build up our parts of the lab in the physical chemistry, it was a gigantic help to meanwhile be able to work on my PhD in the labs across the street. Also, his participation in my projects had an invaluable impact on my work. Not many are as lucky as me to get the insights of two experts on their topic this easily and frequently.

Of course, I also want to thank Prof. Dr. Bernd Smarsly who not only enabled me and my colleagues to work in his labs but who also made sure that we were fully included in his working group. Although perovskite solar cells are not his topic, he still frequently offered valuable advice and was, for example, an enormous help to write a beamline application for my project. I also want to thank him for always being available when I had formal questions.

Furthermore, I want to thank Prof. Dr. Michael Dürr for being part of the disputation committee. I'm happy that this worked since he already evaluated my master thesis on a similar topic and it now feels like a nice circle to have this great committee.

All my work and achievements also wouldn't have been possible without my great current and former co-workers, not only in Gießen but all over the world! There are far too many great people that I had the chance to work with to name them all. Still, I want to use this chance to give a special thanks to Sebastian, with whom I shared an office in my first years and who always offered his help when I needed it, especially in the first weeks and months. Also, Jonas, who had already supervised my master thesis, was an invaluable help to get my research started and I want to thank him that I could always ask for advice on the topic of perovskite solar cells and all other matters. I shouldn't forget to thank Raoul for unforgettable lunch break conversations that brightened my mood even on stressful and bad days.

A big "thank you" goes out to all the students that I had the luck to supervise during my work here. I probably learned at least as much as they did by supervising them. Without them, I would not have been

able to achieve as much results of such a great quality in this amount of time and I wish them all the best on their way. Thank you, Gioele, Anna, Aline, Elena, Raphael, Julian, Manuel, Chiara, and Thomas!

Thank you so much, Sebastian, Jonas, Jan, and Dennis, for checking my dissertation before I will finally print it now.

It’s phenomenal, how much support I received from my friends in all phases of doing my PhD, I will never forget this.

The same goes for my family, I cannot imagine achieving this without all of you having my back!

The last, but for me the most important, thanks go to Franziska and her unconditional support, no matter how hard the times are and how busy I am.

8 Literature

(1) Smil, V. *Energy Transitions: Global and National Perspectives*, 2nd ed.; Praeger, 2016.

(2) Energy Institute. *Statistical Review of World Energy*; 2023.

(3) *Population Data Portal*. https://pdp.unfpa.org/.

(4) National Aeronautics and Space Administration. The Balance of Power in the Earth-Sun System. *Natl. Aeronaut. Sp. Adm.* **2005**.

(5) Kojima, A. et al. Organometal Halide Perovskites as Visible-Light Sensitizers for Photovoltaic Cells. *J. Am. Chem. Soc.* **2009**, *131* (17), 6050–6051. https://doi.org/10.1021/ja809598r.

(6) Zhao, Y. et al. Inactive (PbI2)2RbCl Stabilizes Perovskite Films for Efficient Solar Cells. *Science (80-.).* **2022**, *377* (6605), 531–534. https://doi.org/10.1126/science.abp8873.

(7) *Best Research-Cell Efficiency Chart*. https://www.nrel.gov/pv/cell-efficiency.html.

(8) Faridi, A. W. et al. Synthesis and Characterization of High-Efficiency Halide Perovskite Nanomaterials for Light-Absorbing Applications. *Ind. Eng. Chem. Res.* **2023**, *62* (11), 4494–4502. https://doi.org/10.1021/acs.iecr.2c00416.

(9) Jiang, Q. et al. Planar-Structure Perovskite Solar Cells with Efficiency beyond 21%. *Adv. Mater.* **2017**, *29* (46), 1–7. https://doi.org/10.1002/adma.201703852.

(10) Prasanna, R. et al. Band Gap Tuning via Lattice Contraction and Octahedral Tilting in Perovskite Materials for Photovoltaics. *J. Am. Chem. Soc.* **2017**, *139* (32), 11117–11124. https://doi.org/10.1021/jacs.7b04981.

(11) Kulkarni, S. A. et al. Band-Gap Tuning of Lead Halide Perovskites Using a Sequential Deposition Process. *J. Mater. Chem. A* **2014**, *2* (24), 9221–9225. https://doi.org/10.1039/c4ta00435c.

(12) Guo, J. et al. Ultralong Carrier Lifetime Exceeding 20 Ms in Lead Halide Perovskite Film Enable Efficient Solar Cells. *Adv. Mater.* **2023**, *35* (28), 1–9. https://doi.org/10.1002/adma.202212126.

(13) Li, B. et al. PbCl2-Tuned Inorganic Cubic CsPbBr3(Cl) Perovskite Solar Cells with Enhanced Electron Lifetime, Diffusion Length and Photovoltaic Performance. *J. Power Sources* **2017**, *360*, 11–20. https://doi.org/10.1016/j.jpowsour.2017.05.050.

(14) Oga, H. et al. Improved Understanding of the Electronic and Energetic Landscapes of Perovskite Solar Cells: High Local Charge Carrier Mobility, Reduced Recombination, and Extremely Shallow Traps. *J. Am. Chem. Soc.* **2014**, *136* (39), 13818–13825. https://doi.org/10.1021/ja506936f.

(15) Yin, W. J. et al. Unusual Defect Physics in CH3NH3PbI3 Perovskite Solar Cell Absorber. *Appl. Phys. Lett.* **2014**, *104* (6). https://doi.org/10.1063/1.4864778.

(16) Ma, S. et al. Development of Encapsulation Strategies towards the Commercialization of Perovskite Solar Cells. *Energy Environ. Sci.* **2022**, *15* (1), 13–55. https://doi.org/10.1039/d1ee02882k.

(17) Dong, Q. et al. Encapsulation of Perovskite Solar Cells for High Humidity Conditions. *ChemSusChem* **2016**, *9* (18), 2597–2603. https://doi.org/10.1002/cssc.201600868.

(18) Zhang, X. et al. Recent Progress of Carbon-Based Inorganic Perovskite Solar Cells: From Efficiency to Stability. *Adv. Energy Mater.* **2023**, *13* (33), 1–43. https://doi.org/10.1002/aenm.202201320.

(19) Yu, B. Bin et al. Heterogeneous 2D/3D Tin-Halides Perovskite Solar Cells with Certified Conversion Efficiency Breaking 14%. *Adv. Mater.* **2021**, *33* (36), 1–10. https://doi.org/10.1002/adma.202102055.

(20) Zhu, Z. et al. Smooth and Compact FASnI3Films for Lead-Free Perovskite Solar Cells with over 14% Efficiency. *ACS Energy Lett.* **2022**, *7* (6), 2079–2083. https://doi.org/10.1021/acsenergylett.2c00776.

(21) Jiang, X. et al. One-Step Synthesis of SnI2·(DMSO)x Adducts for High-Performance Tin Perovskite Solar Cells. *J. Am. Chem. Soc.* **2021**, *143* (29), 10970–10976. https://doi.org/10.1021/jacs.1c03032.

(22) Slavney, A. H. et al. A Bismuth-Halide Double Perovskite with Long Carrier Recombination Lifetime for Photovoltaic Applications. *J. Am. Chem. Soc.* **2016**, *138* (7), 2138–2141. https://doi.org/10.1021/jacs.5b13294.

(23) Hoye, R. L. Z. et al. Fundamental Carrier Lifetime Exceeding 1 Ms in Cs2AgBiBr6 Double Perovskite. *Adv. Mater. Interfaces* **2018**, *5* (15), 2–9. https://doi.org/10.1002/admi.201800464.

(24) Li, Z. et al. Understanding the Role of Grain Boundaries on Charge-Carrier and Ion Transport in Cs2AgBiBr6 Thin Films. *Adv. Funct. Mater.* **2021**, *31* (49), 2104981. https://doi.org/10.1002/adfm.202104981.

(25) McClure, E. T. et al. Cs2AgBiX6 (X = Br, Cl): New Visible Light Absorbing, Lead-Free Halide Perovskite Semiconductors. *Chem. Mater.* **2016**, *28* (5), 1348–1354. https://doi.org/10.1021/acs.chemmater.5b04231.

(26) Lei, H. et al. Lead-Free Double Perovskite Cs2AgBiBr6: Fundamentals, Applications, and Perspectives. *Adv. Funct. Mater.* **2021**, *31* (49). https://doi.org/10.1002/adfm.202105898.

(27) Greul, E. et al. Highly Stable, Phase Pure Cs2AgBiBr6 Double Perovskite Thin Films for Optoelectronic Applications. *J. Mater. Chem. A* **2017**, *5* (37), 19972–19981. https://doi.org/10.1039/C7TA06816F.

(28) Igbari, F. et al. Composition Stoichiometry of Cs2AgBiBr6 Films for Highly Efficient Lead-Free Perovskite Solar Cells. *Nano Lett.* **2019**, *19* (3), 2066–2073. https://doi.org/10.1021/acs.nanolett.9b00238.

(29) Du, K. Z. et al. Bandgap Engineering of Lead-Free Double Perovskite Cs2AgBiBr6 through Trivalent Metal Alloying. *Angew. Chemie - Int. Ed.* **2017**, *56* (28), 8158–8162. https://doi.org/10.1002/anie.201703970.

(30) Longo, G. et al. Understanding the Performance-Limiting Factors of Cs2AgBiBr6 Double-Perovskite Solar Cells. *ACS Energy Lett.* **2020**, *5* (7), 2200–2207. https://doi.org/10.1021/acsenergylett.0c01020.

(31) Zhao, D. et al. Overcoming the Limitation of Cs2AgBiBr6 Double Perovskite Solar Cells Through Using Mesoporous TiO2 Electron Extraction Layer. *Energy Environ. Mater.* **2022**, *5* (4), 1317–1322. https://doi.org/10.1002/eem2.12249.

(32) Kentsch, R. et al. Exciton Dynamics and Electron-Phonon Coupling Affect the Photovoltaic Performance of the Cs2AgBiBr6 Double Perovskite. *J. Phys. Chem. C* **2018**, *122* (45), 25940–25947. https://doi.org/10.1021/acs.jpcc.8b09911.

(33) Steele, J. A. et al. Giant Electron–Phonon Coupling and Deep Conduction Band Resonance in Metal Halide Double Perovskite. *ACS Nano* **2018**, *12* (8), 8081–8090. https://doi.org/10.1021/acsnano.8b02936.

(34) Leveillee, J. et al. Phonon-Limited Mobility and Electron-Phonon Coupling in Lead-Free Halide Double Perovskites. *J. Phys. Chem. Lett.* **2021**, *12* (18), 4474–4482. https://doi.org/10.1021/acs.jpclett.1c00841.

(35) Tailor, N. K. et al. Elucidating Polaron Dynamics in Cs2AgBiBr6 Double Perovskite. *J. Phys. Chem. Lett.* **2023**, *14* (3), 730–736. https://doi.org/10.1021/acs.jpclett.2c03541.

(36) Tailor, N. K. et al. Dielectric Relaxation and Polaron Hopping in Cs2AgBiBr6 Halide Double Perovskites. *J. Phys. Chem. C* **2022**, *126* (24), 10199–10208. https://doi.org/10.1021/acs.jpcc.2c02073.

(37) Zhang, Z. et al. Hydrogenated Cs2AgBiBr6 for Significantly Improved Efficiency of Lead-Free Inorganic Double Perovskite Solar Cell. *Nat. Commun.* **2022**, *13* (3397), 1–12. https://doi.org/10.1038/s41467-022-31016-w.

(38) Huang, Y. T. et al. Perovskite-Inspired Materials for Photovoltaics and beyond-from Design to Devices. *Nanotechnology* **2021**, *32* (13), 132004. https://doi.org/10.1088/1361-6528/abcf6d.

(39) Hoye, R. L. Z. Perovskite-Inspired Materials for Energy Applications. *Nanotechnology* **2023**, *34* (41), 410201. https://doi.org/10.1088/1361-6528/ace171.

(40) Rühle, S. Tabulated Values of the Shockley-Queisser Limit for Single Junction Solar Cells. *Sol. Energy* **2016**, *130*, 139–147. https://doi.org/10.1016/j.solener.2016.02.015.

(41) Wu, M. J. et al. Bandgap Engineering Enhances the Performance of Mixed-Cation Perovskite Materials for Indoor Photovoltaic Applications. *Adv. Energy Mater.* **2019**, *9* (37), 1–9. https://doi.org/10.1002/aenm.201901863.

(42) Ho, J. K. W. et al. From 33% to 57%-An Elevated Potential of Efficiency Limit for Indoor Photovoltaics. *J. Mater. Chem. A* **2020**, *8* (4), 1717–1723. https://doi.org/10.1039/c9ta11894b.

(43) Jarosz, G. et al. Effect of Band Gap on Power Conversion Efficiency of Single-Junction Semiconductor Photovoltaic Cells under White Light Phosphor-Based LED Illumination. *Mater. Sci. Semicond. Process.* **2020**, *107* (October 2019). https://doi.org/10.1016/j.mssp.2019.104812.

(44) Saha, A. et al. Performance Evaluation of Single-Junction Indoor Photovoltaic Devices for Different Absorber Bandgaps under Spectrally Varying White Light-Emitting Diodes. *IEEE J. Photovoltaics* **2020**, *10* (2), 539–545. https://doi.org/10.1109/JPHOTOV.2019.2959938.

(45) Pecunia, V. et al. Emerging Indoor Photovoltaic Technologies for Sustainable Internet of Things. *Adv. Energy Mater.* **2021**, *11* (29), 2100698. https://doi.org/https://doi.org/10.1002/aenm.202100698.

(46) Peng, Y. et al. Lead-Free Perovskite-Inspired Absorbers for Indoor Photovoltaics. *Adv. Energy Mater.* **2021**, *11* (1), 2002761. https://doi.org/https://doi.org/10.1002/aenm.202002761.

(47) De Wolf, S.; Aydin, E. Tandems Have the Power. *Science* **2023**, *381* (6653), 30–31. https://doi.org/10.1126/science.adi6278.

(48) Stoumpos, C. C. et al. Ruddlesden-Popper Hybrid Lead Iodide Perovskite 2D Homologous Semiconductors. *Chem. Mater.* **2016**, *28* (8), 2852–2867. https://doi.org/10.1021/acs.chemmater.6b00847.

(49) Connor, B. A. et al. Layered Halide Double Perovskites: Dimensional Reduction of Cs2AgBiBr6. *J. Am. Chem. Soc.* **2018**, *140* (15), 5235–5240. https://doi.org/10.1021/jacs.8b01543.

(50) Chen, Y. et al. 2D Ruddlesden–Popper Perovskites for Optoelectronics. *Adv. Mater.* **2018**, *30* (2), 1–15. https://doi.org/10.1002/adma.201703487.

(51) Chen, Y. et al. Optoelectronic Properties of Mixed Iodide-Bromide Perovskites from First-Principles Computational Modeling and Experiment. *J. Phys. Chem. Lett.* **2022**, *13* (18), 4184–4192. https://doi.org/10.1021/acs.jpclett.2c00938.

(52) Uddin, M. A. et al. Halide Exchange and Surface Modification of Metal Halide Perovskite Nanocrystals with Alkyltrichlorosilanes. *Nanoscale* **2018**, *10* (35), 16919–16927. https://doi.org/10.1039/c8nr04763d.

(53) Nedelcu, G. et al. Fast Anion-Exchange in Highly Luminescent Nanocrystals of Cesium Lead Halide Perovskites (CsPbX3, X = Cl, Br, I). *Nano Lett.* **2015**, *15* (8), 5635–5640. https://doi.org/10.1021/acs.nanolett.5b02404.

(54) Koscher, B. A. et al. Surface- vs Diffusion-Limited Mechanisms of Anion Exchange in CsPbBr3 Nanocrystal Cubes Revealed through Kinetic Studies. *J. Am. Chem. Soc.* **2016**, *138* (37), 12065–12068. https://doi.org/10.1021/jacs.6b08178.

(55) Saliba, M. et al. Incorporation of Rubidium Cations into Perovskite Solar Cells Improves Photovoltaic Performance. *Science (80-.).* **2016**, *354* (6309), 206–209. https://doi.org/https://doi.org/10.1126/science.aah5557.

(56) Pering, S. R.; Cameron, P. J. The Effect of Multiple Ion Substitutions on Halide Ion Migration in Perovskite Solar Cells. *Mater. Adv.* **2022**, *3* (21), 7918–7924. https://doi.org/10.1039/d2ma00619g.

(57) A, K. et al. Organometal Halide Perovskites as Visible-Light Sensitizers for Photovoltaic Cells. *J. Am. Chem. Soc.* **2009**, *131* (17), 6050–6051.

(58) Kim, D. I. et al. A High-efficiency and Stable Perovskite Solar Cell Fabricated in Ambient Air Using a Polyaniline Passivation Layer. *Sci. Rep.* **2022**, *12* (1), 1–10. https://doi.org/10.1038/s41598-021-04547-3.

(59) Hu, Y. et al. Understanding the Role of Cesium and Rubidium Additives in Perovskite Solar Cells: Trap States, Charge Transport, and Recombination. *Adv. Energy Mater.* **2018**, *8* (16), 1–11. https://doi.org/10.1002/aenm.201703057.

(60) Lee, M. M. et al. Efficient Hybrid Solar Cells Based on Meso-Superstructured Organometal Halide Perovskites. *Science (80-.).* **2012**, *338* (6107), 643–647. https://doi.org/https://doi.org/10.1126/science.1228604.

(61) Webb, T. et al. Device Architecture Engineering: Progress toward Next Generation Perovskite Solar Cells. *Adv. Funct. Mater.* **2021**, *31* (35). https://doi.org/10.1002/adfm.202103121.

(62) Yin, X. et al. Novel NiO Nanoforest Architecture for Efficient Inverted Mesoporous Perovskite Solar Cells. *ACS Appl. Mater. Interfaces* **2019**, *11* (47), 44308–44314. https://doi.org/10.1021/acsami.9b15820.

(63) Mali, S. S. et al. Nanoporous P-Type NiOx Electrode for p-i-n Inverted Perovskite Solar Cell toward Air Stability. *Mater. Today* **2018**, *21* (5), 483–500. https://doi.org/10.1016/j.mattod.2017.12.002.

(64) Boschloo, G. Can Alternative Module Design Help to Overcome Stability Problems of Perovskite Photovoltaics? *ACS Energy Lett.* **2023**, *8* (2), 1147–1151. https://doi.org/10.1021/acsenergylett.2c02841.

(65) Chen, J. et al. Solar Cell Efficiency Exceeding 25% through Rb-Based Perovskitoid Scaffold Stabilizing the Buried Perovskite Surface. *ACS Energy Lett.* **2022**, *7* (10), 3685–3694. https://doi.org/10.1021/acsenergylett.2c01661.

(66) Yang, T. et al. One-Stone-for-Two-Birds Strategy to Attain beyond 25% Perovskite Solar Cells. *Nat. Commun.* **2023**, *14* (1). https://doi.org/10.1038/s41467-023-36229-1.

(67) Ren, G. et al. Strategies of Modifying Spiro-OMeTAD Materials for Perovskite Solar Cells: A Review. *J. Mater. Chem. A* **2021**, *9* (8), 4589–4625. https://doi.org/10.1039/d0ta11564a.

(68) Rombach, F. M. et al. Lessons Learned from Spiro-OMeTAD and PTAA in Perovskite Solar Cells. *Energy Environ. Sci.* **2021**, *14* (10), 5161–5190. https://doi.org/10.1039/d1ee02095a.

(69) Zheng, L. et al. Inverted Perovskite/Silicon V-Shaped Tandem Solar Cells with 27.6% Efficiency via Self-Assembled Monolayer-Modified Nickel Oxide Layer. *J. Mater. Chem. A* **2022**, *10* (13), 7251–7262. https://doi.org/10.1039/d1ta10313j.

(70) Al-Ashouri, A. et al. Monolithic Perovskite/Silicon Tandem Solar Cell with >29% Efficiency by Enhanced Hole Extraction. *Science (80-.).* **2020**, *370* (6522), 1300–1309. https://doi.org/10.1126/science.abd4016.

(71) Xie, H. et al. Hole Transport Free Flexible Perovskite Solar Cells with Cost-Effective Carbon Electrodes. *Nanotechnology* **2020**, *32* (10). https://doi.org/10.1088/1361-6528/abcf70.

(72) Hu, Y. et al. Flexible Perovskite Solar Cells with High Power-Per-Weight: Progress, Application, and Perspectives. *ACS Energy Lett.* **2021**, *6* (8), 2917–2943. https://doi.org/10.1021/acsenergylett.1c01193.

(73) Wojciechowski, K.; Forgács, D. Commercial Applications of Indoor Photovoltaics Based on Flexible Perovskite Solar Cells. *ACS Energy Lett.* **2022**, *7* (10), 3729–3733. https://doi.org/10.1021/acsenergylett.2c01976.

(74) Feleki, B. T. et al. Development of a Perovskite Solar Cell Architecture for Opaque Substrates. *Sol. RRL* **2020**. https://doi.org/10.1002/solr.202000385.

(75) Feleki, B. T. et al. Perovskite Solar Cells on Polymer-Coated Smooth and Rough Steel Substrates. *Sol. RRL* **2022**, *6* (4). https://doi.org/10.1002/solr.202100898.

(76) Zhu, W. et al. Band Alignment Engineering Towards High Efficiency Carbon-Based Inorganic Planar CsPbIBr2 Perovskite Solar Cells. *ChemSusChem* **2019**, *12* (10), 2318–2325. https://doi.org/10.1002/cssc.201900611.

(77) Zhao, B. et al. The Role of Interface between Electron Transport Layer and Perovskite in Halogen Migration and Stabilizing Perovskite Solar Cells with Cs4SnO4. *J. Mater. Chem. A* **2018**, *6* (46), 23797–23804. https://doi.org/10.1039/c8ta09382b.

(78) Yang, D. et al. Surface Optimization to Eliminate Hysteresis for Record Efficiency Planar Perovskite Solar Cells. *Energy Environ. Sci.* **2016**, *9* (10), 3071–3078. https://doi.org/10.1039/c6ee02139e.

(79) Sirtl, M. T. et al. 2D/3D Hybrid Cs2AgBiBr6 Double Perovskite Solar Cells: Improved Energy Level Alignment for Higher Contact-Selectivity and Large Open Circuit Voltage. *Adv. Energy Mater.* **2022**, *12* (7), 2103215. https://doi.org/10.1002/aenm.202103215.

(80) Weber, S. A. L. et al. How the Formation of Interfacial Charge Causes Hysteresis in Perovskite Solar Cells. *Energy Environ. Sci.* **2018**, *11* (9), 2404–2413. https://doi.org/10.1039/c8ee01447g.

(81) Guerrero, A. et al. Electrical Field Profile and Doping in Planar Lead Halide Perovskite Solar Cells. *Appl. Phys. Lett.* **2014**, *105* (13). https://doi.org/10.1063/1.4896779.

(82) Jiang, C. S. et al. Carrier Separation and Transport in Perovskite Solar Cells Studied by Nanometre-Scale Profiling of Electrical Potential. *Nat. Commun.* **2015**, *6*, 1–10. https://doi.org/10.1038/ncomms9397.

(83) Ebadi, F. et al. Coupled Ionic-Electronic Equivalent Circuit to Describe Asymmetric Rise and Decay of Photovoltage Profile in Perovskite Solar Cells. *Sci. Rep.* **2019**, *9* (1), 1–9. https://doi.org/10.1038/s41598-019-48505-6.

(84) Wu, C. et al. All Electrospray Printing of Carbon-Based Cost-Effective Perovskite Solar Cells. *Adv. Funct. Mater.* **2021**, *31* (6), 1–9. https://doi.org/10.1002/adfm.202006803.

(85) Cai, M. et al. Cost-Performance Analysis of Perovskite Solar Modules. *Adv. Sci.* **2017**, *4* (1). https://doi.org/10.1002/advs.201600269.

(86) Čulík, P. et al. Design and Cost Analysis of 100 MW Perovskite Solar Panel Manufacturing Process in Different Locations. *ACS Energy Lett.* **2022**, *7* (9), 3039–3044. https://doi.org/10.1021/acsenergylett.2c01728.

(87) Chang, N. L. et al. Manufacturing Cost and Market Potential Analysis of Demonstrated Roll-to-Roll Perovskite Photovoltaic Cell Processes. *Sol. Energy Mater. Sol. Cells* **2018**, *174* (May 2017), 314–324. https://doi.org/10.1016/j.solmat.2017.08.038.

(88) Kajal, P. et al. Costing Analysis of Scalable Carbon-Based Perovskite Modules Using Bottom Up Technique. *Glob. Challenges* **2022**, *6* (2). https://doi.org/10.1002/gch2.202100070.

(89) Sepalage, G. A. et al. Can Laminated Carbon Challenge Gold? Toward Universal, Scalable, and Low-Cost Carbon Electrodes for Perovskite Solar Cells. *Adv. Mater. Technol.* **2022**, *7* (6), 1–11. https://doi.org/10.1002/admt.202101148.

(90) Domanski, K. et al. Not All That Glitters Is Gold: Metal-Migration-Induced Degradation in Perovskite Solar Cells. *ACS Nano* **2016**, *10* (6), 6306–6314. https://doi.org/10.1021/acsnano.6b02613.

(91) Svanström, S. et al. Degradation Mechanism of Silver Metal Deposited on Lead Halide Perovskites. *ACS Appl. Mater. Interfaces* **2020**, *12* (6), 7212–7221. https://doi.org/10.1021/acsami.9b20315.

(92) Yan, K. et al. High-Performance Graphene-Based Hole Conductor-Free Perovskite Solar Cells: Schottky Junction Enhanced Hole Extraction and Electron Blocking. *Small* **2015**, *11* (19), 2269–2274. https://doi.org/10.1002/smll.201403348.

(93) Wu, Z. et al. Highly Efficient and Stable Perovskite Solar Cells via Modification of Energy Levels at the Perovskite/Carbon Electrode Interface. *Adv. Mater.* **2019**, *31* (11), 1–7. https://doi.org/10.1002/adma.201804284.

(94) Öcebe, A. et al. Gas-Quenching Approach for Fabricating Cs2AgBiBr6 Thin Films in Ambient Environment for Lead-Free All-Inorganic Perovskite Solar Cells with Carbon Electrodes. *Energy Technol.* **2023**, *11* (10), 1–9. https://doi.org/10.1002/ente.202300407.

(95) Ma, X. et al. Study on the Performance of CuBr2 Doped Cs2AgBiBr6 Perovskite Solar Cells with Carbon Electrode and without a Hole-Transporting Layer. *Mater. Sci. Semicond. Process.* **2023**, *164* (May), 107618. https://doi.org/10.1016/j.mssp.2023.107618.

(96) Li, J. et al. Alkali Metal Ion-Regulated Lead-Free, All-Inorganic Double Perovskites for HTM-Free, Carbon-Based Solar Cells. *ACS Appl. Mater. Interfaces* **2020**, *12* (42), 47408–47415. https://doi.org/10.1021/acsami.0c11770.

(97) Li, J. et al. Suppressing Interfacial Shunt Loss via Functional Polymer for Performance Improvement of Lead-Free Cs2AgBiBr6 Double Perovskite Solar Cells. *Sol. RRL* **2021**, *2100791*, 34–39. https://doi.org/10.1002/solr.202100791.

(98) Liu, S. et al. Thermodynamically Regulated Preparation of High Performance for Carbon-Based Cs2AgBiBr6 Perovskite Solar Cells. *Mater. Sci. Semicond. Process.* **2023**, *154* (October 2022), 107193. https://doi.org/10.1016/j.mssp.2022.107193.

(99) Li, J. et al. Pinning Bromide Ion with Ionic Liquid in Lead-Free Cs2AgBiBr6 Double Perovskite Solar Cells. *Adv. Funct. Mater.* **2022**, *32* (25), 2112991. https://doi.org/10.1002/adfm.202112991.

(100) Sirtl, M. T. et al. Optoelectronic Properties of Cs2AgBiBr6Thin Films: The Influence of Precursor Stoichiometry. *ACS Appl. Energy Mater.* **2020**, *3* (12), 11597–11609. https://doi.org/10.1021/acsaem.0c01308.

(101) Yang, J. et al. Band Structure Engineering of Cs2AgBiBr6 Perovskite through Order−Disordered Transition: A First-Principle Study. *J. Phys. Chem. Lett.* **2018**, *9*, 31–35. https://doi.org/10.1021/acs.jpclett.7b02992.

(102) Hadi, M. A. et al. Indirect to Direct Band Gap Transition through Order to Disorder Transformation of Cs2AgBiBr6 via Creating Antisite Defects for Optoelectronic and Photovoltaic Applications. *RSC Adv.* **2022**, *12* (24), 15461–15469. https://doi.org/10.1039/d1ra06308a.

(103) Shadabroo, M. S. et al. Dimethyl Sulfoxide Vapor-Assisted Cs2AgBiBr6 Homogenous Film Deposition for Solar Cell Application. *ACS Appl. Energy Mater.* **2021**, *4* (7), 6797–6805. https://doi.org/10.1021/acsaem.1c00894.

(104) Wang, B. et al. Photoactive Zn-Chlorophyll Hole Transporter-Sensitized Lead-Free Cs2AgBiBr6 Perovskite Solar Cells. *Sol. RRL* **2020**, *4* (7), 2–8. https://doi.org/10.1002/solr.202000166.

(105) Zhang, L. et al. Regulating Film Crystallization Kinetics with Thiourea Additive in Cs2AgBiBr6 Solar Cells. *J. Phys. D. Appl. Phys.* **2023**, *56* (7), 075501. https://doi.org/https://doi.org/10.1088/1361-6463/acad11.

(106) Wu, C. et al. The Dawn of Lead-Free Perovskite Solar Cell: Highly Stable Double Perovskite Cs2AgBiBr6 Film. *Adv. Sci.* **2018**, *5* (3), 2–9. https://doi.org/10.1002/advs.201700759.

(107) Gao, W. et al. High-Quality Cs2AgBiBr6 Double Perovskite Film for Lead-Free Inverted Planar Heterojunction Solar Cells with 2.2 % Efficiency. *ChemPhysChem* **2018**, *19* (14), 1696–1700. https://doi.org/10.1002/cphc.201800346.

(108) Yang, X. et al. Simultaneous Power Conversion Efficiency and Stability Enhancement of Cs2AgBiBr6 Lead-Free Inorganic Perovskite Solar Cell through Adopting a Multifunctional Dye Interlayer. *Adv. Funct. Mater.* **2020**, *30* (23). https://doi.org/10.1002/adfm.202001557.

(109) Daem, N. et al. Spray-Coated Lead-Free Cs2AgBiBr6 Double Perovskite Solar Cells with High Open-Circuit Voltage. *Sol. RRL* **2021**, *5* (9). https://doi.org/10.1002/solr.202100422.

(110) Fan, P. et al. Single-Source Vapor-Deposited Cs2AgBiBr6 Thin Films for Lead-Free Perovskite Solar Cells. *Nanomaterials* **2019**, *9* (23), 1760. https://doi.org/https://doi.org/10.3390/nano9121760.

(111) Peng, H. et al. Phase-Controlled Strategy for High-Quality Single-Source Vapor- Deposited Cs2AgBiBr6 Thin Films. *ACS Appl. Energy Mater.* **2022**, *5* (12), 15058–15068. https://doi.org/10.1021/acsaem.2c02724.

(112) Xiao, B. et al. Band Matching Strategy for All-Inorganic Cs2AgBiBr6Double Perovskite Solar Cells with High Photovoltage. *ACS Appl. Mater. Interfaces* **2021**, *13* (31), 37027–37034. https://doi.org/10.1021/acsami.1c07169.

(113) Wang, M. et al. High-Quality Sequential-Vapor-Deposited Cs2AgBiBr6 Thin Films for Lead-Free Perovskite Solar Cells. *Sol. RRL* **2018**, *2* (12), 1–6. https://doi.org/10.1002/solr.201800217.

(114) Rodkey, N. et al. Pulsed Laser Deposition of Cs2AgBiBr6: From Mechanochemically Synthesized Powders to Dry, Single-Step Deposition. *Chem. Mater.* **2021**, *33* (18), 7417–7422. https://doi.org/10.1021/acs.chemmater.1c02054.

(115) Xiao, Z. et al. Thermodynamic Stability and Defect Chemistry of Bismuth-Based Lead-Free Double Perovskites. *Chem. Sustain. Energy Mater.* **2016**, *9* (18), 2628–2633. https://doi.org/10.1002/cssc.201600771.

(116) Bekenstein, Y. et al. The Making and Breaking of Lead-Free Double Perovskite Nanocrystals of Cesium Silver–Bismuth Halide Compositions. *Nano Lett.* **2018**, *18* (6), 3502–3508. https://doi.org/10.1021/acs.nanolett.8b00560.

(117) Wang, Y. et al. Encapsulation and Stability Testing of Perovskite Solar Cells for Real Life Applications. *ACS Mater. Au* **2021**, *2* (3), 215–236. https://doi.org/10.1021/acsmaterialsau.1c00045.

(118) Emery, Q. et al. Encapsulation and Outdoor Testing of Perovskite Solar Cells: Comparing Industrially Relevant Process with a Simplified Lab Procedure. *ACS Appl. Mater. Interfaces* **2022**, *14* (4), 5159–5167. https://doi.org/10.1021/acsami.1c14720.

(119) Xiang, L. et al. Progress on the Stability and Encapsulation Techniques of Perovskite Solar Cells. *Org. Electron.* **2022**, *106* (July 2022), 106515. https://doi.org/10.1016/j.orgel.2022.106515.

(120) Savory, C. N. et al. Can Pb-Free Halide Double Perovskites Support High-Efficiency Solar Cells? *ACS Energy Lett.* **2016**, *1* (5), 949–955. https://doi.org/10.1021/acsenergylett.6b00471.

(121) Mohandes, A. et al. Numerical Simulation of Inorganic Cs2AgBiBr6 as a Lead-Free Perovskite Using Device Simulation SCAPS-1D. *Opt. Quantum Electron.* **2021**, *53* (6), 1–22. https://doi.org/10.1007/s11082-021-02959-z.

(122) Alanazi, T. I. Design and Device Numerical Analysis of Lead-Free Cs2AgBiBr6 Double Perovskite Solar Cell. *Crystals* **2023**, *13* (2), 267. https://doi.org/https://doi.org/10.3390/cryst13020267.

(123) Li, Z. et al. Single-Layered MXene Nanosheets Doping TiO2for Efficient and Stable Double Perovskite Solar Cells. *J. Am. Chem. Soc.* **2021**, *143* (6), 2593–2600. https://doi.org/10.1021/jacs.0c12739.

(124) Li, Q. et al. High-Pressure Band-Gap Engineering in Lead-Free Cs2AgBiBr6 Double Perovskite. *Angew. Chemie - Int. Ed.* **2017**, *56* (50), 15969–15973. https://doi.org/10.1002/anie.201708684.

(125) Jiang, H. et al. Ion Exchange for Halide Perovskite: From Nanocrystal to Bulk Materials. *Nano Sel.* **2021**, *2* (11), 2040–2060. https://doi.org/10.1002/nano.202100084.

(126) Protesescu, L. et al. Nanocrystals of Cesium Lead Halide Perovskites (CsPbX3, X = Cl, Br, and I): Novel Optoelectronic Materials Showing Bright Emission with Wide Color Gamut. *Nano Lett.* **2015**, *15* (6), 3692–3696. https://doi.org/10.1021/nl5048779.

(127) Tripathi, M. N. et al. Structural, Elastic, Electronic and Optical Properties of Lead-Free Halide Double Perovskite Cs2AgBiX6 (X = Cl, Br, and I). *Mater. Res. Express* **2019**, *6* (11). https://doi.org/10.1088/2053-1591/ab48ba.

(128) Absike, H. et al. Optoelectronic and Photovoltaic Properties of Cs2AgBiX6 (X = Br, Cl, or I) Halide Double Perovskite for Solar Cells: Insight from Density Functional Theory. *Int. J. Energy Res.* **2022**, *46* (8), 11053–11064. https://doi.org/10.1002/er.7907.

(129) Kubicki, D. J. et al. Halide Mixing and Phase Segregation in Cs2AgBiX6(X = Cl, Br, and I) Double Perovskites from Cesium-133 Solid-State NMR and Optical Spectroscopy. *Chem. Mater.* **2020**, *32* (19), 8129–8138. https://doi.org/10.1021/acs.chemmater.0c01255.

(130) Li, Y. et al. Composition and Illumination-Driven Phase Segregation in Hybrid Perovskite Cs2AgBi(Br1-XIx)6. *J. Phys. Chem. C* **2023**, *127* (32), 16061–16070. https://doi.org/10.1021/acs.jpcc.3c02994.

(131) Wu, H. et al. Mixed-Halide Double Perovskite Cs2AgBiX6 (X=Br, I) with Tunable Optical Properties via Anion Exchange. *Chem. Sustain. Energy Mater.* **2021**, *14* (20), 4507–4515. https://doi.org/10.1002/cssc.202101146.

(132) Kluherz, K. T. et al. Structure and Stability of the Iodide Elpasolite, Cs2AgBiI6. *Chem. Mater.* **2023**, *35* (14), 5699–5708. https://doi.org/10.1021/acs.chemmater.3c01511.

(133) Pai, N. et al. Solution Processable Direct Bandgap Copper-Silver-Bismuth Iodide Photovoltaics: Compositional Control of Dimensionality and Optoelectronic Properties. *Adv. Energy Mater.* **2022**, *12* (32). https://doi.org/10.1002/aenm.202201482.

(134) Hutter, E. M. et al. Band-Like Charge Transport in Cs2AgBiBr6 and Mixed Antimony-Bismuth Cs2AgBi1-XSbxBr6 Halide Double Perovskites. *ACS Omega* **2018**, *3* (9), 11655–11662. https://doi.org/10.1021/acsomega.8b01705.

(135) Kumar, A. et al. Mixed Bismuth-Antimony-Based Double Perovskite Nanocrystals for Solar Cell Application. *Int. J. Energy Res.* **2021**, *45* (11), 16769–16780. https://doi.org/10.1002/er.6924.

(136) Ou, Y. et al. Boosting the Stability and Efficiency of Cs2AgBiBr6 Perovskite Solar Cells via Zn Doping. *Opt. Mater. (Amst).* **2022**, *129* (July 2021), 112452. https://doi.org/10.1016/j.optmat.2022.112452.

(137) Zhang, Z. et al. Improvement of Cs2AgBiBr6 Double Perovskite Solar Cell by Rubidium Doping. *Org. Electron.* **2019**, *74* (November 2019), 204–210. https://doi.org/10.1016/j.orgel.2019.06.037.

(138) He, Y. et al. Design and Performance Exploration of a Lead-Free All-Inorganic Hydrogenated Cs2AgBiBr6-Based Double Perovskite Solar Cell: A Numerical Modeling Study. *Sol. RRL* **2023**, *7* (10), 1–20. https://doi.org/10.1002/solr.202300030.

(139) Liu, G. et al. Extending Absorption of Cs2AgBiBr6 to Near-Infrared Region (≈1350 Nm) with Intermediate Band. *Adv. Funct. Mater.* **2022**, *32* (12), 1–8. https://doi.org/10.1002/adfm.202109891.

(140) Ji, F. et al. Near-Infrared Light-Responsive Cu-Doped Cs2AgBiBr6. *Adv. Funct. Mater.* **2020**, *30* (51), 1–7. https://doi.org/10.1002/adfm.202005521.

(141) Wang, S. et al. Improved Optical Properties of Lead-Free Double Perovskite Cs2AgBiBr6 Nanocrystals via Na Ions Doping. *Adv. Opt. Mater.* **2023**, *11* (10), 1–8. https://doi.org/10.1002/adom.202202745.

(142) Tran, M. N. et al. Reactive Physical Vapor Deposition of Yb-Doped Lead-Free Double Perovskite Cs2AgBiBr6with 95% Photoluminescence Quantum Yield. *ACS Appl. Electron. Mater.* **2022**, *4* (9), 4588–4594. https://doi.org/10.1021/acsaelm.2c00788.

(143) Tran, M. N. et al. High Photoluminescence Quantum Yield Near-Infrared Emission from a Lead-Free Ytterbium-Doped Double Perovskite. *Mater. Horizons* **2022**, *9* (8), 2191–2197. https://doi.org/10.1039/d2mh00483f.

(144) Goldschmidt, V. M. Die Gesetze Der Krystallochemie. *Naturwissenschaften* **1926**, *14*, 477–485. https://doi.org/https://doi.org/10.1007/BF01507527.

(145) Li, Z. et al. Stabilizing Perovskite Structures by Tuning Tolerance Factor: Formation of Formamidinium and Cesium Lead Iodide Solid-State Alloys. *Chem. Mater.* **2016**, *28* (1), 284–292. https://doi.org/10.1021/acs.chemmater.5b04107.

(146) Zheng, F. et al. Revealing the Role of Methylammonium Chloride for Improving the Performance of 2D Perovskite Solar Cells. *ACS Appl. Mater. Interfaces* **2020**, *12* (23), 25980–25990. https://doi.org/10.1021/acsami.0c05714.

(147) Connor, B. A. et al. Dimensional Reduction of the Small-Bandgap Double Perovskite Cs2AgTlBr6. *Chem. Sci.* **2020**, *11* (29), 7708–7715. https://doi.org/10.1039/d0sc01580f.

(148) Jung, M. H. Exploration of Two-Dimensional Perovskites Incorporating Methylammonium for High Performance Solar Cells. *CrystEngComm* **2021**, *23* (5), 1181–1200. https://doi.org/10.1039/d0ce01469a.

(149) Lu, L. et al. Two-Dimensional Guanidine-Based Hybrid Perovskites with Strong Dichroism for Multiwavelength Polarization-Sensitive Detection. *Chem. - A Eur. J.* **2021**, *27* (36), 9267–9271. https://doi.org/10.1002/chem.202100691.

(150) Qin, C. et al. Carrier Dynamics in Two-Dimensional Perovskites: Dion-Jacobson: Vs. Ruddlesden-Popper Thin Films. *J. Mater. Chem. A* **2022**, *10* (6), 3069–3076. https://doi.org/10.1039/d1ta09549h.

(151) Liu, R. et al. Layered Low-Dimensional Ruddlesden-Popper and Dion-Jacobson Perovskites: From Material Properties to Photovoltaic Device Performance. *ChemSusChem* **2023**. https://doi.org/10.1002/cssc.202300736.

(152) Ghosh, D. et al. Charge Carrier Dynamics in Two-Dimensional Hybrid Perovskites: Dion-Jacobson: Vs. Ruddlesden-Popper Phases. *J. Mater. Chem. A* **2020**, *8* (42), 22009–22022. https://doi.org/10.1039/d0ta07205b.

(153) Chen, M. et al. Two-Dimensional Lead-Free Double Perovskite with Superior Stability and Optoelectronic Properties for Solar Cell Application. *J. Phys. Chem. C* **2022**, *126* (35), 14824–14831. https://doi.org/10.1021/acs.jpcc.2c03646.

(154) Zhang, Y. et al. Highly Efficient Guanidinium-Based Quasi 2D Perovskite Solar Cells via a Two-Step Post-Treatment Process. *Small Methods* **2019**, *3* (11), 1–9. https://doi.org/10.1002/smtd.201900375.

(155) Ortiz-Cervantes, C. et al. Two-Dimensional Halide Perovskites in Solar Cells: 2D or Not 2D? *ChemSusChem* **2019**, *12* (8), 1560–1575. https://doi.org/10.1002/cssc.201802992.

(156) Ishihara, T. et al. Exciton State in Two-Dimensional Perovskite Semiconductor (C10H21NH3)2PbI4. *Solid State Commun.* **1989**, *69* (9), 933–936. https://doi.org/10.1016/0038-1098(89)90935-6.

(157) Hong, X. et al. Dielectric Confinement Effect on Excitons in PbI4-Based Layered Semiconductors. *Phys. Rev. B* **1992**, *45* (12), 6961–6964. https://doi.org/10.1103/PhysRevB.45.6961.

(158) Ziegler, J. D. et al. Excitons at the Phase Transition of 2D Hybrid Perovskites. *ACS Photonics* **2022**, *9* (11), 3609–3616. https://doi.org/10.1021/acsphotonics.2c01035.

(159) Chen, A. Z. et al. Origin of Vertical Orientation in Two-Dimensional Metal Halide Perovskites and Its Effect on Photovoltaic Performance. *Nat. Commun.* **2018**, *9* (1), 1–7. https://doi.org/10.1038/s41467-018-03757-0.

(160) Chen, A. Z. et al. Understanding the Formation of Vertical Orientation in Two-Dimensional Metal Halide Perovskite Thin Films. *Chem. Mater.* **2019**, *31* (4), 1336–1343. https://doi.org/10.1021/acs.chemmater.8b04531.

(161) Lin, Y. et al. Enhanced Thermal Stability in Perovskite Solar Cells by Assembling 2D/3D Stacking Structures. *J. Phys. Chem. Lett.* **2018**, *9* (3), 654–658. https://doi.org/10.1021/acs.jpclett.7b02679.

(162) Cheng, P. et al. Highly Efficient Ruddlesden-Popper Halide Perovskite PA2MA4Pb5I16 Solar Cells. *ACS Energy Lett.* **2018**, *3* (8), 1975–1982. https://doi.org/10.1021/acsenergylett.8b01153.

(163) Zhang, J. et al. Binary Solvent Engineering for High-Performance Two-Dimensional Perovskite Solar Cells. *ACS Sustain. Chem. Eng.* **2019**, *7* (3), 3487–3495. https://doi.org/10.1021/acssuschemeng.8b05734.

(164) Ma, C. et al. 2D Perovskites with Short Interlayer Distance for High-Performance Solar Cell Application. *Adv. Mater.* **2018**, *30* (22), 2–7. https://doi.org/10.1002/adma.201800710.

(165) Zhang, F. et al. Enhanced Charge Transport in 2D Perovskites via Fluorination of Organic Cation. *J. Am. Chem. Soc.* **2019**, *141* (14), 5972–5979. https://doi.org/10.1021/jacs.9b00972.

(166) Smith, I. C. et al. A Layered Hybrid Perovskite Solar-Cell Absorber with Enhanced Moisture Stability. *Angew. Chemie - Int. Ed.* **2014**, *53* (42), 11232–11235. https://doi.org/10.1002/anie.201406466.

(167) Yao, D. et al. 2D-3D Mixed Organic-Inorganic Perovskite Layers for Solar Cells with Enhanced Efficiency and Stability Induced by n-Propylammonium Iodide Additives. *ACS Appl. Mater. Interfaces* **2019**, *11* (33), 29753–29764. https://doi.org/10.1021/acsami.9b06305.

(168) Mitzi, D. B. et al. Conducting Layered Organic-Inorganic Halides Containing 〈110〉-Oriented Perovskite Sheets. *Science (80-.).* **1995**, *267* (5203), 1473–1476. https://doi.org/10.1126/science.267.5203.1473.

(169) Pantaler, M. et al. Revealing Weak Dimensional Confinement Effects in Excitonic Silver/Bismuth Double Perovskites. *JACS Au* **2022**, *2* (1), 136–149. https://doi.org/10.1021/jacsau.1c00429.

(170) Hooijer, R. et al. Silver-Bismuth Based 2D Double Perovskites (4FPEA)4AgBiX8 (X = Cl, Br, I): Highly Oriented Thin Films with Large Domain Sizes and Ultrafast Charge-Carrier Localization. *Adv. Opt. Mater.* **2022**, *10* (14). https://doi.org/10.1002/adom.202200354.

(171) Lassoued, M. S. et al. Semiconductivity and High Stability in Centimetric Two-Dimensional Bismuth-Silver Hybrid Double Perovskites. *Mater. Chem. Front.* **2022**, *6* (15), 2135–2142. https://doi.org/10.1039/d2qm00341d.

(172) Gross, R.; Marx, A. *Festkörperphysik*; 2013. https://doi.org/10.1524/9783486714869.

(173) Jana, M. K. et al. Direct-Bandgap 2D Silver-Bismuth Iodide Double Perovskite: The Structure-Directing Influence of an Oligothiophene Spacer Cation. *J. Am. Chem. Soc.* **2019**, *141* (19), 7955–7964. https://doi.org/10.1021/jacs.9b02909.

(174) Shao, M. et al. Over 21% Efficiency Stable 2D Perovskite Solar Cells. *Adv. Mater.* **2022**, *34* (1), 1–10. https://doi.org/10.1002/adma.202107211.

(175) Zhang, Y.; Park, N. G. Quasi-Two-Dimensional Perovskite Solar Cells with Efficiency Exceeding 22%. *ACS Energy Lett.* **2022**, *7* (2), 757–765. https://doi.org/10.1021/acsenergylett.1c02645.

(176) Krishna, A. et al. Mixed Dimensional 2D/3D Hybrid Perovskite Absorbers: The Future of Perovskite Solar Cells? *Adv. Funct. Mater.* **2019**, *29* (8), 1–20. https://doi.org/10.1002/adfm.201806482.

(177) Gebhardt, J.; Elsässer, C. The Electronic Structure of Cs2AgBiBr6 at Room Temperature. *Phys. Status Solidi B* **2022**, *259* (8), 2200124. https://doi.org/10.1002/pssb.202200124.

(178) Grancini, G. et al. One-Year Stable Perovskite Solar Cells by 2D/3D Interface Engineering. *Nat. Commun.* **2017**, *8*, 1–8. https://doi.org/10.1038/ncomms15684.

(179) Wang, Z. et al. Efficient Ambient-Air-Stable Solar Cells with 2D-3D Heterostructured Butylammonium-Caesium-Formamidinium Lead Halide Perovskites. *Nat. Energy* **2017**, *2* (9), 1–10. https://doi.org/10.1038/nenergy.2017.135.

(180) Hauschild, D. et al. Impact of N-Butylammonium Bromide on the Chemical and Electronic Structure of Double-Cation Perovskite Thin Films. *ACS Appl. Mater. Interfaces* **2021**, *13* (44), 53202–53210. https://doi.org/10.1021/acsami.1c15707.

(181) Sidhik, S. et al. Deterministic Fabrication of 3D/2D Perovskite Bilayer Stacks for Durable and Efficient Solar Cells. *Science (80-.).* **2022**, *377* (6613), 1425–1430. https://doi.org/10.1126/science.abq7652.

(182) Bhattacharya, S.; John, S. Beyond 30% Conversion Efficiency in Silicon Solar Cells: A Numerical Demonstration. *Sci. Rep.* **2019**, *9* (1), 1–15. https://doi.org/10.1038/s41598-019-48981-w.

(183) Das, S. et al. High-Performance Flexible Perovskite Solar Cells by Using a Combination of Ultrasonic Spray-Coating and Low Thermal Budget Photonic Curing. *ACS Photonics* **2015**, *2* (6), 680–686. https://doi.org/10.1021/acsphotonics.5b00119.

(184) Zhu, X. et al. Perspectives for the Conversion of Perovskite Indoor Photovoltaics into IoT Reality. *Nanoscale* **2023**, *15* (11), 5167–5180. https://doi.org/10.1039/d2nr07022g.

(185) Liu, X. et al. Boosting the Efficiency of Carbon-Based Planar CsPbBr3 Perovskite Solar Cells by a Modified Multistep Spin-Coating Technique and Interface Engineering. *Nano Energy* **2019**, *56* (October 2018), 184–195. https://doi.org/10.1016/j.nanoen.2018.11.053.

(186) Scriven, L. E. Physics and Applications of DIP Coating and Spin Coating. *MRS Proc.* **1988**, *121*, 717–729. https://doi.org/10.1557/proc-121-717.

(187) Acrivos, A. et al. On the Flow of a Non-Newtonian Liquid on a Rotating Disk. *J. Appl. Phys.* **1960**, *31* (6), 963–968. https://doi.org/10.1063/1.1735785.

(188) Zuo, C. et al. Drop-Casting Method to Screen Ruddlesden-Popper Perovskite Formulations for Use in Solar Cells. *ACS Appl. Mater. Interfaces* **2021**, *13* (47), 56217–56225. https://doi.org/10.1021/acsami.1c17475.

(189) Emslie, A. G. et al. Flow of a Viscous Liquid on a Rotating Disk. *J. Appl. Phys.* **1958**, *29* (5), 858–862. https://doi.org/10.1063/1.1723300.

(190) Grosso, D. How to Exploit the Full Potential of the Dip-Coating Process to Better Control Film Formation. *J. Mater. Chem.* **2011**, *21* (43), 17033–17038. https://doi.org/10.1039/c1jm12837j.

(191) Zuo, C.; Ding, L. Drop-Casting to Make Efficient Perovskite Solar Cells under High Humidity. *Angew. Chemie* **2021**, *133* (20), 11342–11346. https://doi.org/10.1002/ange.202101868.

(192) Howatt, G. N. et al. Fabrication of Thin Ceramic Sheets for Capacitors. *J. Am. Ceram. Soc.* **1947**, *30* (8), 237–242. https://doi.org/https://doi.org/10.1111/j.1151-2916.1947.tb18889.x.

(193) Tang, S. et al. Composition Engineering in Doctor-Blading of Perovskite Solar Cells. *Adv. Energy Mater.* **2017**, *7* (18), 1–7. https://doi.org/10.1002/aenm.201700302.

(194) Patidar, R. et al. Slot-Die Coating of Perovskite Solar Cells: An Overview. *Mater. Today Commun.* **2020**, *22* (September 2019), 100808. https://doi.org/10.1016/j.mtcomm.2019.100808.

(195) Chang, Y.-R. et al. Start-up of Slot Die Coating. *Society* **2009**, *49* (6), 1158–1167. https://doi.org/https://doi.org/10.1002/pen.21360.

(196) Whitaker, J. B. et al. Scalable Slot-Die Coating of High Performance Perovskite Solar Cells. *Sustain. Energy Fuels* **2018**, *2* (11), 2442–2449. https://doi.org/10.1039/c8se00368h.

(197) Aziz, F.; Ismail, A. F. Spray Coating Methods for Polymer Solar Cells Fabrication: A Review. *Mater. Sci. Semicond. Process.* **2015**, *39*, 416–425. https://doi.org/10.1016/j.mssp.2015.05.019.

(198) Bishop, J. E. et al. Fully Spray-Coated Triple-Cation Perovskite Solar Cells. *Sci. Rep.* **2020**, *10* (1), 1–8. https://doi.org/10.1038/s41598-020-63674-5.

(199) Bishop, J. E. et al. Development of Spray-Coated Perovskite Solar Cells. *ACS Appl. Mater. Interfaces* **2020**, *12* (43), 48237–48245. https://doi.org/10.1021/acsami.0c14540.

(200) Christen, H. M.; Eres, G. Recent Advances in Pulsed-Laser Deposition of Complex Oxides. *J. Phys. Condens. Matter* **2008**, *20* (26). https://doi.org/10.1088/0953-8984/20/26/264005.

(201) Wang, H. et al. Pulsed Laser Deposition of CsPbBr3 Films for Application in Perovskite Solar Cells. *ACS Appl. Energy Mater.* **2019**, *2* (3), 2305–2312. https://doi.org/10.1021/acsaem.9b00130.

(202) Joyce, B. A. Molecular Beam Epitaxy. *Reports Prog. Phys.* **1985**, *48*. https://doi.org/10.1088/0034-4885/48/12/002.

(203) Yu, Z. et al. Epitaxial Perovskite Thin Films Grown on Silicon by Molecular Beam Epitaxy. *J. Vac. Sci. Technol. B* **2000**, *18* (3), 1653–1657. https://doi.org/https://doi.org/10.1116/1.591445.

(204) Leskelä, M.; Ritala, M. Atomic Layer Deposition Chemistry: Recent Developments and Future Challenges. *Angew. Chemie - Int. Ed.* **2003**, *42* (45), 5548–5554. https://doi.org/10.1002/anie.200301652.

(205) Sutherland, B. R. et al. Perovskite Thin Films via Atomic Layer Deposition. *Adv. Mater.* **2015**, *27* (1), 53–58. https://doi.org/10.1002/adma.201403965.

(206) Kaliyaraj Selva Kumar, A. et al. A Mini-Review: How Reliable Is the Drop Casting Technique? *Electrochem. commun.* **2020**, *121* (September), 106867. https://doi.org/10.1016/j.elecom.2020.106867.

(207) Razza, S. et al. Research Update: Large-Area Deposition, Coating, Printing, and Processing Techniques for the Upscaling of Perovskite Solar Cell Technology. *APL Mater.* **2016**, *4* (9). https://doi.org/10.1063/1.4962478.

(208) Sahu, N. et al. Fundamental Understanding and Modeling of Spin Coating Process: A Review. *Indian J. Phys.* **2009**, *83* (4), 493–502. https://doi.org/10.1007/s12648-009-0009-z.

(209) Bornside, D. E. et al. Spin Coating: One - Dimensional Model. *J. Appl. Phys.* **1989**, *66* (11), 5185–5193. https://doi.org/https://doi.org/10.1063/1.343754.

(210) Taylor, A. D. et al. A General Approach to High-Efficiency Perovskite Solar Cells by Any Antisolvent. *Nat. Commun.* **2021**, *12* (1), 1–11. https://doi.org/10.1038/s41467-021-22049-8.

(211) Yan, Y. et al. Implementing an Intermittent Spin-Coating Strategy to Enable Bottom-up Crystallization in Layered Halide Perovskites. *Nat. Commun.* **2021**, *12* (1), 1–11. https://doi.org/10.1038/s41467-021-26753-3.

(212) Ghosh, S. et al. Antisolvents in Perovskite Solar Cells: Importance, Issues, and Alternatives. *Adv. Mater. Interfaces* **2020**, *7* (18), 1–24. https://doi.org/10.1002/admi.202000950.

(213) Slegers, S. et al. Surface Roughness Reduction of Additive Manufactured Products by Applying a Functional Coating Using Ultrasonic Spray Coating. *Coatings* **2017**, *7* (12), 1–12. https://doi.org/10.3390/coatings7120208.

(214) *Sono-Tek*. https://www.sono-tek.com/ultrasonic-coating/.

(215) Yasuda, K. et al. Analysis of Concentration Characteristics in Ultrasonic Atomization by Droplet Diameter Distribution. *Ultrason. Sonochem.* **2005**, *12* (1-2 SPEC. ISS.), 37–41. https://doi.org/10.1016/j.ultsonch.2004.05.008.

(216) Kim, J. et al. Numerical Analysis for the Optimum Condition of Ultrasonic Nebulizing. *Jpn. J. Appl. Phys.* **2016**, *55* (7), 3–6. https://doi.org/10.7567/JJAP.55.07KE03.

(217) Bose, S. et al. Process Optimization of Ultrasonic Spray Coating of Polymer Films. *Langmuir* **2013**, *29* (23), 6911–6919. https://doi.org/10.1021/la4010246.

(218) Li, C. et al. Ultrasonic Spray Pyrolysis for Nanoparticles Synthesis. *J. Mater. Sci.* **2004**, *9*, 3647–3657.

(219) Huang, H. et al. Two-Step Ultrasonic Spray Deposition of CH3NH3PbI3 for Efficient and Large-Area Perovskite Solar Cell. *Nano Energy* **2016**, *27*, 352–358. https://doi.org/10.1016/j.nanoen.2016.07.026.

(220) Chang, W. C. et al. Controlled Deposition and Performance Optimization of Perovskite Solar Cells Using Ultrasonic Spray-Coating of Photoactive Layers. *ChemSusChem* **2017**, *10* (7), 1405–1412. https://doi.org/10.1002/cssc.201601711.

(221) Zelewski, S. J. et al. Revealing the Nature of Photoluminescence Emission in the Metal-Halide Double Perovskite. *J. Mater. Chem. C* **2019**, *7* (27), 8350–8356. https://doi.org/10.1039/c9tc02402f.

(222) Schade, L. et al. Structural and Optical Properties of Cs2AgBiBr6 Double Perovskite. *ACS Energy Lett.* **2019**, *4* (1), 299–305. https://doi.org/10.1021/acsenergylett.8b02090.

(223) Ke, B. et al. Homo- And Heterovalent Doping-Mediated Self-Trapped Exciton Emission and Energy Transfer in Mn-Doped Cs2Na1- XAgxBiCl6 Double Perovskites. *J. Phys. Chem. Lett.* **2020**, *11* (1), 340–348. https://doi.org/10.1021/acs.jpclett.9b03387.

(224) Zhou, J. et al. Manipulation of Bi3+/In3+ Transmutation and Mn2+-Doping Effect on the Structure and Optical Properties of Double Perovskite Cs2NaBi1-XInxCl6. *Adv. Opt. Mater.* **2019**, *7* (8), 1–9. https://doi.org/10.1002/adom.201801435.

(225) Ma, J. P. et al. Insights into the Local Structure of Dopants, Doping Efficiency, and Luminescence Properties of Lanthanide-Doped CsPbCl3 Perovskite Nanocrystals. *J. Mater. Chem. C* **2019**, *7* (10), 3037–3048. https://doi.org/10.1039/c9tc00237e.

(226) Liu, Y. et al. Considerably Enhanced Exciton Emission of CsPbCl3 Perovskite Quantum Dots by the Introduction of Potassium and Lanthanide Ions. *Nanoscale* **2018**, *10* (29), 14067–14072. https://doi.org/10.1039/c8nr03581d.

(227) Gan, W. et al. Broad-Band Sensitization in Cr3+-Er3+ Co-Doped Cs2AgInCl6 Double Perovskites with 1.5 Mm Near-Infrared Emission. *Chem. Mater.* **2023**, *35* (14), 5291–5299. https://doi.org/10.1021/acs.chemmater.3c00446.

(228) Cao, L. et al. Strong Self-Trapped Exciton Emission and Highly Efficient Near-Infrared Luminescence in Sb3+-Yb3+ Co-Doped Cs2AgInCl6 Double Perovskite. *Adv. Funct. Mater.* **2023**, *33* (13), 1–9. https://doi.org/10.1002/adfm.202212135.

(229) Jin, S. et al. Compact Ultrabroadband Light-Emitting Diodes Based on Lanthanide-Doped Lead-Free Double Perovskites. *Light Sci. Appl.* **2022**, *11* (1). https://doi.org/10.1038/s41377-022-00739-2.

(230) Cao, D. H. et al. 2D Homologous Perovskites as Light-Absorbing Materials for Solar Cell Applications. *J. Am. Chem. Soc.* **2015**, *137* (24), 7843–7850. https://doi.org/10.1021/jacs.5b03796.

(231) Xu, Z. et al. Exploring Lead-Free Hybrid Double Perovskite Crystals of (BA)2CsAgBiBr7 with Large Mobility-Lifetime Product toward X-Ray Detection. *Angew. Chemie - Int. Ed.* **2019**, *58* (44), 15757–15761. https://doi.org/10.1002/anie.201909815.

(232) Mao, L. et al. Chemical and Structural Diversity of Hybrid Layered Double Perovskite Halides. *J. Am. Chem. Soc.* **2019**, *141* (48), 19099–19109. https://doi.org/10.1021/jacs.9b09945.

(233) Vishnoi, P. et al. Why Are Double Perovskite Iodides so Rare? *J. Phys. Chem. C* **2021**, *125* (21), 11756–11764. https://doi.org/10.1021/acs.jpcc.1c02870.

(234) Yao, Y. et al. (C3H9NI)4AgBiI8: A Direct-Bandgap Layered Double Perovskite Based on a Short-Chain Spacer Cation for Light Absorption. *Chem. Commun.* **2020**, *56* (21), 3206–3209. https://doi.org/10.1039/c9cc07796k.

(235) Knight, A. J. et al. Halide Segregation in Mixed-Halide Perovskites: Influence of A-Site Cations. *ACS Energy Lett.* **2021**, *6* (2), 799–808. https://doi.org/10.1021/acsenergylett.0c02475.

(236) Rury, A. S. et al. Evidence of Defect-Induced Broadband Light Emission from 2D Ag-Bi Double Perovskites Grown at Liquid-Liquid Interfaces. *J. Chem. Phys.* **2023**, *158* (1). https://doi.org/10.1063/5.0134568.

(237) Stolterfoht, M. et al. How To Quantify the Efficiency Potential of Neat Perovskite Films: Perovskite Semiconductors with an Implied Efficiency Exceeding 28%. *Adv. Mater.* **2020**, *32* (17). https://doi.org/10.1002/adma.202000080.

(238) Cacovich, S. et al. Gold and Iodine Diffusion in Large Area Perovskite Solar Cells under Illumination. *Nanoscale* **2017**, *9* (14), 4700–4706. https://doi.org/10.1039/c7nr00784a.

(239) Kasparavicius, E. et al. Long-Term Stability of the Oxidized Hole-Transporting Materials Used in Perovskite Solar Cells. *Chem. - A Eur. J.* **2018**, *24* (39), 9910–9918. https://doi.org/10.1002/chem.201801441.

(240) Murray, A. T. et al. Modular Design of SPIRO-OMeTAD Analogues as Hole Transport Materials in Solar Cells. *Chem. Commun.* **2015**, *51* (43), 8935–8938. https://doi.org/10.1039/c5cc02129d.

(241) Hajikhanmirzaei, L. et al. A Cost-Device Efficiency Balanced Spiro Based Hole Transport Material for Perovskite Solar Cells. *J. Mater. Chem. C* **2020**, *8* (18), 6221–6227. https://doi.org/10.1039/d0tc00196a.

(242) Chang, N. L. et al. A Manufacturing Cost Estimation Method with Uncertainty Analysis and Its Application to Perovskite on Glass Photovoltaic Modules. *Prog. Photovoltaics Res. Appl.* **2017**, *25* (5), 390–405. https://doi.org/10.1002/pip.2871.

(243) Zhang, Z. et al. Big Data Driven Perovskite Solar Cell Stability Analysis. *Nat. Commun.* **2022**, *13* (1). https://doi.org/10.1038/s41467-022-35400-4.

(244) Gan, Y. et al. Advances in the Research of Carbon Electrodes for Perovskite Solar Cells. *Dalt. Trans.* **2023**, *52* (45), 16558–16577. https://doi.org/10.1039/d3dt03136e.

(245) Gao, Q. et al. Commercial Carbon Nanotube as Rear Contacts for Industrial P-Type Silicon Solar Cells with an Efficiency Exceeding 23%. *Carbon N. Y.* **2023**, *202* (P1), 432–437. https://doi.org/10.1016/j.carbon.2022.11.020.

(246) Bautista-López, J. A. et al. Recent Progress in Organic Waste Recycling Materials for Solar Cell Applications. *Environ. Sci. Pollut. Res.* **2023**, *30* (47), 103367–103389. https://doi.org/10.1007/s11356-023-29639-7.

(247) Bai, Y. et al. Interdigitated Back-Contacted Carbon Nanotube–Silicon Solar Cells. *Small Struct.* **2023**, *4* (8), 1–7. https://doi.org/10.1002/sstr.202200375.

(248) Romano, V. et al. Advances in Perovskites for Photovoltaic Applications in Space. *ACS Energy Lett.* **2022**, *7* (8), 2490–2514. https://doi.org/10.1021/acsenergylett.2c01099.

(249) Tu, Y. et al. Perovskite Solar Cells for Space Applications: Progress and Challenges. *Adv. Mater.* **2021**, *33* (21), 1–22. https://doi.org/10.1002/adma.202006545.

(250) Li, H.; Zhang, W. Perovskite Tandem Solar Cells: From Fundamentals to Commercial Deployment. *Chem. Rev.* **2020**, *120* (18), 9835–9950. https://doi.org/10.1021/acs.chemrev.9b00780.

(251) Jošt, M. et al. Monolithic Perovskite Tandem Solar Cells: A Review of the Present Status and Advanced Characterization Methods Toward 30% Efficiency. *Adv. Energy Mater.* **2020**, *10* (26). https://doi.org/10.1002/aenm.201904102.

(252) Lal, N. N. et al. Perovskite Tandem Solar Cells. *Adv. Energy Mater.* **2017**, *7* (18), 1–18. https://doi.org/10.1002/aenm.201602761.

(253) He, X. et al. 40 . 1 % Record Low-Light Solar-Cell Efficiency by Holistic Trap-Passivation Using Micrometer-Thick Perovskite Film. *Adv. Mater.* **2021**, *33* (27), 2100770. https://doi.org/10.1002/adma.202100770.

(254) Cheng, R. et al. Tailoring Triple-Anion Perovskite Material for Indoor Light Harvesting with Restrained Halide Segregation and Record High Efficiency Beyond 36 %. *Adv. Energy Mater.* **2019**, *9* (38), 190980. https://doi.org/10.1002/aenm.201901980.

(255) Dong, C. et al. Lycopene-Based Bionic Membrane for Stable Perovskite Photovoltaics. *Adv. Funct. Mater.* **2021**, *31* (25), 2011242. https://doi.org/10.1002/adfm.202011242.

(256) Li, M. et al. Interface Modification by Ionic Liquid : A Promising Candidate for Indoor Light Harvesting and Stability Improvement of Planar Perovskite Solar Cells. *Adv. Energy Mater.* **2018**, *8* (24), 1801509. https://doi.org/10.1002/aenm.201801509.

(257) Wang, M. et al. Low-Trap-Density CsPbX 3 Film for High-E Ffi Ciency Indoor Photovoltaics. *ACS Appl. Mater. Interfaces* **2022**, *14* (9), 11528–11537. https://doi.org/10.1021/acsami.1c25207.

(258) Mularso, K. T. et al. Recent Strategies for High-Performing Indoor Perovskite Photovoltaics. *Nanomaterials* **2023**, *13* (2). https://doi.org/10.3390/nano13020259.

(259) Wang, B. et al. Organic Dye/Cs2AgBiBr6Double Perovskite Heterojunction Solar Cells. *J. Am. Chem. Soc.* **2021**, *143* (36), 14877–14883. https://doi.org/10.1021/jacs.1c07200.

(260) Raj, A. et al. Investigating the Potential of Lead-Free Double Perovskite Cs2AgBiBr6 Material for Solar Cell Applications: A Theoretical Study. *Energy Res.* **2022**, *46* (10), 13801–13819. https://doi.org/10.1002/er.8099.

(261) Gao, Z. W. et al. Buried Interface Modification in Perovskite Solar Cells: A Materials Perspective. *Adv. Energy Mater.* **2022**, *12* (20), 1–20. https://doi.org/10.1002/aenm.202104030.

(262) Zhai, M. et al. Advancing Lead-Free Cs2AgBiBr6 Perovskite Solar Cells: Challenges and Strategies. *Sol. Energy* **2023**, *253* (December 2022), 563–583. https://doi.org/10.1016/j.solener.2023.02.027.

(263) Mehrabian, M. et al. Effects of Electron Transport Layer Type on the Performance of Pb-Free Cs2AgBiBr6 Double Perovskites: A SCAPS-1D Solar Simulator-Based Study. *Environ. Sci. Pollut. Res. Int.* **2023**, *30* (56), 118754–118763. https://doi.org/10.1007/s11356-023-30732-0.

(264) Shrivastav, N. et al. Optimizing the Performance of Cs2AgBiBr6 Based Solar Cell through Modification of Electron and Hole Transport Layers. *Mater. Today Commun.* **2023**, *36* (May), 106761. https://doi.org/10.1016/j.mtcomm.2023.106761.

(265) Chabri, I. et al. Cs2AgBiBr6-Based Perovskite Solar Cell: A Novel Combination of ITO/CdS/ Cs2AgBiBr6/ CuAlO2/Pt, with Inorganic Charge Transport Layers. *Optik (Stuttg).* **2023**, *274* (December 2022). https://doi.org/10.1016/j.ijleo.2023.170560.

(266) Zimmermann, E. et al. Characterization of Perovskite Solar Cells: Towards a Reliable Measurement Protocol. *APL Mater.* **2016**, *4* (9). https://doi.org/10.1063/1.4960759.

(267) Dunbar, R. B. et al. How Reliable Are Efficiency Measurements of Perovskite Solar Cells? The First Inter-Comparison, between Two Accredited and Eight Non-Accredited Laboratories. *J. Mater. Chem. A* **2017**, *5* (43), 22542–22558. https://doi.org/10.1039/c7ta05609e.

(268) Polyzoidis, C. et al. Indoor Perovskite Photovoltaics for the Internet of Things—Challenges and Opportunities toward Market Uptake. *Adv. Energy Mater.* **2021**, *11* (38), 1–44. https://doi.org/10.1002/aenm.202101854.